IMPROVEMENT OF THERMOELECTRIC PROPERTIES THROUGH MANIPULATION OF THEIR MICROSTRUCTURE: THE EFFECT OF GRAPHENE REINFORCEMENT

A Dissertation submitted in partial satisfaction of the requirements for the degree of

Doctor of Philosophy

in

Mechanical Engineering

Candidate

Sadeq Hooshmand Zaferani

Supervisors

Professor Reza Ghomashchi
School of Mechanical Engineering,
ARC Research Hub for Graphene Enabled Industry Transformation,
Institute for Photonics And Advanced Sensing,
University of Adelaide, AUSTRALIA

Professor Daryoosh Vashaee
Department of Electrical and Computer Engineering,
Department of Materials Science and Engineering,
North Carolina State University, United States

July 2021

DECLARATION OF AUTHORSHIP

Student declaration

I declare that the submitted thesis contains no experimental work that is not my own, except where an acknowledgment has been made and clearly refers to the work of others. According to the journals' policy, I have cited my own published papers for the current PhD work wherever I have used the contents, tables, and figures form the published articles. I give permission for my assessment work to be reproduced and submitted to other academic staff for the purposes of evaluation and to be copied, submitted and retained in a form suitable for electronic checking of plagiarism.

I certify that this work contains no material which has been accepted for the award of any other degree or diploma in my name, in any university or other tertiary institution and, to the best of my knowledge and belief, contains no material previously published or written by another person, except where due reference has been made in the text. In addition, I certify that no part of this work will, in the future, be used in a submission in my name, for any other degree or diploma in any university or other tertiary institution without the prior approval of the University of Adelaide and where applicable, any partner institution responsible for the joint-award of this degree. I acknowledge that copyright of published works contained within this thesis resides with the copyright holder(s) of those works. I also give permission for the digital version of my thesis to be made available on the web, via the University's digital research repository, the Library Search and also through web search engines, unless permission has been granted by the University to restrict access for a period of time. I acknowledge the support I have received for my research through the provision of an Australian Government Research Training Program Scholarship.

Sadeq Hooshmand Zaferani

Date: 16/03/2021

ABSTRACT

Environmental changes and extreme climate-related events are mainly attributed to greenhouse gas (GHG) emissions and are becoming a growing concern. The reported scientific evidence, highlighting such interrelationships, has convinced researchers to look for clean energy sources and improve operational efficiencies, and capture and convert the waste heat into electricity. Since almost two-thirds of energy is converted to heat and wasted, the recovery of waste heat will boost savings in fossil fuel consumption as an abundant source of energy. In this regard, thermoelectric (TE) compounds can be employed to convert the waste heat into electricity, thereby increasing the efficiencies of energy generating operations. Such an approach is even applicable to renewable energy (RE) sources. However, the applications of the thermoelectric converters necessitate the development of advanced, efficient thermoelectric materials with a high level of thermomechanical stability. This doctoral research project aims to develop and modify thermoelectric compounds by manipulating their microstructure and improving their mechanical properties by reinforcement with graphene nanoplates (GNPs). To the best of our knowledge, there is no specific report in the open literature to determine the reinforcing effects of graphene nanofillers (e.g., GNPs) on thermoelectric products. There is a lack of a comprehensive assessment in the scientific and industrial communities in evaluating the advantages and drawbacks of GNPs, as the reinforcing agent on TE compounds. In this dissertation, to assess the performance of the GNPs, three potential thermoelectric compounds, namely MnTe, CoVSn, and $CuSbTe_2$, have been investigated. These designated compounds address the requirements for covering an extended working temperature range from low to high, examining various crystal structures (e.g., Chalcogenides and half-Heusler), and developing environmentally-friendly (i.e., lead-free) TE products. The bulk samples with the addition of small quantities of GNPs (0.25, 0.5, 0.75, and 1 wt. %) were synthesized using powder metallurgy and

fabricated by spark plasma sintering (SPS). The thermoelectric factors, magnetic behavior, microstructure, and mechanical properties of the samples were evaluated and analyzed. Grain growth inhibition is the main consequence of the reinforcing GNPs, which results in an enhancement in the thermoelectric and mechanical characteristics of the nominated TE products. Scattering of electrical carriers and phonons due to the precipitation of the reinforcing GNPs in the matrix, thus providing a higher density of microstructural boundaries, improves the thermoelectric properties. Furthermore, microstructural manipulation, such as crystal/particle size reduction caused by the segregation of the reinforcing GNPs as a second phase in the matrix, enhances the mechanical characteristics of TE compounds, for example, the fracture toughness (K_{IC}) and hardness.

ACKNOWLEDGEMENTS

This work would not be possible without the academic support I have been provided. First and foremost, thanks to my supervisors, Professor Reza Ghomashchi and Professor Daryoosh Vashaee, for the deep care they have given to this project.

Many thanks to Professor Dusan Losic (Director of the ARC Graphene Research Hub) and Dr Jacqui McRae (Manager, ARC Graphene Research Hub) for their support and guidance when presenting the results to the ARC Graphene Hub.

I am also thankful that this work has been supported by an Australian Government Research Training Program Scholarship and The ARC Graphene Enabled Industry Transformation Hub at the University of Adelaide. Also, this project is partially based upon work supported by the National Science Foundation (NSF).

Without the aid of excellent academic staff, completing this project would have been infinitely more difficult. Special thanks also go to Professor Anthony Zander (Head of the School of Mechanical Engineering), Professor Andrei Kotousov (Chair of HDR assessment at the School of Mechanical Engineering), Dr Lei Chen (Postgraduate coordinator at the School of Mechanical Engineering), and Dr.Alison-Jane Hunter (Technical English Editor at the School of Mechanical Engineering).

Special thanks to Professor Veena Misra (Director of the ASSIST Centre) for her support throughout my research at the North Carolina State University, ASSIST center.

Thanks to all the Department of Mechanical Engineering (especially Paula Billington and Terry Utting) at the University of Adelaide, Department of Electrical and Computer Engineering, and ASSIST Centre (Dr Rajinder Khosla, C.J. Gosnell, and Candice Byrd) at the North Carolina State University.

I would like to express my sincere gratitude to Professor Kazem Abhary and Professor Tahereh Ziaian, who supported and encouraged me during this project.

In the end, special thanks to my wife, my family, and friends who provided me invaluable support and care throughout this project.

LIST OF PUBLICATIONS AND CONFERENCE PRESENTATIONS

1) Sadeq Hooshmand Zaferani, Reza Ghomashchi, Daryoosh Vashaee, Strategies for engineering phonon transport in Heusler thermoelectric Compounds, Renewable and Sustainable Energy Reviews 112 (2019) 158‑169.
2) Sadeq Hooshmand Zaferani, Reza Ghomashchi, Daryoosh Vashaee, Thermoelectric, Magnetic, and Mechanical Characteristics of Antiferromagnetic Manganese Telluride Reinforced with Graphene Nanoplates, Adv. Eng. Mater. 2020, 2000816.
3) Sadeq Hooshmand Zaferani, Alireza Darebaghi, Soon-Jik Hong, Daryoosh Vashaee, Reza Ghomashchi, Energies, 2020, 13, 1459; doi:10.3390/en13061459.
4) Sadeq Hooshmand Zaferani, Reza Ghomashchi, Daryoosh Vashaee, Assessment of Thermoelectric, Mechanical and Microstructural Reinforcement Properties of Graphene-mixed Heterostructures, ACS applied energy materials, https://dx.doi.org/10.1021/acsaem.1c00015.
5) Doping Engineering Approaches to Improve Power Factor of Thermoelectric Products, Under review.
6) Sadeq Hooshmand Zaferani, R.Ghomashchi, D.Vashaee, Thermoelectric Properties of P-type MnTe/Graphene Nanocomposites, Advanced Nano and Energy Materials, The University of Western Australia, Perth, Australia, 4-6 December (2019)- Oral presentation.
7) Sadeq Hooshmand Zaferani, R.Ghomashchi, D.Vashaee, S.Hong, Design and Synthesis of Metal-Semiconductor Heterostructured $CoV_{5.6}Sn_{1.6}$, Advanced Nano and Energy Materials, The University of Western Australia, Perth, Australia, 4-6 December (2019)-Poster presentation.

8) Sadeq Hooshmand Zaferani, Daryoosh Vashaee, Soon-Jik Hong, Reza Ghomashchi, Assessment of the Graphene-Based Thermoelectric Nanocomposites, The ARC Research Hub for Graphene Enabled Industry Transformation Workshop, Monash University, Melbourne, (2020)- Oral presentation.

CONTENTS

LIST OF TABLES

LIST OF FIGURES

ABBREVIATIONS

GHGs: Greenhouse gases

RE: Renewable energy

TE: Thermoelectric

TEG: Thermoelectric generator

STEG: Solar Thermoelectric generator

GF: Graphene filler

HH: half-Huesler

TA: Transverse acoustic

LA: Longitudinal acoustic

TEM: Transmission Electron Microscopy

SEM: Scanning Electron Microscopy

FE-SEM: Field emission-SEM

AFM: Atomic Force Microscopy

DSC: Differential Scanning Calorimetry

XRD: X-ray Diffraction

GNF: Graphene nanofiller

GNS: Graphene nanosheet

GNP: Graphene nanoplate

TEC: Thermal expansion coefficient

ΔT: Temperature gradient

SPS: Spark plasma sintering

FEA: Finite element analysis

SYMBOLS

$\boldsymbol{zT}$: Figure of merit of thermoelectric compounds

$\boldsymbol{ZT_M}$: Figure of merit at the average temperature (T_M, between hot and cold junctions) of thermemoelectric generator

$\boldsymbol{S}$: Seebeck coefficient

$\boldsymbol{\sigma}$: Electrical conductivity

$\boldsymbol{\kappa_t}$: Total thermal conductivity

$\boldsymbol{\kappa_l}$: Lattice thermal conductivity

$\boldsymbol{\kappa_e}$: Electronic thermal conductivity

$\boldsymbol{\eta_{max}}$: Maximum efficieny

$\boldsymbol{\omega}$: Frequency

$\boldsymbol{a}$: Lattice constant

$\boldsymbol{e}$: Electron charge

$\boldsymbol{q}$: Wavelength

$\boldsymbol{\beta}$: Constant

$\boldsymbol{T_H}$: Hot surface temperature

$\boldsymbol{T_C}$: Cold surface temperature

$\boldsymbol{T_M}$: Average temperature

$\boldsymbol{\sigma_c}$: Strength of composite

$\boldsymbol{\sigma_m}$: Strength of matrix

$\boldsymbol{G}$: Shear modulus

$\Delta\boldsymbol{C}$: Difference in the TECs

$\boldsymbol{\vartheta}$: Poisson's ratio

$\boldsymbol{E}$: Young’s modulus

$\boldsymbol{\gamma}$: Surface energy

$\boldsymbol{n}$: Carrier concentration

$\boldsymbol{Y}$: Yield strengt

Nothing in life is to be feared, it is only to be understood. Now is the time to understand more, so that we may fear less.

—MARIE CURIE (1867 – 1934)

CHAPTER ONE

INTRODUCTION

Energy crisis and thermoelectricity

Global warming and the resulting climate change can be traced back to human activities, industrial processes, and greenhouse gases (GHGs) emissions [1, 2]. For example, a makeover [3] clarifies that the largest sector for greenhouse gases emission in Australia during the year of 2015 was electricity generation (Figure 1).

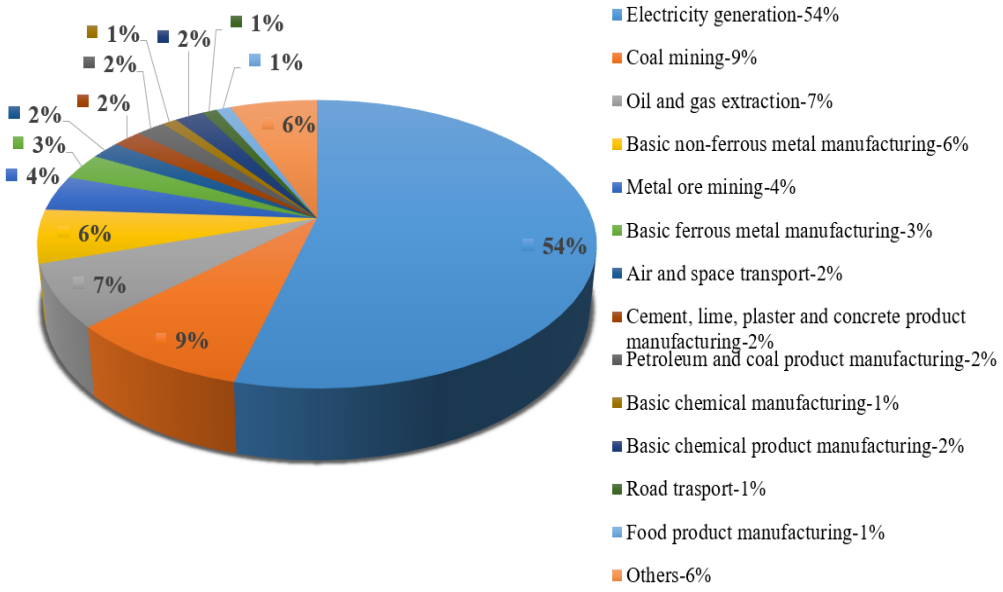

Figure 1: Australia's top greenhouse gases emitters in 2015 by sector [3].

In this field, according to a study conducted by the Lawrence Livermore National Laboratory, in the year 2018, the majority of the rejected energy (waste heat) throughout the total energy production in the United States belongs to electricity generation (38.2%), in comparison with the other sectors, including transportation (28.3%), industrial (26.3%), residential (11.9%), and commercial (9.45%), as illustrated in Figure 2.

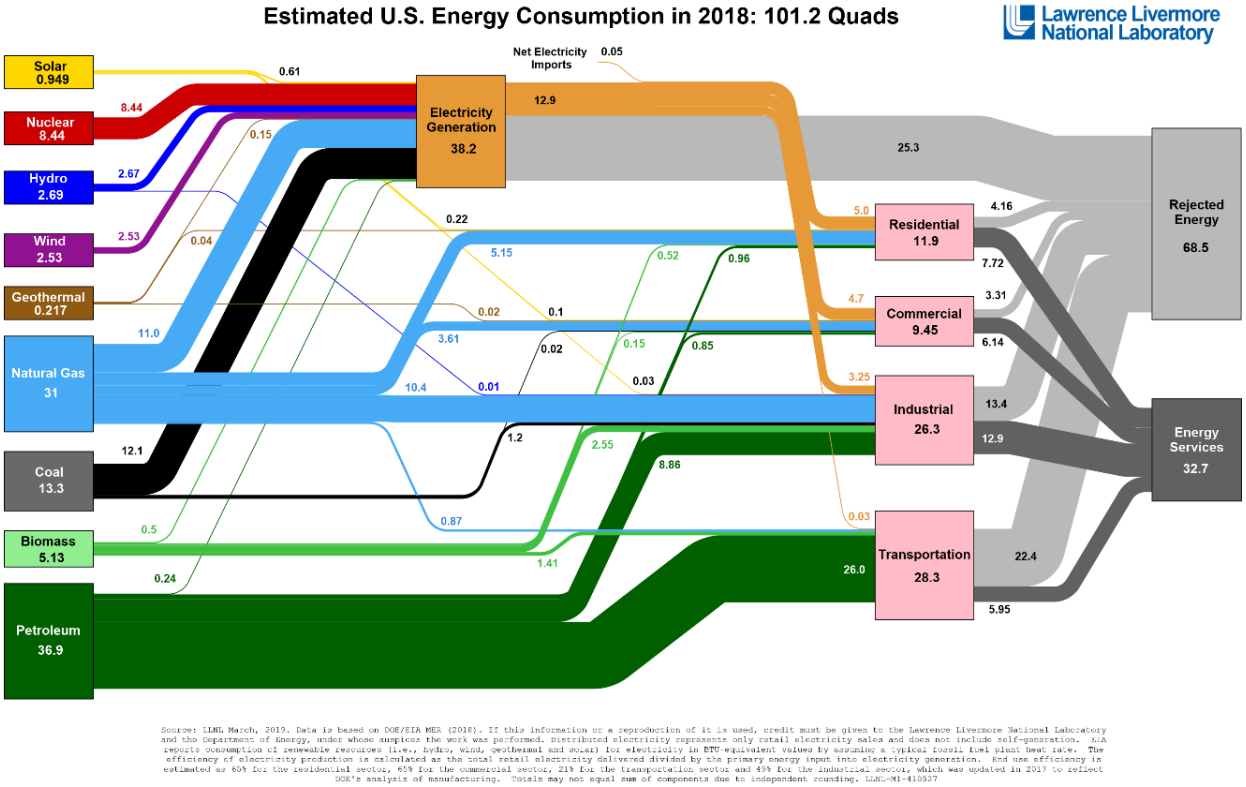

Figure 2: Energy flow diagram of US energy production and consumption. Source: Lawrence Livermore National Laboratory, March 2019. Data is based on DOE/EIA MER (2018). *https://flowcharts.llnl.gov/content/assets/docs/2019_United-States_Energy.pdf*

It may take many years until renewable energies reach a position where they can fully replace fossil fuels. Consequently, other intermediate technologies are required to reduce carbon output (e.g., CO_x) and increase the efficiency of the existing energy-generating technologies during

this transition period. In this regard, Figure 3 illustrates the electricity generation from the fuel energies (Figure 3a) and renewable energy sources (Figure 3b) in the US, which are projected up to 2050. It is anticipated that a greater role for renewable energy sources will be found to satisfy future energy demand, as clearly demonstrated in Figure 4.

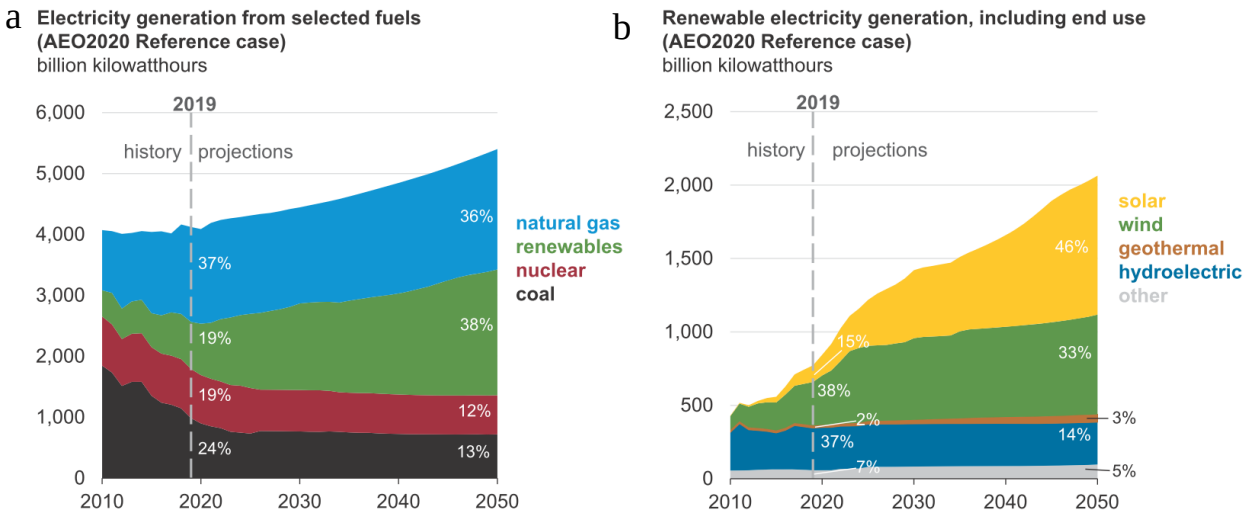

Figure 3: Electricity generation from selected energy resources, a) fuel energies and b) clean energies [4].

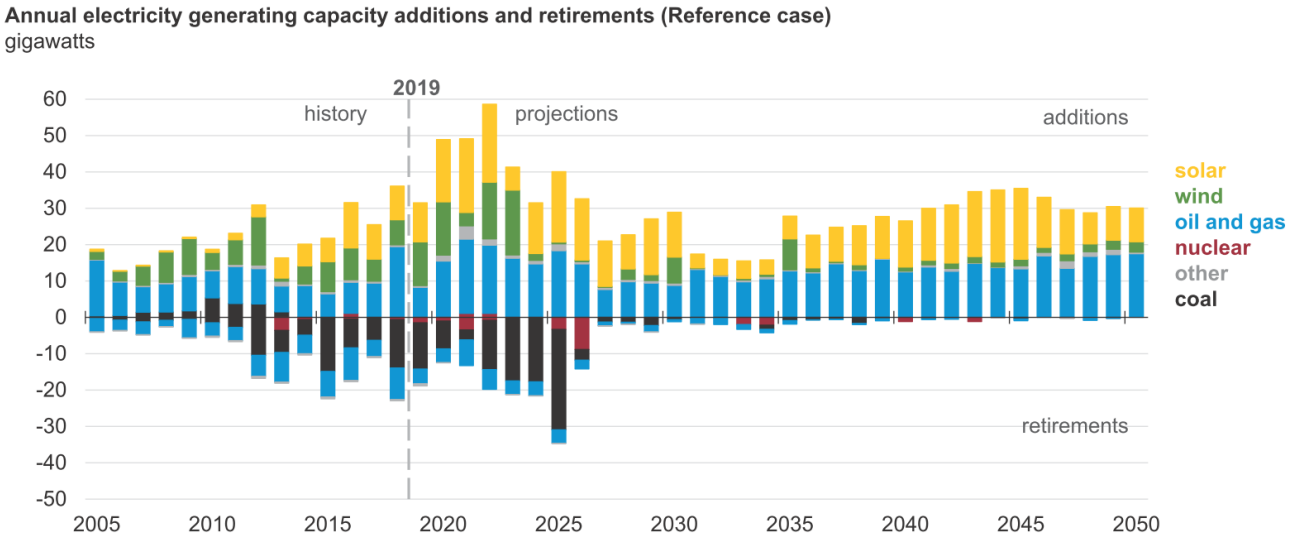

Figure 4: Application of renewable energies in the future [4].

Apparently, the forecast in Figure 4 is based on the trend to date on rapid deployment of clean energy technologies, which is encouraging. In this approach, Figure 5 demonstrates an estimate based on the available energy sources. As depicted in Figure 5, the demand for polluting energies will be replaced by renewable energy types.

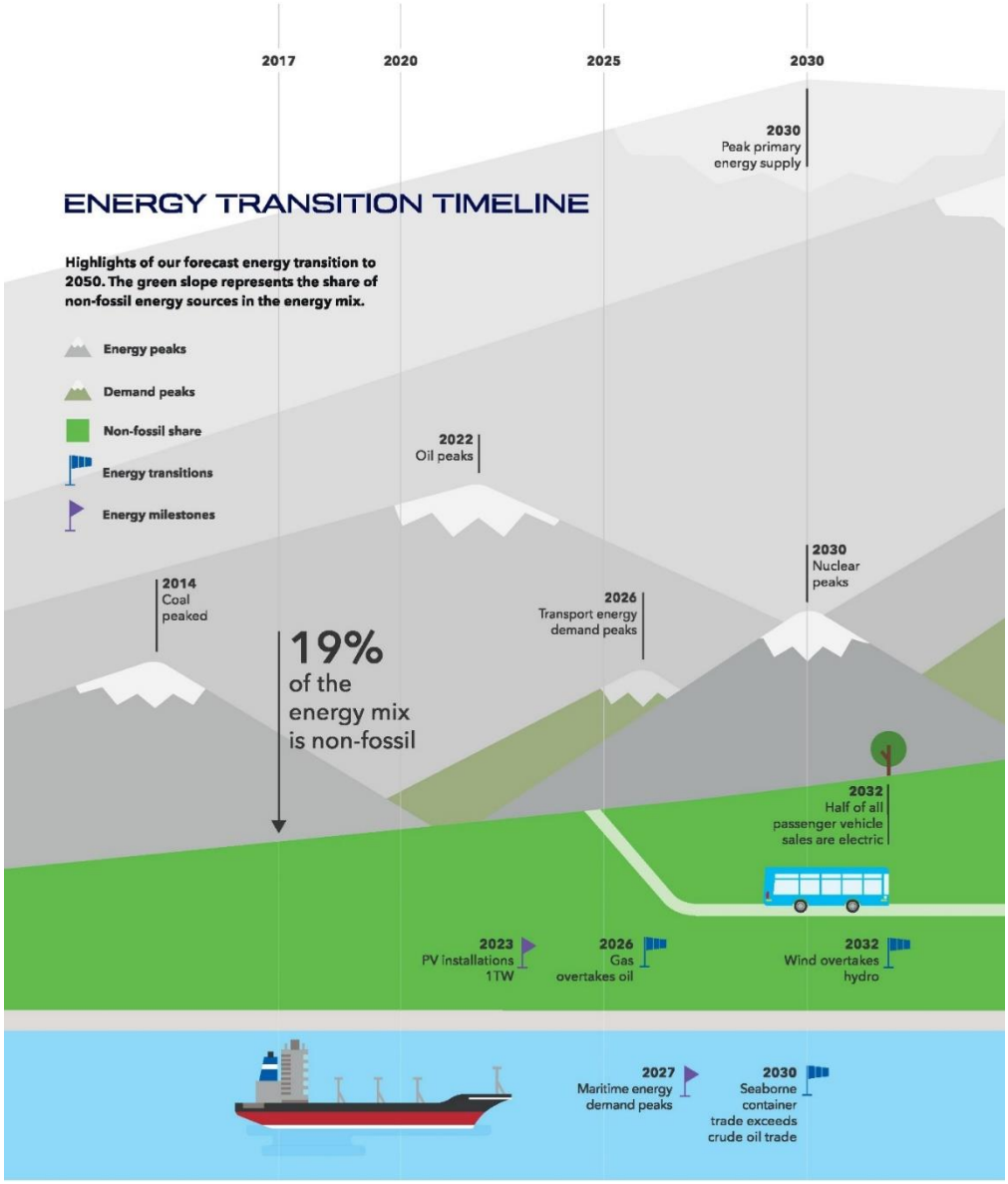

Continued

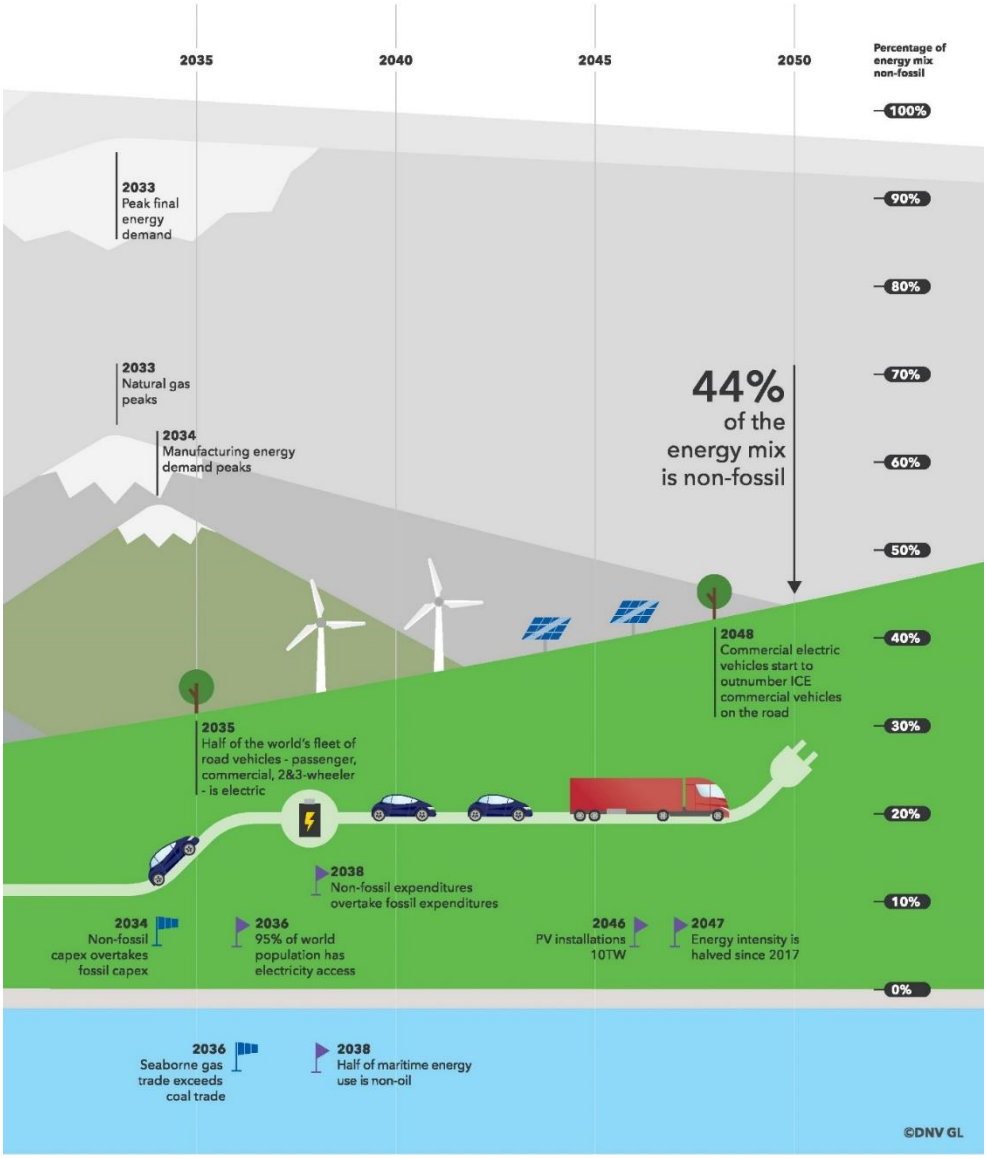

Figure 5: Energy transition timeline. Source: DNV GL Energy Transition Outlook 2019, A Global and Regional Forecast to 2050.

https://www.dnv.com/publications/energy-transition-outlook-2019-162874

Consequently, this growth in the renewable energy industry will impact the projected CO_2 immersion in the electric power sector, as exhibited in Figure 6. As shown in this figure, the average CO_2 emissions decreases with time.

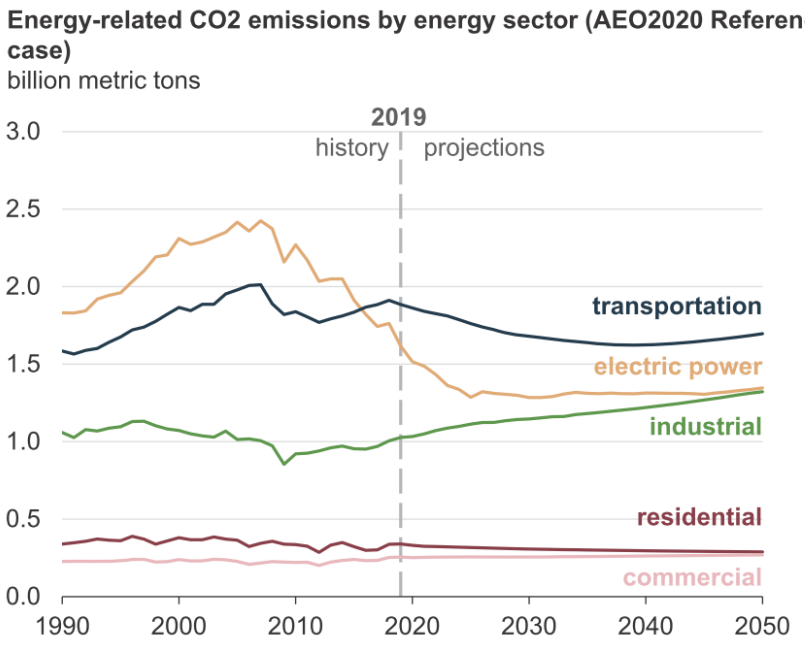

Figure 6: Energy-related CO_2 emissions by energy sector [4].

In this field, energy harvesting from the environment by reliable sources has manifested itself as a worldwide concern. Moreover, due to the low-performance efficiency of industrial processes, the majority of energy is converted into heat, especially in combustion engines, which use fossil fuels in their operations [5, 6]. Therefore, if the conversion of useful energy to waste heat is reduced through more efficient processes, or alternatively the waste heat is converted into more useful energy like electricity, the environmental impact of energy production will be mitigated.

One solution to enabling the capture of waste heat and converting it into electricity is utilizing solid-state energy convertors, such as thermoelectric generators (TEGs). In line with this encouraging trend, the application of thermoelectric generators is considered as the primary potential candidate to capture waste heat, for example in automobile exhaust recovery systems, see Figure 7 [6-8], and to harvest the heating energy from current renewable energy sources (e.g., concentrated solar heat exchangers – shown in Figure 8) [9].

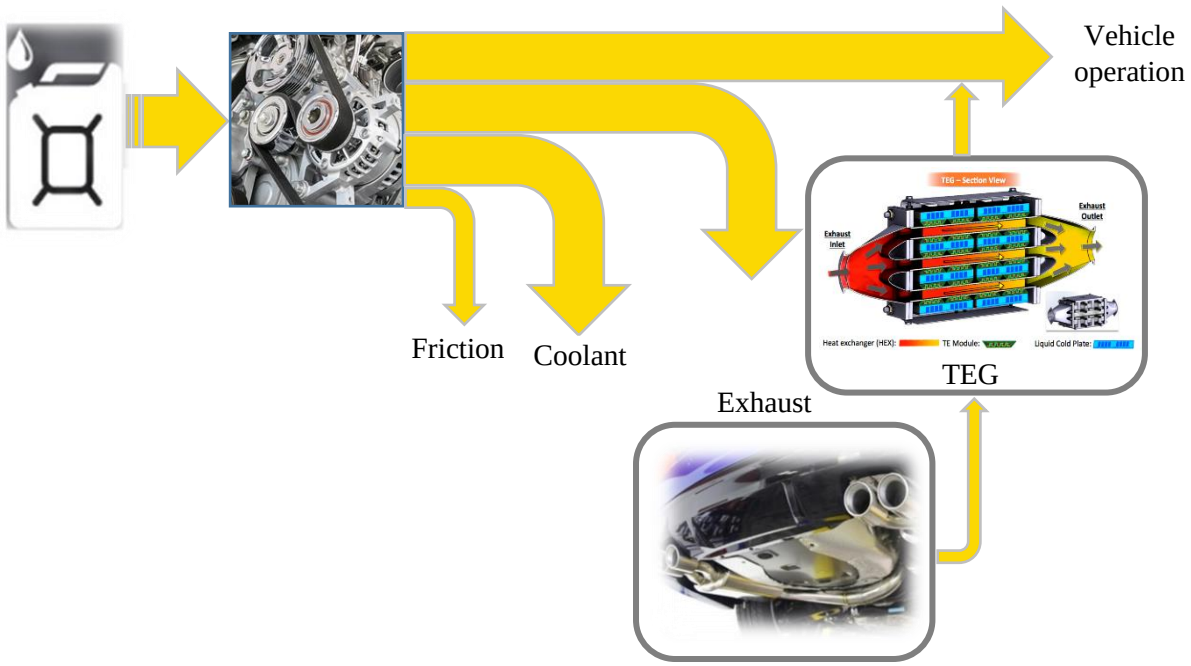

Figure 7: Application of the TEGs in automobile systems. Adapted from ref. [6-8] with permission.

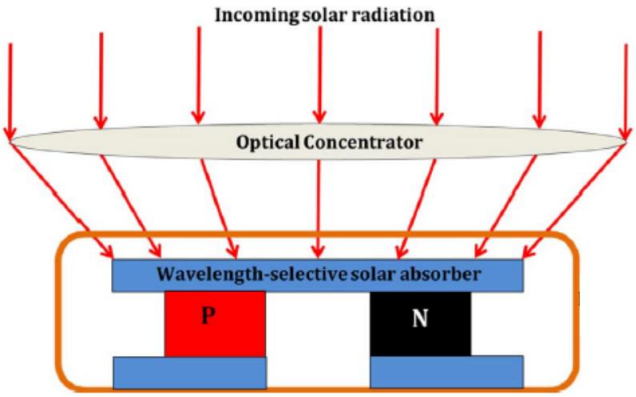

Figure 8: Solar TEG (STEG) for electric generation. Reused from ref. [9] with permission.

As presented in Figure 9, the TEG structure comprises several segments, but the central parts are p and n-type semiconductor junctions. The interaction of the p-type semiconductors with an excess concentration of holes (positive carriers) against the n-type semiconductors with a greater level of electrons (negative carriers) under a temperature gradient (∇T) can produce an electric current [10].

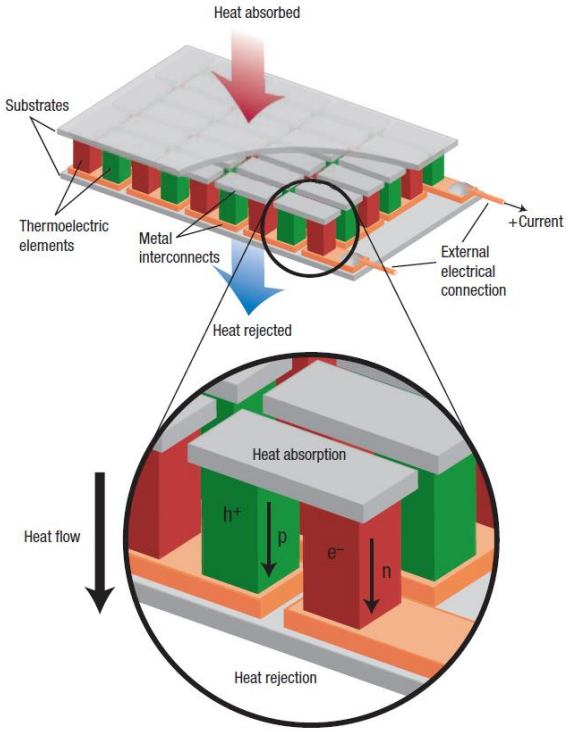

Figure 9: Thermoelectric generator (TEG) structures. Reused from ref. [10] with permission.

The efficiency of thermoelectric generators is very much dependent on the conversion efficiency of the constituent thermoelectric (TE) compounds. Therefore, the introduction of advanced thermoelectric materials is crucial in increasing the waste heat-electricity conversion rate. This is the central theme of the current project; to explore and improve advanced thermoelectric products.

THESIS OUTLINE

CHAPTER ONE explains the concepts of the energy crisis and thermoelectricity.

CHAPTER TWO describes a history of thermoelectricity, thermoelectric products, transition metal chalcogenides, Heusler compounds, graphene nanoplates (GNPs), and their applications.

CHAPTER THREE presents the project aims, objectives, and justifies the selection of thermoelectric compounds.

CHAPTER FOUR focuses on experimental procedures for sintering of composites reinforced with graphene nanoplates (GNPs), and their corresponding tests and experiments.

CHAPTER FIVE analyses thermodynamic stability, magnetic, thermoelectric, and mechanical properties of the MnTe compound, and its GNPs - reinforced products.

CHAPTER SIX examines thermodynamic stability, thermoelectric and mechanical characteristics of CoVSn composition, and its GNPs - reinforced products.

CHAPTER SEVEN discusses thermoelectric and mechanical features of $CuSbTe_2$ composition, and its GNPs - reinforced products.

CHAPTER EIGHT summarizes the conclusion of the studied products, implications for industry, future works, gaps in knowledge, and research directions.

If you want to find the secrets of the universe, think in terms of energy, frequency and vibration.

— NIKOLA TESLA (1856 -1943)

CHAPTER TWO

LITERATURE REVIEW

2.1 History of thermoelectricity

The concept of thermoelectricity (TE) as the direct conversion of the temperature gradient (∇T) to electricity was instigated by the German-Estonian physicist, Thomas Johann Seebeck, in the years between 1821 and 1831 [11, 12]. The Seebeck coefficient (S, V/K) was estimated based on the generated voltage (ΔV) against an imposed temperature difference (ΔT) [7] – Equation 1,

$$S = -\frac{\Delta V}{\Delta T} \qquad (1).$$

Further contributions in this field were reported by Gustav Magnus, who declared the Seebeck voltage is not dependent to the temperature distribution along the intermediate metals connecting the p-n junctions [13]. Later on, the Peltier effect was introduced to show that the heating or cooling are generated by passing an electric current through two dissimilar materials [11, 12]. Furthermore, William Thomson defined the relationship between the Seebeck and Peltier effects [12], and then Edmund Altenkirch calculated the maximum efficiency of the thermoelectric generators [11]. The modern theory of thermoelectricity in materials, however, is due to Abram Fedorovich Ioffe [11], who introduced a dimensionless factor, named a "figure of merit (zT)". It is a metric for evaluating the thermoelectric behaviour (performance) of thermoelectric compounds (materials);

$$zT = \frac{S^2\sigma}{k_e + k_l}T \qquad (2),$$

where S is the Seebeck coefficient (μVK^{-1}), σ is the electrical conductivity ($\Omega^{-1}m^{-1}$), T is temperature (K), and κ_e and κ_l are the electronic, and lattice thermal conductivities ($Wm^{-1}K^{-1}$), respectively [14]. The following chart summarizes the historical trend in thermoelectric development.

1821

Seebeck discovered that a circuit made from two dissimilar materials produces a voltage when their junctions are at different temperatures.

1834

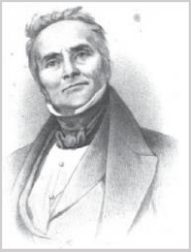

Peltier discovered that passing an electric current through two dissimilar materials produces heating or cooling at their junction. This is known as the "Peltier effect".

1854

William Thomson, also known as Lord Kelvin, found that the Seebeck and Peltier effects are related, indicating that any thermoelectric material can be used to either generate power in a temperature gradient or pump heat with an applied current.

1909-1911

$$zT = \frac{S^2\sigma}{k}T$$

Altenkirch correctly derived the maximum efficiency of a thermoelectric generator (1909) and performance of a cooler (1911), which later developed into the 'thermoelectric figure of merit', zT.

1928

Ioffe developed the modern theory of semiconductor physics in order to describe thermoelectric energy conversion.

1930

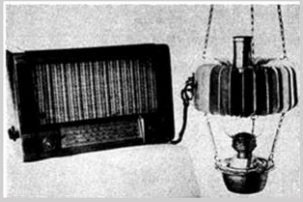

The first radio was powered by thermoelectrics and publicized.

1947

Maria Telkes constructed the first thermoelectric power generator with an efficiency of 5%.

@https://www.britannica.com/biography/Maria-Telkes

1954

H. Julian Goldsmid cooled a surface to 0° C using a thermoelectric Peltier cooler based on Bismuth telluride (Bi_2Te_3).

1959

Westinghouse unveiled a full-size home refrigerator based on Bismuth Telluride (Bi_2Te_3) Peltier thermoelectrics.

1959

US President Dwight D. Eisenhower unveiled the first Radioactive Thermoelectric Generator (RTG). "SNAP III," launched two years later in the first RTG-equipped spacecraft, Transit 4A, to orbit earth as a navigational satellite.
.

1968

SNAP-19 became the first radioisotope thermoelectric generator to be flown on a NASA spacecraft after the simplicity and reliability of thermoelectrics proved to be the most viable way to generate power remotely.

1970

The first cardiac pacemaker powered by a miniature radioisotope thermoelectric generator, made by Medtronic.

1975

A group of entrepreneurs acquired Lead Telluride (PbTe) thermoelectric technology to produce remote terrestrial power generation products.

1977

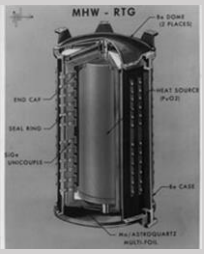

NASA launched Voyagers 1 and 2 powered by MHW-RTG3, a Silicon Germanium (SiGe) thermoelectric generator.

1993

Hicks and Dresselhaus published a theory paper indicating that nanotechnology may offer significant advances in the efficiency of thermoelectric materials, ushering in the modern era of thermoelectrics.

1995

John Fairbanks at the US Department of Energy began a program to develop thermoelectric generators for automotive engines after Porsche did a prototype study using Iron Silicide thermoelectric materials.

Recent decades: 21st century.

Interest in thermoelectricity has continued in recent years and resulted in the development of novel ideas. The research has focused on engineering the microstructures to enhance zT for both bulk and flexible thermoelectric products.

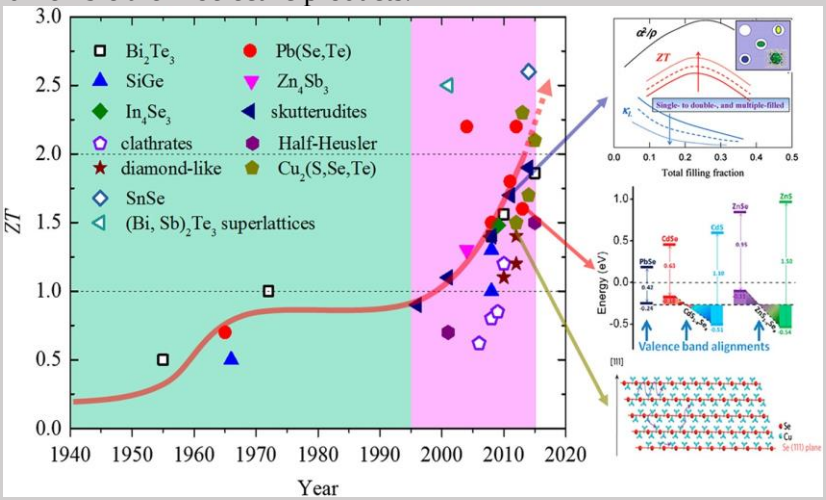

A- Growth trend of zT values for TE materials.

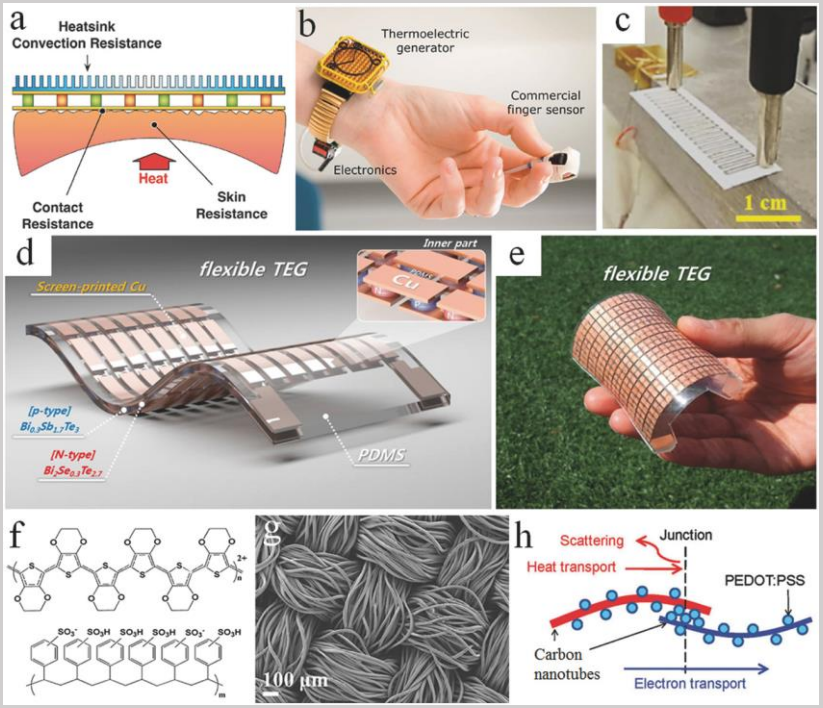

B- a) Schematic of the working principle of wearable TEG, b) An example of a TEG-powered wearable device, c) Paper-based TEG. Reproduced with permission, d) Schematic of a flexible TEG assembled using inorganic modules and e) a photo of the flexible TEG product, f) Chemical structure of poly (3,4-ethylenedioxythiophene):poly(styrenesulfonate) (PEDOT:PSS) and g) SEM image of thermoelectrical polymer coated polyester fabric textile, h) Schematic of carbon nanotube–PEDOT:PSS–carbon nanotube TE junctions.

Figure 10: Historical trends in thermoelectric development [15-17], insets A and B were reused from ref. [18, 19] with permission.

The importance of zT is evident when the maximum efficiency (η_{max}) of the thermoelectric (TE) generators (p and n junction) is calculated as;

$$\eta_{max} = \frac{T_H - T_C}{T_H} \times \frac{\sqrt{1+ZT_M}-1}{\sqrt{1+ZT_M}+\frac{T_C}{T_H}} \qquad (3),$$

where T_H and T_C are the temperatures of the hot and cold surfaces, respectively, and ZT_M is the figure of merit at the average temperature (T_M) of the hot and cold junctions [20].

As evaluated in Equation 3, a larger thermal gradient (ΔT) can increase the TE efficiency. However, it can provide thermal stresses that may compromise the mechanical integrity of the TE compounds. Therefore, in addition to the appropriate thermoelectric characteristics, the TE materials should have thermal and mechanical stabilities to be able to function under harsh conditions.

Significant efforts by the TE community over the last few decades, as summarized in Figure 11, have considered various techniques to improve thermoelectric properties, based on modifying S, σ, and κ [21-25] in terms of materials selection [26-28], manufacturing processes like sintering method selection [29] and nanostructuring [30-32], band engineering [33-39], magnetic interaction [40-42], and lowering the total thermal conductivity ($\kappa_t = \kappa_e + \kappa_l$) [30, 43-47]. It is noteworthy that the mechanisms discussed in Figure 11 may not be applicable to all thermoelectric compounds. Since the requirement for every material maybe different. At the first stage, it is necessary to identify the TE parameters needing improvement. To enhance the power factor ($S^2\sigma$), the electronic properties can be changed by modifying the band structures, such as by reducing the dimensions, modulation doping, employing magnetic dopants, band convergence, and the resonance level. These mechanisms are described in detail in further sections (Section 2.3). Materials selection and

sintering methods are two important factors in developing efficient TE compounds. Since each crystal structure has its own electronic and thermal properties, the proper selection of TE compounds depends on the target application (i.e., target temperature). Reduction in lattice thermal conductivity has been considered as an efficient method to boost the performance of TE materials. This strategy can be achieved either through the sintering process, an example would be recrytallisation via microwave sintering, or doping the compounds with atoms owning different atomic masses and sizes. The methods to reduce thermal conductivity are explained in Section 2.4.

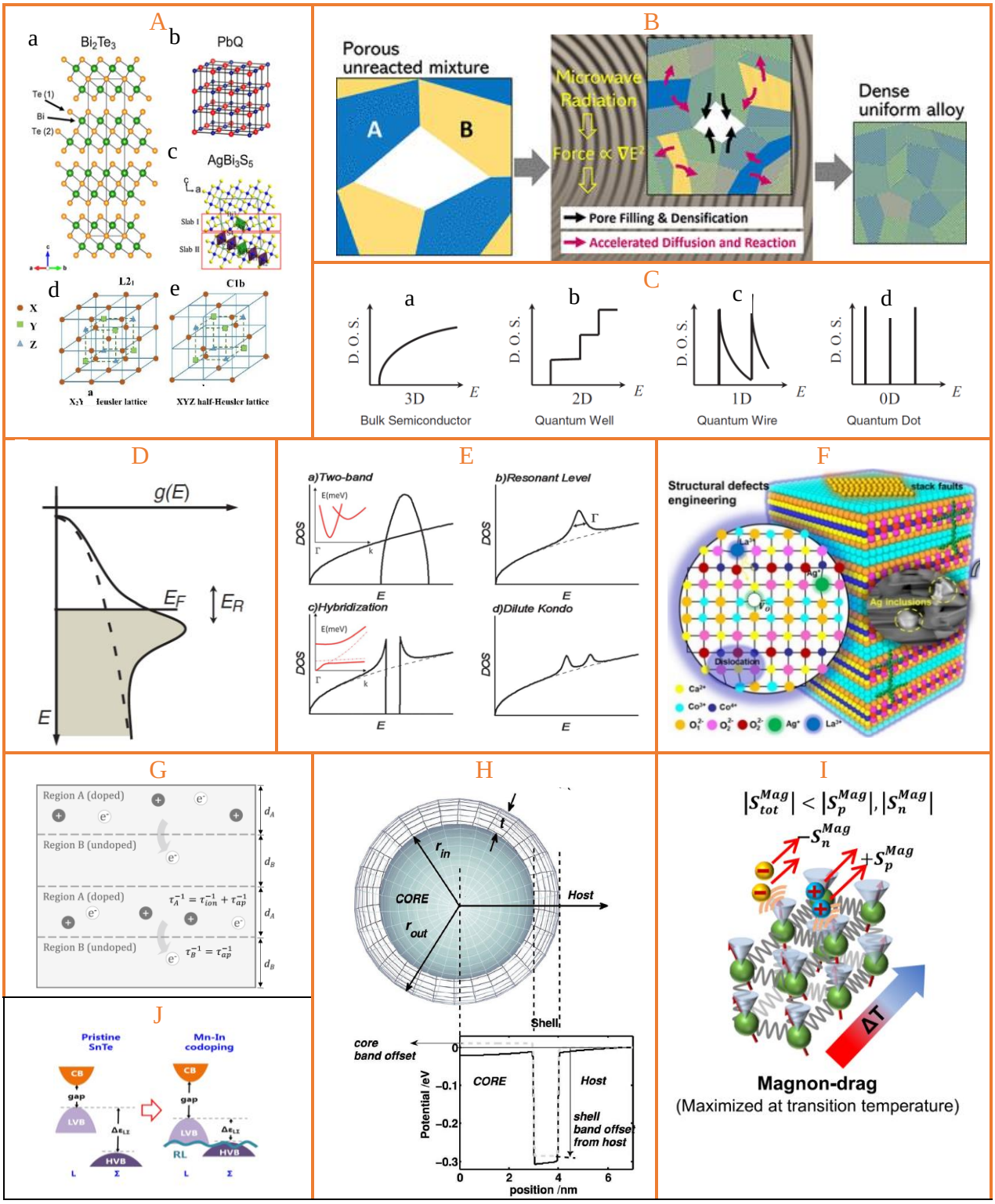
A
a
Bi2Te3
b
PbQ
Te (1)
Bi
Te (2)
c
AgBi3S5
Slab I
Slab II
d
L21
e
C1b
X
Y
Z
X2Y Heusler lattice
XYZ half-Heusler lattice
B
Porous unreacted mixture
A
B
Microwave Radiation
Force ∝ ∇E²
Pore Filling & Densification
Accelerated Diffusion and Reaction
Dense uniform alloy
C
a
b
c
d
D. O. S.
E
3D
2D
1D
0D
Bulk Semiconductor
Quantum Well
Quantum Wire
Quantum Dot
D
g(E)
EF
ER
E
E
a)Two-band
b)Resonant Level
c)Hybridization
d)Dilute Kondo
E(meV)
DOS
Γ
k
F
Structural defects engineering
stack faults
Ag inclusions
Dislocation
Ca2+
Co3+ Co4+
O1 2- O2 2- O2 2-
Ag+
La3+
G
Region A (doped)
Region B (undoped)
Region A (doped)
Region B (undoped)
dA
dB
dA
dB
H
rin
rout
t
CORE
Host
Shell
core band offset
Potential /eV
CORE
Host
shell band offset from host
position /nm
I
Magnon-drag
(Maximized at transition temperature)
ΔT
J
Pristine SnTe
Mn-In codoping
CB
gap
LVB
HVB
RL
L
Σ

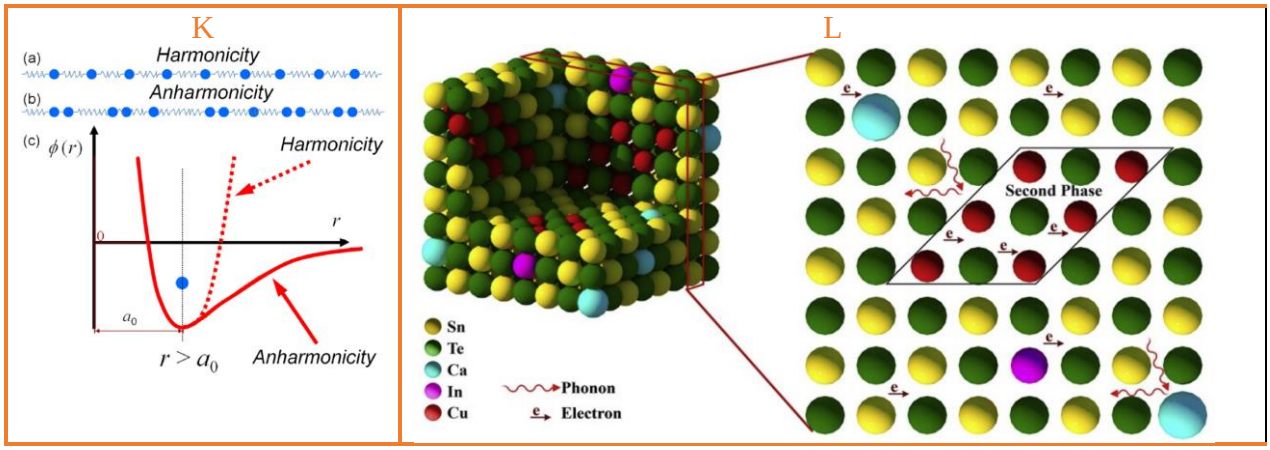

Figure 11: A) Material selection and crystal examples, a) Bi_2Te_3 adopts a layered tetradymite structure, b) PbQ (Q = S, Se, Te) with cubic rocksalt structure, c) $AgBi_3S_5$ with the complex pavonite-type structure, d) full-Heusler crystal, and e) half-Heusler crystal structure, used from refs. [26, 45] with permission, B) Enhancement of diffusion, densification and solid-state reactions in dielectric materials due to interfacial interaction of microwave radiation, used from ref. [29] with permission, C) Electronic density of states for a) a bulk 3D crystalline semiconductor, b) a 2D quantum well, c) a 1D nanowire or nanotube, and d) a 0D quantum dot; enhancing the density of electronic states (DOS) may be useful for enhancing thermoelectric performance, used from ref. [30] with permission, D) Schematic representation of the density of electron states of the valence band of pure PbTe (dashed line) versus Tl-PbTe (solid line) in which a Tl-related level increases the density of states, adopted from ref. [35] with permission, E) Mechanisms used to manipulate the density of states in solids and to increase the thermopower used from ref. [36] with permission, F) Structural defect engineering to boosting the thermoelectric performance of calcium cobaltite composites, used from ref. [48] with permission, G) Model periodic structure consisting of a) doped and b) undoped regions of the same material. Electrons transfer from region A to B, and the transport direction is parallel to the layers, used from ref. [49] with permission, H) a) A cartoon of the core – shell nanoparticle. The potential profile of the nanoparticle is plotted as a function of position in the radial direction. The band offset profile across the core – shell nanoparticle is plotted

with the dashed line and the screened bent potential with the solid line, used from ref. [50] with permission, I) Schematic illustration of magnon-drag, used from ref. [40] with permission, J) Schematic band structure for pristine and Mn–In codoped SnTe, describing synergistic band engineering, used from ref. [51] with permission, K) Schematic illustrations of a) harmonicity (balanced phonon transport), b) anharmonicity (imbalanced phonon transport) c) harmonicity: if an atom is pulled from its equilibrium position during the passage of a phonon, the force that the atom is subjected to is proportional to its displacement, and the proportionality constant of this relationship is called the spring constant, Anharmonicity: the spring constant does not remain constant with atom displacements, which has important consequences when two phonons run into each other, used from ref. [52] with permission, L) Schematic diagram of endotaxial nanostructuring in SnTe systems, used from ref. [53] with permission, M) Dominant modes of phonon scattering versus temperature, used from ref. [45] with permission.

2.2 Thermoelectric materials

There is a range of the thermoelectric materials classified into different groups of clathrates [54-56], skutterudites [57-60], chalcogenides [61-63], and half-Heusler [63-71]. The majority of studies are applied to microstructural manipulation, in order to improve the thermoelectric parameters (S, σ, κ) at various temperatures. In this regard, the stoichiometry of the p and n-type TE compounds is the key variable. For example, Figure 12 shows zT values for thermoelectric products at different temperatures. As illustrated in this figure, different TE compounds with various zT values confirm their dependency on the constituent elements.

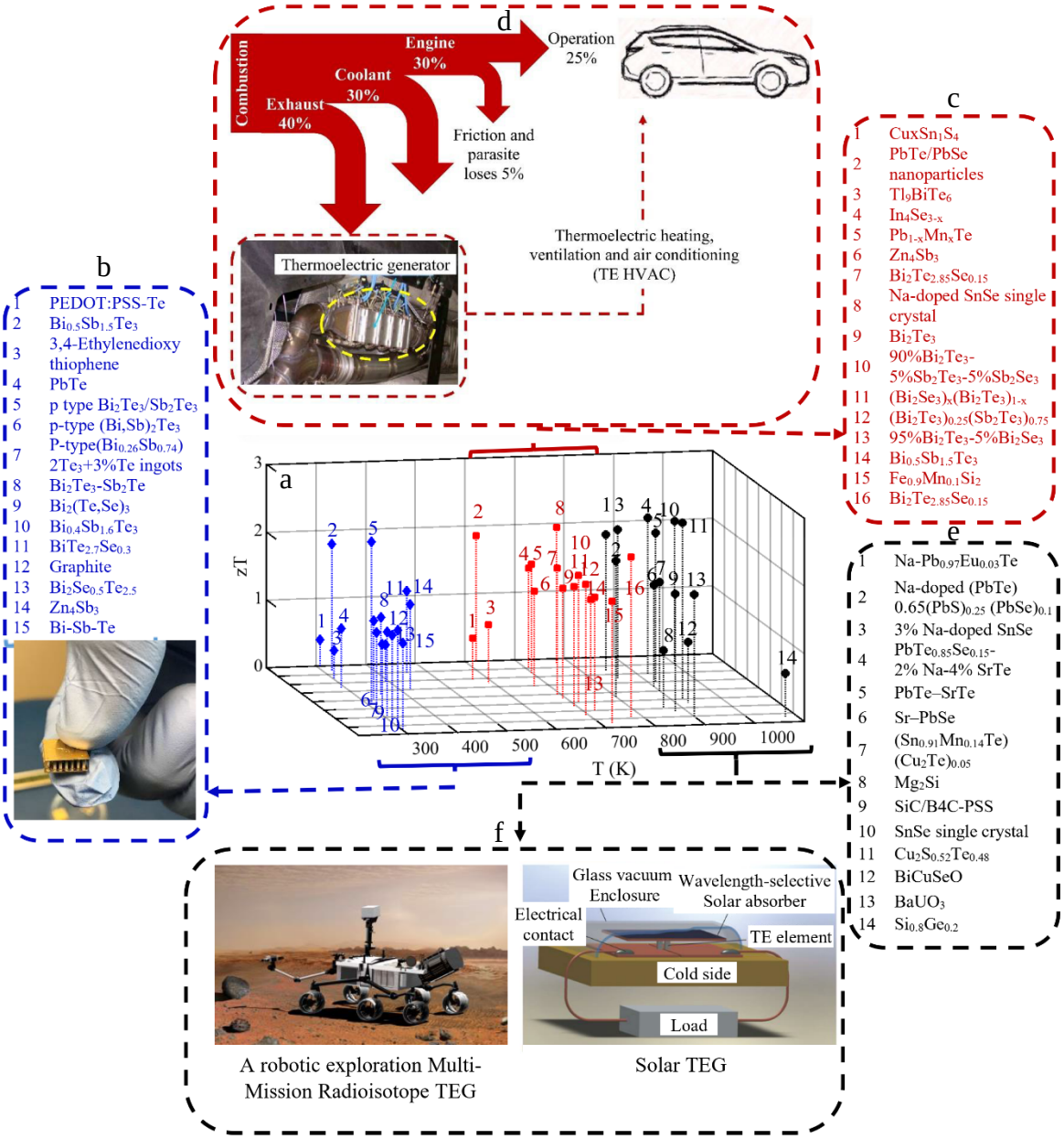

Figure 12: a) Stem chart which classifies the TE materials based on their optimum operation temperatures in three main intervals: low (room temperature to 600K), mid (600 to 850K), and high (850K and more) [19], b) a list of TE compounds, and a TEG operating at room temperature, c) illustrates the TE materials with optimized application in mid temperatures, and an application of TEGs in converting car exhaust heat into electricity (d-adapted from ref. [6, 72], with permission), e) represents the TE compounds with optimum performance at high temperatures, and two examples

of their applications in NASA (f- adapted from ref.[73]), and Solar TEGs (g- adapted from ref.[74], with permission).

The search for developing TE materials reveals the necessity to design products containing nontoxic/eco-friendly elements, sustainable at harsh conditions and high temperatures. Based on the dimensionless figure of merit (Equation 2), there should be a correlation between the thermoelectric parameters to make an efficient TE product with reasonable zT. Therefore, the effective factors, including the Seebeck (S), electrical (σ), and thermal conductivity (κ) must be optimized. As aforementioned, S and σ are mainly related to the electronic band structure (i.e., bandgap), which should be calculated based on the physics relationships. However, thermal conductivities can be modified via microstructure manipulation to increase the carriers' (electronic and heat) scattering, and reduce thermal conductivities.

2.3 Electronic transport properties - power factor ($S^2\sigma$)

The adverse interplay between the Seebeck coefficient and the electrical conductivity via the carrier density ($zT = (S^2 n)\frac{\mu}{\kappa_e+\kappa_l}eT$, n:carrier density, e:elementary charge, μ:carrier mobility) has provided more complexity by boosting the figure of merit by improving the numerator of Equation 2 [75]. Figure 13 exhibits the dependence of the Seebeck coefficient, the electrical conductivity, the power factor, electronic thermal conductivity, and lattice thermal conductivity versus carrier concentration.

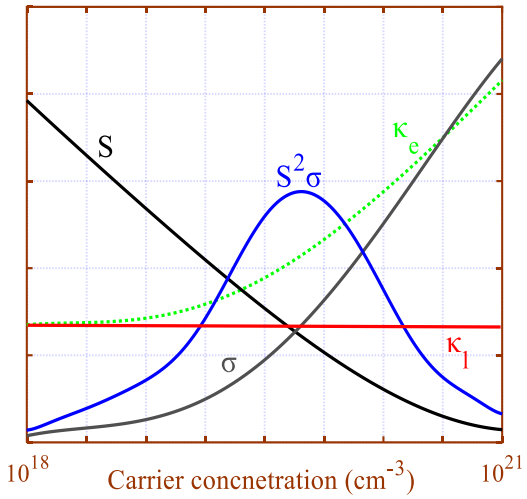

Figure 13: Interdependency of thermoelectric factors via carrier concentrations [75-77].

As shown in this figure, the Seebeck coefficient decreases almost linearly with the carrier concentration; whilst the electrical conductivity increases exponentially versus carrier concentration (as it increases the carrier density exponentially), which leads the power factor $S^2\sigma$ to a peak value [75-77].

Considering the difficulty in simultaneously increasing Seebeck and electrical conductivity has led to the creation of strategies to improve the thermoelectric properties in terms of transport coefficients. Many sophisticated electronic structure modulations and thermal transport optimization strategies have been developed to achieve this goal [23, 29, 30, 33, 35, 36, 41, 42, 45, 49, 50, 78-85], including scattering strategies [24, 75, 86, 87], resonant states, [36, 88, 89], manipulating the band gap [90], and modulation doping [49, 87, 91-96]. The common goal of these techniques is to engineer the band structure and transport factors (e.g., engineering distortions of the electronic density of states near the Fermi energy [36]) in TE compounds, that have been used to independently tune either the electrical conductivity or the Seebeck coefficient, or simultaneously increase, and thus maximize, the power factor ($S^2\sigma$). Important traces in finding fundamental solutions to create a trade-off between the Seebeck and electrical conductivity can be explained based on the following Mott equation, defined for a degenerate semi-conductor [76, 97].

$$S = \frac{\pi^2}{3}\frac{k_B}{q}\,k_B T\left[\frac{\partial \ln(\partial(E))}{\partial E}\right]_{E=E_f} = \frac{\pi^2}{3}\frac{k_B}{q}\,k_B T\left[\frac{1}{n}\frac{\partial n(E)}{\partial E} + \frac{1}{\mu}\frac{\partial \mu(E)}{\partial E}\right]_{E=E_f} \quad (4),$$

where k_B is the Boltzmann constant, q is the electron charge, E is the electron energy, τ is the carrier relaxation time, and E_F is the Fermi energy.

Increasing the density of state (DOS) near E_F can improve the Seebeck factor. Hicks and Dresselhaus [98, 99] proposed the use of quantum size effects in low-dimensional materials to make sharp features in the density of states and improve the Seebeck coefficient. Reduced dimensionality has offered a strategy to enhance the figure of merit, based on various concepts including 1) enhancement of the density of states near E_F, causing an improvement of the Seebeck coefficient, 2) increasing carrier mobility at a given carrier concentration via quantum confinement, doping strategies, and modulation doping, 3) considering the advantage of the anisotropic Fermi surfaces in multi-valley semiconductors, 4) increasing phonon scattering against barrier well interfaces, 5) the presence of different temperature dependences of the transport features and intrinsic carrier excitations in low dimensional systems in comparison with 3D systems [100]. Their model suggested that should a material be a good thermoelectric in 3D (bulk), it would be better in 2D (plane), and still better in lD (wire), with various levels of effectiveness, depending on the materials used [100]. In another work, Ren et al. [101] reviewed the size effect in low-dimensional thermoelectric materials through the quantum confinement effect on carriers (the enhancement of electronic density of states, semimetal to semiconductor transition, and carrier pocket engineering), the effect of phonon confinement, and interface scattering on lattice thermal conductivity. Heremans et al. [36] discussed four approaches to increasing the power factor ($S^2\sigma$) by engineering the electronic density of states (DOS) near the Fermi energy based on two-band structures, resonant levels (i.e., virtual bound states), hybridization gaps, and dilute Kondo alloys.

From the second term in Equation 4, S can be modified by the change in τ (i.e., mobility) through approaches such as filtering/scattering of charged carriers with low energy using energy barriers. As shown in Figure 14, carrier filtering happens due to the band bending at the energy barrier and

leads to a change in τ (i.e., mobility). This band alignment can be induced by the introduction of inclusions as dopants [76].

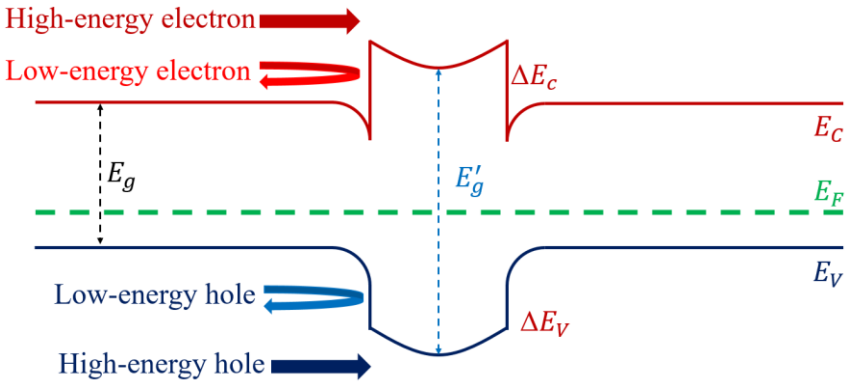

Figure 14: Carrier filtering due to the band alignment, adapted from ref. [76] with permission.

Electronic band-structure engineering using doping strategies is regarded as an important method to enhance the power factor ($S^2\sigma$) by essentially optimizing the carrier concentration (i.e., achieving an optimum carrier concentration) to control electrical conductivity and the Seebeck coefficient [37]. Dutta et al. [86] have discussed various electronic-structure modulation strategies and their recent developments, with a brief background of the underlying ideas. Uniform doping or alloying can significantly modify electrical conductivity and improve the Seebeck coefficient; however, mobility can be impacted. High carrier mobility plays an important role in obtaining potentially high thermoelectric performance. Carrier mobility can be improved by modifying the band structure, as well as by controlling the carrier scattering mechanism (e.g., modulation doping) [24, 102]. Several factors should be considered for using an appropriate method. For example, the nanoparticles may not be treated as scattering centres because the nanoparticle diameters (~20 nm) are much larger than the electron mean free paths (1-2 nm) [103]. To enhance the Seebeck coefficient, other mechanisms have been employed, mainly by distorting the electronic structure, such as band convergence and resonant state formation [87, 104].

2.3.1 Magnetic dopants

The potential of physical, chemical and structural modification at the nanometre scale is considered an important route for developing high-performance thermoelectric compounds [105]. In this regard, the concept of magnetism, the magnetic moment, and charged carrier interactions have been studied to improve the efficiency of several compounds [106]. In 1971, Fischer [107] discussed the electronic characteristics of dilute magnetic alloys/composites and presented a variety of anomalies attributable to the interaction between the magnetic moments of the magnetic impurities (dopants) and the conduction band electrons of the matrix. Later, in 1982, Furdyna [108] reviewed the electrical, magnetic, and optical properties of diluted magnetic semiconductors (DMS), sometimes referred to as "semi-magnetic" semiconductors. The diluted magnetic semiconductors discussed in the mentioned work contain substitutional Mn^{++} ions randomly distributed in the diluted magnetic semiconductor (DMS) lattice. These compounds are ternary semiconductor alloys, whose lattices are made up based on the partial substitution of magnetic ions. For example, $Cd_{1-x}Mn_xTe$ and $Hg_{1-x}Mn_xTe$ are two alloys of those systems. In the case of Mn ion, the half-filled $3d^5$ shell of Mn^{++} is highly localized at the ion site and contains five electrons with aligned spins, providing each individual ion with a magnetic moment equal to five Bohr magnetons. In the above-mentioned doped compositions with Mn atoms, the Mn^{++} ions, and their interactions amongst themselves, determine the magnetic characteristics of DMS [108]. These features are interesting for understanding and characterizing the behaviour of a disordered magnetic system. The small content of added transition or rare-earth impurities creates magnetic characteristics in the nonmagnetic host lattice and modified compositions with magnetic features. These properties are attributable to exchange splitting, arising from the magnetic interactions among the host lattice and the dopant cationic states, which provides the novel and interesting physical properties [109, 110]. As semiconductors, these alloys display interesting and important tunability, such as in the energy gap and the effective mass, etc., via composition control [108]. As an example, the tunability of the

energy gap by composition has been shown via substituting Mn instead of Hg in an $Hg_{1-x}Mn_xTe$ compound (Figure 15). As shown in this figure, the parent HgTe is a zero-gap semiconductor caused by the energy sequence of the Γ6 and the Γ8 bands. Replacement of Hg by Mn changes the relative distance of the Γ6 and Γ8 bands, creating a drastic impact on the band-structure dependent characteristics, for instance the effective carrier mass [108].

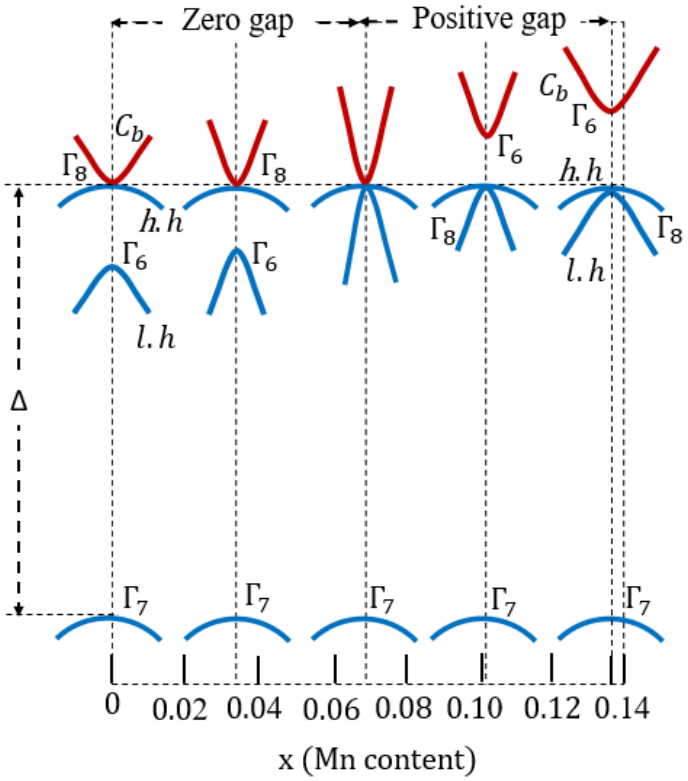

Figure 15: Band structure of $Hg_{1-x}Mn_xTe$ at the centre of the Brillouin zone (the Γ-point) for various compositions of the alloy. Δ denotes spin-orbit splitting, C_b conduction band, $h.h$ and $l.h$ stand for heavy and light holes, respectively, adapted from ref. [108] with permission.

In addition, DMSs are of interest for their magnetic appearances as disordered magnetic alloys, providing, for example, the spin glass transition, antiferromagnetic cluster formation, etc., [108]. The presence of localized magnetic ions in these semiconductors leads to an exchange interaction between the *sp* band electrons and the *d* electrons associated with transition-metal ions (e.g., Mn^{++}), resulting in extremely large Zeeman splitting of electronic levels [108]. Zeeman splitting [111] of

the free-exciton ground-state creates one of the most direct and convenient situations for scaling the exchange effects in wide-gap DMS. These spin-dependent properties also provide some other effects, such as the giant Faraday rotation, the magnetic-field-induced metal-insulator transition, and the formation of bound magnetic polarons [109]. Moreover, the existence of magnetic ions in the DMS lattice enables spin-spin exchange interactions between the localized magnetic moments and the band electrons. This interaction influences the energy band and impurity level parameters of the semiconductor [108].

Zener [112] proposed a simple model for the interaction between the magnetic impurity and the conduction band electrons of the matrix. This work discussed the interaction between the electrons of the d shells in the transition metals by considering three principles: 1) the spin correlation between the electrons in the incomplete d shell of a single atom is essentially the same when the atom forms part of a solid as when it is isolated in the gaseous state. Also, this coupling is formed by the direct exchange between the incomplete d shells of nearest neighbours. 2) The exchange integral between d shells of adjacent atoms has always had the same sign. This coupling is created by the exchange between the conduction band electrons and the inner d electrons. The direct interaction between d shells of adjacent atoms is thus of such a sign and tends to make an antiferromagnetic configuration of the d shell spins. Therefore, in the first two principles, the direct exchange interaction tends to align the spins of the incomplete d shell in an antiferromagnetic manner, and this tendency will be stronger for the larger spin of the d shells. 3) The spin of an incomplete d shell is strongly coupled to the spin of the conduction band electrons. This coupling provides alignment of the spins in the incomplete d shells in a ferromagnetic manner. This case happens if the indirect coupling dominates over the direct coupling between adjacent d shells, therefore ferromagnetism is possible [112].

It is worth noting that the magnetic moment of the impurity vanishes if this coupling with the conduction band electrons is large compared with the interaction between the d-electrons of the

impurity [107]. If the transition metal atoms are dissolved in a matrix, and contain only completed inner shells, the transition metal atoms have ordered positions such that they are not nearest neighbours of one another. In such an alloy there would be no exchange between the incomplete d shells [113].

In the field of doping engineering with magnetic dopants, nanoparticles with magnetic characteristics can result in magnetoelectric features and influence the thermoelectric properties via different effects, such as carrier spiral motion (carrier trapping-releasing) [114], magnon (spin wave) excitations [42, 107, 115, 116], carrier scattering (enhancing the carrier effective mass) [106, 117, 118], and phonon scattering [114]. A research paper [117] reported on natural chalcopyrite minerals ($Cu_{1+x}Fe_{1-x}S_2$) obtained from a deep-sea hydrothermal vent with thermoelectric properties in the low x region. They detected electron-magnon scattering and a large effective mass in this region, based on the strong coupling of doped carriers and antiferromagnetic spins, resulting in the natural enhancement of thermoelectric characteristics during mineralization reactions.

Recently, the work by Wei et al. [119] demonstrated that magnetic doping is an effective strategy to modify the thermoelectric performance of p-type $Bi_{0.5}Sb_{1.5}Te_3$. However, the results showed that the ferromagnetic Fe/Co elements could not easily enter the $Bi_{0.5}Sb_{1.5}Te_3$ lattice, unlike diamagnetic Pb. This process was explained with the concept of the “like dissolves like” rule. Moreover, it was reported that ferromagnetic Fe/Co atoms hardly replaced Bi/Sb since Fe/Co needs to fight against the spin splitting to enter the $Bi_{0.5}Sb_{1.5}Te_3$ lattice. According to the analysis, by constantly keeping the doping content, Fe and Co provided much lower hole carriers in comparison with Pb, due to their larger carrier thermal activation energies. Therefore, Fe and Co were indicated as very applicable dopants for fine modification of the carrier concentration. The Fe/Co-doped samples showed higher Seebeck coefficients and lower carrier mobilities than the Pb-doped sample because the doped magnetic atoms (Co and Fe) created additional carrier scattering. Finally, zT values of about 1.05 and 1.15 near room temperature were reported for the samples with 1.71 atomic % Co

and 1.80 atomic % Fe, respectively. Furthermore, at the solid solubility limit, the excess Fe/ Co appeared in the impurity phases [119].

Charge carrier interactions with local magnetic moments may result in increasing the charge carrier effective mass, and consequently enhancing thermopower. Vaney et al. [106] doped bulk bismuth telluride samples with chromium to make n-type dilute magnetic $Bi_{2-x}Cr_xTe_3$ ($0<x<0.1$) compounds. The results indicated that by neutral replacement of Bi with Cr (i.e., isovalent substitution of Bi with Cr atoms), the resulting compound, $Bi_{1.99}Cr_{0.01}Te_3$, had an enhanced power factor, decreased thermal conductivity, and thus an improved zT . The magnetic interactions caused by the magnetic moment carried by Cr atoms increased the electrons' effective mass and enhanced the thermopower. Combined with the decrease in lattice thermal conductivity, the overall performance of these compounds was enhanced by 25% at constant carrier concentration. The result indicated an enhancement principle, such that the magnetic interactions are effective at high temperatures above the transition temperature, unlike magnon drag, which is dependent on ordering and, typically, on a low temperature effect [106]. Another work [118] presented that the carriers in $CuGa_{1-x}Mn_xTe_2$ were strongly correlated with the Mn magnetic moments due to the magnetic and magnetotransport effects. This type of local interaction enhanced the holes' effective mass, resulting in relatively high Seebeck coefficients. Strong interactions between the Mn magnetic moments and charge carriers were inferred, based on the large negative Weiss temperature in the magnetic susceptibility, and a distinctive anomalous Hall effect [118]. In this regard, Tang et al. [120] employed Mn to preserve the large Seebeck coefficient of BiCuSeO alloys, also improving the carrier mobility, and thus enhancing the electrical conductivity by light element Li doping. Spin entropy due to the spin degeneracies of magnetic transition metals is another effect of magnetic element doping. The spin entropy current created by free spins contributes to enhancement of the Seebeck coefficient in materials [120].

In the later sections, two main impacts of magnetic nanoparticles on electrical conductivity and the Seebeck coefficient, in terms of carrier scattering/trapping and spin-entropy interaction, will be evaluated and discussed.

2.3.1.1 Carrier Scattering/Trapping

According to Maxwell's electromagnetic theory, magnetic impurities (i.e., magnetic dopants) may change the movement direction of the moving charged carriers due to the Lorentz force interaction, while the velocity magnitude is preserved. Based on this theory, charged particles (electrons and holes) confined to circular paths or helices are trapped by magnetic impurities due to the Lorentz force [105, 114]. Zhao et al. [114] classified the electrons' motion based on their movement direction versus their magnetic field. Those electrons with velocities parallel to the magnetic field Figure 16) move linearly and are not affected by the magnetic field (Figure 16b and c). Those electrons with their velocity direction perpendicular to the magnetic field (Figure 16d), are formed with circular paths in the ferromagnetism state (Figure 16e). These electrons will move linearly in the paramagnetism state, as shown in Figure 16f. Those electrons with velocities having components parallel and perpendicular to the magnetic field (Figure 16g) move in a spiral pattern. These electrons are trapped by magnetic nanoparticles in the ferromagnetism state (Figure 16h).The trapped electrons are released with linear movement in the paramagnetism state, as demonstrated in Figure 16i.

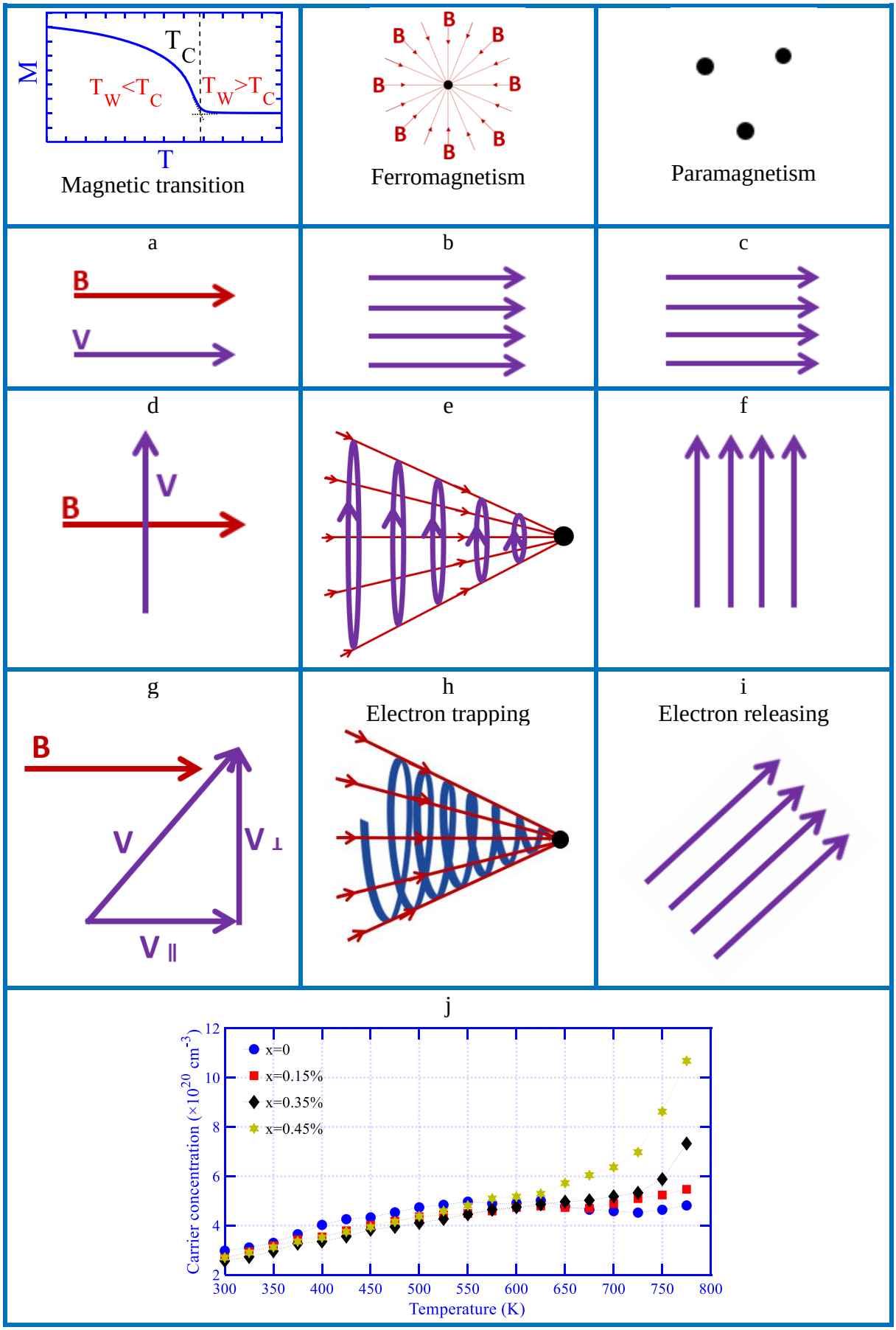
M
T
T_C
T_W<T_C
T_W>T_C
Magnetic transition
B
Ferromagnetism
Paramagnetism
a
b
c
B
V
d
e
f
B
V
g
h
Electron trapping
i
Electron releasing
B
V
V ⊥
V ∥
j
x=0
x=0.15%
x=0.35%
x=0.45%
Carrier concentration (×10^20 cm^-3)
Temperature (K)
2
4
6
8
10
12
300
350
400
450
500
550
600
650
700
750
800

Figure 16: Effect of permanent magnet nanoparticles on electrical transport. a-c) carrier velocity direction is parallel to the magnetic field direction, d-f) carrier velocity direction is perpendicular to the magnetic field direction, g-i) carrier velocity direction components are parallel and perpendicular to the magnetic field direction, and j) change in carrier connotation versus temperature for xBaM/$Ba_{0.3}In_{0.3}Co_4Sb_{12}$ magnetic nanocomposites. The carrier concentration increases at temperatures above T_C,- magnetic temperature transition, which releases the trapped carriers, adapted from ref. [114] with permission.

The above-mentioned results were experimentally evaluated by the significant increase in carrier concertation of (x ($BaFe_{12}O_{19}$) nanoparticles, xBaM)/$Ba_{0.3}In_{0.3}Co_4Sb_{12}$ above T_C=675 K, (Figure 16j), which shows that the BaM-nanoparticles lowered the carrier concentrations of xBaM/$Ba_{0.3}In_{0.3}Co_4Sb_{12}$ at a low temperature range (T<675K). Based on the "electron repository" role of the BaM-nanoparticles in xBaM/ $Ba_{0.3}In_{0.3}Co_4Sb_{12}$, the magnetic nanoparticles trap electrons below the T_C and release the trapped electrons above the T_C [114]. Similarly, another work [121] evaluated the addition of $BaFe_{12}O_{19}$ magnetic nanoparticles to the $In_{0.25}Co_4Sb_{12}$ matrix and observed two results: 1) the addition of $BaFe_{12}O_{19}$ nanoparticles reduced the grain size of the In-filled $CoSb_3$ matrix and increased the defects, causing an increase in carrier density; 2) electron capturing due to the generated magnetic field by $BaFe_{12}O_{19}$ magnetic nanoparticles in the low-temperature range below 550 K resulted in a decrease in carrier concentration. In temperatures above 550 K, $BaFe_{12}O_{19}$ magnetic nanoparticles with a paramagnetic state released the trapped electrons because of the disappearance of the micromagnetic field interaction with the magnetic nanoparticles [121].

Embedded magnetic nanoparticles in thermoelectric compositions may act as scattering centres for the phonons at nanometre scales. In particular, magnetic nanoparticles in a superparamagnetic state cause additional electron and phonon scattering due to the random turning of the magnetic domain

[105]. The introduction of superparamagnetic nanoparticles into a thermoelectric compound may provide a new method of manipulating electron and phonon transport simultaneously at nanometre scales [105]. The superparamagnetic behaviour of nanoparticles may result in three types of thermo-electromagnetic effects: 1) charge transfer from the magnetic inclusions to the matrix, 2) multiple electron scattering by superparamagnetic fluctuations, and 3) phonon scattering caused by both the magnetic fluctuations and the nanostructures [105]. Theoretically, soft-magnet transition-metals, such as Fe, Co and Ni nanoparticles, can experience a magnetic transition from ferromagnetism to superparamagnetism if the magnetocrystalline anisotropy energy is equivalent to/smaller than the thermal energy. The above-mentioned work [105] showed dual control of phonon- and electron-transport properties by embedding soft-magnetic nanoparticles (Co nanoparticles) in $xCo/Ba_{0.3}In_{0.3}Co_4Sb_{12}$ ($x = 0.1\%$) thermoelectric particles to optimize the transport parameters of electrical conductivity (σ), Seebeck (S), and thermal conductivity (κ). The results show the presence of an important mechanism for multiple scattering of electrons induced by superparamagnetic Co nanoparticles. In the superparamagnetic state, the magnetic moment of Co nanoparticles is not rigid and is changed randomly, which may result in a multiple scattering mechanism. The resultant multiple scattering is similar to the Kondo effect, in which the conduction electrons experience multiple scattering caused by antiferromagnetic coupling [105].

2.3.1.2 Magnon (spin wave) excitations

In addition to spin fluctuations caused by magnetic transition, the effect of magnon (spin wave) excitations should be considered for thermoelectric compounds doped with magnetic nanoparticles. Magnons in magnetic compositions interact with electrons throughout the bulk of the material. One measurable consequence of this interaction is the magnon-drag thermopower result due to thermagnonic heat flux dragging along the electronic charge carriers [122]. Blatt et al. [123] first suggested the magnon drag thermopower is the dominant mechanism behind the high thermopower (Seebeck, S) of elemental Fe. Grannemann et al. [124] measured a consistent decrease created by

the magnon-drag contribution to the Peltier coefficient via field quenching for $Ni_{66}Cu_{34}$. Lucassen et al. [125], pointed out a relationship between the dissipative spin-transfer-torque parameter (β) and the contribution of magnon drag to the thermoelectric power in conducting ferromagnets. They showed that this parameter is dependent on the ratio of the magnon-drag thermopower and the magnon heat conductivity.

Watzman et al. [122] showed that magnon drag directs the thermopower of elemental Fe in the temperature range from 2 to 80 K, of elemental Co from 150 to 600 K, and of elemental Ni from 50 to 500 K. This work presents two theoretical models for magnon-drag thermopower, 1) hydrodynamic theory based purely on nonrelativistic, Galilean, spin-preserving electron-magnon scattering, and 2) based on spin-motive forces, where the thermopower created by the electric current pumped via the dynamic magnetization associated with a magnon heat flux [122]. In the above-mentioned research, magnons and electrons were treated as two fluids, by only considering the interaction between the two fluids with no further electron-phonon or magnon scatterings. As a result, the authors suggest that the magnon-drag thermopower (S_{md}) is proportional to the magnon heat capacity (C_m), $S_{md} \propto C_m \propto T^{3/2}$ [122].

In general, thermopower in ferromagnetic materials is achieved through collaborations of various parameters, including phonon diffusion, phonon drag, magnon drag, and spin wave fluctuations, as illustrated in Equation 5 [117, 126].

Low temperature — Magnon drag effect — Spin-wave fluctuation

$$S = S_0 + S_1 T + S_{3/2} T^{3/2} + S_3 T^3 + S_4 T^4 \quad (5).$$

Phonon diffusion — Phonon drag

Phonon drag [127], a well-established principle in thermoelectricity, is central to thermopower generation (i.e., electrons' drag and movement) and is created by nonequilibrium phonons' energy under a temperature gradient (∇T). Similarly, in the magnon drag process, the magnons owning

nonequilibrium energy levels transfer momentum to the conduction electrons [128] by moving from the hot side to the cold region. In this process, the spin disorder increases with temperature due to thermal excitation and results in higher levels of magnetic entropy [129]. Schlickeiser et al. [129] studied thermally-driven magnetic domain wall (DW) motion via magnonic spin currents and showed that the temperature gradient makes a torque term, thereby maximizing the magnetic entropy. Also, they reported that the maximum change in entropy (ΔS) occurs at a temperature slightly below the Curie temperature (T_C) [129]. In this regard, the spin caloritronic (i.e., the Spin Seebeck effect) evaluates the transport of spin, charge, entropy, and energy in magnetic systems [129-132]. The spin Seebeck effect is based on the spin caloritronic phenomenon and defines the occurrence of spin currents or spin accumulation by temperature gradients [129-132]. The extra degree of freedom produced by the electron spin and magnetic order may result in strategies to increase thermoelectric efficiency [133, 134]. In this field, the total Seebeck coefficient for spin-polarized metals is described by Equation 6 [133, 134],

$$S = \frac{\sigma^{\uparrow}S^{\uparrow}+\sigma^{\downarrow}S^{\downarrow}}{\sigma^{\uparrow}+\sigma^{\downarrow}} \qquad (6),$$

in which, $S^{\uparrow}, \sigma^{\uparrow}$ and $S^{\downarrow}, \sigma^{\downarrow}$ are the Seebeck coefficient and electrical conductivity for spin up and spin down electrons, respectively.

The magnon-/spin wave fluctuation-related effects are defined on the basis of thermally nonequilibrium spin currents [135]. The electronic entropy is indicated to be increased due to spin fluctuations. In this field, thermopower, roughly regarded as the entropy, is transferred by a charge carrier, and can be improved through spin fluctuations in the vicinity of the magnetic ordering. Studies [135, 136] show that spin fluctuations in ferromagnetic metals can cause a peak in the Seebeck coefficient around Curie temperature, and are characteristic to the spin fluctuation energy. Tsujii et al. [135] presented that the power factor can be enhanced by incorporating magnetic interactions in ferromagnetic metals via the spin fluctuation caused by itinerant electrons. They

showed the weak ferromagnetism at T_C with a small magnetic moment for electron doped Heusler alloys, $Fe_2V_{1-x}T_xAl_{1-y}Si_y$. The results displayed an enhancement (20% improvement in the power factor) around T_C in comparison with cases in which the spin fluctuation was suppressed under an applied magnetic field to support the merit of using spin fluctuation to further enhance thermoelectric properties.

Mayer et al. [115] modelled two possible contributions to the thermopower, including diffusion and exchange effects ($S = S_{diffusion} + S_{exchange}$). They expressed the thermopower due to diffusion by considering the density of states:

$$S_{diffusion} = \frac{\int (E-E_f)\frac{dF(E)}{dE} g_{del}(E)dE}{eT\int \frac{dF(E)}{dE} g(E)_{del}dE} \qquad (7),$$

where $g_{del}(E)$ is the delocalized density of states and $F(E)$ is the Fermi-Dirac distribution function. In dilute magnetic semiconductors, another additional contribution to the thermopower originating from the exchange interaction was considered according to Kondo's derivation, expressed as:

$$S_{exchange} = S_0 \frac{T}{T+T_0} \qquad (8),$$

where T_0 is the Kondo temperature and S_0 is a temperature independent parameter defined in terms of the exchange integral, spin operator, resistivity, potential, and physical constants [115].

Kondo [137] explained that conduction band electrons may change their spin states by being scattered against the magnetic impurities. By considering the effect of magnon drag on thermopower, another work [40] derived a theoretical model for magnon-bipolar carrier drag thermopower, based on the magnon-carrier interaction lifetimes. This research reported the experimental observation of magnon-carrier drag thermopower in *n*-type and intrinsic ferromagnetic semiconductors. The *p*-type antiferromagnetic MnTe was doped with different amounts of Cr to produce nondegenerate and *n*-type semiconductors of various carrier concentrations. They applied the following expressions, based on the fundamental theory of

diffusion and drag thermopower in intrinsic semiconductors, for the thermopowers due to diffusion (S_n^{diff}), and magnon-carrier drag (S_n^{drag}) [40]:

$$S_n^{diff} = -\frac{k_B}{e}\left[\left(ln\frac{N_C}{n}\right) + \left(r + \frac{5}{2}\right)\right] \qquad (9),$$

$$S_n^{drag} = -\frac{m_n^* C^2}{eT}\,\frac{\tau_m}{\tau_{em}}\,\frac{\tau_{me}}{(\tau_m + \tau_{me})} \qquad (10),$$

in which, n is the carrier concentration, r shows the electronic scattering parameter, m^* denotes the effective carrier mass, C is the magnon group velocity, T is temperature, τ_m is the magnon lifetime due to all scatterings but charge carriers (magnon-magnon scattering), τ_{em} is the charge carrier relaxation time due to scattering by magnons (carrier-on-magnon scattering), and τ_{me} is the magnon relaxation time due to scattering by charge carriers (magnon-on-carrier scattering). $\eta = ln\frac{N_c}{n} = \frac{E_c - E_F}{k_B T}$ is the reduced chemical potential energy of the carriers, and $(r + \frac{5}{2})$ is used as the reduced kinetic energy of the carrier.

The above-mentioned studies reveal the importance of magnon (spin wave) excitation's effects on thermoelectric compounds doped with magnetic nanoparticles. In addition to thermopower, the electrical conductivity of ferromagnetic metals was reported with an anomalous temperature dependence below the Curie temperature (T_C) [138]. This observation has been interpreted by Mott [139] on the basis of the band model, and by Kasuya [140] on the basis of the localized d-electron model. The anomalous Hall effect (AHE) and the magnetoresistance have been explained theoretically by Karplus and Luttinger [141, 142] and by Smie [143] on the basis of the band model. Nagaosa et al. [144] comprehensively reviewed experimental and theoretical studies of the AHE and readers are referred to this work for further discussion. Here, we are focusing on the relevance of the intrinsic mechanisms in magnetic compositions with spin-orbit coupling, for instance diluted magnetic semiconductors. The evidence of the magnetic moment-carrier interaction characterized by measuring the Hall resistance and the AHE is good evidence of the correlation between carriers

and magnetic moments [118]. The anomalous Hall effect has deep roots in the history of electricity and magnetism. In 1879, Edwin H. Hall [145] showed that when a current-carrying conductor is located in a magnetic field, the Lorentz force influences its electrons against one side of the conductor. Later [146], he reported this effect to be ten times larger in ferromagnetic iron in comparison with nonmagnetic conductors. The well-known ferromagnetic feedback of charge carriers in ferromagnetic semiconductors is defined as AHE [147]. In the other words, the emergence of voltage transverse in response to the applied current and external magnetic field with respect to the magnetization is attributable to asymmetric carrier scattering by magnetic impurities in the existence of spin-orbit association [147].

The Hall resistivity is generally expressed as an empirical relationship between ρ_{xy} (Hall resistivity), H_z (applied perpendicular field Hz), and M_z (magnetization),

$$\rho_{xy} = R_o H_z + R_s M_z \qquad (11),$$

where the first term corresponds to the normal Hall contribution, and the second term represents the contribution of the anomalous Hall effect (AHE). R_o and R_s are ordinary and anomalous Hall coefficients, respectively [135, 144, 147]. Experimental investigators showed that the dependence of the Hall resistivity (ρ_{xy}) on an applied perpendicular field (H_z) is qualitatively different in ferromagnetic and nonmagnetic conductors. The Hall resistivity increases linearly versus H_z, by considering the Lorentz force. However, in ferromagnets, ρ_{xy} initially increases steeply in weak H_z, but saturates at a large value, which is nearly H_z independent [144, 147].

Hidemi et al. [147] evaluated the anomalous Hall effect governed by electron doping in a room-temperature transparent ferromagnetic semiconductor, namely rutile $Ti_{1-x}Co_xO_{2-\delta}$ (of oxygen deficiency, δ). As illustrated in Figure 17, ρ_{xy} increases rapidly up to 0.2 T versus the magnetic field, and gradually decreases linearly with any further increasing magnetic field. This behaviour exhibits that the anomalous part of ρ_{xy} (ρ_{AHE}), proportional to magnetization, is mainly found in a lower magnetic field, while the ordinary part of Hall resistance (ρ_{OHE}) remains.

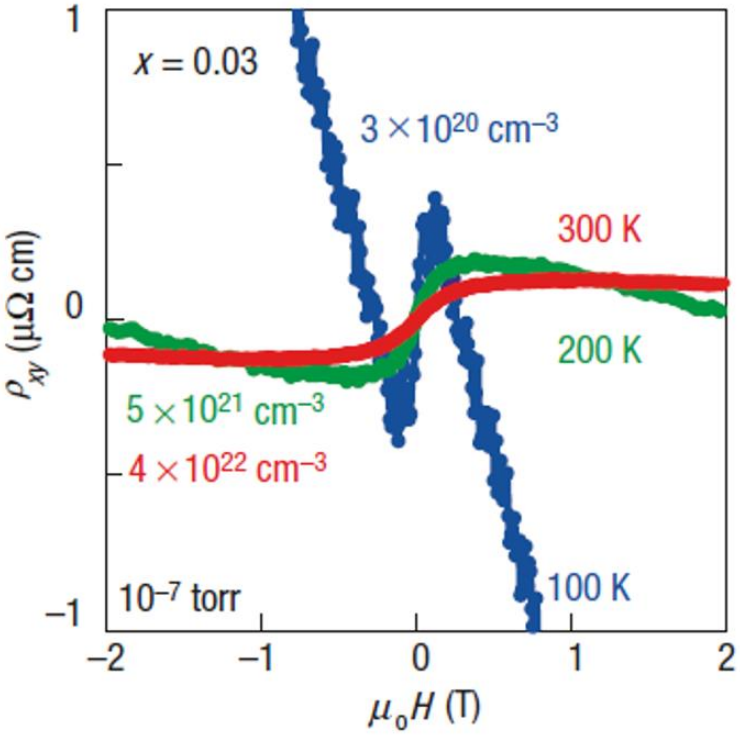

Figure 17:Magnetic-field dependence of Hall resistivity (ρ_{xy}) for $Ti_{1-x}Co_xO_{2-\delta}$. $\rho_{xy} = R_OB + R_s\mu_0M$ (B: magnetic induction, μ_0: magnetic permeability, M: magnetization, Ro: ordinary Hall coefficient, R_s: anomalous Hall coefficient), reused from ref. [147] with permission.

On the basis of the intrinsic influence of the AHE, by applying an external electric force on ferromagnetic conductors, electrons achieve an additional impact on their group velocity, as an anomalous velocity, which is perpendicular to the electric field and implies a contribution to the Hall conductivity σ_{xy} [144].

2.3.2 Modulation doping

As clearly mentioned above, increased carrier mobility results in higher zT values via increasing electrical conductivity. Through the doping strategies available to increase electrical conductivity, modulation doping has been proven as an efficient method to increase carrier mobility and thus thermoelectric performance. This method, in and of itself as a mechanism and in combination with other enhancement mechanisms to improve thermoelectric performance, was originally proposed by Dresselhaus and Hicks [98] and has been considered in various studies [49, 50, 80, 82, 83, 93,

148]. The modulation doping process, unlike conventional uniform doping (alloying), results in atomic scale structural changes, similar to phase-separated (heterostructured) composites [148]. The reasons and motivations for employing this technique as a form of remote doping in developing thermoelectric compounds mainly focus on the achievement of high carrier concentrations, without decreasing the carrier mobility – caused by scattering – by avoiding the scattering created by ionized impurities [37, 49, 75]. This technique has been widely used in thin film devices designed to improve electrical conductivity. In general, these devices are made of three layers, including a doped layer to provide charge carriers, an undoped layer to serve as a charge transport channel with no parent impurity atoms, and a third layer serving as a thin spacer layer between the doped and undoped layers. This layer acts as a separator to avoid impurity diffusion from the doped layer into those that are undoped [102]. In terms of the doped/undoped layer interface, the moving of electrons/holes from the doped to the undoped layer will proceed if the doped layer has a higher/lower conduction/valence band edge against the undoped one for n/p-type doped semiconductors [102]. Otherwise, the Schottky barrier will disrupt the electrical transport and the effect of modulation doping will be diminished. Similarly, in bulk samples (3D), the ionized nanoparticles come from the doping nanograins, while the host matrix is left either undoped or lightly doped.

Figure 18a presents a list of thermoelectric compounds, which employ the modulation doping method to improve their thermoelectric properties, combined with other factors (e.g., a reduction in lattice thermal conductivity).

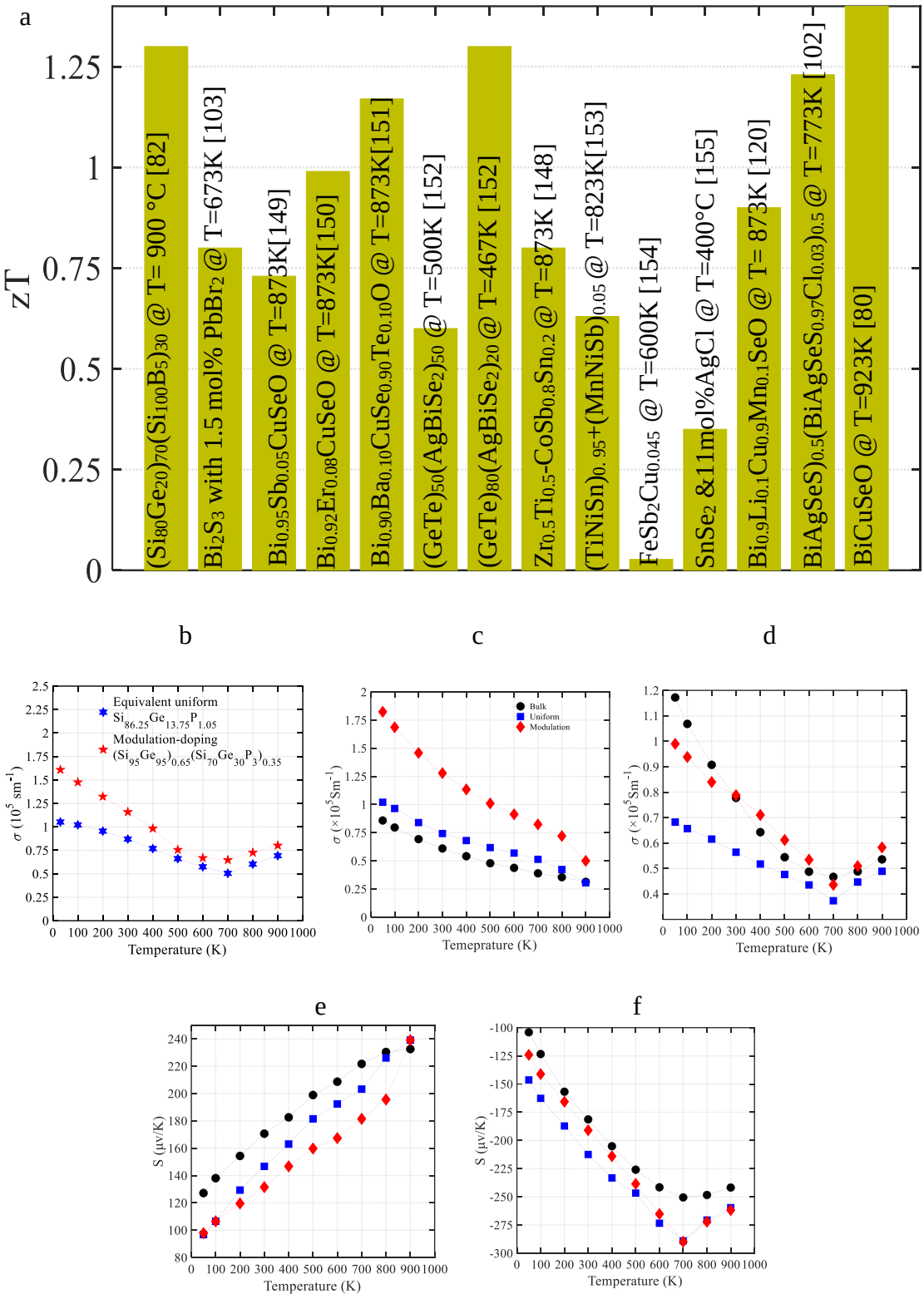

Figure 18: a) Thermoelectric compounds which employ the modulation doping method to improve thermoelectric properties combined with other factors (e.g., reduction in lattice thermal conductivity) b) Comparison of modulation-doping with uniform impurity doping data for the

optimally-doped matrix of $Si_{95}Ge_5P_2$ [82], c) Temperature-dependent electrical conductivity, $(Si_{80}Ge_{20})_{70}(Si_{100}B_5)_{30}$ (modulation doping), $Si_{86}Ge_{14}B_{1.5}$ (uniformly alloyed single-phase nanocomposite), p-type SiGe (bulk alloy), d) Temperature-dependent electrical conductivity, $(Si_{80}Ge_{20})_{80}(Si_{100}P_3)_{20}$ (modulation doping), $Si_{84}Ge_{16}B_{0.6}$ (uniformly alloyed single-phase nanocomposite), n-type SiGe (bulk alloy), e) Temperature-dependent Seebeck coefficient, $(Si_{80}Ge_{20})_{70}(Si_{100}B_5)_{30}$ (modulation doping), $Si_{86}Ge_{14}B_{1.5}$ (uniformly alloyed single-phase nanocomposite), p-type SiGe (bulk alloy), f) Temperature-dependent Seebeck coefficient, $(Si_{80}Ge_{20})_{80}(Si_{100}P_3)_{20}$ (modulation doping), $Si_{84}Ge_{16}B_{0.6}$ (uniformly alloyed single-phase nanocomposite), n-type SiGe (bulk alloy) [83].

Research [82] compared modulation-doping with uniform impurity doping data for an optimally doped matrix, $Si_{95}Ge_5P_2$ (Figure 18b). As shown in this figure, over the whole temperature range, the modulation-doped sample has a higher electrical conductivity due to higher carrier mobility than the equivalent uniform sample (e.g., 36.42 $cm^2V^{-1}s^{-1}$ (modulation doped sample), 24.26 $cm^2V^{-1}s^{-1}$ (uniform counterpart)). The difference is relatively large at low temperatures but becomes smaller as the temperature increases, since electron-phonon scattering increases with temperature and starts to dominate at high temperatures [82]. One issue in the modulation doping scheme is increasing the electronic part of the thermal conductivity due to the produced enhancement in electrical conductivity. Such an increase in the electronic part is unavoidable since charge carriers are also heat carriers. Moreover, the new phase (dopants) may have higher thermal conductivity than the matrix, which would result in higher total thermal conductivity [82]. In this regard, strategies such as nanostructuring may be helpful to reduce thermal conductivity due to the modulation-doping scheme [82]. Zebarjadi et al. [83] considered a two-phase composite ($A\&B$) and estimated the electrical conductivity of the composites based on the following equation:

$$\frac{1}{\sigma_{AB}} = \frac{V_A}{en_A\mu_A} + \frac{V_B}{en_B\mu_B} \qquad (12),$$

where n_A and n_B stand for the modified carrier densities, and μ_A and μ_B show the carrier mobilities in grains A and B, respectively. To obtain the Seebeck coefficient of the two-phase composite, they assumed two connected grains in series. The Seebeck coefficients added up with the thermal resistance weight as:

$$S_{AB} = \frac{\frac{S_A V_A}{\kappa_A} + \frac{S_B V_B}{\kappa_B}}{\frac{V_A}{\kappa_A} + \frac{V_B}{\kappa_B}} \qquad (13).$$

Here, S_A and S_B denote the Seebeck coefficients of grains A and B, respectively; and κ_A and κ_B are their corresponding thermal conductivities [83]. The results showed that using two types of grains provides another strategy to improve the performance of the thermoelectric bulk compound via enhancing the power factor in addition to a reduction in thermal conductivity. The results show that the electrical conductivity of the modulation-doped samples is higher than that of their equivalent uniformly doped nanostructured samples in both n-type and p-type compositions (Figure 18c and d). In contrast, the difference between the Seebeck coefficient for the two types of samples is less significant (Figure 18e and f) [83].

Some findings were suggested in the above-mentioned works to obtain maximum benefit from the modulation-doping strategy [82, 83]. Both types of grains in the modulation-doped samples should be fabricated of good thermoelectric compounds with low-lattice thermal conductivity [83]. The band edge of the conduction/valence band of nanoparticles should be higher/lower than that of the host; therefore, the carriers can transfer from the nanoparticle to the host [83]. The nanoparticles should create proper band alignments with the matrix to facilitate the carrier's flow from the nanoparticles into the matrix [82]. In nanocomposites formed by two consolidated grains, however, the band alignment may be influenced by applied tension on the grains and thus create possible dangling bonds, trapped charges at the interfaces, and the presence of impurities at the boundaries [82]. Using a host matrix with a larger effective mass compared with that of the nanoparticles – the ones with a low density of states compared with the matrix – is an effective strategy to increase the

number of available states inside the host matrix, and therefore to promote the flow of charge from the nanoparticles into the host matrix [82, 83]. Therefore, by engineering the Fermi level and designing the right compositions, the modulation doping strategy could have significant potential to improve the performance of thermoelectric compounds [83].

Another work [80] quantitatively evaluated the effects of modulation doping on improving electrical conductivity, based on self-consistent effective medium theory [156]. The effective electrical conductivity (σ_{eff}) value of a heterogeneous composite consisting of two phases of undoped (σ_A) and doped (σ_B) regions was calculated based on the following expression:

$$V_A \frac{\sigma_A - \sigma_{eff}}{\sigma_A + 2\sigma_{eff}} + V_B \frac{\sigma_B - \sigma_{eff}}{\sigma_B - 2\sigma_{eff}} = 0 \qquad (14),$$

where V_A and V_B are the volume fractions of phases A and B, respectively.

Jovovic et al. [79] showed that the thermoelectric properties of $AgSbTe_2$ are modified by doping the material p-type. The overall zT of both Na-doped and Tl-doped $AgSbTe_2$ reached values in excess of 1 at 400 K and remained higher than 0.8 near and above room temperature. It is noteworthy that the diffusion between the matrix and the nanoparticles via a solid solution should be considered in the modulation-doping process. In a work [153], modulation doping of half-metallic MnNiSb in the TiNiSn system was evaluated by using spark plasma sintering.

It was found that MnNiSb dissolves into the TiNiSn matrix and forms a heavily doped $Ti_{1-x}Mn_xNiSn_{1-x}Sb_x$ phase, which leads to a largely enhanced carrier concentration and a slight increase of carrier mobility. As a result, the electrical conductivity and power factor of the modulation doped compounds are greatly improved. A maximum power factor of 45×10^{-4} $WK^{-2}m^{-1}$ is obtained at a temperature of 750 K for the modulation doping system $(TiNiSn)_{1-x}+(MnNiSb)_x$ with x=0.05. They also reported a reduction in the lattice thermal conductivity due to the enhanced phonon scattering. Benefitting from the improved power factor and reduced lattice thermal conductivity, a peak zT of 0.63 was reported at a temperature of 823 K for x = 0.05, which is about 70% higher than the peak zT of TiNiSn [153].

In further steps, the idea of using of anti-resonance nanoparticle methods was mentioned as an important advance for enhancing the power factor in thermoelectric compounds [50]. In this work [50], a sharp dip in the scattering cross section function versus carrier energy is referred to as anti-resonant scattering. Two ways were mentioned for this concept to enhance thermoelectric performance, including 1) since such dopants are invisible to the conduction carriers, their interaction scattering cross section with the conduction carriers is minimal. The anti-resonant doping results in lower carrier scattering at high carrier concentrations and mitigates the side effects of conventional doping, thereby improving electrical conductivity. 2) The sharp scattering dip may create sharp features in the relaxation times and hence in the differential conductivity. Moreover, the results were expected to provide an actual thermal conductivity reduction caused by a large acoustic mismatch between the core-shell and the host matrix materials. Therefore, the anti-resonance strategy applied to the nanoparticle-doped samples points to a direction that can be used to improve the three parameters determining performance (zT) for doped thermoelectric compounds [50]. In a further advance, another research paper [81], aimed to embed nanoparticles in a host semiconductor with a size comparable with electronic wavelengths, making them "invisible" to the electron transport. The results indicated possible applications of the ''electron cloaks'' when designing energy harvesting, conversion technologies, electronic switches, and sensors. They showed that this system is adequate to cloak the nanoparticles from being distinguished by electrons with specific energies and hence the total achieved scattering cross section is smaller than 0.01% of the physical cross section.

2.3.3 Band convergence

Goldsmid et al. [33] evaluated the manipulation of the density of states function as a promising approach to improve the power factor, by means such as the introduction of impurity bands. The results expressed the contributions from carriers in an impurity band to the Seebeck coefficient and electrical conductivity in terms of the Fermi energy, alongside the position of the impurity levels

relative to the edge of the main band [33]. Band engineering is one of the core strategies to improve the performance of thermoelectric compounds. Excellent progress has recently been made through band engineering, such as band convergence [76, 157-166], leading to modifications in both the electrical conductivity and Seebeck coefficient. In this regard, the energy-alignment of multiple electronic band pockets at the band edge – widely named band convergence – is one of the most successful approaches for systematic enhancement of electronic performance of thermoelectric compounds [162-168]. Hong et al. [169] provide numerical investigations into the effects of band convergence on the electronic properties. Figure 19 shows a list of thermoelectric compounds that have been used with the band convergence approach combined with other factors (e.g., a reduction in lattice thermal conductivity) to improve thermoelectric performance.

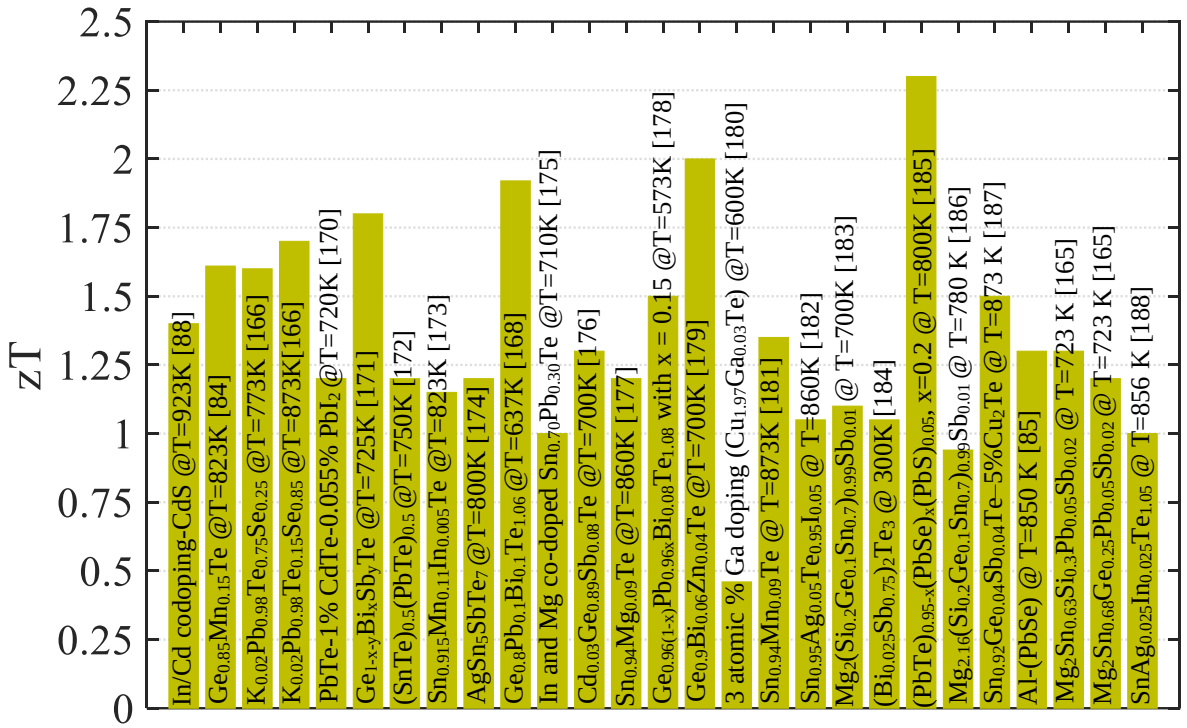

Figure 19: List of thermoelectric compounds using the band convergence approach combined with other enhancing methods to improve thermoelectric efficiency.

As shown in Figure 19, band convergence has been used to enhance the thermoelectric performance of chalcogenides. Rocksalt structured thermoelectric chalcogenides, such as PbTe, PbSe, and SnTe have been introduced as the top candidates for mid to high temperature applications, while their p-type thermoelectric efficiencies can be improved by aligning the valence bands [88, 169]. In this regard, SnTe has emerged as an environmentally-friendly alternative to the conventional thermoelectric compound PbTe, which contains the toxic element (Pb) [53]. One issue that limits the application of SnTe is its electronic structure. Similar to PbTe and PbSe, tin telluride (SnTe) has two valence bands: the light-hole valence band at the L point of the highly symmetrical Brillouin zone, and the other one the heavy-hole valence band lying at the Σ point energetically below the L point [157]. In contrast with the small band gap (0.18 eV, 300 K) [157], pristine SnTe has a much larger band offset between its two valence bands [88, 157, 189]. The room-temperature energy separation (ΔE) between the so-called upper light-hole band at the L point (Brillouin zone) and lower heavy-hole band at the Σ point of SnTe (~0.3-0.4 eV) is much bigger than in PbTe (ΔE ~0.17 eV) [88, 157, 175]. This large ΔE in SnTe prevents significant contribution of heavy-hole bands to the Seebeck coefficient for SnTe [88, 157, 175]. Moreover, the very small band gap of SnTe is not useful for retaining high thermoelectric performance at high temperatures because of its bipolar diffusion. Another reason why pristine SnTe is not considered to be a promising thermoelectric material is the ultra-high hole density (>10^{21}cm^{-3}) caused by the very large number of intrinsic Sn lattice vacancies [157, 175].

Recently, a work [53] reported an improved high power factor and thermoelectric performance of SnTe through the synergy of resonance levels, band convergence, and nanostructuring. The results show that the coexistence of resonant levels via In-doping and band convergence with Ca-doping made an improvement in the Seebeck coefficient, and thus power factor [53]. A Ca and In co-doped structure such as $Sn_{24}In_1Ca_2Te_{27}$ exhibits a higher density of state attributable to the In-doping.

Figure 20 illustrates the light-heavy valence offset $\Delta E_{L-\Sigma}$ for pristine SnTe, In-doped SnTe, and Ca and In co-doped SnTe compounds.

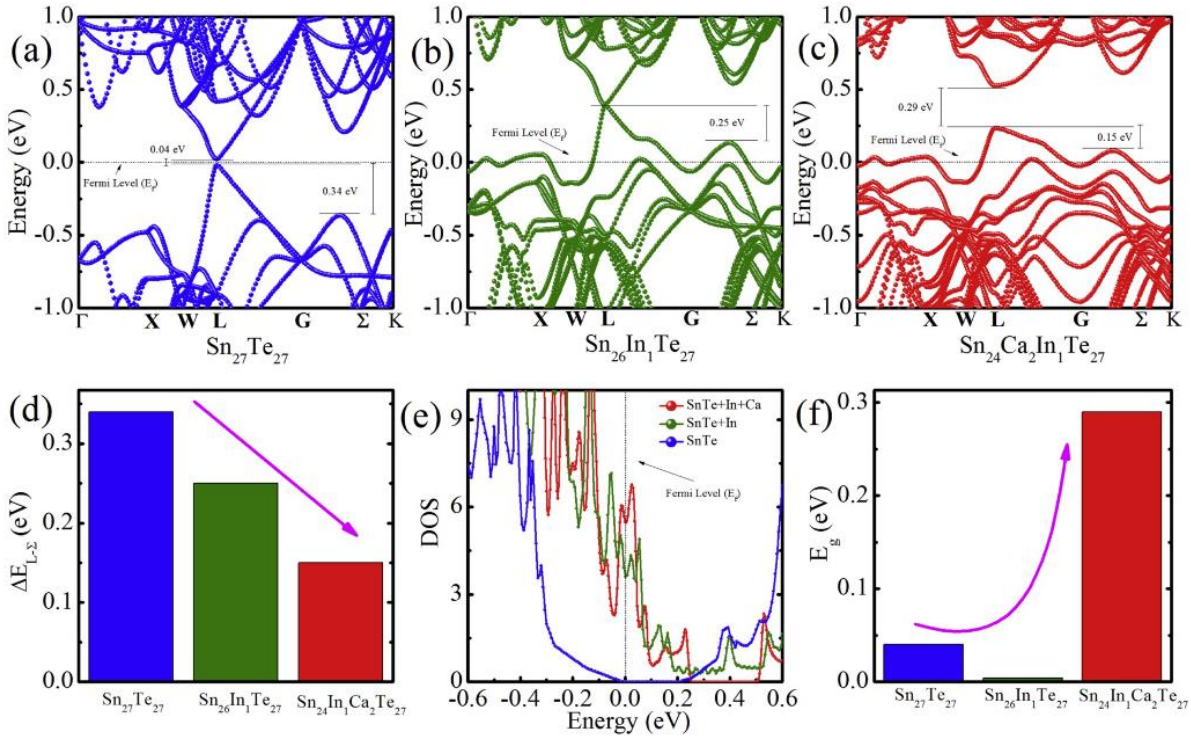

Figure 20: DFT calculation of the energy band structure a) $Sn_{27}Te_{27}$, b) $Sn_{26}In_1Te_{27}$, c) $Sn_{26}In_1Ca_2Te_{27}$, d) light-heavy valence offset $\Delta E_{L-\Sigma}$ for $Sn_{27}Te_{27}$, $Sn_{26}In_1Te_{27}$, and $Sn_{26}In_1Ca_2Te_{27}$, e) density of states of $Sn_{27}Te_{27}$, $Sn_{26}In_1Te_{27}$, and $Sn_{26}In_1Ca_2Te_{27}$ near the Fermi level, f) energy gap E_g for $Sn_{27}Te_{27}$, $Sn_{26}In_1Te_{27}$, and $Sn_{26}In_1Ca_2Te_{27}$, adapted from ref. [53] with permission.

Pristine SnTe has a large valance offset of $\Delta E_{L-\Sigma}$ =0.34 eV (Figure 20a), while In-doped compounds reduce the gap to 0.25 eV (Figure 20b), and the addition of Ca further reduces the valance offset to 0.15 eV (Figure 20c and 9). The comparison of conduction and valence band gaps (E_g) – as shown in Figure 20e and f – shows that the bandgaps of the SnTe and $Sn_{24}Ca_2InTe_{27}$ expand from 0.04 to 0.29 eV, respectively [53]. In other research [190], PbSe, as an attractive thermoelectric material, was mixed with $NaSbSe_2$ to make $NaPb_mSbSe_{m+2}$ and produce a new p-type, PbSe-based thermoelectrics. The calculations based on density functional theory and photoemission spectroscopy demonstrate that introduction of $NaSbSe_2$ decreases the energy separation between

the L- and Σ-valence bands and provides an enhancement in the power factors under a temperature of 700 K. Two beneficial effects were reported for alloying $NaSbSe_2$ into PbSe in terms of thermoelectric characteristics, based on the reduction of the energy separation between L- and Σ-valence bands, which increased the density of states' effective mass and thus the power factors, and enabled the creation of strong point-defect phonon scattering, which decreases the thermal conductivity without nanostructuring [190]. Kanatzidis et al. [84] present the DFT calculations of the electronic structure regarding modifications of the valence band structure GeTe via the introduction of Mn. The band calculations show that the conduction bands are made mostly based on Ge 4p states and the valence bands chiefly based on Te 5p states for both the rhombohedral and rock-salt structures. On the basis of the calculations for the rhombohedral $Ge_{1-x}Mn_xTe$ structure, the energy difference between the first and second valence band maxima decreases to 0.04 eV for $Ge_{25}Mn_2Te_{27}$ in comparison with pristine GeTe (0.15 eV), which signifies that band convergence of the two valence bands has occurred. However, that energy difference stays unchanged for $Ge_{26}MnTe_{27}$ as 0.14 eV. Moreover, the addition of MnTe (i.e., Mn-doping) into GeTe created a new state in the band gap, regardless of the crystal structures being either rhombohedral (Figure 21 a-c) or rock-salt cubic (Figure 21 e-g), attributable to Mn 3d states, – displayed in red dots in Figure 21.

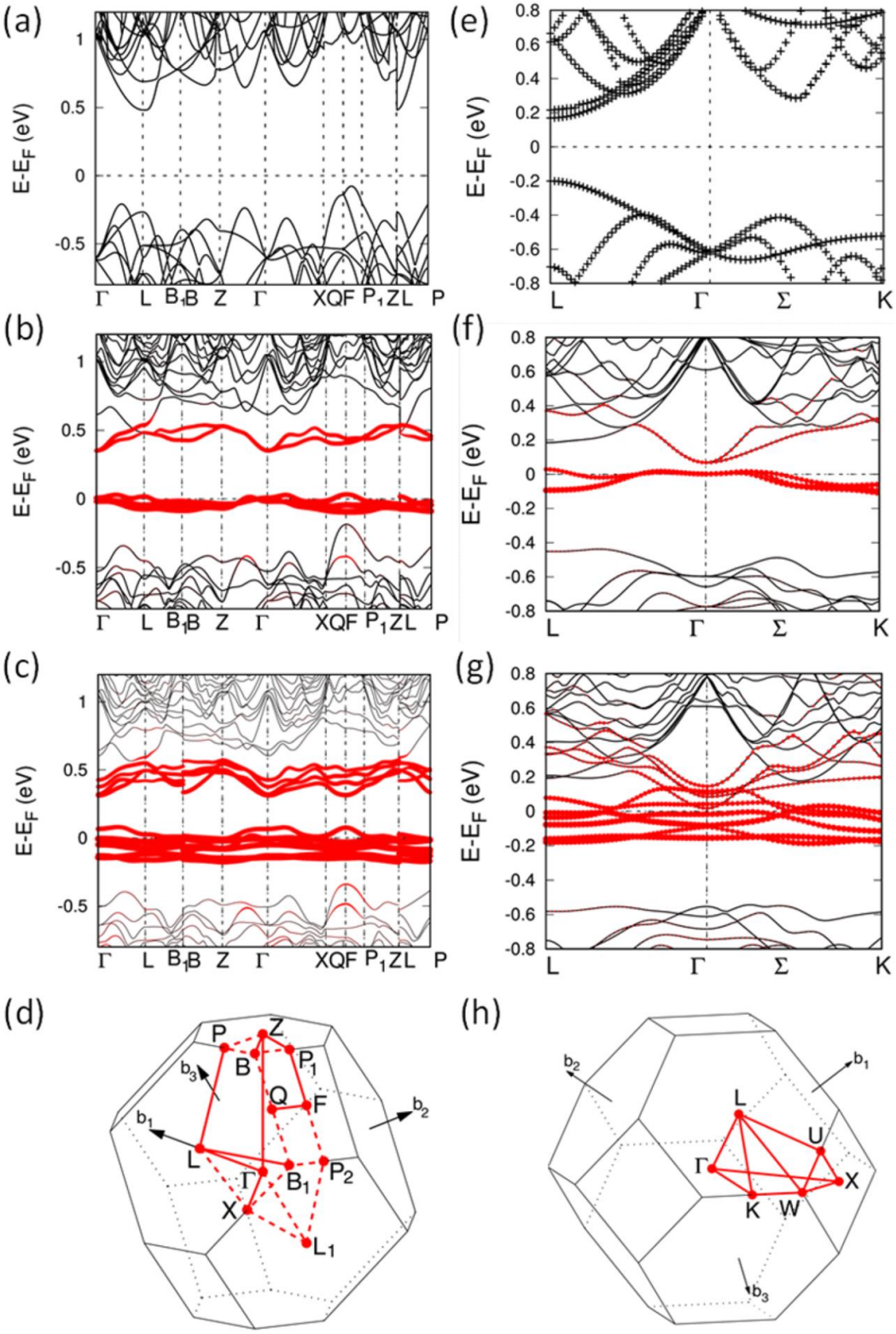

Figure 21: Band structure of $Ge_{27-x}Mn_xTe_{27}$ (x=0,1,2) compounds in (a-c) a low temperature rhombohedral structure, d) Brillouin zones of GeTe with a low temperature rhombohedral structure, (e-g) a high temperature cubic structure, and h) Brillouin zones of GeTe with a high

temperature cubic structure. MnTe creates some impurity states in the band gap, as illustrated by the red dots, reused from ref. [84] with permission.

As illustrated in Figure 21, alloying with MnTe enhances convergence of the two valence bands of $Ge_{1-x}Mn_xTe$, both in the rhombohedral and the rock-salt cubic phase. In addition, introduction of MnTe provides the extra states in the gap for both the low temperature rhombohedral phase (Figure 21a-c), and the high temperature cubic phase (Figure 21 e-g). At high temperatures (as exhibited in Figure 21e-g), the main involvement to the hole transport is achieved from the valence band maximum at the L and Σ points of the Brillouin zone. In pure GeTe with a cubic structure (Figure 21e), the energy difference between the valence band maxima at the L and Σ points is about 0.21 eV, while after the introduction of MnTe, the energy difference of $Ge_{26}MnTe_{27}$ and $Ge_{25}Mn_2Te_{27}$ reduces to 0.05 and 0.01 eV, respectively [84].

Implementing the band convergence – engineering bands with different energies to have the same energy via raising or lowering to align bands – via alloying is linked to the underlying nature of the chemical bonds in thermoelectric compounds [76, 158]. In this field, depending on the materials and the positions of the band in the Brillouin zone, the energy of the band may vary with the changing bonding interactions in the alloys [76, 158]. Therefore, by considering the collaboration of both light (L-band) and heavy (Σ-band) valences, the Hall carrier concentration and Seebeck coefficients can be expressed as follows:

$$n_H = \frac{(n_L\mu_L + n_\Sigma\mu_\Sigma)^2}{(n_L\mu_L^2 + n_\Sigma\mu_\Sigma^2)} \qquad (15),$$

$$S = \frac{\sigma_L S_L + \sigma_\Sigma S_\Sigma}{\sigma_L + \sigma_\Sigma} \qquad (16),$$

where, n, μ, and S stand for the carrier concentration, mobility, and Seebeck coefficient, respectively [162].

Here the question is when the band convergence is effective to enhance the thermoelectric properties. One idea that should be considered is the presence of another band near the primary

band, which mostly associates to the carrier transport. For n-type compounds, the second band should be located with an energy above the primary band. For p-type materials, a second band with an energy just below the primary band is a strong candidate that can contribute to in band convergence [76]. As an obvious reported outcome for the band convergence strategy, unlike band flattening, the effectively converged light and heavy valence/conduction bands increase the band degeneracy (N_V), and thus enhance the density state effective mass (m_d^*) with no significant reduction of mobility [76, 165]. As abovementioned and represented in Equation 18 (heavily doped TE materials), a high Seebeck coefficient can be achieved by manipulating the density state effective mass (m_d^*) through band convergence, even though it does not result in any reduction in electrical conductivity (σ), as happens in the case of band flattening [76, 86].

$$S = \frac{8\pi^2 k_B^2 T}{3eh^2}\left(\frac{\pi}{3n}\right)^{3/2} m_d^* \qquad (17).$$

The relationship of m_d^* and the effective mass of the single Fermi pocket (m_b^*) is expressed as Equation 19 [76, 86]:

$$m_d^* = N_V^{2/3} m_b^* \qquad (18).$$

During the band convergence, N_V and consequently m_d^* (becoming heavier) are increased, while the m_b^* stays constant. However, band flattening will increase m_b^* instead of N_V. Based on the calculated expression (Equation 19) [76] for electrical conductivity (σ) through collaboration of N_V and m_b^*, it is clear that the band flattening decreases σ:

$$\sigma = \left(\frac{2}{3}\right)^2 \frac{e^2 h}{\pi^{5/2}} \frac{N_V C_l}{m_b^* \Xi^2} F_0(\eta) \qquad (19).$$

Here, the band-related parameters of C_l, and Ξ are the elastic constant, and the deformation potential, respectively. Therefore, according to Equation 19, band convergence provides greater N_V with constant m_b^*, which results in a higher σ. However, band flattening m_b^* is increased with a constant N_V, which reduces σ. Hence, band convergence is an effective approach to optimize the power factor, as it improves both the Seebeck coefficients and electrical conductivity [76]. Recently,

Parkand et al. [167] investigated the behaviours of band convergence helpful for thermoelectrics, based on the additional inter-band scattering of carriers to other bands caused by band convergence. They performed first-principles treatment of electron-phonon (e-ph) scattering in $CaMg_2Sb_2$-$CaZn_2Sb_2$ Zintl alloy and full Heusler Sr_2SbAu to demonstrate the benefit of band convergence based on inter-band scattering. The results highlighted that electron-phonon scattering among the bands can intrinsically cancel out the advantage of band convergence, specifically in the case of bands converging at one k-point. Also, they stated that multi-band convergence at a single k-point (e.g., in the Zintl alloy) is much less advantageous than multi-pocket convergence at distant k-points, such as in the full Heuslers. Generally, the electronic states within the few k_BT around the Fermi energy associate in the thermoelectric transport. Therefore, band convergence can be used to have a greater number of closely-spaced electronic bands around the Fermi energy, (i.e., increasing the N_V) via tuning of the periodical band structure [86, 173].

2.3.4 Resonance level

Local distortion of the density of states (DOS) via formation of resonant states near the Fermi level is regarded as an efficient strategy to improve the Seebeck coefficient [36, 88, 89, 191]. Mahan and Sofo [78] derived a mathematical function for the thermoelectric figure of merit, based on the transport distribution. A delta-shaped transport distribution was mentioned to maximize the thermoelectric properties. The results designated that a narrow energy distribution of the electrons contributing to the transport process is required to achieve maximum thermoelectric efficiency. One of the possible realizations of this idea was discussed, based on a situation in which the conduction or valence band of the host semiconductor resonates with one energy level of a localized atom [78]. Heremans et al. [35] explored improving the Seebeck coefficient via a distortion of the electronic density of states and reported successful implementation using the thallium (Tl) impurity levels in lead telluride (PbTe). Such band structure engineering resulted in a doubling of zT in p-type PbTe to above 1.5 at a temperature of 773 K. This local improvement in DOS within a small energy range

can be realized when the dopant energy level resonates with the valence or conduction band of the host semiconductor compounds. A fundamental relationship between this local increase in DOS and S is given by the Mott expression (Equation 20) [97, 104, 170]:

$$S = \frac{\pi^2}{3}\frac{k_B}{q}\, k_B T \left\{\frac{d[\ln(\sigma(E))]}{dE}\right\}_{E=E_F}$$

$$= \frac{\pi^2}{3}\frac{k_B}{q}\, k_B T \left\{\frac{1}{n}\frac{dn(E)}{dE} + \frac{1}{\mu}\frac{d\mu(E)}{dE}\right\}_{E=E_F} \quad (20),$$

where k_B is the Boltzmann constant, e is the electronic charge, $\sigma(E)$ is the energy-dependent electrical conductivity, E_F is the Fermi energy, $n(E)$ is the energy-dependent carrier concentration, and $\mu(E)$ is the energy-dependent mobility.

The idea of the resonance level (i.e., the virtual bound state) has been considered in condensed matter physics and evaluated in various studies [86, 97, 104, 170]. To adequately achieve the benefits of this scenario, the resonance levels need to be appropriately located near the Fermi level to significantly enhance the Seebeck coefficient at a constant carrier concentration [170]. Consequently, tuning of the carrier concentration is required to locate the Fermi level around the resonance level [170]. As represented by Equation 21, the Seebeck coefficients can be increased by two mechanisms: either an increased energy-dependence of $n(E)$, a strong energy dependence in the electronic density of states, or an increased energy dependence of $\mu(E)$; for instance, by a scattering mechanism that strongly depends on the charge-carrier's energy [36, 86, 97]. In other words, the resonant levels can enhance the Seebeck coefficient based on two mechanisms, including carriers in extended states, such as the plane-wave-like wave function formed by dopant impurities to carry electricity and heat, and thus contribute to the Seebeck coefficient in a nearly temperature-independent way; furthermore, resonant scattering provides an electron energy filtering effect, and increases the Seebeck coefficient specifically at low temperatures, where the electron-phonon interactions are weaker [157]. The resonance level strategy can be achievable through the doping mechanism, in which the energy band of the isolated dopant impurity locates above the conduction

band edge of the host or below the valence band edge. The smaller width of the resonant level would result in larger distortion in the electronic density of states, leading to larger improvement in the Seebeck coefficient [86]. Figure 22 displays the calculated DOS (Figure 22a) for pristine SnTe, Mn-doped, In-doped, Mn-In co-doped compounds, and the schematic band structure, based on the resonant level (RL) and band convergence (Figure 22b). As illustrated in this Figure, for In-doping ($In_xSn_{1-x}Te$) an obvious DOS peak is located about 0.2 eV lower than the edge of the band gap, indicating a very local resonant level resulting from the In-Te antibonding state. The DOS near the top of the valence band for the Mn-doped compound ($Sn_{1-x}Mn_xTe$) is significantly higher than for the pristine SnTe, which resulted based on the band convergence of the light and heavy valence bands. The Mn-In co-doped compounds show the DOS peak created by In-doping after incorporating Mn atoms in the lattice. Based on the calculations, the increased DOS near the top of the valence band is still higher than that of In-doped SnTe, which confirms the presence of the resonant state in Mn, In co-doped SnTe compounds. Both the resonant level of In-doping and band convergence of Mn-doping were reported to be effective in improving the S and $S^2\sigma$ for pristine SnTe [173].

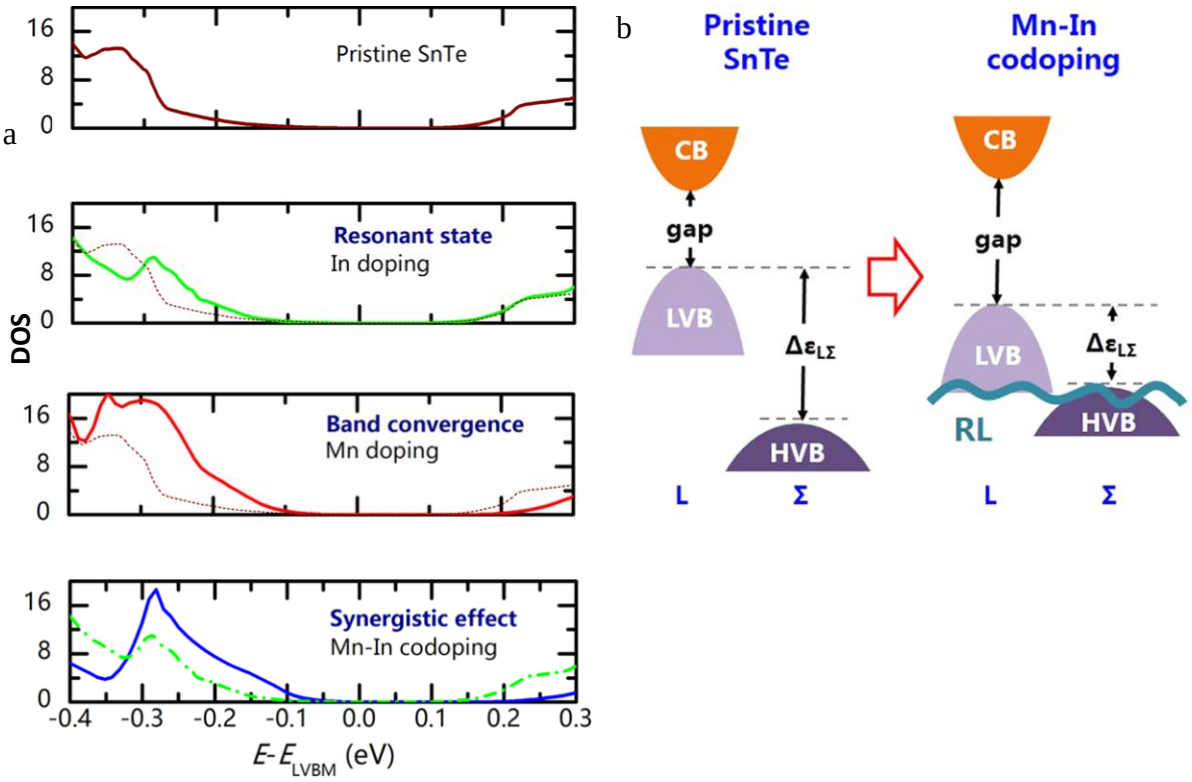

Figure 22: a) Calculated DOS for pristine SnTe and its In-doped, Mn-doped and In, Mn co-doped compounds with spin-orbit coupling. The top of the light valence band is at 0 eV, b) Schematic band structure for pristine and In-Mn co-doped compounds to show the presence of resonant levels and band convergence [173].

Chen et al. [85] reported n-type PbSe thermoelectric compounds with a figure of merit (zT) of 1.3 (300% higher than pristine PbSe) at a temperature of 850 K through the introduction of aluminium (Al) into lead selenide (PbSe). This zT was achieved by a combination of a high Seebeck coefficient resulting from the resonant states in the conduction band caused by the Al dopant (i.e., an increase of the local DOS near the Fermi level), and low thermal conductivity due to the presence of the nanosized phonon scattering centres, such as numerous distinctive microstructures, Pb depleted discs, small grains, and 10 nm sub-grains [85]. It is noteworthy that the resonant state, as a distortion of the DOS, may largely decrease σ owing to the reduction in carrier mobility (μ) at high doping levels. Therefore, lower resonant state doping and higher band convergence doping are preferred

[173]. Resonant levels, in contrast, do not necessarily involve d-levels, but can arise from s and p-levels, especially in semiconductors [36].

Moreover, because of the Fermi level pinning, not all resonant impurities are favourable to thermoelectric power improvement [192]. This can be explained based on the position of such levels inside the conduction band. For example, if the resonant levels locate very deep inside the band, then the required carrier concentration may not be achieved to place the Fermi level at the modified density [192]. Furthermore, to implement the performance of the resonance levels in thermoelectric compounds, the resonance levels must contribute to the charge conduction and should not trap the charge carriers; also, the background density of states should be negligible [192].

2.3.5 Dopant stability

Thermoelectric compounds are usually made based on heavy doping with impurity atoms to provide the required carrier concentration for good thermoelectric performance [50]. Generally, any substitution via introduction/substitution of different atom sizes and masses tends to induce strain-stress impact or mass fluctuations in the crystal lattice [148]. In this field, elastic stiffness constants, as the important characteristics, are used to evaluate the elastic properties of the compounds. The number of independent elastic constants is usually reduced if the systems have symmetry elements. Mouhat et al. [193] explained the generic elastic stability conditions for crystals (Table 1). The generalized tensorial form of Hook's law for the strain-stress relationship in a crystal can be expressed as:

$$\sigma_i = C_{ij}\varepsilon_j \qquad (21).$$

For instance, in the case of cubic crystals, the conditions of stability reduce to a very simple form:

$$C_{11} - C_{12} > 0, C_{11} + 2C_{12} > 0, C_{44} > 0 \quad (22).$$

The above equations for the cubic crystal system are well known [193-196]. However, there are many other promising thermoelectric compounds with crystal structures different from the cubic crystal structure [45, 197-199].

The elastic behaviours of a lattice are described by its matrix of second-order elastic constants:

$$C_{ij} = \frac{1}{V_0}\left(\frac{\partial^2 E}{\partial \varepsilon_i \, \partial \varepsilon_j}\right) \quad (23).$$

Here E is the energy of the crystal, V_0 its equilibrium volume, and ε denotes a strain [193].

Table 1: Elastic stability conditions for crystals. The elastic matrix (also called the stiffness matrix) has size 6 × 6 and is symmetrical. It is composed of 21 independent components [193].

Crystal structure and matrix components	Born stability criteria
$\mathbf{C_{cubic}} = \begin{pmatrix} \mathbf{C_{11}} & \mathbf{C_{12}} & \mathbf{C_{12}} & & & \\ . & \mathbf{C_{11}} & \mathbf{C_{12}} & & & \\ . & . & \mathbf{C_{11}} & & & \\ & & & \mathbf{C_{44}} & & \\ & & & & \mathbf{C_{44}} & \\ & & & & & \mathbf{C_{44}} \end{pmatrix}$	$C_{11} - C_{12} > 0,$ $C_{11} + 2C_{12} > 0,$ $C_{44} > 0$
$\mathbf{C_{hexa,tetra\ I\ (4/mmm)}} = \begin{pmatrix} \mathbf{C_{11}} & \mathbf{C_{12}} & \mathbf{C_{13}} & & & \\ . & \mathbf{C_{11}} & \mathbf{C_{13}} & & & \\ . & . & \mathbf{C_{33}} & & & \\ & & & \mathbf{C_{44}} & & \\ & & & & \mathbf{C_{44}} & \\ & & & & & \mathbf{C_{66}} \end{pmatrix}$	$C_{66} = (C_{11} - C_{12})/2$ $C_{11} > \lvert C_{12}\rvert,$ $2C_{13}^2 < C_{33}(C_{11} + C_{12}),$ $C_{44} > 0, C_{66} > 0$
$\mathbf{C_{tetra\ II\ (4/m)}} = \begin{pmatrix} \mathbf{C_{11}} & \mathbf{C_{12}} & \mathbf{C_{13}} & & & \mathbf{C_{16}} \\ . & \mathbf{C_{11}} & \mathbf{C_{13}} & & & \mathbf{-C_{16}} \\ . & . & \mathbf{C_{33}} & & & \\ & & & \mathbf{C_{44}} & & \\ & & & & \mathbf{C_{44}} & \\ . & . & & & & \mathbf{C_{66}} \end{pmatrix}$	$C_{11} > \lvert C_{12}\rvert,$ $2C_{13}^2 < C_{33}(C_{11} + C_{12}),$ $C_{44} > 0, 2C_{16}^2 < C_{66}(C_{11} - C_{12})$

$\mathbf{C_{rhombo\ I}} = \begin{pmatrix} \mathbf{C_{11}} & \mathbf{C_{12}} & \mathbf{C_{13}} & \mathbf{C_{14}} & & \\ . & \mathbf{C_{11}} & \mathbf{C_{13}} & \mathbf{-C_{14}} & & \\ . & . & \mathbf{C_{33}} & & & \\ . & . & & \mathbf{C_{44}} & & \\ & & & & \mathbf{C_{44}} & \mathbf{C_{14}} \\ & & & & . & \mathbf{C_{66}} \end{pmatrix}$	$C_{11} > \lvert C_{12}\rvert, C_{44} > 0,$ $C_{13}^2 < \frac{1}{2}C_{33}(C_{11} + C_{12}),$ $C_{14}^2 < \frac{1}{2}C_{44}(C_{11} - C_{12}) \equiv C_{44}C_{66}$
$\mathbf{C_{rhombo\ II}} = \begin{pmatrix} \mathbf{C_{11}} & \mathbf{C_{12}} & \mathbf{C_{13}} & \mathbf{C_{14}} & \mathbf{C_{15}} & \\ . & \mathbf{C_{11}} & \mathbf{C_{13}} & \mathbf{-C_{14}} & \mathbf{-C_{15}} & \\ . & . & \mathbf{C_{33}} & & & \\ . & . & & \mathbf{C_{44}} & & \mathbf{-C_{15}} \\ . & . & & & \mathbf{C_{44}} & \mathbf{C_{14}} \\ & & & . & . & \mathbf{C_{66}} \end{pmatrix}$	$C_{11} > \lvert C_{12}\rvert, C_{44} > 0,$ $C_{13}^2 < \frac{1}{2}C_{33}(C_{11} + C_{12}),$ $C_{14}^2 + C_{15}^2 < \frac{1}{2}C_{44} \ldots$ $\ldots (C_{11} - C_{12}) \equiv C_{44}C_{66}$
$\mathbf{C_{ortho}} = \begin{pmatrix} \mathbf{C_{11}} & \mathbf{C_{12}} & \mathbf{C_{13}} & & & \\ . & \mathbf{C_{22}} & \mathbf{C_{23}} & & & \\ . & . & \mathbf{C_{33}} & & & \\ . & & & \mathbf{C_{44}} & & \\ . & & & & \mathbf{C_{55}} & \\ & & & & & \mathbf{C_{66}} \end{pmatrix}$	$C_{11} > 0, C_{11}C_{22} > C_{12}^2$ $C_{11}C_{22}C_{33} + 2C_{12}C_{13}C_{23} - C_{11}C_{23}^2$ $- C_{22}C_{13}^2 - C_{33}C_{12}^2 > 0$ $C_{44} > 0, C_{55} > 0, C_{66} > 0$

In addition, these elastic parameters are linked with other mechanical features through empirical expressions, expressed as follows [200, 201]:

$E = \frac{9BG}{3B+G}$ (24),

$B = \frac{C_{11}+2C_{12}}{3}$ (25),

$\vartheta = \frac{3B-2G}{2(3B+G)}$ (26),

$A = \frac{2C_{44}}{C_{11}-C_{12}}$ (27),

where E and B are Young's and Bulk's moduli respectively, ϑ stands for Poisson's ratio, and A shows the anisotropy ratio. Based on the Poisson's ratio, the stability condition of the material against the shear presents the ratio of transverse strain to the longitudinal strain and provides information about the nature of bonding forces among the constituent atoms in a compound. A low

value of the Poisson's ratio shows a large compression of volume and a higher value indicates plasticity [200, 201]. The solubility limit, optimizing the chemical potential, [158] chemical instability in air at high temperatures, elemental toxicity [120], electronic structure, and physical properties, [153] should be considered in developing the thermoelectrics. In the magnetic doping scenario, strong hybridization between transition metal d-states and the anion p-state is an important parameter contributing to ferromagnetism stabilization [110].

Electronegativity difference ($\Delta\chi$) is a scale to evaluate the covalency of the bonding in a material [202]. For example, large $\langle\Delta\chi\rangle$ shows ionic bonding, which results in the carrier's scattering by polar optical phonons and a reduction of the carrier mobility [202]. Slack [203] pointed out that materials with a small electronegativity difference between their constituent atoms show high mobility values. $\langle\Delta\chi\rangle \leq 0.5$ has been proposed as an initial screening value in the search for good thermoelectric compounds (e.g., $\langle\Delta\chi\rangle_{Bi_2Te_3}$=0.3) [202, 203]. Skutterudites (e.g., $\langle\Delta\chi\rangle$=0.11 for $CoSb_3$) were first identified based on this screening process. Also, this is one of the reasons for the poor performance of oxides as thermoelectric materials (e.g., $\langle\Delta\chi\rangle_{ZnO}$=1.79 and $\langle\Delta\chi\rangle_{SrTiO_3}$=2.2) [202]. This effect should be considered in the doping process. In a work [166], K^+ and Na^+ dopant substitution instead of Pb^{2+} in the PbTe and PbSe systems were evaluated, in which both K and Na have lower Pauling electronegativities than Pb. The solubilities of K and Na were reported based on the electronegativity difference of the average anion (Te^{2-} or Se^{2-}) and cation (Pb^{2+} together with K^+or Na^+) after doping. In general, a larger electronegativity difference provides higher solubility. Because K has a lower electronegativity (0.82) in comparison with Na (0.93), the average cation electronegativity after doping was determined as being lower for the K-doped samples. In the case of PbTe, a lower average cation electronegativity decreased the electronegativity difference, depending on the difference for Te^{2-} and Pb^{2+} without doping: therefore, K showed less solubility than Na in PbTe. Unlike for PbSe, a lower average cation electronegativity widened the

electronegativity difference, depending on Se^{2-} and Pb^{2+} without doping; therefore, K provided a higher solubility than Na in PbSe [166].

Thermodynamic stability of the structures can be evaluated based on the calculation of the enthalpy of formation (ΔH_f), as expressed in Equation 28 [110, 195]:

$$\Delta H_f = E_{total}(A_nB_mC_l) - nE_A - mE_B - lE_C \quad (28),$$

in which, $E_{total}(A_nB_mC_l)$ represents the total ground state energies of the compounds and nE_A mE_B and lE_C are energies per unit cell of the individual constituents in their bulk forms at the ground state, and l, m, and n represent the number of A, B, and C atoms per unit cell, respectively. The negative ΔH_f confirms that the investigated structures are stable [110, 195].

In this regard, cohesive energy (E_{Coh}), as an important thermodynamical physical aspect, defines the capability of the material/compounds and determines the required energy to break the intermolecular physical links within the lattice structure. Cohesive energy per atom of a crystal A_xB_y, with x and y as the number of A and B atoms respectively, can be examined as follows [110, 200, 204]:

$$E_{Cohesive}^{A_xB_y} = \frac{[xE_{atom}^{A} + yE_{atom}^{B}] - E_{A_xB_y}}{x+y} \quad (29).$$

This energy is mainly applied to dissociate a solid into its constituent atoms or into basic structure blocks. It estimates the nature and strength of forces that hold the atoms together in a solid.

2.4 Lattice thermal conductivity (κ_l)-Phonon scattering mechanisms

In quantum mechanics, phonons are defined as a unit of vibrational energy arising from the atomic oscillation within a crystal lattice in a single frequency and transferring the thermal energy. There are two types of phonons to carry thermal energy within solids, including acoustic phonons as the coherent displacement of atoms in the direction of propagation (e.g., a sound wave in air), and optical phonon with an incoherent motion of the two neighbouring atoms in the opposite direction.

Figure 23 illustrates the schematic of the optical and acoustic components of phonon energy for two atoms [205].

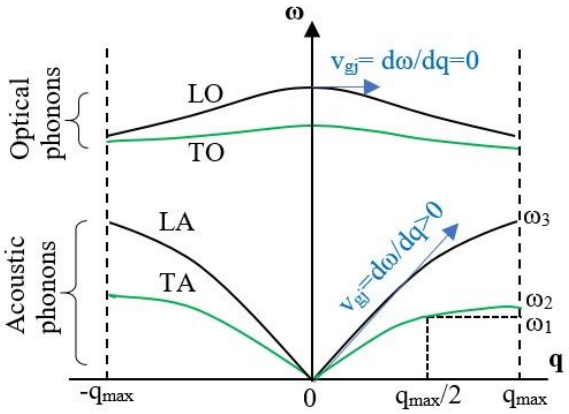

Figure 23: Acoustic and optical branches for phonon radiation (reused from ref.[45]).

As depicted in Figure 23, the group velocity (the speed of energy propagation) of the acoustic branches of phonon radiation, $V_g = {d\omega}/{dq}$, is more than zero ($V_g > 0$). The optical branches, however, have a group velocity equal to zero ($V_g \approx 0$) as q (the wave vector, which is a vector point in the direction of propagation of the phonon energy wave) tends to zero.

Also, in a solid, if A represents the number of atoms in a unit cell, the number of phonon branches will be $3A$, from which three branches are acoustic and the remaining (3A-3) are optical [206]. In addition, Table 2 represents the classification of acoustic and optical branches as longitudinal and transverse with their respective counts [206].

Table 2: Classification of phonon radiation energies for acoustic and optical branches [45].

Phonon type	Longitudinal	Transverse
Acoustic	1	2
Optical	A-1	2(A-1)

Both the acoustic and optical components of phonon energy can propagate both transversally and longitudinally within the crystalline solids, as schematically illustrated in Figure 24. The transverse acoustic (TA) (Figure 24a) branches have low frequency and are characteristic of low temperatures; while the longitudinal acoustic (LA) (Figure 24b) types are dominant at high temperatures and have high frequencies.

Figure 24: a) Tranverse Wave, b) Longitudinal Wave [45].

It is noteworthy that having a higher number of atoms (A) in a unit cell can be a recipe for obtaining lower thermal conductivity in the TE compounds, because the number of optical components of the phonon energy will increase. Also, absorbed energy can be transferred partially by the acoustic branches. Therefore, the remaining energy is attributed to the optical branches, which have a negligible contribution in heat transfer with zero propagation speed. Moreover, due to the limited phonon frequency (~10 THz), by increasing the optical branches, the acoustic phonon frequency declines, because the acoustic branches transfer only a partial amount of energy in the crystal. This fact influences the lattice thermal conductivity at a higher temperature in which the high-frequency phonons are the majority of heat carriers [206].

Therefore, to control the thermal conductivity, the phonon transition needs to be obstructed [207, 208] with appropriate strategies. The schematic diagram in Figure 25 illustrates the appropriate phonon scattering strategies against the temperature range.

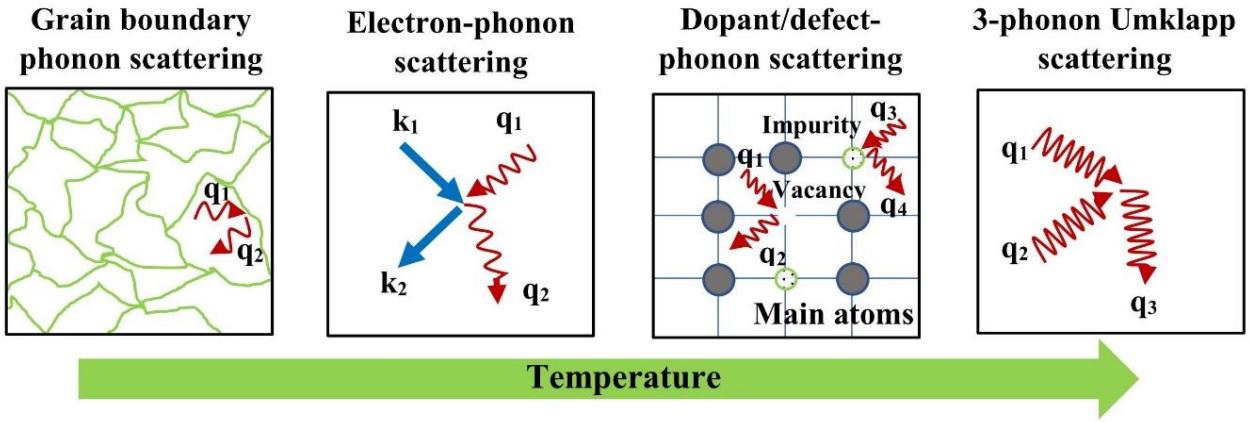

Figure 25: Phonon scattering mechanisms against the temperature ranges [45].

The results reported by [209, 210] showed that by employing the scattering mechanisms, the zT increases as the thermal conductivity decreases. However, precaution must be taken in decoupling the electrical and thermal conductivities. This means the introduction of the scattering barriers for phonon transfer may decrease the electrical conductivities. In this case, high values of σ/κ and n/κ_l (n: concentration of charged carriers) ratios can be regarded as a measure to promote decoupling between thermal and electrical conductivities, and arriving at high zT values [211, 212].

2.5 Electronic thermal conductivity (κ_e)

Reducing the vibrational component of total thermal conductivity (κ_t) – lattice thermal conductivity (κ_l) – has chiefly been considered in developing optimized thermoelectric products [45]. Besides attempting to reduce κ_l, the electronic thermal conductivity (κ_e) linked to the electrical conductivity also needs to be controlled and decreased [213-216]. In this regard, comprehending the impact of physical and chemical bonds on lattice dynamics and phonon transport can often evolve the highly efficient TEs by controlling the total thermal conductivity ($\kappa_t = \kappa_l + \kappa_e$) [217-219]. Observing a great interest in disconnecting the κ_l from κ_e, accurate calculation of the Lorenz number (L) is a principle step to indicating the precise contribution of electrical conductivity (σ) to κ_t via the Wiedemann-Franz relationship ($\kappa_e = L\sigma T$, T: absolute temperature) [213, 220, 221]. Selection of advanced materials with low Lorenz numbers will reveal the TE compounds with (1) low κ_e to

avoid violating the energy conversion factor (figure of merit-$zT = \frac{S^2\sigma}{\kappa_l+\kappa_e}T$), (2) high electrical conductivity ($\sigma = ne\mu$, n: carrier concentration, μ: carrier mobility, e: electron elementary charge), and (3) high power factor ($PF = S^2\sigma$, S: Seebeck coefficient) [213, 216]. By approximating the κ_l equal to zero, zT_{max} inversely relates to S^2/L, which highlights the Lorenz number contribution to optimizing the TE products [213, 222, 223]. In addition, an imprecise Lorenz number may not accurately evaluate TE materials to see whether they are approaching their amorphous margin of κ_l, or still require a greater reduction in thermal conductivity [216]. In this regard, the Wiedemann-Franz law can calculate κ_e for metals containing electrons as the main heat carriers, based on the reported Lorenz number – 2.45×10^{-8} $W\Omega K^{-2}$ – (the classic free electron model) [224]. In research [78] by Mahan and Sofo, the thermoelectric factors and Lorenz number were extracted from the transport function. Later, Mahan and Bartkowiak [225] stated that the Wiedemann-Franz law based on the classic free electron model ($L=2.45\times10^{-8}$ $W\Omega K^{-2}$) is not a law of physics, but is roughly true as a "rule of thumb". For example, a non-degenerate Lorenz number of a single parabolic band (SPB) is defined to be about 1.5 to 3.0×10^{-8} $W\Omega K^{-2}$, depending on the main scattering sources, such as ionized impurity, acoustic phonon, etc. [216, 226]. Therefore, this law within the defined Lorenz number of 2.45×10^{-8} $W\Omega K^{-2}$ cannot identify the relative contributions of κ_e and κ_l to κ_t precisely for all compounds; specifically, for those with complex scattering mechanisms or non-parabolicity bands, such as PbTe, SnS and SnSe [216, 227-230]. McKinney et al. [213] investigated the yield of a reduced Lorenz number via energy filtering and its subsequent associated impacts on zT. They reported that the zT of well-known thermoelectric compounds can be enhanced by lowering the Lorenz number due to the multi-band intervalley scattering. Several works [213, 220, 224, 231, 232] have studied the Lorenz number calculation through decoupling the lattice and electronic thermal conductivities. In this field, a transverse magnetic field with either high ($\mu B >> 1$) [224] or intermediate ($\mu B \approx 1$) [233-236] magnetic fields can be used to calculate the Lorenz numbers. Lukas et.al [220] applied a magnetothermal resistance (MTR) method developed by Goldsmid [234-

236] to extract the Lorenz number at low to intermediate magnetic fields. In this technique, the electrical and total thermal conductivities were measured under a constant temperature but varying transverse magnetic fields to follow the relationship of $\kappa(B)_{total} = LT\sigma(B) + \kappa_l$.

2.6 Transition metal chalcogenides

Metal chalcogenide (MC) compounds have achieved significant attention with the development of one-dimensional (e.g., nanorods, nanostrings, nanotubes), two-dimensional (e.g., nanosheets, nanoplates), and three-dimensional (e.g., nanocubes, nanostars) structures [237, 238]. Chalcogens are the chemical elements of group 16 in the periodic table, including oxygen (O), sulfur (S), selenium (Se), tellurium (Te), and polonium (Po). A transition metal chalcogenide (TMC) is a chemical compound consisting of at least one chalcogen anion (group 16) and one electropositive transition metal element (elements from group 3 to group 12). However, the chalcogenide term is more generally applied to sulfides, selenides, and tellurides than the oxides and polonium compounds. This statement can be attributed to extremely strong non-metallic characteristics of oxygen and high metallic features of the polonium element. There is a range of transition metal chalcogenides with numerous structures and compositions, for example Cu_2S, $CuSe$, $MnSe_2$, $CoSe_2$,Fe_3S_4, ScS_2, TiS_2, $TiSe_2$, CrS_2, FeS_2, $FeSe_2$, $CdTe$, HgS, etc. These compounds combine the non-metallic characteristics of chalcogens and the unfilled d-orbitals of transition metals. Moreover, the transition metal chalcogenides can be classified based on either the chalcogen elements, such as sulfides, selenides, tellurides, and multi-chalcogen based, or the number of elements, including binary, ternary, quaternary, etc. Even though most of the main group metal chalcogenides own stoichiometric compounds, transition metal chalcogenides can easily form off-stoichiometric compounds because of their unfilled d-orbitals. In this regard, non-stoichiometric binary TMCs can be divided into chalcogen rich phases, for example TiS_2, TaS_2, and metal rich phases, such as Ta_6S, Ta_2S. Furthermore, the transition, structural features and types of TMCs are

dependent on size of atoms, valence electron concentrations, metal-chalcogen bonding, chalcogen-chalcogen, and metal-metal bondings [239, 240].

2.7 Heusler compounds

Heusler compounds are divided into full- and half-Heusler types, based on ternary intermetallic materials [70, 241-245] with a stoichiometric composition of X_2YZ and XYZ, respectively [14, 246]. The full-Heusler alloys (FH) have an $L2_1$ cubic crystal structure with fcc lattice unit cells, containing four atoms as X at $(1/4,1/4,1/4)$ and $(3/4,3/4,3/4)$, Y at $(1/2,1/2,1/2)$, and Z at $(0,0,0)$ in Wyckoff coordinates, with a corresponding space group of $Fm-3m$ (No. 225) [14, 246]. Also, the half-Heusler alloys have a $C1_b$ cubic crystal structure with the absence of one of the X sub-lattices, and the corresponding space group of $F-43m$ (No. 216) [14, 246].

In the above-mentioned compositions, generally, X is filled with a high valence transition element, Y is substituted with a lower valence transition metal atom, and, finally, Z is an element in the III–V columns of the periodic table with $s-p$ type valence electrons [14, 246].

Figure 26 demonstrates the atomic arrangements for the full-Heusler, half-Heusler, and their corresponding elements in the periodic table.

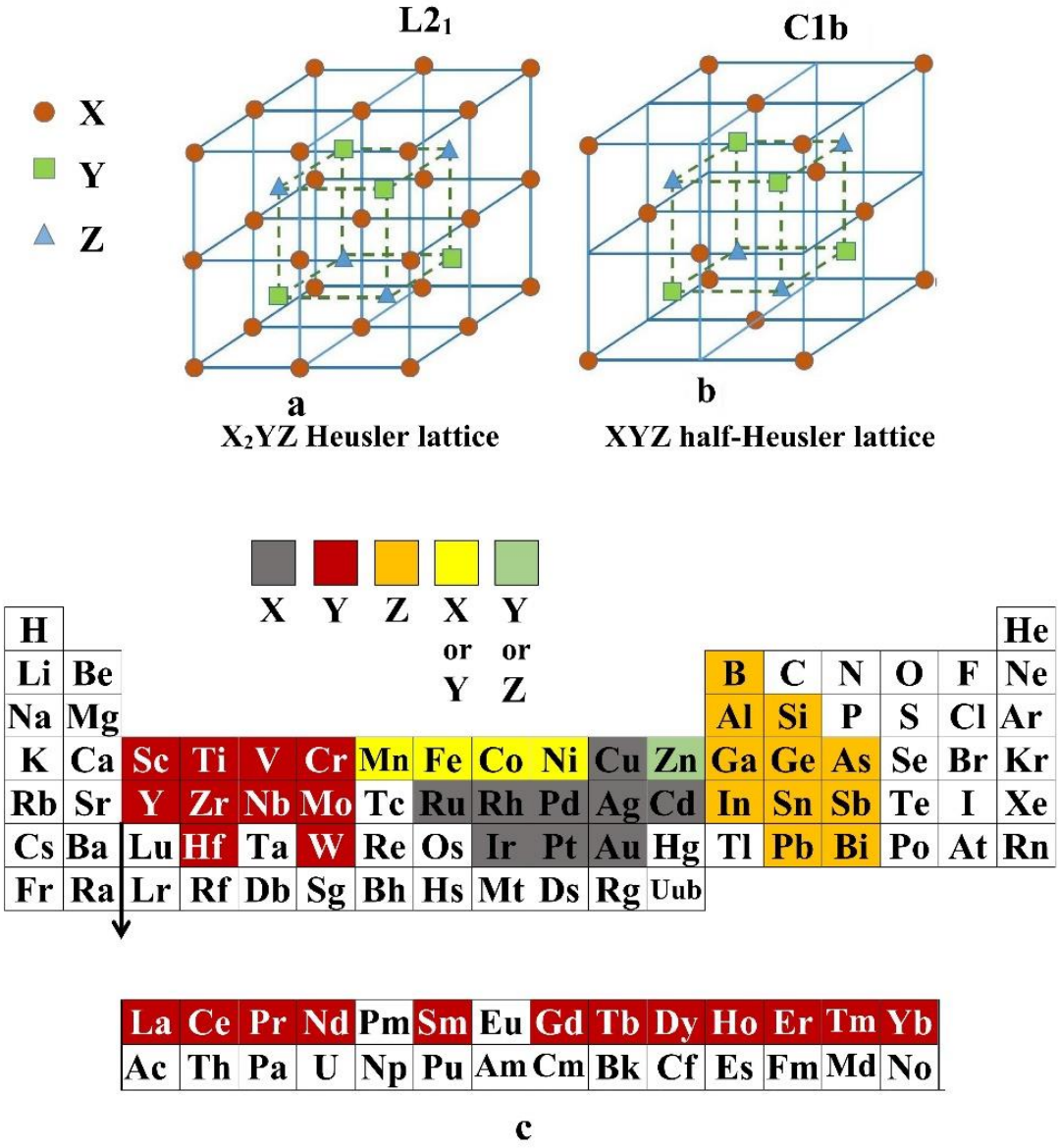

Figure 26: (a) full-Heusler crystal structures, (b) half-Heusler, and (c) specific elements in the Heusler alloys [45].

In the half-Heusler compounds, the distance of the elements in the *Y* locations is more than the full Heusler alloys (X_2YZ), causing less overlap of the d-like wave functions and, consequently, enlarging the band gaps in the density of states (DOS). This feature of the half-Heusler alloys provides them with a wide range of electronic and magnetic properties [247]. Moreover, these compounds can be tuned to obtain the desired electrical, thermal, and mechanical characteristics via composition/structural modification [248, 249]. In this regard, element doping with different

orbitals can be employed for engineering the electronic structural and improving zT – modifying the Seebeck coefficient and electrical conductivity [14, 207]. Unlike traditional experimental efforts for discovering new TE materials, density functional theory (DFT) as the basis of ab initio calculations [250], enables researchers to analyse and model the TE characteristics of half-Heusler alloys [251-254]. In spite of the strong motivation in theoretical investigation of half-Heusler TEs, accurate calculation of their TE characteristics has been challenging due to their complicated crystal structure and elemental properties. The main issue is to what extent the calculated wave functions based on the element locations in the XYZ crystal structure (e.g., the MgAgAs ordered arrangement) coincides with real synthesized half-Heusler samples.

2.8 Graphene products and applications

For the first time, standing graphene was discovered by Andre Geim and Konstantin Novoselov in 2004 [255], who were consequently awarded a Nobel prize for this work in 2011 [256]. Graphene owns a hexagonal structure (Figure 27) with an sp^2 covalent bond among the atoms in the network and a Van der Waals bond between the layers. It has two main types (Figure 27b), based on their edge structures, including Zigzag and Armchair types [257].

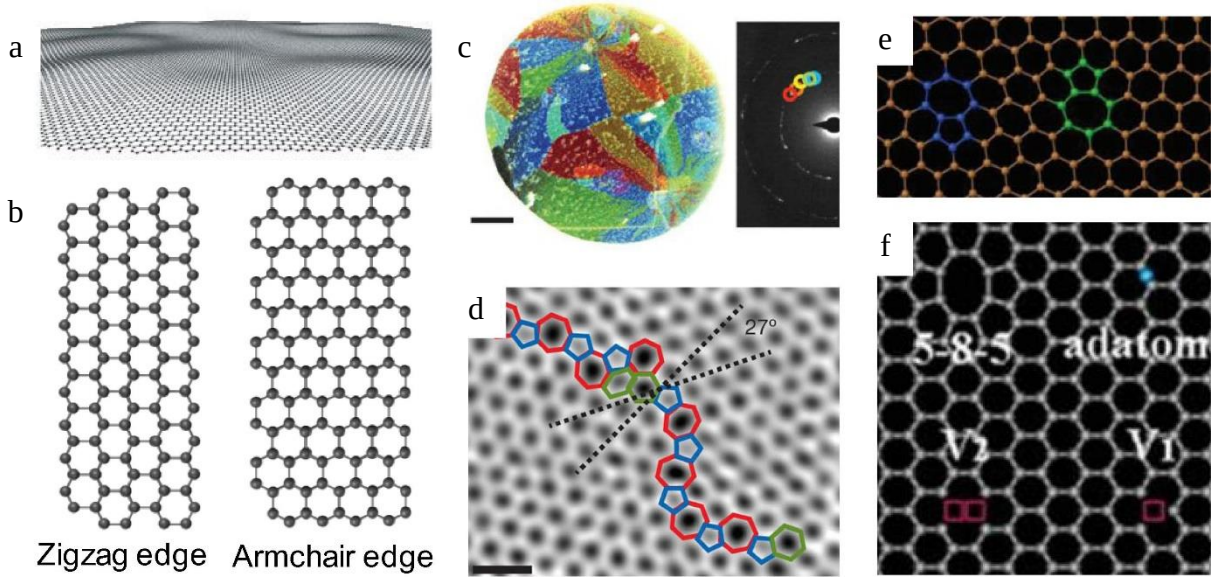

Figure 27: Structure and morphology of graphene. a) Corrugated graphene, b) Zigzag edge GNR and armchair edge GNR, [257] c) Left panel: grains emanated from a few points, Right panel: diffraction pattern taken from a region in the left image. The diffraction pattern reveals that this area is polycrystalline, d) Atomic-resolution ADF-STEM images of graphene crystals, e) Dislocation pair in graphene, f) Four defect types in graphene: an adatom, unrelaxed vacancies (V_1 and V_2) and a 5-8-5 rearrangement. Reused from ref. [258] with permission.

Graphene with a single atomic layer of sp^2 hybridized carbon atoms has several remarkable characteristics, such as thermoelectricity [208, 259-262], high Young's modulus (~1TPa) [263], tensile strength (~125 GPa) [263], high thermal conductivity (~2,000 W/mK) [264], high electron mobility (~200,000 cm^2/Vs) [264], high electrical conductivity (~6000 S/m) [265], and high specific surface area (2640 m^2/g) [266]. To date, graphene-based nanomaterials have demonstrated diverse applications such as in the electronic [267-270], biomedical [271-273], coating [274-276], and food industries [277-280]. Zhong et.al [258] summarized the percentage of graphene-based published research articles in numerous fields, as shown in Figure 28:

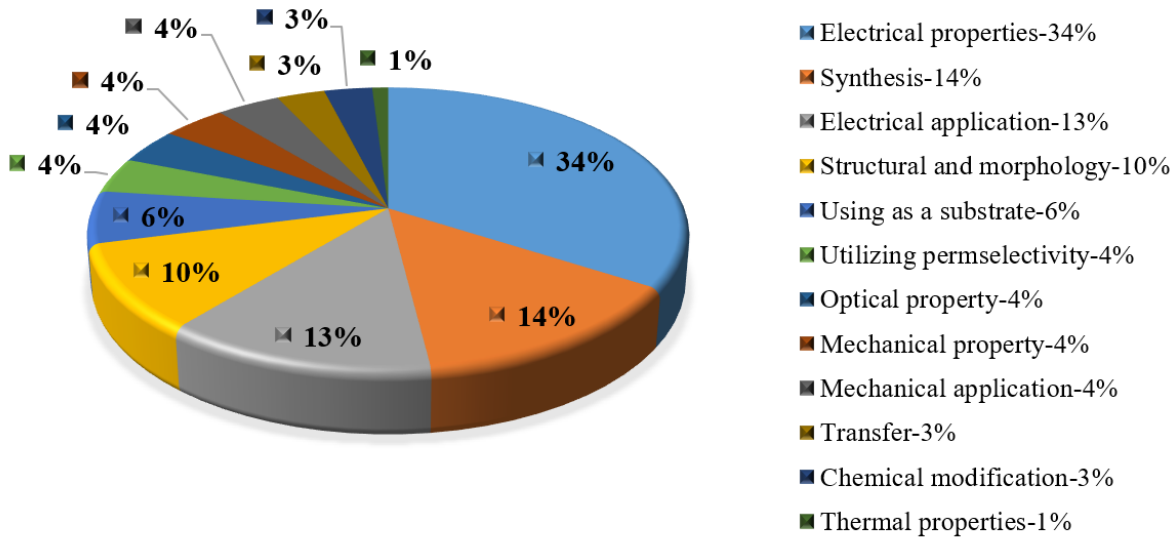

Figure 28: Classification of the published articles regarding graphene applications [257].

Encouraged by such interesting findings, graphene compounds (i.e., few layer graphene (FLG), reduced graphene oxide (RGO), etc.) were also tested to modify the efficiencies of thermoelectric compounds through microstructural manipulation [211, 281-284]; however, the outcomes were more complex due to the fact that the multilayer graphene (i.e. stacked single graphene layers) may not possess the same effect as the 2D defect-free single layer graphene [285-287].

The impact of graphene inclusion on the TE factors is summarized in Figure 29 through the critical analysis of several studies. In this figure, the Seebeck coefficients (S), electrical conductivity (σ), thermal conductivity ($\kappa_t = \kappa_l + \kappa_e$), and their contribution in the unit-less parameter of the figure of merit ($zT = \frac{S^2\sigma}{\kappa}T$) for pristine TE compounds and their graphene-reinforced compositions are presented.

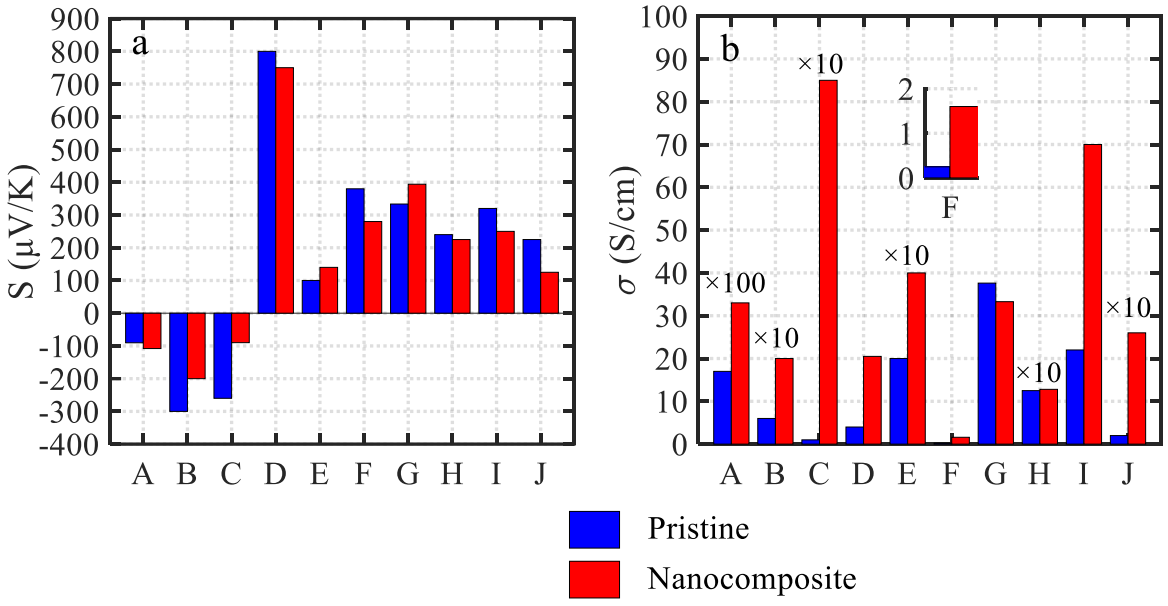

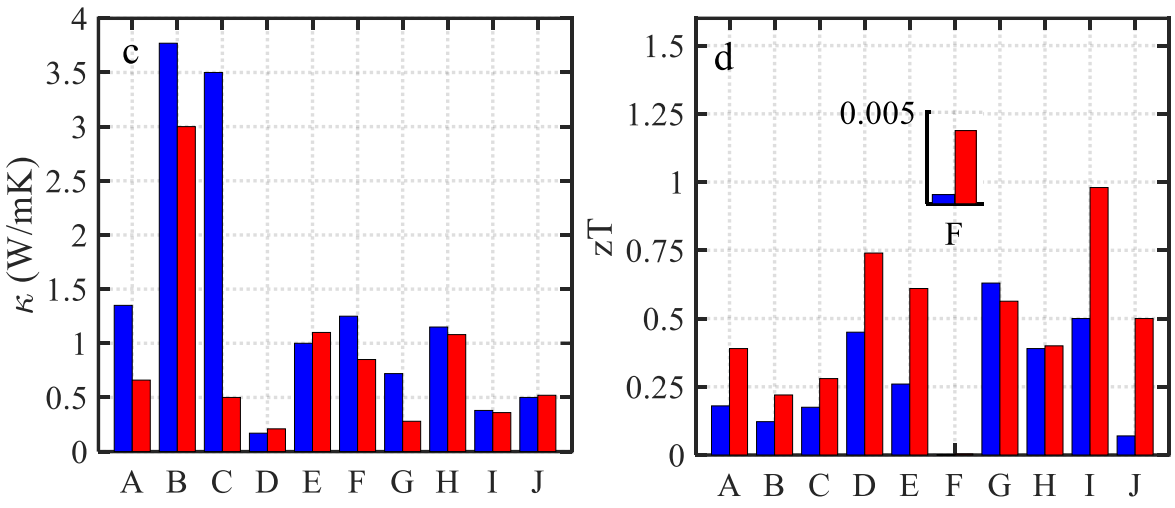

Figure 29: TE characteristics of the pristine and graphene-reinforced nanocomposites, a) Seebeck coefficients, b) electrical conductivities, c) lattice thermal conductivity (E and H which show total thermal conductivity) and d) dimensionless figure-of-merit (zT)- A) $Bi_{0.85}Sb_{0.15}$-0.5wt.%G [211], B) Nb-doped $SrTiO_3$-RGO [288], C) $Zn_{0.98}Al_{0.02}O$-1.5wt.%RGO [289], D) p-Phenediamino-modified graphene (PDG) [290], E) $CoSb_3$/G[291], F) $LaCoO_3$-0.01 wt.% G [292], G) MnTe-GNPs [41], H) $CuInTe_2$/G (80:1) mass ratio [212], I) SnSe-3.2 wt% MoS_2/G [281].

As shown in Figure 29, graphene compounds have shown various impacts on thermoelectric compounds. In the following sections, the scientific and engineering aspects of the graphene effects on electrical and thermal transport and the mechanical properties of thermoelectric compounds are discussed.

2.8.1 Graphene impact on the thermoelectric properties

2.8.1.1 Seebeck coefficient

As aforementioned, the Seebeck coefficient of a degenerate semiconductor and the carrier mobility can be expressed by [293, 294]:

$$S = \frac{\pi^2 k_B^2 T}{3q}\left[\frac{\partial \ln(\partial(E))}{\partial E}\right]_{E=E_f} = \frac{\pi^2 k_B^2 T}{3q}\left[\frac{1}{n}\frac{\partial n(E)}{\partial E} + \frac{1}{\mu}\frac{\partial \mu(E)}{\partial E}\right]_{E=E_f} \quad (30),$$

$$\mu(E) = q\tau(E)/m_d^* \quad (31),$$

where E is the energy, n (E) stands for the energy-dependent carrier density and m_d^* is the effective mass of the charge carrier, while n, μ, q, K_B, E_f, and τ are the carrier concertation, carrier mobility, carrier charge, Boltzmann constant, Fermi energy, and charge carrier relaxation time, respectively. Assuming a parabolic energy band and the dependency of the relaxation time (τ) on the energy and scattering factor (λ) via $(\tau = \tau_0 E^{\lambda - \frac{1}{2}})$ (τ_0 is an energy-independent constant) [293, 294], Equation 32 can be written as [294]:

$$S \approx \frac{\pi^2 k_B^2 T}{3q} \left[\frac{N(E)}{n} + \frac{\lambda - \frac{1}{2}}{Ef} \right]_{E=E_f} \qquad (32),$$

where $N(E)$ is the electronic density of the states. Based on Equation 7, the Seebeck coefficient depends directly on the scattering factor (λ) and is inversely affected by the charge carriers' concentration if the other parameters remain unchanged. It is well established that graphene reinforcement and its segregation at the grain boundaries (GBs) can lead to a grain size reduction in nanocomposites when compared with a pristine matrix, by preventing welding or grain growth during milling and sintering, respectively [41, 212, 283]. The electrical characteristics of a sample with single crystal and polycrystalline may differ due to the effect of the grain/crystal boundaries [295]. However, the impact of the grain-boundaries on the scattering of carriers is significant in cases where the mean free length (l) of carriers is larger than or comparable to the crystal/grain size (d) [295]. The intrinsic tendency for carrier localization is created by the presence of energetic disorder, caused by the structural inhomogeneity and chemical impurities at the grain boundaries [296-298]. This atomic disorder at the grain/crystal boundaries may provide an electrical-charge potential barrier (scattering regions) or traps [295-299]. The reason for this phenomenon is that the atoms near GBs are usually distributed irregularly, so the electronic couplings between atoms in different grains may change and thus prevent/disrupt the charge-carriers' transport from one grain to the other [300]. This process can create the traps, which may also be classified as valleys (i.e.,

states of lower energy) or barriers (i.e. higher energy states), by considering their energetic position with respect to the transport level [299, 301, 302].

As shown in Figure 30, four scenarios may occur at the grain boundaries when considering the disturbed carrier concentration in these areas. If the structural inhomogeneity of the lattice at the grain boundaries creates electron donors near the VBM, hole traps are made (Figure 30a). Conversely, electron acceptors near the VBM act as dopants, making a barrier for holes [303, 304] (Figure 30b). Similar behaviours apply to CBM [304, 305]. The electron acceptors make a trap for electrons (Figure 30c), while the electron donors create a barrier for electrons (Figure 30d) [304, 305].

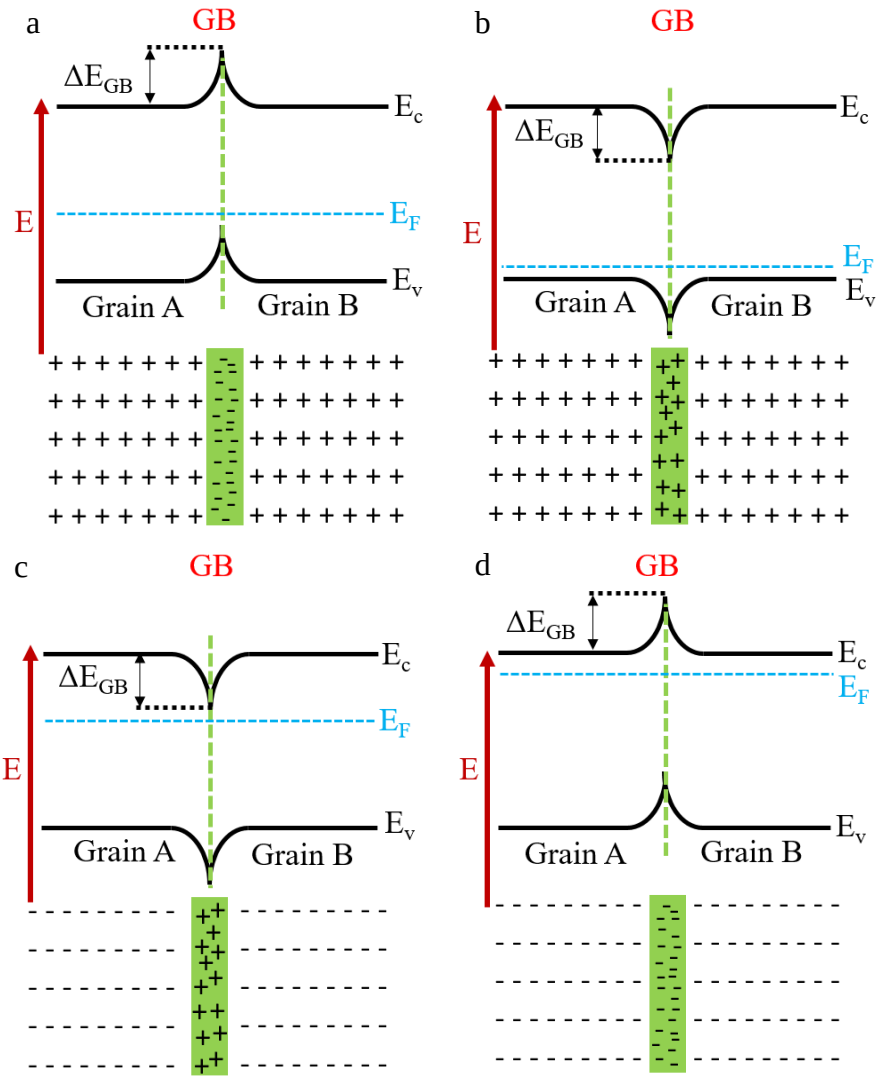

Figure 30: Schematic diagrams of a) hole trap, b) hole barrier, c) electron trap, and d) electron barrier [306].

There are further effects from the inclusion of graphene due to the formation of various lattice defects such as vacancies, antisites, etc., some of which can introduce extra charge carriers or compensate for some of the donors or acceptors in the lattice [307-311]. However, in the case of graphene segregation, there are some other questions that need to be clarified, such as how the newly-created graphene-matrix interfaces can affect electrical transport. The effect of graphene segregation at the grain interfaces can be evaluated based on the possible band alignment, depending on the work functions of the graphene and the main matrix. As illustrated in Figure 31, the type of contact (Schottky or Ohmic) at the graphene-matrix interfaces depends on the type of the majority carriers in the matrices, electrons or holes. As shown in Figure 31, Schottky barriers occur at the graphene-matrix interfaces for both n and p-type semiconductors when the graphene work function (Φ_G) is larger and smaller than the semiconductor work function (Φ_S), respectively (Figure 31 a, b). In this case, there is an interface potential barrier (E_b), which preferentially scatters the low energy carriers more than the others, resulting in carriers energy filtering. In contrast, for the case of ohmic contact, there is no potential barrier, and all the carriers can pass through the interface (Figure 31 c, d), although they can still experience scattering due to potential energy variations at the interface.

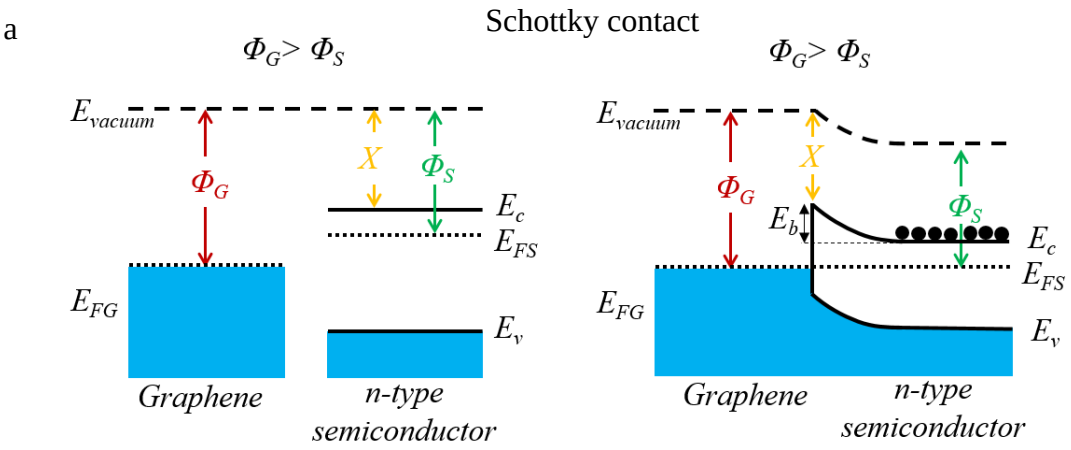

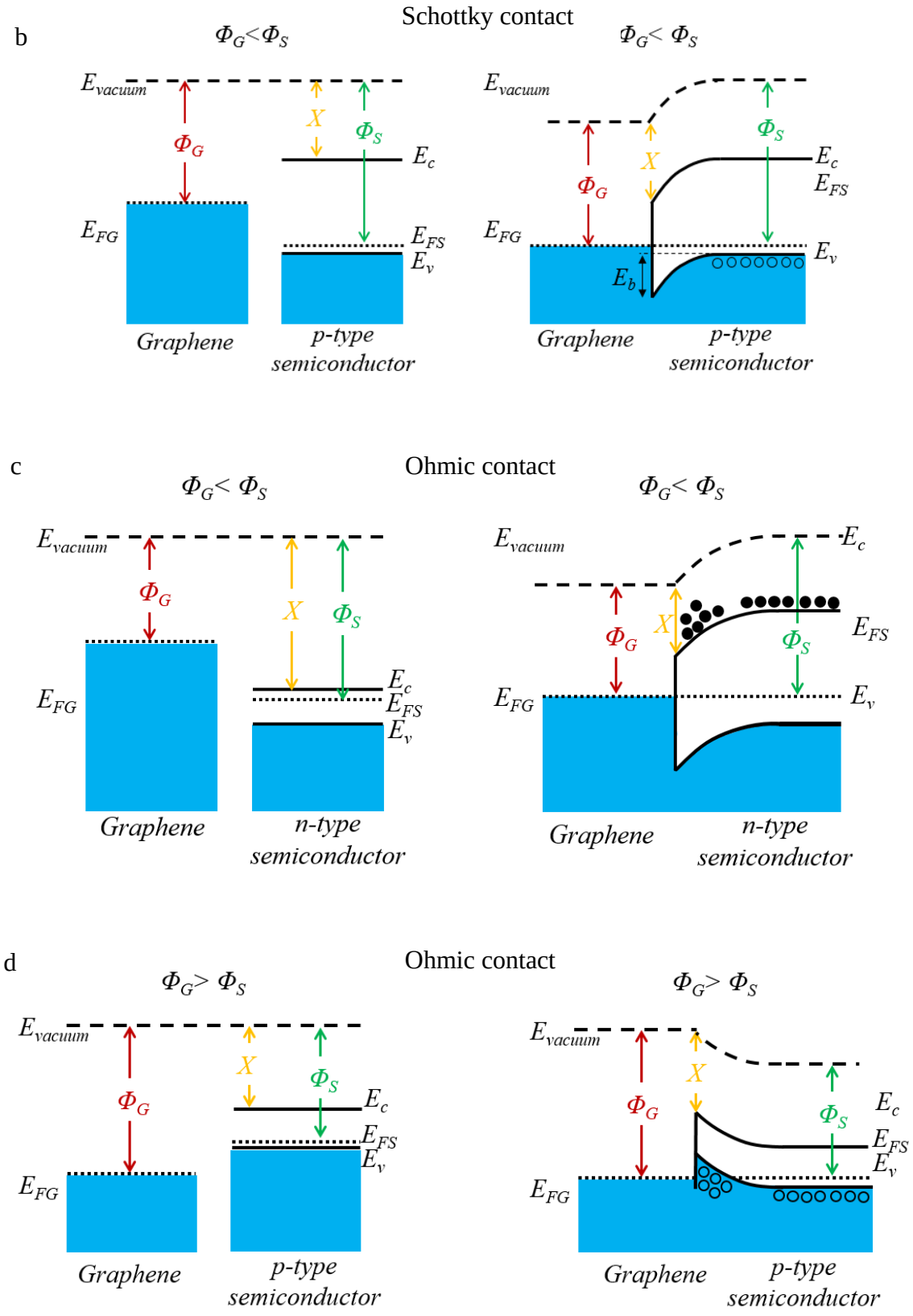

Figure 31: Schematic diagrams of various types of contacts and band alignments at the graphene-matrix interface [306].

Therefore, these extra boundaries due to smaller grain sizes – caused by graphene segregation and grain growth blocking – and graphene-matrix interfaces may provide an energy filtering effect for the charge carriers (electrons or holes). The consequence of energy filtering is strong scattering of low energy carriers, leading to a reduction in electrical conductivity and simultaneously increasing the Seebeck coefficients [43, 312-314].

2.8.1.2 Electrical conductivity

The addition of graphene to the TE materials can result in either an increase or a decrease in the electrical conductivity overall (Figure 29b). This is due to the graphene manipulating the carrier concentration (n) or the mobility (μ), according to the Mott equation $\sigma = en\mu$ [211, 212, 283, 284, 307]. The higher or lower carrier concentration depends on how the graphene affects the crystal imperfections and interacts with the charge donating centres in the material [284, 307, 315]. The graphene-embedded compounds may introduce a larger carrier concentration, but the resultant nanostructuring (i.e., grain growth prevention) provides more grain boundary barriers and thus further charges carrier scattering, leading to a decrease in carrier mobility [211, 212]. Therefore, one must consider both the carrier mobility of the matrix (μ_m) and the associate carrier mobility to the interface (μ_{in}) to estimate the total mobility of the nanocomposites (Equation 33) [307, 316],

$$\frac{1}{\mu_T} = \frac{1}{\mu_m} + \frac{1}{\mu_{in}} \qquad (33).$$

There are various models and approximations for interface mobility. One approximation is given by [307, 316]:

$$\mu_{in} = L_q \left(\frac{1}{2\pi m^* k_B T}\right)^{0.5} \exp\left(-\frac{E_b}{k_B T}\right) \qquad (34),$$

where L_q is the mean path between two adjacent potential barriers, E_b shows the height of the potentials (energy) at the interfaces (Figure 31a,b), k_B is the Boltzmann constant, $m^*$is the effective mass of the charge carriers, and T is the absolute temperature.

2.8.1.3 Lattice thermal conductivity

Figure 29c shows that the graphene addition in all the listed materials reduces the lattice thermal conductivity. The main mechanism is expected to be the phonon scattering against the grain boundaries [212], which happens effectively at the low to medium temperature range [45]. Based on Matthiessen's rule [45, 317], the total relaxation time of phonons τ_c (Equation 10) is related to various relaxation times, including τ_U (umklapp), τ_N (normal), τ_{e-ph} (Electron phonon), τ_{pd} (point defect), τ_{i-ph} (impurity-phonon), τ_{Ref} (regular reflection and refraction), τ_{Diff} (diffusive scattering due to the corrugation of the GB) and τ_{Ray} (Rayleigh scattering), as follows:

$$\frac{1}{\tau_c} = \frac{1}{\tau_U} + \frac{1}{\tau_N} + \frac{1}{\tau_{e-ph}} + \frac{1}{\tau_{pd}} + \frac{1}{\tau_{i-ph}} + \frac{1}{\tau_{\text{Ref}}} + \frac{1}{\tau_{Diff}} + \frac{1}{\tau_{Ray}} \qquad (35),$$

in which τ_{Ref}, τ_{Diff}, and τ_{Ray} depend on the grain boundary scattering, as described in Table 3.

Table 3: Phonon scattering strategies against the grain boundaries [45].

Scattering Strategies	Parameters and relations	Parameters	Definitions
GB regular reflection and refraction	$\tau_{\text{Ref}} \sim \ell_{GB} v_{gj}^{-1} (\Delta\nu)^{-2}$	ℓ_{GB}	Mean distance of the GBs
GB diffusive scattering	$\tau_{\text{Diff}} \sim \ell_{GB} v_{gj}^{-1} \left(\frac{k_B \theta_j}{\hbar\omega}\right)^2 \frac{1}{\eta}$	v_{gj}	Group velocity for the corresponding phonon modes
GB Rayleigh scattering	$\tau_{\text{Ray}} \sim \left(\frac{v_{gj}}{\ell_{GB}}\right)^3 \left(\frac{\theta_j}{T\omega}\right)^4 \Xi$	$\Delta\nu$	Difference in refraction indices of the elastic waves in different grains
		k_B	Boltzmann constant

	θ_j	Debye temperature
	η	A parameter that characterizes the degree of the corrugation of the GB (typically 1< <10)
	$\hbar$	(ħ=h/2π), h is the Plank's constant
	ω	Phonon frequency
	Ξ	A constant dependent on the details of the grain boundary characteristics
	T	Absolute temperature

It is noteworthy that the graphene compounds can contribute to the electronic thermal conductivity ($\kappa_t = \kappa_l + \kappa_e$), based on the Wiedemann-Franz law ($\kappa_e = L\sigma T, L$: Lorentz number), the relationship that maps the electrical conductivity to the electronic thermal conductivity (κ_e) [225]. In cases where the electrical conductivity increases significantly, there may be a trade-off between the increase in the electronic and reduction in the lattice thermal conductivities to determine the effect of graphene on the total thermal conductivity [213].

Li et al. [318] obtained a significant reduction in thermal conductivity (from ~0.8W/mK to ~0.4W/mK at a temperature of 873K) by adding 0.15 wt.% graphene in the Cu_2Se matrix. The reduction of the lattice thermal conductivity was associated with a frequency mismatch in the phonon density of states in between the carbon honeycomb phases and the cubic Cu_2Se. Another study [319] reported thermal conductivity of 2.5 W/mK for the 0.25 vol. % graphene/Cu_2SnSe_3 compound at room temperature, which was 12% lower than that of pristine Cu_2SnSe_3. In this study,

the extra barriers created by the graphene addition were mentioned as the reason for the phonon scattering and the reduction of the thermal conductivity of the nanocomposites.

2.9 Mechanical stability of thermoelectrics

A thermal gradient is a mandatory requirement for the efficient performance of thermoelectric generators. In this regard, thermomechanical stability is an essential factor, which enables the thermoelectric generators to resist under the thermomechanical shocks created by the thermal gradient. Strengthening the thermoelectric generators against the mechanical stresses highlights the importance of reinforcement for the thermoelectric legs [320].

There are several mechanisms used to improve the mechanical characteristics of metallic alloys, for example precipitation hardening, solid solution, work hardening, grain refining, and dispersion strengthening [321].

In the field of strengthening the alloys, Table 4 presents the resultant changes in mechanical characteristics due to mixing with graphene products.

Table 4: Optimized mechanical features reinforced by graphene products.

Matrix	Graphene compounds/ mixing ratios	Optimum mechanical characteristic	Reference
Al	Graphene nanoplates/ 0.25, 0.5, 1.0 wt.%	98% increment in tensile strength	[322]
AZ31 Mg alloy	Graphene nanoplatelets/ 0.3 wt.%	Tensile fracture strain, microhardness	[323]
Al2024	Few-layer graphene/ 0.7 vol.%	Achieves a tensile strength of 700 MPa	[324]

Sn-8Zn-3Bi solder alloys	Graphene nanosheets/ 0.1 wt.%	9.1% increment in the Vickers hardness, (29.9HV).	[325]
Sn-3.0Ag-0.5Cu	Graphene nanoplatelets/ 0.05 wt.%	13.9 % increment elongation and 17 % in the ultimate tensile strength.	[326]
Al5083	Graphene nanoplatelets/ 1.0wt.%	50% increment in the yield strength and ultimate tensile strength.	[263]
Mg–6Zn alloy	Graphene nanoplatelets/ Mg–6Zn–1.5GNP	43.3% increment in hardness.	[327]
2009Al	Graphene nanoplatelets/ 1 wt.%	30.5% in increment in yield strength and 23.3% in ultimate strength.	[328]
AZ91 powders Mg alloy	Reduced graphene oxide/0.5 wt.%	85.7% and 61.4% increments in yield strength and elongation, respectively	[329]
AZ91 alloy powders-Mg	Graphene nanosheets/ 0.5 wt. %	76.2% and 24.3% increments in yield strength and elongation, respectively.	[330]
Al	Graphene nanofillers/ 0.50 wt.%	50% increment in yield strength.	[331]

Al	Graphene nanoplates/ 0.25, 0.50, and 1.0 wt.%	Hardness improvement	[332]
Mg-1%Al-1%Sn-0.18%	Graphene nanoplates/ 0.18 wt.%	Tensile strength (i.e., from 236 to 269 MPa).	[333]
Mg-3%Al alloy	Graphene nano-platelets/ 0.1, 0.3, and 0.5 wt-%	Improvement in micro-hardness and compressive response, the ductility under compressive loading for composite samples remained higher than 20%.	[334]

By considering the application of graphene nanofillers (GNFs) to strengthen the thermoelectric products, four mechanisms, including grain refining, load transferring, local dislocation, and Orowan, and Griffith [322, 324-326, 329, 333, 335] have been mainly studied, and are discussed in the subsequent sections.

2.9.1 Grain growth prevention

Grain refinement, through graphene decorating of the grains, has been suggested as an effective method to improve the mechanical characteristics of nanocomposites [325, 335]. Graphene reinforcement of alloy matrices – graphene precipitation in the grain/particle boundaries – inhibits grain growth in the sintering process. In this regard, the Hall-Petch criteria explains the manipulation of mechanical factors, specifically yield strength and hardness by grain size reduction, as follows:

$\sigma_y = \sigma_0 + \frac{K_\sigma}{\sqrt{d}}$ [331, 336] (36),

$H = H_0 + \frac{K_H}{\sqrt{d}}$ [336] (37),

where σ_y and H are the yield strength and hardness when grain growth is prevented by the reinforced GNPs, respectively; also, K_σ and K_H, (slope of the straight line when σ_y or H is plotted against $\frac{1}{\sqrt{d}}$), H_0, and σ_0 are materials constants (friction stress opposing motion of dislocation). Furthermore, geometry mismatch may result from the presence of non-reacting graphene/matrix interfaces. The existence of an inharmonious geometry amongst the graphene precipitates at the grain boundaries, and can punch the dislocations and strengthen the nanocomposites [322].

In the graphene-reinforced alloys, there are several regions with stress concentration/accumulations in the proximity of graphene nanofillers (GNPs) due to their high specific interface areas with the matrices. Accordingly, this factor can obstruct the dislocation movement and lead to mechanical stabilities in the nanocomposite [324]. It is noteworthy that the above-mentioned phenomenon can be observed in the optimum reinforcing percentage of GNPs. In this regard, Figure 32 illustrates how the agglomerated graphene nanoplates at the alloy matrix (a CoVSn compound in this figure) may not be able to prevent crack growth.

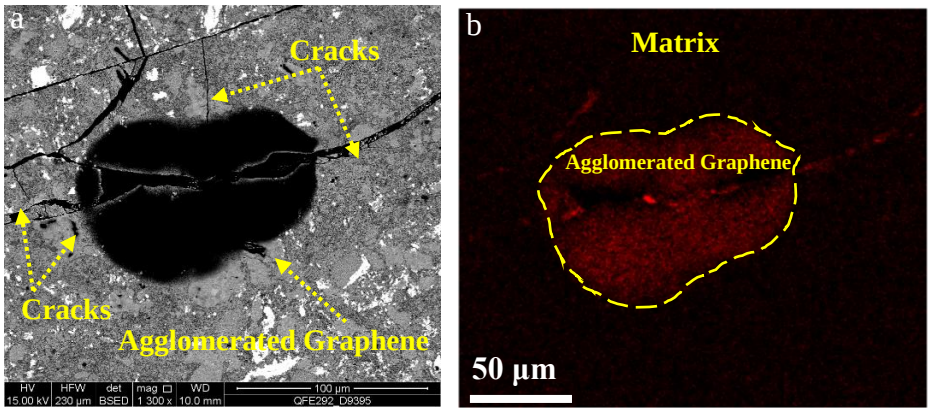

Figure 32: Graphene nanoplates (GNPs) agglomeration at the CoVSn- 1 wt.% GNPs, a) back-scattered electron image, and b) carbon x-ray map [306].

Equation 38 calculates the strengthening efficiency of reinforcement (R) [335], based on the strengths of the composite (σ_c), matrix (σ_m), and reinforcement volume fraction (V_r).

$$R = \frac{\sigma_c - \sigma_m}{V_r \sigma_m} \qquad (38).$$

Based on this equation, increasing the reinforcement volume above the optimum value may not enhance the reinforced strength, as represented in Figure 32.

2.9.2 Load transferring

There are three main factors that control the load transfer mechanism in the nanocomposites, including the reinforcement geometry, volume fraction, and bonding strength among the matrices and nanofillers [322, 326, 329, 333, 335]. By reinforcing a matrix with GNPs, the tight bonding (interlocking) due to the large interface areas of the GNPs/matrix enhances the load transferring between the graphene and matrices [322, 326, 329, 333, 335].

The formation of strong bonding was reported by Bhadauria et al. [322] through TEM analysis of the interface. This confirmed the presence of a clean interface with good metallurgical bonding between the GNP reinforcement and the Al matrix – see Figure 33a. The high-resolution TEM image of the interface region, illustrated in Figure 33b, reveals the nature of the bonding between the graphene and Al matrix.

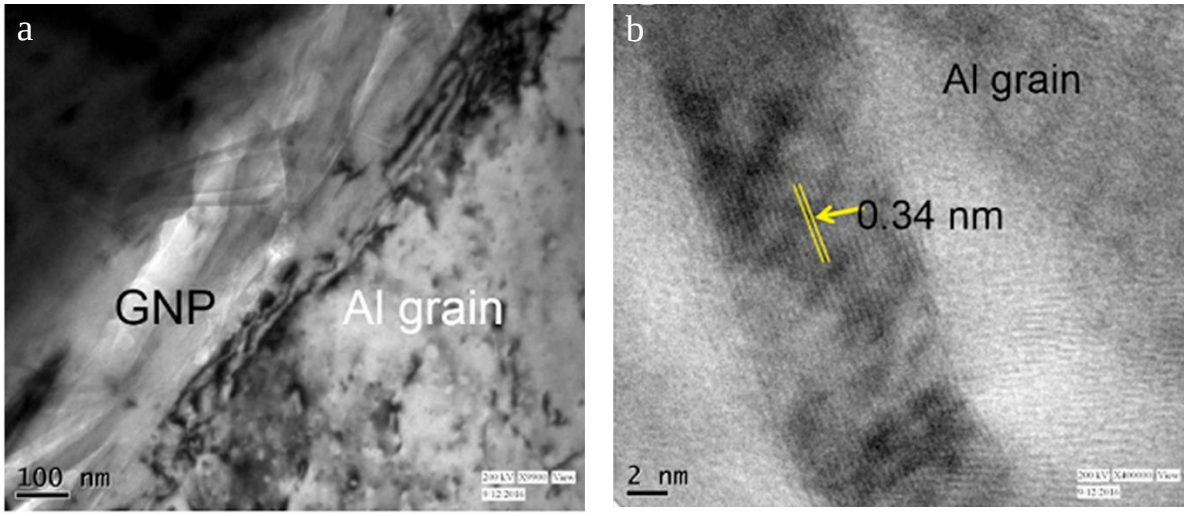

Figure 33: TEM micrographs showing the Al-GNP interface, and (b) High resolution TEM image, showing graphene layers in GNP, along with its interface structure with an Al-matrix [306].

In this case, Equation 14 can estimate the nanocomposite strength via the volume fraction and interfacial areas [323, 324, 337],

$$\sigma_{nanocomposite} = V_r\left(\frac{A}{CS}\right)\left(\frac{\tau}{2}\right) + \sigma_m V_m \qquad (39),$$

where V_r shows the reinforcement's volume fraction; A and CS are interfacial surfaces and cross sections of reinforcements, respectively; τ stands for shear stress, σ_m is the matrix strength and V_m is the matrix's volume fraction. According to this equation, at the optimum dispersed GNPs in the matrix, the interfacial surfaces (A) increase and the reinforcement's cross section (CS) decreases, which leads to an enhancement of the nanocomposite strength. In other words, a matrix reinforced by GNPs provides more effective interfaces and facilitates the load transfer from the matrices into GNPs via shear stress [331]. This mechanism causes the load distribution to prevent any local stress concentrations in the matrices and any subsequent nanocomposite failures.

2.9.3 Difference in thermal expansion coefficients (TECs)

Several studies [322, 326, 329, 333, 335] have discussed and analysed dislocation generation due to the differences in the thermal expansion coefficients (TECs), contributing to matrices and GNPs. In this field, Equation 40 describes the effective parameters in strength improvement, based on the TEC differences [337, 338];

$$\sigma_{TEC} = \alpha G b\sqrt{\frac{12\Delta T\Delta C}{bd}} \qquad (40),$$

where, α is constant, G shows the shear modulus, b represents the magnitude of Burger's vector, ΔT is the temperature gradient between the process and the ambient, ΔC states the TEC difference and d is the particle size.

As shown in this equation, the residual stress creation due to the TEC difference is directly related to ΔC. Moreover, the mismatch in the TECs caused dislocations at the interfacial areas and extra residual stress [327]. Equation 41 estimates the change in strength based on the density of the dislocations. In this equation, α is the geometric constant, μ_m shows the matrix shear modulus, b represents the Burger vector magnitude and ρ is the dislocation density [327].

$$\Delta\sigma = \alpha\mu_m b\sqrt{\rho} \qquad (41).$$

As represented in this equation, well-dispersed GNPs with a high level of interface areas with the matrix generate residual stress.

2.9.4 Orowan and Griffith criteria

Orowan reinforcement [322, 326, 329, 333, 335] is another mechanism that has been evaluated for reinforcing the matrix using GNPs. In this process, graphene may pile up the dislocations and prevent them from transferring freely throughout the matrix. Consequently, the dislocations need to pass around the graphene nanoplates due to their high mechanical stability. This extension in the dislocation paths (loops) results in higher ductility for the nanocomposites. Furthermore, these loops can create back stresses and prevent dislocation motions [322, 337]. Equation 42 [337, 338] describes the strengths of this mechanism, based on effective parameters, such as:

$$\sigma_o = \frac{Gb}{2\pi\sqrt{1-\frac{\vartheta}{1.28}\left[\frac{1}{\sqrt{V_r}}-1\right]d}}\ln\frac{d}{1.27b} \qquad (42),$$

in which G states the shear modulus, b is the Burger's vector magnitude, ϑ is the Poisson's ratio, V_r is the reinforcement volume fraction, and d is the particle grain size.

Candidate thermoelectric materials for waste heat recovery applications, such as heavily doped semiconductors and ceramic oxides, are predominately brittle materials [339]. By considering this important feature, the performance of the GNPs in strengthening the thermoelectric compounds against brittle fracture can be estimated via Griffith's fracture criterion (Equation 43). In this

equation, the critical stress intensity factor ($K_c = \sigma_c\sqrt{\pi a_0}$) depends on the Young's modulus (E) and surface energy (γ) (i.e.: the edge energy for 2D materials like graphene).

$$K_c = \sigma_c = \sqrt{\pi a_0} = \sqrt{2\gamma E} \qquad (43).$$

Also a_0 stands for the half crack length and σ_c shows the critical stress at the fracture onset [340, 341].

Nevertheless, there is a crack length restriction (up to 10 nm) when using the Griffith criteria [342, 343], but as per an adequate dispersion for GNPs, these reinforcements with a high Young's modulus can improve the nanocomposite strength [344], as follows:

$$E_c = E_{Gr}X_{Gr} + E_mX_m \qquad (44),$$

where E_c shows the Young's modulus of the nanocomposites, and E_{Gr}, E_m, X_{Gr} and X_m are the Young's modulus and volume fractions of the graphene nanoplates and matrices, respectively.

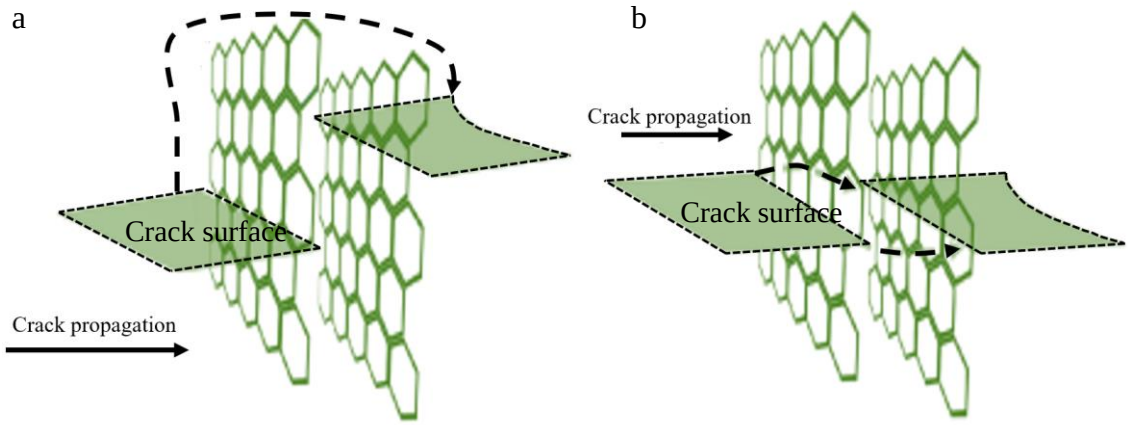

Figure 34: Schematic of crack growth inhibition by a) crack deflection, b) crack bifurcation/pinning [306].

Moreover, Figure 34 demonstrates schematically the crack growth blocking or halting by GNFs. This process can be also interpreted based on Equation 18, in which increasing the nanocomposite Young's modulus (E) and raising K_{IC} – fracture toughness – results in a lower cracking tendency.

There are only two ways to live your life. One is as though nothing is a miracle. The other is as though everything is a miracle.
— Albert Einstein (1879 - 1955)

CHAPTER THREE

PROJECT AIM, OBJECTIVES, AND JUSTIFICATION OF THE PROJECT TREND

Graphene nanoplates (GNPs) owing significant electrical and mechanical features have been suggested as potential improvements for thermoelectric (TE) products in order to achieve adequate efficiency and firmness as the main body constituent for the development of thermoelectric generators (TEGs). They should enable the TEGs to function effectively in a harsh environment (in terms of temperature fluctuations) under a range of thermo-mechanical stresses. In this field, there are some compounds that have either been predicted or evaluated experimentally to show promising thermoelectric characteristics. Based on the literature review and to the best of our knowledge, there is no specific report in the open literature to determine the reinforcing effects of graphene nanofillers (e.g., GNPs) on advanced thermoelectric compounds. In other words, there is a lack of a comprehensive assessment in the scientific community evaluating the advantages and drawbacks (side effects) of GNPs as the reinforcing agent for TE compounds.

The overall aim of this project is to study the effect of graphene reinforcement on the thermoelectric and mechanical characteristics of TE products. At the beginning, it was hypothesized that the grain growth inhibition created by the GNP precipitation could potentially manipulate the microstructure. Therefore, the effects of the microstructural development are evaluated in terms of reinforcing the thermoelectric products, alongside modifying their TE factors, including the Seebeck (S), electrical conductivity (σ), and lattice thermal conductivity (k_l). Consequently, three different thermoelectric compounds with various working temperatures have been nominated to cover thermoelectric applications from low to high temperature ranges. The nominated thermoelectric compounds are MnTe, CoVSn, and $CuSbTe_2$, which provide interesting features within their thermoelectricity, such as their crystal structure (Chalcogenide and half-Heusler), magnetic properties (magnetic contributions), and environmentally-friendly properties (Lead-free compounds). Further sections describe the important features of the abovementioned compositions.

3.1 MnTe

Along with discovering novel TE compounds and continued interest in developing efficient chalcogenide TE materials [35, 218, 219, 345-347], Lead-free MnTe, as an antiferromagnetic (AFM) transition metal semiconductor, has shown potential as an efficient TE material. MnTe has a Néel temperature (T_N) of 307–310 K [348, 349] and a band gap of 1.27 eV [348, 350, 351], with a high Seebeck coefficient (~450 μV/K) [350, 352] and spin-wave excitation (magnon) drag effect [351, 353, 354]. Also, in contrast with other manganese chalcogenides, such as MnO, MnS and MnSe, which form with a cubic NaCl type crystal structure, MnTe has a hexagonal NiAs structure in its ground state [350] (Figure 35).

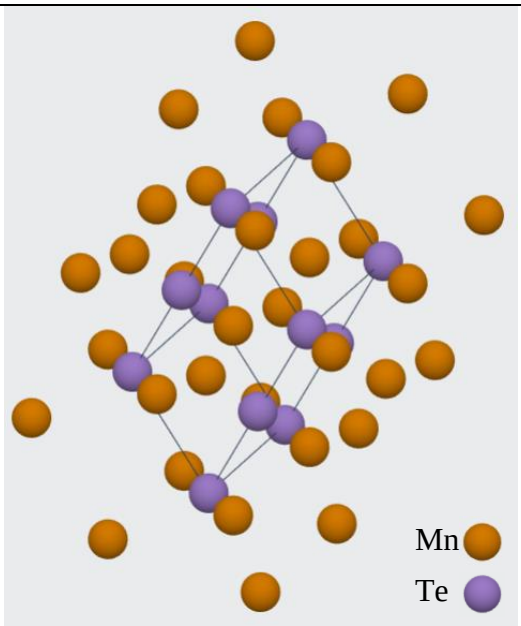

Figure 35: Atomic arrangement of MnTe. Source: materials project [355]. Mn^{2+} is bonded to six equivalent Te_2- atoms to form a mixture of edge, face, and corner-sharing $MnTe_6$ octahedra. The corner-sharing octahedral tilt angles are 51°. All Mn–Te bond lengths are 2.85 Å. Te_2- is bonded in a 6-coordinate geometry to six equivalent Mn^{2+} atoms.

This material has been investigated since the 1930s [356, 357] either as an un-doped MnTe [358-361] or as doped compounds, such as MnTeLi [359], $(GeTe)_{1-x}(MnTe)_x$ [362, 363], $(Ge, Pb)_{1-x}Mn_xTe$ [364], $Cd_{1-x}Mn_xTe$ [365], $Sn_{1-x}Mn_xTe$ [366] and $Zn_{1-x}Mn_xTe$ [367]. However, there are two features of poor electrical conductivity and crystal structure instability that may compromise the potential of the MnTe compound as an efficient TE material. The poor electrical conductivity originates from a low hole concentration (~10^{18} cm^{-3} in comparison with the carrier concentration 10^{19}-10^{21} cm^{-3} in the state-of-the-art TE tellurides) [350, 368, 369], and the crystal structure instability is due to Te/Mn ion migration. Both may alter the properties of MnTe-based devices during service time [353, 370], and therefore warrant further investigation for improvement.

In order to overcome the above-mentioned drawbacks for MnTe as a potential TE material, attempts have been made to reinforce it with graphene nanoplates (GNPs) to investigate if the high electrical

conductivity of GNPs can compensate for the low charge carrier concentration, while preventing Mn migration and inducing thermomechanical stability through interaction with the grain structure. As for the latter, mechanical sustainability due to graphene addition may result through grain/crystal growth inhibition or size reduction, load transfer, dislocation density increase, and Orowan strengthening. In this project, the magnetic, thermoelectric and mechanical factors of GNP reinforced MnTe compounds are characterised based on their microstructure manipulation and analysis.

3.2 CoVSn

There has been substantial progress in thermoelectric materials over the last two decades. Thermoelectric technology, which was mainly based on alloys of bismuth telluride [371] for Peltier cooling modules, or silicon-germanium alloys [372] for radioisotope thermoelectric generators used in NASA spacecraft, has expanded to new compounds for power generation and cooling [10]. New materials and material structures have been discovered with considerably enhanced thermoelectric properties [373]. In particular, some materials like half-Heusler (HH) alloys show an inherently large thermoelectric power factor, although they have generally higher thermal conductivity than alloys such as Skutterudites [374] and Clathrates. Since the thermal conductivity can be decreased by structural engineering, their potential to provide inherently significant power factors has recently attracted much attention. Indeed, a new class of half-Heusler compounds was predicted with low thermal conductivity [375]. In this regard, the sheer number of HH compounds to investigate is vast, and computational and predictive methods to shortlist the promising ones has become essential to make quick progress. First principle studies [376] and thermodynamic calculations [333] are some of the main methods to predict the new materials. Notably, the half-Heusler alloys with the cubic crystal structure of $C1b$ (no.216) and the atomic arrangement of XYZ [377] have attracted much attention due to their unusual thermoelectric characteristics, high-temperature stability, and their doping capabilities (Figure 36,Table 5).

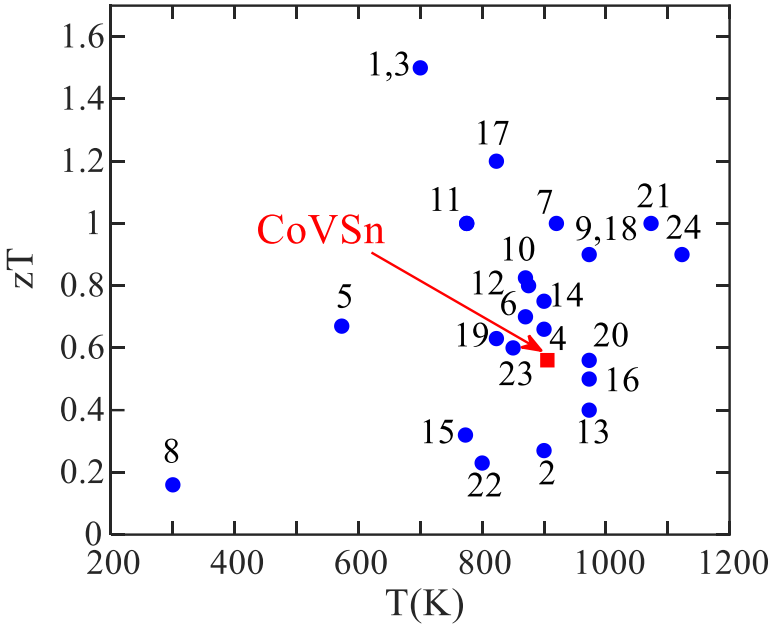

Figure 36: Selected alloys with their corresponding TE properties that have been studied as half-Heusler (the numbers are the items given in Table 5) [378].

Table 5: Compounds cited in Figure 36 [378].

Item	Compound	Ref.	Item	Compound	Ref.
1	$Ti_{0.5}(Zr_{0.5}Hf_{0.5})_{0.5}NiSn_{0.998}Sb_{0.002}$	[379]	13	NbCoSb	[380]
2	$TiCo_{0.95}Ni_{0.05}Sb$	[381]	14	Zr,Ni,Sn	[382]
3	$(Zr_{0.5}Hf_{0.5})_{0.5}Ti_{0.5}NiSn_{0.998}Sb_{0.002}$	[383]	15	Ti,Ni,Sn	[384]
4	$Ti_{0.5}(ZrHf)_{0.49}Nb_{0.01}Ni_{0.9}Pd_{0.1}Sn_{0.98}Sb_{0.02}$	[385]	16	VCoSb	[386]
5	$ZrNiSn_{0.98}Sb_{0.02}$	[387]	17	$Ti_{0.5}Zr_{0.5}NiSn_{0.98}Sb_{0.02}$	[12]
6	$(Hf_{0.6}Zr_{0.4})_{0.99}Y_{0.01}NiSn_{0.98}Sb_{0.02}$	[388]	18	$(Hf_{0.25}Zr_{0.75})_{0.995}Nb_{0.005}NiSn$	[67]
7	$Hf_{0.75}Zr_{0.25}NiSn_{0.99}Sb_{0.01}$	[389]	19	$(TiNiSn)_{0.95}+(MnNiSb)_{0.05}$	[153]

8	1.5% Y-Sb-doped Ti-Ni-Sn	[390]	20	$NbCoSb_{0.8}Sn_{0.2}$	[391]
9	$TiCoSb_{0.8}Sn_{0.2}$	[392]	21	$Zr_{0.5}Hf_{0.5}Co_{0.9}Ni_{0.1}Sb$	[393]
10	$(Zr_{0.3}Hf_{0.65}Ta_{0.05})NiSn$	[394]	22	$ZrCo_{0.97}Pd_{0.03}Bi$	[395]
11	$(Ti_{0.4}(Zr_{0.5}Hf_{0.5})_{0.6})_{0.99}Ta_{0.01}NiSn$	[396]	23	$TiNi_{1.06}Sn_{0.81}Sb_{0.17}$	[397]
12	$ZrNiSn_{0.99}Sb_{0.01}$	[398]	24	$Nb_{0.83}CoSb$	[399]
Predicted TE factors of CoVSn compound, κ=4.1 W/mK, S=175 μV K^{-1}, zT=0.53 at 900 K.					[400]

In 1995, Ögüt et al. [401] predicted CoVSn with MgAgAs ($C1b$) crystal structure would be a semiconductor intermetallic using DFT band structure calculations. The atomic arrangement of CoVSn is demonstrated in Figure 37.

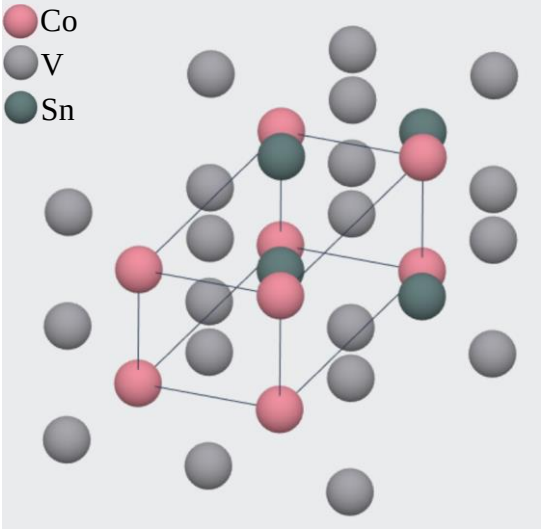

Figure 37: Atomic arrangement of CoVSn. Source: materials project [355]. V is bonded in a body-centred cubic geometry to four equivalent Co and four equivalent Sn atoms. All V–Co bond lengths are 2.57 Å. All V–Sn bond lengths are 2.57 Å. Co is bonded to four equivalent V atoms to form distorted CoV_4 tetrahedra that share corners with four equivalent SnV_4 tetrahedra, corners with twelve equivalent CoV_4 tetrahedra, and edges with six equivalent SnV_4 tetrahedra. Sn is bonded to four equivalent V atoms to form distorted SnV_4 tetrahedra that share corners with four equivalent

CoV_4 tetrahedra, corners with twelve equivalent SnV_4 tetrahedra, and edges with six equivalent CoV_4 tetrahedra.

Another study [402] applied the full-potential linear muffin-tin orbital (FP-LMTO) method to evaluate the electronic properties of CoVSn alloy and showed an indirect energy bandgap of 0.75 eV. Shi et al. [403], calculated the electronic structure using the modified Becke-Johnson (MBJ) potential. Also, the transport coefficients were computed employing Boltzmann theory within the constant scattering time approximation. Moreover, spin-orbit coupling (SOC) was considered in the electronic and transport calculations. Figure 38 shows the calculated electronic band structure and density of states (DOS) of CoVSn alloy [402]. Based on this electronic structure, the alloy was predicted as a p-type semiconductor with a bandgap (W-X) of 0.85 eV.

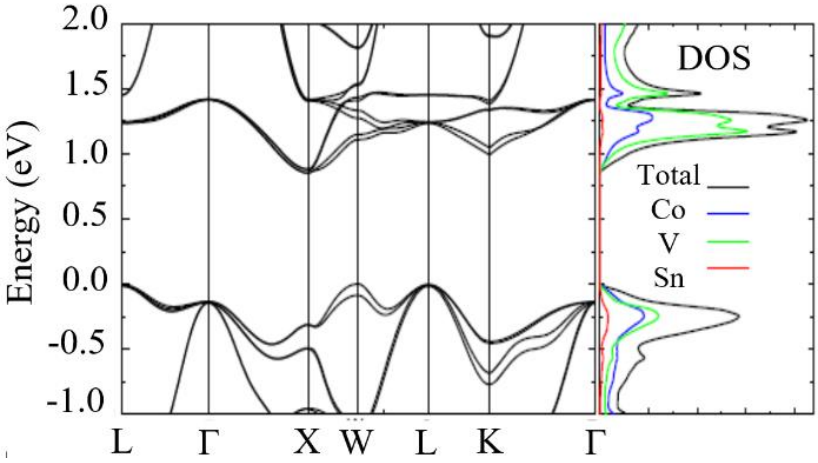

Figure 38: Calculated electronic band structure and density of states (DOS) of CoVSn alloy [378].

In the mentioned study, the maximum Seebeck coefficient with a carrier concentration of 1.0×10^{21} cm^{-3} was calculated at a temperature of 1150 K as 340 µV/K [402]. Zeeshan et al. [71] carried out combined ab initio and semiclassical calculations based on Boltzmann transport theory and determined the maximum doping concentration of the p-type CoVSn alloy. Assuming a relaxation time of 10^{-15} s for V- and Cr-group doping, they estimated a Seebeck coefficient of 175 µV/K and a maximum power factor in the range of 11-23 $\mu W/K^{-2}$ at optimum 0.26 e/uc p-type doping. This

value of power factor is comparable with the power factor of many effective HH thermoelectric alloys.

Despite the wide range of theoretical studies on CoVSn alloy, with promising predicted thermoelectric characteristics, to the best of our knowledge, there is no report on the thermoelectric characterization of synthesized samples of this alloy in the open literature. In this project, the microstructure, thermodynamic stability, thermoelectric and mechanical factors of pristine and GNP reinforced CoVSn compositions are characterised and analysed.

3.3 $CuSbTe_2$

By 1958, $CuSbTe_2$ had been studied for its crystal structure [404-406] and electrical properties [407]. In 2017, Chen et al. [408] calculated the electronic band structure (Figure 39) of this compound and reported its effective electron mass equal to $m_e^{DOS} \approx 0.25m_0$ for a single conduction band (CB).

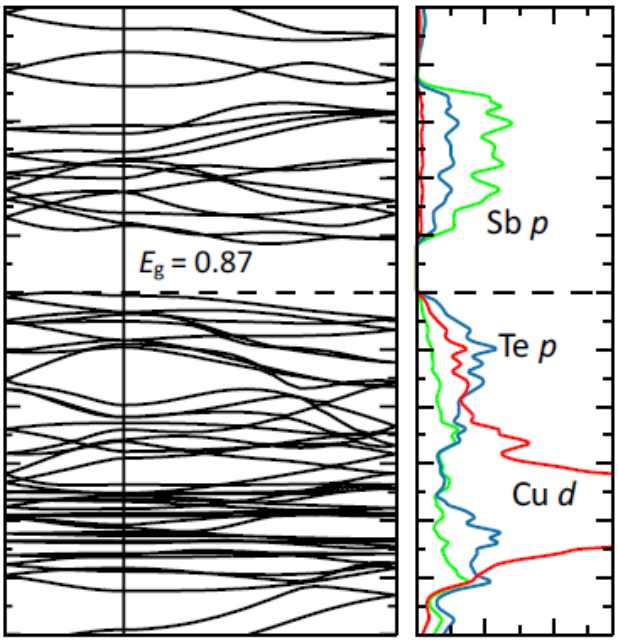

Figure 39: Electronic band structure and the local, atomic- and angular-resolved density of state (LDOS) of $CuSbTe_2$ adapted from ref. [408] with permission.

It should also be pointed out that, unlike most materials operating in thermoelectric power generation, $CuSbTe_2$ is lead-free and thus is regarded as an environmentally-friendly product. However, there is a need for comprehensive analysis of this composition through its microstructure and thermoelectric characterization. In this project, $CuSbTe_2$ and its GNP-reinforced composites are evaluated based on their microstructure, thermoelectric, and mechanical characteristics.

No great discovery was ever made without a bold guess.

— ISAAC NEWTON (1643 - 1727)

CHAPTER FOUR

EXPERIMENTAL PROCEDURE

This chapter explains the experimental procedures to synthesize and characterise the nominated TE composites. According to the objectives discussed in chapter three, powder metallurgy was selected to fabricate different samples with various concentrations of graphene nanoplates. Moreover, through powder metallurgy, specifically in the step of mechanical alloying and milling, the narrow-distribution size powder was produced as the basis for graphene reinforcing. Importantly, the nominated thermoelectric compounds, including MnTe, CoVSn, and $CuSbTe_2$ have different physical characteristics, such as melting temperatures. By using powder metallurgy, the specific elemental parts can be mixed and then synthesized based on the appropriate sintering and annealing procedures. It is noteworthy that several procedures were tried for each compound and the optimized processes were used to sinter the nominated TE compositions. In further steps, sintered samples were analysed and assessed by crystallography methods, such as x-ray diffraction methods. Subsequently, thermoelectric properties, including S, σ, and κ were measured. The electronic parameters, namely carrier mobility, and concentration were determined by measuring Hall coefficients and the Van der Pauw technique. Magnetic characterization was used for the samples with magnetic properties (i.e., MnTe). Microscopic evaluation was performed to characterize the microstructure of the nominated samples. Moreover, hardness measurement was carried out to

characterize mechanical properties and the impact of graphene nanoplates reinforcement. Each step of the mentioned experimental procedures is described in detail in subsequent sections.

4.1 Powder metallurgy

4.1.1 MnTe-GNPs

The pure chunks of Mn and Te elements (Alfa Aesar Co., 99.9% commercial purity, Ward Hill, MA, USA.) with an atomic ratio of 1: 1, were weighed and mixed under an argon gas atmosphere inside the Glovebox station (Figure 40a). In the first step, the mixture was poured into a P-7 milling cup filled with steel balls (D=10mm) with a 3: 1 ball/powder weight ratio (Figure 40b). The milling process was implemented by a planetary P-7 FRITSCH ball mill under a milling rate of 600 RPM for twenty-four hours (Figure 40c).

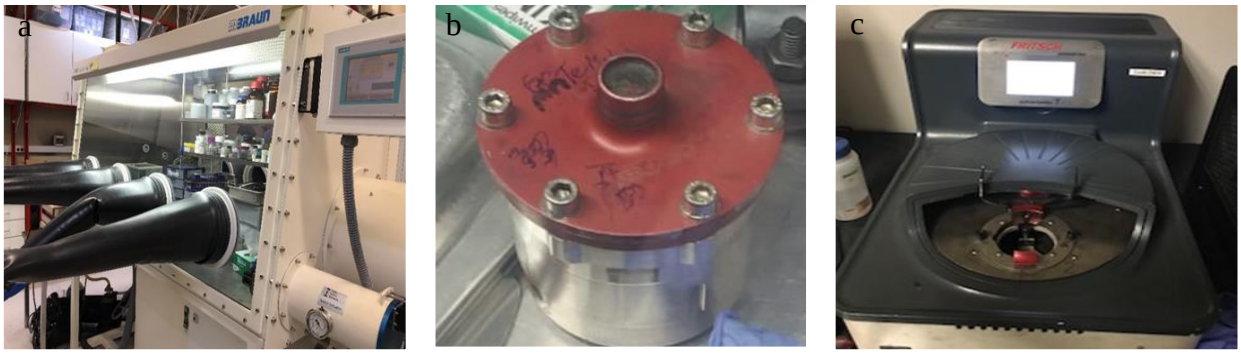

Figure 40: a) Glovebox station, b) P-7 milling cup, and c) P-7 FRITSCH ball milling machine.

After mechanical mixing of the Mn and Te chunks, the alloy powder was sealed off in a quartz tube. To perform this step, the powdered mixture was poured into a quartz tube (OD=20mm) and attached to a sealing valve, all inside the Glovebox, under the argon gas atmosphere (Figure 41a and b). After sealing the valve, the assembled valve was shifted outside the Glovebox and the inlet port was connected to a vacuum pump to create a partial vacuum pressure (~5 torr). Subsequently, the quartz tube was heated up to melt and seal, using an oxyacetylene flame (Figure 41c).

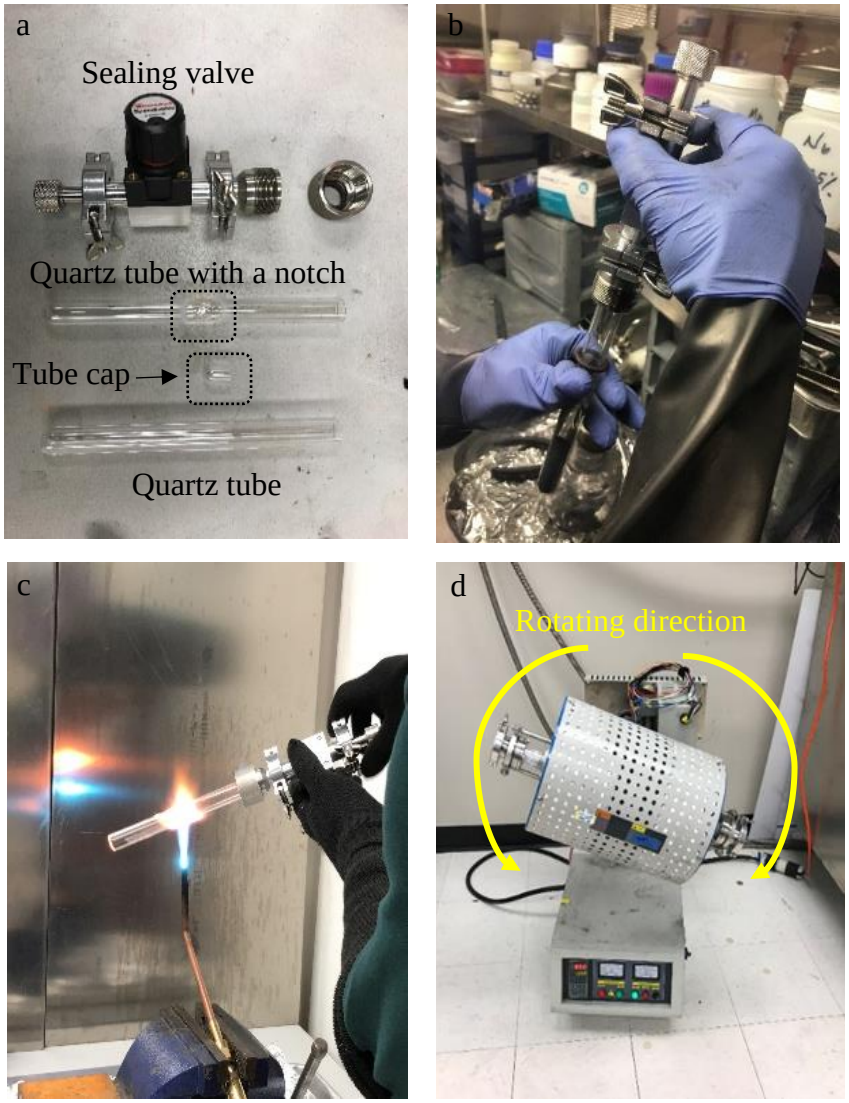

Figure 41: a) Quartz tube and sealing valve, b) Sealing the mechanically alloyed powder under an argon gas atmosphere inside the Glovebox via a sealing valve, c) Sealing the quartz tube containing the mechanically alloyed powder using a flame, and d) Rocking furnace with rotational movement to mix the powder during the annealing process.

Subsequently, the sealed off compound powder was annealed in a rotating furnace at 750°C for twenty-four hours (Figure 41d). In this step, the powder mixture further homogenized during the furnace rotation and annealing process. After completing the annealing process, the alloyed powder was further milled in a P-7 FRITSCH ball mill machine with a milling rate of 150 RPM for four

hours. In the next step, MnTe-xGNP composite powders (x: 0.25, 0.5, 0.75, and 1 wt. %) were prepared by mixing the synthesized MnTe powder and Graphene nanoparticles (GNPs, average particle size 3nm, surface area 500 m^2/g, Alfa Aesar) under the argon gas atmosphere. In this process, a planetary micro ball-mill was used for one hour, containing steel balls (D=1mm) with a ball/powder volume ratio of 1: 1.

4.1.2 CoVSn-GNPs

For the sample preparation of CoVSn composition, elemental powders of Co, V, and Sn (Alfa Aesar Co., 99.9% commercial purity, Ward Hill, MA, USA.) based on a stoichiometric atomic ratio of 1: 1: 1 were weighed and mixed under an inert atmosphere (argon gas, P= ~2.2mbar) inside a Glovebox (Figure 42) to eliminate any potential oxidation.

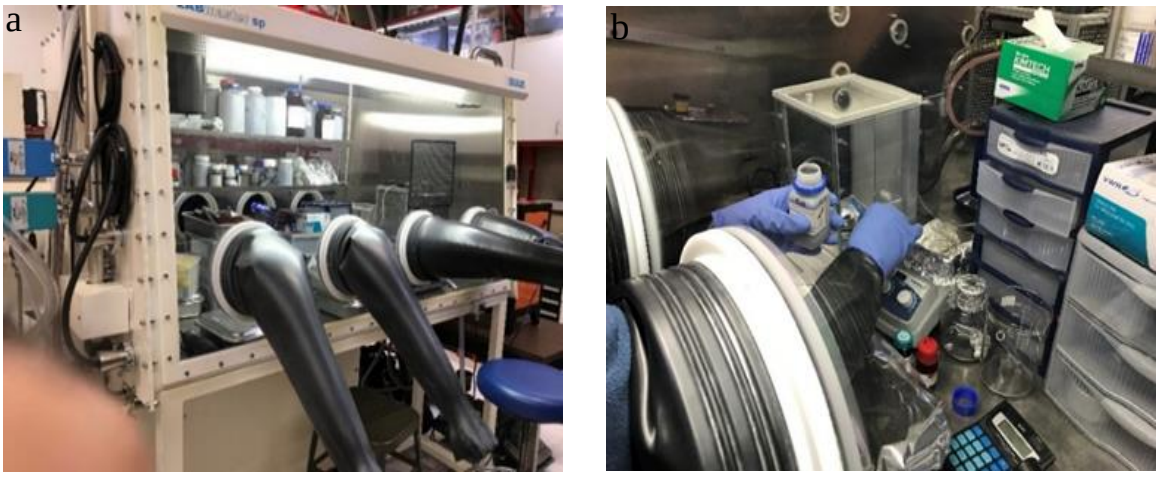

Figure 42: a) Glovebox station for the CoVSn sample preparation, b) element weighing inside the Glovebox.

The powder mixture of the CoVSn composition was mechanically milled by a planetary ball mill (SPEX-6, Metuchen, NJ, USA, 5:1 ball-powder weights, steel ball diameter=10 cm) for thirty hours (Figure 43). It is noteworthy that all the mechanical alloying steps, including pouring the elemental powder into the milling cup, sealing, and powder mixture inspection (to check for any sticking on the cup inner wall) were implemented inside the Glovebox under argon gas pressure (Figure 42).

Figure 43: a) SPEX-6 ball milling machine contents, b) steel balls (D=10mm) inside a clean milling cup, c-e) photos of the inspection steps and trial-error checking to find the best ball-powder ratio and milling time, and f) successfully produced alloyed powder with no sticking to the cup wall.

After mechanical alloying of the powdered mixture, the premixed alloy needed to be sealed off in a quartz tube for annealing through the same process as described for the MnTe compound (Figure

41a-c). The sealed powdered composition inside the quartz tube was annealed at a temperature of 900°C for time intervals of twenty, forty, and eighty hours (Figure 44).

Figure 44: Sealed off quartz tubes for annealing.

The CoVSn composition, after annealing, was then reinforced by Graphene nanoparticles (GNPs) (average particle size 3nm, surface area 500 m^2/g, Alfa Aesar). CoVSn-xGNP composite powders (x: 0.25, 0.5, 0.75, and 1 wt. %) were prepared via milling by a planetary micro ball-mill for one hour, containing steel balls (D = 1mm) with a ball/powder volume ratio of 1: 1.

4.1.3 $CuSbTe_2$-GNPs

The pure chunks of Cu, Sb, and Te elements (Alfa Aesar Co., 99.9% commercial purity, Ward Hill, MA, USA.) were mixed with a stoichiometric atomic ratio of $CuSbTe_2$ (Cu:Sb:Te, 1: 1: 2) and loaded into a quartz tube under an argon gas atmosphere inside the Glovebox (Figure 45a), and then sealed off, as explained for the MnTe compound (Figure 41a-c, Figure 45b). In the next step, the mixed elements (Cu, Sb, and Te) were heated in a pre-melting step (T=~600°C) to expedite the alloying process. The melting and solidification steps were repeated three times to ensure an homogenous alloy. Due to the low melting temperature of $CuSbTe_2$ (T_m=530 °C) [409], complete melting occurred during the heating process by using an oxyacetylene flame heating (Figure 45c), and resulted in a solid ingot after cooling (Figure 45d).

Figure 45: a) Glovebox station, b) sealing valve assembly, c) melting the premixed elements of $CuSbTe_2$, and d) a solidified $CuSbTe_2$ ingot.

In order to produce a uniform alloyed powder, the as-solidified ingot was milled in a P-6 FRITSCH ball mill (Figure 46a) containing 10 mm Zirconia balls with a ball/powder ratio of 10: 1 at a milling rate of 400 RPM for three hours (Figure 46b).

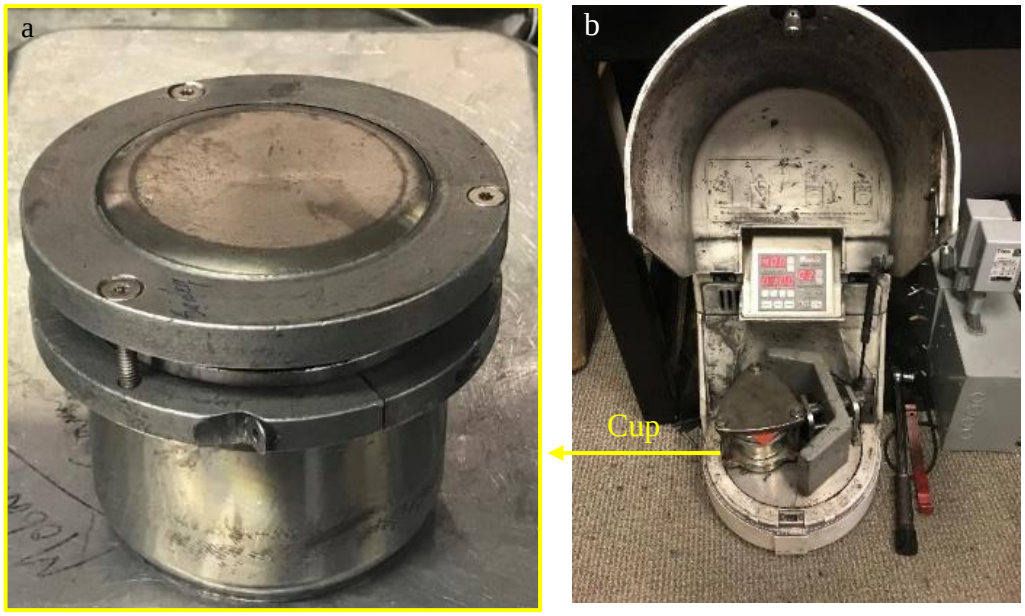

Figure 46: P-6 milling cup and b) P-6 FRITSCH ball milling machine.

After the mechanical milling of the ingot, the powdered composition was poured into a quartz tube and sealed off with an oxyacetylene flame under vacuum pressure of about 5 torr (Figure 47a). The powder in the sealed off quartz tube was annealed at a temperature of 450 °C for twenty-four hours in a rocking furnace with rotation (Figure 47b).

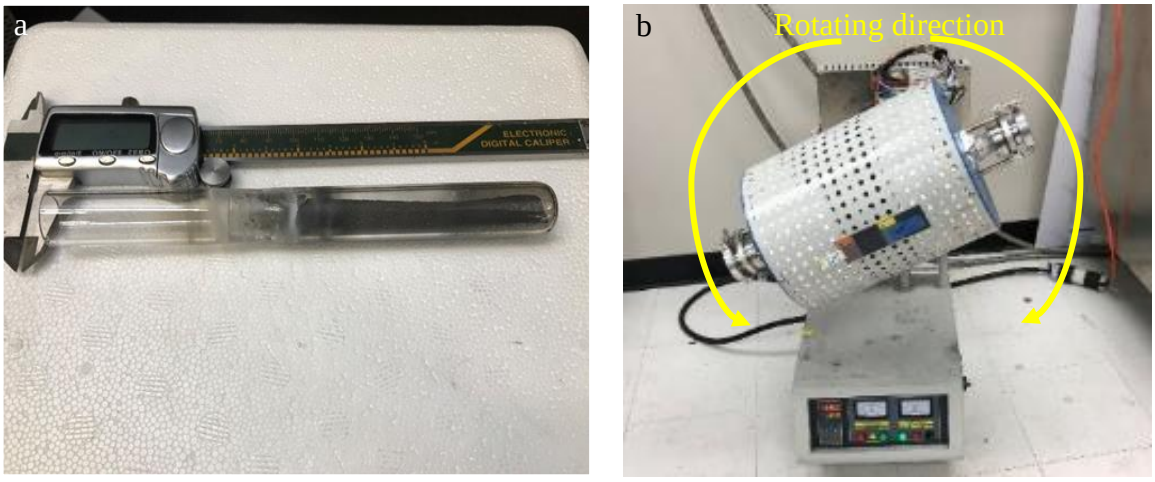

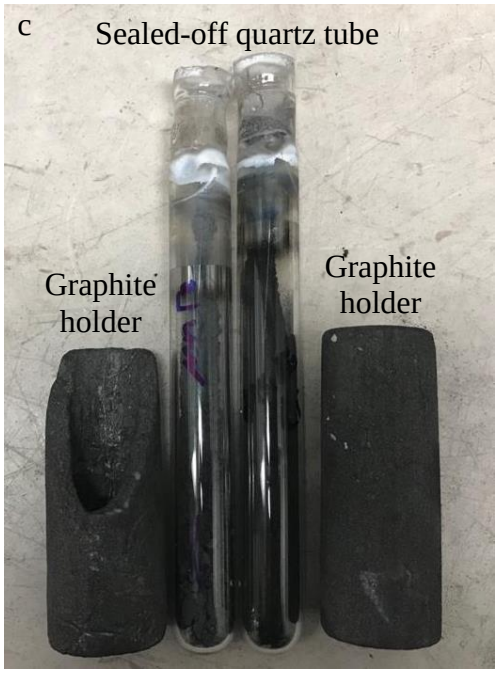

Figure 47: a) Sealing off quartz tube containing the $CuSbTe_2$ powder to anneal, b) Rotating rocking furnace, and c) Annealed $CuSbTe_2$ powder.

In the next step, the annealed powder was milled in a P-6 cup (Figure 46a) containing 10 mm Zirconia balls (ball/powder ratio of 10: 1) in a FRITSCH milling machine under a rotation speed of 400 RPM for 3 hours (Figure 46b).

$CuSbTe_2$-xGNP composite powders (x: 0.25, 0.5, 0.75, and 1 wt. %) were prepared by the milling process as described for the MnTe- xGNP composite powders.

4.2 Bulk sample production

The powder of the pristine and GNP-reinforced composites for the MnTe, CoVSn, and $CuSbTe_2$ compounds were sieved inside the Glovebox (under an argon gas atmosphere) using a test sieve with a mesh size of 63µm (USA standard Test Sieve, ASTM E-11 specification, W.S. TYLER[1]), as shown in Figure 48.

[1] https://wstyler.com/particle-analysis/test-sieves/

Figure 48: Standard test sieve to sieve and measure the powder particle size before the spark plasma sintering step.

The bulk samples were fabricated using the spark plasma sintering (SPS) technique. In this step, the required weights of the green alloy powders for a volume of a cylinder with a diameter of 6 mm and a length of 10-14 mm were loaded into a graphite die with an inner diameter of 6 mm. Two more graphite spacers and rods with diameter of ~ 6 mm were used as the punches for transferring the pressure and connecting the electrical circuit during the heating time (Figure 49). Three to five bulk samples were produced for each composition.

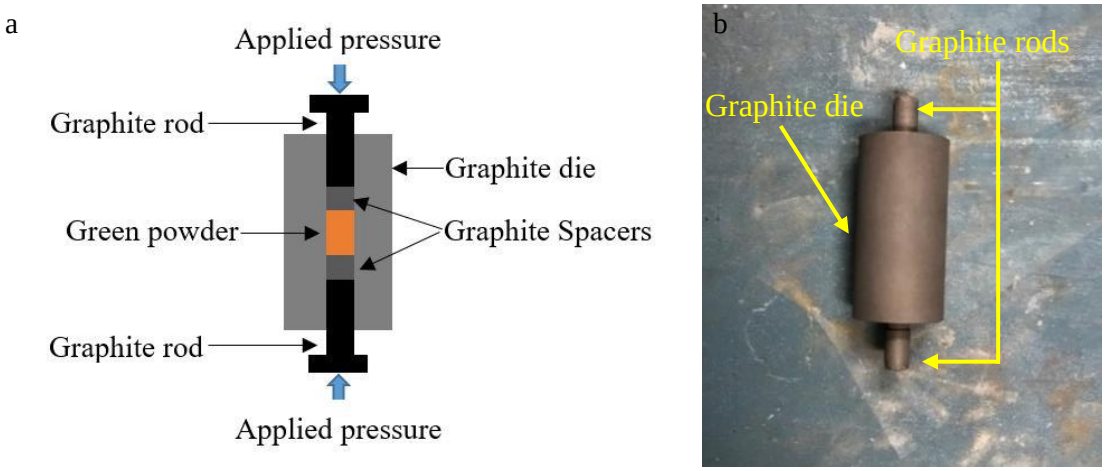

Figure 49: a) Schematic of the graphite die and interiors set up, b) expected graphite die containing green powder and graphite rods.

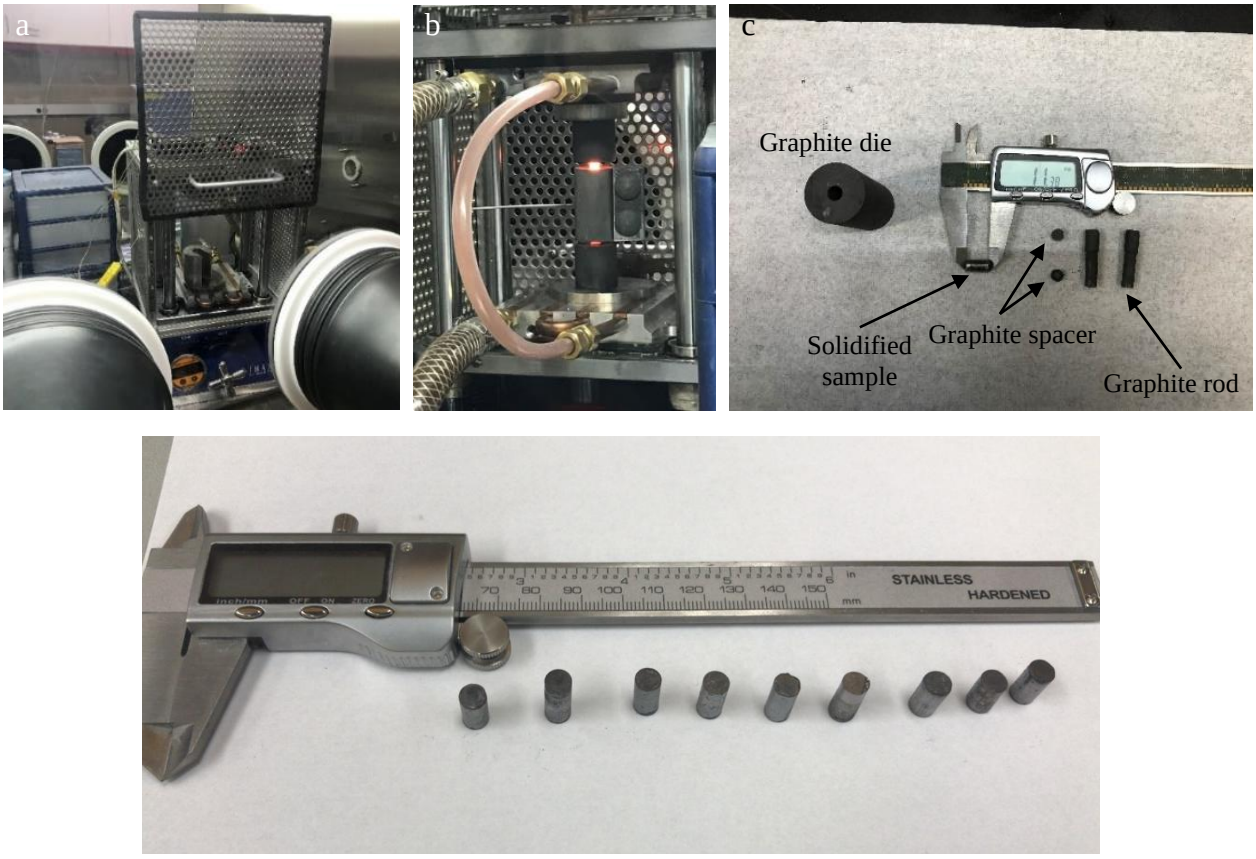

Figure 50: Spark plasma sintering (SPS) setup (a-c), d) Examples of sintered samples.

Based on the physical properties of the nominated thermoelectric compounds, the sintering temperatures were different, as shown in Table 6. However, the applied pressure and soaking time were the same for all the samples, at 42 MPa and twenty minutes, respectively. Also, the sintering process was completed under the argon gas atmosphere (Glovebox) to eliminate any risk of oxidation (Figure 50).

Table 6: Applied pressure and temperature in the SPS process for the studied samples. All samples were sintered for twenty minutes.

Composite	Applied pressure (MPa)	Temperature (°C)
MnTe-xGNPs	42	1000

(x: 0, 0.25, 0.5, 0.75, and 1 wt. %)		
CoVSn-xGNPs (x: 0, 0.25, 0.5, 0.75, and 1 wt. %)	42	850
$CuSbTe_2$-xGNPs (x: 0, 0.25, 0.5, 0.75, and 1 wt. %)	42	450

4.3 Density measurement

The bulk sample average density (to be ≈98-99% of the ideal density) was measured by the Archimedes method, with isopropyl alcohol as a displacement medium (Figure 51). The results of this measurement were used to calculate the thermal conductivity.

Figure 51: Archimedes experimental setup for measuring the sample density.

4.4 Crystal structure characterization

The phase identification via the X-ray diffraction analysis of the studied compositions, including the MnTe, CoVSn, $CuSbTe_2$ compositions and their GNP-reinforced composites, was implemented by a MiniFlex 300/600 model diffractometer used Cu x-ray radiation generated with 40 kV, 15 mA

and a scan rate of 3 deg/min, as shown in Figure 52. The XRD results were analysed using integrated X-ray powder diffraction software (PDXL) based on the available CIF (crystal information file) for each crystal structure.

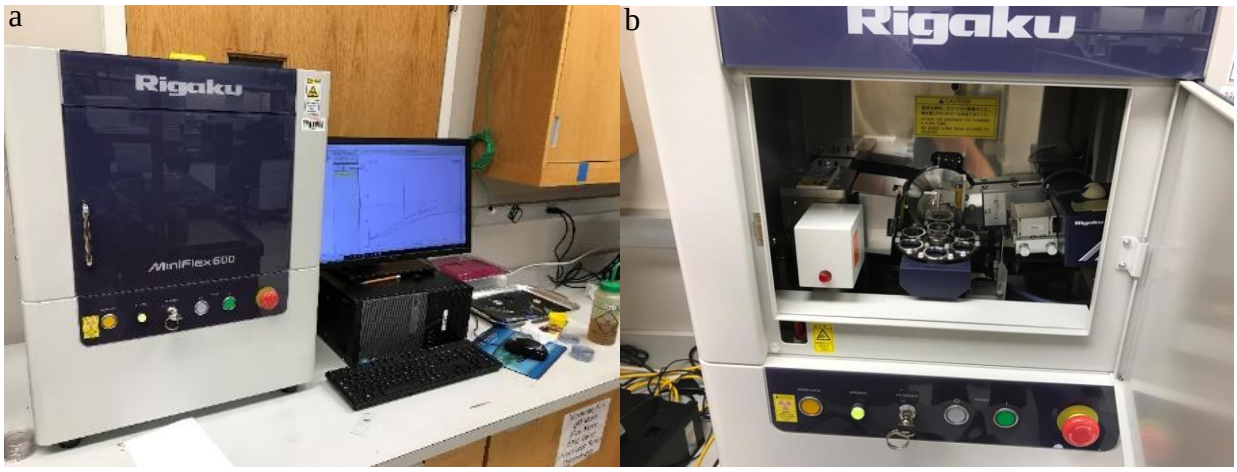

Figure 52: a) XRD characterization machine, b) view of sample holders.

4.5 Measurement of Seebeck coefficients and electrical conductivity

The electrical resistivity was measured by using Linseis-LSR3 (LSR3, LINSEIS, Selb, Germany) equipment under an He environment for the same temperature range. The Seebeck coefficient was measured simultaneously (Figure 53 a and b). The samples were prepared in the cylindrical shapes (L=10-14mm and D=6mm) (Figure 53c). The samples' surfaces were degreased by isopropyl alcohol to reduce any error in the electrical and temperature measurements (Figure 53d). In addition, carbon paste and carbon sheets were used to create proper electrical and thermal contacts for the measuring probes. The commercial LINSEIS software calculates the thermopower from a single temperature gradient (ΔT) and voltage difference (ΔV), which is often erroneous. Therefore, the measurement was performed for five different temperature gradients, and each measurement was repeated four times and then averaged. The thermopower was calculated from the slope of the

line fitted to five separate temperature and voltage differences. The accuracy of the measurement was verified by inspecting the linear fit to the ($\Delta T - \Delta V$) data set (Figure 54).

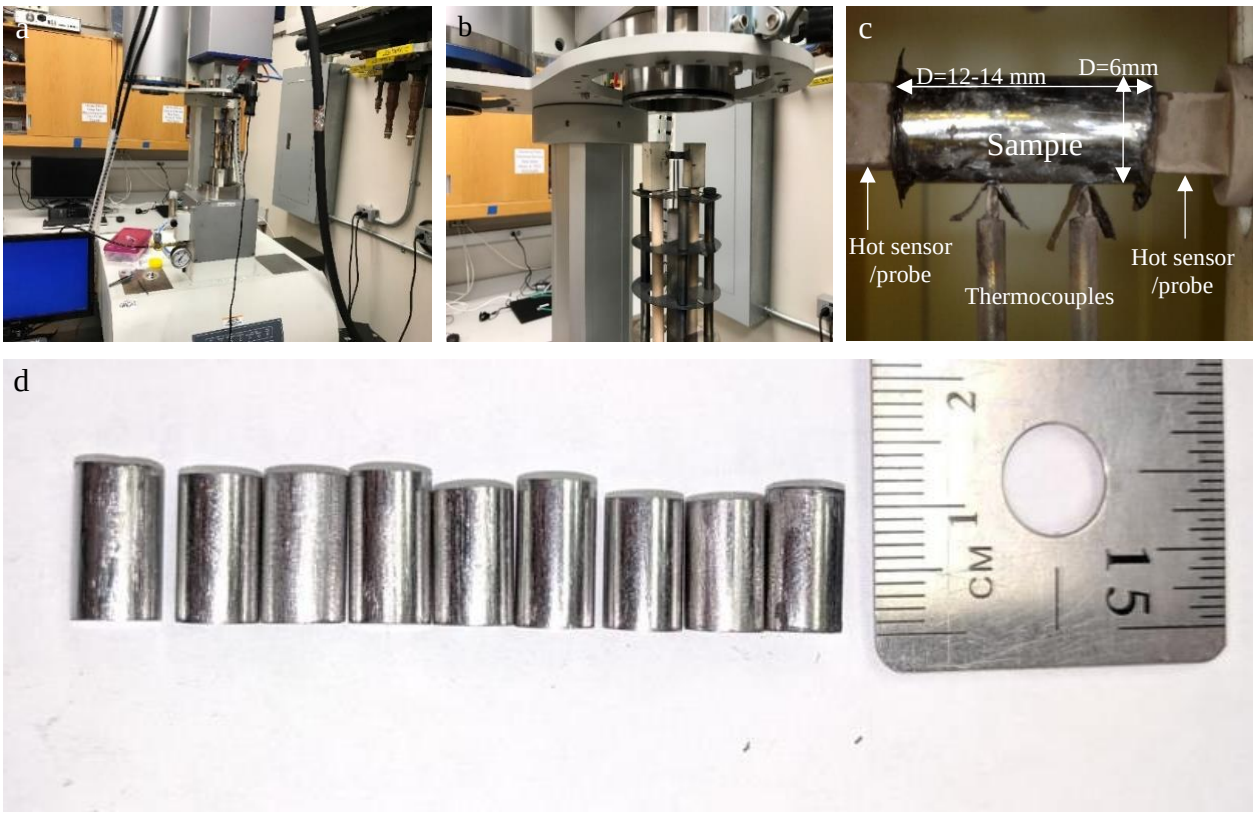

Figure 53: a) LINSEIS -LSR3 machine and b, c) sample set up, d) Prepared samples with shiny clean surface to measure S and σ.

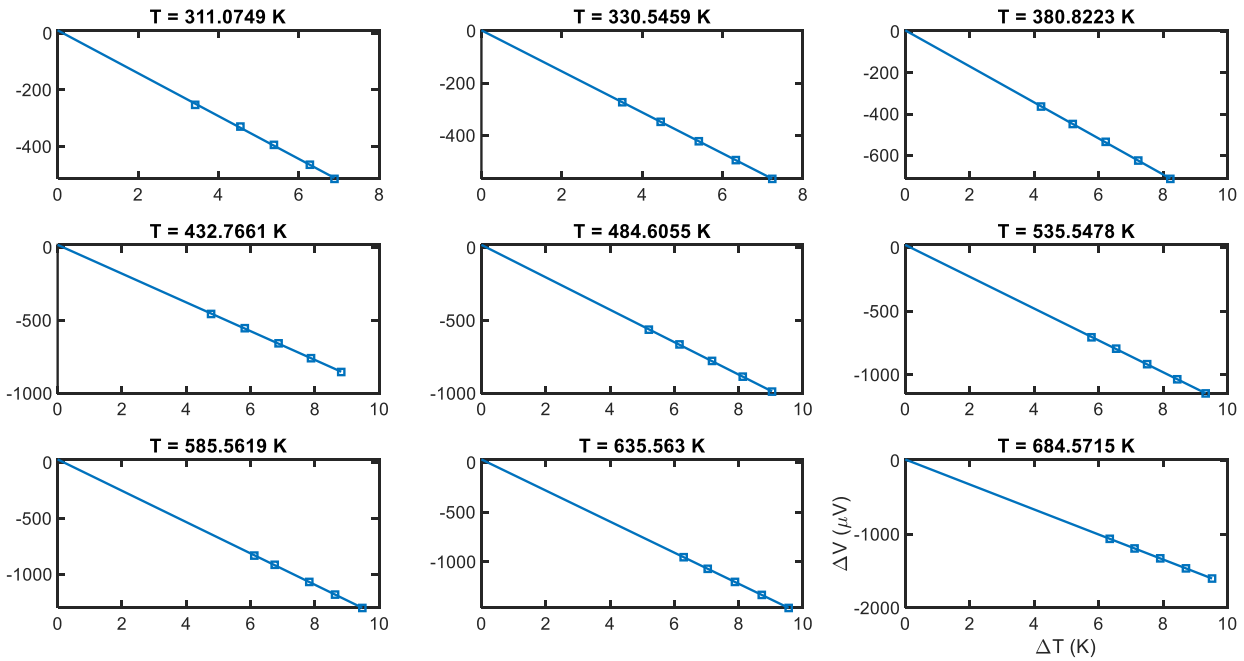

Figure 54: Linear fit to the ($\Delta T - \Delta V$) data set.

4.6 Measurement of heat capacity and thermal diffusivity

The thermal conductivity (κ) was calculated by using $\kappa = D\rho C_p$, where ρ (g.cm^{-3}) is the sample density. The specific heat capacity C_p (J. Kg^{-1}K^{-1}) and thermal diffusivity D (m^2.s^{-1}) were measured by the laser flash method on the LINSEIS LFA instrument (Figure 55). The samples were prepared in the form of thin discs with diameters of 6 mm and thicknesses of 0.5-0.6 mm. The samples were coated with a carbon spray, based on the device's instructions.

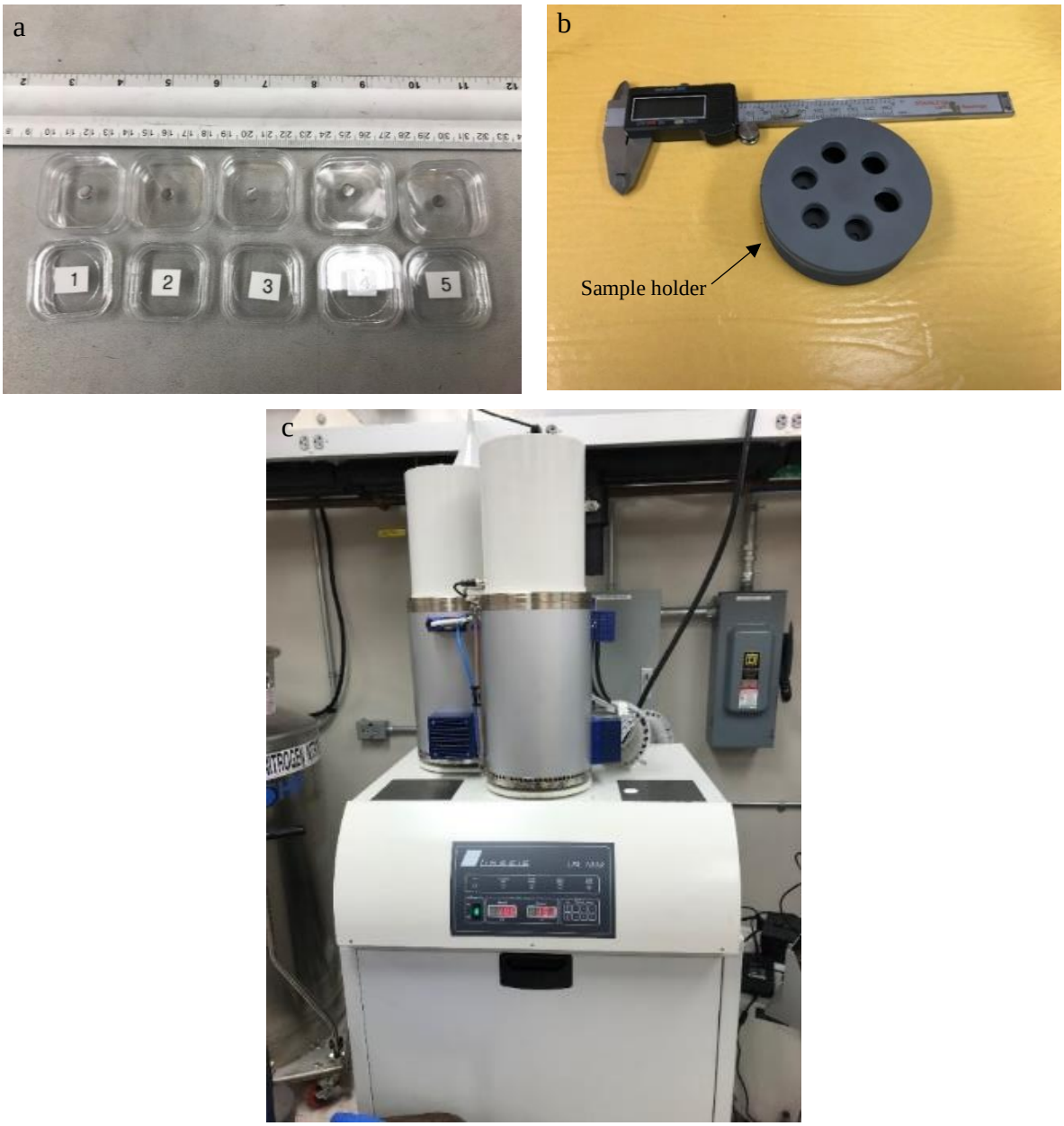

Figure 55: a) Sample preparation, b) sample holder, and c) LINSEIS LFA instrument.

4.7 Magnetic characterization

The DynaCool physical property measurement system (PPMS) was used to characterize the magnetic and electrical transport properties of the potential thermoelectric compounds (MnTe, CoVSn, $CuSbTe_2$, and their GNP-reinforced composites) in an environment where the magnetic field and temperature were well-controlled (Figure 56).

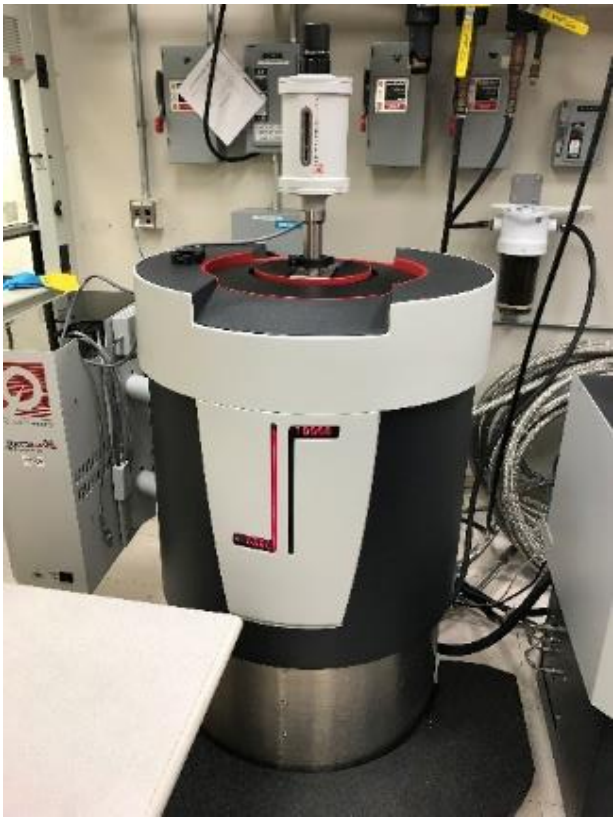

Figure 56: Physical Property Measurement System (PPMS) (Dynacool).

The geometries of samples were typically thin strips (L=~5mm, W=~3mm, and t=0.5-0.7mm) to measure the magnetic behaviours by magnetic susceptibility via the vibrating sample magnetometry (VSM) option (Figure 57), and thin discs (D=6mm and t=0.5-0.7mm) to measure electrical transport properties (e.g., Electrical transport measurements by the electrical transport option (ETO) – Figure 58).

The VSM option is a fully automated DC magnetometer. This measurement is accomplished by oscillating the sample in a pickup coil and synchronously detecting the induced voltage [410-412].

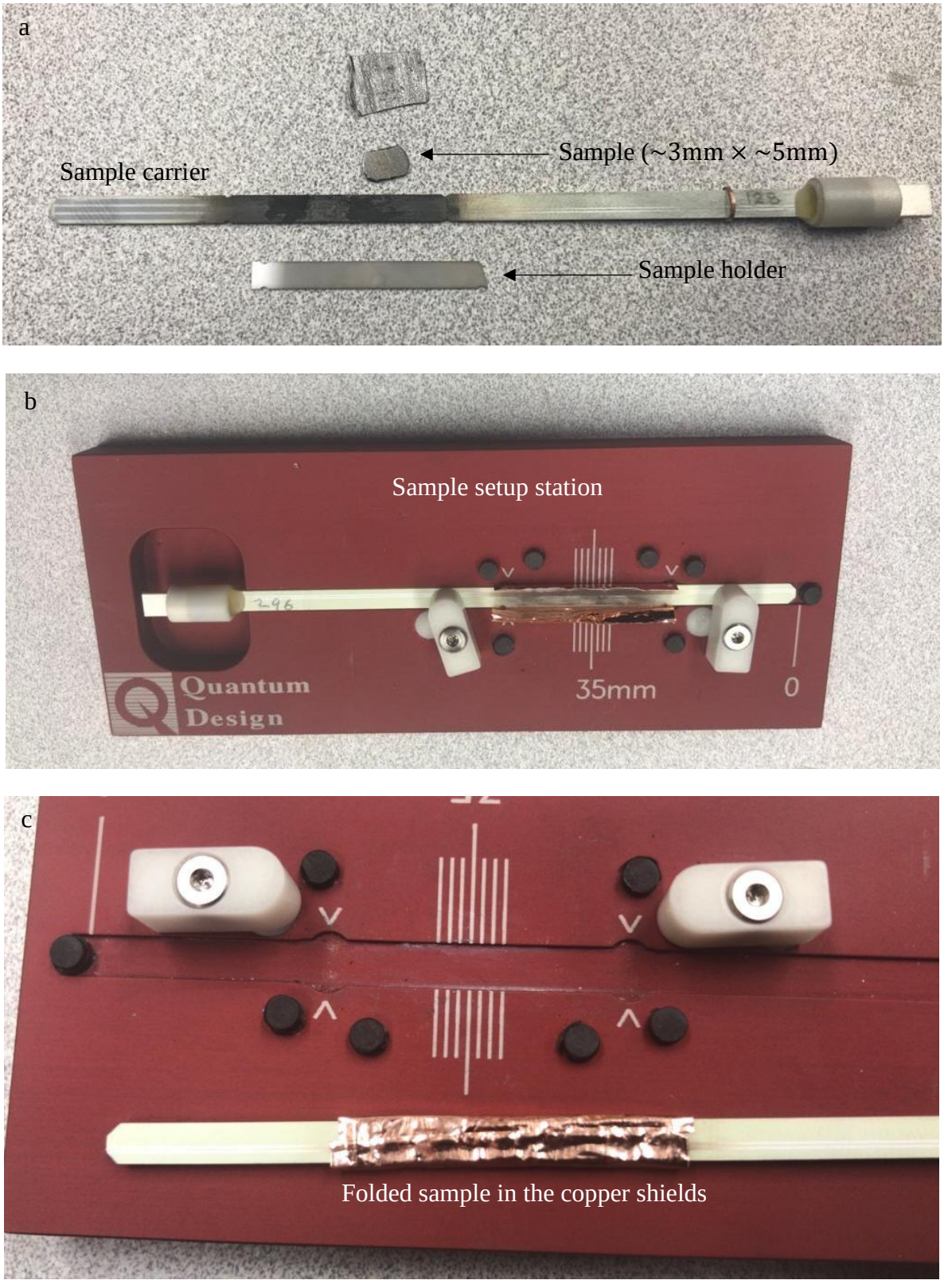

Figure 57: VSM sample preparation (c), and setup (b,c).

At room temperature, the carrier densities (n_H) and mobility (μ_H) were measured by measuring the Hall coefficients (R_H) using the Van der Pauw method by the DC resistance puck and setup (Figure 58a,b), and electrical transport option (ETO) (Figure 58c). n_H values were calculated by $n_H = \frac{1}{eR_H}$, (e is the charge of an electron) and carrier mobility was calculated based on $\mu_H = \frac{\sigma}{en_H}$.

a

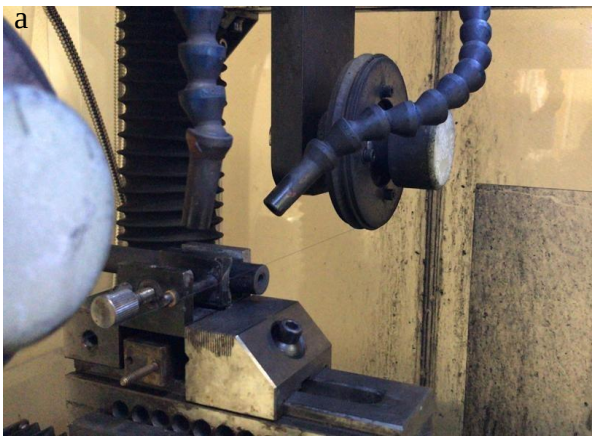

b

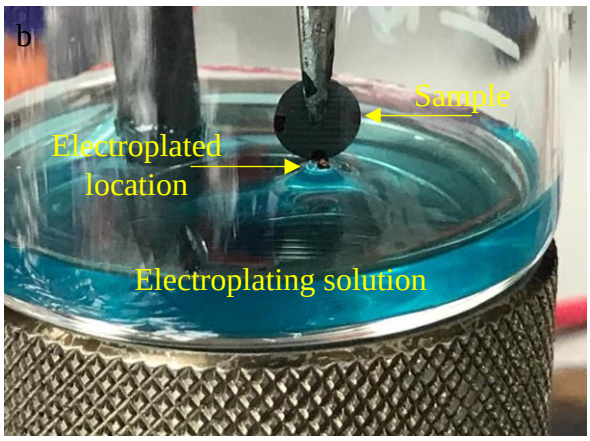

c

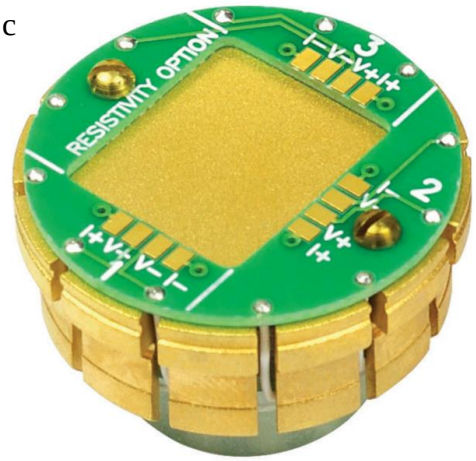

d

e

Sample (Thin disc) D= 6mm, t=0.6mm

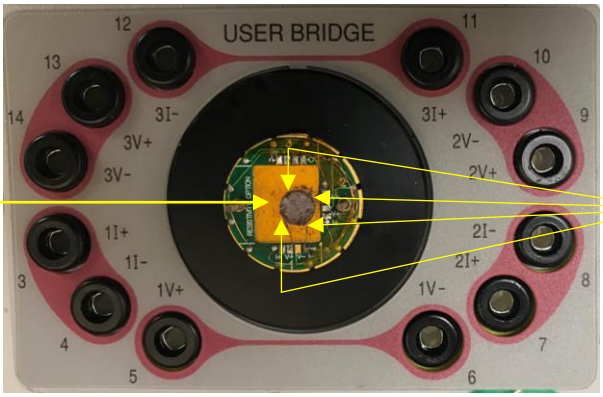

Connecting wires

Figure 58: a) Wire cutting machine to cut the sample with a thickness of 0.5-0.7mm, b) electroplating setup to prepare the connection point and reduce the electrical resistance at the contact points, c) resistivity puck, d) sample wiring test station, and e) sample setup for Hall measurements.

4.8 Microstructure Analysis

Microstructural analysis is performed to characterise the impact of graphene nanoplate reinforcement on the nominated TE samples. This method is capable of showing the precipitation of graphene nanoplates on the particle/grain boundaries. The sample preparation as a preliminary step for microstructural analysis is also presented.

4.8.1 Sample preparation

In order to study the microstructure and measure hardness, the samples were typically mounted in Bakelite by employing the Struers CitoPress-5 automatic mounting machine, as shown in Figure 59, and under the conditions described in Table 7.

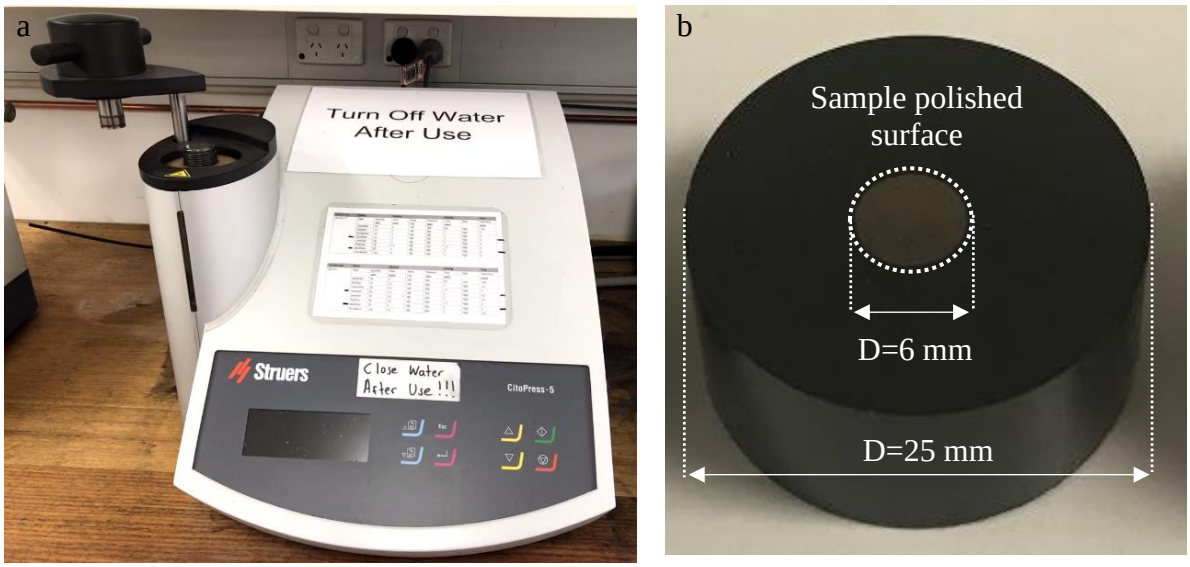

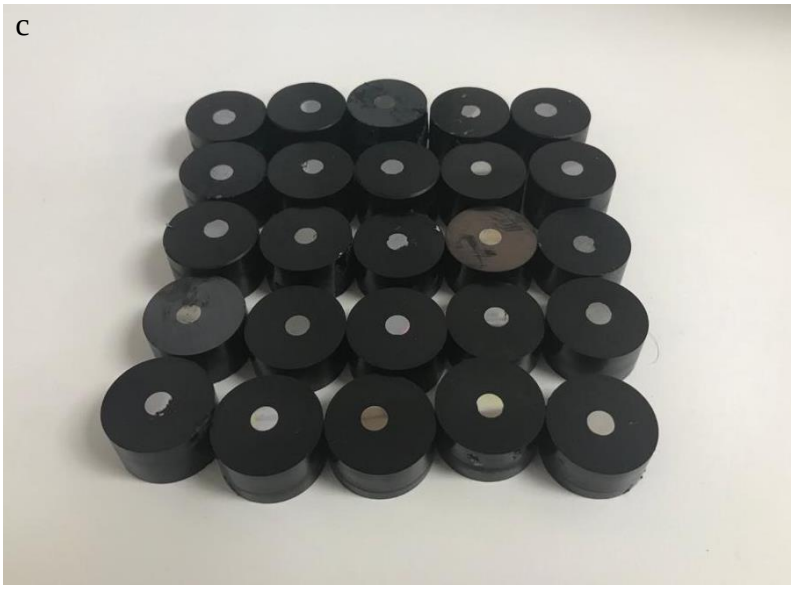

Figure 59: a) Struers CitoPress-5 automatic mounting machine, b) Dimension of a mounted specimen, and c) Example of prepared samples for microscopic analysis.

Table 7: Hot mounting parameters.

Items	Heating			Cooling
	Heating time (min)	Temperature (ºC)	Applied pressure (bar)	Cooling time (min)
Multi-fast resin	3	180	300	2

4.8.2 Polishing

Polishing took place on a Struers Tegramin 25 automatic polisher, as shown in Figure 60. Rough grinding was completed on 220, 500 and 1200 grit diamond impregnated disks. Polishing was carried out by using 9 μm, 3 μm, 1 μm diamond suspensions and 0.04 μm colloidal silica abrasives, following a short colloidal silica polishing time to prepare the samples for optical microscopy or electron microscopy analysis. The polishing procedures presented in Table 8, Table 9, and Table

10 were used for the surface preparation of MnTe-xGNPs, CoVSn-xGNPs, and $CuSbTe_2$-xGNPs (x: 0, 0.25, 0.5, 0.75, and 1 wt. %) composites, respectively.

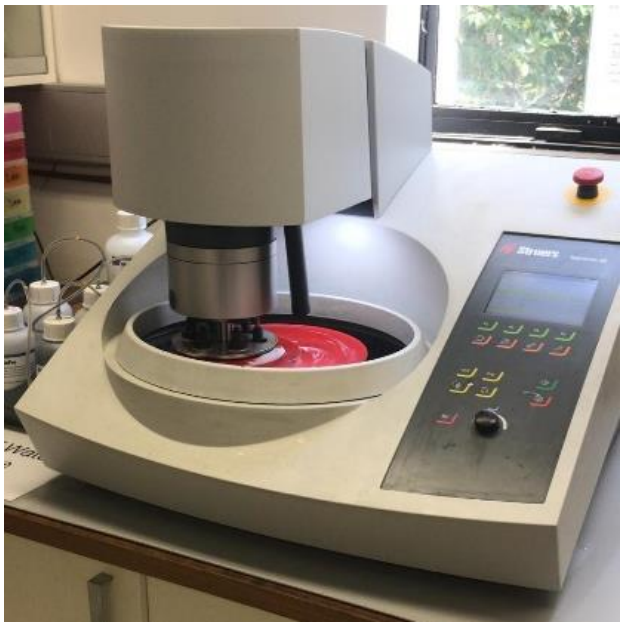

Figure 60: Struers Tegramin 25 automatic polisher.

Table 8: Polishing process for MnTe -xGNPs (x: 0, 0.25, 0.5, 0.75, and 1 wt. %), used media: Ethanol.

Compound	Step	Time (min)	RPM Head/Body	Rotation	Force (psi)	Abrasive
MnTe-xGNPs (x: 0, 0.25, 0.5, 0.75, and 1 wt. %)	1	3.00	150/150	Co-rotation	35	500 grit diamond disk

	2	3.00	150/150	Co-rotation	30	1200 grit diamond disk
	3	3.00	150/150	Co-rotation	25	9 μm diamond suspension
	4	3.00	150/150	Co-rotation	20	3 μm diamond suspension
	5	4.00	150/150	Co-rotation	20	1 μm diamond suspension
	6	7.00	150/150	Counter	15	0.04 μm Colloidal Silica

Table 9: Polishing process for CoVSn-xGNPs (x: 0, 0.25, 0.5, 0.75, and 1 wt. %).

Compound	Step	Time (min)	RPM Head/Body	Rotation	Force (psi)	Abrasive

CoVSn-xGNPs (x: 0, 0.25, 0.5, 0.75 and 1 wt. %)	1	3.00	150/300	Co-rotation	35	220 grit diamond disk
	2	3.00	150/150	Co-rotation	35	500 grit diamond disk
	3	5.00	150/150	Co-rotation	30	1200 grit diamond disk
	4	5.00	150/150	Co-rotation	25	9 μm diamond suspension
	5	3.00	150/150	Co-rotation	20	3 μm diamond suspension
	6	3.00	150/150	Co-rotation	20	1 μm diamond suspension
	7	7.00	150/150	Counter	15	0.04 μm Colloidal Silica

Table 10: Polishing process for CuSbTe2-xGNPs (x: 0, 0.25, 0.5, 0.75, and 1 wt. %).

Compound	Step	Time (min)	RPM Head/Body	Rotation	Force (psi)	Abrasive
$CuSbTe_2$-xGNPs (x: 0, 0.25, 0.5, 0.75, and 1 wt. %)	1	2.00	150/150	Co-rotation	35	500 grit diamond disk
	2	3.00	150/150	Co-rotation	30	1200 grit diamond disk
	3	3.00	150/150	Co-rotation	25	9 μm diamond suspension
	4	4.00	150/150	Co-rotation	20	3 μm diamond suspension
	5	4.00	150/150	Co-rotation	20	1 μm diamond suspension
	6	7.00	150/150	Counter	15	0.04 μm Colloidal Silica

The time spent for polishing the samples by the colloidal silica in step seven depends on the specimen's composition. Between the different polishing steps, the samples were rinsed with water or ethanol and then placed in a bath of ethanol under an ultrasonic cleaning process. The samples were cleaned for at least five minutes and then dried with ethanol and hot air.

4.8.3 Optical Microscopy

Optical microscopy took place using a Zeiss AXIO Imager.M2m reflected light optical microscope fortified with bright field, dark field and cross-polarization filters. The microscope provides a 10× ocular and 5×, 10×, 20×, 50×, and 100× objectives (Figure 61). Images were analysed with Axiovision software version 4.9.1.

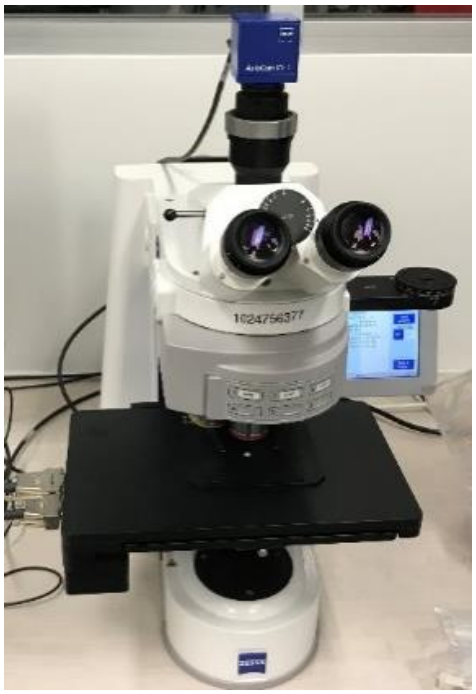

Figure 61: Zeiss Axio Imager.M2m optical microscope.

4.8.4 Electron Microscopy

The electron microscopy was performed at Adelaide Microscopy; a branch of the Australian Microscopy and Microanalysis Research Facility (AMMRF). Electron microscopy was employed to generate scanning electron microscopy (SEM) images of the microstructure, Energy dispersive

X-ray spectroscopy analysis of phases within the microstructure and to create Electron backscatter diffraction (EBSD) maps.

4.8.4.1 Scanning electron microscopy (SEM)

General scanning electron microscopy (SEM) imaging was accomplished at Adelaide Microscopy on the FEI Quanta 450 FEG Environmental Scanning Electron Microscope (ESEM) shown in Figure 62. The microscope contained both secondary and backscatter electron detectors and is equipped with an Oxford Ultim Max Large Area SDD EDS detector. A carbon tape was used to bridge the connection from the sample surface to the standard 25 mm diameter stub.

Figure 62: Quanta 450 FEG ESEM.

4.9 Hardness measurement

The hardness (H) is a mechanical feature often measured for thermoelectric materials and other brittle compounds via nanoindentation or microindentation. Hardness testing is relatively quick, straightforward, and needs only a planar specimen surface [339]. Vickers' hardness is a determination of the material resistance against the plastic deformation. A Vickers' hardness indenter imposes a constant load over a time period (10-15 seconds) according to the ASTM E384 standard [413]. In a Vickers' hardness tester, there is a square base pyramid (diamond) built-in tip

angle of 136º - see Figure 63a. The applied force to this indenter results in a square with diagonals d_1 and d_2, as demonstrated in Figure 63b.

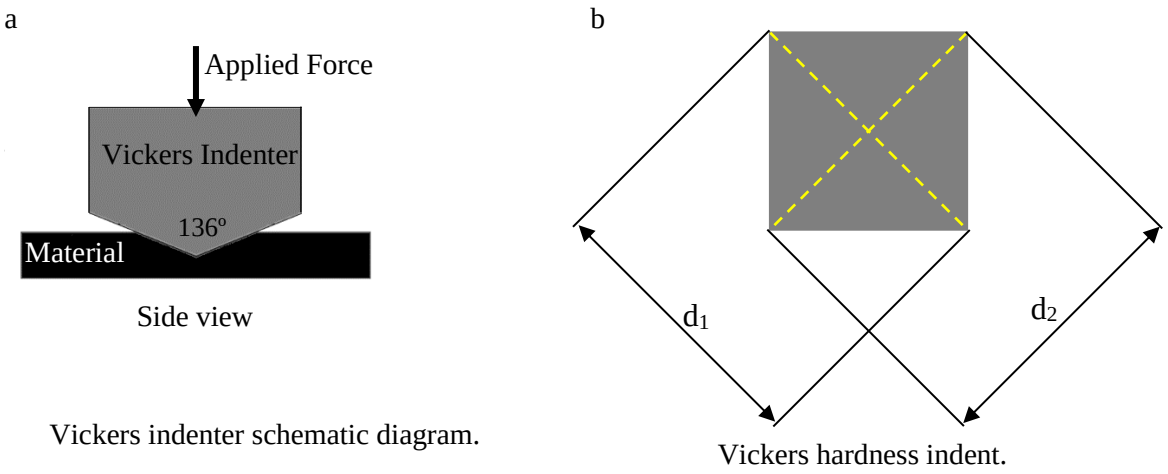

Vickers indenter schematic diagram.

Vickers hardness indent.

Figure 63: Schematic diagram of a) Vickers hardness indenter and b) the indent produced.

The Vickers' hardness number can be calculated based on the applied force and resultant area. The area of the indent is determined based on the average diagonal length, including d_1 and d_2, Equation 45.

$$A = \frac{d^2}{2\sin(\frac{136^\circ}{2})}\ [mm^2] \qquad (45),$$

$$HV = \frac{F}{A} = \frac{F \times 2\sin(\frac{136^\circ}{2})}{d^2}\ [\frac{kgf}{mm^2}] \qquad (46),$$

$$HV \approx \frac{0.1891 \times F}{d^2}\ [\frac{N}{mm^2}] \qquad (47),$$

where F is in Newtons and d is in mm.

Vickers' hardness testing was performed by a LECO LM700AT microhardness tester, with an applied force of 1000 g and a dwell time of 10 s, presented in Figure 64 according to the ASTM E384-17 standard [413].

Figure 64: LECO LM700AT Vickers' microhardness tester.

Based on the ASTM E384-17 standard, the subsequent hardness indents were created in the spaces greater than 3× the diagonal length of the indent (typically 500 μm intervals) to eliminate any influence from previous indents on the further measured hardness and mechanical properties.

> Equipped with his five senses, man explores the universe around him and calls the adventure Science.
>
> — Edwin Hubble (1889 - 1953)

CHAPTER FIVE

RESULTS AND DISCUSSION- MnTe-xGNPs (x: 0, 0.25, 0.5, 0.75, and 1 wt.%)

This section of the project explains the results of the thermoelectric, mechanical, and microstructural analysis of the MnTe compounds reinforced with the Graphene nanoplates (GNPs), at various weight percents, including 0,0.25, 0.5, 0.75, and 1. Figure 65a exhibits the XRD pattern for the synthesized MnTe compound, in which the majority of the diffraction peaks can be well indexed with NiAs-type crystal structure (section 3.1) in good agreement with the literature (Figure 65b) [361]. This observation confirms the successful synthesis of pristine MnTe powder to be reinforced by graphene nanoplates.

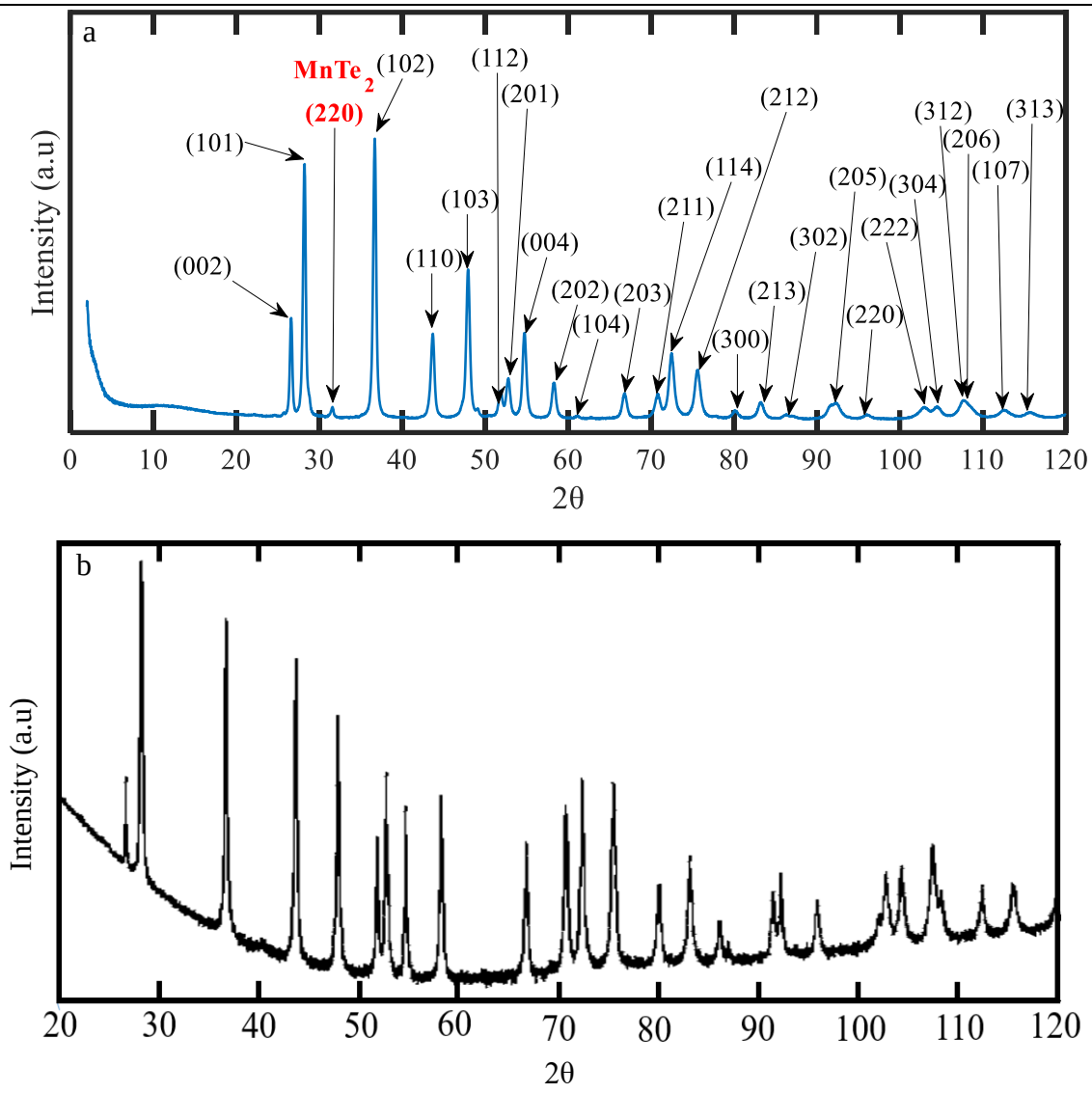

Figure 65: XRD spectra of the MnTe sintered powder, a) current work, b) literature [361].

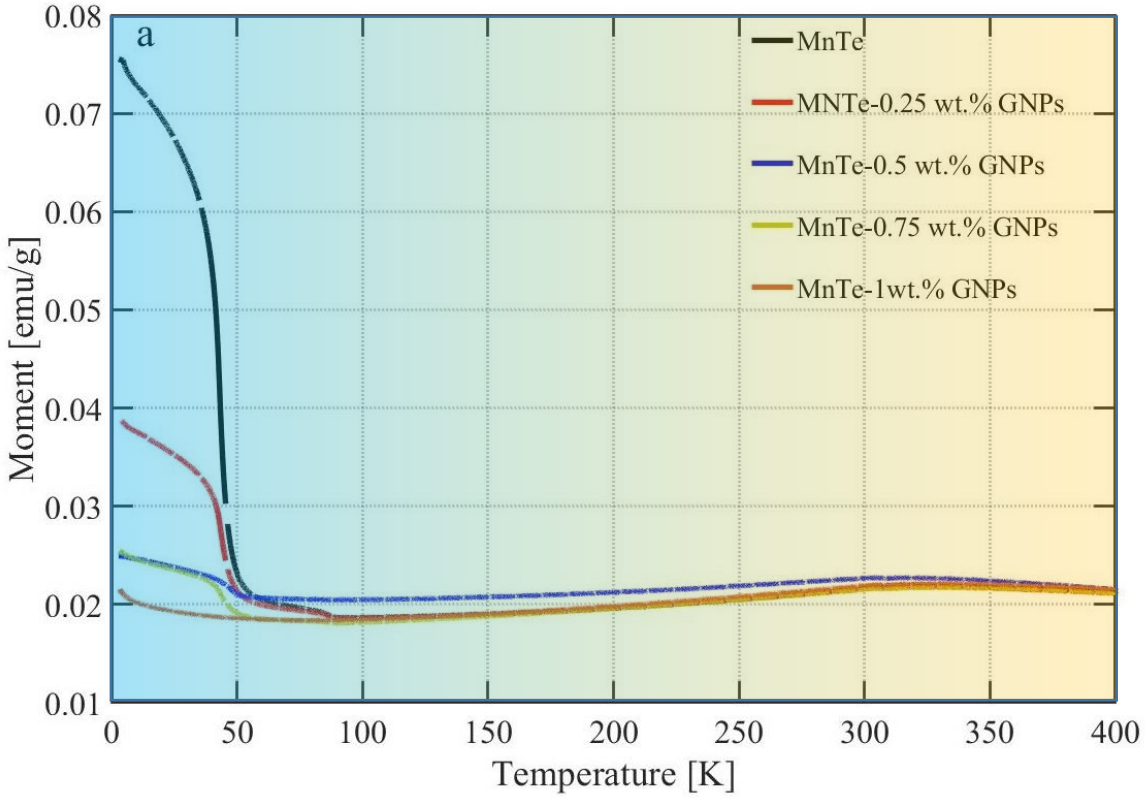
a
MnTe
MNTe-0.25 wt.% GNPs
MnTe-0.5 wt.% GNPs
MnTe-0.75 wt.% GNPs
MnTe-1wt.% GNPs
Moment [emu/g]
Temperature [K]

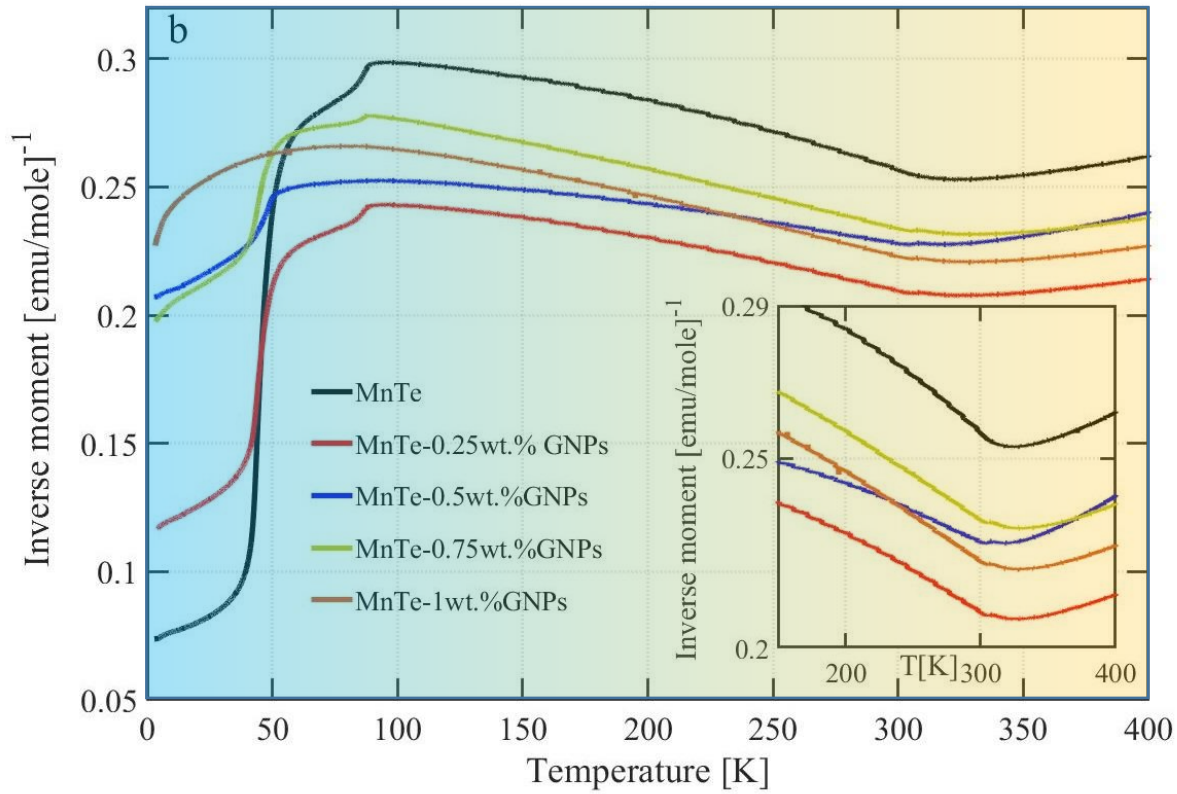
b
MnTe
MnTe-0.25wt.% GNPs
MnTe-0.5wt.%GNPs
MnTe-0.75wt.%GNPs
MnTe-1wt.%GNPs
Inverse moment [emu/mole]-1
Temperature [K]
T[K]

Figure 66: Magnetic susceptibility of the MnTe-GNP compounds versus temperature under a magnetic field of 0.1T (1000 Oe), a) moment, b) inverse moment [41].

Magnetic characterization of the MnTe and MnTe-GNP compounds indicates that the Néel temperature ($T_N \cong 307K$) [348, 349] remains almost unaffected by the GNP addition (Figure 66b-inset). The pristine MnTe shows a ferromagnetic (FM) phase over a temperature range of 0-50K (Figure 66a). The associated magnetic moment is smaller in the samples with greater GNP. Therefore, this reduction must be attributed to the dispersion of GNP in the MnTe matrix. The magnetic susceptibility (Figure 66a) shows a Curie temperature at the interval of 40-50 K. This observation indicates a probable existence of Mn_3O_4, since its Curie temperature is around 43 K [414]. Moreover, the XRD spectra, shown in Figure 67, reveals a minor peak ($2\theta=49.2^o$), which can be made to disappear by increasing the GNPs mixing ratios (Figure 67-inset). All GNP reinforced MnTe samples, except the MnTe- 0.25 wt.% GNP, also show XRD peaks at about $2\theta=40.7^o$ and $2\theta=56.6^o$, associated with the $Mn_{23}C_6$ phase [415]. The disappearance of the Mn_3O_4 XRD lines in the GNP-reinforced samples and the emergence of the $Mn_{23}C_6$ lines suggest a chemical reaction is taking place between the bulk material and the GNPs (Figure 67-inset). The comparison of the formation energies for Mn_3O_4 [416] and $Mn_{23}C_6$ [417] confirms that $Mn_{23}C_6$ is chemically more stable than Mn_3O_4. Since $Mn_{23}C_6$ is energetically more favourable, it is highly possible that in a thermally activated reaction, GNP reduces Mn_3O_4 to make $Mn_{23}C_6$, as evidenced by the disappearance of Mn_3O_4 lines in the XRD data.

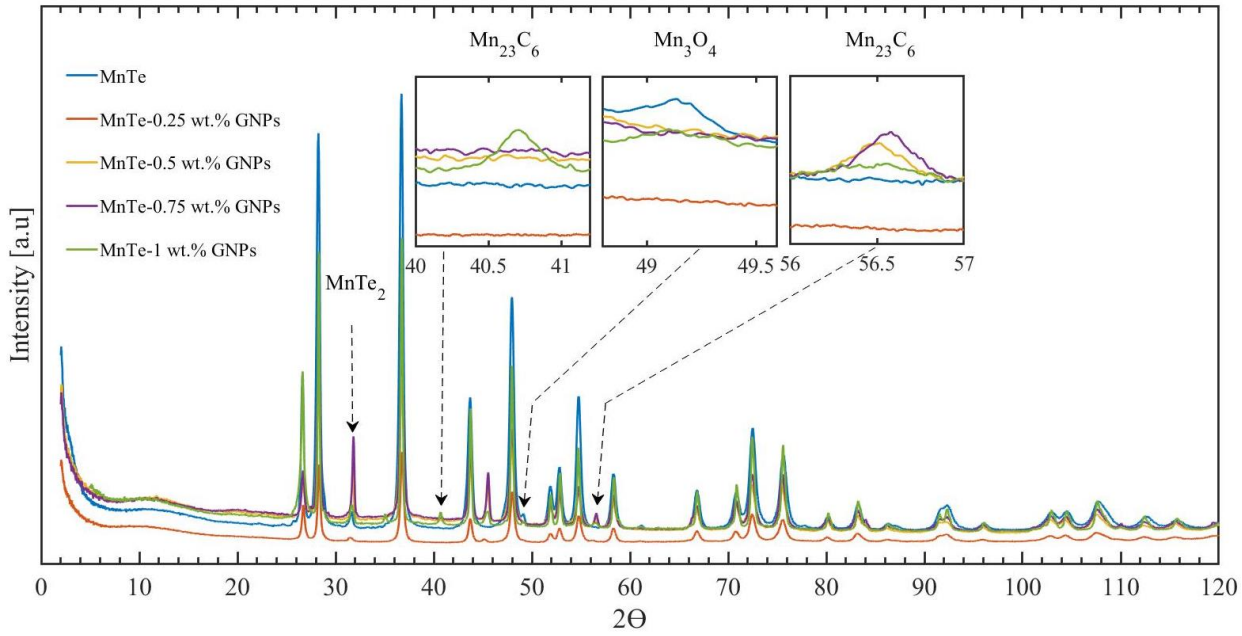

Figure 67: XRD spectrum showing the diffraction peaks for the GNP-MnTe samples. The formation of $Mn_{23}C_6$ peaks confirms the chemical interaction of Mn-C in addition to the formation of a Te-rich phase, $MnTe_2$ [41].

The Mn reaction with carbon consumes Mn, leading to Te rich domains that favour the formation of $MnTe_2$, as confirmed by the XRD peak at 2Θ=32 (Figure 67). The formation of the $MnTe_2$ phase can be explained by thermodynamic consideration [418, 419], based on three reaction steps for the formation of MnTe alloy in the current study,

1) $2Mn + 2Te \rightarrow MnTe_2 + Mn + Q_1$ @ mechanical alloying and milling, ($MnTe_2$ standard heat of formation = -26.4 kcal/mol) [420],
2) $MnTe_2 \rightarrow MnTe + Te$ @ annealing process (T:750 ºC) and spark plasma sintering (T:950 ºC)
3) $Mn + Te \rightarrow MnTe$, (MnTe standard heat of formation = -13.27 kcal/mol) [421].

It is worth noting that the second and third synthesis steps can happen simultaneously during the SPS process of the bulk samples. While these steps are likely to be completed in pristine MnTe samples, in the GNP-reinforced MnTe, the second reaction may not proceed further to the third one,

as the unreacted Mn can react with the carbon atoms (achieved by defected GNPs during the mechanical alloying) and create the stable manganese carbide of $Mn_{23}C_6$ (Figure 67) [415, 422]. In other words, $Mn_{23}C_6$ acts as a competitive phase with standard heat of formation of -58.5 kcal/mol [415] against the MnTe and $MnTe_2$ phases, with the heat of formation equal to -13.27 kcal/mol [421] and -26.4 kcal/mol [420], respectively.

Consistent with these claims, the equilibrium Mn-C phase diagram (Figure 68a) confirms that the $Mn_{23}C_6$ is stable up to a temperature of 1034 ºC, which is higher than the melting point of $MnTe_2$ (T=735ºC-Figure 68 b). Consequently, Figure 67 illustrates higher peak intensities for $Mn_{23}C_6$ and $MnTe_2$ in the samples containing more GNP (i.e., 0.75 and 1 wt.% GNPs), which almost compromises their magnetic properties (Figure 66) in comparison with the pristine MnTe. It is noteworthy that the GNPs were mixed rather than doped (atomic substitution) into the MnTe matrix; therefore there is no major variation observed in the lattice parameters calculated for the MnTe-GNPs samples (Table 11).

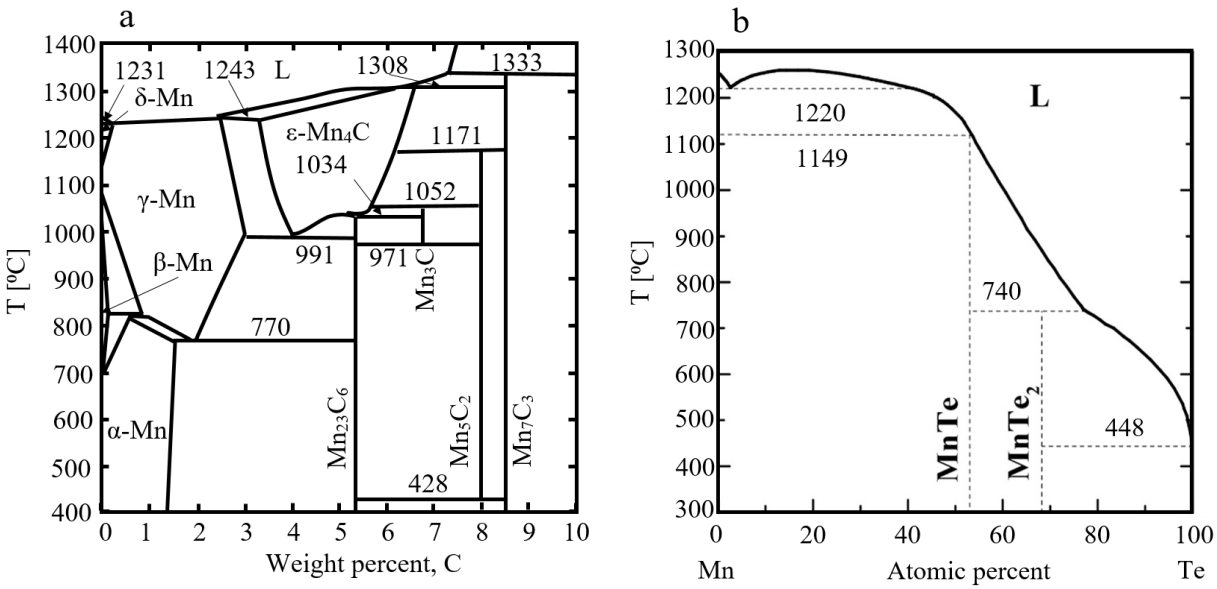

Figure 68: a) Mn-C binary phase diagram, b) Mn-Te phase diagrams [41].

Table 11: Lattice parameters of MnTe-GNPs samples calculated by PDXL software according to the XRD results.

Parameters	MnTe	MnTe-0.25wt.% GNPs	MnTe-0.5wt.% GNPs	MnTe-0.75wt.% GNPs	MnTe-1wt.% GNPs
a (ang), α=90°	4.1496	4.1491	4.1505	4.1497	4.1457
b (ang),β=90°	4.1496	4.1491	4.1505	4.1497	4.1457
c (ang), γ=120°	6.7161	6.7119	6.7242	6.7157	6.7170

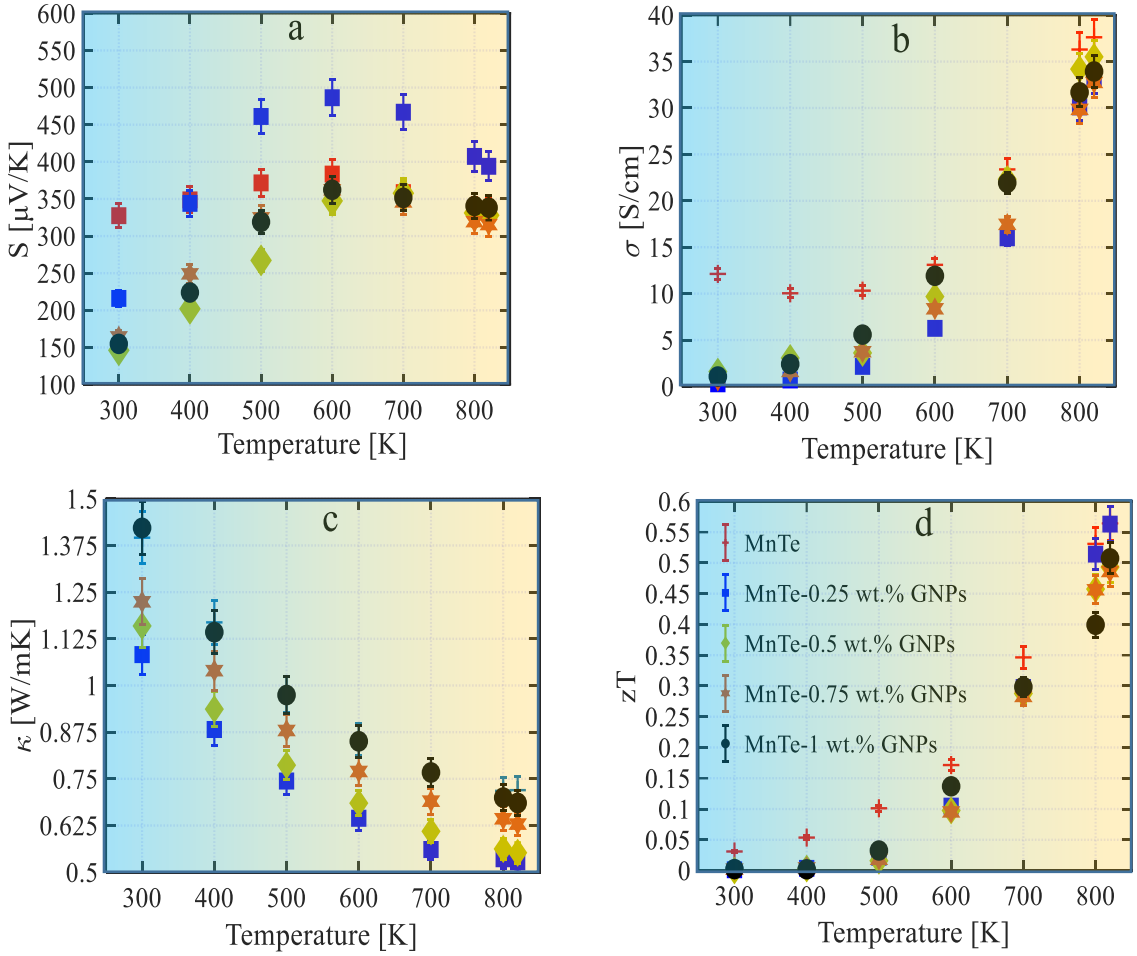

Figure 69: The temperature-dependent thermoelectric characteristics of the MnTe-xGNP compounds.

The temperature-dependent thermoelectric characteristics of MnTe-GNP compounds are presented in Figure 69 versus temperature from 300 K to 820 K. The observed transport characteristics of the

p-type MnTe near its Néel temperature (~307 K) have already been noted in several reports [423-425]. GNP mixing did not make a significant difference to the electrical conductivity at high temperatures. However, the room temperature electrical conductivity dropped with GNP inclusion. Electrical conductivity (σ) relates directly to the carrier concentration (n) and mobility (μ), i.e., $\sigma = en\mu$. To determine the impact of the graphene reinforcement on carrier concentration and mobility, the Hall effect data for two selected samples, namely MnTe and MnTe-1 wt.% GNP, were measured, as shown in Figure 70.

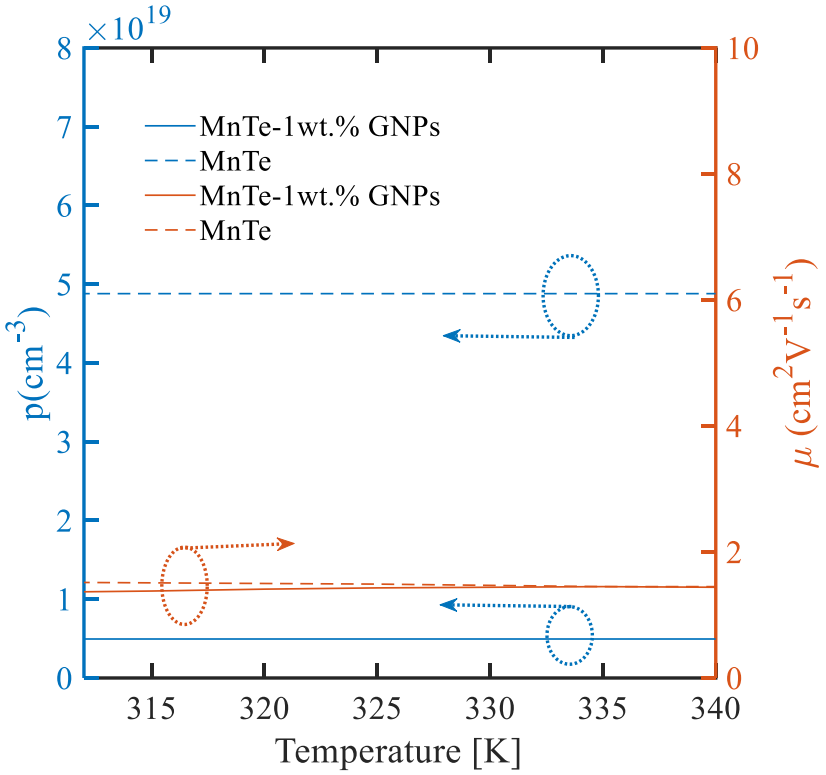

Figure 70: Carrier concentration (left axis) and Carrier mobility (right axis) for two selected samples. MnTe (broken line) and MnTe-1wt.%GNPs (solid line) [41].

The low-temperature side of the Hall data is limited to ~312K to stay away from the Néel temperature, where the critical fluctuations can distort the Hall voltage. As shown in the figure, the Hall data is in good agreement with the trends observed in the thermopower data. MnTe-1 wt.% GNP shows about 10× smaller hole concentration than MnTe. The electrical conductivity of this

sample is also about the same order more diminutive than that of MnTe. The doping mechanism in pure MnTe is by stoichiometry and defects. For example, uncompensated ions such as Mn^{1+} – Mn vacancies, as the major types of defect in MnTe, can donate a hole to the crystal [426, 427]. GNP introduces carbon to the system that may compensate some of such defects and reduce the hole concentration in MnTe, which can explain the smaller hole concentration in MnTe-1 wt.% GNP. The hole mobility for both samples is in the same order, which may seem counter-intuitive, considering the larger density of the interfaces in MnTe-1 wt% GNP. To understand the insensitivity of the carrier mobility to the interface scattering in MnTe, one must take into consideration the magnetic properties. In AFM MnTe, the dominant scattering mechanism near and above the Néel temperature is due to spin-disorder scattering [428]. This scattering is about one to two orders of magnitude stronger than any other one in the material. For example, the relaxation times due to the acoustic phonons and impurity scatterings are typically in the range of picoseconds or fractions of picoseconds. However, the spin-disorder scattering in MnTe is in the range of a few ten femtoseconds [42]. GNP addition will add more interface scattering to the material, though such defect scatterings are in the picosecond ranges and will not affect the carrier mobility significantly. Therefore, the larger Seebeck coefficient alongside the smaller electrical conductivity of MnTe-GNP samples, all indicate a lower carrier concentration in the GNP-added samples.

The segregation of the graphene phase (GNPs) at the microstructural boundaries is illustrated in Figure 71 (a,b). Moreover, Figure 71c illustrates the results of the x-ray line scan of the GNP (carbon) distribution in the microstructure. As shown in this figure, the path of this line was arranged to cross the microstructural boundaries containing the GNP precipitation. Based on the results, by passing through the boundary regions, the carbon peaks increase, which confirms the precipitation of GNPs at the boundaries. It is noteworthy that the interfaces may scatter the low energy carriers preferentially more than the high energy ones and thereby contribute to enhancing the Seebeck coefficient, or energy filtering mechanism [32, 429]. However, considering the lower carrier

concentration of MnTe-GNPs samples, energy filtering does not seem to be the dominant factor responsible for the observed improvement of the Seebeck coefficient in the paramagnetic region.

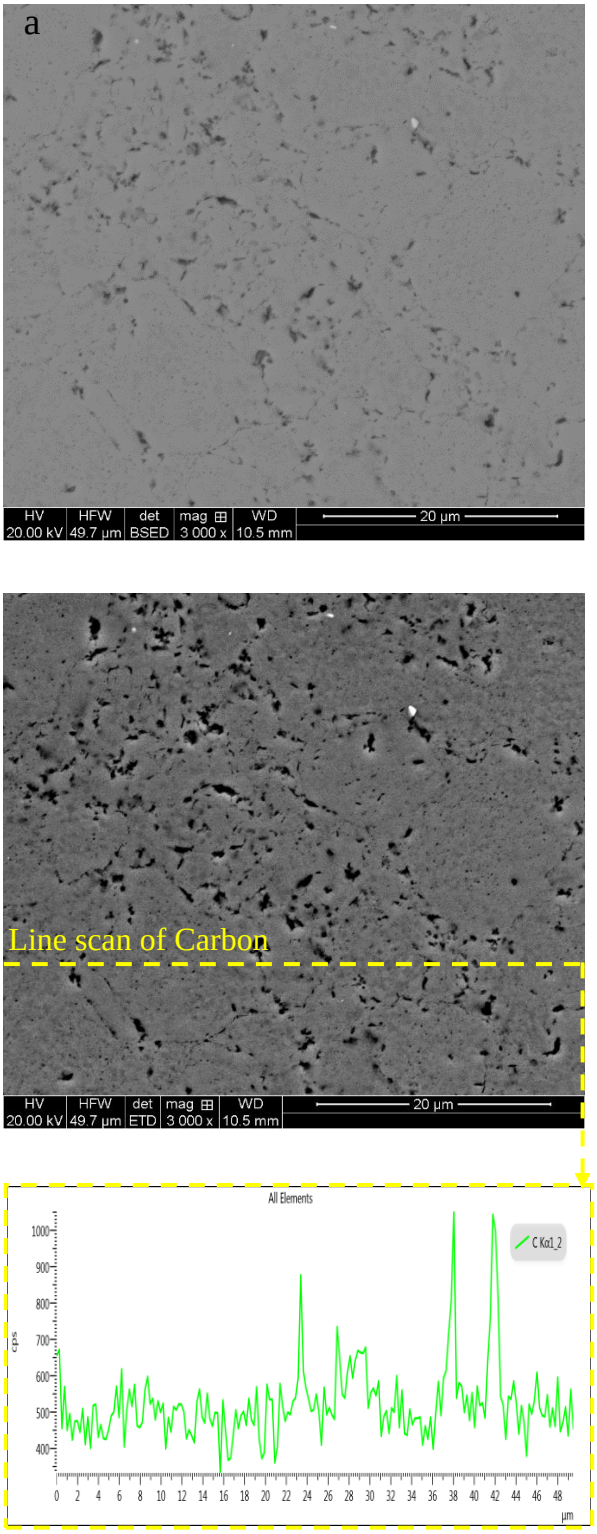

Figure 71: Graphene precipitation at the microstructural boundaries in the GNP-reinforced MnTe sample, a) BSE image, b) Micrograph, and c) x-ray line scan of Carbon distribution [41].

Concurrently, the thermal conductivities have also been reduced (Figure 69b), owing to the interface scattering of the acoustic phonons in the MnTe-GNP matrix [206, 430]. Overall, the samples with 0.5, 0.75, and 1wt.% GNPs did not show enhanced TE characteristics as much as the sample with 0.25 wt.% GNPs, despite the higher amount of GNP concentration.

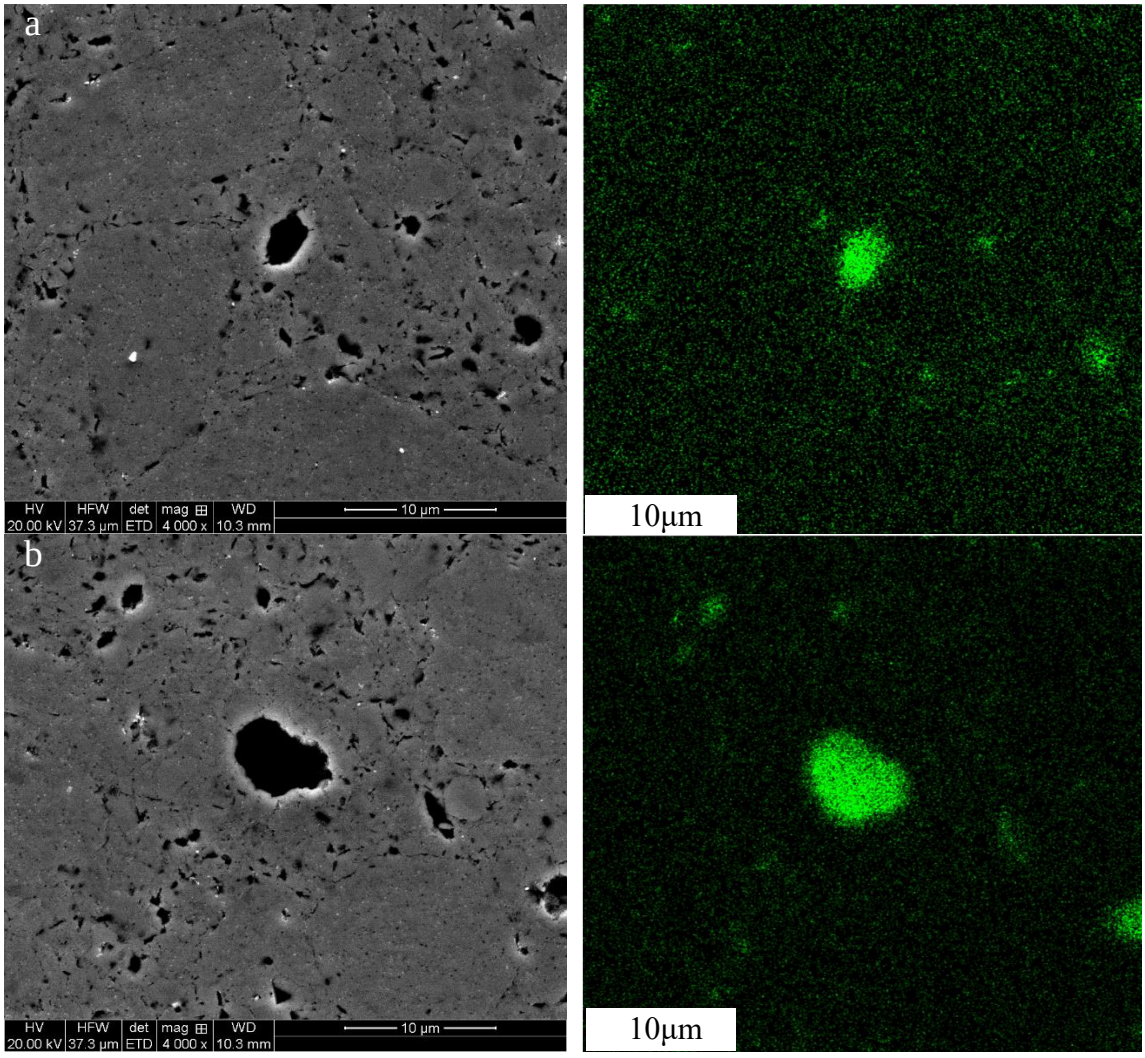

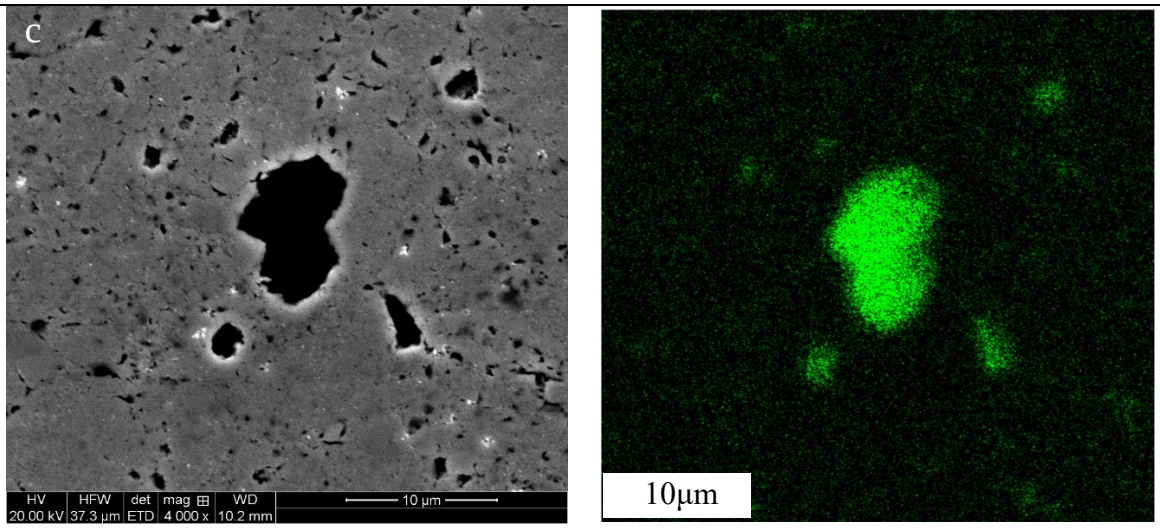

Figure 72: Graphene agglomeration in, a) MnTe-0.5 wt.% GNPs (left), and Carbon distribution X-ray map (right), b) MnTe-0.75 wt.% GNPs (left), and Carbon distribution X-ray map (right), and c) MnTe-1 wt.% GNPs (left), and Carbon distribution X-ray map (right) [41].

This may be attributed to a few reasons such as the lack of uniform dispersion of GNPs in the mixing ratios greater than 0.25wt.% GNPs (Figure 72), as similarly reported in another study [319]. Also, the phase impurities generated by GNP reaction with MnTe can deteriorate the thermoelectric properties. GNP is also a pseudo-metallic phase with a small Seebeck coefficient; hence, an excessive amount of GNP can lead to the reduction of the thermopower. To this end, the zT_{max} was determined approximately as ~0.56 at 820K for the MnTe-0.25wt.% GNP compound (Figure 69b).

Table 12: Microstructure and mechanical characteristics of the MnTe-GNP samples [41].

Sample	MnTe	MnTe-0.25 wt.%GNPs	MnTe-0.5 wt.%GNPs	MnTe-0.75 wt.%GNPs	MnTe-1wt.%GNPs
Porosity area percent	0.6	1.12	0.5	0.5	0.65
Hardness (MPa)	1442	882	1497	1514	1379

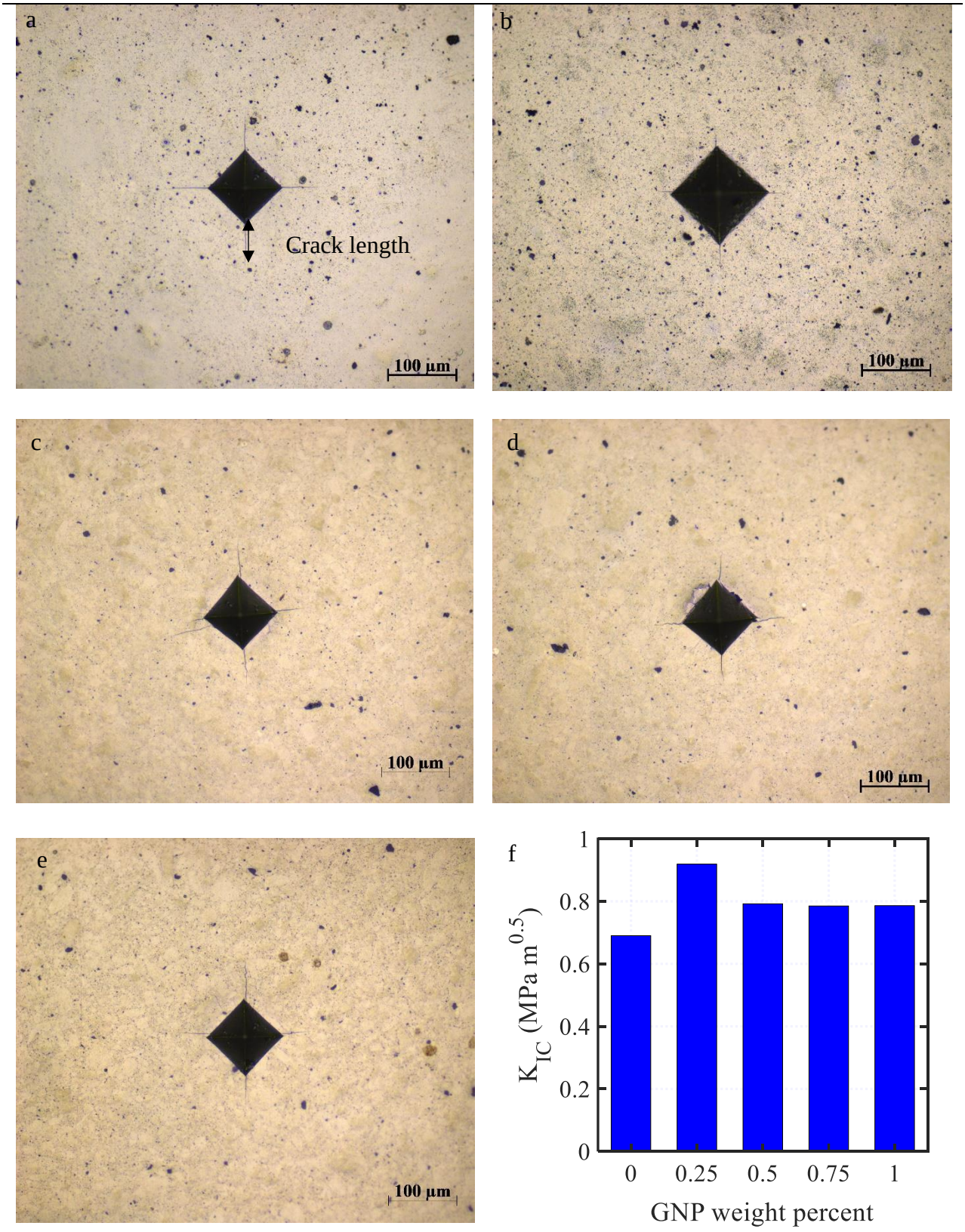

Figure 73: Crack length measurement to calculate the fracture toughness of MnTe-GNPs composites.

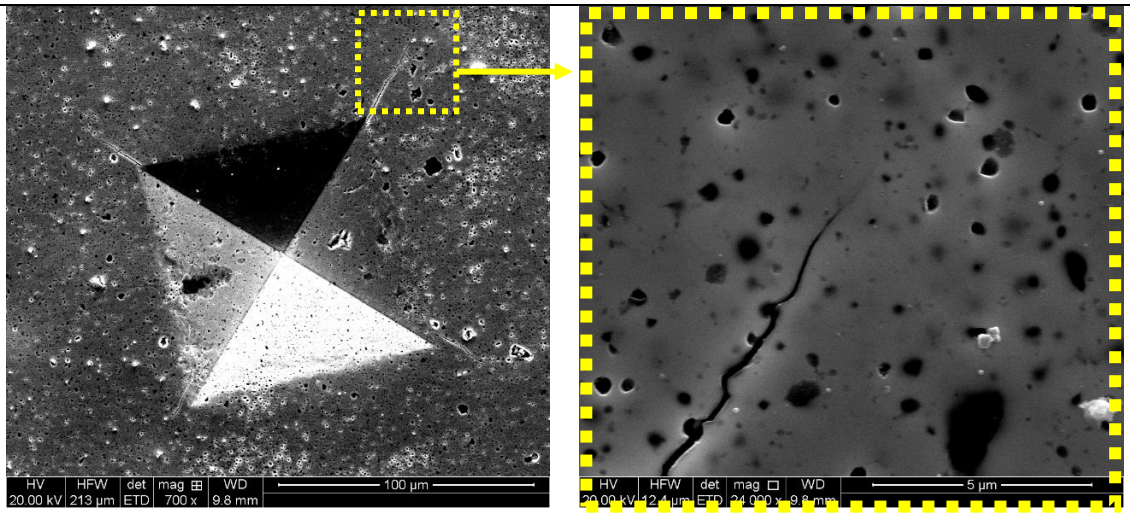

Figure 74: Micro-crack formation due to the Vickers' microhardness test (left side) and crack propagation path for 0.25 wt.% GNP-MnTe (right side) [41].

The mechanical characteristics of the MnTe-GNP compounds were evaluated through the measurement of Vickers' microhardness and calculation of the fracture toughness, as given in Table Table 12 and Figure 73. Fracture toughness (K_{IC}, MPa$\sqrt{\text{m}}$) values were calculated according to the Shetty equation $K_{IC} = 0.0899\sqrt{\frac{HP}{4l}}$ [431-433], where H, P and l are the hardness, applied load of indentation, and indentation crack length, respectively. The average of the radial crack length was calculated from five indentations measured for each specimen. The calculations exhibit higher fracture toughness values for the samples containing 0.25 wt.% GNPs (Figure 73f). Based on the illustrated crack growth path (Figure 74b), the presence of porosity in the bulk materials may influence the crack deflection [434], making the cracks reinitiate after passing through the pores. Moreover, the presence of porosity appears to have influenced the hardness values such that the samples with a higher concentration of porosity showed lower hardness (Table 12). The increase in porosity with GNP reinforcement may be attributed to the fact that in the SPS process of pristine MnTe, the local Joule heating produces melting at the particle contacts, and the applied force brings about the closure of interparticle voids [435]. In contrast, in the GNP-reinforced samples, MnTe particles are separated by GNPs, preventing them from joining together due to the low wettability

for graphene due to the MnTe matrix. [436, 437]. Furthermore, the formation of the impurity $Mn_{23}C_6$ phase (Figure 67) in the GNP-reinforced samples (GNPs ≥0.5wt.%), which is expected to increase with increasing GNP content, could increase the hardness values, as carbides are hard and brittle [436].

An experiment is a question which science poses to Nature and a measurement is the recording of Nature's answer.
— MAX PLANCK (1858 - 1947)

CHAPTER SIX

RESULTS AND DISCUSSION- CoVSn-xGNPs (x:0, 0.25, 0.5, 0.75, and 1 wt.%)

This section of the project evaluates and analyses the thermoelectric, mechancial, and microstrcuture of CoVSn composition reinforced with the Graphene nanoplates (GNPs), in various weight percents, including 0, 0.25, 0.5, 0.75, and 1. Since the thermoelectric experimental realization of this composition has not been studied in the open research database, in the first step, the synthesis and thermoelectric characterization of the pristine CoVSn are presented and discussed. Figure 75 shows the XRD data of the CoVSn powder after 15hr and 30hr milling and that of the SPS-consolidated bulk sample prepared from the sintered powder mixture. The XRD patterns of the SPS-consolidated CoVSn bulk sample revealed the presence of three binary intermetallics, namely SnV_3, Co_2Sn, and Co_3V, in addition to the non-stoichiometry CoVSn half-Heusler alloy. Therefore, the synthesized compound is shown to be a multi-phase material. Furthermore, the BSE image and the EDS maps of the material, as shown in Figure 76, illustrate a heterogeneous microstructure, which agrees with the observation from the XRD analysis. The non-uniform dispersion of the

elements of Co, V, and Sn evidence the presence of a multiphase structure with various micro-clusters.

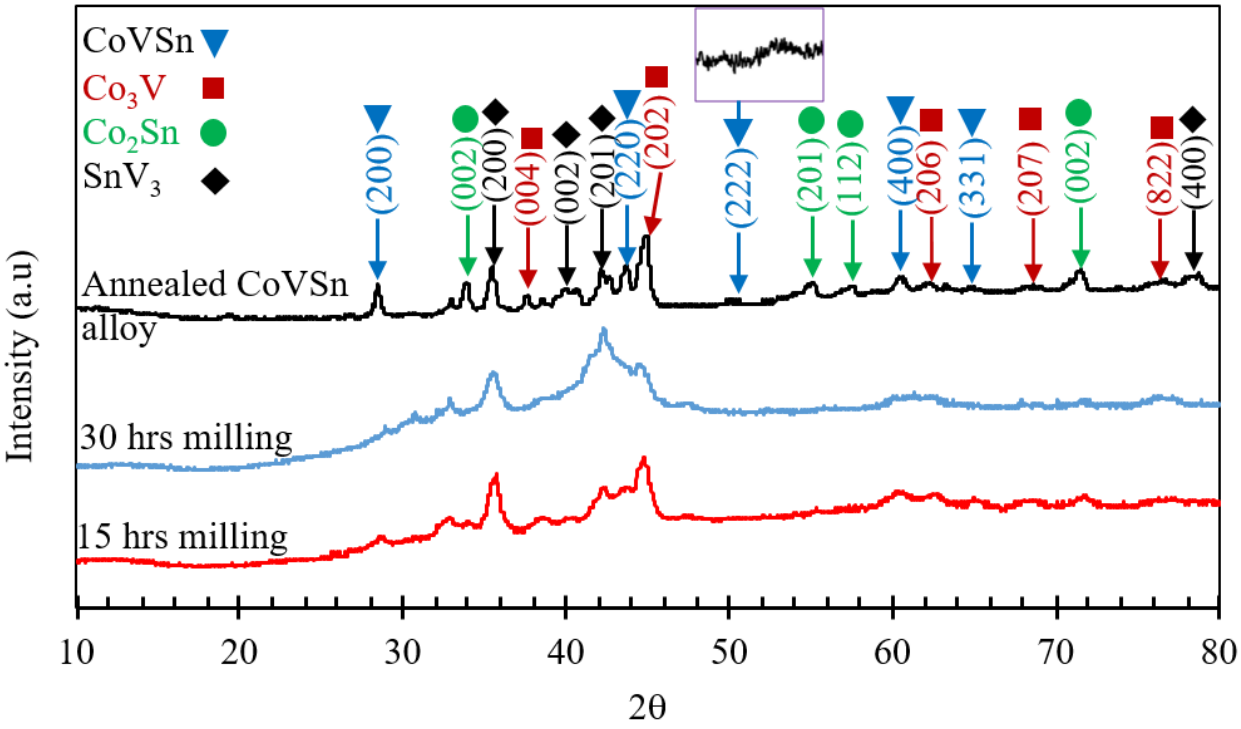

Figure 75: XRD patterns of the synthesized CoVSn compound [378].

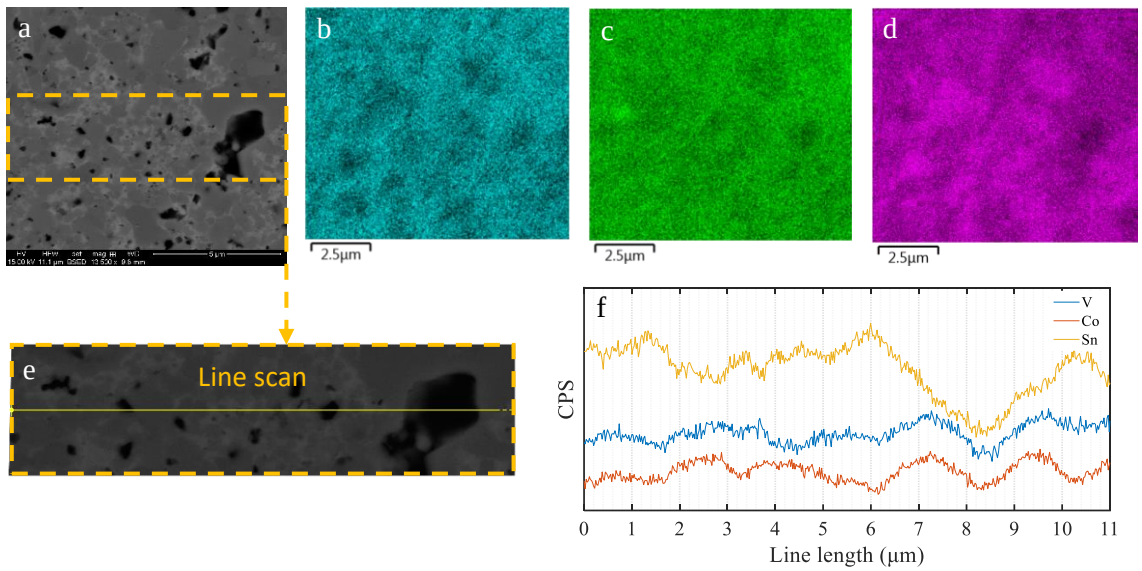

Figure 76 : a) BSE micrograph of the SPS-consolidated CoVSn composition and EDS-maps of b) Co, c) V, and (d) Sn, e) line scan, and f) element distribution along the line scan (e) [378].

Figure 77 shows the thermoelectric parameters S, σ, κ (thermal conductivity), and zT of the synthesized compound over a temperature range of 300 to 800 K. The Seebeck coefficient is negative, indicating an n-type semiconductor. This is in contrast with the theoretical prediction that the CoVSn compound should be a p-type semiconductor [71, 438]. The physical properties of the Heusler-based compound are generally highly related to the crystallographic order [439]. The observed multiphase structure (Figure 75) combines metallic characteristics due to the presence of intermetallics, such as SnV_3, Co_2Sn, and Co_3V. Therefore, the carrier type of the composition cannot be assigned to a single-phase half-Heusler CoVSn compound.

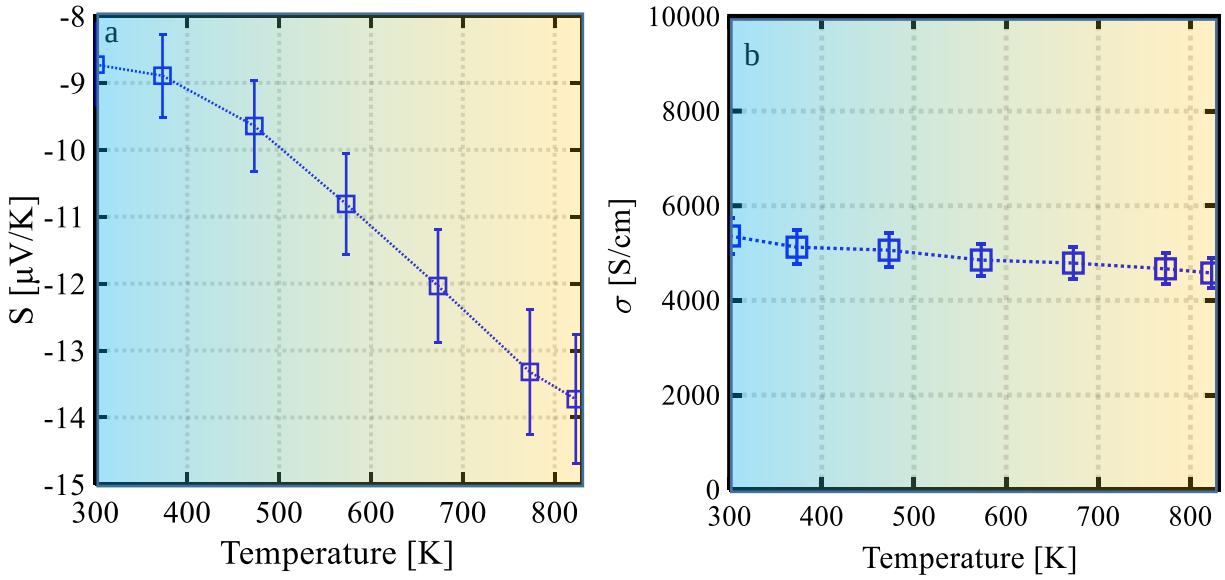

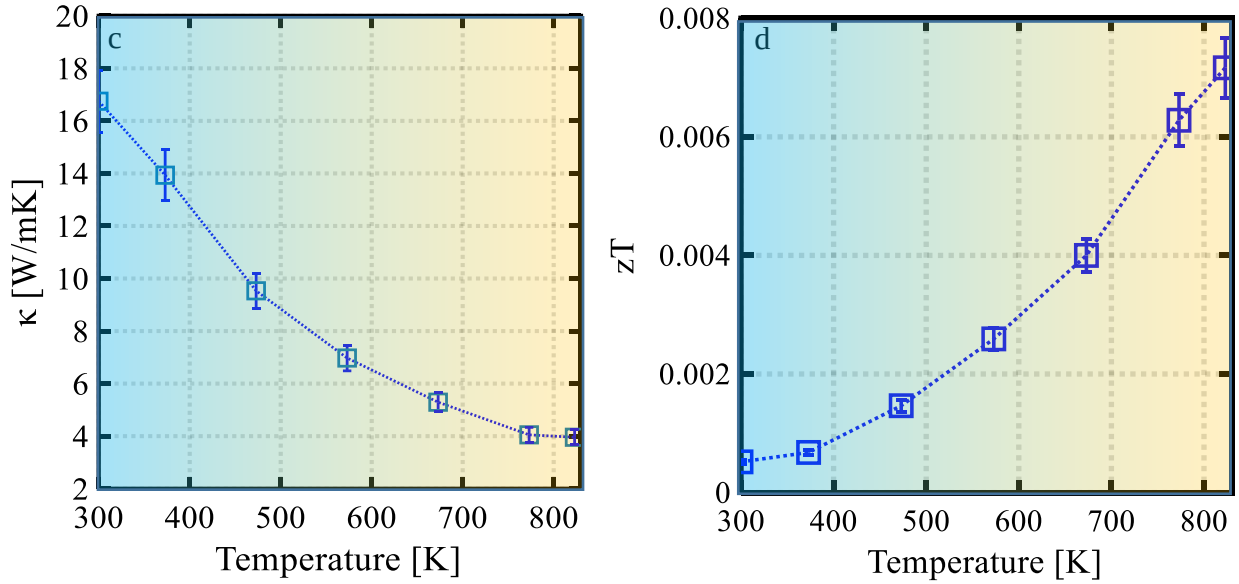

Figure 77: Temperature-dependent thermoelectric parameters of CoVSn compounds.

As illustrated in Figure 75, the multi-phase structure containing various intermetallic compounds with both semiconductor and metallic characteristics provides semiconductor-metal interfaces [440]. The CoVSn compound containing the intermetallic phases has both ionic and covalent bonds. The presence of both ionic and covalent bonds in CoVSn (VSn: ionic-rock salt, $CoSn$: covalent-Zinc blend) can influence the stability of the semiconductor-metal interfaces (i.e., interface behaviour) [441]. The metal-semiconductor contact lines up the chemical potentials and develops a Schottky barrier at the interface that can lead to distinctive chemical and electrical properties, which are different from the bulk compounds [442]. It is instructive to look at the thermodynamics of the ternary phase diagram of CoVSn. Such data are not currently available, it being a new alloy. Therefore, the ternary phase diagrams of the Co-V-Sn were calculated over the temperature ranges of interest: 25 °C and 1200 °C. The Thermo-Calc 2016a package was used for this calculation. Figure 78 shows the ternary phase diagrams at the selected temperatures of 25, 600, 900, and 1100 °C.

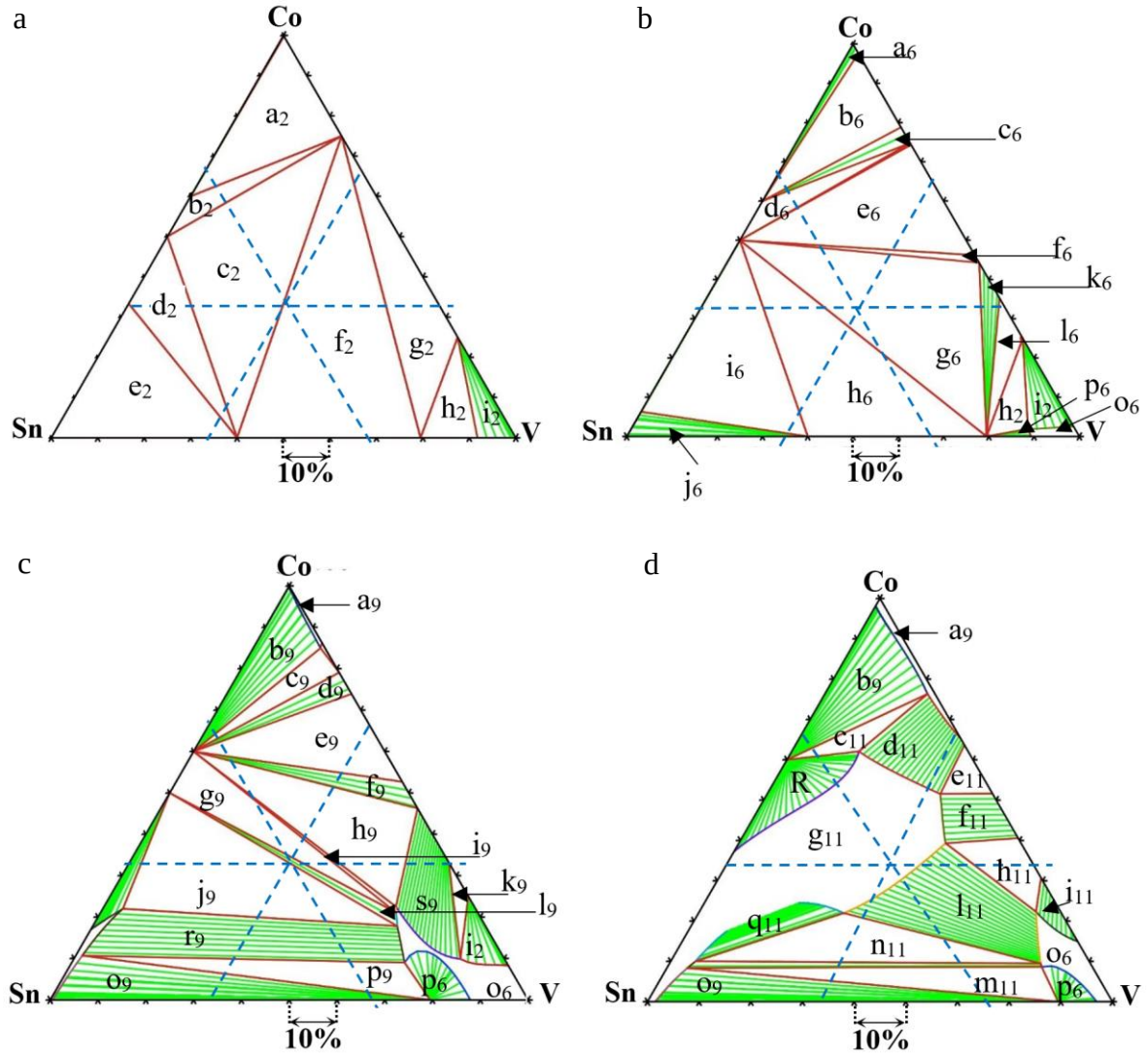

Figure 78 : Calculated ternary phase diagrams (atomic ratio) of Co-V-Sn at a) 25, b) 600, c) 900, and d) 1100 °C. Crossing point showed a composition of 1:1:1 of atomic percent and weight percent of Co: 26 wt. %, V: 22 wt. % and Sn: 52 wt. %. The Thermo-Calc package was employed to calculate the ternary phase diagrams under atmospheric pressure [378].

Table 13: Phase compositions of the nominated areas in Figure 78 [378].

Temperature (°C)	Label	Phase (s)
25	a_2	Co_3Sn_2_A+HCP_A3+HCP_ORD
	b_2	Co_3Sn_2_A+CoSn+HCP_ORD

	c_2	CoSn+HCP_ORD+Sn_3V_2
	d_2	CoSn+$CoSn_2$+ Sn_3V_2
	e_2	BCT_A5+ $CoSn_2$+ Sn_3V_2
	f_2	HCP_ORD+Sn_3V_2+ SnV_3
	g_2	CoV_3_A15+HCP_ORD+ SnV_3
	h_2	BCC_B2+CoV_3_A15+ SnV_3
	i_2	BCC_B2+CoV_3_A15
600	a_6	Co_3Sn_2_A +FCC_L12
	b_6	Co_3Sn_2_B+FCC_L12+HCP_ORD
	c_6	Co_3Sn_2_B+ HCP_ORD
	d_6	Co_3Sn_2_B+CoSn+ HCP_ORD
	e_6	ALTA_SIGMA(V,Co) +CoSn+HCP_ORD
	f_6	ALTA_SIGMA (V, Co)+ CoSn
	g_6	ALTA_SIGMA(V, Co)+ CoSn+ SnV_3
	h_6	CoSn+Sn_3V_2+ SnV_3
	i_6	LIQUID+CoSn+ Sn_3V_2
	j_6	LIQUID+Sn_3V_2
	k_6	ALTA_SIGMA(V, Co) + SnV_3
	l_6	ALTA_SIGMA(V, Co) +CoV_3_A15+ SnV_3
	h_2	BCC_B2+CoV_3_A15+ SnV_3
	i_2	BCC_B2+CoV_3_A15
	o_6	BCC_B2
	p_6	BCC_B2+SnV_3
900	a_9	FCC_L12

	b_9	Co_3Sn_2_B+ FCC_L12
	c_9	Co_3Sn_2_B + FCC_L12+ HCP_ORD
	d_9	Co_3Sn_2_B + HCP_ORD
	e_9	ALTA_SIGMA(V, Co) + Co_3Sn_2_B + HCP_ORD
	f_9	ALTA_SIGMA(V, Co) + Co_3Sn_2_B
	g_9	Co_3Sn_2_B+BCC_B2+CoSn
	h_9	ALTA_SIGMA(V, Co) + Co_3Sn_2_B+BCC_B2
	i_9	BCC_B2+Co_3Sn_2_B
	j_9	LIQUID+BCC_B2+CoSn
	k_9	ALTA_SIGMA (V, Co)+ CoV_3_A15+BCC_B2
	l_9	BCC_B2+CoSn
	i_2	BCC_B2+CoV_3_A15
	o_6	BCC_B2
	o_9	LIQUID+ SnV_3
	p_9	LIQUID+BCC_B2+ SnV_3
	p_6	BCC_B2+ SnV_3
	r_9	LIQUID+BCC_B2
	s_9	ALTA_SIGMA(V, Co) +BCC_B2
1100	a_9	FCC_L12
	b_9	Co_3Sn_2_B+ FCC_L12
	c_{11}	LIQUID+ Co_3Sn_2_B+ FCC_L12
	d_{11}	LIQUID+ FCC_L12
	e_{11}	LIQUID+ ALTA_SIGMA
	f_{11}	LIQUID+ ALTA_SIGMA (V, Co)+FCC_L12

	g_{11}	LIQUID
	h_{11}	LIQUID+ ALTA_SIGMA(V, Co)+ BCC_B2
	i_{11}	ALTA_SIGMA (V, Co)+ BCC_B2
	o_6	BCC_B2
	p_6	BCC_B2+ SnV_3
	l_{11}	LIQUID+ BCC_B2
	m_{11}	LIQUID+ LIQUID #2+SnV_3
	n_{11}	LIQUID+ LIQUID #2+ BCC_B2
	l_{11}	LIQUID+ BCC_B2
	o_9	LIQUID+ SnV_3
	q_{11}	LIQUID+ LIQUID #2

Table 14: Phase composition of CoVSn compound (1:1:1) at a temperature of 25 to 1100 °C [378].

T (°C)	Phase/ Crystal structure/Elements
25	CoSn, HCP_ORD (Co, V) and Sn_3V_2
100	SnV_3, HCP_ORD (Co, V) and Sn_3V_2
200	SnV_3, HCP_ORD (Co, V) and Sn_3V_2
300	CoSn, HCP_ORD (Co, V) and Sn_3V_2
400	CoSn, HCP_ORD (Co, V) and Sn_3V_2
500	CoSn, HCP_ORD (Co, V) and Sn_3V_2
600	CoSn, SnV_3, ALTA_SIGMA (V, CO)
700	SnV_3, BCC_B2 (Co,V,Sn), ALTA_SIGMA (V, Co)
800	Equilibrium line between two areas of (CoSn, BCC_B2 (Co,V,Sn)) and (ALTA_SIGMA (V, Co), CoSn, BCC_B2 (Co,V,Sn))

900	Equilibrium line between two areas of (CoSn, BCC_B2 (Co,V,Sn)) and (LIQUID, CoSn, BCC_B2 (Co,V,Sn))
1000	LIQUID, BCC_B2 (Co,V,Sn)
1100	LIQUID

Table 14 lists the different phases at the centre of the phase diagram, i.e., the equal atomic concentration of the elements, over 100-degree temperature steps from 25 to 1100 °C. These diagrams further confirm that at thermodynamic equilibrium, the material decomposes into multiple phases, as listed in the Table 14, which agrees with the observation in the microstructural analysis (Figure 75, Figure 76).

As shown in Table 14, there is no single phase of CoVSn, but there are mainly binary compounds of $CoSn$, SnV_3, Co_3V, and Sn_2V_3. Our observation of the multiphase structure, containing three binary intermetallics, contradicts previous studies [438, 443]. In the theoretical analysis of this composition $(1:1:1)$ [438], the calculated phase diagram showed a specific area for the stable CoVSn compound, although the presence of this single-phase alloy was not experimentally confirmed. Therefore, the CoVSn compound can be regarded as having a heterostructural composition.

The following section experimentally reports the potential mechanisms by which the graphene addition may modify the thermoelectric, microstructure and mechanical properties of the heterostructure CoVSn composition. Here the associated impacts of graphene nanoplates (GNPs) within participation in the CoVSn microstructure are analysed and represented.

The segregation of GNPs at GBs is shown in Figure 79, presenting the range of the average crystal size of CoVSn-GNPs heterostructure compounds estimated from the XRD analysis. The GNP addition has resulted in smaller crystallites, which are saturated at approximately 15-18 nm. The segregation of GNPs at the grain boundaries, creating new microstructural interfaces and providing

extra boundaries, influenced the thermoelectric properties (Figure 80). The reduction of thermal conductivity is clearly illustrated in Figure 80a. Phonon scattering against the microstructural boundaries (grain/crystal boundaries and GNP distribution as a second phase) can be regarded as a reason for reducing the thermal conductivities. Based on the results, the primary reduction occurred at a lower temperature due to the main impact of phonon scattering with a longer wavelength (low frequencies) against the grain boundaries [45].

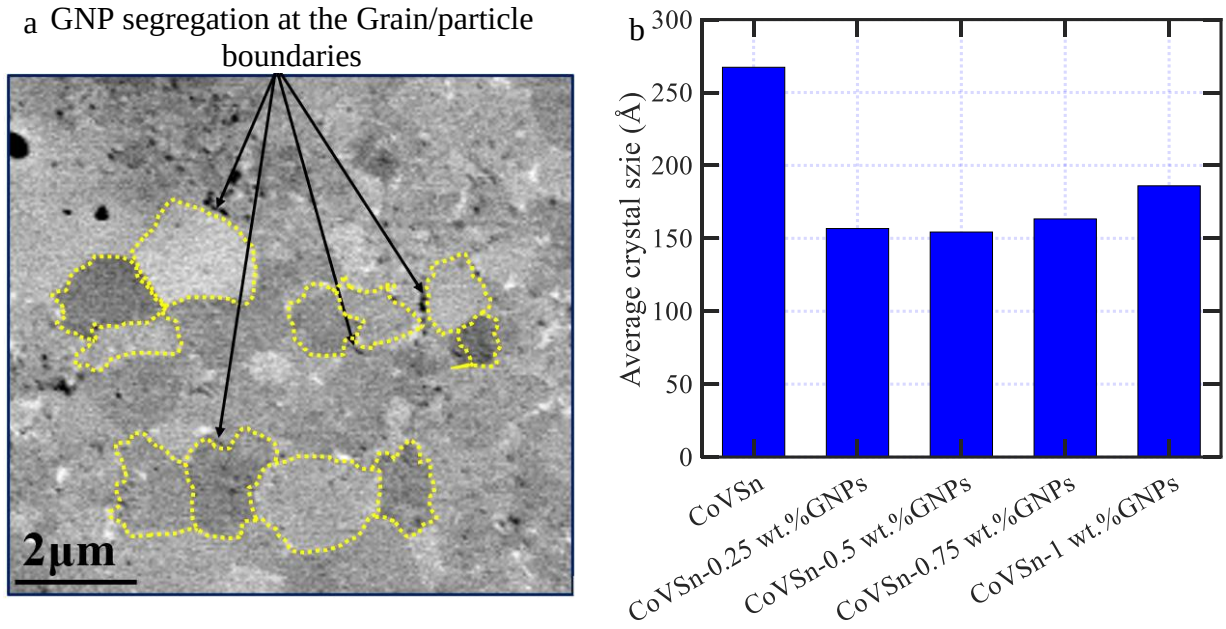

Figure 79: a) GNP segregation at the Grain/particle boundaries, and b) Average crystal size of CoVSn heterostructure composition[306].

Figure 80b shows the electrical conductivities of the samples after reinforcing with GNPs, which are in the range of conductive compounds. Moreover, Figure 80c illustrates the negative Seebeck coefficients for the samples to confirm the presence of electrons as the majority carriers. However, for the compounds with more than 0.5 wt.% GNPs, there is a disruption in the improvement of the TE characteristics. This can be attributed to a lack of uniform GNP dispersion in the matrix and formation of the agglomerated GNPs regions, as shown in Figure 81, which is also reported for other nanocomposites [319, 444].

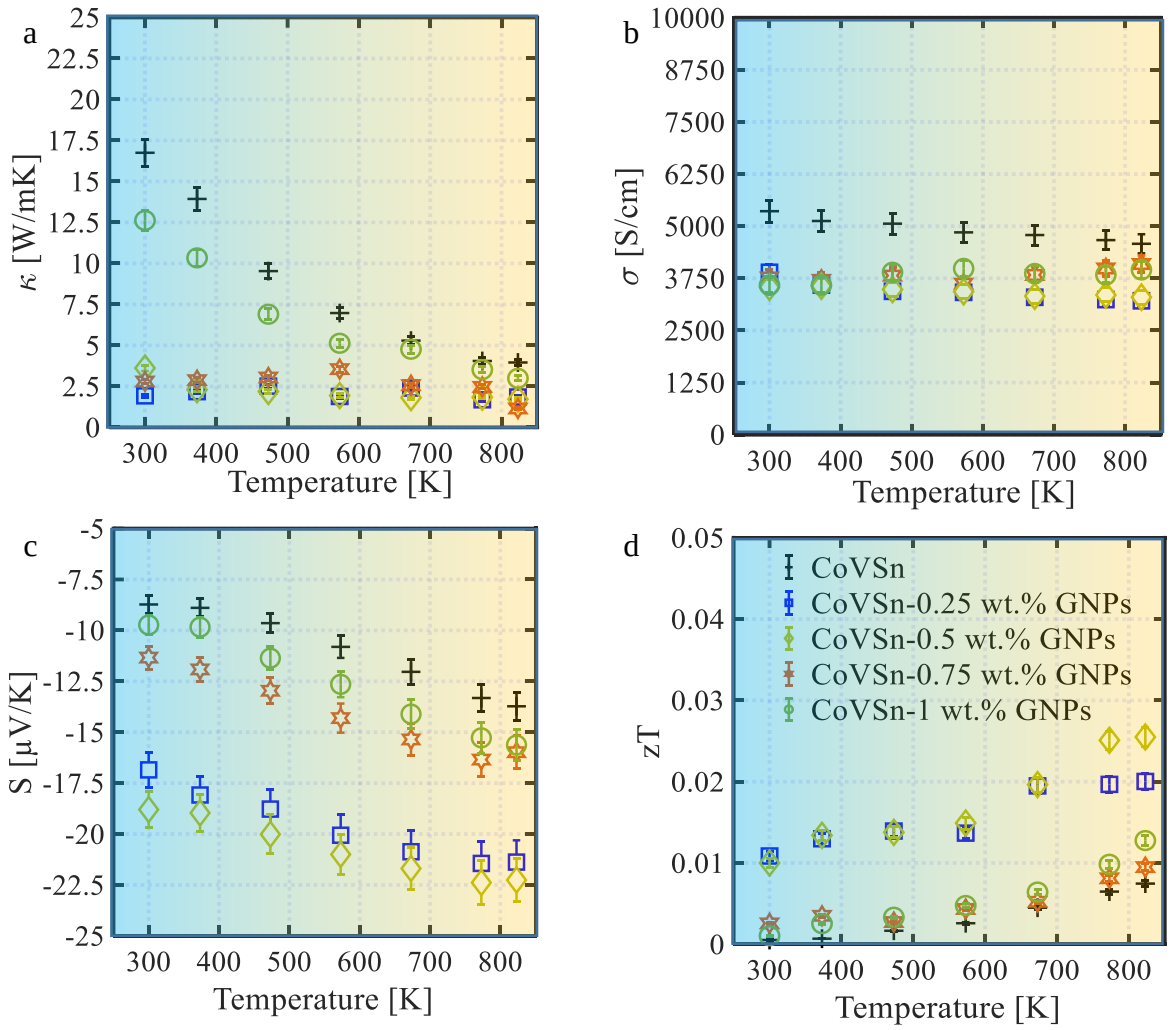

Figure 80: Temperature-dependent thermoelectric characteristics of CoVSn-GNP heterostructure compounds[306].

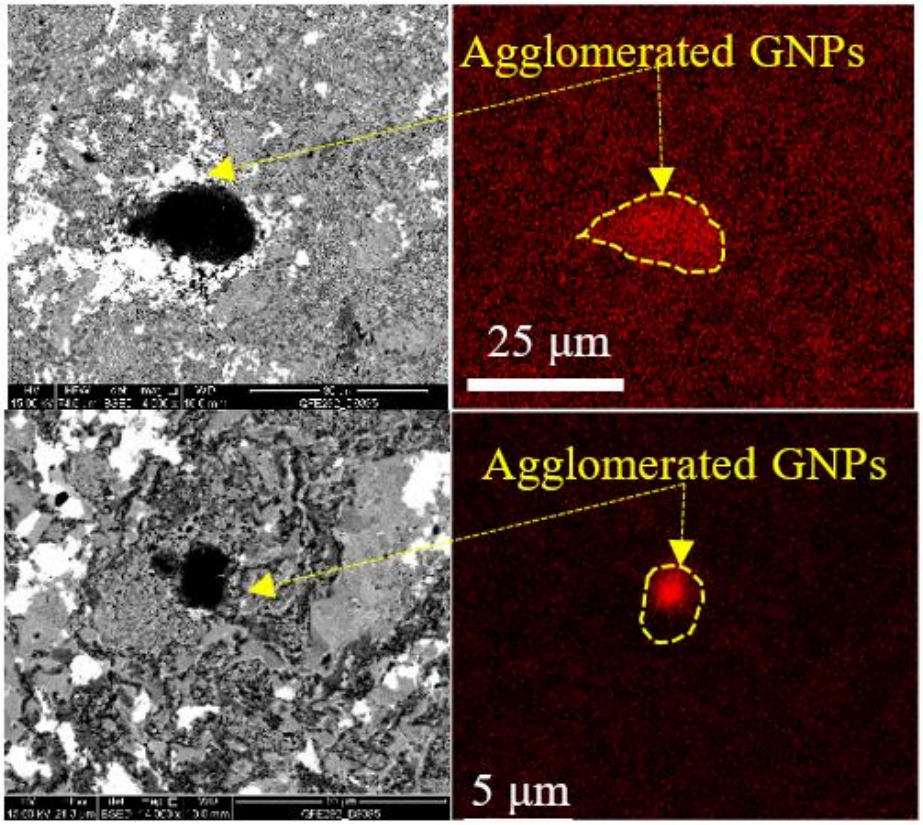

Figure 81: Backscattered electron micrographs with respective X-ray maps illustrating the GNP agglomerations in the matrix of CoVSn- 1w.t.% GNPs nanocomposite[306].

Moreover, the microstructural analysis revealed multiphase microconstituents for the CoVSn-GNPs (e.g., CoVSn-1 wt.% GNPs-Figure 82), similar to the pristine CoVSn sample, as abovementioned and discussed in [378].

Figure 82 shows the elemental dispersion via x-ray mapping. It can be seen that the distributions of the main three elements, Co, V, and Sn, are not uniform, which confirms the presence of a multiphase microstructure. Comparison with the multiphase microstructure of the pristine CoVSn shows that the incorporation of GNPs does not influence the formation of the constituent phases in the microstructure.

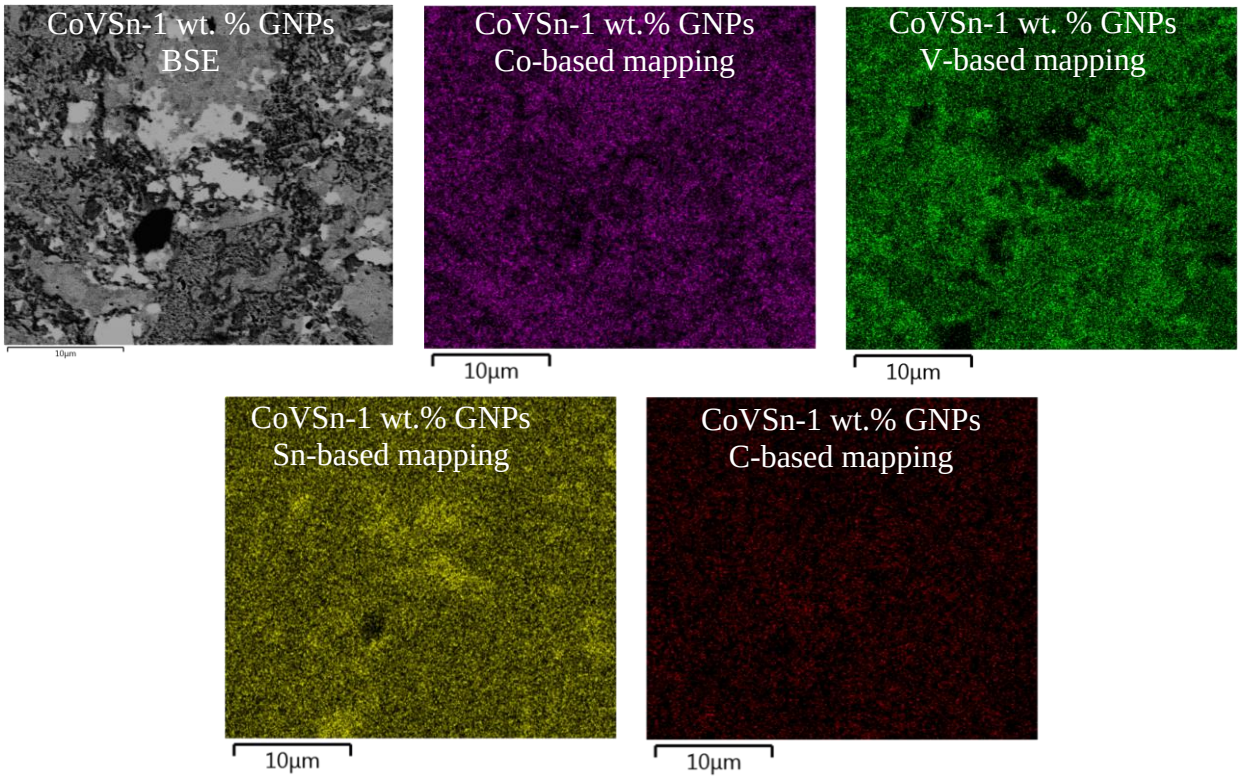

Figure 82: Backscattered electron micrograph along with X-ray maps showing the formation of multiphase structure in CoVSn-1wt.% GNP[306].

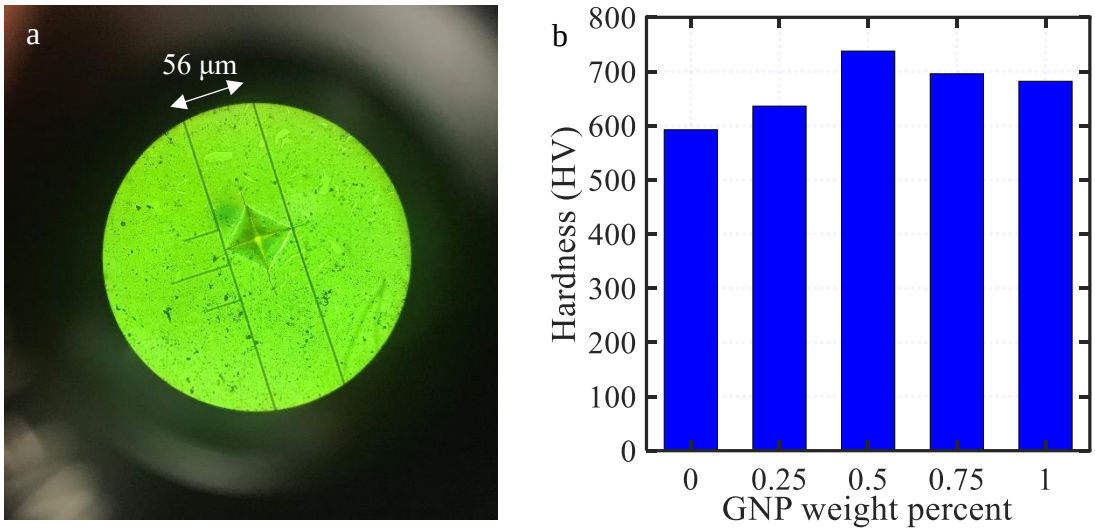

Figure 83: a) Vickers' hardness indication, b) Hardness measurement results of CoVSn-GNPs compounds.

Figure 83 illustrates the hardness measurement results of the studied heterostructure compositions after reinforcement with the GNPs. The average hardness of the samples containing GNPs is higher than for the pristine sample. This result can be explained by considering the presence of the GNPs as a second phase in the matrix and the smaller average crystal size: leading to extra microstructural barriers (Hall-Petch effect [336]). In this regard, the dispersion of GNPs in the matrix is expected to hinder dislocation movements [445] and, consequently, strengthen the GNP-reinforced CoVSn heterostructure composition. It appears that the optimum concentration of GNPs to achieve the highest hardness is about 0.5%, and the further addition of GNPs reduces the hardness. Such an outcome may be attributed to the GNPs' distribution. A higher GNP concentration results in their agglomeration (Figure 81) and thus reduces the hardness.

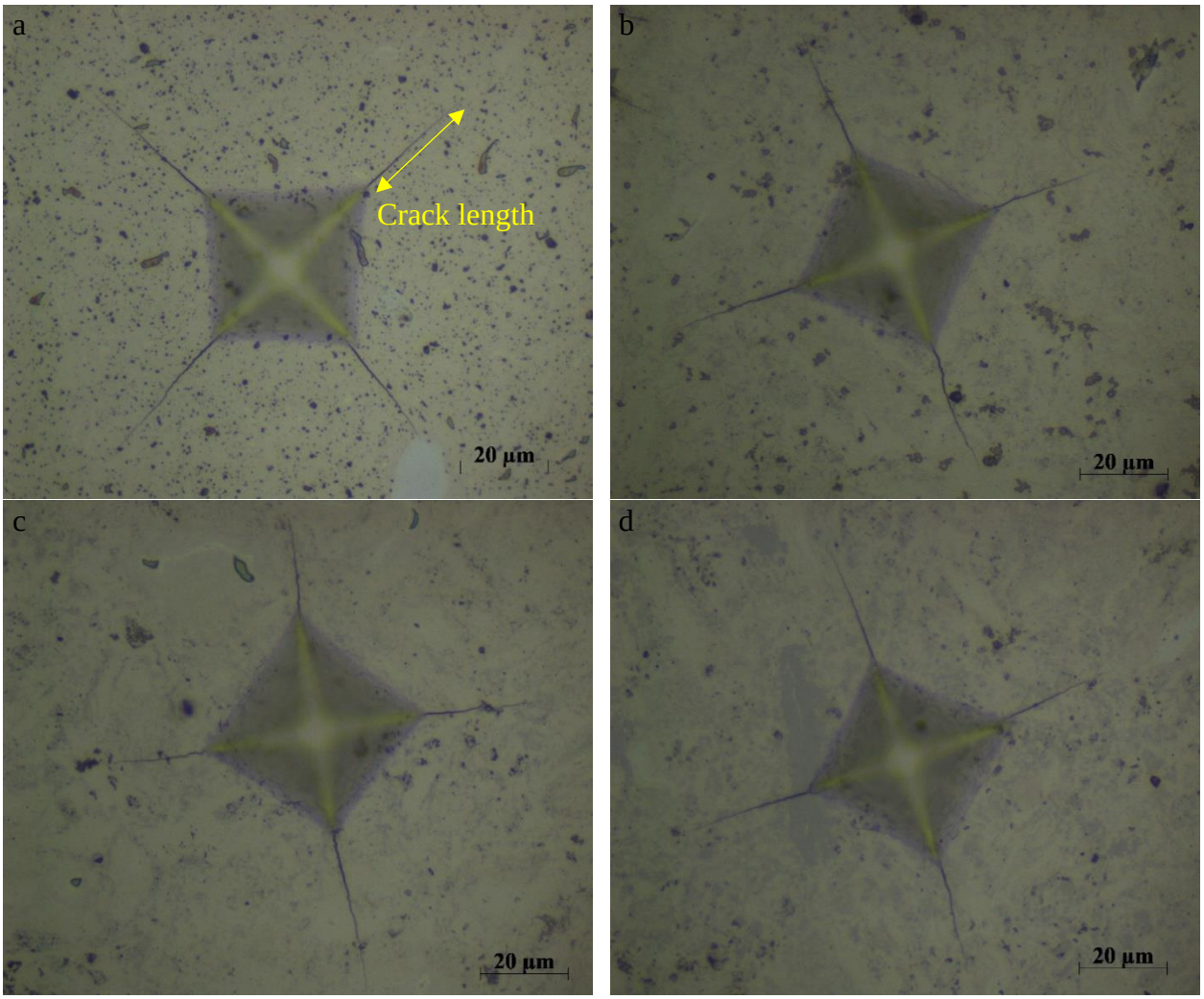

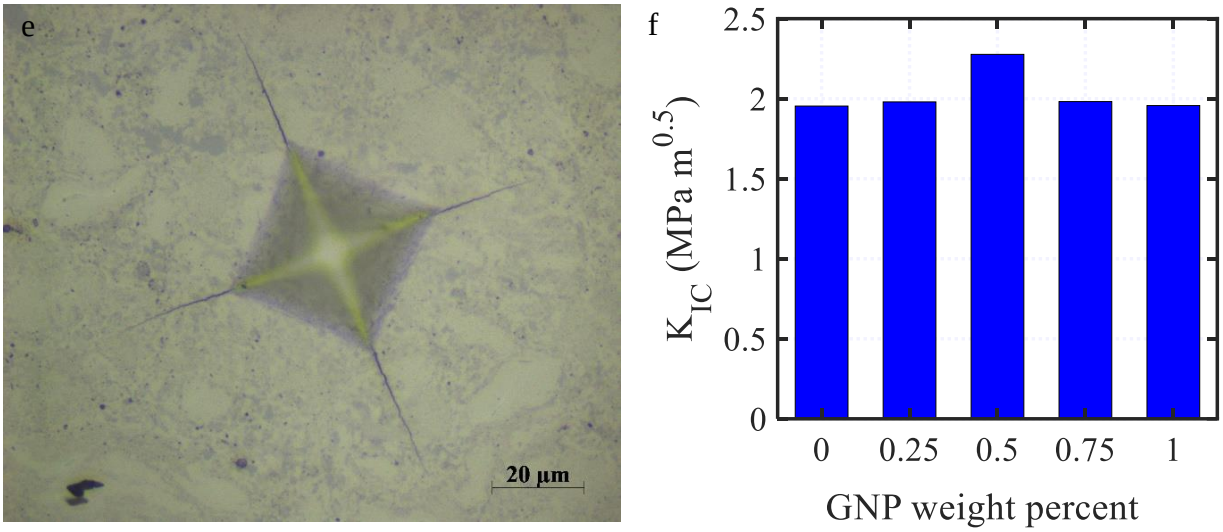

Figure 84: Crack length measurement to calculate the fracture toughness of the CoVSn-GNPs for a) CoVSn, b) CoVSn-0.25 wt.% GNPs, c) CoVSn-0.5 wt.% GNPs, d) CoVSn-0.75 wt.% GNPs, and e) CoVSn-1 wt.% GNPs, f) Fracture toughness calculations[306].

Fracture toughness (K_{IC}, MPa$\sqrt{\text{m}}$) values were calculated based on the Shetty equation $K_{IC} = 0.0899\sqrt{\frac{HP}{4l}}$ [431-433]. Here H, P and l are the hardness, applied load of indentation, and indentation crack length, respectively. The average of the radial crack length was calculated from five indentations measured for each specimen (Figure 84). The calculations exhibit higher fracture toughness values for the samples containing 0.5 wt.% GNPs (Figure 84f). However, the other samples have a fracture toughness at a similar range. The fracture toughness is affected by the average intercept of grain, in which, by crossing the crack through the boundary between two grains/crystal, it must turn/change direction to bring itself into line with the cleavage plane of the next grain/crystal [446-449]. Therefore, more turns of the crack requires more energy for crack propagation [446-449]. Consequently, the compositions owning small grains/crystal sizes can absorb more loading energy before crack propagation [446-449]. This is observed for the CoVSn-0.5 wt.% GNPs. As shown in Figure 79b, the measured samples reinforced with 0.5 wt.% GNPs have the smallest crystal sizes and thus a higher density of microstructural boundaries to enhance the fracture toughness, as reported in Figure 84f.

Until man duplicates a blade of grass, nature can laugh at his so-called scientific knowledge.

— THOMAS EDISON (1847 -1931)

CHAPTER SEVEN

RESULTS AND DISCUSSION- $CuSbTe_2$- xGNPs (x: 0, 0.25, 0.5, 0.75, and 1 wt.%)

This section of the project analyses the thermoelectric, mechanical, and microstructural characteristics of $CuSbTe_2$ composition, reinforced with the Graphene nanoplates (GNPs) in various weight percents (wt.%) of 0, 0.25, 0.5, 0.75, and 1.

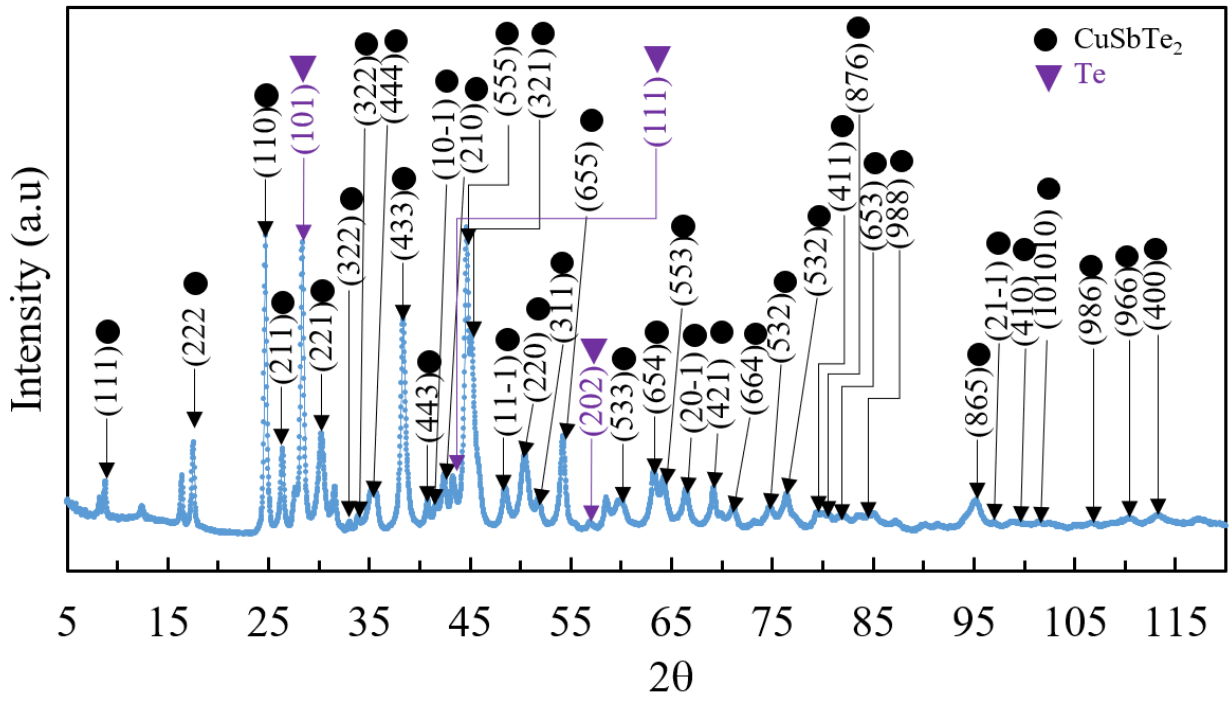

Figure *85*a demonstrates the XRD diffraction peaks of $CuSbTe_2$ composition, which exhibits an acceptable range in comparison with the reported research document [407,409].

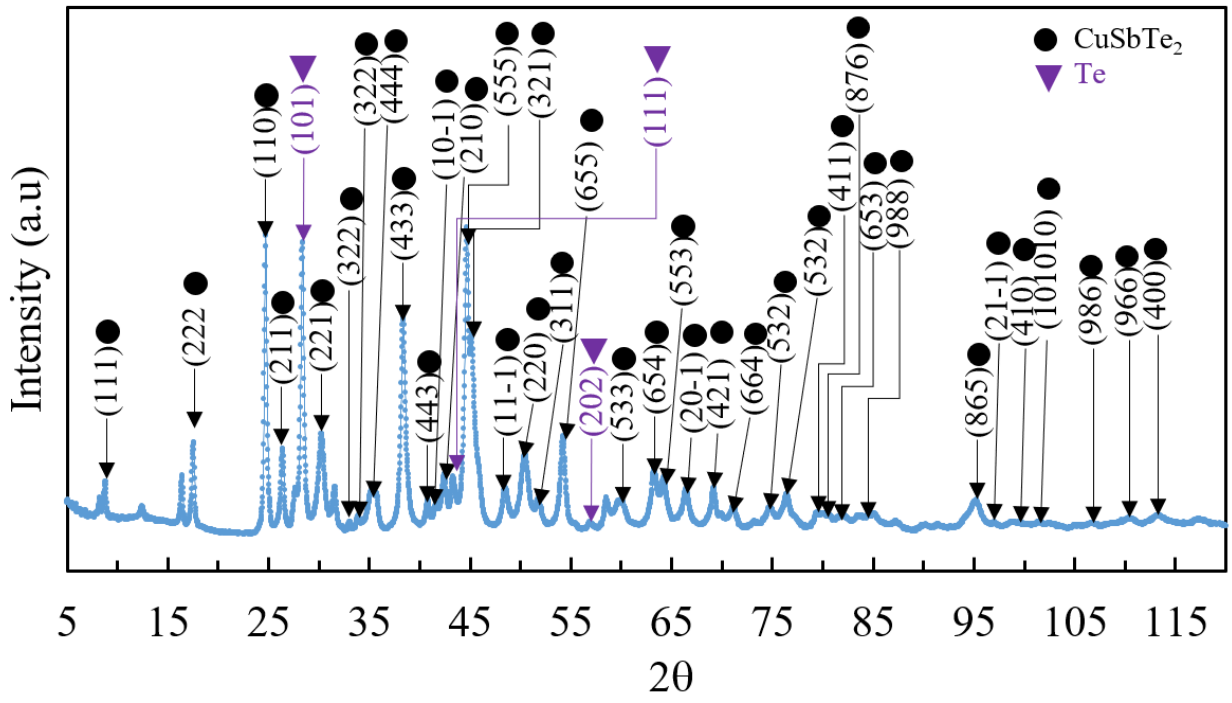

Figure 85: XRD diffraction of $CuSbTe_2$ fabricated by spark plasma sintering.

At the first attempt, the thermoelectric factors of the bulk pristine samples (0 wt.% GNPs) were measured (see Figure 86). The results exhibited the positive Seebeck coefficients, which classify this compound as a P-type thermoelectric compound (Figure 86a). The change in the electrical conductivity versus temperature (Figure 86b) demonstrates a degenerated behaviour, since the electrical conductivity decreases by increasing the temperature [450]. Figure 86c presents thermal conductivity of $CuSbTe_2$ composition. Due to the high electrical conductivity of $CuSbTe_2$ compositions, the electronic thermal conductivity ($\kappa_e = L\sigma T$, L: Lorenz number, σ: electrical conductivity, and T: temperature) highly impact the total thermal conductivity ($\kappa_t = \kappa_{e^+} \kappa_l$) (section 2.5).

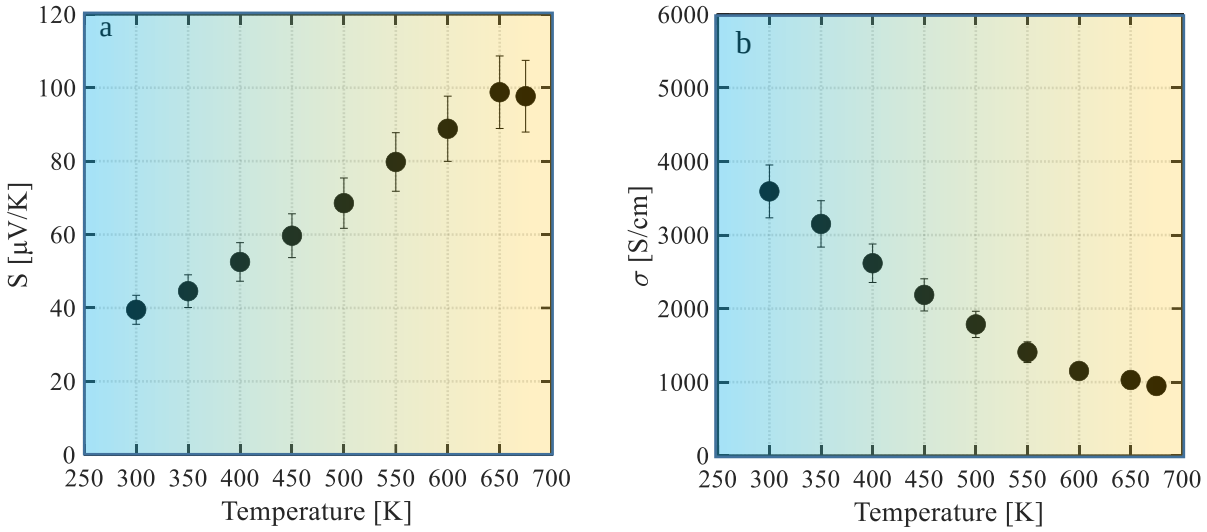

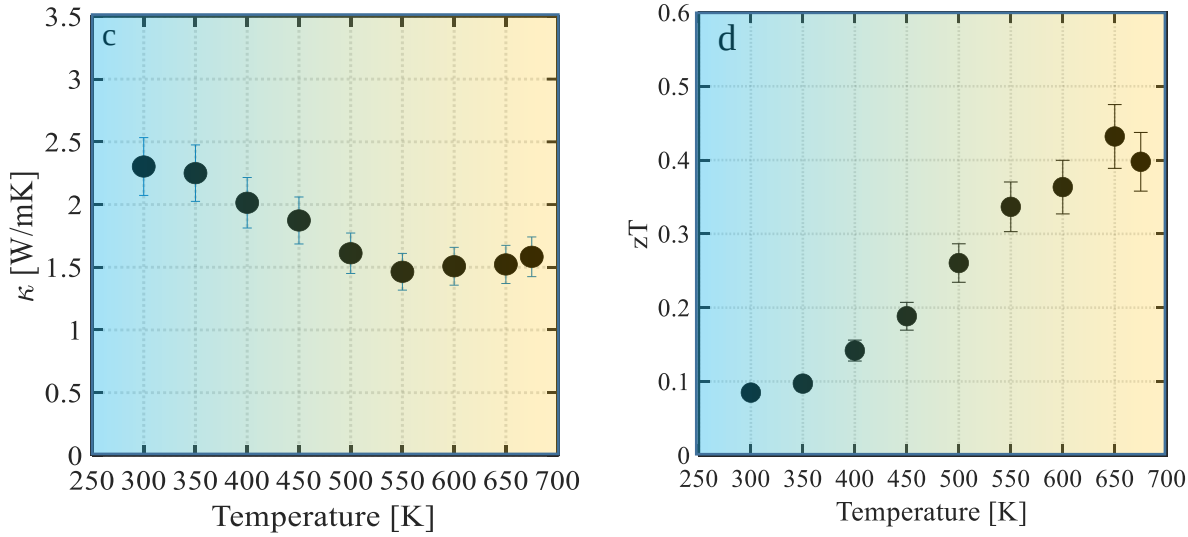

Figure 86: Temperature-dependent thermoelectric properties of $CuSbTe_2$, a) Seebeck coefficients, b) electrical conductivity, c) thermal conductivity, and d) zT.

In further steps, to evaluate the effects of graphene, the thermoelectric characteristics of the GNP-reinforced $CuSbTe_2$ compositions were evaluated based on the measured thermoelectric factors, as demonstrated in Figure 87.

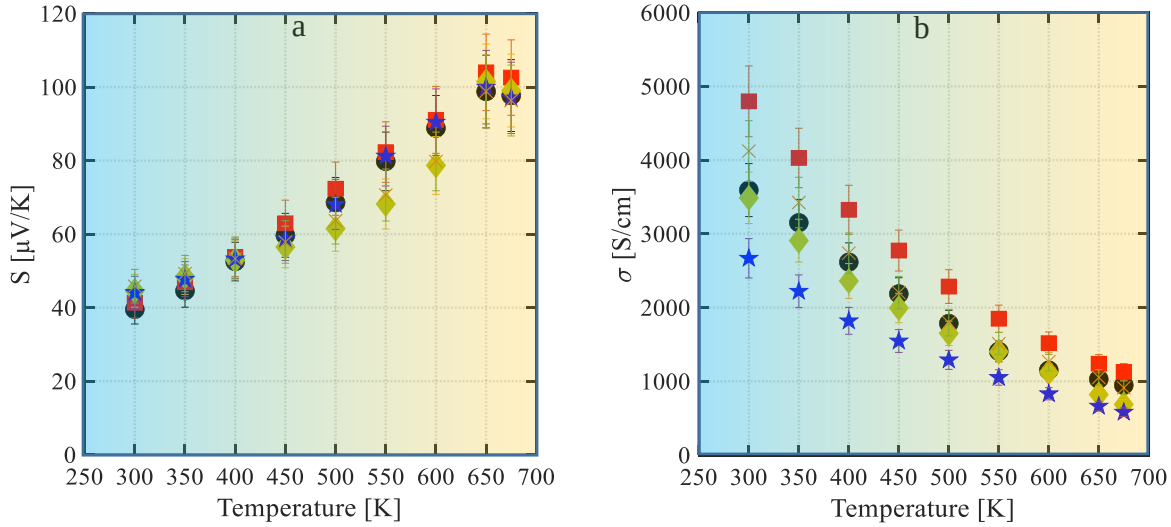

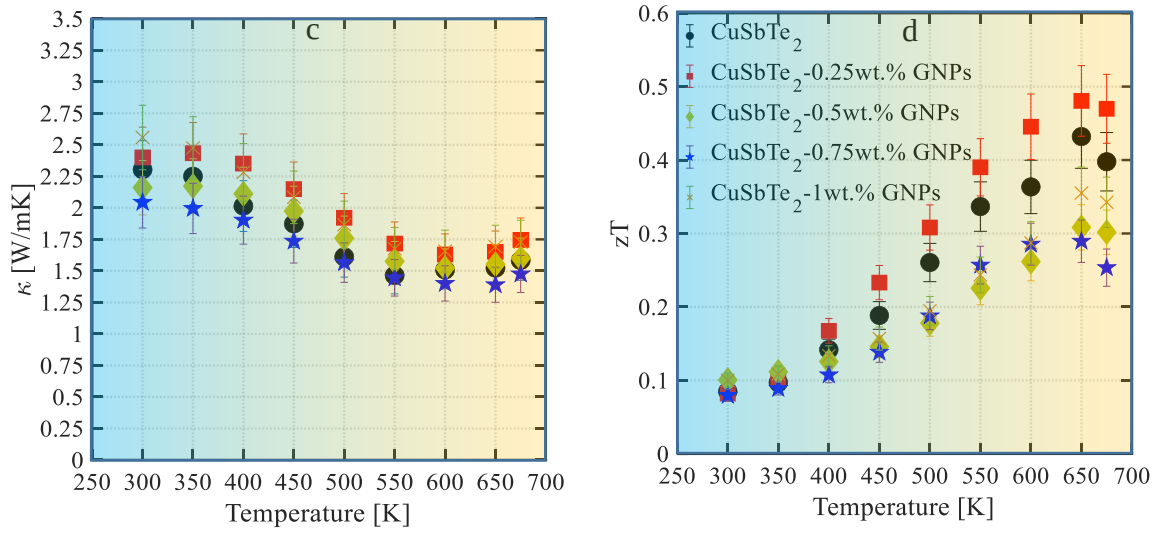

Figure 87: Temperature-dependent thermoelectric characteristics of the $CuSbTe_2$-GNPs composites, $CuSbTe_2$ (Black circle), $CuSbTe_2$-0.25 wt.% GNPs (Red square), $CuSbTe_2$-0.5 wt.% GNPs (Green diamond), $CuSbTe_2$-0.75 wt.% GNPs (Blue pentagram), $CuSbTe_2$-1wt.% GNPs (Orange cross).

As shown in Figure 87a, the addition of GNPs did not provide a major impact on the Seebeck coefficients, in which the measured Seebeck coefficients of $CuSbTe_2$-GNPs composites – with GNP concentrations from 0 to 1 wt.% – are at the same range. Also, all the measured Seebeck coefficients of the composites are positive as p-type semiconductors. However, there is a reduction in both electrical and thermal conductivities with increasing GNP concentrations. Due to the high electrical conductivity (Figure 87b) of $CuSbTe_2$ composition, the electronic part of the thermal conductivity ($\kappa_e = L\sigma T$, L: Lorenz number, σ: electrical conductivity, and T: temperature) chiefly control the total thermal conductivity ($\kappa_t = \kappa_e + \kappa_l$). This can be observed by comparing the behaviours of the electrical conductivities (Figure 87b) and total thermal conductivities (Figure 87c) of the $CuSbTe_2$-GNPs composites versus temperature. Based on the results, the reduction trend in total thermal conductivity is the same as the electrical conductivity against the GNPs mixing ratios.

In a further step, the microstructural analysis revealed a reduction in grain (crystal) size with increasing GNP additions, see Figure 88. This observation is attributable to the segregation of the Graphene at the boundaries, as illustrated in Figure 89.

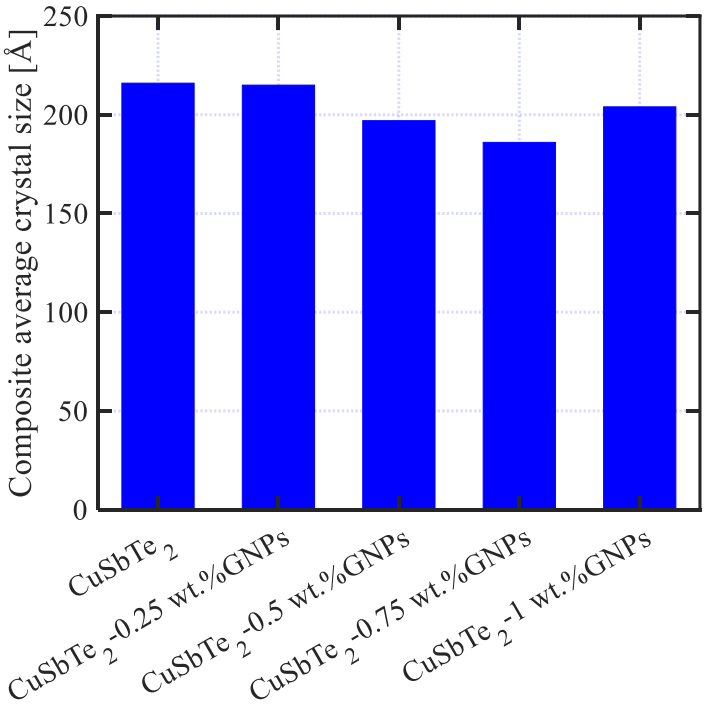

Figure 88: Crystal size of the $CuSbTe_2$-GNP compounds.

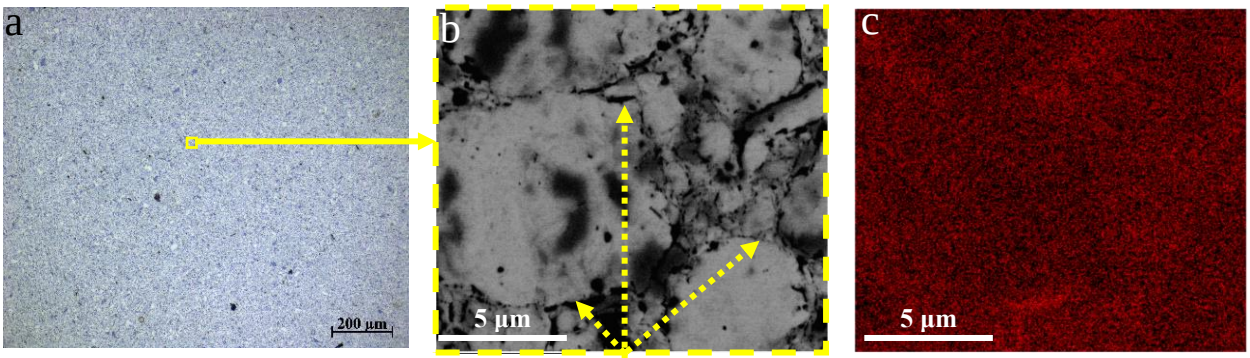

Graphene nanoplate precipitation at the grain/particle boundaries.

Figure 89: Microscopic observation of the GNP-reinforced $CuSbTe_2$ a) SEM micrograph showing some degree of segregation of GNP (shown by arrows), b) BSE micrograph showing preferential

GNP segregation at the grain boundaries, and c) X-ray map of (b) to highlight the graphene segregation at the boundaries.

Table 15: Carrier mobility and carrier concentrations of the $CuSbTe_2$- GNPs composites.

Compound	$CuSbTe_2$	$CuSbTe_2$- 0.25wt.% GNPs	$CuSbTe_2$- 0.5wt.% GNPs	$CuSbTe_2$- 0.75wt.% GNPs	$CuSbTe_2$- 1wt.% GNPs
Carrier concentration (cm^{-3}) @ T=300K	0.4×10^{21}	0.3×10^{21}	0.31×10^{21}	0.31×10^{21}	0.3×10^{21}
Carrier mobility (cm^2/Vs) @ T=300K	69	90	70	50	90

As demonstrated in Figure 88 and Figure 89, the precipitation of the graphene phases at the microstructural boundaries led to the reduction of the crystal sizes. This shows that graphene precipitation prevents particle/crystal growth during sintering. Therefore, the density of the microstructural boundaries (particle/crystal boundaries) as the main source of carrier scattering increased. The electrical characteristics of the samples confirm this conclusion, in which the carriers' mobility is lower for the samples with smaller crystal sizes, as shown in Table 15. However, as the mixing ratio of GNPs increased, the evidence of agglomeration reduced the

effectiveness of GNP in refining the structure. In this field, Figure 90 clearly exhibits the graphene agglomeration that violates the performance of the appropriate GNPs' dispersion, and subsequent improvement of thermoelectric factors (Figure 87d). This behaviour by graphene nanofillers has been also reported in other work [451].

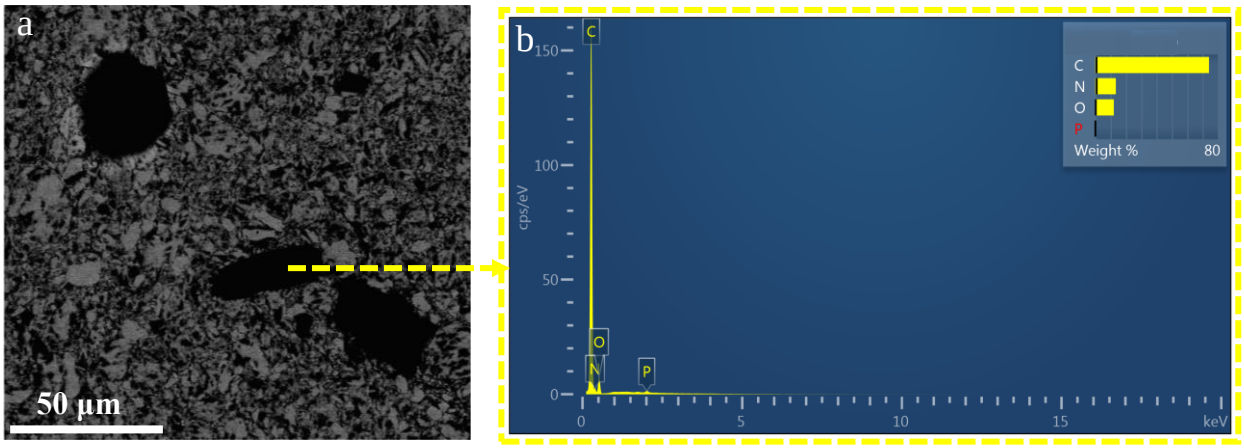

Figure 90: Scanning electron microscopy image a) agglomerated GNP, and b) X-ray point spectrum of the agglomerated GNPs.

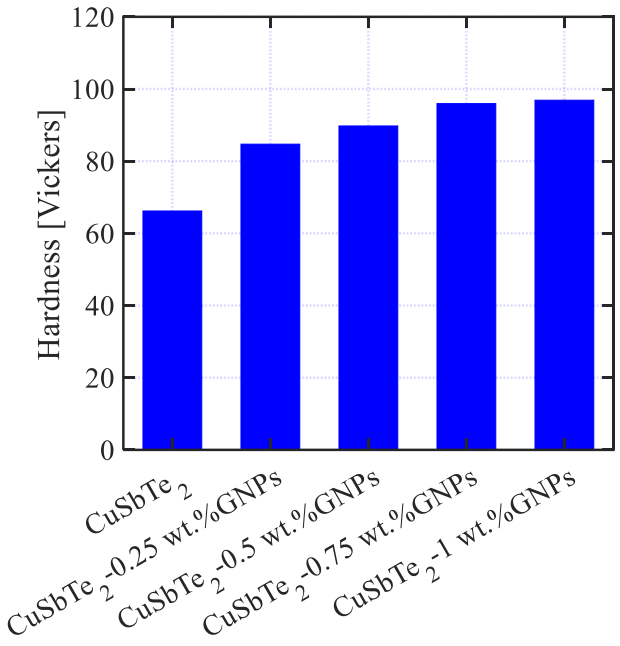

Figure 91: Vickers hardness for the $CuSbTe_2$- GNPs compounds.

The effects of the GNPs on the mechanical characteristics were evaluated because their precipitation at the microstructure reduced the particle/crystal sizes due to the particle/crystal growth inhibition during the sintering process (Figure 88). A hardness measurement was implemented using Vickers' hardness to assess the effects of the GNP reinforcement on the microstructure of the $CuSbTe_2$-GNP composites (Figure 91). The results showed that the reinforcement of $CuSbTe_2$ compositions by blending with GNPs enhanced the Vickers' hardness. The reduction of the particle/crystal sizes (in accordance with the Hall-Petch criteria [331, 452]) via the presence of GNPs as a second phase at the microstructural boundaries improves the hardness values (Figure 88). Based on the Hall-Petch effect, the presence of more grain/crystal boundaries halts the dislocation movements (i.e., piles up the dislocations) and they cannot follow their ways through the subsequent grains/crystals.

The love for all living creatures is the most noble attribute of man.
— CHARLES DARWIN (1809 - 1882)

CHAPTER EIGHT

CONCLUSION

In response to the greenhouse gas emissions associated with worldwide energy generation, thermoelectric compounds offer economic and environmental benefits through emission-free conversion of the waste heat (thermal gradients) into electrical energy. While most efforts have been focused on the design and optimization of novel thermoelectric products, solutions for simultaneous enhancement of their mechanical stabilities, when the compounds experience cycled thermomechanical stresses in service operation, have taken less attention. To respond to the need for improving the thermoelectric and mechanical characteristics, the overall aim of this project is evaluating the graphene reinforcement (graphene nanoplates-GNPs), applied to the thermoelectric products. It is well established that graphene reinforcement and its segregation at the particle/grain/crystal boundaries leads to a grain size reduction in thermoelectric compositions (MnTe, CoVSn, and $CuSbTe_2$), when compared with a pristine matrix, by preventing welding or particle/grain/crystal growth during milling and sintering, respectively. Moreover, the segregation of GNPs at the grain boundaries – creating new microstructural interfaces – and providing extra boundaries influences the thermoelectric properties. Therefore, these extra boundaries due to smaller particle/grain/crystal sizes, caused by graphene segregation and particle/grain/crystal

growth blocking, and graphene-matrix interfaces provide an energy filtering effect for the charge carriers (electrons or holes). The consequence of energy filtering is the strong scattering of the low energy carriers, leading to a reduction in the electrical conductivity and simultaneously increasing the Seebeck coefficients. Furthermore, a reduction in thermal conductivity is clearly observed. Phonon scattering against the microstructural boundaries (particle/crystal boundaries and GNP distribution as a second phase) is regarded as a reason for reducing the thermal conductivities. The hardness measurement results of the studied compositions (MnTe, CoVSn, and $CuSbTe_2$) after reinforcement with the GNPs showed that the average hardness of the samples containing GNPs is higher than that of the pristine samples. This result is explained by considering the presence of the GNPs as a second phase in the matrix and smaller average particle/grain/crystal sizes – extra microstructural barriers (the Hall-Petch effect). In this regard, the dispersion of GNPs in the matrix is expected to hinder dislocation movements and, consequently, strengthen the GNP-reinforced compositions.

However, since the effects of GNP reinforcement are different for the studied thermoelectric compounds, the following sections summarize the observed impact of the GNPs on the nominated TEs.

8.1 Summarized results

8.1.1 MnTe-GNPs

The XRD pattern for the synthesized MnTe compound showed the majority of the diffraction peaks, which can be well indexed with NiAs-type crystal structure, to be in good accordance with the literature. Magnetic characterization of the MnTe and MnTe-GNP compounds indicates that the Néel temperature ($T_N \cong 307K$) remains almost unaffected by GNP reinforcement. The pristine MnTe shows a ferromagnetic (FM) phase over a temperature range of 0-50K. The associated magnetic moment is smaller in the samples with more reinforcing GNPs. Therefore, this reduction must be

attributed to the dispersion of GNP in the MnTe matrix. The magnetic susceptibility exhibits a Curie temperature at the interval of 40-50 K. This observation indicates the probable existence of Mn_3O_4, since its Curie temperature is around 43 K. Moreover, the XRD spectra results have a minor peak ($2\theta=49.2^o$), which disappears after increasing the GNPs' reinforcing ratios. All GNP-reinforced MnTe samples, except the MnTe- 0.25 wt.% GNP, also demonstrate XRD peaks at about $2\theta=40.7^o$ and $2\theta=56.6^o$, related to the $Mn_{23}C_6$ phase. The disappearance of the Mn_3O_4 XRD lines in the GNP-reinforced MnTe compounds and the emergence of the $Mn_{23}C_6$ lines suggest a chemical reaction is taking place between the bulk material and the GNPs. The comparison of the formation energies for Mn_3O_4 and $Mn_{23}C_6$ confirms that $Mn_{23}C_6$ is chemically more stable than Mn_3O_4. Since $Mn_{23}C_6$ is energetically more favourable, it is highly possible that in a thermally-activated reaction, GNP reduces Mn_3O_4 to make $Mn_{23}C_6$, as proved by the vanishing of Mn_3O_4 lines in the XRD data. Consequently, the thermoelectric factors (S, σ, κ, and zT) and mechanical properties of the GNPs-reinforced samples were evaluated and analysed. Nearly 33% improvement was observed in the fracture toughness (K_{IC}) of MnTe reinforced with 0.25 wt.% GNPs, compared with the pristine MnTe samples. The results also identified an improved modification in the thermoelectric features, mainly in the Seebeck coefficients (27% increase) and thermal conductivity (34% decrease) for the samples mixed with 0.25 wt.% GNPs, in comparison with the pristine MnTe samples at a temperature of 600K.

8.1.2 CoVSn-GNPs

The XRD patterns of the SPS-consolidated CoVSn bulk sample disclosed the presence of three binary intermetallics, including SnV_3, Co_2Sn, and Co_3V. Therefore, the synthesized compound is demonstrated to be a multi-phase compound. Furthermore, the BSE image and the EDS maps of the microstructure exhibited a heterogeneous texture, which confirms the observations from the XRD results. The non-uniform dispersion of the elements of Co, V, and Sn evidences the existence of a

multiphase structure with various micro-clusters. The thermoelectric factors of S, σ, κ, and zT for the synthesized compound were measured at a temperature range of 300 to 825 K. The Seebeck coefficient is negative, indicating an n-type semiconductor. This is in contrast with the theoretical prediction that the CoVSn compound should be a p-type semiconductor. The physical characteristics of the Heusler-based compounds are generally highly related to the crystallographic order. The observed multiphase structure combines metallic and semiconductor characteristics due to the presence of intermetallics, such as SnV_3, Co_2Sn, and Co_3V. Hence, the carrier type of the composition cannot be assigned to the single-phase half-Heusler CoVSn compound. It is instructive to look at the thermodynamics of the ternary phase diagram of CoVSn. Therefore, the ternary phase diagrams of the Co-V-Sn were calculated over the temperatures range of interest: 25 °C and 1200 °C. The Thermo-Calc 2016a package was used for this calculation. The diagrams further confirm that at thermodynamic equilibrium, the material decomposes into multiple phases, which agrees with the observation in the microstructural analysis. In fact, according to the ternary phase diagrams of Co-V-Sn compositions, there is no single phase of CoVSn, but there are mainly binary compounds of $CoSn$, SnV_3, Co_3V, and Sn_2V_3. Therefore, the CoVSn compound can be regarded as a heterostructural composition.

Consequently, the potential mechanisms were evaluated by which the graphene addition may modify the thermoelectric, microstructural and mechanical properties of the heterostructural CoVSn composition. Here, the associated impacts of graphene nanoplates (GNPs) within participation in the CoVSn microstructure are analysed and represented.

The segregation of GNPs at GBs presents the range of the average crystal size of CoVSn-GNPs heterostructural compounds estimated from the XRD analysis, in which the GNP addition has resulted in smaller crystallites, which are saturated at approximately 15-18 nm. The segregation of GNPs at the grain boundaries, creating new microstructural interfaces and providing extra boundaries, influenced the thermoelectric properties. The reduction in thermal conductivity is

clearly observed. Phonon scattering against the microstructural boundaries (particle/crystal boundaries and GNP distribution as a second phase) can be regarded as a reason for reducing the thermal conductivities. Based on the results, the primary reduction occurred at a lower temperature due to the main impact of phonon scattering with a longer wavelength (low frequencies) against the grain boundaries. The electrical conductivities results showed that the samples, after reinforcement with GNPs, are in the range of conductive compounds. Moreover, the Seebeck measurement illustrated the negative Seebeck coefficients for the samples to confirm the presence of electrons as the majority carriers. However, for the compounds with more than 0.5 wt.% GNPs, there is a disruption in the improvement of the TE characteristics. This can be attributed to a lack of uniform GNP dispersion in the matrix and formation of the agglomerated GNP regions.

Moreover, the microstructural analysis revealed multiphase microconstituents for the CoVSn-GNPs (e.g., CoVSn-1 wt.% GNPs), is similar to the pristine CoVSn sample. The results showed that the distributions of the main three elements, Co, V, and Sn, are not uniform, which confirms the presence of a multiphase microstructure. The comparison with the multiphase microstructure of the pristine CoVSn shows that the incorporation of GNPs does not influence the formation of the constituent phases in the microstructure.

The hardness measurement results of the studied heterostructure compositions after reinforcement with the GNPs showed that the average hardness of the samples containing GNPs is higher than for the pristine sample. This result can be explained by considering the presence of the GNPs as a second phase in the matrix and the smaller average crystal size – extra microstructural barriers (the Hall-Petch effect). In this regard, the dispersion of GNPs in the matrix is expected to hinder dislocation movements and, consequently, strengthen the GNP-reinforced CoVSn heterostructure composition. It appears that the optimum concentration of GNPs to achieve the highest hardness is about 0.5% (735 HV), and the further addition of GNPs reduces the hardness. Such an outcome

may be attributed to the GNPs' distribution. A higher GNP concentration results in their agglomeration and thus reduces the hardness in the samples reinforced with GNPs above 0.5 wt.%.

8.1.3 $CuSbTe_2$-GNPs

The XRD diffraction peaks of $CuSbTe_2$ alloy exhibited a good agreement with the research document to confirm the successful synthesis of the composition. At the first stage, the thermoelectric factors of the bulk pristine samples (0 wt. % GNPs) were measured. The results exhibited the positive Seebeck coefficients, which classify this compound as a p-type thermoelectric composition. The change in the electrical conductivity versus temperature demonstrates a degenerated behaviour, since the electrical conductivity decreases by increasing the temperature.

The addition of GNPs did not provide a major impact on the Seebeck coefficients, as the measured Seebeck coefficients of the composites are at the same range. Also, all the measured Seebeck coefficients of the composites are positive as p-type semiconductors. However, there is a reduction in both electrical and thermal conductivities with increasing GNP concentrations. Due to the high electrical conductivity of $CuSbTe_2$ compositions, the electronic thermal conductivity ($\kappa_e = L\sigma T$, L: Lorenz number, σ: electrical conductivity, and T: temperature) highly impact the total thermal conductivity ($\kappa_{t=} \kappa_{e+} \kappa_l$). This can be observed by comparing the behaviours of the electrical conductivities and total thermal conductivities versus the temperature and GNP concentration. Based on the results, the reduction trend in the total thermal conductivity is the same as for the electrical thermal conductivity results based on the GNPs' mixing ratios.

In a further step, the microstructural analysis revealed a reduction in grain (crystal) size with increasing GNP addition. This observation is attributable to the segregation of the Graphene at the boundaries. The precipitation of the graphene phases at the microstructural boundaries led to the reduction of the crystal sizes. This shows that graphene precipitation prevents grain/crystal growth during sintering. Therefore, the density of microstructural boundaries (grain/crystal boundaries) as the main source of carrier scattering increased. The electrical characteristics of the samples confirms

this statement, in which the carriers' mobility is lower for the samples with smaller crystal sizes. However, as the mixing ratio of GNPs increased, the evidence of agglomeration reduced the effectiveness of the GNP in refining the structure. The graphene agglomeration violates the performance of the appropriate GNPs' dispersion, and subsequent improvement of thermoelectric factors. The effects of the GNPs' precipitation at the microstructure and hence reduction in crystal sizes were evaluated in terms of the mechanical characteristics. A hardness measurement was implemented using Vickers' hardness to assess the effects of the GNP reinforcement on the microstructure of the $CuSbTe_2$-GNP composites. The results showed that the reinforcement of $CuSbTe_2$ compositions by blending with GNPs enhanced the Vickers' hardness. The reduction of the crystal sizes (in accordance with the Hall-Petch criteria) and presence of GNPs as a second phase improves the hardness values. Based on the Hall-Petch effect, the presence of more grain/crystal boundaries halts the dislocation movements (i.e., piles up the dislocations) and they cannot follow their way through the next grains/crystals.

8.2 Future Works

Since this project has added significant knowledge to the open scientific database, it is clear that new gaps and future engineering research directions have been created. The future works of this group, based on the current PhD work, are classified as follows:

1) Evaluation of the effects of Graphene products on the stability of the thermoelectric compounds used for subzero thermoelectric cooling (TEC) systems.
2) Assessment of the physics of $CuSbTe_2$ based on Density Functional Theory (i.e., $ab\ initio$ calculations). According to the observed behaviour for $CuSbTe_2$, there is a degree of complexity in its electronic structure and dominant scattering mechanisms, which highlights a need for an extra analysis of its physics (e.g., $ab\ initio$ calculations).
3) Application of other sintering processes such as microwave could be interesting to highlight if the sintering process is of any importance.

REFERENCES

[1] Eri Saikawa Geoff Martins,Effectiveness of state climate and energy policies in reducing power-sector CO2 emissions,Nature Climate Change,7 (2017) 912–919.

[2] Steven Goh Talal Yusaf, J.A. Borserios,Potential of renewable energy alternatives in Australia,Renewable and Sustainable Energy Reviews,15 (2011) 2214–2221.

[3] Energy Makeover. (2018). Australia's Top 20 Greenhouse Gas Emitters.

[4] Annual Energy Outlook 2020 with projections to 2050, January 2020, U.S. Energy Information Administration Office of Energy Analysis, U.S. Department of Energy, Washington, DC 20585, This publication is on the Web at: https://www.eia.gov/aeo.

[5] Annual Energy Outlook 2020 with projections to 2050, U.S. Energy Information Administration Office of Energy Analysis, U.S. Department of Energy, Washington, DC 20585, January 2020, https://www.eia.gov/aeo.

[6] FRANCIS R. STABLER JIHUI YANG, Automotive Applications of Thermoelectric Materials, Journal of ELECTRONIC MATERIALS, Vol. 38, No. 7, 2009s.

[7] A.L.O. Maran O.H. Ando Junior, N.C. Henaos,A review of the development and applications of thermoelectric microgenerators for energy harvesting,Renewable and Sustainable Energy Reviews,91 (2018) 376–393.

[8] Yanliang Zhang ,Thermoelectric Advances to Capture Waste Heat in Automobiles, ACS Energy Lett. 2018, 3, 1523−1524.

[9] A. Akbarzadeh L.C. Ding, L. Tans,A review of power generation with thermoelectric system and its alternative with solar ponds,Renewable and Sustainable Energy Reviews,81 (2018) 799–812.

[10] Eric S. Toberer G. Jeffrey Snyders,Complex thermoelectric materials,nature materials,7 (2008) 105-114.

[11] Susanna Sirotinskaya Alexandre Polozine, Lírio Schaeffers,History of Development of Thermoelectric Materials for Electric Power Generation and Criteria of their Quality,Materials Research Society,17 (2014) 1260-1267.

[12] Itziar Hoces Prospero J. Taroni, Natalie Stingelin,Martin Heeney, Emiliano Bilottis,Thermoelectric Materials: A Brief Historical Survey from Metal Junctions and Inorganic Semiconductors to Organic Polymers,Isr. J. Chem.,54 (2014) 534 – 552.

[13] Brief History of Thermoelectrics. Available: http://www.thermoelectrics.caltech.edu/thermoelectrics/history.html.

[14] H.G.Schoberth J.M.Mena, T.Gruhn, H.Emmerichs,Ab initio study of domain structures in half-metallic CoTi1-xMnxSb and thermoelectric CoTi1-xScxSb half-Heusler alloys,Journal of Alloys and Compounds,650 (2015) 728-740.

[15] Punith. N , G. M. Swamy, Shivasharana Yalagi, 2015, A Thermoelectric Generator Systems Forwaste Heat Recovery- A Review, INTERNATIONAL JOURNAL OF ENGINEERING RESEARCH & TECHNOLOGY (IJERT) NCERAME – 2015 (Volume 3 – Issue 17).

[16] Brief History of Thermoelectrics, Northwestern Materials Science and Engineering, Website: http://thermoelectrics.matsci.northwestern.edu/thermoelectrics/history.html.

[17] Thermoelectrics History Timeline, Copyright © 2009-2020, Alphabet Energy, Inc. http://www.alphabetenergy.com/thermoelectrics-timeline/.

[18] Lili Xi Jiong Yang, Wujie Qiu, Lihua Wu, Xun Shi, Lidong Chen, Jihui Yang, Wenqing Zhang, Ctirad Uher, David J Singhs,On the tuning of electrical and thermal transport in thermoelectrics: an integrated theory–experiment perspective,npj Computational Materials, Nature,2 (2016) 1-17.

[19] Lei Yang, Zhi-Gang Chen, Matthew S. Dargusch, Jin Zou, High Performance Thermoelectric Materials: Progress and Their Applications, Adv. Energy Mater. 2018, 8, 1701797, DOI: 10.1002/aenm.201701797, 1-28.

[20] In-Ho Kim Muhammad Usman, Hyung-Jo Jungs,Improving thermoelectric energy harvesting efficiency by using graphene,AIP ADVANCES,6 (2016) 1-7.

[21] Maxwell T. Dylla, Alexander Dunn , Shashwat Anand , Anubhav Jain ,G. Jeffrey Snyder, Machine Learning Chemical Guidelines for Engineering Electronic Structures in Half-Heusler Thermoelectric Materials, AAAS, Research, Volume 2020, Article ID 6375171, 8 pages, https://doi.org/10.34133/2020/6375171.

[22] Zhou, J., Shin, H.D., Chen, K. et al. Direct observation of large electron–phonon interaction effect on phonon heat transport. Nat Commun 11, 6040 (2020). https://doi.org/10.1038/s41467-020-19938-9.

[23] Feiyu Qin,Sergey A. Nikolaev,Ady Suwardi,Maxwell Wood,Yingcai Zhu, Xianyi Tan, Umut Aydemir, Yang Ren, Qingyu Yan, Lei Hu, G. Jeffrey Snyder, Crystal Structure and Atomic Vacancy Optimized Thermoelectric Properties in Gadolinium Selenides, Chem. Mater. 2020, XXXX, XXX, XXX-XXX,Publication Date:November 26, 2020,https://doi.org/10.1021/acs.chemmater.0c03581.

[24] Jun Maoa, Jing Shuaia, Shaowei Songa, Yixuan Wu, Rebecca Dally, Jiawei Zhou, Zihang Liu, Jifeng Sun, Qinyong Zhang, Clarina dela Cruz, Stephen Wilson, Yanzhong Pei, David J. Singh, Gang Chen, Ching-Wu Chu, Zhifeng Ren, Manipulation of ionized impurity scattering for achieving high thermoelectric performance in n-type Mg3Sb2-based materials, PNAS, 114, 40, October 3, 2017, 10548–10553, www.pnas.org/cgi/doi/10.1073/pnas.1711725114.

[25] R. Lu, A. Olvera, T. Bailey, J. Fu, X. Su, I. Veremchuk, Z. Yin, B. Buchannan, C. Uher, X. Tang, Y. Grin and P. F. Poudeu, Mater. Adv., 2021, DOI: 10.1039/D0MA00912A.

[26] Davide Beretta, Neophytos Neophytou, James M. Hodges, Mercouri G. Kanatzidis, Dario Narducci, Marisol Martin- Gonzalez, Matt Beekman, Benjamin Balke, Giacomo Cerretti, Wolfgang Tremel, Alexandra Zevalkink, Anna I. Hofmann, Christian Müller, Bernhard Dörling, Mariano Campoy-Quiles, Mario Caironi,Thermoelectrics: From history, a window to the future, Materials Science and Engineering: R: Reports, Volume 138, 2019, 100501,https://doi.org/10.1016/j.mser.2018.09.001.

[27] Pingjun Ying, Ran He, Jun Mao, Qihao Zhang, Heiko Reith, Jiehe Sui, Zhifeng Ren, Kornelius Nielsch, Gabi Schierning, Towards tellurium-free thermoelectric modules for power generation from low-grade heat, NATURE COMMUNICATIONS, (2021) 12:1121, https://doi.org/10.1038/s41467-021-21391-1.

[28] Sumanta Sarkar, Xia Hua, Shiqiang Hao, Xiaomi Zhang, Trevor P. Bailey, Tyler J. Slade, Poya Yasaei, Rachel J. Korkosz, Gangjian Tan, Ctirad Uher, Vinayak P. Dravid, Chris Wolverton, Mercouri G. Kanatzidis, Dissociation of GaSb in n-Type PbTe: off-Centered Gallium Atom and Weak Electron−Phonon Coupling Provide High Thermoelectric Performance, Chem. Mater., https://dx.doi.org/10.1021/acs.chemmater.0c04854, 2021.

[29] https://dx.doi.org/10.1021/acsami.0c09719.
[30] Mildred S. Dresselhaus, Gang Chen, Ming Y. Tang, Ronggui Yang, Hohyun Lee, Dezhi Wang, Zhifeng Ren, Jean-Pierre Fleurial, Pawan Gogna, New Directions for Low-Dimensional Thermoelectric Materials, Adv. Mater. 2007, 19, 1043–1053.
[31] Mona Zebarjadi, Jian Yang, Kevin Lukas, Boris Kozinsky, Bo Yu, Mildred S. Dresselhaus, Cyril Opeil, Zhifeng Ren, Gang Chen, Role of phonon dispersion in studying phonon mean free paths in skutterudites, Journal of Applied Physics 112, 044305 (2012); https://doi.org/10.1063/1.4747911.
[32] M. S. Dresselhaus A. J. Minnich, Z. F. Ren, G. Chens,Bulk nanostructured thermoelectric materials: current research and future prospects,Energy Environ. Sci.,2 (2009) 466–479.
[33] H. J. GOLDSMID, Impurity Band Effects in Thermoelectric Materials, Journal of ELECTRONIC MATERIALS, Vol. 41, No. 8, 2012.
[34] Yanzhong Pei, Heng Wang G. J. Snyder, Band Engineering of Thermoelectric Materials, Adv. Mater. 2012, 24, 6125–6135.
[35] Joseph P. Heremans, Vladimir Jovovic, Eric S. Toberer, Ali Saramat, Ken Kurosaki, Anek Charoenphakdee, Shinsuke Yamanaka, G. Jeffrey Snyder, Enhancement of Thermoelectric Efficiency in PbTe by Distortion of the Electronic Density of States, Science 25 Jul 2008:Vol. 321, Issue 5888, pp. 554-557, DOI: 10.1126/science.1159725.
[36] Joseph P. Heremans, Bartlomiej Wiendlocha, Audrey M. Chamoire, Resonant levels in bulk thermoelectric semiconductors, Energy Environ. Sci., 2012, 5, 5510.
[37] Heng Wang, Xianlong Cao, Yoshiki Takagiwa, G. Jeffrey Snyder, Higher mobility in bulk semiconductors by separating the dopants from the chargeconducting band – a case study of thermoelectric PbSe, Mater. Horiz., 2015, 2, 323.
[38] Chathurangi Kumarasinghe, Neophytos Neophytou, Band alignment and scattering considerations for enhancing the thermoelectric power factor of complex materials: The case of Co-based half-Heusler alloys, Phys. Rev. B 99, 195202 (2019).
[39] Yu Pan, Feng-Ren Fan, Xiaochen Hong, Bin He, Congcong Le, Walter Schnelle, Yangkun He, Kazuki Imasato, Horst Borrmann, Christian Hess, Bernd Büchner, Yan Sun, Chenguang Fu, G. Jeffrey Snyder, Claudia Felser, Thermoelectric Properties of Novel Semimetals: A Case Study of YbMnSb2, Adv. Mater. 2021, 33, 2003168, DOI: 10.1002/adma.202003168.
[40] Md Mobarak Hossain Polash, Daryoosh Vashaee, Magnon-bipolar carrier drag thermopower in antiferromagnetic/ferromagnetic semiconductors: Theoretical formulation and experimental evidence, PHYSICAL REVIEW B 102, 045202 (2020).
[41] Sadeq Hooshmand Zaferani, Reza Ghomashchi, Daryoosh Vashaee, Thermoelectric, Magnetic, and Mechanical Characteristics of Antiferromagnetic Manganese Telluride Reinforced with Graphene Nanoplates, Adv. Eng. Mater. 2020, 2000816.
[42] Y. Zheng, T. Lu, M. M. H. Polash, M. Rasoulianboroujeni, N. Liu, M. E. Manley, Y. Deng, P. J. Sun, X. L. Chen, R. P. Hermann, D. Vashaee, J. P. Heremans, H. Zhao, Paramagnon drag in high thermoelectric figure of merit Li-doped MnTe, Sci. Adv., 5(9), eaat9461 (2019).
[43] Biplab Paul, Ajay Kumar V, P. Banerji, Embedded Ag-rich nanodots in PbTe: Enhancement of thermoelectric properties through energy filtering of the carriers, J. Appl. Phys. 108, 064322 (2010); https://doi.org/10.1063/1.3488621.
[44] Zong-Yue Li, Jing-Feng Li, Wen-Yang Zhao, Qing Tan, Tian-Ran Wei, Chao-Feng Wu, Zhi-Bo Xing, PbTe-based thermoelectric nanocomposites with reduced thermal

conductivity by SiC nanodispersion, Appl. Phys. Lett. 104, 113905 (2014); https://doi.org/10.1063/1.4869220.

[45] Sadeq Hooshmand Zaferani, Reza Ghomashchi, Daryoosh Vashaee, Strategies for engineering phonon transport in Heusler thermoelectric compounds, Renewable and Sustainable Energy Reviews 112 (2019) 158–169.

[46] Jingpeng Li, Shiqiang Hao, Shangqing Qu, Christopher Wolverton, Jing Zhao, Yonggang Wang, In4Pb5.5Sb5S19: A Stable Quaternary Chalcogenide with Low Thermal Conductivity,Inorg. Chem. 2020, XXXX, XXX, XXX-XXX, https://doi.org/10.1021/acs.inorgchem.0c02966.

[47] L. Xie, J. H. Feng, R. Li, J. Q. He, First-Principles Study of Anharmonic Lattice Dynamics in Low Thermal Conductivity AgCrSe2: Evidence for a Large Resonant Four-Phonon Scattering, Phys. Rev. Lett. 125, 245901 – Published 9 December 2020,

[48] ACS Appl. Mater. Interfaces 2020, 12, 19, 21623-21632.

[49] Matt Beekman, Grigory Heaton, Thomas M. Linker, David C. Johnson, Material considerations for thermoelectric enhancement via modulation doping, Applied Physics A (2020) 126:517, https://doi.org/10.1007/s00339-020-03673-5.

[50] Mona Zebarjadi , Bolin Liao , Keivan Esfarjani , Mildred Dresselhaus , Gang Chen, Enhancing the Thermoelectric Power Factor by Using Invisible Dopants, Adv. Mater. 2013, 25, 1577–1582.

[51] Ling Wang, Xiaojian Tan, Guoqiang Liu, Jingtao Xu, Hezhu Shao, Bo Yu, Haochuan Jiang, Song Yue, Jun Jiang, Manipulating Band Convergence and Resonant State in Thermoelectric Material SnTe by Mn−In Codoping, ACS Energy Lett. 2017, 2, 1203−1207, DOI: 10.1021/acsenergylett.7b00285.

[52] Xiao Zhang, Li-Dong Zhao, Thermoelectric materials: Energy conversion between heat and electricity, Journal of Materiomics 1 (2015) 92-105.

[53] Tanveer Hussain, Xiaotong Li, Mazhar Hussain Danish, Mutee Ur Rehman, Jian Zhang, Di Li, Guang Chen, Guodong Tang, Realizing high thermoelectric performance in eco-friendly SnTe via synergistic resonance levels, band convergence and endotaxial nanostructuring with Cu2Te, Nano Energy 73 (2020) 104832.

[54] G. Rogl M. Falmbigl, P. Rogl, M. Kriegisch, H. Müller, E. Bauer, M. Reinecker, W. Schranzs,Thermal expansion of thermoelectric type-I-clathrates,JOURNAL OF APPLIED PHYSICS,108 (2010).

[55] Yuta Sasaki Kengo Kishimoto, Tsuyoshi Koyanagi, Kenji Ohoyama, Koji Akais,Crystal structure and thermoelectric properties of KxBa82xZnyGe462y clathrates,JOURNAL OF APPLIED PHYSICS,111 (2012) 1-8.

[56] Holger Kleinkes,New bulk Materials for Thermoelectric Power Generation: Clathrates and Complex Antimonides,Chem. Mater.,22 (2010) 604–611.

[57] R. H. Liu P. F. Qiu, J. Yang, X. Shi, X. Y. Huang, W. Zhang, L. D. Chen, Jihui Yang, D. J. Singhs,Thermoelectric properties of Ni-doped CeFe4Sb12 skutterudites,JOURNAL OF APPLIED PHYSICS,111 (2012) 1-7.

[58] R Anbalagan R C Mallik, K K Raut, A Bali, E Royanian, E Bauer2, G Rogl, P Rogls,Thermoelectric properties of Bi-added Co4Sb12 skutterudites,J. Phys.: Condens. Matter,25 (2013).

[59] P. Puneet Y. Dong, T. M. Tritt, J. Martin, G. S. Nolass,High temperature thermoelectric properties of p-type skutterudites BaxYbyCo4-zFezSb12,JOURNAL OF APPLIED PHYSICS,112 (2012) 1-5.

[60] Z. Ye J.Y. Cho, M.M. Tessema , R.A. Waldo, J.R. Salvador, J. Yang b,⇑, W. Cai,H. Wangs,Thermoelectric properties of p-type skutterudites YbxFe3.5Ni0.5Sb12 (0.8< x <1),Acta Materialia,60 (2012) 2104–2110.

[61] Katja M. Kleinke Mohamed Oudah, and Holger Kleinkes,Thermoelectric Properties of the Quaternary Chalcogenides BaCu5.9STe6 and BaCu5.9SeTe6,Inorg. Chem.,54 (2015) 845−849.

[62] Dan Qin Xu-Jin Ge, Kai-Lun Yao, Jing-Tao Lüs,First-principles study of thermoelectric transport properties of monolayer gallium chalcogenides,J. Phys. D: Appl. Phys.,50 (2017) 1-6.

[63] Niels Bindzus Sofie Kastbjerg , Martin Søndergaard , Simon Johnsen , Nina Lock ,Mogens Christensen , Masaki Takata , Mark A. Spackman , and Bo Brummerstedt Iversens,Direct Evidence of Cation Disorder in Thermoelectric Lead Chalcogenides PbTe and PbS,Adv. Funct. Mater.,23 (2013) 5477–5483.

[64] F. Failamani A. Tavassoli, A. Grytsiv, G. Rogl, P. Heinrich, H. Müller,E. Bauer, M. Zehetbauer, P. Rogls,On the Half-Heusler compounds Nb1-x{Ti,Zr,Hf}xFeSb: Phase relations, thermoelectric properties at low and high temperature, and mechanical properties,Acta Materialia,135 (2017) 263e276.

[65] TSUNEHIRO TAKEUCHI AKIO YAMAMOTOs,The Potential of FeVSb Half-Heusler Phase for Practical Thermoelectric Material,Journal of ELECTRONIC MATERIALS,46 (2017) 3200-3206.

[66] Xiuwen Zhang Feng Yan, Yonggang G. Yu, Liping Yu, Arpun Nagaraja, Thomas O. Mason, Alex Zungers,Design and discovery of a novel half-Heusler transparent hole conductor made of all-metallic heavy elements,NATURE COMMUNICATIONS,6 (2015) 1-8.

[67] Yumei Wang Hao Zhang, Keshab Dahal, Jun Mao, Lihong Huang,Qinyong Zhang , Zhifeng Rens,Thermoelectric properties of n-type half-Heusler compounds (Hf0.25Zr0.75)1exNbxNiSn,Acta Materialia,113 (2016) 41-47.

[68] Kaiyang Xia Junjie Yu, Xinbing Zhao,Tiejun Zhus,High performance p-type half-Heusler thermoelectric materials,J. Phys. D: Appl. Phys.,51 (2018) 1-15.

[69] D. Fuks M. Kaller, Y. Gelbsteins,Sc solubility in p-type half-Heusler (Ti1-cScc)NiSn thermoelectric alloys,Journal of Alloys and Compounds,729 (2017) 446-452.

[70] Jennifer Schmitt Wolfgang G. Zeier, Geoffroy Hautier, Umut Aydemir,Zachary M. Gibbs, Claudia Felser, G. Jeffrey Snyders,Engineering half-Heusler thermoelectric materials using Zintl chemistry,NATURE REVIEWS, MATERIALS,1 (2016) 1-10.

[71] Harish K. Singh Mohd Zeeshan, Jeroen van den Brink, Hem C. Kandpals,Ab initio design of new cobalt-based half-Heusler materials for thermoelectric applications,PHYSICAL REVIEW MATERIALS,1 (2017) 075407-1-075407-9.

[72] John Fairbanks, THERMOELECTRIC APPLICATIONS IN VEHICLES STATUS 2008, U.S. Department of Energy Washington, D.C., U.S.A. 20585.

[73] Photo courtesy of NASA/JPLCaltech, https://www.energy.gov/sites/prod/files/styles/borealis_photo_gallery_large_respondsmall/public/mars_rover_MMGTG_0.png?itok=8S2HxJhI.

[74] Daniel Kraemer, Bed Poudel, Hsien-Ping Feng, J. Christopher Caylor, Bo Yu, Xiao Yan, Yi Ma, Xiaowei Wang, Dezhi Wang, Andrew Muto, Kenneth McEnaney, Matteo Chiesa, Zhifeng Ren, Gang Chen , High-performance flat-panel solar thermoelectric generators with high thermal concentration, Nature Materials volume 10, pages532–538(2011).

[75] Neophytos Neophytou, Mischa Thesberg, Modulation doping and energy filtering as effective ways to improve the thermoelectric power factor, J Comput Electron (2016) 15:16–26, DOI 10.1007/s10825-016-0792-7.

[76] Kyu Hyoung Lee, Sang-il Kim, Hyun-Sik Kim, Sung Wng Kim, Band Convergence in Thermoelectric Materials: Theoretical Background and Consideration on Bi−Sb−Te Alloys, ACS Appl. Energy Mater. 2020, 3, 2214−2223.

[77] Khalid Bin Masood, Pushpendra Kumar , R A Singh, Jai Singh, Odyssey of thermoelectric materials: foundation of the complex structure, J. Phys. Commun. 2 (2018) 062001, ,

[78] J. O. Sofo G. D. Mahan, The best thermoelectric, Proc. Natl. Acad. Sci. USA, Vol. 93, pp. 7436-7439, July 1996s.

[79] V. JOVOVIC, J.P. HEREMANS, Doping Effects on the Thermoelectric Properties of AgSbTe2, Journal of ELECTRONIC MATERIALS, Vol. 38, No. 7, 2009.

[80] Yan-Ling Pei, Haijun Wu, Di Wu, Fengshan Zheng, Jiaqing He, High Thermoelectric Performance Realized in a BiCuSeO System by Improving Carrier Mobility through 3D Modulation Doping, J. Am. Chem. Soc. 2014, 136, 13902−13908.

[81] Bolin Liao, Mona Zebarjadi, Keivan Esfarjani, Gang Chen, Cloaking Core-Shell Nanoparticles from Conducting Electrons in Solids, PRL 109, 126806 (2012), 10.1103/PhysRevLett.109.126806.

[82] Bo Yu, Mona Zebarjadi, Hui Wang, Kevin Lukas, Hengzhi Wang,Dezhi Wang, Cyril Opeil,Mildred Dresselhaus, Gang Chen,Zhifeng Ren, Enhancement of Thermoelectric Properties by Modulation-Doping in Silicon Germanium Alloy Nanocomposites, Nano Lett. 2012, 12, 2077−2082, dx.doi.org/10.1021/nl3003045.

[83] Mona Zebarjadi, Giri Joshi, Gaohua Zhu, Bo Yu, Austin Minnich, Yucheng Lan, Xiaowei Wang,Mildred Dresselhaus, Zhifeng Ren, Gang Chen, Power Factor Enhancement by Modulation Doping in Bulk Nanocomposites, Nano Lett. 2011, 11, 2225–2230, dx.doi.org/10.1021/nl201206d.

[84] Zheng Zheng, Xianli Su, Rigui Deng, Constantinos Stoumpos, Hongyao Xie, Wei Liu, Yonggao Yan, Shiqiang Hao, Ctirad Uher, Chris Wolverton, Mercouri G. Kanatzidis, Xinfeng Tang, Rhombohedral to Cubic Conversion of GeTe via MnTe Alloying Leads to Ultralow Thermal Conductivity, Electronic Band Convergence, and High Thermoelectric Performance, J. Am. Chem. Soc. 2018, 140, 2673−2686.

[85] Qinyong Zhang, Hui Wang, Weishu Liu, Hengzhi Wang, Bo Yu,b Qian Zhang, Zhiting Tian, George Ni,Sangyeop Lee, Keivan Esfarjani, Gang Chen, Zhifeng Ren, Enhancement of thermoelectric figure-of-merit by resonant states of aluminium doping in lead selenide, Energy Environ. Sci., 2012, 5, 5246.

[86] Moinak Dutta, Tanmoy Ghosh, Kanishka Biswas, Electronic structure modulation strategies in high-performance thermoelectrics, APL Mater. 8, 040910 (2020); doi: 10.1063/5.0002129.

[87] L. W. Whitlow, T. Hirano, Superlattice applications to thermoelectricity, Journal of Applied Physics 78, 5460 (1995); https://doi.org/10.1063/1.359661.

[88] Gangjian Tan, Fengyuan Shi, Shiqiang Hao, Hang Chi, Li-Dong Zhao, Ctirad Uher,Chris Wolverton, Vinayak P. Dravid, Mercouri G. Kanatzidis, Codoping in SnTe: Enhancement of Thermoelectric Performance through Synergy of Resonance Levels and Band Convergence, J. Am. Chem. Soc. 2015, 137, 5100−5112.

[89] Lihua Wu, Xin Li, Shanyu Wang, Tiansong Zhang, Jiong Yang, Wenqing Zhang, Lidong Chen, Jihui Yang, Resonant level-induced high thermoelectric response in indium-doped GeTe, NPG Asia Materials (2017) 9, e343; doi:10.1038/am.2016.203.

[90] Dianta Ginting, Chan-Chieh Lin, Lydia Rathnam, Gareoung Kim, Jae Hyun Yun, Hyeon Seob So, Hosun Lee, Byung-Kyu Yu, Sung-Jin Kim, Kyunghan Ahn, Jong-Soo Rhyee, Enhancement of Thermoelectric Performance in Na-Doped Pb0.6Sn0.4Te0.95−xSexS0.05 via Breaking the Inversion Symmetry, Band Convergence, and Nanostructuring by Multiple Elements Doping, ACS Appl. Mater. Interfaces 2018, 10, 11613−11622.

[91] S. R. Bauers, D. R. Merrill, D. B. Moore, D. C. Johnson, Carrier dilution in TiSe2 based intergrowth compounds for enhanced thermoelectric performance, J. Mater. Chem. C, 2015,3, 10451.

[92] A. Samarelli, L. Ferre Llin, S. Cecchi, J. Frigerio, T. Etzelstorfer, E. M€uller, Y. Zhang,J. R. Watling, D. Chrastina, G. Isella, J. Stangl, J. P. Hague, J. M. R. Weaver,P. Dobson, D. J. Paul, The thermoelectric properties of Ge/SiGe modulation doped superlattices,J. Appl. Phys. 113, 233704 (2013); https://doi.org/10.1063/1.4811228.

[93] Wei Wu, Wenxin Liu, Fengrong Yu, Enhancement of thermoelectric performance through synergy of Pb acceptor doping and superstructure modulation for p-type Bi2Te3, Journal of Materials Science: Materials in Electronics (2020) 31:1200–1209, https://doi.org/10.1007/s10854-019-02631-z.

[94] Xiao-Xi Peng, Xuan Qiao, Shuai Luo, Jun-An Yao, Yun-Fei Zhang, Fei-Peng Du, Modulating Carrier Type for Enhanced Thermoelectric Performance of Single-Walled Carbon Nanotubes/Polyethyleneimine Composites, Polymers 2019, 11, 1295; doi:10.3390/polym11081295,

[95] Jun Wang, Bo-Yu Zhang, Hui-Jun Kang, Yan Lia, Xinba Yaer, Jing-Feng Li,Qing Tan, Shuai Zhang, Guo-Hua Fan, Cheng-Yan Liu, Lei Miao, Ding Nan, ong-Min Wang, Li-Dong Zhao, Record high thermoelectric performance in bulk SrTiO3 via nano-scale modulation doping, Nano Energy 35 (2017) 387–395.

[96] Dongwook Lee, Sayed Youssef Sayed, Sangyeop Lee, Chris Adam Kuryak,Jiawei Zhou, Gang Chen, Yang Shao-Horn, Quantitative analyses of enhanced thermoelectric properties of modulation-doped PEDOT:PSS/undoped Si (001) nanoscale heterostructures, Nanoscale, 2016, 8, 19754.

[97] Joseph P. Heremans, Vladimir Jovovic, Eric S. Toberer, Ali Saramat, Ken Kurosaki, Anek Charoenphakdee, Shinsuke Yamanaka, G. Jeffrey Snyder, Enhancement of Thermoelectric Efficiency in PbTe by Distortion of the Electronic Density of States, Science 321 (5888), 554-557, DOI: 10.1126/science.1159725,

[98] L. D. Hicks, M. S. Dresselhaus, Thermoelectric figure of merit of a one-dimensional conductor, PHYSICAL REVIEW 8, VOLUME 47, NUMBER 24, 1993.

[99] L. D. Hicks, M. S. Dresselhaus, Effect of quantum-well structures on the thermoelectric figure of merit, PHYSICAL REVIEW 8 VOLUME 47, 1993-I.

[100] M. S. Dresselhaus, T. Koga, X. Sun, S. B. Cronin, K.L. Wang, G. Chen, Low Dimensional Thermoelectrics, 16th International Conference on Thermoelectrics (1997).

[101] Jun Mao, Zihang Liu, Zhifeng Ren, Size effect in thermoelectric materials, npj Quantum Materials (2016) 1, 16028; doi:10.1038/npjquantmats.2016.28; published online 9 December 2016.

[102] Di Wu , Yanling Pei , Zhe Wang , Haijun Wu , Li Huang , Li-Dong Zhao , Jiaqing He, Signifi cantly Enhanced Thermoelectric Performance in n-type Heterogeneous BiAgSeS Composites, Adv. Funct. Mater. 2014, 24, 7763–7771.

[103] Jun Guo, Yi-Xin Zhang, Zi-Yuan Wang, Fengshan Zheng, Zhen-Hua Ge, Jiecai Fu, Jing Feng, High thermoelectric properties realized in earth-abundant Bi2S3 bulk via carrier modulation and multi-nano-precipitates synergy, Nano Energy 78 (2020) 105227.

[104] Subhajit Roychowdhury, Manisha Samanta, Suresh Perumal, Kanishka Biswas, Germanium Chalcogenide Thermoelectrics: Electronic Structure Modulation and Low Lattice Thermal Conductivity, Chem. Mater. 2018, 30, 5799−5813.

[105] Wenyu Zhao, Zhiyuan Liu, Zhigang Sun, Qingjie Zhang, Ping Wei, Xin Mu, Hongyu Zhou, Cuncheng Li, Shifang Ma, Danqi He, Pengxia Ji, Wanting Zhu, Xiaolei Nie, Xianli Su, Xinfeng Tang, Baogen Shen, Xiaoli Dong, Jihui Yang,Yong Liu, Jing Shi, Superparamagnetic enhancement of thermoelectric performance, Nature 549, 247–251 (2017); doi:10.1038/nature23667.

[106] J.-B. Vaney, S. Aminorroaya Yamini, H. Takaki, K. Kobayashi, N. Kobayashi,T. Mori, Magnetism-mediated thermoelectric performance of the Cr-doped bismuth telluride tetradymite, Materials Today Physics 9 (2019) 100090.

[107] K. FISCHER, Theory of Dilute Magnetic Alloys, phys. stat. sol. (b) 46, 11 (1971).

[108] J. K. Furdyna, Diluted magnetic semiconductors: An interface of semiconductor physics and magnetism (invited), Journal of Applied Physics 53, 7637 (1982); https://doi.org/10.1063/1.330137.

[109] J. K. Furdyna, Diluted magnetic semiconductors, Journal of Applied Physics 64, R29 (1988); https://doi.org/10.1063/1.341700.

[110] Q. Mahmood, S. Khalil, M. Hassan, A. Laref, Systematic DFT study of the impact of anionic variations on the physical properties of Cd1-xMnxX (X=S, Se, Te; x=6.25%), Materials Research Bulletin, 107 (2018) 225-235.

[111] S. Sergeenkov, J. Mucha, M. Pekala, V. Drozd, and M. Ausloos, Influence of Zeeman splitting and thermally excited polaron states on magnetoelectrical and magnetothermal properties of magnetoresistive polycrystalline manganite La0.8Sr0.2MnO3, J. Appl. Phys. 102, 083916 (2007); https://doi.org/10.1063/1.2802189.

[112] C. Zener, Interaction between the d bhells in the transition metals, Physical Review, Vol 81, No 4, February 1951, 440-44,.

[113] Antiferromagnetism. Theory of Suyerexchange Interaction, Physical review, Vol 79, No 2, Juy 15, 1950 (350-356).

[114] Wenyu Zhao, Zhiyuan Liu, Ping Wei, Qingjie Zhang, Wanting Zhu, Xianli Su, Xinfeng Tang, Jihui Yang, Yong Liu, Jing Shi, Yimin Chao, Siqi Lin, Yanzhong Pei, Magnetoelectric interaction and transport behaviours in magnetic nanocomposite thermoelectric materials, NATURE NANOTECHNOLOGY,VOL 12, JANUARY 2017.

[115] M. A. Mayer, P. R. Stone, N. Miller, H. M. Smith III, O. D. Dubon, E. E. Haller, K. M. Yu, W. Walukiewicz, X. Liu, J. K. Furdyna, Electronic structure of Ga1−xMnxAs analyzed according to hole-concentration-dependent measurements, PHYSICAL REVIEW B 81, 045205 (2010).

[116] M. M. H. Polash, F. Mohaddes, M. Rasoulianboroujeni, D. Vashaee, Magnon-drag thermopower in antiferromagnets versus ferromagnets, J. Mater. Chem. C, 8(12), 4049-4057 (2020).

[117] Ran Ang, Atta Ullah Khan, Naohito Tsujii, Ken Takai, Ryuhei Nakamura, Takao Mori, Thermoelectricity Generation and Electron–Magnon Scattering in a Natural Chalcopyrite Mineral from a Deep-Sea Hydrothermal Vent, Angew. Chem. Int. Ed. 2015, 54, 12909 – 12913.

[118] Fahim Ahmed, Naohito Tsujii, Takao Mori, Thermoelectric properties of CuGa1xMnxTe2:power factor enhancement by incorporation of magnetic ions, Mater. Chem. A, 2017, 5, 7545.

[119] Zichen Wei, Chenyang Wang, Jiye Zhang, Jiong Yang, Zhili Li, Qidong Zhang, Pengfei Luo, Wenqing Zhang, Enke Liu, Jun Luo, Precise Regulation of Carrier Concentration in Thermoelectric BiSbTe Alloys via Magnetic Doping, ACS Appl. Mater. Interfaces 2020, 12, 20653−20663.

[120] Jun Tang, Rui Xu, Jian Zhang, Di Li, Weiping Zhou, Xiaotong Li, Zhihe Wang, Feng Xu,Guodong Tang, Guang Chen, Light Element Doping and Introducing Spin Entropy: An Effective Strategy for Enhancement of Thermoelectric Properties in BiCuSeO, ACS Appl. Mater. Interfaces 2019, 11, 15543−15551.

[121] Zhiyuan Liu, Jianglong Zhu, Ping Wei, Wanting Zhu, Wenyu Zhao, Ailin Xia, Dong Xu, Ying Lei, Jian Yu, Candidate for Magnetic Doping Agent and High-Temperature Thermoelectric Performance Enhancer: Hard Magnetic M-type BaFe12O19 Nanometer Suspension, ACS Appl. Mater. Interfaces 2019, 11, 45875−45884.

[122] Sarah J. Watzman, Rembert A. Duine, Yaroslav Tserkovnyak, Stephen R. Boona, Hyungyu Jin, Arati Prakash, Yuanhua Zheng, Joseph P. Heremans, Magnon-drag thermopower and Nernst coefficient in Fe, Co, and Ni, Phys. Rev. B 94, 144407, Published 11 October 2016.

[123] F. J. Blatt, D. J. Flood, V. Rowe, P. A. Schroeder, Magnon-drag thermopower in iron, Phys. Rev. Lett. 18, (1967) 395–396.

[124] G. N. Grannemann, L. Berger, Magnon-drag Peltier effect in a Ni-Cu alloy, hys. Rev. B 13, 2072, 1 March 1976, https://doi.org/10.1103/PhysRevB.13.2072.

[125] M. E. Lucassen, C. H. Wong, R. A. Duine, Y. Tserkovnyak, Spin-transfer mechanism for magnon-drag thermopower, Appl. Phys. Lett. 99, 262506 (2011); https://doi.org/10.1063/1.3672207.

[126] G. Venkataiah, P. Venugopal Reddy, Magnon drag contribution to thermopower of Nd0.67Sr0.33MnO3 nanocrystalline Manganites, Journal of Applied Physics 106, 033706 (2009); doi: 10.1063/1.3191680. 2-8.

[127] Frank J.Blatt, "Phonon Drag," in Thermoelectric Power of Metals, Frank J. BlattPeter A. SchroederCarl L. FoilesDenis Greig, Ed., ed New York and London: Springer, 1976.

[128] Hiroto Adachi et al 2013 Rep. Prog. Phys. 76 036501.

[129] F. Schlickeiser, U. Ritzmann, D. Hinzke, U. Nowak, Role of Entropy in Domain Wall Motion in Thermal Gradients, Erschienen in: Physical Review Letters ; 113 (2014), 9. – 097201 https://dx.doi.org/10.1103/PhysRevLett.113.097201.

[130] Johnson, M. Silsbee, R. H. Thermodynamic analysis of interfacial transport and of the thermomagnetoelectric system. Phys. Rev. B 35, 4959–4972 (1987).

[131] Shi, J. et al. Field-dependent thermoelectric power and thermal conductivity in multilayered and granular giant magnetoresistive systems. Phys. Rev. B 54, 15273–15283 (1996).

[132] Gravier, L., Guisan, S. S., Reuse, F. & Ansermet, J-Ph. Spin-dependent Peltier effect of perpendicular currents in multilayered nanowires. Phys. Rev. B 73, 052410 (2006).

[133] Bauer, G. E. W., Saitoh, E., & van Wees, B. J. (2012). Spin caloritronics. Nature Materials, 11(5), 391-399. https://doi.org/10.1038/NMAT3301.

[134] RSC Adv., 2016, 6, 80302.

[135] Naohito Tsujii, Akinori Nishide, Jun Hayakawa, Takao Mori, Observation of enhanced thermopower due to spin fluctuation in weak itinerant ferromagnet, Sci. Adv. 2019;5: eaat5935.

[136] Takuya Okabe, Spin-fluctuation drag thermopower of nearly ferromagnetic metals, J. Phys.: Condens. Matter 22 115604, 2010.

[137] J. Kondo, Giant Thermo-Electric Power of Dilute Magnetic Alloys, Progress of Theoretical Physics, Volume 34, Issue 3, September 1965, Pages 372–382, https://doi.org/10.1143/PTP.34.372.

[138] Jun Kondo, Anomalous Hall Effect and Magnetoresistance of Ferromagnetic Metals, Progress of Theoretical Physics, Vol. 27, No. 4, April 1962 (772-792).

[139] N F Mott,A discussion of the transition metals on the basis of quantum mechanics, Proceedings of the Physical Society, Volume 47, Number 4. 1935 , 571.

[140] Tadao Kasuya,Electrical Resistance of Ferromagnetic Metals, Progress of Theoretical Physics, Volume 16, Issue 1, July 1956, Pages 58–63, https://doi.org/10.1143/PTP.16.58.

[141] Robert Karplus, J. M. Luttinger, Hall Effect in Ferromagnetics, Phys. Rev. 95, 1954, 1154-1160.

[142] J. M. Luttinger, Theory of the Hall Effect in Ferromagnetic Substances, Phys. Rev. 112, 1958 (739-751).

[143] J.Smit, The spontaneous hall effect in ferromagnetics II, Physica, Volume 24, Issues 1–5, 1958, Pages 39-51, https://doi.org/10.1016/S0031-8914(58)93541-9.

[144] Naoto Nagaosa, Jairo Sinova, Shigeki Onoda, A. H. MacDonald, N. P. Ong, Anomalous Hall effect, REVIEWS OF MODERN PHYSICS, VOLUME 82, APRIL–JUNE 2010 (1539-1592).

[145] E. H. Hall, On a New Action of the Magnet on Electric Currents, American Journal of Mathematics , Sep., 1879, Vol. 2, No. 3 (Sep., 1879), pp. 287-292, Published by: The Johns Hopkins University Press, Stable URL: https://www.jstor.org/stable/2369245.

[146] E.H. Hall Ph.D. (1881) XVIII. On the “Rotational Coefficient” in nickel and cobalt, The London, Edinburgh, and Dublin Philosophical Magazine and Journal of Science, 12:74, 157-172, DOI: 10.1080/14786448108627086.

[147] Hidemi Toyosaki,Tomoteru Fukumura, Yasuhiro Yamada, Kiyomi Nakajima, Toyohiro Chikyow, Tetsuya Hasegawa, Hideomi Koinuma, Masashi Kawasaki, Anomalous Hall

effect governed by electron doping in a room-temperature transparent ferromagnetic semiconductor, nature materials, VOL 3, APRIL 2004.

[148] Nagendra S. Chauhan , Sivaiah Bathula,Bhasker Gahtori, Yury V. Kolen'ko, Ajay Dhar, Enhanced Thermoelectric Performance in Hf-Free p-Type (Ti,Zr)CoSb Half-Heusler Alloys, Journal of ELECTRONIC MATERIALS, Vol. 48, No. 10, 2019, https://doi.org/10.1007/s11664-019-07486-y.

[149] Bo Feng, Guangqiang Li, Yanhui Hou, Chengcheng Zhang, Chengpeng Jiang, Jie Hu, Qiusheng Xiang, Yawei Li, Zhu He, Xi'an Fan, Enhanced thermoelectric properties of Sb-doped BiCuSeO due to decreased band gap, Journal of Alloys and Compounds 712 (2017) 386-393.

[150] Bo Feng, Guangqiang Li, Zhao Pan, Xiaoming Hu, Peihai Liu, Yawei LiZhu He, Xi'an Fan, Enhanced thermoelectric performances in BiCuSeO oxyselenides via Er and 3D modulation doping, Ceramics International 45 (2019) 4493–4498.

[151] Bo Feng, Guangqiang Li, Zhao Pan, Xiaoming Hu, Peihai Liua, Zhu Hea,Yawei Li, Xi'an Fan, Enhanced thermoelectric performance in BiCuSeO oxyselenides via Ba/Te dual-site substitution and 3D modulation doping, Journal of Solid State Chemistry 266 (2018) 297–303.

[152] Manisha Samanta, Tanmoy Ghosh, Raagya Arora, Umesh V. Waghmare, Kanishka Biswas, Realization of Both n- and p-Type GeTe Thermoelectrics: Electronic Structure Modulation by AgBiSe2 Alloying, J. Am. Chem. Soc. 2019, 141, 19505−19512.

[153] Chenguang Fu Tanya Berry, Gudrun Auffermann, Gerhard H. Fecher, Walter Schnelle, Federico Serrano-Sanchez, Yuan Yue, Hong Liang, Claudia Felsers,Enhancing Thermoelectric Performance of TiNiSn Half-Heusler Compounds via Modulation Doping,Chem. Mater.,29 (2017) 7042−7048.

[154] Machhindra Koirala, Huaizhou Zhao, Mani Pokharel, Shuo Chen, Tulashi Dahal, Cyril Opeil, Gang Chen, Zhifeng Ren, Thermoelectric property enhancement by Cu nanoparticles in nanostructured FeSb2, APPLIED PHYSICS LETTERS 102, 213111 (2013).

[155] Shaohai Wu, Hengquan Yang, Zhengsen Wu, Chengyan Liu, Lei Miao, Jie Gao,Xiaoyang Wang, Xiuxia Wang, Chengjin Shen, Jacques G. Noudem, Jun Wang, Enhancement of Thermoelectric Performance of Layered SnSe2 by Synergistic Modulation of Carrier Concentration and Suppression of Lattice Thermal Conductivity, ACS Appl. Energy Mater. 2019, 2, 8481−8490.

[156] Ce-Wen Nan, Physics Of Inhomogeneous Inorganic Materials, Progress in Materials Science Vol. 37, pp. 1-116, 1993.

[157] Li Juan Zhang, Peng Qin, Chao Han, Jian Li Wang, Zhen Hua Ge, Qiao Sun, Zhen Xiang Cheng, Zhen Li, Shi Xue Dou, Enhanced thermoelectric performance through synergy of resonance levels and valence band convergence via Q/In (Q ¼ Mg, Ag, Bi) co-doping, J. Mater. Chem. A, 2018, 6,2507.

[158] Riley Hanus, Xingyu Guo, Yinglu Tang, Guodong Li, G. Jeffrey Snyder,Wolfgang G. Zeier, A Chemical Understanding of the Band Convergence in Thermoelectric CoSb3 Skutterudites: Influence of Electron Population, Local Thermal Expansion, and Bonding Interactions, Chem. Mater. 2017, 29, 1156−1164.

[159] Zhiwei Chen, Zhengzhong Jian, Wen Li, Yunjie Chang, Binghui Ge, Riley Hanus, Jiong Yang, Yue Chen, Mingxin Huang, Gerald Jeffrey Snyder, Yanzhong Pei, Lattice

Dislocations Enhancing Thermoelectric PbTe in Addition to Band Convergence, Adv. Mater. 2017, 29, 1606768.

[160] Xiaohua Liu, Tiejun Zhu, Heng Wang, Lipeng Hu, Hanhui Xie, Guangyu Jiang, G. Jeffrey Snyder, Xinbing Zhao, Low Electron Scattering Potentials in High Performance Mg2Si0.45Sn 0.55 Based Thermoelectric Solid Solutions with Band Convergence, Adv. Energy Mater. 2013, 3, 1238–1244.

[161] Min Hong, Yuan Wang, Weidi Liu, Syo Matsumura, Hao Wang, Jin Zou, Zhi-Gang Chen, Arrays of Planar Vacancies in Superior Thermoelectric Ge1−x−yCdxBiyTe with Band Convergence, Adv. Energy Mater. 2018, 8, 1801837.

[162] Dianta Ginting, Chan-Chieh Lin, Gareoung Kim, Jae Hyun Yun, Byung-Kyu Yu, Sung-Jin Kim, Kyunghan Ahn, Jong-Soo Rhyee, Enhancement of thermoelectric performance via weak disordering of topological crystalline insulators and band convergence by Se alloying in Pb0.5Sn0.5Te1-xSex, J. Mater. Chem. A, 2018, 6, 5870.

[163] Wenqi Lu, Tiantian He, Shuang Li, Xinru Zuo, Yao Zheng, Xunuo Lou, Jian Zhang, Di Li, Jizi Liu, Guodong Tang, Thermoelectric performance of nanostructured In/Pb codoped SnTe with band convergence and resonant level prepared via a green and facile hydrothermal method, Nanoscale, 2020, 12, 5857.

[164] U.Sandhya Shenoy, D.Krishna Bhat, Enhanced thermoelectric properties of vanadium doped SrTiO3: A resonant dopant approach, Journal of Alloys and Compounds 832 (2020) 154958.

[165] Jun Mao, Yumei Wang, Binghui Ge, Qing Jie, Zihang Liu, Udara Saparamadu, Weishu Liu, Zhifeng Ren, Thermoelectric performance enhancement of Mg2Sn based solid solutions by band convergence and phonon scattering via Pb and Si/Ge substitution for Sn, Phys. Chem. Chem. Phys., 2016, 18, 20726.

[166] Qian Zhang, Feng Cao, Weishu Liu, Kevin Lukas, Bo Yu, Shuo Chen, Cyril Opeil, David Broido,Gang Chen, Zhifeng Ren, Heavy Doping and Band Engineering by Potassium to Improve the Thermoelectric Figure of Merit in p-Type PbTe, PbSe, and PbTe1−ySey, J. Am. Chem. Soc. 2012, 134, 10031−10038.

[167] Junsoo Park, Max Dylla, Yi Xia, Max Wood, G. Jeffrey Snyder, Anubhav Jain, When Band Convergence is Not Beneficial for Thermoelectrics, spinarXiv:2012.02272v1 [cond-mat.mtrl-sci] 3 Dec 2020.

[168] Peigen Li, Teng Ding, Junqin Li, Chunxiao Zhang, Yubo Dou, Yu Li, Lipeng Hu, Fusheng Liu, Chaohua Zhang, Positive Effect of Ge Vacancies on Facilitating Band Convergence and Suppressing Bipolar Transport in GeTe-Based Alloys for High Thermoelectric Performance, Adv. Funct. Mater. 2020, 30, 1910059.

[169] Min Hong, Zhi-Gang Chen, Yanzhong Pei, Lei Yang, Jin Zou, Limit of zT enhancement in rocksalt structured chalcogenides by band convergence, PHYSICAL REVIEW B 94, 161201(R) (2016).

[170] Kyunghan Ahn, Mi-Kyung Han, Jiaqing He, John Androulakis,Sedat Ballikaya, Ctirad Uher, Vinayak P. Dravid, Mercouri G. Kanatzidis, Exploring Resonance Levels and Nanostructuring in the PbTe-CdTe System and Enhancement of the Thermoelectric Figure of Merit, J. AM. CHEM. SOC. 2010, 132, 5227–5235.

[171] Suresh Perumal, Pavithra Bellare, U. Sandhya Shenoy, Umesh V. Waghmare, Kanishka Biswas, Low Thermal Conductivity and High Thermoelectric Performance in Sb and Bi

Codoped GeTe: Complementary Effect of Band Convergence and Nanostructuring, Chem. Mater. 2017, 29, 10426−10435.

[172] Sajid Ahmad, Ajay Singh, Shovit Bhattacharya, M. Navaneethan, Ranita Basu, Ranu Bhatt, Pritam Sarkar, K. N. Meshram, A. K. Debnath, K. P. Muthe, D. K. Aswal, Band Convergence and Phonon Scattering Mediated Improved Thermoelectric Performance of SnTe−PbTe Nanocomposites, ACS Appl. Energy Mater. 2020, 3, 8882−8891.

[173] Ling Wang, Xiaojian Tan, Guoqiang Liu, Jingtao Xu, Hezhu Shao, Bo Yu, Haochuan Jiang,Song Yue, Jun Jiang, Manipulating Band Convergence and Resonant State in Thermoelectric Material SnTe by Mn−In Codoping, ACS Energy Lett. 2017, 2, 1203−1207.

[174] Gangjian Tan, Shiqiang Hao, Riley C. Hanus, Xiaomi Zhang, Shashwat Anand, Trevor P. Bailey, Alexander J. E. Rettie, Xianli Su, Ctirad Uher, Vinayak P. Dravid, G. Jeffrey Snyder, Chris Wolverton, Mercouri G. Kanatzidis, High Thermoelectric Performance in SnTe−AgSbTe2 Alloys from Lattice Softening, Giant Phonon−Vacancy Scattering, and Valence Band Convergence, ACS Energy Lett. 2018, 3, 705−712.

[175] Subhajit Roychowdhury, U. Sandhya Shenoy, Umesh V. Waghmare, Kanishka Biswas, An enhanced Seebeck coefficient and high thermoelectric performance in p-type In and Mg co-doped Sn1xPbxTe via the co-adjuvant effect of the resonance level and heavy hole valence band, J. Mater. Chem. C, 2017, 5, 5737.

[176] Evariste Nshimyimana, Shiqiang Hao, Xianli Su, Cheng Zhang, Wei Liu, Yonggao Yan, Ctirad Uher, Chris Wolverton, Mercouri G. Kanatzidis, Xinfeng Tang, Discordant nature of Cd in GeTe enhances phonon scattering and improves band convergence for high thermoelectric performance, J. Mater. Chem. A, 2020, 8,1193.

[177] Ananya Banik, U. Sandhya Shenoy, Shashwat Anand, Umesh V. Waghmare, Kanishka Biswas, Mg Alloying in SnTe Facilitates Valence Band Convergence and Optimizes Thermoelectric Properties, Chem. Mater. 2015, 27, 581−587.

[178] Yamei Feng, Junqin Li, Yu Li, Teng Ding, Chunxiao Zhang, Lipeng Hu, Fusheng Liu, Weiqin Ao, Chaohua Zhang, Band convergence and carrier-density fine-tuning as the electronic origin of high-average thermoelectric performance in Pb-doped GeTebased alloys, J. Mater. Chem. A, 2020, 8,11370.

[179] Zhe Guo, Qiang Zhang, Hongxiang Wang, Xiaojian Tan, Fanfan Shi,Chenglong Xiong, Na Man, Haoyang Hu, Guoqiang Liu, Jun Jiang, Bi–Zn codoping in GeTe synergistically enhances band convergence and phonon scattering for high thermoelectric performance, J. Mater. Chem. A, 2020, 8, 21642.

[180] Sayan Sarkar, Prashant K. Sarswat, Shrikant Saini, Paolo Mele, Michael L. Free, Synergistic effect of band convergence and carrier transport on enhancing the thermoelectric performance of Ga doped Cu2Te at medium temperatures, Scientific Reports, (2019) 9:8180, https://doi.org/10.1038/s41598-019-43911-2.

[181] Fengkai Guo, Bo Cui, Yuan Liu, Xianfu Meng, Jian Cao, Yang Zhang, Ran He, Weishu Liu, Haijun Wu, Stephen J. Pennycook, Wei Cai, Jiehe Sui, Thermoelectric SnTe with Band Convergence, Dense Dislocations, and Interstitials through Sn Self-Compensation and Mn Alloying, Small 2018, 14, 1802615, DOI: 10.1002/smll.201802615.

[182] Ananya Banik, Kanishka Biswas, AgI alloyingin SnTe boosts the thermoelectric performance via simultaneous valence band convergence and carrier concentration optimization, Journal of Solid State Chemistry 242 (2016) 43–49.

[183] Zhengliang Du, Xiaolu Chen, Mengyi Yan, Enhanced thermoelectric properties of Sn-rich quaternary Mg2Si0.25Ge0.05Sn0.7 based solid solutions by band convergence in addition to scattering of point defects, Journal of Solid State Chemistry 271 (2019) 67–73.

[184] Hyun-Sik Kim, Nicholas A. Heinz, Zachary M. Gibbs, Yinglu Tang, Stephen D. Kang, G. Jeffrey Snyder, High thermoelectric performance in (Bi0.25Sb0.75)2Te3 due to band convergence and improved by carrier concentration control, Materials Today, Volume 20, Number 8,October 2017.

[185] Dianta Ginting, Chan-Chieh Lin, R. Lydia, Hyeon Seob So, Hosun Lee, Junpil Hwang, Woochul Kim, Rabih Al Rahal Al Orabi, Jong-Soo Rhyee, High thermoelectric performance in pseudo quaternary compounds of (PbTe)0.95-x(PbSe)x(PbS)0.05 by simultaneous band convergence and nano precipitation, Acta Materialia 131 (2017) 98-109.

[186] Z.L. Du, H.L. Gao, J.L. Cui, Thermoelectric performance of quaternary Mg2(1þx)Si0.2Ge0.1Sn0.7 ($0.06 \leq x \leq 0.12$) solid solutions with band convergence, Current Applied Physics 15 (2015) 784-788.

[187] Xiaotong Li, Jizi Liu, Shuang Li, Jian Zhang, Di Li, Rui Xu, Qingtang Zhang, Xuemei Zhang, Biao Xu, Yongsheng Zhang, Feng Xu, Guodong Tang, Synergistic band convergence and endotaxial nanostructuring: Achieving ultralow lattice thermal conductivity and high figure of merit in eco-friendly SnTe, Nano Energy 67 (2020) 104261.

[188] Ananya Banik, U. Sandhya Shenoy, Sujoy Saha, Umesh V. Waghmare, Kanishka Biswas, High Power Factor and Enhanced Thermoelectric Performance of SnTe-AgInTe2: Synergistic Effect of Resonance Level and Valence Band Convergence, J. Am. Chem. Soc. 2016, 138, 13068−13075.

[189] Wen Li, Linglang Zheng, Binghui Ge, Siqi Lin, Xinyue Zhang, Zhiwei Chen, Yunjie Chang, Yanzhong Pei,Promoting SnTe as an Eco-Friendly Solution for p-PbTe Thermoelectric via Band Convergence and Interstitial Defects, Adv. Mater. 2017, 29, 1605887.

[190] Tyler J. Slade, Trevor P. Bailey, Jann A. Grovogui, Xia Hua, Xiaomi Zhang, Jimmy Jiahong Kuo, Ido Hadar, G. Jeffrey Snyder, Chris Wolverton, Vinayak P. Dravid, Ctirad Uher, Mercouri G. Kanatzidis, High Thermoelectric Performance in PbSe–NaSbSe2 Alloys from Valence Band Convergence and Low Thermal Conductivity, Adv. Energy Mater. 2019, 9, 1901377.

[191] Zhenghao Hou, Dongyang Wang, Tao Hong, Yongxin Qin, Shang Peng Guangtao Wang, Jinfeng Wang, Xiang Gao, Zhiwei Huang, Li-Dong Zhao, Boosting thermoelectric performance of n-type PbS through synergistically integrating In resonant level and Cu dynamic doping , Journal of Physics and Chemistry of Solids,Volume 148, January 2021, 109640.

[192] P. K. Rawat, B. Paul, P. Banerji, Exploration of Zn Resonance Levels and Thermoelectric Properties in I-Doped PbTe with ZnTe Nanostructures, ACS Appl. Mater. Interfaces 2014, 6, 3995−4004.

[193] Felix Mouhat, Francois-Xavier Coudert, Necessary and sufficient elastic stability conditions in various crystal systems, PHYSICAL REVIEW B 90, 224104 (2014).

[194] Anita Rani, Ranjan Kumar, Stability and electronic properties of Cd0.75Mn0.25S and Cd0.75Mn0.25Se in B3 phase, Appl. Phys. A (2015) 120:775–784, DOI 10.1007/s00339-015-9255-4.

[195] Q. Mahmood, M. Hassan, Muhammad Rashid, Bakhtiar Ul Haq, A. Laref, The systematic study of mechanical, thermoelectric and optical properties of lead based halides by first principle approach, Physica B: Condensed Matter 571 (2019) 87–92.

[196] Enamul Haque, M. Anwar Hossain, First-principles study of elastic, electronic, thermodynamic, and thermoelectric transport properties of TaCoSn, Results in Physics 10 (2018) 458–465.

[197] Juan Li, Xinyue Zhang, Zhiwei Chen, Siqi Lin, Wen Li, Jiahong Shen, Ian T. Witting, Alireza Faghaninia, Yue Chen, Anubhav Jain, Lidong Chen, G. Jeffrey Snyder, Yanzhong Pei, Low-Symmetry RhombohedralGeTe Thermoelectrics, Joule2, 976–987, May 16, 2018.

[198] Jiawei Zhang, Ruiheng Liu, Nian Cheng, Yubo Zhang, Jihui Yang, Ctirad Uher, Xun Shi, Lidong Chen, Wenqing Zhang, High-Performance Pseudocubic Thermoelectric Materials from Non-cubic Chalcopyrite Compounds, Adv. Mater. 2014, 26, 3848–3853.

[199] Zhiwei Huang, Li-Dong Zhao, Symmetry and asymmetry in thermoelectrics, J. Mater. Chem. C, 2020, 8, 12054-12061.

[200] Saveer Ahmad Khandy, Dinesh C. Gupta, Magneto-electronic, mechanical, thermoelectric and thermodynamic properties of ductile perovskite Ba2SmNbO6, Materials Chemistry and Physics 239 (2020) 121983,

[201] Sajad Ahmad Dar, Vipul Srivastava, Umesh Kumar Sakalle, Structural, elastic, mechanical, electronic, magnetic, thermoelectric and thermodynamic investigation of half metallic double perovskite oxide Sr2MnTaO6, Journal of Magnetism and Magnetic Materials 484 (2019) 298–306.

[202] Arash Mehdizadeh Dehkordi, Mona Zebarjadi, Jian He, Terry M. Tritt, Thermoelectric power factor: Enhancement mechanisms and strategies for higher performance thermoelectric materials, Materials Science and Engineering R 97 (2015) 1–22.

[203] G.A. Slack, in: D.M. Rowe (Ed.), CRC Handbook of Thermoelectrics, CRC Press, London, 1995, p. 407.

[204] Shakeel Ahmad Sofi, Dinesh C. Gupta, Investigation of high pressure and temperature study of thermo-physical properties in semiconducting Fe2ZrSi Heusler, Physica B 577 (2020) 411792.

[205] Creative Commons Attribution-Noncommercial-Share Alike 3.0 United States License. Lattice Vibrations. Available: https://eng.libretexts.org/Core/Materials_Science/Electronic_Properties/Lattice_Vibrations

[206] W. Kims,Strategies for engineering phonon transport in thermoelectrics,J. Mater. Chem. C,3 (2015) 10336--10348.

[207] Vladan Stevanovic´ Prashun Gorai, Eric S. Toberers,Computationally guided discovery of thermoelectric materials,NATURE REVIEWS, MATERIALS,2 (2017) 1-16.

[208] Alexander A. Balandins,Thermal properties of graphene and nanostructured carbon materials,nature materials,10 (2011) 569-581.

[209] Chris Wolverton Vancho Kocevskis,Designing High-Efficiency Nanostructured Two-Phase Heusler Thermoelectrics,Chem. Mater.,29 (2017) 9386-9398.

[210] Giri Joshi Xiao Yan, Weishu Liu, Yucheng Lan, Hui Wang, Sangyeop Lee, J. W. Simonson,S. J. Poon, T. M. Tritt, Gang Chen, Z. F. Rens,Enhanced Thermoelectric Figure of Merit of p-Type Half-Heuslers,Nano Lett.,11 (2011) 556–560.

[211] Mohamed N.A. Nasr Mohamed S. El-Asfoury, Koichi Nakamura, Ahmed Abdel-Moneims,Enhanced thermoelectric performance of Bi85Sb15-graphene composite by modulation carrier transport and density of state effective mass,Journal of Alloys and Compounds,745 (2018) 331-340.

[212] Chongyin Yang Haijie Chen, Huili Liu, Ganghua Zhang, Dongyun Wan, Fuqiang Huangs,Thermoelectric properties of CuInTe2/graphene composites,Cryst Eng Comm,15 (2013,) 6648–6651.

[213] Robert W. McKinney, Prashun Gorai,Vladan Stevanovi´c, Eric S. Toberer, Search for new thermoelectric materials with low Lorenz number, J. Mater. Chem. A, 2017,5, 17302-17311.

[214] Xufeng Wang, Vahid Askarpour, Jesse Maassen, Mark Lundstrom, On the calculation of Lorenz numbers for complex thermoelectric materials, JOURNAL OF APPLIED PHYSICS 123, 055104 (2018).

[215] Huili Liu , Xun Yuan , Ping Lu , Xun Shi , Fangfang Xu , Ying He , Yunshan Tang , Shengqiang Bai , Wenqing Zhang , Lidong Chen , Yue Lin , Lei Shi , He Lin , Xingyu Gao , Xingmin Zhang , Hang Chi , Ctirad Uher, Ultrahigh Thermoelectric Performance by Electron and Phonon Critical Scattering in Cu 2 Se 1-x I x, Adv.Mater.2013, 25, 6607–6612.

[216] Mischa Thesberg, Hans Kosina, Neophytos Neophytou, On the Lorenz number of multiband materials, PHYSICAL REVIEW B 95, 125206 (2017).

[217] Pingjun Ying, Xin Li, Yancheng Wang, Jiong Yang, Chenguang Fu, Wenqing Zhang, Xinbing Zhao, Tiejun Zhu, Hierarchical Chemical Bonds Contributing to the Intrinsically Low Thermal Conductivity in α-MgAgSb Thermoelectric Materials, Adv. Funct.Mater.2017, 27, 1604145.

[218] Michele D. Nielsen, Vidvuds Ozolins, Joseph P. Heremans, Lone pair electrons minimize lattice thermal conductivity,Energy Environ. Sci., 2013, 6, 570–578.

[219] D. T. Morelli, V. Jovovic, J. P. Heremans, Intrinsically Minimal Thermal Conductivity in Cubic I-V-VI2 Semiconductors, Physicl Review Letters, 2008,035901-1-4. DOI: 10.1103/PhysRevLett.101.035901.

[220] K. C. Lukas, W. S. Liu, G. Joshi, M. Zebarjadi, M. S. Dresselhaus, Z. F. Ren, G. Chen, C. P. Opeil, Experimental determination of the Lorenz number in Cu0.01Bi2Te2.7Se0.3 and Bi0.88Sb0.12, PHYSICAL REVIEW B 85, 205410 (2012).

[221] Anatolie Casian, Violation of the Wiedemann-Franz law in quasi-one-dimensional organic crystals, PHYSICAL REVIEW B 81, 155415 (2010).

[222] David J. Singh, Doping-dependent thermopower of PbTe from Boltzmann transport calculations, PHYSICAL REVIEW B 81, 195217 (2010).

[223] Michael W. Gaultois, Taylor D. Sparks, How much improvement in thermoelectric performance can come from reducing thermal conductivity?, APPLIED PHYSICS LETTERS 104, 113906 (2014).

[224] G. S. Kumar, G. PrasadR. O. Pohl, Experimental determinations of the Lorenz number, Journal of Materials Science, 28, 16 (1993), 4261–4272.

[225] G. D. Mahan and M. Bartkowiak, Wiedemann–Franz law at boundaries, Appl. Phys. Lett., 74, p. 953, 1999.

[226] Wang H., Pei Y., LaLonde A.D., Jeffery Snyder G. (2013) Material Design Considerations Based on Thermoelectric Quality Factor. In: Koumoto K., Mori T. (eds) Thermoelectric Nanomaterials. Springer Series in Materials Science, vol 182. Springer, Berlin, Heidelberg.

[227] Yanzhong Pei, Xiaoya Shi, Aaron LaLonde, Heng Wang, Lidong Chen, G. Jeffrey Snyder, Convergence of electronic bands for high performance bulk thermoelectrics, Nature, 473, (2011) 66–69.

[228] Ruiqiang Guo, Xinjiang Wang, Youdi Kuang, Baoling Huang, First-principles study of anisotropic thermoelectric transport properties of IV-VI semiconductor compounds SnSe and SnS, Phys. Rev. B 92, 115202, 2015.

[229] Li-Dong Zhao, Shih-Han Lo, Yongsheng Zhang, Hui Sun, Gangjian Tan, Ctirad Uher, C. Wolverton, Vinayak P. Dravid, Mercouri G. Kanatzidis, Ultralow thermal conductivity and high thermoelectric figure of merit in SnSe crystals, Nature, 508, (2014) 373–377.

[230] Li-Dong Zhao, Gangjian Tan, Shiqiang Hao, Jiaqing He, Yanling Pei, Hang Chi, Heng Wang, Shengkai Gong, Huibin Xu, Vinayak P. Dravid, Ctirad Uher, G. Jeffrey Snyder, Chris Wolverton, Mercouri G. Kanatzidis, Ultrahigh power factor and thermoelectric performance in hole-doped single-crystal SnSe, Science 08 Jan 2016:Vol. 351, Issue 6269, pp. 141-144, DOI: 10.1126/science.aad3749.

[231] N. Hsieh, M. E. Fine, The Lorenz ratio and electron transport properties of NbO, J. Appl. Phys. 52, 2876 (1981), https://doi.org/10.1063/1.329021.

[232] Hyun-Sik Kim , Zachary M. Gibbs, Yinglu Tang, Heng Wang, G. Jeffrey Snyder, Characterization of Lorenz number with Seebeck coefficient measurement, APL MATERIALS 3, 041506 (2015).

[233] G. K. White, S. B. Woods, The thermal and electrical resistivity of bismuth and antimony at low temperatures, Philos. Mag. 3, 342 (1958) 342-359.

[234] D. Armitage, H. J. Goldsmid, The thermal conductivity of cadmium arsenide, J. Phys. C 2,11, (1969) 2138-2145.

[235] C. Uher, H. J. Goldsmid, Separation of the Electronic and Lattice Thermal Conductivities in Bismuth Crystals, Phys. Status Solidi B 65, 765 (1974) 765-772.

[236] J. W. Sharp, E. H. Volckmann, H. J. Goldsmid, The Thermal Conductivity of Polycrystalline Bi88Sb12, Phys. Status Solidi A 185, 2 (2001) 257 -265.

[237] Daniel Kraemer, Bed Poudel, Hsien-Ping Feng, J. Christopher Caylor, Bo Yu, Xiao Yan , Yi Ma, Xiaowei Wang, Dezhi Wang, Andrew Muto, Kenneth McEnaney, Matteo Chiesa, Zhifeng Ren, Gang Chen, High-performance flat-panel solar thermoelectric generators with high thermal concentration, NATURE MATERIALS, VOL 10,JULY 2011.

[238] A.K. Geim, K.S. Novoselov, The rise of graphene, Nat. Mater. 6 (2007) 183–191.

[239] Francesco Devillanova, W.-W. D. M., Handbook of Chalcogen Chemistry: New Perspectives in Sulfur, Selenium and Tellurium. 2013; Vol. 2.

[240] Poon, J.-f.; Singh, V. P.; Yan, J.; Engman, L., Regenerable Antioxidants—Introduction of Chalcogen Substituents into Tocopherols. Chemistry – A European Journal 2015, 21 (6), 2447-2457.

[241] G. Joseph Poon, "Chapter 2 Electronic and thermoelectric properties of Half-Heusler alloys," in Semiconductors and Semimetals. vol. 70, ed: Elsevier 2001, pp. 37-75.

[242] Anke Weidenkaff Wenjie Xie, Xinfeng Tang, Qingjie Zhang , Joseph Poon, Terry M. Tritts,Recent Advances in Nanostructured Thermoelectric Half-Heusler Compounds,Nanomaterials,2 (2012) 379-412.

[243] Corey Oses Stefano Sanvito, Junkai Xue,Anurag Tiwari, Mario Zic, Thomas Archer,Pelin Tozman, Munuswamy Venkatesan, Michael Coey, Stefano Curtarolos,Accelerated discovery of new magnets in the Heusler alloy family,Sci. Adv.,3 (2017) 1-9.

[244] R. Ghomashchi R. Ahamed, Z. Xie, L. Chen, P. Munroe, S. Xus,Powder processing and characterisation of a quinary Ni-Mn-Co-Sn-Cu Heusler alloy,Powder Technology,324 (2018) 69–75.

[245] Riaz Ahamed Ahamed Khan, Reza Ghomashchi, Zonghan Xie , Lei Chen, Ferromagnetic Shape Memory Heusler Materials: Synthesis, Microstructure Characterization and Magnetostructural Properties,Materials,11 (2018) 1-34.

[246] S.Ramasubramanian R.Mohankumar, M.Rajagopalan, M.Manivel Raja, S.V.Kamat, J.Kumars,Effect of Fe substitution on the electronic structure, magnetic and thermoelectric properties of Co2FeSi full Heusler alloy: A first principle study,Computational Materials Science,109 (2015) 34-40.

[247] Janusz Tobola, Jacques Pierre, Electronic phase diagram of the XTZ (X5Fe, Co, Ni; T5Ti, V, Zr, Nb,q Mn; Z5Sn, Sb) semi-Heusler compounds, Journal of Alloys and Compounds 296 (2000) 243–252.

[248] Matthias Schrade, Kristian Berland, Simen N. H. Eliassen, Matylda N. Guzik, Cristina Echevarria-Bonet, Magnus H. Sørby, Petra Jenuš, Bjørn C. Hauback, Raluca Tofan, Anette E. Gunnæs, Clas Persson, Ole M. Løvvik, Terje G. Finstad, The role of grain boundary scattering in reducing the thermal conductivity of polycrystalline XNiSn (X = Hf, Zr, Ti) half-Heusler alloys, SCIENTIFIC REPORTS, 7: 13760 , DOI:10.1038/s41598-017-14013-8,2017.

[249] Ki Sung Kim, Young-Min Kim, Hyeona Mun, Jisoo Kim, Jucheol Park, Albina Y. Borisevich, Kyu Hyoung Lee Sung Wng Kim, Direct Observation of Inherent Atomic-Scale Defect Disorders responsible for High-Performance Ti1-xHfxNiSn1-ySby Half-Heusler Thermoelectric Alloys, Adv. Mater. 2017, 29, 1702091, 1-11. DOI: 0.1002/adma.201702091.

[250] Dipendra Jha, Vishu Gupta, Logan Ward, Zijiang Yang, Christopher Wolverton, Ian Foster, Wei-keng Liao, Alok Choudhary, Ankit Agrawal, Enabling deeper learning on big data for materials informatics applications, Scientific Reports, (2021), 11:4244 | https://doi.org/10.1038/s41598-021-83193-1.

[251] Hangtian Zhu, Jun Mao, Yuwei Li, Jifeng Sun, Yumei Wang, Qing Zhu, Guannan Li, Qichen Song, Jiawei Zhou, Yuhao Fu, Ran He, Tian Tong, Zihang Liu, Wuyang Ren, Li You, Zhiming Wang, Jun Luo, Andrei Sotnikov, Jiming Bao, Kornelius Nielsch, Gang Chen, David J. Singh, Zhifeng Ren, Discovery of TaFeSb-based half-Heuslers with high thermoelectric performance,Nature Communications, (2019) 10:270.

[252] Alexander Page, P.F.P. Poudeu, Ctirad Uher, A first-principles approach to half-Heusler thermoelectrics: Accelerated prediction and understanding of material properties, J Materiomics 2 (2016) 104-113.

[253] L. Li A. J. Hong, R. He, J. J. Gong, Z. B. Yan, K. F. Wang, J. -M. Liu, Z. F. Rens,Full-scale computation for all the thermoelectric property parameters of half-Heusler compounds,Scientific Reports, Nature,6 (2016) 1-12.

[254] Yongwoo Shin Anubhav Jain, Kristin A. Perssons,Computational predictions of energy materials using density functional theory,NATURE REVIEWS | MATERIALS,1 (2016) 1-13.

[255] A. K. Geim K. S. Novoselov, S. V. Morozov, D. Jiang, Y. Zhang, S. V. Dubonos, I. V. Grigorieva, A. A. Firsovs,Electric Field Effect in Atomically Thin Carbon Films,SCIENCE,306 (2004) 666-669.

[256] Andre K. Geims,Nobel Lecture: Random walk to graphene,REVIEWS OF MODERN PHYSICS,83 (2011) 851-862.

[257] Zhen Zhen Yujia Zhong, Hongwei Zhu s,Graphene: Fundamental research and potential applications,FlatChem,4 (2017) 20-32.

[258] Yujia Zhong, Zhen Zhen, Hongwei Zhu, Graphene: Fundamental research and potential applications, FlatChem 4 (2017) 20-32.

[259] Jing Guo Yijian Ouyangs,A theoretical study on thermoelectric properties of graphene nanoribbons,Appl. Phys. Lett.,94 (2009) 1-3.

[260] Genene T. Mola Tabitha A. Amollo, M. S. K. Kirui, Vincent O. Nyamoris,Graphene for Thermoelectric Applications: Prospects and Challenges,Critical Reviews in Solid State and Materials Sciences,43 133-157.

[261] Duc Hau Huynh Md Sharafat Hossain, Liming Jiang, Sharmin Rahman,Phuong Duc Nguyen, Feras Al-Dirini, Faruque Hossain, Je-Hyeong Bahke, Efstratios Skafidasa,s,Investigating enhanced thermoelectric performance of graphene-based nano-structures,Nanoscale,10 (2018,) 4786–4792.

[262] Duc Hau Huynh Md Sharafat Hossain, Phuong Duc Nguyen, Liming Jiang, Thanh Cong Nguyen, Feras Al-Dirini, Faruque M. Hossain, Efstratios Skafidass,Enhanced thermoelectric performance of graphene nanoribbon-based devices,JOURNAL OF APPLIED PHYSICS,119 (2016) 1-7.

[263] CongXu Haiping Zhang, WenlongXiao, KeiAmeyama, ChaoliMas,Enhanced mechanical properties of Al5083 alloy with graphene nanoplates prepared by ballmilling and hot extrusion,Materials Science & Engineering A,658 (2016) 8-15.

[264] Ryan A. Shaffer Thomas E. Beechem, John Nogan, Taisuke Ohta, Allister B. Hamilton, Anthony E. McDonald, Stephen W. Howells,Self-Heating and Failure in Scalable Graphene Devices,Scientific Reports, Nature,6 (2016) 1-8.

[265] Smita Mohanty Ruchi Aradhana, Sanjay Kumar Nayaks,Comparison of mechanical, electrical and thermal properties in graphene oxide and reduced graphene oxide filled epoxy nanocomposite adhesives,Polymer,141 (2018) 109-123.

[266] Jae Hong Kim Keon-Woo Kim, Sunghun Cho, Kwonwoo Shin, Se Hyun Kims,Scalable high-performance graphene paper with enhanced electrical and mechanical properties,Thin Solid Films,632 (2017) 50-54.

[267] F.schwierz, Graphene transistors, nature nanotechnology, VOL 5, JULY 2010. ,

[268] Y.W.Son, M.L. Cohen, S.G. Louie, Half-metallic graphene nanoribbons, nature letters, Vol 444,16 November 2006, doi:10.1038/nature05180..

[269] F. Bonaccorso, Z. Sun, T. Hasan and A. C. Ferrari, Graphene photonics and optoelectronics, NATURE PHOTONICS, VOL 4, SEPTEMBER 2010.

[270] O.V. Yazyev, S.G. Louie, Electronic transport in polycrystalline graphene, NATURE MATERIALS , VOL 9, OCTOBER 2010.

[271] K.Kostarelos, K.S. Novoselov, Graphene devices for life, NATURE NANOTECHNOLOGY ,VOL 9 , OCTOBER 2014.

[272] S. Syama, P. V. Mohanan, Comprehensive Application of Graphene: Emphasis on Biomedical Concerns, Nano-Micro Lett. (2019) 11:6.

[273] C.J. Bullock, C.Bussy, Biocompatibility Considerations in the Design of Graphene Biomedical Materials, Adv. Mater. Interfaces 2019, 1900229.

[274] M.J.Nine, D.N.H.Tran, A.El Mekawy, D.Losic, Interlayer growth of borates for highly adhesive graphene coatings with enhanced abrasion resistance, fire-retardant and antibacterial ability, Carbon Volume 117, June 2017, Pages 252-262.

[275] M.J.Nine, S.Kabiri,T.T.T.Diana, N.H.Tran, D.Losic, Electrostatic powder coatings of pristine graphene: A new approach for coating of granular and fibril substrates, Applied Surface Science Volume 441, 31 May 2018, Pages 187-193.

[276] M. J. Nine,M. A. Cole, D. N. H. Tran, D. Losic, Graphene: a multipurpose material for protective coatings, Journal of Materials Chemistry A , Issue 24, 2015.

[277] A. Rahimi, M.A.Zanjanchi, S.Bakhtiari, M, Dehsaraei, Selective determination of caffeine in foods with 3D-graphene based ultrasound-assisted magnetic solid phase extraction, Food Chemistry Volume 262, 1 October 2018, Pages 206-214.

[278] M.Wang, Mi.Cui, M.Zhao, H.Cao, Sensitive determination of Amaranth in foods using graphene nanomeshes , Journal of Electroanalytical Chemistry Volume 809, 15 January 2018, Pages 117-124.

[279] Y.Xie, Y.Li, L.Niu, H.Wang, H.Qian, W.Yao, A novel surface-enhanced Raman scattering sensor to detect prohibited colorants in food by graphene/silver nanocomposite , Talanta, Volume 100, 15 October 2012, Pages 32-37.

[280] ACS Appl. Mater. Interfaces 2016, 8, 15, 9994-10004.

[281] Jianxiao Si Shidan Yang, Qingmei Su, Haifei Wus,Enhanced thermoelectric performance of SnSe doped with layered MoS2/graphene,Materials Letters,193 (2017) 146–149.

[282] Eun Sil Lee Jin Il Kim, Jong-Young Kim, Soon-Mok Choi, Kyu Hyoung Lee, Won-Seon Seos,Thermoelectric properties.of unoxidized graphene/Bi2Te2.7Se0.3 composites synthesized by exfoliation/re-assembly method,P hys. Status Solidi RRL,8 (2014) 357–361.

[283] Kyunghan Ahn Weon Ho Shin, Mahn Jeong, Jeong Seop Yoon, Jae Min Song,Soonil Lee, Won Seon Seo, Young Soo Lims,Enhanced thermoelectric performance of reduced graphene oxide incorporated bismuth-antimony-telluride by lattice thermal conductivity reduction,Journal of Alloys and Compounds,718 (2017) 342-348.

[284] Simrjit Singh Sunil Kumar, Punit Kumar Dhawan, R R Yadav, Neeraj Khares,Effect of graphene nanofillers on the enhanced thermoelectric properties of Bi2Te3 nanosheets: elucidating the role of interface in de-coupling the electrical and thermal characteristics,Nanotechnology,29 (2018) 1-9.

[285] Karim Kakaei, Mehdi D. Esrafili, Ali Ehsani, Chapter 2 - Atomic Properties and Electronic Structure, Interface Science and Technology, Volume 27, 2019, Pages 23-66.

[286] Johan Nilsson, A. H. Castro Neto, F. Guinea, N. M. R. Peres, Electronic Properties of Graphene Multilayers, PHYSICAL REVIEW LETTERS, 97, 266801 (2006).

[287] Tabitha A. Amollo, Genene T. Mola, M. S. K. Kirui, Vincent O. Nyamori, Stacking order dependent electric field tuning of the band gap in graphene multilayers, Physical Review B 81, 115432 (2010).

[288] Cao Wu, Jia Li, Yuchi Fan, Juanjuan Xing, Hui Gu, Zhenxing Zhou,Xiaofang Lu, Qihao Zhang, Lianjun Wang, Wan Jiang, The effect of reduced graphene oxide on microstructure and thermoelectric properties of Nb-doped A-site-deficient SrTiO3 ceramics, Journal of Alloys and Compounds 786 (2019) 884-893.

[289] Dongsheng Chen, Yan Zhao, Yani Chen, Biao Wang, Haiyan Chen, Jun Zhou, Ziqi Liang, One-Step Chemical Synthesis of ZnO/Graphene Oxide Molecular Hybrids for High-Temperature Thermoelectric Applications, ACS Appl. Mater. Interfaces 2015, 7, 3224−3230.

[290] Yen-Hao Lin, Tsung-Chi Lee, Yu-Sheng Hsiao, Wei-Keng Lin, Wha-Tzong Whang, Chun-Hua Chen, Facile Synthesis of Diamino-Modified Graphene/Polyaniline Semi-Interpenetrating Networks with Practical High Thermoelectric Performance, ACS Appl. Mater. Interfaces 2018, 10, 4946−4952.

[291] Bin Feng, Jian Xie, Gaoshao Cao, Tiejun Zhua, Xinbing Zhao, Enhanced thermoelectric properties of p-type CoSb3/graphene nanocomposite, J. Mater. Chem. A, 2013, 1, 13111–13119.

[292] Ashutosh Kumar , Karuna Kumari, S. J. Ray, Ajay D. Thakur, Graphene mediated resistive switching and thermoelectric behavior in lanthanum cobaltate, J. Appl. Phys. 127, 235103 (2020); https://doi.org/10.1063/5.0009666.

[293] Joseph P. Heremans, Christopher M. Thrush, Donald T. Morelli, Thermopower enhancement in PbTe with Pb precipitates, J. Appl. Phys. 98, 063703 (2005); https://doi.org/10.1063/1.2037209.

[294] Yuanyue Li, Yunchen Dou, Xiaoying Qin, Jian Zhang, Hongxing Xin, Di Li,Chunjun Song, Tianhua Zou, Yongfei Liu, Cong Li, Enhanced thermoelectric figure of merit in p-type b-Zn4Sb3/Bi0.4Sb1.6Te3 nanocomposites, RSC Adv., 2016, 6, 12243-12248.

[295] V.I. Kaydanov, T.J. Coutts, D.L. Young, Studies of Band Structure and Free-Carrier Scattering in Transparent Conducting Oxides Based on Combined Measurements of Electron Transport Phenomena, Presented at the Material Research Society Workshop, Denver, Colorado, June 19–20, 2000.

[296] Szu-Ying Wang Anna K. Hailey , Yuanzhen Chen , Marcia M. Payne , John E.Anthony , Vitaly Podzorov, Yueh-Lin Loo, Quantifying the Energy Barriers and Elucidating the Charge Transport Mechanisms across Interspherulite Boundaries in Solution-Processed Organic Semiconductor Thin Films, Adv. Funct. Mater. 2015, 25, 5662–5668s.

[297] Kanan Puntambekar, Jinping Dong, Greg Haugstad, C. Daniel Frisbie, Structural and Electrostatic Complexity at a Pentacene/Insulator Interface, Adv. Funct. Mater. 2006, 16, 879–884.

[298] lS.Yogev, R.Matsubara, M.Nakamura, Y.Rosenwaks, Local charge accumulation and trapping in grain boundaries of pentacene thin film transistors, Organic Electronics Volume 11, Issue 11, November 2010, Pages 1729-1735.

[299] I. Vladimirov, M. Kühn, T. Geßner, F. May , R. T. Weitz, Energy barriers at grain boundaries dominate charge carrier transport in an electron-conductive organic semiconductor, Scientific Reports, 8, Article number: 14868 (2018).

[300] Guangjun Nan, Zesheng Li, Modeling of charge transport in polycrystalline sexithiophene from quantum charge transfer rate theory beyond the first-order perturbation, Organic Electronics, Volume 12, Issue 12, December 2011, Pages 2198-2206.

[301] Florian Steiner, Carl Poelking, Dorota Niedzialek, Denis Andrienko, Jenny Nelson, Influence of orientation mismatch on charge transport across grain boundaries in tri-isopropylsilylethynyl (TIPS) pentacene thin films, Phys. Chem. Chem. Phys., 2017,19, 10854-10862.

[302] R. A. Street, D. Knipp, A. R. Völkel, Hole transport in polycrystalline pentacene transistors, Appl. Phys. Lett. 80, 1658 (2002); https://doi.org/10.1063/1.1456549.

[303] Chuan Qian, Jia Sun, Lei Zhang, Han Huang, Junliang Yang, Yongli Gao, Crystal-Domain Orientation and Boundary in Highly Ordered Organic Semiconductor Thin Film, J. Phys. Chem. C 2015, 119, 27, 14965–14971.

[304] L. G. Kaake, P. F. Barbara, X.-Y. Zhu, Intrinsic Charge Trapping in Organic and Polymeric Semiconductors: A Physical Chemistry Perspective, J. Phys. Chem. Lett. 2010, 1, 3, 628–635.

[305] Robert Baier,Caspar Leendertz, DanielAbou-Ras, Martha Ch.Lux-Steiner, Sascha Sadewasser, Properties of electronic potential barriers at grain boundaries in Cu(In,Ga)Se2 thin films, Solar Energy Materials and Solar Cells Volume 130, November 2014, Pages 124-131.

[306] Sadeq Hooshmand Zaferani, Reza Ghomashchi, Daryoosh Vashaee, An Assessment of Thermoelectric, Mechanical and Microstructural Reinforcement Properties of Graphene-mixed Heterostructures, ACS Applied Energy Materials, https://dx.doi.org/10.1021/acsaem.1c00015.

[307] Xiaoying Qin Cong Li, Yuanyue Li, Di Li, Jian Zhang, Haifeng Guo, Hongxing Xin, Chunjun Songs,Simultaneous increase in conductivity and phonon scattering in a graphene nanosheets/(Bi2Te3)0.2(Sb2Te3)0.8 thermoelectric nanocomposite,Journal of Alloys and Compounds,661 (2016) 389e395.

[308] Guillaume Colas Yiyi Wang, Tobin Filleters,Improvements in the mechanical properties of carbon nanotube fibers through graphene oxide interlocking,Carbon,98 (2016).

[309] Chien-Neng Liao Sin-Shien Lins,Effect of ball milling and post treatment on crystal defects and transport properties of Bi2(Se,Te)3 compounds,J. Appl. Phys.,110 (2011) 1-7.

[310] Chien-Neng Liao Meng-Pei Lus,Mechanical and thermal processing effects on crystal defects and thermoelectric transport properties of Bi2(Se,Te)3 compounds,Journal of Alloys and Compounds,571 (2013) 178–182.

[311] Wei Li Yecheng Zhou, Minghui Wu, Li-Dong Zhao, Jiaqing He, Su-Huai Wei, Li Huangs,Influence of defects on the thermoelectricity in SnSe: A comprehensive theoretical study,Physical review,97 (2018) 1-8.

[312] Xinghua Shi Zahra Zamanipour, Arash M. Dehkordi, Jerzy S. Krasinski, Daryoosh Vashaees,The effect of synthesis parameters on transport properties of nanostructured bulk thermoelectric p-type silicon germanium alloy,Physica Status Solidi (a),209 (2012) 2049-2058.

[313] Mildred S. Dresselhaus, Gang Chen, Zhifeng Ren, Jean-Pierre Fleurial, Pawan Gogna, Ming Y. Tang, Daryoosh Vashaee, Hohyun Lee, Xiaowei Wang, Giri Joshi, Gaohua Zhu, De-zhi Wang, Richard G. Blair, Sabah K. Bux, Richard B Kaner less, Nanocomposites To Enhance ZT in Thermoelectrics.Mater. Res. Soc. Symp. Proc. Vol. 1044, 2008 Materials Research Society, doi:10.1557/PROC-1044-U02-04.

[314] Milad Mohebali, Yin Liu, Lobat Tayebi, Jerzy S. Krasinski, Daryoosh Vashaee, Thermoelectric Figure of Merit of Bulk FeSi2-Si0.8Ge0.2 Nanocomposite and a Comparison with β-FeSi2, Renewable Energy, Volume 74, February 2015, Pages 940–947.

[315] J. Horak, K. Cermak, L. Koudelka, J. Phys. Chem. Solids 47 (1986) 805.

[316] Vishakha Kaushik Khushboo Agarwal, Deepak Varandani, Ajay Dhar, B.R. Mehtas,Nanoscale thermoelectric properties of Bi2Te3 – Graphene nanocomposites: Conducting atomic force, scanning thermal and kelvin probe microscopy studies,Journal of Alloys and Compounds,(2016).

[317] Ferry, D.K., Semiconductor transport. 2000, London: Taylor & Francis.

[318] Meng Li, David L.Cortie, Jixing Liu,Dehong Yu, Sheik Md. Kazi NazrulIslam, LanlingZhao, David R.G.Mitchell, Richard A.Mole, Michael B.Cortie, Shixue Dou, Xiaolin Wang, Ultra-high thermoelectric performance in graphene incorporated Cu2Se: Role of mismatching phonon modes, Nano Energy Volume 53, November 2018, Pages 993-1002.

[319] D. Zhao, X. Wang, D.Wu, Enhanced Thermoelectric Properties of Graphene/Cu2SnSe3 Composites, Crystals 2017, 7, 71; doi:10.3390/cryst7030071.

[320] Guodong Li, Qi An, Bo Duan, Leah Borgsmiller, Muath Al Malki, Matthias Agne, Umut Aydemir, Pengcheng Zhai, Qingjie Zhang, Sergey I. Morozov, William A. Goddard III, G. Jeffrey Snyder, Fracture toughness of thermoelectric materials, Materials Science & Engineering R 144 (2021) 100607.

[321] Jayanta Mondal Hansang Kwon, Khaled A. AlOgab, V€aino Sammelselg, Miyazaki Takamichi, Akira Kawaski, Marc Leparouxs,Graphene oxide-reinforced aluminum alloy matrix composite materials fabricated by powder metallurgy,Journal of Alloys and Compounds,698 (2017) 807-813.

[322] Alok Bhadauria, Lavish K. Singh, Tapas Laha,Effect of physio-chemically functionalized graphene nanoplatelet reinforcement on tensile properties of aluminum nanocomposite synthesized via spark plasma sintering, Journal of Alloys and Compounds, 748 (2018) 783-793.

[323] Fusheng Pan Muhammad Rashad, Jianyue Zhang, Muhammad Asifs,Use of high energy ball milling to study the role of graphene nanoplatelets and carbon nanotubes reinforced magnesium alloy,Journal of Alloys and Compounds,646 (2015) 223-232.

[324] D.H. Bae S.E. Shins,Deformation behavior of aluminum alloy matrix composites reinforced with few-layer graphene,Composites: Part A,78 (2015) 42-47.

[325] Xiao Hu, Y.C. Chan, Kaili Zhang, K.C. Yung, Effect of graphene doping on microstructural and mechanical properties of Sn–8Zn–3Bi solder joints together with electromigration analysis,Journal of Alloys and Compounds, 580 (2013) 162-171.

[326] Ashutosh Sharma, Heung-Rak Sohn, Jae Pil Jung, Effect of Graphene Nanoplatelets on Wetting, Microstructure, and Tensile Characteristics of Sn-3.0Ag-0.5Cu (SAC) Alloy, Metallurgical and materials transactions A, 47, (2016) 494–503. ,(2016).

[327] Fusheng Pan Muhammad Rashad, Muhammad Asifs,Exploring mechanical behavior of Mg–6Zn alloy reinforced with graphene nanoplatelets,Materials Science & Engineering A,649 (2016) 263-269.

[328] Z.Y. Liu Z.W. Zhang, B.L. Xiao, D.R. Ni, Z.Y. Mas,High efficiency dispersal and strengthening of graphene reinforced aluminum alloy composites fabricated by powder metallurgy combined with friction stir processing,Carbon,135 (2018) 215-223.

[329] Qiu-hong Yuan, Zhi-qiang Qiu, Guo-hua Zhou, Xiao-shu Zeng, Lan Luo, Xi-Xin Rao, Yan Ding, Yong Liu, Interfacial design and strengthening mechanisms of AZ91 alloy reinforced with in-situ reduced graphene oxide,Materials Characterization,138 (2018) 215-228.

[330] Guo-hua Zhou Qiu-hong Yuan, Lin Liao, Yong Liu, Lan Luos,Interfacial structure in AZ91 alloy composites reinforced by graphene nanosheets,Carbon,127 (2018) 177-186.

[331] S.L.Dai S.J. Yan, X.Y.Zhang, C.Yang, Q.H.Hong, J.Z.Chen a, Z.M.Lins,Investigating aluminum alloy reinforced by graphene nanoflakes,Materials Science & Engineering A,612 (2014) 440-444.

[332] D. Bolaños-Morales R. Pérez-Bustamante, J. Bonilla-Martínez, I. Estrada-Guel, R. Martínez-Sánchezs,Microstructural and hardness behavior of graphene-nanoplatelets/aluminum composites synthesized by mechanical alloying,Journal of Alloys and Compounds,615 (2014) S578-S582.

[333] Muhammad Rashad, Fusheng Pan, Muhammad Asif, Aitao Tang, Powder metallurgy of Mg–1%Al–1%Sn alloy reinforced with low content of graphene nanoplatelets (GNPs), Journal of Industrial and Engineering Chemistry, 20 (2014), 4250-4255.

[334] Ashis Mallick Pravir Kumar, Milli Suchita Kujur, Khin Sandar Tun, Rajashekhara Shabadi, Manoj Guptas,Strength of Mg–3%Al alloy in presence of graphene nano-platelets as reinforcement,MATERIALS SCIENCE AND TECHNOLOGY,(2018) 1-10.

[335] Hongyan Yue, Longhui Yao, Xin Gao, Shaolin Zhang, Erjun Guo, Hong Zhang, Xuanyu Lin, Bao Wang,Effect of ball-milling and graphene contents on the mechanical properties and fracture mechanisms of graphene nanosheets reinforced copper matrix composites,Journal of Alloys and Compounds,691 (2017), 775-762.

[336] A. S. Taha, F. H. Hammad, Application of the Hall-Petch Relation to Microhardness Measurements on Al, Cu, Al-MD 105, and Al-Cu Alloys, phys. stat. sol. (a) 119, 455 (1990).

[337] Jun SHEN Tao ZHANG, Lu-qiang LÜ, Chun-min WANG, Jia-xin SANG, Dong WUs,Effects of graphene nanoplates on microstructures and mechanical properties of NSA-TIG welded AZ31 magnesium alloy joints,Trans. Nonferrous Met. Soc. China,27 (2017) 1285-1293.

[338] Lei Zhang Xinyu Liu, Yi Xus,Microstructure and mechanical properties of graphene reinforced Fe50Mn30Co10Cr10 high-entropy alloy composites synthesized by MA and SPS,Appl. Phys. A,567 (2017) 1-7.

[339] D. M. Rowe, Thermoelectrics and Its Energy Harvesting, Modules, Systems, And Applications in Thermoelectrics , CRC PressTaylor & Francis Group, © 2012 by Taylor & Francis Group, LLC, ISBN:978-1-4665-6030-7. NEWYORK.

[340] Rafael A. Soler-Crespo Zhaoxu Meng, Wenjie Xia, Wei Gao, Luis Ruiz, Horacio D. Espinosa, Sinan Ketens,A coarse-grained model for the mechanical behavior of graphene oxide,Carbon,117 (2017) 476-487.

[341] P.R. Budarapu B. Javvaji, V.K. Sutrakar, D. Roy Mahapatra, M. Paggi, G. Zi , T. Rabczuks,Mechanical properties of Graphene: Molecular dynamics simulations correlated to continuum based scaling laws,Computational Materials Science,125 (2016) 319–327.

[342] Qiheng Tang Feng Liu, Tzu-Chiang Wangs,Intrinsic Notch Effect Leads to Breakdown of Griffith Criterion in Graphene,small,13 (2017) 1-8.

[343] H. Jerry Qi Hanqing Yin, Feifei Fan, Ting Zhu, Baolin Wang, Yujie Weis,Griffith Criterion for Brittle Fracture in Graphene,Nano Lett.,15 (2015) 1918−1924.

[344] Qing-Xiang Pei Jing-Yang Chung Viacheslav Sorkin, Cheng-Hsin Chiu, Yong-Wei Zhangs,Mechanical properties and failure behaviour of graphene/silicene/graphene heterostructures,J. Phys. D: Appl. Phys.,50 (2017).

[345] T.Caillat, M.Carle, P.Pierrat, H.Scherrer, S.Scherrer, Thermoelectric properties of (BixSb1−x)2Te3 single crystal solid solutions grown by the T.H.M. method, Journal of Physics and Chemistry of Solids Volume 53, Issue 8, August 1992, Pages 1121-1129.

[346] Huili Liu, Xun Shi, Fangfang Xu , Linlin Zhang , Wenqing Zhang, Lidong Chen, Qiang Li, Ctirad Uher, Tristan Day, G. Jeffrey Snyder, Copper ion liquid-like thermoelectrics, Nat Mater. 2012 Mar 11;11(5):422-425. doi: 10.1038/nmat3273.

[347] R. Watanabe, R. Yoshimi, M. Shirai, T. Tanigaki, M. Kawamura, A. Tsukazaki, K. S. Takahashi, R. Arita, M. Kawasaki, Y. Tokura, Emergence of interfacial conduction and ferromagnetism in MnTe/InP, Appl. Phys. Lett. 113, 181602 (2018); https://doi.org/10.1063/1.5050446.

[348] C. Ferrer-Roca, A. Segura, C. Reig, V. Munoz, Temperature and pressure dependence of the optical absorption in hexagonal MnTe, Phys. Rev.B 61, 13679 (2000).

[349] K. Walther, Ultrasonic relaxation at Neel temperature and nuclear acoustic resonance in MnTe, Solid State Commun. 5, 399 (1967).

[350] Wenjie Xie, Sascha Populoh, Krzysztof Gałązka, Xingxing Xiao, Leyre Sagarna, Yufei Liu, Matthias Trottmann, Jian He, Anke Weidenkaff, Thermoelectric study of crossroads material MnTe via sulfur doping, J. Appl. Phys. 115, 103707 (2014); https://doi.org/10.1063/1.4868584.

[351] Sai Mu, Raphaël P. Hermann, Stéphane Gorsse, Huaizhou Zhao, Michael E. Manley, Phonons, magnons, and lattice thermal transport in antiferromagnetic semiconductor MnTe, PHYSICAL REVIEW MATERIALS 3, 025403 (2019).

[352] Yangyang Ren, Junyou Yang, Qinghui Jiang, Dan Zhang, Zhiwei Zhou, Xin Li, Jiwu Xin, Xu He, Synergistic effect by Na doping and S substitution for high thermoelectric performance of p-type MnTe, J. Mater. Chem. C, 2017, 5, 5076-5082.

[353] M. Jouannea, W. Szuszkiewiczb, J.F. Morhangea, M.A. Kanehisa", J.M. Hartmannc, H. Mariettec, E. Dynowskab, G. Karczewskib, T. Wojtowiczb, J. Kossutb, J. Barnasd, Magnons in layered MnTe/CdTe structures, Journal of Crystal Growth 184/185 (1998) 947-951.

[354] L. Yang, Z. H. Wang, Z. D. Zhang, Electrical properties of NiAs-type MnTe films with preferred crystallographic plane of (110), J. Appl. Phys. 119, 045304 (2016); https://doi.org/10.1063/1.4940950.

[355] A. Jain*, S.P. Ong*, G. Hautier, W. Chen, W.D. Richards, S. Dacek, S. Cholia, D. Gunter, D. Skinner, G. Ceder, K.A. Persson (*=equal contributions) The Materials Project: A materials genome approach to accelerating materials innovation APL Materials, 2013, 1(1), 011002.,doi:10.1063/1.4812323.

[356] K. K. Kelley, The Specific Heats at Low Temperatures of Manganese, Manganous Selenide, and Manganous Telluride, J. Am. Chem. Soc. 61,1, (1939) 203-207.

[357] C. F. Squire, Antiferromagnetism in Some Manganous Compounds, Phys. Rev. 56, 922 (1939).

[358] J. W. Allen, G. Lucovsky, and J. C. Mikkelsen, Optical properties and electronic structure of crossroads material MnTe, Solid State Communications, Vol. 24, pp. 367—370, 1977.

[359] A.J. Panson, W.D. Johnston, A study of substituted MnTe, J. Inorg. Nucl. Chem., 1964. Vol., 26 pp. 705 to 710.

[360] Koji Ando, Kenichi Takahashi ', Takashi Okuda, Zinc-blende MnTe: magnetic properties, Journal of Magnetism and Magnetic Materials 104-107 (1992) 993-994.

[361] W. Szuszkiewicz, E. Dynowska, B. Witkowska, B. Hennion, Spin-wave measurements on hexagonal MnTe of NiAs -type structure by inelastic neutron scatteringPhys.Rev. B 73, 104403 (2006).

[362] R. W. Cochrane, M. Plischke, J. O. Strom-Olsen, Magnetion studies of (GeTe)1-x(MnTe)x seudobinary alloys, Physical Review B Vol 9, 7, (1974) 3013-3021.

[363] W. D. Johnston, D. E. Sestrich, The MnTe-GeTe phase diagram, J..Vnorg. Nucl. Chem., 1961 Vol. 19, pp. 229 to 236.

[364] T. Hamasaki, Magnetic properties of (Ge, Pb)1-xMnxTe, Solid State Communications,Vol. 32, PP. 1069-1073.

[365] R. Triboulet, G. Didier, Growth and characterization oF Cd1-xMnxTe and MnTe crystals; contribution to the CdTe-MnTe pseudo-binary phase diagram determination, Journal of Crystal Growth 52 (1981) 614-618.

[366] Gangjian Tan, Fengyuan Shi, Shiqiang Hao, Hang Chi, Trevor P. Bailey, Li-Dong Zhao,Ctirad Uher, Chris Wolverton,Vinayak P. Dravid, Mercouri G. Kanatzidis, Valence Band Modification and High Thermoelectric Performance in SnTe Heavily Alloyed with MnTe, J. Am. Chem. Soc. 2015, 137, 11507−11516.

[367] T. M. Giebultowicz, P. KIosowski, N. Samarth, H. Luo, J. K. Furdyna, Neutron-diffraction studies of zinc-blende MnTe epitaxial films and MnTe/ZnTe superlattices: The effect of strain and dilution on a strongly frustrated fcc antiferromagnet, Physical review B, volume 48, number 17 1 november 1993-i, 12817-12833.

[368] Y. Magnin, T. Diep, Monte Carlo study of magnetic resistivity in semiconducting MnTe, Phys. Rev. B 85, 184413 (2012).

[369] Abdul Basit , Junyou Yang, Qinghui Jiang, Jiwu Xin , Xin Li , Sihui Li , Suwei Li, Qiang Long, Simultaneous regulation of electrical and thermal transport properties in MnTe chalcogenides via the incorporation of p-type Sb2Te3, J. Mater. Chem. A, 2018, 6,23473.,

[370] A. Gaj, W. Grieshaber, C. Bodin-Deshayes, Cibert, Magneto-optical study of interface mixing in the CdTe-(Cd, Mn)Te system, Physical review B volume 50, number 8 15 august 1994.

[371] M. Bouroushian, Electrochemistry of Metal Chalcogenides, Springer Science&Business Media, Heidelberg (2010).

[372] Shaohua Zhang,PhD thesis,Transition metal chalcogenides based molecular probes in biomedical applications, University of Wollongong, 2017.

[373] Shafai, C.; Brett, M. J. Optimization of Bi2Te3 thin films for microintegrated Peltier heat pumps. J. Vac. Sci. Technol. A., 1997,15,2798-2801.

[374] Scoville, A. N.; Bajgar, C.; Vandersande, J.; Fleurial, J. High figure-of-merit n-type SiGe/GaP alloys, IECEC '91; Proceedings of the 26th Intersociety Energy Conversion Engineering Conference, Boston, MA, USA, Aug. 4-9, 1991. Vol. 3 (A92-50672 21-44). La Grange Park, IL, American Nuclear Society, 1991, p. 224-229.

[375] A.M. Tishin, Y.I. Spichkin, Recent progress in magnetocaloric effect: Mechanisms and potential applications, International Journal of Refrigeration, 37, (2014)223 -229.

[376] Shuying Cheng Qiao Zheng, Hongjie Jia, Hong Zhang, Si Liu, Yunfeng Lai, Jinling Yu, Haifang Zhous,Flexible polymer solar cells based on Ag metallic grids and functional reduced graphene oxide composite electrode,J. Phys. D: Appl. Phys.,50 (2017) 1-6.

[377] Abhay Kumar Singhs,SeZnSb alloy and its nano tubes, graphene composites properties,AIP ADVANCES,3 (2013) 1-11.

[378] Sadeq Hooshmand Zaferani, Alireza Darebaghi, Soon-Jik Hong, Daryoosh Vashaee, Reza Ghomashchi, Experimental Realization of Heavily p-doped Half-Heusler CoVSn Compound, Energies 2020, 13, 1459; doi:10.3390/en13061459, 1-11.

[379] Hermann,R. P. ; Jin,R. ; Schweika,W.; Grandjean,F.; Mandrus, D.; Sales,B. C.; Long, G. J. Einstein oscillators in thallium filled antimony skutterudites, Phys. Rev. Lett.,2003, 90,1-4.,

[380] Ran He Lihong Huang, Shuo Chen , Hao Zhang , Keshab Dahal , Haiqing Zhou , Hui Wang , Qinyong Zhang, Zhifeng Rens,A new n-type half-Heusler thermoelectric material NbCoSb,Materials Research Bulletin,70 (2015) 773-778.

[381] Chude Feng Min Zhou, Lidong Chen, Xiangyang Huangs,Effects of partial substitution of Co by Ni on the high-temperature thermoelectric properties of TiCoSb-based half-Heusler compounds,Journal of Alloys and Compounds,391 (2005) 194-197.

[382] Bentien, A. ; Christensen, M.; Bryan, J. D.; Sanchez, A.; Paschen, S.; Steglich, F.; Stucky, G. D. ; Iversen, B. B. Thermal conductivity of thermoelectric clathrates, Phys. Rev. B,2004,69,1-5.

[383] N. Shutoh S. Sakuradas,Effect of Ti substitution on the thermoelectric properties of (Zr,Hf)NiSn half-Heusler compounds,Applied physics letters,86 (2005).

[384] A. Rajput D. K. Misra, A. Bhardwaj, N. S. Chauhan, Sanjay Singhs,Enhanced power factor and reduced thermal conductivity of a half-Heusler derivative Ti9Ni7Sn8: A bulk nanocomposite thermoelectric material,Applied physics letters,106 (2015) 1-5.

[385] Anand,S.; Wood,M.; Wolverton,C.; Snyder, G. J., An Enormous Class of Double Half-Heusler Compounds with Low Thermal Conductivity, 2019, arXiv:1901.09800 cond-mat.mtrl-sci.

[386] Yumei Wang Hao Zhang, Lihong Huang, Shuo Chen, Heshab Dahal,Dezhi Wang, Zhifeng Rens,Synthesis and thermoelectric properties of n-type half-Heusler compound VCoSb with valence electron count of 19,Journal of Alloys and Compounds,654 (2016) 321-326.

[387] Tetsuya Kobayashi Shigeru Katsuyamas,Effect of mechanical milling on thermoelectric properties of half-Heusler ZrNiSn0.98Sb0.02 intermetallic compound,Materials Science and Engineering: B,166 (2010) 99-103.

[388] K. Xiao T. J. Zhu, C. Yu, J. J. Shen, S. H. Yang, A. J. Zhou, X. B. Zhao, J. He s,Effects of yttrium doping on the thermoelectric properties of Hf0.6Zr0.4NiSn0.98Sb0.02 half-Heusler alloys,JOURNAL OF APPLIED PHYSICS,108 (2010).

[389] Xiao Yan Giri Joshi, Hengzhi Wang, Weishu Liu, Gang Chen, Zhifeng Rens,Enhancement in Thermoelectric Figure-Of-Merit of an N-Type Half-Heusler Compound by the Nanocomposite Approach,Adv. Energy Mater,1 (2011) 643-647.

[390] Masato Matsubara Hirofumi Hazama, Ryoji Asahis,Thermoelectric Properties of Off-Stoichiometric Ti-Ni-Sn Half-Heusler Systems,Journal of ELECTRONIC MATERIALS,41 (2012) 1730-1734.

[391] Qinyong Zhang Lihong Huang, Yumei Wang, Ran He, Jing Shuai, Jianjun Zhang, Chao Wang, Zhifeng Rens,The effect of Sn doping on thermoelectric performance of n-type half-Heusler NbCoSb,Phys. Chem. Chem. Phys.,19 (2017) 25683-25690.

[392] Benjamin Balke Elisabeth Rausch, Siham Ouardib, Claudia Felsers,Enhanced thermoelectric performance in the p-type half-Heusler (Ti/Zr/Hf)CoSb0.8Sn0.2 system via phase separation,Phys Chem Chem Phys,16 (2014) 25258-62.

[393] Shutohs, S. S.N.;Thermoelectric properties of the TiX(Zr0.5Hf0.5)1-XNiSn half-Heusler compounds, J. Alloys Compd.,2005, 389, 204-208.

[394] Sascha Populoh Krzysztof Gałązka, Wenjie Xie, Songhak Yoon, Gesine Saucke, Jürg Hulliger, Anke Weidenkaffs,Improved thermoelectric performance of (Zr0.3Hf0.7)NiSn half-Heusler compounds by Ta substitution,JOURNAL OF APPLIED PHYSICS,115 (2014).

[395] Min Zuo Degang Zhao , Lin Bo, Yongpeng Wangs,Synthesis and Thermoelectric Properties of Pd-Doped ZrCoBi Half-Heusler Compounds,Materials & Design,11 (2018) 1-9.

[396] Hao Zhang Huiyuan Gengs,Effects of phase separation on the thermoelectric properties of (Ti, Zr, Hf)NiSn half-Heusler alloys,JOURNAL OF APPLIED PHYSICS,116 (2014).

[397] Xiaoshuang Li Yinglu Tang, Lukas H. J. Martin, Eduardo Cuervo Reyes, Toni Ivas, Christian Leinenbach, Shashwat Anand, Matthew Peters, G. Jeffrey Snyder, Corsin Battaglias,Impact of Ni content on the thermoelectric properties of half-Heusler TiNiSn,Energy & Environmental Science,11 (2018) 311-320.

[398] Yanan Wang Shasha Li, Hui Wang, Yue Chens,Mechanical failure of graphene and the anharmonic phonon coupling mechanisms,Carbon,126 (2018) 404-409.

[399] Hui Li Xuesong Ge, Lin Wu, Ping Li, Xindong Mu, Yijun Jiangs,Improved mechanical and barrier properties of starch film with reduced graphene oxide modified by SDBS,J. APPL. POLYM. SCI.,(2017).

[400] Jeroen van den Brink Mohd Zeeshan, Hem C. Kandpal1s,Hole-doped cobalt-based Heusler phases as prospective high-performance high-temperature thermoelectrics,PHYSICAL REVIEW MATERIALS,1 (2017) 074401-1-074401-4.

[401] Karin M. Rabe Serdar ¨O˘g¨uts,Band gap and stability in the ternary intermetallic compounds NiSnM (M = Ti, Zr, Hf): A first principles study,arXiv:mtrl-th/9411001v2 12 May 1995,(2008).

[402] D.Rached M. Hichour b, R.Khenata, M.Rabah, M.Merabet, AliH.Reshak,S. BinOmran, R.Ahmedfs,Theoretical investigations of NiTiSn and CoVSn compounds,Journal of Physicsand Chemistry of Solids,((2012)) 975–981.

[403] Thakur Prasad Yadava Shashank Shekhar Mishra, Semanti Mukhopadhyay, Ram Manohar Yadav, Vajapeyajula Srinivasa Subrahmanyam, Nilay Krishna Mukhopadhyay, Onkar Nath Srivastavas,Rapidly Quenched Ni45Fe5Mn40Sn10 Heusler Alloys,Materials Research Society,18 (2015) 101-105.

[404] Zhuse, V. P., Sergeeva, V. M., Shtrum, E. L.: Sov. Phys. Tech. Phys. 3 (1958) 1925 (transl. from Zh.Tekhn. Fiz. 28 (1958).

[405] Petrov, A. V., Shtrum, E. L.: Sov. Phys. Solid State 4 (1962) 1061.

[406] O. Madelung, U. Rössler, M. Schulz (ed.), CuSbTe2 crystal structure, physical properties: Datasheet from Landolt-Börnstein - Group III Condensed Matter · Volume 41E: "Ternary

Compounds, Organic Semiconductors" in SpringerMaterials, 10.1007/10717201_184 (Springer-Verlag Berlin Heidelberg © 2000), (https://doi.org/10.1007/10717201_184).

[407] Laila I. Soliman, Aziza M. Abo El Soad, Hamdia A. Zayed, Sammer A. El Ghfar, Structural And Electrical Properties Of Cusbte2, Cusbse2 And Cusbs2 Chalcogenide This Films, Fizika A 11 (2002) 4, 139-152.

[408] Rongzhen Chen, Clas Persson, High absorption coefficients of the CuSb(Se,Te)2 and CuBi(S,Se)2 alloys enable high-efficient 100 nm thin-film photovoltaics, EPJ Photovoltaics 8, 85504 (2017). DOI: 10.1051/epjpv/2017005.

[409] $CuSbTe_2$ crystal structure, physical properties: Datasheet from Landolt-Börnstein - Group III Condensed Matter · Volume 41E: "Ternary Compounds, Organic Semiconductors" in SpringerMaterials (https://dx.doi.org/10.1007/10717201_184), O. Madelung, U. Rössler, and M. Schulz, Editors., Springer-Verlag Berlin Heidelberg.

[410] https://www.ornl.gov/content/physical-property-measurement system#:~:text=The%20DynaCool%20physical%20property%20measurement,thin%20film%2C%20and%20powder%20form,

[411] https://www.qdusa.com/products/ppms.html.

[412] https://www.qdusa.com/.

[413] ASTM International. E384: Standard Test Method for Knoop and Vickers Hardness of Materials. In: ASTM Stand (2012), pp. 1-43.

[414] Chan Woong Na, Doo Suk Han, Dae Sung Kim, Jeunghee Park, Yoon Tae Jeon, Gangho Lee, Myung-Hwa Jung, Ferromagnetism of MnO and Mn3O4 nanowires, Appl. Phys. Lett. 87, 142504 (2005); https://doi.org/10.1063/1.2061849.

[415] Dawson, W.M., Sale, F.R. Enthalpy of formation of manganese carbide, Mn23C6 . MTA 11, 1849–1852 (1980) doi:10.1007/BF02655100.

[416] K. T. Jacob, A. Kumar, G. Rajitha, Y. Waseda, Thermodynamic Data for Mn3O4, Mn2O3 and MnO2, High Temp. Mater. Proc., Vol. 30 (2011), pp. 459–472.

[417] U. V. Choudary, Y. A. Chang, Gibbs energies of formation of Mn3C, M(Fe,Mn)3C and Mn23C6 from the ternary phase equilibria in the Fe-Mn-C system, CALPHAD vol. 2, No. 2, pp. 169-185.

[418] Zhiliang Li, Jin-Feng Dong, Fu-Hua Sun, Shinsuke Hirono, Jing-Feng Li, Significant Enhancement of the Thermoelectric Performance of Higher Manganese Silicide by Incorporating MnTe Nanophase Derived from Te Nanowire, Chem. Mater. 2017, 29, 7378−7389.

[419] Xiaoyu She, Xianli Su,Hongyao Xie,Jiefei Fu,Yonggao Yan,Wei Liu, Pierre Ferdinand Poudeu Poudeu, Xinfeng Tang, Ultrafast Synthesis and Thermoelectric Properties of Mn 1+ xTe ompounds, ACS Appl. Mater. Interfaces 2018, 10, 25519−25528.

[420] Heribert Wiedemeier, Growth of single crystals by vapour transport, Technical report, NASA, Nov, 1987.

[421] V Vassiliev, M Bykov, M Gambino, JP Bros, Thermodynamic investigation of the manganese-tellurium system, J. Chim. Phys., Vol. 90 (1993), pp. 463–476.

[422] Mingqi Liu, John M. Cowley, Encapsulation of manganese carbides within carbon nanotubes and nanoparticles, Carbon, Vol. 33, No. 6, pp. 749-756, 1995.

[423] J. D.Wasscher, Electrical transport phenomena in MnTe, an antiferromagnetic semiconductor.Eindhoven: Technische Hogeschool Eindhoven., (1969), https://doi.org/10.6100/IR43336.

[424] E. Uchida, H. Kondoh, N. Fukuoka, Magnetic and Electrical Properties of Manganese Telluride, J. phys. Soc. Japan 11, 27, 1956.

[425] H. Yadaka, T. Harada, E. Hirahara, Magnetic Properties of Manganese Telluride Single Crystals, J. phys. Soc. Japan 17, 875, 1962.

[426] Yidong Xu,Wen Li, ChenWang, Zhiwei Chen, YixuanWu, Xinyue Zhang, Juan Li,Siqi Lin, Yue Chen, Yanzhong Pei, MnTe2 as a novel promising thermoelectric material, Journal of Materiomics 4 (2018) 215-220.

[427] W. D. Johnston, R. C. Miller, D. H. Damon, Electrical properties of some compounds having the pyrite or marcasite structure, J. Less-Common Metals. 8 (1965) 272-287.

[428] C. Hass, Spin-Disorder Scattering and Magnetoresistance of Magnetic Semiconductors, Phys. Rev. 168, 531, 1968.

[429] Daryoosh Vashaee, Ali Shakouri, Improved Thermoelectric Power Factor in Metal-Based Superlattices, Phys. Rev. Lett., 2004, 92, 106103.

[430] W. Kims, Strategies for engineering phonon transport in thermoelectrics,J. Mater. Chem. C,3 (2015) 10336--10348.

[431] Kalaimani Markandan, Jit Kai Chin, Michelle T.T. Tan, Study on Mechanical Properties of Zirconia-Alumina Based Ceramics, 625, 2014, 81-84. https://doi.org/10.4028/www.scientific.net/AMM.625.81.

[432] D. K. Shetty, I. G. Wright, P. N. Mincer,A. H. Clauer, Indentation fracture of WC-Co cermets, JOURNAL OF MATERIALS SCIENCE 20 (1985) 1873-1882.

[433] Lenka Kvetkova´,Annama´ria Duszova´, Pavol Hvizdoš, Ja´n Dusza, Pe´ter Kunb, Csaba Bala´zsi, Fracture toughness and toughening mechanisms in graphene platelet reinforced Si3N4 composites, Scripta Materialia 66 (2012) 793-796.

[434] Joulaee N, Makradi A, Ahzi S, Khaleel MA. Fracture Toughness and Crack Deflection in Porous Multilayered Ceramics: Application to NiO-YSZ. Materials Science Forum 2007;553:69–74. https://doi.org/10.4028/www.scientific.net/msf.553.69.

[435] Baoli Du, Francesco Gucci, Harshit Porwal, Salvatore Grasso, Amit Mahajan, Mike J. Reece, Flash spark plasma sintering of magnesium silicide stannide with improved thermoelectric properties, J. Mater. Chem. C, 2017,5, 1514-1521.

[436] Mevlut Gurbuz, Tugba Mutuk, Effect of process parameters on hardness and microstructure of graphene reinforced titanium composites, Journal of Composite Materials, 52, 2018,, 543-551.

[437] Hamid Reza Ezatpour, Seyed Abolkarim Sajjadi, Mohsen Haddad Sabzevar, Yizhong Huang, Investigation of microstructure and mechanical properties of Al6061-nanocomposite fabricated by stir casting, Materials and Design 55 (2014) 921–928.

[438] W. M. Hongliang Shi, David S. Parker, Mao-Hua Du, David J. Singhs, Prospective high thermoelectric performance of the heavily p-doped half-Heusler compound CoVSn, PHYSICAL REVIEW B,1 (2017) 195207-1-195207-6.

[439] J Tobola, J Pierre, S Kaprzyk, R V Skolozdra, M A Kouacou, Crossover from semiconductor to magnetic metal in semi-Heusler phases as a function of valence electron concentration, J. Phys.: Condens. Matter 10 (1998) 1013–1032.

[440] Pierre Villars (Chief Editor), PAULING FILE in: Inorganic Solid Phases, Springer Materials (online database), Springer, Heidelberg (ed.) Springer Materials Co2Sn (Co1.5Sn ht) Crystal Structure- https://materials.springer.com/isp/crystallographic/docs/sd_0454900sd_0454900 (Springer-Verlag GmbH, Heidelberg, © 2016).

[441] L. J. Brillson, Metal-semiconductor interfaces, Surface Science 299/300, 1994 (909-927).

[442] I.P. Batra, E. Tekman, S. Ciraci, Theory of schottky barrier and Metallization, Progress in Surface Science, 36, 1991 (289-361).

[443] Y. Öner C. S. Lue, D. G. Naugle, and Joseph H. Ross, Jrs,Magnetism of New Semi-Heusler Compounds FeVSn and CoVSn,IEEE TRANSACTIONS ON MAGNETICS,37 (2001) 2138-2141.

[444] H. Ghodrati, R. Ghomashchi, Effect of Graphene Dispersion and Interfacial bonding on the Mechanical Properties of Metal Matrix Composites: An Overview, FlatChem (2019), doi: https://doi.org/10.1016/j.flatc.2019.100113.

[445] Hong-chuan Cao, Yi-long Liang, The microstructures and mechanical properties ofgraphene-reinforced titanium matrix composites, Journal of Alloys and Compounds 812 (2020) 152057, 1-10.

[446] J.Pacyna, A.Mazur, Relationship between grain size and fracture toughness of tool steel. Steel Research, 57, (1986) 577-585. https://doi.org/10.1002/srin.198600828.

[447] Fracture Failure of Engineering Materials, Copyright © 1998-2005 by Pichai Rusmee, https://my.mech.utah.edu/~rusmeeha/labNotes/fracture1.html.

[448] W.B.Shou , D.Q.Yi , H.Q.Liu , C.Tang, F.H.Shen, B.Wang, Effect of grain size on the fatigue crack growth behavior of 2524-T3 aluminum alloy. Arch Civ Mech Eng. 2016;16:304–312.

[449] Qi Zhao, Zhiyi Liu, Yangcheng Hu, Fudong Li, Cheng Luo, Shasha Li, Texture effect on fatigue crack propagation in aluminium alloys: an overview, Materials Science and Technology, 35:15, 1789-1802 (2019), DOI: 10.1080/02670836.2019.1651954,

[450] Ying Lei, Wensheng Gao, Yu Li, Rundong Wan, Wen Chen, Rui Zheng, Leiqiang Ma, Hongwei Zhou, Structure and thermoelectric performance of Ti-filled and Te-doped skutterudite TixCo4Sb11.5Te0.5 bulks fabricated by combination of microwave synthesis and spark plasma sintering, Materials Letters 233 (2018) 166–169.

[451] Fei-Peng Du, Nan-Nan Cao, Yun-Fei, Zhang, Ping Fu,Yan-Guang Wu, Zhi-Dong Lin, Run Shi, Abbas Amini, Chun Cheng, PEDOT:PSS/graphene quantum dots films with enhanced thermoelectric properties via strong interfacial interaction and phase separation, Scientific Reports, 8, (Apr 2018): 1-12. DOI:10.1038/s41598-018-24632-4.

[452] K.R. Sriraman, S. Ganesh Sundara Raman, S.K. Seshadri, Influence of crystallite size on the hardness and fatigue life of steel samples coated with electrodeposited nanocrystalline Ni–W alloys, Materials Letters 61 (2007) 715–718.

APPENDIX A

Published papers

Renewable and Sustainable Energy Reviews 112 (2019) 158–169

Contents lists available at ScienceDirect

Renewable and Sustainable Energy Reviews

journal homepage: www.elsevier.com/locate/rser

Strategies for engineering phonon transport in Heusler thermoelectric compounds

Sadeq Hooshmand Zaferani[a,c,*], Reza Ghomashchi[a,b,**], Daryoosh Vashaee[c,d,***]

[a] School of Mechanical Engineering, University of Adelaide, SA, 5005, Australia
[b] ARC Research Hub for Graphene Enabled Industry Transformation, University of Adelaide, Adelaide, SA, 5005, Australia
[c] Department of Electrical and Computer Engineering, North Carolina State University, NC, 27606, United States
[d] Department of Materials Science and Engineering, North Carolina State University, NC, 27606, United States

ARTICLE INFO

Keywords:
Thermoelectricity
Heusler alloys
Thermal conductivity
Phonon scattering
Waste heat recovery

ABSTRACT

Thermoelectric generators, which can convert waste heat directly into electricity, are promising candidates for capturing low-grade heat and enhancing the efficiency of the heat engines. This would lead to decreasing the fossil fuel usage and greenhouse gas emission. Many Heusler compounds have been studied for thermoelectric application due to their desired characteristics such as sizeable thermoelectric power factor, non-toxicity, and high stability over a wide temperature range. The primary restriction for Heusler thermoelectric materials has been their high lattice thermal conductivity, which reduces their thermoelectric figure of merit. Several strategies have been carried out to ameliorate this restriction by engineering the phonon transport properties. This article discusses several approaches such as bulk nanostructuring, the creation of point defects and vacancies, impurity doping, and multiphase engineering of the material structure for reducing the thermal conductivity of the Heusler compounds. The effectiveness of each of these methods depends on temperature; hence, the working temperature must be taken into account when designing the material structure and the composition to achieve the optimum performance for practical applications.

1. Introduction

Climate change as a result of global warming may be traced back to human activities, industrial processes, and greenhouse gas emission [1,2]. In this field, the application of renewable energy and the practical use of waste heat are very appealing fields of study [3–6]. Apparently, the trend is encouraging as based on the report of "international energy agency, world energy outlook 2017", there has been a rapid deployment of clean energy technologies and an indirect falling costs [7]. One of the available techniques towards improving energy efficiency is to endeavor to convert the wasted thermal energy back into more useful energy such as electricity. Thermoelectric generators (TEGs), capable of converting waste heat directly into electricity, have already attracted worldwide attention as evidenced by the expansion of research activities on thermoelectric materials and manufacturing of TE modules and systems. Waste heat recovery is an environmentally friendly method which not only reduces the consumption of fossil fuels for energy production but also decreases waste heat emissions [8–11].

For thermoelectric materials, the dimensionless figure of merit (zT) is a measure for evaluating the efficiency of energy conversion and is defined as:

$$zT = \frac{S^2\sigma}{\kappa_e + \kappa_l}T \quad (1)$$

where S is the Seebeck coefficient (VK^{-1}), σ is the electrical conductivity ($\Omega^{-1}m^{-1}$), T is temperature (K), κ_e and κ_l are the electronic and the lattice thermal conductivities ($Wm^{-1}K^{-1}$), respectively [12,13]. With the advances in new thermoelectric materials, the thermoelectric technology is growing to find new market space for power generation, cooling, or detection and imaging applications [14–17]. Consequently, new types of thermoelectric devices and fabrication techniques are also being developed [18,19]. High-performance thermoelectric materials have been promoted following new designs such as the reduction of the thermal conductivity by using larger phonon

* Corresponding author. School of Mechanical Engineering, University of Adelaide, SA, 5005, Australia.
** Corresponding author. School of Mechanical Engineering, University of Adelaide, SA, 5005, Australia.
*** Corresponding author. Department of Electrical and Computer Engineering, North Carolina State University, NC, 27606, United States.
E-mail addresses: sadeq.hooshmandzaferani@adelaide.edu.au (S. Hooshmand Zaferani), reza.ghomashchi@adelaie.edu.au (R. Ghomashchi), d.vashaee@ncsu.edu (D. Vashaee).

https://doi.org/10.1016/j.rser.2019.05.051
Received 23 September 2018; Received in revised form 3 May 2019; Accepted 22 May 2019

scattering via nanostructuring [20,21] and nano-inclusions [22–24] as well as the increase of the power factor by designing complex structures [25–29], creating of resonant energy levels close to the band edges [30], using low dimensional structures [31–33], and via carrier filtering [34–36]. New materials based on bulk heterostructures, or nanocomposites, have especially taken considerations because of their simplicity of manufacture and similarity with the current type of the thermoelectric devices. Even though nanostructuring techniques have turned out to be gainful in numerous material frameworks because of the inherent spectral discrepancies of the electron and phonon transport parameters [37], these strategies are also linked to the degradation of the charge carrier mobility or have less efficiency at high working temperatures. Therefore, in a few materials, they have resulted in a significant decrease in the power factor prompting little or no enhancement of the figure-of-merit [20,38,39].

In this regard, Heusler alloys have a simple lattice structure and as such phonon characteristics compared to those of the caged structures like Skutterudites [40–42] and Clathrates [43–45]. Therefore, they generally have higher thermal conductivity while also a more substantial thermoelectric power factor. Therefore, methods for reducing the thermal conduction in Heusler based alloys are highly desired. Concerning material selection, it is desired to find compounds containing nontoxic and eco-friendly elements with no or little rare earth components, which are sustainable in harsh condition and at high temperature In this field, the Heusler compounds have attracted much attention due to their particular characteristics as non-toxic materials with magnetic or semiconducting behavior and also remarkable stability at various temperature intervals [46,47].

These compounds are divided into full- and half-Heusler types which are based on ternary intermetallic materials [48–53] with the stoichiometric composition of X_2YZ and XYZ, respectively [12,54]. The full-Heusler alloys (X_2YZ) have an $L2_1$ structure with fcc lattice unit cells containing four atoms as X at (1/4,1/4,1/4) and (3/4,3/4,3/4), Y at (1/2,1/2,1/2) and Z at (0,0,0) in Wyckoff coordinates, and their corresponding space group is Fm-3m (No. 225) [12,54]. Also, the half-Heusler alloys have a C1b structure with the absence of one of the X sub-lattices, and the corresponding space group of F-43 m (No. 216) [12,54].

In the mentioned compositions, generally, X is filled with a high valence transition element, Y is substituted with a lower valence transition metal atom, and finally, Z is an element in the III–V columns of the periodic table with s-p type valence electrons [12,54].

Fig. 1 shows the atomic arrangements for the full-Heusler and half-Heusler alloys and the elements, which have been carried out in these compounds.

Traditionally, high thermal conductivity ($\kappa = \kappa_e + \kappa_l$) has been the main drawback of the Heusler TE alloys. The dominant part of this thermal conductivity is κ_l due to lattice vibration which is represented by phonons [58,59]. Generally, phonons are described in quantum mechanics as a unit of vibrational energy that arises from oscillating atoms within a crystal lattice, which can have different frequencies, and are responsible for transferring the thermal energy. There are two types of phonons to carry thermal energy within solids, (i) acoustic phonons which are representing the coherent displacement of atoms in parallel (longitudinal) or perpendicular (transverse) to the propagation and (ii) optical phonons, corresponding to the incoherent motion of the two neighboring atoms in the opposite direction.

Fig. 2.b shows the schematic optical and acoustic components of phonon energies based on the dispersion of two atoms with masses of m_1 and m_2 (equation (2)) [60].

$$\omega^2 = \beta\left(\frac{1}{m_1} + \frac{1}{m_2}\right) \pm \sqrt{\left(\frac{1}{m_1} + \frac{1}{m_2}\right)^2 - \frac{4sin^2qa}{m_1 m_2}} \tag{2}$$

Here ω is the frequency, a the lattice constant, q the phonon wave vector, and β a constant related to the atomic bonds.

As depicted in Fig. 2.a, in the acoustic branches, including longitudinal (LA) and transverse (TA) modes, the group velocities of all the acoustic branches, $V_{gj} = d\omega_j/dq$ (j = LA, TA), are higher than that of the longitudinal optical (LO) and transverse optical (TO) modes with their velocity being nearly zero at $q \approx 0$. The transverse mode makes either a doubly degenerate or two separate branches. In each classification, the transverse modes have lower group velocity than the longitudinal ones due to the higher frequency of the longitudinal modes at a specific wave vector. In other words, the longitudinal branches generally carry more energies in comparison to the transverse branches with the same momentum.

In a solid, if A represents the number of atoms in a unit cell, the outcome will be 3A phonon branches, in which, three branches are acoustic, and the rest are optical. Also, Table 1 shows the classification of acoustic and optical branches as longitudinal and transverse with their counts [61].

Moreover, both the acoustic and optical components of phonon energy propagate transversally and longitudinally within the crystalline solids as schematically illustrated in Fig. 2.b. In respect to the application temperature range, the transverse acoustic (TA) (Fig. 2b) branches have low frequency and are characteristics of low temperature while the longitudinal acoustic (LA) (Fig. 2b) types have higher frequencies and are dominant at high temperature.

It is worth noting that a higher number of atoms (A) in a unit cell can be a recipe for obtaining lower thermal conductivity. Because, when the number of optical components of the phonon energy increases, the absorbed energy can be transferred less by the acoustic branches. In this case, more energy is attributed to the optical branches, which have a negligible contribution to heat transfer ascribed to their low group velocity. Moreover, due to the limited phonon frequency (~10 THz), by increasing the optical branches, the acoustic phonon frequency declines as the acoustic branches transfer only a partial amount of energy in the crystal. This fact influences the lattice thermal conductivity mostly at high temperature in which the high-frequency phonons are the majority of heat carriers [61].

To reduce thermal conductivity, one needs to somehow obstruct the phonon transport [62,63] with appropriate strategies. The choice of phonon scattering approach is based on the application temperature range, which may include strategies such as nanostructuring [62–66], impurity/vacancy doping [67] and designing a multiphase matrix [12]. Consequently, a comprehensive understanding of the phonon scattering mechanisms is required for optimum engineering of the material structure. The following section discusses the central phonon scattering mechanisms useful for the Heusler TEs.

2. Thermal conductivity of heusler compounds

The lattice thermal conductivity in the isotropic Debye approximation can be described based on Holland's model [68]:

$$\kappa = \frac{1}{3}\left(2I_{T_0} + 2I_{T_U} + I_L\right) \tag{3}$$

where

$$I_j = \frac{k_B}{2\pi^2 v_{gj}}\left(\frac{k_B}{\hbar}\right)^3 \int_{x_{j_2}}^{x_{j_1}} \tau_{cj} \frac{x^4 e^x}{(e^x - 1)^2} dx \tag{4}$$

Here $x = \hbar\omega/k_B T$ is a dimensionless parameter, k_B is the Boltzmann constant, h is the Plank's constant ($\hbar = h/2\pi$), θ_j and v_{gj} are the Debye temperature and the group velocity for the corresponding phonon modes, respectively, T states the absolute temperature, ω is the phonon frequency, and τ_{cj} shows the total scattering relaxation time for the corresponding phonon branch.

Parameters j, x_{j_1}, x_{j_2}, and x_{j_3} are defined in Table 2.

ω_1 corresponds to $q_{max}/2$ where the transverse branch becomes almost flat (Fig. 2a). This is the frequency where umklapp processes are

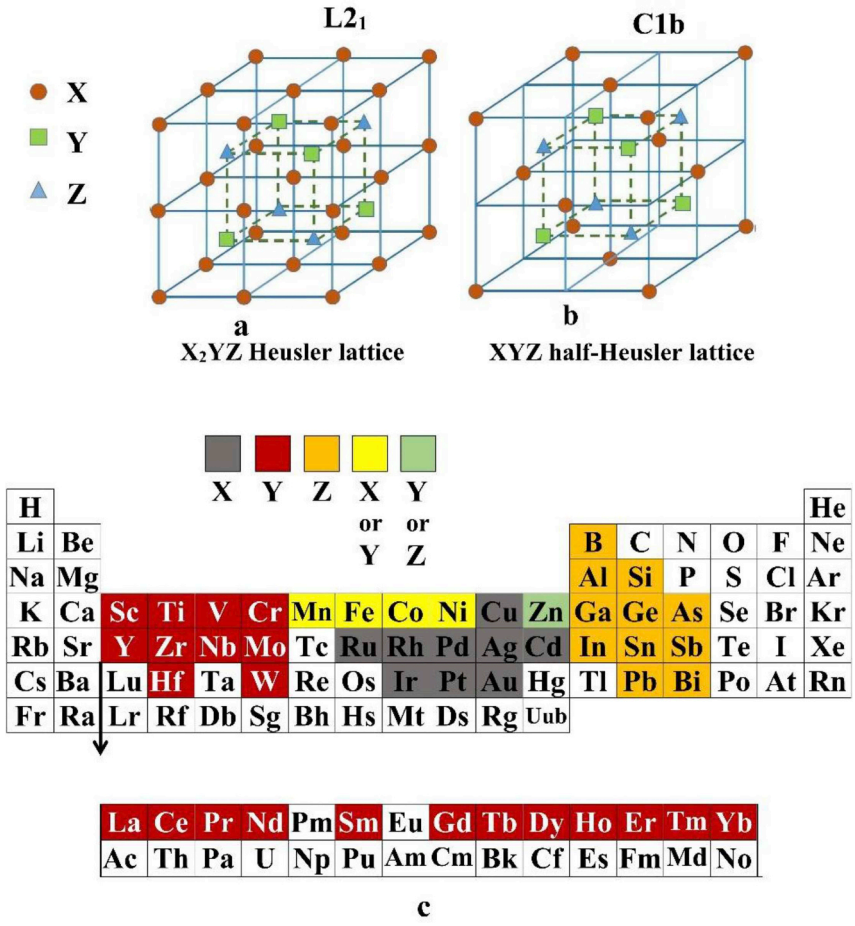

Fig. 1. (a) full-Heusler crystal structures and (b) half-Heusler, (c) specific elements in the Heusler alloys (adapted from Refs. [55–57]).

supposed to start. ω_2 and ω_3 are the zone-boundary frequencies for the transverse and longitudinal phonons, respectively.

This model reduces to the Callaway's model [69,70] if the longitudinal phonons dominate the thermal conduction. Callaway's formalism makes no distinction between transverse and longitudinal phonon modes and the sum over phonon polarization is set equal to three, and an average phonon velocity is used everywhere. Therefore, the Callaway model becomes less accurate when the temperature increases. Holland's model, also, although not being as accurate as the first principle methods, enables obtaining detailed information about the effect of different phonon scattering mechanisms on lattice thermal conductivity in a convenient way. There are several main contributing scattering sources within solid structures incorporated in the phonon scattering relaxation time. Table 3 lists the summary of the main phonon scattering mechanisms and the corresponding relaxation times including, grain boundary phonon scattering, impurity-phonon mass fluctuation scattering, point defect (alloy) scattering, three-phonon scattering due to the normal (N) and umklapp (U) processes, and electron-phonon scattering.

Table 1
The number of acoustic and optical branches in a solid with A atom in the unit cell.

	Longitudinal	Transverse
Acoustic	1	2
Optical	A-1	2(A-1)

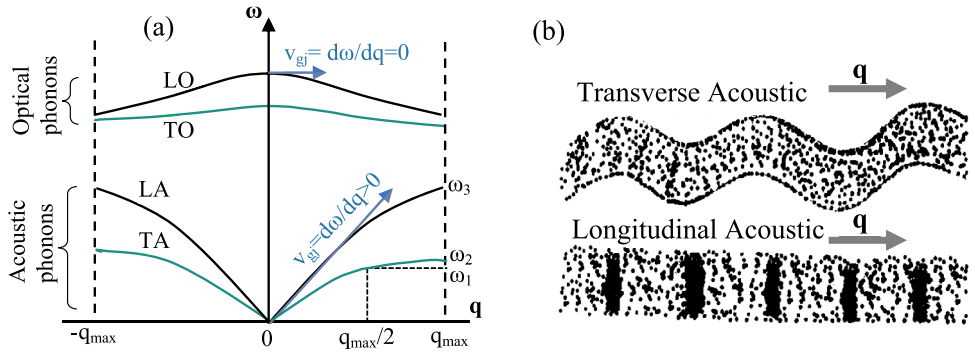

Fig. 2. Schematic acoustic and optical phonon branches for a diatomic lattice.

Table 2
Parameters used in equations (3) and (4).

Parameters	Values		
j	T_0	T_U	L
$\boldsymbol{x}_{j_1}$	0	$\hbar\omega_1/k_B$	0
$\boldsymbol{x}_{j_2}$	$\hbar\omega_1/k_B$	$\hbar\omega_2/k_B$	$\hbar\omega_3/k_B$

Here M is the total average mass for the alloy, γ is the Grüneisen constant (or the anharmonicity parameter), a is the atomic size determined by the cubic root of the atomic volume, and β is the ratio of the normal three phonon-scattering rate to the umklapp three-phonon-scattering rate, which is assumed temperature-independent. Electron-phonon relaxation timeτ_{e-ph}, is given by Ziman [74,75] in which v_s is the sound velocity, k_B is the Boltzmann constant, E_a is the deformation potential, m_d is the density-of-states effective mass, ρ is the mass density, and E_F is the Fermi energy. y_i, M_i, and $a_i$in the relaxation time due to point defects are the fractional concentration, mass, and atomic size of each element in the alloy respectively, where $M = \sum_i f_i M_i$and $a = \sum_i f_i a_i$. ε_s determines the contribution of strain disorder to point defect scattering of phonons. If the lattice constants of the elements in the compound do not differ largely, the effect of strain is small compared with the mass fluctuation. The phonon relaxation time due to scattering by impurity atoms is calculated based on a single atomic site, in which f_i is the fractional concentration of the impurity atom i, and M_i is its mass. Due to the substitutional replacement of the host atoms by impurities, the doping-phonon scattering in Heusler alloys can happen via both the mass fluctuating and atomic interaction. Therefore, it follows a similar trend as that of the point defects.

Grain boundaries can introduce three different types of scattering of phonons: (1) regular reflection and refractionτ_{Ref},(2) diffusive scattering due to the corrugation of the GB, τ_{Diff}, and (3) Rayleigh scattering, τ_{Ray} [76,77]. Diffusive scattering is related to the physical defects at the GB, such as vacancy. Rayleigh scattering arises from the mass and bond stiffness differences between the host alloy and the spherical grains such as precipitated regions of impurities. The mean free path due to regular reflection and refraction is approximately constant as listed in the table. Here $\ell_{GB}$is the mean distance of the GBs, and $\Delta\nu$ is the difference of refraction indices of the elastic waves in different grains. This can arise, for example, due to the different orientation of the crystal in the adjacent grains. If the crystal orientation is slightly rotated by an angle δ, one can estimate $\Delta\nu \approx \delta$. If the GB region is much smaller than the wavelengths of the excited phonons, the diffusive scattering relaxation time changes with ω^{-2}. The phonon relaxation time with respect to such a diffusive scattering is shown in Table 3, in which η is a parameter that characterizes the degree of the corrugation of the GB (typically $1 < \eta < 10$). For the case of Rayleigh scattering, in which Ξ is some constant dependent on the details of the grain boundary characteristics, the approximation is valid for low frequency phonons. At high frequencies the exponent of ω decreases and eventually at very high frequencies, the scattering is almost frequency-independent and is in the same form as that of the regular reflections and refractions at the GBs [76,77].

Once all the different relaxation times are calculated, the total relaxation time of phonons τ_c can be given by Matthiessen's rule [78] as follows:

$$\frac{1}{\tau_c} = \frac{1}{\tau_U} + \frac{1}{\tau_N} + \frac{1}{\tau_{e-ph}} + \frac{1}{\tau_{pd}} + \frac{1}{\tau_{i-ph}} + \frac{1}{\tau_{Ref}} + \frac{1}{\tau_{Diff}} + \frac{1}{\tau_{Ray}} \quad (5)$$

However, the strength and effectiveness of each scattering mechanism is temperature dependent. At low temperature and low frequency, grain boundary phonon scattering is often ruling, and at a sufficiently high temperature and high phonon frequency, the Umklapp scattering of phonon by other phonons becomes dominant. At the intermediate temperature and frequency (between the two limits) electron-phonon and point defect scattering, e.g., by dopants, vacancies, and alloy element substitution can become important (Fig. 3). Therefore, the working temperature must be considered when engineering the structure for optimum performance from the scattering resources.

3. Scattering mechanisms

To reduce the thermal conductivity of Heusler TE alloys, one may engineer various sources of the phonon scattering such as grain boundaries or inter-phase boundaries (interface), interstitial or substitutional atoms, impurities, point defects (e.g., substitutional, vacancies) and precipitates [48]. Over approximately the last ten years, many of these techniques have been successfully implemented. Table 4 shows a range of Heusler compounds synthesized and the executed phonon scattering mechanisms within the working temperature range. The success of producing appropriate sample is dependent on the process parameters such as time, temperature, dopant and the degree of porosity. As represented in this table, the mass fluctuating is a practical method of phonon scattering, which has been employed in various alloys such as $Yb_{13.82}Pr_{0.18}Mn_{1.01}Sb_{10.99}$ $La_{2.2}Ca_{0.78}Te_4$ and $Ti_{0.5}Zr_{0.5}NiSn_{0.994}Sb_{0.006}$ leading to zT values of 1.2, 1.2 and 1, respectively.

Table 3
Phonon scattering relaxation time [71–73].

Scattering Strategies	Parameters and relations
GB regular reflection and refraction	$\tau_{Ref} \sim \ell_{GB} v_{gj}^{-1} (\Delta\nu)^{-2}$
GB diffusive scattering	$\tau_{Diff} \sim \ell_{GB} v_{gj}^{-1} \left(\frac{k_B \theta_j}{\hbar\omega}\right)^2 \frac{1}{\eta}$
GB Rayleigh scattering	$\tau_{Ray} \sim \left(\frac{v_{gj}}{\ell_{GB}}\right)^3 \left(\frac{\theta_j}{T\omega}\right)^4 \Xi$
Impurity-phonon mass fluctuation	$\frac{1}{\tau_{i-ph}} = \left(\frac{a}{v_{gj}}\right)^3 \left(\frac{k_B T}{\hbar}\right)^4 \sum_i f_i \left(1 - \frac{M_i}{M}\right)^2 x^4$
Point defect	$\frac{1}{\tau_{PD}} = \left(\frac{a}{v_{gj}}\right)^3 \left(\frac{k_B T}{\hbar}\right)^4 \sum_i \left[y_i \left(1 - \frac{M_i}{M}\right)^2 + \varepsilon_s y_i \left(1 - \frac{a_i}{a}\right)^2 \right] x^4$
3-phonon Umklapp process	$\tau_u^{-1} = \frac{20\pi}{3} \hbar N_A \left(\frac{6\pi^2}{4}\right)^{1/3} \times \frac{1 + \frac{5}{9}\beta}{1+\beta} \frac{\gamma^2}{M a^2} \left(\frac{T}{\theta_j}\right)^3 x^2$
Normal three-phonon scattering	$\tau_N = \beta \tau_u$
Electron-phonon	$\tau_{e-ph}^{-1} = E_a^2 m_d^3 v_{gj} / 4\pi\hbar^4 \rho \left(\frac{1}{2} m_d v_{gj}^2 / k_B T\right) \times \ln \left(\frac{1 + \exp\left(-\left(\frac{1}{2} m_d v_{gj}^2 / k_B T\right) + E_F / k_B T - x^2 / 16 \left(\frac{1}{2} m_d v_{gj}^2 / k_B T\right) + x/2\right)}{1 + \exp\left(-\left(\frac{1}{2} m_d v_{gj}^2 / k_B T\right) + E_F / k_B T - x^2 / 16 \left(\frac{1}{2} m_d v_{gj}^2 / k_B T\right) - x/2\right)} \right)$

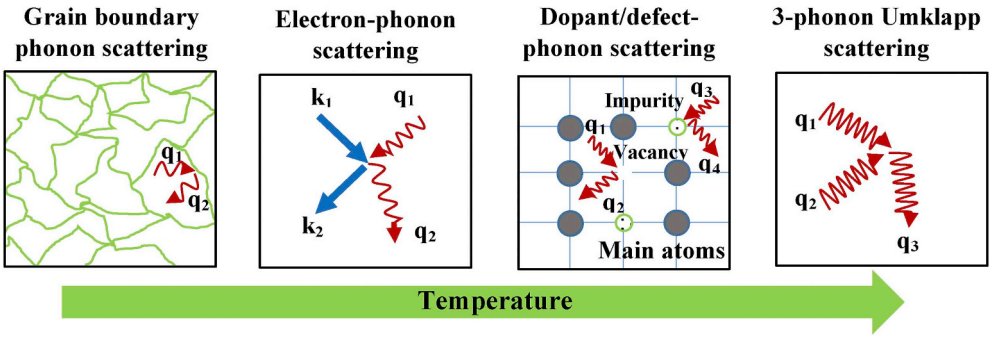

Fig. 3. Dominant modes of the phonon scattering versus temperature (adapted from Ref. [61]).

3.1. Grain boundaries scattering

Grain boundaries as phonon scatterers can be employed in designing the TE materials. The correlation between phonon coherencies and the mean free path, the wavelength, and grain size (characterized length) have impacts on phonon dispersion. Thermal conductivity decreases when the effective phonon mean free path is greater than the grain or crystal size [94]. Since phonon mean free path is a function on the wavelength, and wavelength itself is dependent on temperature as per Wien's displacement law ($\lambda_{max}.T$ = constant), grain boundaries can be the significant scattering sources at low temperature [92,93].

For the Heusler TE alloys, nano-sized grains [47,63,64] and high-density of grain boundaries have resulted in phonon scattering and reduced the lattice thermal conductivity. For example, the reported lattice thermal conductivity of the polycrystalline $Zr_{0.5}Hf_{0.5}Co_{1-x}Rh_xSb_{0.99}Sn_{0.01}$ was 3.7 $Wm^{-1}K^{-1}$ at 300 K in structures with grain sizes of 80-175 nm. Mikami et al. [95] used spark plasma sintering to synthesize $Fe_2VAl_{0.9}Si_{0.1}$/Bi composites via incorporating different amounts of Bi to yield a composite structure containing micrometer-sized Bi grains and nanometer-sized Fe_2VAl grains. The results showed the inclusion of nanometer-sized microstructural constituents of $Fe_2VAl_{0.9}Si_{0.1}$ has reduced thermal conductivity [95].

Also, Katsuyama et al. [96] studied the effects of grain refining via the milling process on the thermal conductivity of half-Heusler $ZrNiSn_{0.98}Sb_{0.02}$ alloys. Fig. 4 illustrates the grain size reduction of this alloy with increasing the milling time.

Table 5 compares the TE properties of different samples. As represented in the table, the thermal conductivity lowers with the milling time in the 3 and 5-h milled samples due to the grain refinement, hence; a higher concentration of the grain boundaries.

It is noted that the sample milled for three hours has higher Seebeck coefficient than the one milled for five hours resulting in a higher zT. The grain refinement can lead to the formation of various defects such as vacancies, antisites, dislocations, etc., some of which can introduce charge carriers into the lattice [97–99]. The lower Seebeck coefficient and higher electrical conductivity of the 5-h milled sample indicates a higher carrier concentration, which can be the reason for the smaller power factor if the carrier concentration is away from the optimum value [97,100]. There is also a limit for the grain size below which the carrier mobility is impaired more than the phonon transport, which can lead to smaller zT [97,100].

In another study [101], the relation between the average grain size and the lattice thermal conductivity was evaluated for $TiNiSn_{1-x}Sb_x$ alloy as shown in Fig. 5.

In this study, the lattice thermal conductivities were characterized against the average grain size in the temperature range up to 300 K. As shown in Fig. 5, by decreasing the average grain diameters, the lattice thermal conductivity decreased due to the interface phonon scattering. It should be noted that the grain boundaries can also act as potential obstacles to hinder the charge carrier transport and decrease electrical conductivity [47]. In some materials, the effect is significant, that the zT does not improve noticeably or even reduces [102,103].

Therefore, the decoupling of thermal and electrical conductivities is desired. El-Asfoury et al. [104] used graphene to decouple the κ and σ

Table 4
List of Heusler TE compounds with dominant scattering sources and the corresponding temperature range.

Heusler TE Compound	Engineering Strategy	Effective Temperature Range (K)	Scattering Mechanism	ZT Max	Ref.
ZrNiSn	Y or Sb doping	–	Mass fluctuating	0.28	[58]
$Ti_{0.3}(ZrHf)_{0.69}V_{0.01}Ni_{0.9}Pd_{0.1}Sn_{0.99}Sb_{0.01}$	Ti substitution at the Zr and Hf site	820	Mass fluctuating	0.92	[79]
$Ti_{0.5}(ZrHf)_{0.49}Nb_{0.01}Ni_{0.9}$ $Pd_{0.1}Sn_{0.98}Sb_{0.02}$	Nb substitution at the IV metal site	900	Mass fluctuating	0.66	[80]
$Mg_2Si_{0.8}Sn_{0.2}$	Sb doping	740	Mass fluctuating	0.95	[81]
$Zr_{0.5}Hf_{0.5}Co_{0.4}Rh_{0.6}$ $Sb_{0.8}Sn_{0.2}$	Variation of CoSb particle size range	775	Grain boundary scattering	0.18	[82]
$Zr_{0.7}Hf_{0.3}NiSn$	Phase separation	350	Multi-phase interface scattering	0.007	[83]
ZrNiSn, $(Zr_{0.5}$, $Hf_{0.5})NiSn$	Ni and/or Co antisites, structural vacancies	775	Mass fluctuating	0.03	[84]
$Zr(Ni,Co_{0.2})Sn$					
$Ti_{0.3}Zr_{0.35}Hf_{0.35}Ni_{1.01}Sn$	Phase separation	350–500	Multi-phase interface scattering	0.68	[85]
$Cu_{12}Sb_{3.39}Te_{0.61}S_{13}$	Te doping	623	Mass fluctuating	0.8	[86]
$AgSbSe_2$	Sb deficiencies	300–610	Mass fluctuating	1	[87]
$Yb_{13.82}Pr_{0.18}Mn_{1.01}Sb_{10.99}$	(RE = Pr and Sm) doping	1275	Mass fluctuating	1.2	[88]
CoSbS	Nickel doping	873	Mass fluctuating	0.5	[89]
$La_{2.2}Ca_{0.78}Te_4$	Calcium doping	1273	Mass fluctuating	1.2	[90]
$Bi_2Te_{2.2}Se_{0.8}$	Point defecting and Se Content changing	473	Mass fluctuating	0.82	[91]
$Ti_{0.25}Hf_{0.75}CoSb_{0.85}Sn_{0.15}$	Phase separation	710	Multi-phase interface scattering	1.2	[92]
$Zr_{0.25}Hf_{0.25}Ti_{0.5}NiSn_{0.994}Sb_{0.006}$	Nano-sized precipitates	500	Mass fluctuating	0.91	[93]
$(Ti_{0.2},Zr_{0.8})Ni_{1.1}Sn$	FH-nanoprecipitates and Ti, Zr point defects	870	Mass fluctuating	0.81	[65]
$Ru_2VAl_{0.25}Ga_{0.75}$	Variation of Ga content	400	Mass fluctuating	0.006	[69]
$Ti_{0.5}Zr_{0.5}NiSn_{0.994}Sb_{0.006}$	HfO_2 doping	500	Mass fluctuating	1	[47]

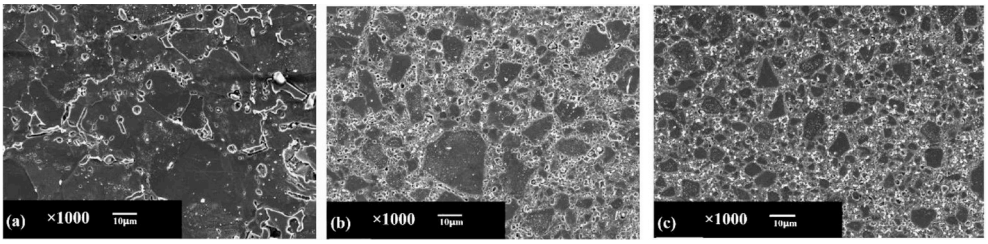

Fig. 4. SEM illustration of grain size reduction due to the milling process in the consolidated samples, a) 0 h, b) 3 h, c) 5 h (ref. [96] with permission).

of the $Bi_{85}Sb_{15}$ compound. In this work, graphene was incorporated in the microstructure to decorate the grain boundaries and prevent crystal growth. Also, the decrease in electrical conductivity was compensated by increasing the carrier concentration (n) via the graphene doping [104–106]. It is also noteworthy that high values of σ/κ and n/κ_l ratios can be regarded as a measure to promote decoupling between thermal and electrical conductivities and arriving at high zT values [104,107].

3.2. Mass fluctuation

Mass fluctuating can also promote the phonon scattering and lower the lattice thermal conductivity [101,108,109]. The magnitude of the mass difference at the interfaces is a crucial parameter in reducing the thermal conductivity [61]. By increasing the temperature, the phonon's wavelength decrease, and these short wavelengths can be scattered more efficiently by mass fluctuation defects such as dislocations, impurities, vacancies and alloy atoms [67].

Also, the change in atomic mass impacts the group velocities. Based on equation (6), by considering the sound speed in solids (V_s) as the group velocity of phonons, via changing the density (ρ) and/or chemical bonding (E), the group velocity will be altered, as well.

$$V_s = \sqrt{\frac{E}{\rho}} \tag{6}$$

Therefore, by selecting the high atomic mass dopant/impurity elements and/or weak chemical bonds, the sound speed will reduce and result in the reduction of thermal conductivity [62,66,67]. This issue can be explained based on the spring-mass system (equation (7)).

$$F = m_i \times a_i = m_i.(d^2X_i/dt^2) = K_i \times X_i \tag{7}$$

In this system, the phonons can be scattered based on the variation in mass (m_i) and/or spring constant (K_i), here representing the atomic bonding. Therefore, atomic substitution/doping is an effective method for modifying phonon transport similar to changing m_i or K_i (Fig. 6).

The change in the mass and/or spring constant occurs due to the presence of impurities or vacancies which can cause mass fluctuation [67]. Moreover, the mass fluctuation can also lead to electric potential disturbance; therefore, it can be employed for energy filtering of both phonons and electrons. This can occur at the interfaces between two different elements or structures. Chai et al. [65] investigated the interfaces between full-Heusler and half Heusler phases to prevent the low energy phonons from passing through the solid structure.

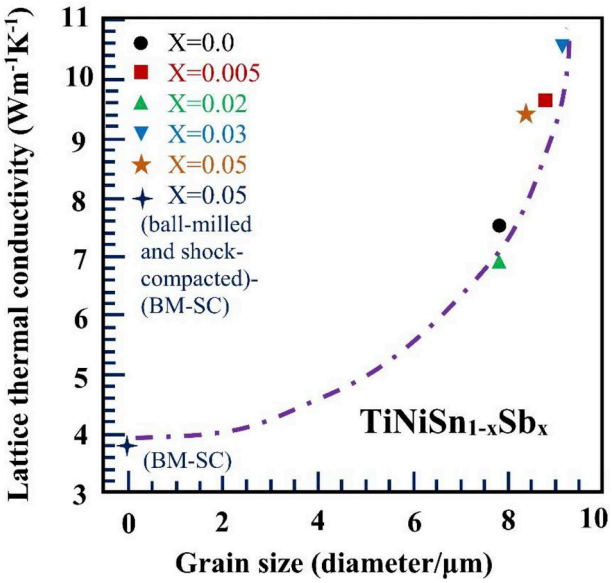

Fig. 5. Relation between the grain size and the lattice thermal conductivity (adapted from Ref. [101]).

In this field, Berry et al. [110] investigated the effects of the mass fluctuating strategy via modulation doping (dissolving) of half-metallic MnNiSb in the TiNiSn alloy and forming a heavily doped $Ti_{1-x}Mn_xNiSn_{1-x}Sb_x$ phase. The results showed the enhancement of the thermoelectric characteristics (Table 6) with a maximum zT value of 0.63 in x = 0.05, at 823 K.

Fig. 7 illustrates BSE images of the modulation doping systems with various amounts of MnNiSb. Based on this image, the matrix was mainly the pristine TiNiSn phase, containing the heavily doped $Ti_{1-x}Mn_xNiSn_{1-x}Sb_x$ with a random distribution. This change in mass caused the fluctuation which led to phonon scattering and reduction of thermal conductivities from about 6.35 to 5.65 $WK^{-1}m^{-1}$at 823 k [110].

Furthermore, nanoinclusions, or nanograins, can provide some barriers to prevent the low energy carriers from propagating through the solid. Hence, both σ and κ will be modified which can generate greater zT values depending on the effectiveness of the barrier on each property [111].

Table 5
Thermoelectric parameters of ZrNiSn alloy after doping with Sb and also refining under the milling process at a temperature of 573 K (adapted from Ref. [96]).

Alloy	S (μVK^{-1})	σ (Scm^{-1})	PF (μWm^{-1}K^{-2})	κ (Wm^{-1}K^{-1})	zT
ZrNiSn	−293	400	3500	7.3	0.25
$ZrNiSn_{0.98}Sb_{0.02}$ 0 h milling	−55	2000	4900	6.7	0.42
$ZrNiSn_{0.98}Sb_{0.02}$ 3 h milling	−180	1724	6700	5.75	0.67
$ZrNiSn_{0.98}Sb_{0.02}$ 5 h milling	−75	1923	5400	5.7	0.55

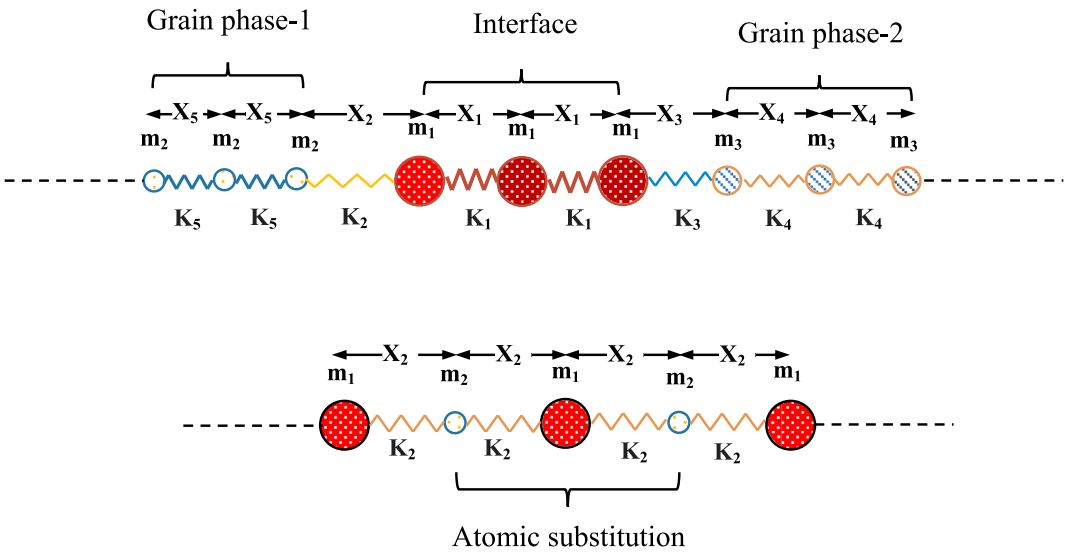

Fig. 6. Motion of atoms in spring system a) using an interface layer with three ranges of atoms, b) atomic substation.

Table 6
Thermoelectric parameters of $(TiNiSn)_{0.95}$ + $(MnNiSb)_{0.05}$ alloy at 823 K [110].

Alloy	S (μVK^{-1})	σ (Scm^{-1})	κ_L ($Wm^{-1}K^{-1}$)	zT
$(TiNiSn)_{0.95}$ + $(MnNiSb)_{0.05}$	−160	1700	3.5@823K	0.63
TiNiSn	−150	1100	4.25 @723K	0.35

In another study, Maji et al. [84] observed the drastic descend of the lattice thermal conductivity in $Zr_{0.5}Hf_{0.5}Co_{1-x}Rh_xSb_{0.99}Sn_{0.01}$ half-Heusler alloy via mass and strain fluctuation by Rh substitution at the Co sites. The effect of Sb doping on thermoelectric characteristics of the full-Heusler Fe_2VAl alloy was evaluated [112]. The results showed that the thermal conductivity remarkably decreased by the Sb substitution of the Al atoms. In this case, the mass fluctuating occurred in the $Fe_2VAl_{1-x}Sb_x$ alloy was due to the large mass difference of Sb and the constituent elements [112]. In another study [79], Zr, Hf, and Ti were utilized to change the mass and strain field caused by their different masses and atomic radii in the $Ti_x(ZrHf)_{0.99-x}V_{0.01}Ni_{0.9}Pd_{0.1}Sn_{0.99}Sb_{0.01}$ half-Heusler alloy. Based on the results, the best thermoelectric properties achieved were $S = -206\ \mu VK^{-1}$, $\sigma = 1408.5\ Scm^{-1}$, $\kappa = 5.13\ W\,m^{-1}\,K^{-1}$, and finally, $zT = 0.92$ at 820 K for x_{Ti} equals to 0.3.

As shown in Fig. 3, vacancies or voids can also provide mass fluctuations. Vacancies can be regarded as weightless nano-sized impurities or point defects which can scatter high-frequency phonons. Lee et al. [80] illustrated the influences of the vacancies on thermal conductivity by increasing the Nb concentration in $Ti_{0.5}(ZrHf)_{0.49}Nb_xNi_{0.9}Pd_{0.1}Sn_{0.98}Sb_{0.02}$, which induced voids in NiSn phase. The sample showed a thermal conductivity reduction from 6.20 to 5 $WK^{-1}m^{-1}$ with the highest zT of 0.66 at 900 k.

The electrical conductivity may be reduced substantially by the addition of the alloying element in the Heusler TEs. The added elements can interact with the Heusler alloy constituent elements either by dissolving (substitutionally or interstitially) in the matrix or forming the second phase precipitates both of which impacting the electrical conductivity [113]. Therefore, the trade-off between the thermal and electrical conductivities must be carefully considered in the mass fluctuation engineering similar to the other scattering strategies, e.g., nanostructuring [25].

3.3. Multi-phases phonon scattering

Another effective technique to scatter phonon is based on the multi-phase engineering of the material structure. Domain interfaces corresponding to multi-phases can generate mass or lattice spacing discontinuity that can scatter phonons, and reduce the lattice thermal conductivity [12,64,114]. In the multi-phase structures, the coexisting Heusler phases (half or full) can be modeled by introducing different K_i and m_i values (equation (7)) corresponding to the different atoms and chemical bonds. The variations in the K_i and m_i lead to scatterings at the phase interfaces affecting the thermal conductivity. At sufficiently large grain sizes, each phase has its own physical properties (and

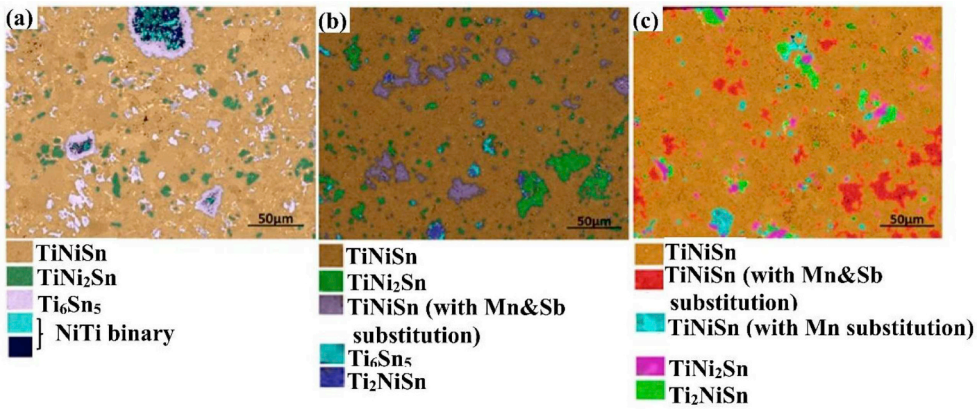

Fig. 7. Backscatter electron (BSE) images of $(TiNiSn)_{1-x}$ + $(MnNiSb)_x$ system: (a) x = 0, (b) x = 0.05, and (c) x = 0.1 (Ref. [110] with permission).

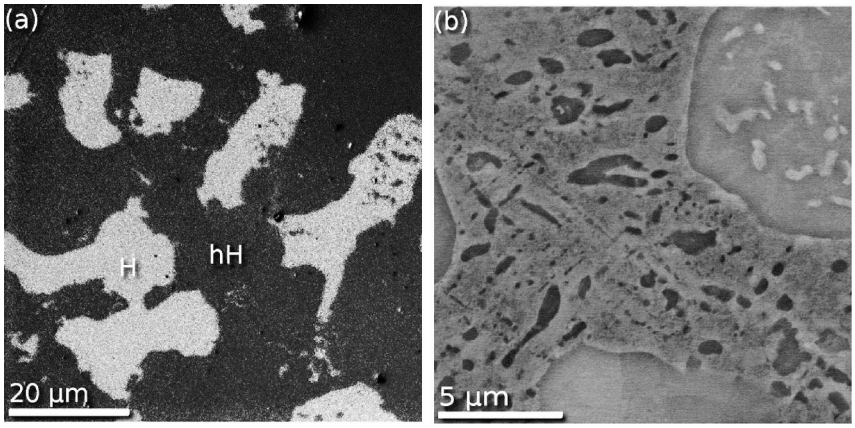

Fig. 8. (a) Optical and (b) scanning electron images of polished surfaces of the binary phase $TiNi_{1.15}Sn$ alloy. In (a), H stands for the $TiNi_2Sn$ full-Heusler alloy, and hH shows the TiNiSn half-Heusler phase (hH). (b) Illustration of a region containing half-Heusler precipitates. (Ref. [118] with permission).

phonon group velocity), and the multi-phase effect can be modeled merely by a phonon scattering causing by the interfaces. However, when the domains become small and comparable to the dominant phonon wavelengths, the individual phase properties alter. In that case, the phonon dispersion (and velocity) changes, and the models based on an effective medium, such as coherent potential approximation, are more appropriate [115–117]. Douglas [118] showed the effects of phase separation on the thermoelectric factors of half-Heusler TiNiSn in corresponding to the presence of phase-segregated Heusler $TiNi_2Sn$ alloy. In this study, the $TiNi_{1.15}Sn$ containing two phases of $TiNi_2Sn$ and TiNiSn (Fig. 8) showed a significant reduction of the thermal conductivity by nearly 10%–30%. Hence, the zT value increased by about 25% compared to that of the TiNiSn alloy reaching 0.44 at 800 K.

Also, as shown in Table 4, the phase separation strategy was carried out successfully to enhance the zT value of the $Ti_{0.25}Hf_{0.75}CoSb_{0.85}Sn_{0.15}$ alloy to around 1.2 at 710 K. In this study, the phase separated half-Heusler $Ti_{0.25}Hf_{0.75}CoSb_{0.85}Sn_{0.15}$ alloy was synthesized, which showed the reduction of thermal conductivities.

Solidification and cooling procedures can influence the phase decomposition because the atomic diffusion is dependent on the cooling rates and temperatures. Consequently, the formation of the new phases can interfere with phonon transport due to differences in phase structure and atomic arrangement [12]. Fig. 9 shows the effects of temperature on phase transformation and segregation of CoVSn compounds within a specific mole percent to the alloy mixture.

According to Table 7, the phase composition can be adjusted by temperature leading to the formation of one to three different phases at each specific molar ratio of the elements in CoVSn (Fig. 9). Each phase has its own thermal and electrical properties; therefore, the composite material can take a wide range of properties depending on the choice of the molar ratios and the temperature of thermal treatment. Thus by controlling the temperature, the multiphase structures could be engineered to introduce the required conditions towards phonon scattering at the phase boundaries.

Schwall et al. [83] evaluated the effects of phase separation on the thermal conductivities of the half-Heusler $Zr_{(1-x)}Hf_xNiSn$ series. They showed that the samples with more phases have higher electrical conductivity, but lower thermal conductivity, despite their higher electronic thermal conductivity. The small thermal conductivity of these samples was associated with the phase separation, which leads to increased interfacial phonon scattering.

Similar to the mass fluctuation mechanism, energy filtering may also occur at the interface of the domains [119]. For example, Agarwal et al. [105] doped graphene into Bi_2Te_3 to make energy filtering that not only decreased the thermal conductivity but also improved the Seebeck coefficient ($S = -117$ ($\mu V.K^{-1}$)). The samples showed $zT = 0.92$ near 405 K. It was concluded that the phase separation induced sub-micron multi-phase domains, which acted as scattering centers and reduced the thermal conductivity.

4. Dominant phonon scattering mechanisms in heusler crystal structures

Heusler alloys can be conveniently doped by replacing the elements in the fcc sub-lattices with other atoms to optimize their thermoelectric properties [55]. The optimum doping concentration often moves the peak of the figure-of-merit of these alloys to the moderate temperature ranges [49,120]. In this range of temperature, the impurity scattering is often significant and dominates the phonon transport as schematically shown in Fig. 10.

To demonstrate the underlying physics of the trend observed in Fig. 10, as a case study of a half-Heusler alloy, the thermal conductivity of NiTiSn was calculated and compared with the experimental data (Fig. 11a) [121]. The variation of phonon mean free path (MFP) versus phonon wavelength was also calculated as shown in Fig. 11.b. This plot demonstrates the contributions of various phonon wavelengths and MFP to the thermal conductivity. Model calculations followed the methodology described in Refs. [102,122].

In Fig. 11.b, the green dot-line following by the blue, and red dot-lines represent the contribution of phonons with MFP > 100 nm to the accumulated thermal conductivities (κ_l) at the temperatures of 300 K and 650 K, respectively. Based on this figure, the phonons with MFP > 100 nm contribute to the thermal conductivities equal to 4.8 W/mk at a temperature of 300K. In other word, if all the phonons with MFP > 100 nm are 100% scattered, the thermal conductivities will be reduced by the amount of 4.8 W/mk. However, at a higher temperature of 650K, by eliminating the phonons with the MFP > 100 nm, the thermal conductivity is reduced only by the amount of 2.4 W/mk. Therefore, nanostructuring is much less effective at 650 K (by ~50%) compared to at 300 K. Note that material with grain sizes of 100 nm does not necessarily filter all the phonons with MFP > 100 nm. As discussed earlier, phonons can experience different types of scattering at an interface leading to different kinds of relaxation times such as due to reflection and refraction, diffusive, or Rayleigh scattering. Therefore, the hard cuts as shown in Fig. 11.b are the extreme cases, and in practice, one would need much smaller grains than 100 nm to filter all or most of the phonons with MFP > 100 nm.

Fig. 11.b also shows that the low energy phonons with high MFPs have a small contribution to the overall thermal conductivity, especially at higher temperatures where the half Heusler material has a high zT. In contrast, the accumulated thermal conductivity increases significantly versus phonon energies although the high-energy phonons have smaller MFPs, mainly due to the larger density of states at higher energy.

As mentioned earlier, the scattering of these high-energy (short

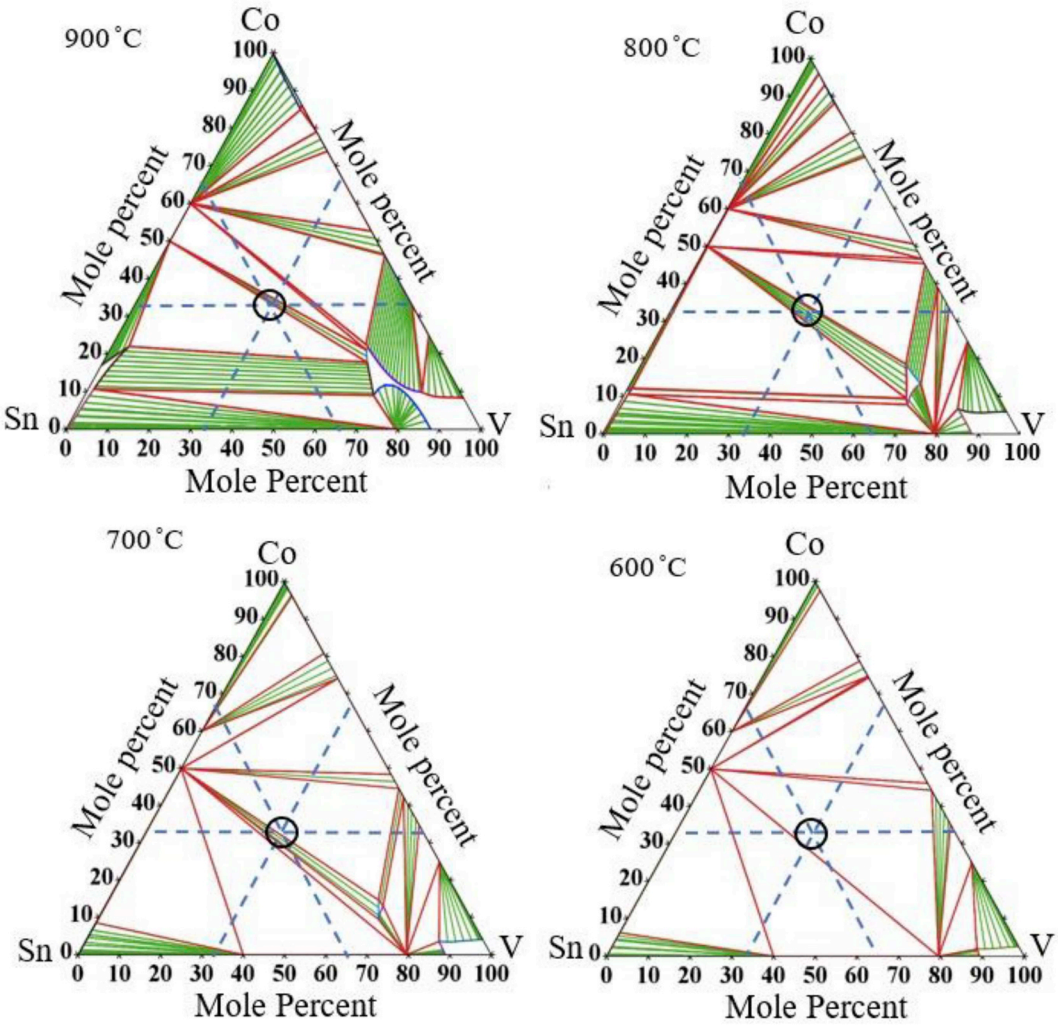

Fig. 9. Multiphase formation by controlling the synthesis temperature of CoVSn.

Table 7
Phase composition of CoVSn alloys at 600,700,800 and 900 °C as mentioned in Fig. 9.

T (°C)	Phase/Crystal structure/Elements
900	Equilibrium line between two areas of (CoSn, BCC (Co,V,Sn)) and (Liquid, CoSn, BCC (Co,V,Sn))
800	Equilibrium line between two areas of (CoSn, BCC (Co,V,Sn)) and (ALTA_Sigma (V, Co), CoSn, BCC (Co,V,Sn))
700	ALTA_Sigma (V, Co)+ CoSn+BCC (Co,V,Sn)
600	ALTA_Sigma (V, Co)+ CoSn+SnV_3

wavelength) phonons is most efficient through mass and lattice constant fluctuation such as by point defect strategy. Both a_i and M_i in the point defect relaxation time can be manipulated readily by substitutional doping in Heusler compounds to decrease the lattice thermal conductivity effectively.

5. Summary

Thermoelectric generators can contribute to controlling global warming by generating electrical power from low-grade heat which is otherwise wasted in mechanical engines or industrial processes. Heusler semiconductors are known as eco-friendly materials with potentially good thermoelectric properties. The high lattice thermal conductivity of these compounds, however, limited their effectiveness. The transport of

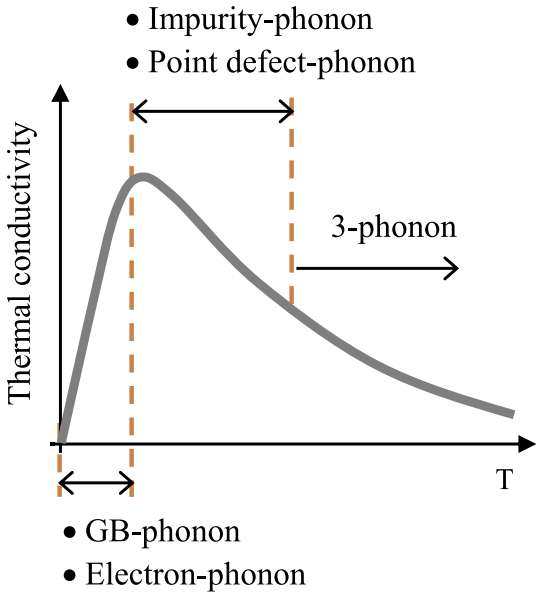

Fig. 10. Dominant phonon scattering mechanisms versus temperature.

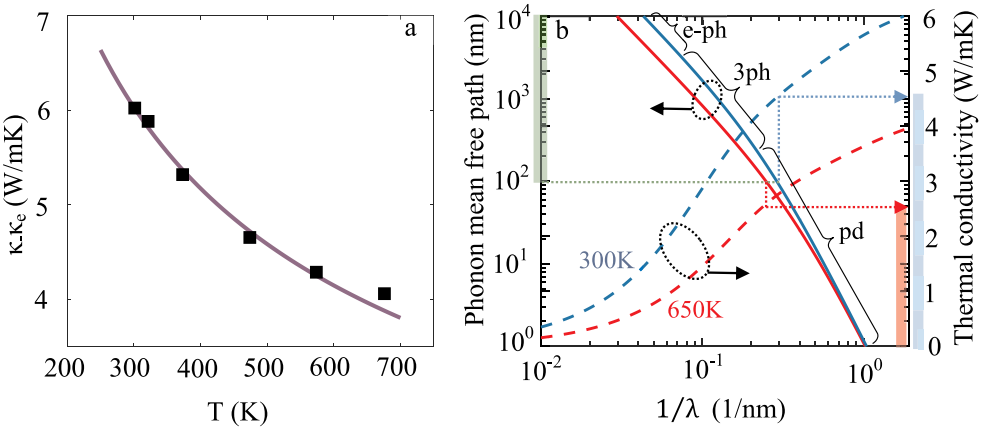

Fig. 11. (a) Thermal conductivity of NiTeSn half-Heusler alloy versus temperature (Symbols: experimental data adapted from Ref. [121] with permission. Line: Theoretical modeling). (b) Comparison of the corresponding phonon mean free path and accumulated thermal conductivity versus reciprocal of phonon wavelength at 300 K and 650 K (e-ph: electron-phonon; 3ph: 3-phonon; pd: point defect).

phonons as the primary heat carriers are to be impaired to reduce thermal conductivity. The critical phonon engineering strategies applicable to Heusler compounds were discussed. These strategies must be implemented according to the working temperature to deliver an effectively low thermal conductivity in practice. At low temperature, the acoustic branches with long wavelength are mainly responsible for heat transfer. These acoustic branches can be distracted by grain/crystal boundaries with length scales comparable to the phonon wavelength. When the grain size is less than the mean free path of these phonons, the thermal conductivity is reduced significantly. By increasing the temperature, the phonons occupy higher frequency states creating mid to short wavelength phonons. In this region, the mass and lattice spacing fluctuations can be more effective in phonon scattering. This can be achieved via substitutional doping of various elements into the Heusler alloy with a large discrepancy of masses and strain fields. The domain interfaces in the multi-phase structures can also generate mass and lattice spacing discontinuities and decrease the thermal conductivity in the medium temperature range. At high temperature, the phonon scattering is often dominated by 3-phonon scattering which is a function of the Grüneisen constant (or the anharmonicity parameter) and is effectively independent of the grain sizes. Among the discussed phonon scattering strategies, the mass and lattice constant fluctuations, due to point defects and/or elemental substitutions, are the most effective methods for improving the thermoelectric performance of Heusler compounds over their optimum working temperature. It should be noted that because of the trade-off between the thermal and the electrical conductivity, the phonon scattering strategies must be implemented carefully as sometimes these methods may cause a significant reduction of the thermoelectric power factor.

Acknowledgment

This work has been supported by the Australian Government Research Training Program Scholarship and The ARC Research Hub for Graphene Enabled Industry Transformation at the University of Adelaide. Also, this study is partially based upon work supported by the National Science Foundation (NSF) under grant numbers ECCS-1351533, ECCS-1711253, and CMMI-1363485.

References

[1] Geoff Martin ES. Effectiveness of state climate and energy policies in reducing power-sector CO2 emissions. Nat Clim Change 2017;7:912–9.
[2] Makeover E. Australia's top 20 greenhouse gas emitters. 2018.
[3] Martin Drechsler JE, Lange Martin, Frank Masurowski, Meyerho Jürgen, Oehlmann Malte. Efficient and equitable spatial allocation of renewable power plants at the country scale. Nat Energy 2017;2:1–9.
[4] Talal Yusaf SG, Borserio JA. Potential of renewable energy alternatives in Australia. Renew Sustain Energy Rev 2011;15:2214–21.
[5] Pragya Nema RKN. Saroj Rangnekar, Minimization of green house gases emission by using hybrid energy system for telephony base station site application. Renew Sustain Energy Rev 2010;14:1635–9.
[6] Zaferani SH. Energy sources, economic policies and sustainable technologies. Environmental science & engineering. Houston, TX 77072: SP LLC Publisher; 2017.
[7] World energy outlook-2017 (WEO-2017). 2017 Available from: http://www.iea.org.
[8] Yadav MK, B.S. First principles study of thermoelectric properties of Li-based half-Heusler alloys. J Alloy Comp 2015;622:388–93.
[9] Ding LC, A.A, Tan L. A review of power generation with thermoelectric system and its alternative with solar ponds. Renew Sustain Energy Rev 2018;81:799–812.
[10] Elsheikh Mohamed Hamid, D.A.S, Sabri Mohd Faizul Mohd, Said Suhana Binti Mohd, Hassan Masjuki Haji, Bashir Mohamed Bashir Ali, Mohamad Mahazani. A review on the moelectric renewable energy : principle parameters that affect their performance. Renew Sustain Energy Rev 2014;30:337–55.
[11] Xi Hongxia, Luo Lingai, Fraisse Gilles. Development and applications of solar-based thermoelectric technologies. Renew Sustain Energy Rev 2007;11:923–36.
[12] Mena JM, H.G.S, Gruhn T, Emmerich H. Ab initio study of domain structures in half-metallic CoTi1-xMnxSb and thermoelectric CoTi1-xScxSb half-Heusler alloys. J Alloy Comp 2015;650:728–40.
[13] Zaferani SH. Using silane products on fabrication of polymer-based nanocomposite for thin film thermoelectric devices. Renew Sustain Energy Rev 2017;71:359–64.
[14] Abdolvand R, Vashaee D. Nanowire thermoelectric infrared detector. WO patent 2013, abdolvand reza. Vashaee Daryoosh USA; Sep. 26, 2013.
[15] D Vashaee AS. HgCdTe superlattices for solid-state cryogenic refrigeration. Appl Phys Lett 2006;88(13). 132110-132110.
[16] Amirkoushyar Ziabari MZ, Vashaee Daryoosh, Ali Shakouri. Nanoscale solid-state cooling: a review. Rep Prog Phys 2016;79.
[17] F Suarez DP, Ladd C, Vashaee D, Dickey MD, Öztürk MC. Flexible thermoelectric generator using bulk legs and liquid metal interconnects for wearable electronics. Appl Energy 2017;202:736–45.
[18] Lobat Tayebi ZZ, Vashaee Daryoosh. Design optimization of microfabricated thermoelectric devices for solar power generation. Renew Energy 2014;66:166–73.
[19] Nozariasbmarz A, A.T.R, Zamanipour Z, Krasinski JS, Tayebi L, Vashaee D. Enhancement of thermoelectric power factor of silicon germanium films grown by electrophoresis deposition. Scripta Mater 2013;69(7):549–52.
[20] Zahra Zamanipour XS, Dehkordi Arash M, Krasinski Jerzy S, Vashaee Daryoosh. The effect of synthesis parameters on transport properties of nanostructured bulk thermoelectric p-type silicon germanium alloy. Phys Status Solidi 2012;209(10):2049–58.
[21] Zamanipour Z, X.S, Mozafari M, Krasinski JS, Tayebi L, Vashaee D. Synthesis, characterization, and thermoelectric properties of nanostructured bulk p-type MnSi1.73, MnSi1.75, and MnSi1.77. Ceram Int 2013;39(3):2353–8.
[22] Sumithra S, T NJ, Misra DK, Nolting WM, Poudeu PFP, Stokes KL. Adv. Energy Mater. 2011;1:1141–7.
[23] Zamanipour Z, V D. J Appl Phys 2012;112.
[24] Zamanipour Zahra, V D. Comparison of thermoelectric properties of p-type nanostructured bulk Si0.8Ge0.2 alloy with Si0.8Ge0.2 composites embedded with CrSi2 nano-inclusions. J Appl Phys 2012;112.
[25] Snyder GJ, T.E.S. Complex thermoelectric materials. Nat Mater 2008;7(2):105–14.
[26] P Norouzzadeh CM, Vashaee D. J Phys Condens Matter 2013;25(47).
[27] P Norouzzadeh CM, Vashaee D. J Appl Phys 2013;114(16).
[28] Norouzzadeh Payam, M CW, Vashaee Daryoosh. Prediction of giant thermoelectric power factor in type-VIII clathrate Si46. Nature 2014(4):7028. Scientific Reports.
[29] Norouzzadeh P, M CW, Vashaee D. Prediction of a large number of electron pockets near the band edges in type-VIII clathrate Si46 and its physical properties from first principles. J Phys: Condens Matter 2013;25.
[30] Heremans JP, V.J, Toberer ES, Saramat A, Kurosaki K, Charoenpakdee A, Yamanaka S, Snyder G. Science 2008;32(554).
[31] Vashaee D, Z Y, Shakouri A, Zeng G, Chiu YJ. Phys Rev B 2006;74(19).
[32] Daryoosh Vashaee JC, Zhang Yan, Ali Shakouri, Zeng Gehong, LaBounty Chris, Fan Xiaofeng, Piprek Joachim, Bowers John E, Croke Edward. MODELING AND OPTIMIZATION OF SINGLE-ELEMENT BULK SiGe THIN-FILM COOLERS. Microscale Thermophys Eng 2004;8(2):99–118.

[33] Zide JMO, V D, Bian ZX, Zeng G, Bowers JE, Shakouri A, Gossard AC. Phys Rev B Condens Matter 2006;74.
[34] Vashaee D, S A. Phys Rev Lett 2004;92(10).
[35] Vashaee D, S A. J Appl Phys 2004;95(3).
[36] Vashaee D, S A. J Appl Phys 2007;101(5):1–5.
[37] Payam Norouzzadeh KFE, Vashaee Daryoosh. The effect of nanostructuring on the spectral population of electrons and phonons. J Alloy Comp 2018;753:234–8.
[38] Milad Mohebali YL, Tayebi Lobat, Krasinski Jerzy S, Vashaee Daryoosh. Thermoelectric figure of merit of bulk FeSi2-Si0.8Ge0.2 nanocomposite and a comparison with β-FeSi2. Renew Energy 2015;74:940–7.
[39] Amin Nozariasbmarz ZZ, Norouzzadeh Payam, Krasinski Jerzy S, Vashaee Daryoosh. Enhanced thermoelectric performance in a metal/semiconductor nanocomposite of iron silicide/silicon germanium. RSC Adv 2016;6:49643–50.
[40] Keppens V, M D, Sales B, Chakoumakos B, Dai P, Coldea R, Maple M, Gajewski D, Freeman E, Bennington S. Nature 1998;395(876). (London).
[41] Hermann RP, J R, Schweika W, Grandjean F, Mandrus D, Sales BC, Long GJ. Phys Rev Lett 2003;90.
[42] Koza MM, J MR, Viennois R, Mutka H, Girard L, Ravot D. Nat Mater 2007;7(805).
[43] Norouzzadeh Payam, C.W.M. Daryoosh Vashaee, Phonon dynamics in type VIII Si clathrates: beyond the rattler concept. Phys Rev B 2017;95.
[44] Norouzzadeh P, C.W.M, Vashaee D. Electronic, elastic, vibrational, and thermodynamic properties of type-VIII clathrates Ba8Ga16Sn30 and Ba8Al16Sn30 by first principles. J Appl Phys 2013;114.
[45] Norouzzadeh P, C.W.M, Vashaee D. Structural, electronic, phonon and thermodynamic properties of hypothetical type-VIII clathrates Ba8Si46 and Ba8Al16Si30 from first principles. J Alloy Comp 2013;587:474–80.
[46] Ahmed R, N.S.M, Ul Haq B, Shaari A, Alfaifi S, Butt FK, Muhamad MN, Ahmed M, Tahir SA. Investigations of electronic and thermoelectric properties of half-Heusler alloys XMgN (X=Li, Na, K) by first-principles calculations. Mater Des 2017;136:196–203.
[47] Visconti A, N C, Leforestier J, Mingo N, Bernard-Granger G. Influence of the addition of HfO2 particles on the thermoelectric properties of an N-type half-Heusler alloy sintered by spark plasma sintering. J Alloy Comp 2017;709:36–41.
[48] Poon GJ. Chapter 2 Electronic and thermoelectric properties of Half-Heusler alloys. Semiconductors and semimetals. Elsevier; 2001. p. 37–75.
[49] Wenjie Xie AW, Tang Xinfeng, Zhang Qingjie, Poon Joseph, Tritt Terry M. Recent advances in nanostructured thermoelectric half-heusler compounds. Nanomaterials 2012;2:379–412.
[50] Zeier Wolfgang G, J.S, Hautier Geoffroy, Aydemir Umut, Gibbs Zachary M, Felser Claudia, Jeffrey Snyder G. Engineering half-Heusler thermoelectric materials using Zintl chemistry. Nat Rev Mater 2016;1:1–10.
[51] Stefano Sanvito CO, Xue Junkai, Tiwari Anurag, Zic Mario, Archer Thomas, Tozman Pelin, Venkatesan Munuswamy, Coey Michael, Curtarolo Stefano. Accelerated discovery of new magnets in the Heusler alloy family. Sci Adv 2017;3:1–9.
[52] Ahamed R, G R, Xie Z, Chen L, Munroe P, Xu S. Powder processing and characterisation of a quinary Ni-Mn-Co-Sn-Cu Heusler alloy. Powder Technol 2018;324:69–75.
[53] Ferromagnetic shape memory heusler materials: synthesis, microstructure characterization and magnetostructural properties. Materials 2018;11(988):1–34.
[54] Mohankumar R, S.R, Rajagopalan M, Manivel Raja M, Kamat SV, Kumar J. Effect of Fe substitution on the electronic structure, magnetic and thermoelectric properties of Co2FeSi full Heusler alloy: a first principle study. Comput Mater Sci 2015;109:34–40.
[55] Tanja Graf CF, Parkin Stuart SP. Simple rules for the understanding of Heusler compounds. Prog Solid State Chem 2011;39:1–50.
[56] Galanakis I. Theory of heusler and full-heusler compounds. In: Felser AHC, editor. Heusler alloys. Springer; 2016.
[57] Gunn C. Periodic table Available from: http://www.science-teachers.com/printable_periodic_tables.htm.
[58] Katsuyama S, R.M, Ito M. Thermoelectric properties of half-Heusler alloys Zr1−xYxNiSn1−ySby. J Alloy Comp 2007;428:262–7.
[59] Kaller M, D.F, Gelbstein Y. Sc solubility in p-type half-Heusler (Ti1-cScc)NiSn thermoelectric alloys. J Alloy Comp 2017;729:446–52.
[60] Misra PK. Phonons and lattice vibrations. Physics of condened matter. US: Elsevier; 2011. p. 688.
[61] Kim W. Strategies for engineering phonon transport in thermoelectrics. J Mater Chem C 2015;3:10336–48.
[62] Prashun Gorai VS, Toberer Eric S. Computationally guided discovery of thermoelectric materials. Nat Rev Mater 2017;2:1–16.
[63] Balandin AA. Thermal properties of graphene and nanostructured carbon materials. Nat Mater 2011;10:569–81.
[64] Matthias Schrade KB, Eliassen Simen NH, Guzik Matylda N, Echevarria-Bonet Cristina, Sørby Magnus H, Jenuš Petra, Hauback Bjørn C, Tofan Raluca, Gunnæs Anette E, Persson Clas, Løvvik Ole M, Finstad Terje G. The role of grain boundary scattering in reducing the thermal conductivity of polycrystalline XNiSn (X = Hf, Zr, Ti) half-Heusler alloys. Sci Rep Nat 2017;7:1–7.
[65] Yaw Wang Chai TO, Kenjo Takahiro, Kimura Yoshisato. The effect of an isoelectronic TieZr substitution on Heusler nanoprecipitation and the thermoelectric properties of a (Ti0.2,Zr0.8) Ni1.1Sn half-Heusler alloy. J Alloy Comp 2016;662:566–77.
[66] Jiong Yang LX, Qiu Wujie, Wu Lihua, Shi Xun, Chen Lidong, Yang Jihui, Zhang Wenqing, Uher Ctirad, Singh David J. On the tuning of electrical and thermal transport in thermoelectrics: an integrated theory–experiment perspective. npj Comput Mater Nat 2016;2:1–17.
[67] Kittel C. Introduction to solid state physics. New York: John Wiley & Sons; 2004.
[68] Holland MG. Analysis of lattice thermal conductivity*. Phys Rev 1963;132(6):2461–71.
[69] Ramachandran B, Y.H.L, Kuo YK, Kuo CN, Gippius AA, Lue CS. Thermoelectric properties of Heusler-type Ru2VAl1−xGax alloys. Intermetallics 2018;92:36–41.
[70] Steigmeier EF,AB. Phys Rev 1964;136(A1149).
[71] Callaway J. Model for lattice thermal conductivity at low temperatures. Phys Rev 1959;113(1046).
[72] Nikhil Satyala PN. Daryoosh vashaee, nano bulk thermoelectrics: concepts, techniques, and modeling. Thermoelectrics at nanoscale. Springer; 2014. p. 141–83.
[73] Nikhil Satyala DV. Modeling of thermoelectric properties of magnesium silicide (Mg2Si). J Electron Mater 2012;41(6):1785–91.
[74] Ziman JM. Philos Mag 1957;2(192).
[75] Ziman RM. Philos Mag 1956;1(191).
[76] Pomeranchuk I. On the thermal conductivity of dielectrics. Phys Rev 1941:60.
[77] Pomeranchuk I. On the thermal conductivity of dielectrics at temperatures lower than that of debye. J Phys 1942;6(6):235–50.
[78] Ferry DK. Semiconductor transport. London: Taylor & Francis; 2000.
[79] Lee P, S.C.T, Chao L. High-temperature thermoelectric properties of Tix(ZrHf)0.99−xV0.01Ni0.9Pd0.1Sn0.99Sb0.01 half-Heusler alloys. J Alloy Comp 2010;496:620–3.
[80] Lee P, L.C. High-temperature thermoelectric properties of Ti0.5(ZrHf)0.5−xNbxNi0.9Pd0.1Sn0.98Sb0.02 half-Heusler alloys. J Alloy Comp 2010;504:192–6.
[81] de Boor J, S.G, Kolb H, Dasgupta T, Mueller E. Thermoelectric transport and microstructure of optimized Mg2Si0.8Sn0.2. J Mater Chem C 2015;3:10467–75.
[82] Maji P, J.P.A.M, Zhou X, Chi H, Uher C, Poudeu PFP. Thermoelectric performance of nanostructured p-type Zr0.5Hf0.5Co0.4Rh0.6Sb1−xSnx half-Heusler alloys. J Solid State Chem 2013;202:70–6.
[83] Michael Schwall BB. On the phase separation in n-type thermoelectric half-heusler materials. Materials 2018;649(11).
[84] Pramathesh Maji NT, Misra DineshK, HeikeGabrisch Kevin Stokes, Poudeu PierreFP. Effects ofRhonthethermoelectricperformanceofthe p-type Zr0.5Hf0.5Co1xRhxSb0.99Sn0.01 half-Heusler alloys. J Solid State Chem 2010;183:1120–6.
[85] Appel O, T.Z, Kalabukhov S, Beeri O, Gelbstein Y. Morphological effects on the thermoelectric properties of Ti0.3Zr0.35Hf0.35Ni1+dSn alloys following phase separation. J Mater Chem C 2015;3:11653–9.
[86] Bouyrie Y, C.C, Ohorodniichuk V, Malaman B, Dauscher A, Tobola J, Lenoir B. Crystal structure, electronic band structure and high-temperature thermoelectric properties of Te-substituted tetrahedrites Cu12Sb4-xTexS13 ($0.5 \le x \le 2.0$). J Mater Chem C 2015;3:10476–87.
[87] Biswas SNGaK. Sb deficiencies control hole transport and boost the thermoelectric performance of p-type AgSbSe2. J Mater Chem C 2015;3:10415–21.
[88] Hu Y, S.K.B, Grebenkemper JH, Kauzlarich SM. The effect of light rare earth element substitution in Yb14MnSb11 on thermoelectric properties. J Mater Chem C 2015;3:10566–73.
[89] Liu Z, G H, Shuai J, Wang Z, Mao J, Jie Q, Wang D, Cai W, Sui J, Ren Z. The effect of Nickel doping on electron and phonon transport in n-type nanostructured thermoelectric material CoSbS. J Mater Chem C 2015;3:10442–50.
[90] Ma JM, S.M.C, Zeier WG, Vo T, Allmen PV, Snyder GJ, Kaner RB, Fleurial J, Bux SK. Mechanochemical synthesis and high temperature thermoelectric properties of calcium-doped lanthanum telluride La 3 - x Ca x Te 4. J Mater Chem C 2015;3:10459–66.
[91] Pan Y, T.W, Wu C, Li J. Electrical and thermal transport properties of spark plasma sintered n-type Bi2Te3-xSex alloys: the combined effect of point defect and Se content. J Mater Chem C 2015;3:10583–9.
[92] Rausch E, B.B, Stahlhofen JM, Ouardi S, Burkhardt U, Felser C. Fine tuning of thermoelectric performance in phase-separated half-Heusler compounds. J Mater Chem C 2015;3:10409–14.
[93] Visconti A, G GB, Navone C, Leforestier J, Mingo N. Microstructure investigations and thermoelectric properties of an N-type Half-Heusler alloy sintered by spark plasma sintering. Scripta Mater 2016;123:100–4.
[94] Chen G. Nanoscale energy transport and conversion. New York: Oxford University Press; 2005.
[95] Mikami M, K.K. Effect of Bi addition on microstructure and thermoelectric properties of Heusler Fe2VAl-sintered alloy. J Alloy Comp 2008;466:530–4.
[96] Shigeru Katsuyama TK. Effect of mechanical milling on thermoelectric properties of half-Heusler ZrNiSn0.98Sb0.02 intermetallic compound. Mater Sci Eng, B 2010;166(1):99–103.
[97] Sin-Shien Lin C-NL. Effect of ball milling and post treatment on crystal defects and transport properties of Bi2(Se,Te)3 compounds. J Appl Phys 2011;110:1–7.
[98] Meng-Pei Lu C-NL. Mechanical and thermal processing effects on crystal defects and thermoelectric transport properties of Bi2(Se,Te)3 compounds. J Alloy Comp 2013;571:178–82.
[99] Yecheng Zhou WL, Wu Minghui, Zhao Li-Dong, He Jiaqing, Wei Su-Huai, Huang Li. Influence of defects on the thermoelectricity in SnSe: a comprehensive theoretical study. Phys Rev 2018;97:1–8.
[100] Son JH, M.W.O.B.S.K.S.D.P, Min BK, Kim MH, Lee HW. Effect of ball milling time on the thermoelectric properties of p-type (Bi,Sb)2Te3. J Alloys Comp 2013;566:168–74.
[101] Bhattachary S, M.J.S, Russell M, Tritt TM, Xia Y, Ponnambalam V, Poon SJ, Thadhani N. Effect of boundary scattering on the thermal conductivity of TiNiSn-based half-Heusler alloys. Phys Rev B 2008;77(18).
[102] Nikhil Satyala DV. The effect of crystallite size on thermoelectric properties of bulk nanostructured magnesium silicide (Mg2Si) compounds. Appl Phys Lett 2012;100(7).
[103] Payam Norouzzadeh ZZ, Krasinski Jerzy S, Vashaee Daryoosh. The effect of nanostructuring on thermoelectric transport properties of p-type higher manganese

silicide MnSi1.73. J Appl Phys 2012;112(12):1–7.
[104] Mohamed S, El-Asfoury MNAN, Nakamura Koichi, Abdel-Moneim Ahmed. Enhanced thermoelectric performance of Bi85Sb15-graphene composite by modulation carrier transport and density of state effective mass. J Alloy Comp 2018;745:331–40.
[105] Khushboo Agarwal VK, Varandani Deepak, Dhar Ajay, Mehta BR. Nanoscale thermoelectric properties of Bi2Te3 e Graphene nanocomposites: conducting atomic force, scanning thermal and kelvin probe microscopy studies. J Alloy Comp 2016;681:394–401.
[106] Shupin Zhang AL, Sun Kangning. Thermoelectric properties of Graphene/Mn0.7Zn0.3Fe2O4 composites. Ceram Int 2017;43:8643–7.
[107] Haijie Chen CY, Liu Huili, Zhang Ganghua, Wan Dongyun, Huang Fuqiang. Thermoelectric properties of CuInTe2/graphene composites. CrystEngComm 2013;15:6648–51.
[108] Chenguang Fu HX, Zhu TJ, Xie Jian, Zhao XB. Enhanced phonon scattering by mass and strain field fluctuations in Nb substituted FeVSb half-Heusler thermoelectric materials. J Appl Phys 2012;112(12).
[109] Ben Huang PZ, Xuqiu Yang, Guodong LI. Effects of mass fluctuation on thermal transport properties in bulk Bi2Te3. J Electron Mater 2016;46(5):2797–806.
[110] Tanya Berry CF, Auffermann Gudrun, Fecher Gerhard H, Walter Schnelle, Serrano-Sanchez Federico, Yuan Yue, Liang Hong. Claudia felser, enhancing thermoelectric performance of TiNiSn half-heusler compounds via modulation doping. Chem Mater 2017;29:7042–8.
[111] Mohamed S, El-Asfoury MNAN, Nakamura Koichi, Abdel-Moneim Ahmed. Thermoelectric power factor performance of Bi85Sb15/graphene composite. Jpn J Appl Phys 2016;55:1–5.
[112] Mikami M, S.T, Kobayashi K. Thermoelectric properties of Sb-doped Heusler Fe2VAl alloy. J Alloy Comp 2009;484:444–8.
[113] Chai YW, K.Y, Kimura Y. Intrinsic point defects in thermoelectric half-Heusler alloys. Scripta Mater 2014;83:13–6.
[114] Michael Schwallab BB. Phase separation as a key to a thermoelectric high efficiency. Phys Chem Chem Phys 2013;15:1868–72.
[115] Soven P. Coherent-potential model of substitutional disordered alloys. Phys Rev 1967;809(156).
[116] Sheng P. Introduction to wave scattering, localization and mesoscopic phenomena. Berlin Heidelberg: Springer-Verlag; 2006.
[117] Economou EN. Green's function in quantum physics. New York: Springer-Verlag; 1979.
[118] Jason E, Douglas, B CS, Miao Mao-Sheng, Torbet Chris J, Stucky Galen D, Pollock Tresa M, Seshadri Ram. Enhanced thermoelectric properties of bulk TiNiSn via formation of a TiNi2Sn second phase. Appl Phys Lett 2012;101(18).
[119] Yuewen Zhang HM, Bing Sun a, Liu Binwu, Liu Haiqiang, Kong Lingjiao, Liu Baomin, Jia Xiaopeng, Chen Xin. Thermoelectric performance of graphene composited BiSbTe bulks by high pressure synthesis. J Alloy Comp 2017;715:344–8.
[120] Shuo Chen ZR. Recent progress of half-Heusler for moderate temperature thermoelectric applications. Mater Today 2013;16(10):387–95.
[121] Hiroaki Muta TK, Kurosaki Ken, Yamanaka Shinsuke. High-temperature thermoelectric properties of Nb-doped MNiSn (M = Ti, Zr) half-Heusler compound. J Alloy Comp 2009;469:50–5.
[122] Minnich AJ, L H, Wang XW, Joshi G, Dresselhaus MS, Ren ZF, Chen G, Vashaee D. Modeling study of thermoelectric SiGe nanocomposites. Phys Rev B 2009:80.

ACS APPLIED ENERGY MATERIALS

www.acsaem.org Article

Assessment of Thermoelectric, Mechanical, and Microstructural Reinforcement Properties of Graphene-Mixed Heterostructures

Sadeq Hooshmand Zaferani, Reza Ghomashchi,* and Daryoosh Vashaee*

Cite This: https://dx.doi.org/10.1021/acsaem.1c00015 Read Online

ACCESS | Metrics & More | Article Recommendations | Supporting Information

ABSTRACT: We examine the role of graphene nanoplates (GNPs) in the critical properties of thermoelectric GNP nanocomposites. After a detailed analysis of the thermoelectric, microstructural, and mechanical characteristics of such nanocomposites, we present a case study based on CoVSn-GNP heterostructures. It is shown that GNPs can improve the mechanical properties without deteriorating the thermoelectric properties of the material. CoVSn-GNP bulk composites are fabricated using powder metallurgy and spark plasma sintering with a GNP weight percentage range of 0−1. All samples with the addition of GNPs showed improved mechanical properties compared with pristine CoVSn. The sample with 0.5 wt % GNPs showed the highest value of Vickers Hardness (737 HV) among all of the studied compositions. Moreover, the fracture toughness was higher for the samples with a lower average crystal size. The concentration and dispersion of GNPs did not significantly change the CoVSn multiphase microstructure; however, it influenced the thermoelectric factors by reducing the thermal conductivity and increasing the Seebeck coefficient, leading to the enhancement of the thermoelectric figure of merit.

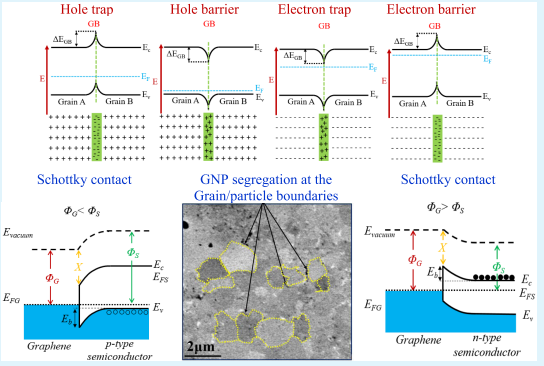

KEYWORDS: *graphene nanoplates, heterostructure composition, thermoelectrics, nanostructuring, CoVSn*

1. INTRODUCTION

To date, graphene-based nanomaterials have demonstrated remarkable characteristics in diverse applications such as the electronic,[1,2] biomedical,[3,4] coating,[5,6] and food industries.[7,8] Encouraged by such interesting findings, graphene compounds, such as few-layer graphene (FLG) and reduced graphene oxide (RGO), were also tested to modify the efficiencies of thermoelectric (TE) compounds through microstructural manipulation of TE materials.[9−11] However, the outcome is more complicated because multilayer graphene (i.e., stacked single graphene layers) may not possess the same effect as the two-dimensional (2D) defect-free single-layer graphene.[12−14] The impact of graphene inclusion on TE factors is summarized in Figure 1 through the critical analysis of several studies. In this figure, we have presented the Seebeck coefficient (S), electrical conductivity (σ), and thermal conductivity ($\kappa = \kappa_l$ (lattice) + κ_e(electronic)) and their contribution to the unit-less parameter of the figure of merit ($zT = S^2\sigma/\kappa\ T$) for both pristine TE compounds and their graphene-reinforced compositions.

As shown in Figure 1, graphene compounds have been shown to have various impacts on thermoelectric products. In the following sections, the scientific and engineering aspects of graphene's effects on electrical and thermal transport and the mechanical properties of thermoelectric compounds are discussed.

1.1. Graphene Impact on the Thermoelectric Properties.

1.1.1. Seebeck Coefficient. The Seebeck coefficient of a degenerate semiconductor and the carrier mobility can be expressed by[24,25]

$$S = \frac{\pi^2}{3}\frac{k_B^2 T}{q}\left[\frac{\partial(\ln(\sigma(E))}{\partial E}\right]_{E=E_f} = \frac{\pi^2 k_B^2 T}{3q}\left[\frac{1}{n}\frac{\partial n(E)}{\partial E} + \frac{1}{\mu}\frac{\partial \mu(E)}{\partial E}\right]_{E=E_f} \quad (1)$$

$$\mu(E) = q\tau(E)/m_d^* \quad (2)$$

where E is the energy, $n(E)$ stands for the energy-dependent carrier density, and m_d^* is the effective mass of the charge carrier, while n, μ, q, K_B, E_f, and τ are the carrier concentration, carrier mobility, carrier charge, Boltzmann constant, Fermi energy, and charge carrier relaxation time, respectively. Assuming a parabolic energy band and the dependency of the relaxation time (τ) on the energy and the

Received: January 3, 2021
Accepted: March 11, 2021

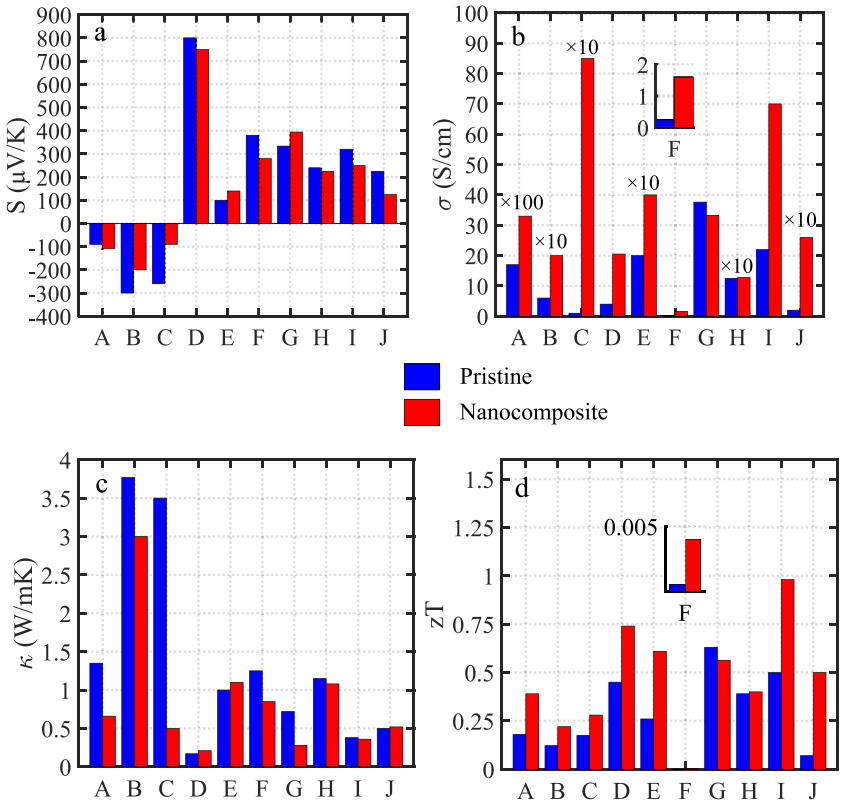

Figure 1. TE characteristics of pristine and graphene-reinforced nanocomposites, (a) Seebeck coefficients, (b) electrical conductivities, (c) lattice thermal conductivity (E and H show the total thermal conductivity), and (d) dimensionless figure of merit (zT): (A) $Bi_{0.85}Sb_{0.15}$-0.5 wt %G (T = 280 K),[15] (B) Nb-doped $SrTiO_3$-RGO (T = 800 K),[16] (C) $Zn_{0.98}Al_{0.02}O$-1.5 wt %RGO (T = 900 °C),[17] (D) *p*-phenediamino-modified graphene (PDG) (RT),[18] (E) $CoSb_3$/G (T = 800 K),[19] (F) $LaCoO_3$-0.01 wt % G (T = 300 K),[20] (G) MnTe-GNPs (T = 823 K),[21] (H) $CuInTe_2$/G (80:1) mass ratio (T = 700 K),[22] (I) SnSe-3.2 wt % MoS_2/G (T = 810 K).[23]

scattering factor (λ) via ($\tau = \tau_0 E^{\lambda}$) ($\tau_0$ is an energy-independent constant),[24,25] eq 1 can be written as[25]

$$S \approx \frac{\pi^2 k_B^2 T}{3q}\left[\frac{N(E)}{n} + \frac{\lambda}{Ef}\right]_{E=E_f} \quad (3)$$

where $N(E)$ is the electronic density of states. According to eq 3, the Seebeck coefficient depends directly on the scattering factor (λ) and is inversely affected by the charge carriers' concentration if the other parameters remain unchanged. It is well established that graphene reinforcement and its segregation at the grain boundaries (GBs) can lead to a grain size reduction in nanocomposites, when compared with a pristine matrix, by preventing welding or grain growth during milling and sintering, respectively.[9,21,22] The electrical characteristics of the sample with a single crystal and a polycrystalline structure may differ due to the effect of the grain/crystal boundaries.[26] However, the impact of the grain boundaries on the scattering of carriers is significant in case the mean free length (l) of carriers is larger than or comparable with the crystal/grain size (d).[26] The intrinsic tendency for carrier localization is created due to the presence of energetic disorder, caused by structural inhomogeneity and chemical impurities at the grain boundaries.[27,28] At the grain/crystal boundaries, this atomic disorder may provide electrical charge potential barriers (scattering regions) or traps.[27,28] The reason for this phenomenon is that the atoms near GBs are usually distributed irregularly, so the electronic couplings between atoms in different grains may change and thus prevent/disrupt the charge carriers' transport from one grain to the other.[29] This process can create traps, which may be classified as valleys (i.e., lower energy states) or barriers (i.e., higher energy states) by considering their energetic position with respect to the transport level.[30,31]

As shown in Figure 2, four scenarios may occur at the grain boundaries by considering the disturbed carrier concentration in these areas. If the structural inhomogeneity of the lattice at the grain boundaries creates electron donors near the valence-band maximum (VBM), hole traps are made (Figure 2a). Conversely, electron acceptors near the VBM act as dopants, making a barrier for holes[32,33] (Figure 2b). Similar behaviors apply to the cognitive bias modification (CBM).[33,34] The electron acceptors make a trap for electrons (Figure 2c), while the electron donors create a barrier for electrons (Figure 2d).[33,34]

There are further effects from the inclusion of graphene due to the formation of various lattice defects such as vacancies, antisites, etc., some of which can introduce extra charge carriers or compensate some of the donors or acceptors in the lattice.[38,39] However, in the case of graphene segregation, there are some other questions that need to be clarified, such as how the newly created graphene-matrix interfaces can affect electrical transport. The effect of graphene segregation at the grain interfaces can be evaluated, based on the possible band alignment, depending on the work functions of graphene and the main matrix. As illustrated in Figure 3, the type of contact (Schottky or

https://dx.doi.org/10.1021/acsaem.1c00015
ACS Appl. Energy Mater. XXXX, XXX, XXX−XXX

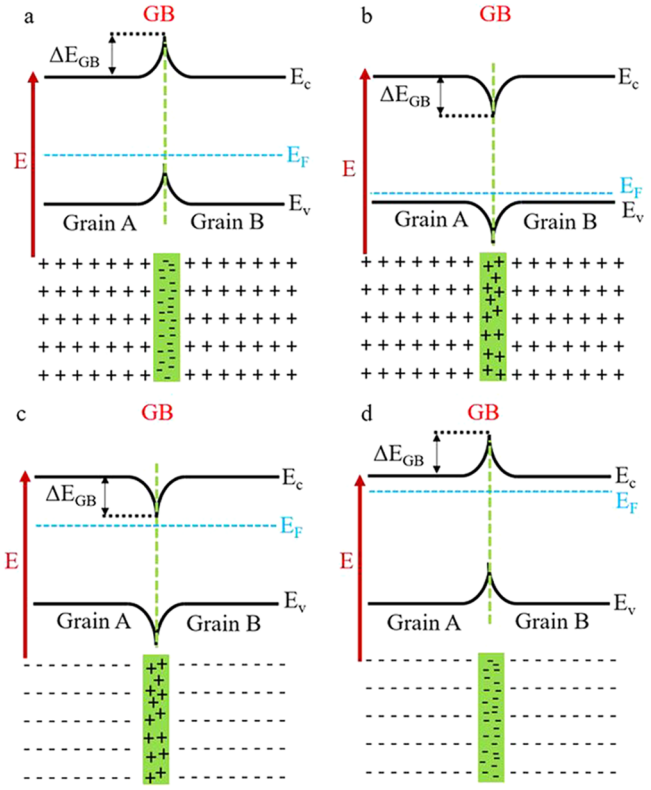

Figure 2. Schematic diagrams of (a) hole trap, (b) hole barrier, (c) electron trap, and (d) electron barrier. Adapted from ref 35−37.

ohmic) at the graphene-matrix interfaces depends on the type of the majority carriers in the matrix: electrons or holes. As shown in Figure 3, Schottky barriers occur at the graphene-matrix interfaces for both n- and p-type semiconductors when the graphene work function (Φ_G) is larger and smaller than the semiconductor work function (Φ_S), respectively (Figure 3a,b). In this case, there is an interface potential barrier (E_b), which scatters the low energy carriers preferentially more than the others, resulting in carrier energy filtering. In contrast, for the ohmic contact, there is no potential barrier, and all of the carriers can pass the interface (Figure 3c,d), although they can still experience scatterings due to potential energy variations at the interface.

Therefore, these extra boundaries due to smaller grain sizes—caused by graphene segregation and grain growth blocking—and graphene-matrix interfaces may provide an energy filtering effect for the charge carriers (electrons or holes). The consequence of energy filtering is the strong scattering of the low energy carriers, leading to reduced electrical conductivity and simultaneously increasing the Seebeck coefficient.[40,41]

1.1.2. Electrical Conductivity. The addition of graphene to the TE materials can result in either an increase or a decrease in the electrical conductivity (Figure 1b). This is due to graphene manipulating either the carrier concentration (n) or the mobility (μ), according to the Mott equation $\sigma = en\mu$.[9,22,38] The higher or lower carrier concentration depends on how graphene affects the crystal imperfections and interacts with the charge-donating centers in the material.[42,43] The graphene-embedded compounds may introduce a larger carrier concentration, but the resultant nanostructuring (i.e., grain growth prevention) provides more grain boundary barriers and thus further charge carrier scattering, leading to a decrease in the carrier mobility.[15,22] Therefore, one must consider both the carrier mobility of the matrix (μ_m) and the associated one to the interface (μ_{in}) to estimate the total mobility of the nanocomposites (eq 4),[38,44]

$$\frac{1}{\mu_T} = \frac{1}{\mu_m} + \frac{1}{\mu_{in}} \tag{4}$$

There are various models and approximations for interface mobility. One approximation is given by[38,44]

$$\mu_{in} = L_q\left(\frac{1}{2\pi m^* k_B T}\right)^{0.5} \exp\left(-\frac{E_b}{k_B T}\right) \tag{5}$$

where L_q is the mean path between two adjacent potential barriers, E_b shows the height of the potentials (energy) at the interfaces (Figure 3a,b), k_B is the Boltzmann constant, m^* is the effective mass of the charge carriers, and T is the absolute temperature.

1.1.3. Lattice Thermal Conductivity. Figure 1c shows that the addition of graphene in all of the listed materials reduces the lattice thermal conductivity. The primary mechanism is expected to be the phonon scattering against the grain boundaries,[22] which happens effectively at the low to medium temperature range.[45] Based on Matthiessen's rule,[45,46] the total relaxation time of phonons, τ_c (eq 6) is related to various relaxation times, including τ_U (Umklapp), τ_N (normal), $\tau_{e\text{-}ph}$ (electron phonon), τ_{pd} (point defect), $\tau_{i\text{-}ph}$ (impurity phonon), τ_{Ref} (regular reflection and refraction), τ_{Diff} (diffusive scattering due to the corrugation of the GB), and τ_{Ray} (Rayleigh scattering), as follows

$$\frac{1}{\tau_c} = \frac{1}{\tau_U} + \frac{1}{\tau_N} + \frac{1}{\tau_{e-ph}} + \frac{1}{\tau_{pd}} + \frac{1}{\tau_{i-ph}} + \frac{1}{\tau_{Ref}} + \frac{1}{\tau_{Diff}} + \frac{1}{\tau_{Ray}} \tag{6}$$

in which τ_{Ref}, τ_{Diff}, and τ_{Ray} depend on the grain boundary scattering, as described in Table 1.

It is noteworthy that graphene compounds can contribute to the electronic thermal conductivity ($\kappa = \kappa_e + \kappa_l$), based on the Wiedemann−Franz law (κ_e: $L\sigma T$, L: Lorentz number), the relationship that maps the electrical conductivity to the electronic thermal conductivity (κ_e).[47] In the cases where the electrical conductivity increases significantly, there may be a tradeoff between the increase of the electronic and reduction of the lattice thermal conductivities to determine the effect of graphene on the total thermal conductivity.[48]

Li et al.[49] obtained a significant reduction in thermal conductivity (from ∼0.8 to ∼0.4 W m^{-1} K^{-1} at a temperature of 873 K) by adding 0.15 wt % graphene in the Cu_2Se matrix. The reduction of the lattice thermal conductivity was associated with a frequency mismatch in the phonon density of states between carbon honeycomb phases and cubic Cu_2Se. Another study[50] reported a thermal conductivity of 2.5 W m^{-1} K^{-1} for a 0.25 vol % graphene/Cu_2SnSe_3 compound at room temperature, which was 12% lower than that of pristine Cu_2SnSe_3. In this study, the extra barriers created by the addition of graphene were mentioned as the reason for the phonon scattering and the reduction of the thermal conductivity of the nanocomposites.

1.2. Graphene's Mechanical Reinforcing Criteria.

1.2.1. Grain Refining. Grain refinement, through graphene

https://dx.doi.org/10.1021/acsaem.1c00015
ACS Appl. Energy Mater. XXXX, XXX, XXX−XXX

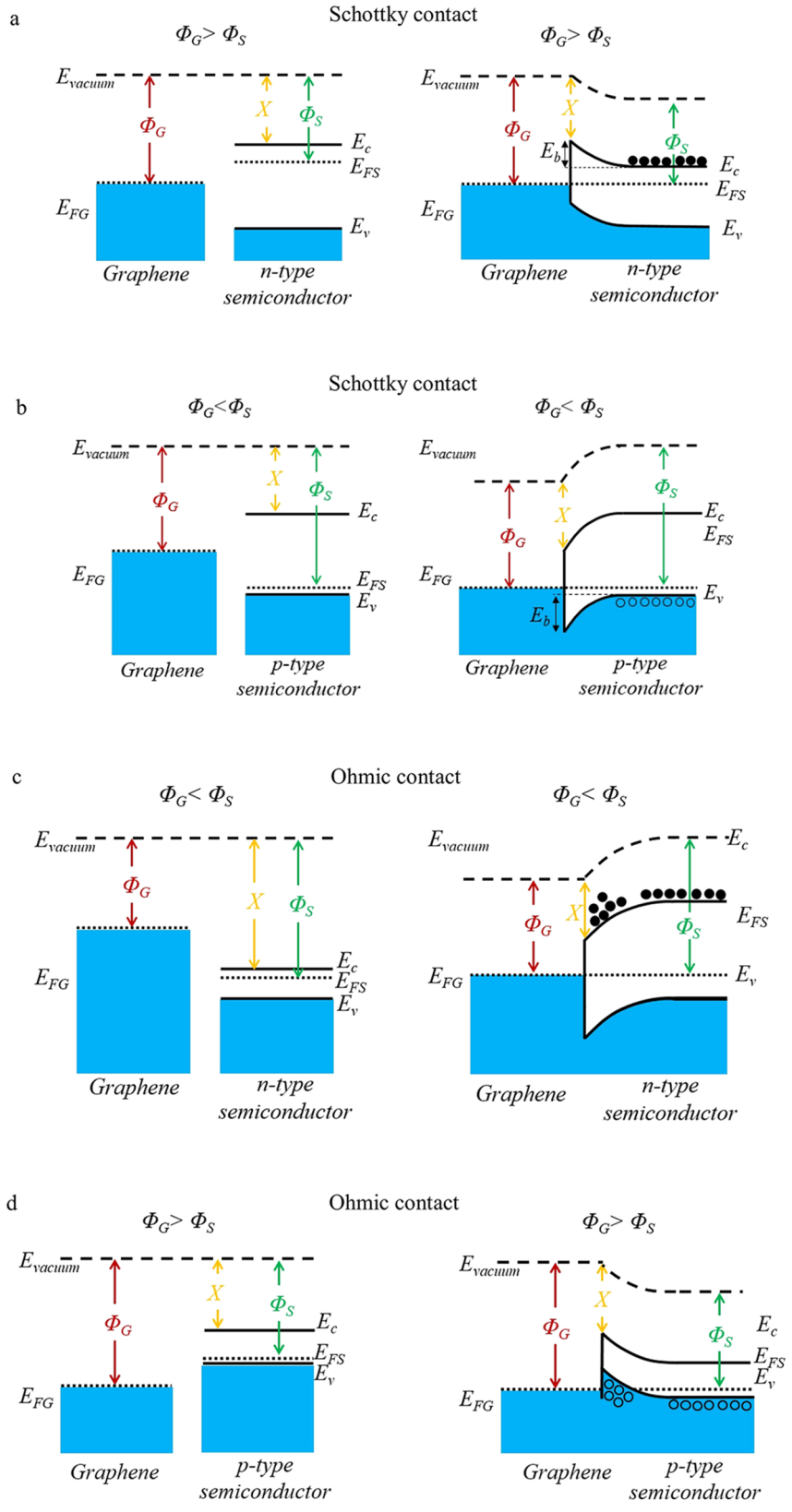

Figure 3. Schematic diagram of various contacts and band alignments at the graphene-matrix interface, (a) Schottky contact for graphene/n-type semiconductor, (b) Schottky contact for graphene/p-type semiconductor, (c) Ohmic contact for graphene/n-type semiconductor, and (d) ohmic contact for graphene/p-type semiconductor.

decoration of the grains, has been suggested as an effective method to improve the mechanical characteristics of nanocomposites.[51,52] Graphene addition to many granular alloys, due to graphene segregation at the grain/particle boundaries, inhibits the grain growth during the sintering process. In this regard, the Hall−Petch criteria explain the

https://dx.doi.org/10.1021/acsaem.1c00015
ACS Appl. Energy Mater. XXXX, XXX, XXX−XXX

Table 1. Phonon Scattering Strategies against the Grain Boundaries[45]

scattering strategies	parameters and relations	parameters	definitions
GB regular reflection and refraction	$\tau_{Ref} \sim l_{GB}\nu_{gj}^{-1}(\Delta\nu)^{-2}$	l_{GB}	mean distance of the GBs
GB diffusive scattering	$\tau_{Diff} \sim l_{GB}\nu_{gj}^{-1}\left(\frac{k_B\theta_j}{\hbar\omega}\right)^2\frac{1}{\eta}$	ν_{gj}	group velocity for the corresponding phonon modes
GB Rayleigh scattering	$\tau_{Ray} \sim \left(\frac{\nu_{gj}}{l_{GB}}\right)^3\left(\frac{\theta_j}{T\omega}\right)^4\Xi$	$\Delta\nu$	difference in the refraction indices of the elastic waves in different grains
		k_B	Boltzmann constant
		θ_j	Debye temperature
		η	a parameter that characterizes the degree of the corrugation of the GB (typically $1 \ll 10$)
		$\hbar$	($\hbar = h/2\pi$), h is Plank's constant
		ω	phonon frequency
		Ξ	a constant, dependent on the details of the grain boundary characteristics
		T	absolute temperature

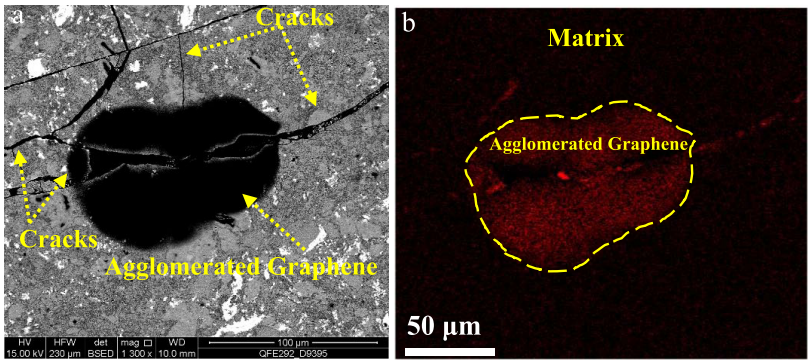

Figure 4. Graphene nanoplate (GNP) agglomeration at CoVSn- 1 wt % GNPs: (a) backscattered electron image and (b) carbon X-ray map.

manipulation of mechanical factors, specifically yield strength and hardness by grain size (d) reduction as follows[53,54]

$$\sigma_y = \sigma_0 + \frac{K_\sigma}{\sqrt{d}} \tag{7}$$

$$H = H_0 + \frac{K_H}{\sqrt{d}} \tag{8}$$

where σ_y and H are the yield strength and hardness when grain growth is prevented by the reinforced GNPs, respectively; also, K_σ, K_H (slope of the straight line when σ_y or H is plotted against $1/\sqrt{d}$), H_0, and σ_0 are materials constants (friction stress opposing the motion of dislocation).

Furthermore, geometry mismatch may result from the presence of nonreacting graphene/matrix interfaces. The existence of an inharmonious geometry among the graphene segregates at the grain boundaries and within the grains can pin down the dislocations and thus strengthen the nanocomposites.[55]

In the graphene-reinforced alloys, several regions are the potential stress concentration/accumulations in the proximity of graphene nanoplates (GNPs) due to their high specific interface areas with the matrix. Accordingly, this factor can obstruct the dislocation movement and lead to mechanical stabilities in the nanocomposite.[56] It is noteworthy that the abovementioned phenomenon can be observed in the optimum reinforcing percentage and distribution of GNPs.[57] In this regard, Figure 4 illustrates how the agglomerated graphene nanoplates at the alloy matrix (a CoVSn compound in this figure) may not be able to prevent the crack growth or even create a crack. This issue emphasizes the importance of optimization of the graphene-mixing ratio to achieve a uniform distribution.

Equation 9 calculates the strengthening efficiency of reinforcement (R),[51] based on the strengths of the composite (σ_c), matrix (σ_m), and reinforcement volume fraction (V_r).

$$R = \frac{\sigma_c - \sigma_m}{V_r\sigma_m} \tag{9}$$

Based on this equation, increasing the reinforcement volume above the optimum value may not enhance the reinforced strength, as illustrated in Figure 4.

1.2.2. Load Transferring. Three main factors control the load transfer mechanism in the nanocomposites, namely, the reinforcement geometry, volume fraction, and bonding strength among the matrices and nanofillers.[51] By reinforcing a matrix with GNPs, the tight bonding (interlocking) due to the large interface areas of the GNPs/matrix enhances the load transfer between graphene and the matrices.[51] The formation of strong bonding was reported by Bhadauria et al.[55] through the transmission electron microscopy (TEM) analysis of the interface (Figure 5a). The results revealed a clean interface with good metallurgical bonding between GNP reinforcement and the Al matrix, which can improve the load transfer between graphene and the matrix. The high-resolution TEM image of the interface region, illustrated in Figure 5b, reveals the nature of the bonding between graphene and the Al matrix.

https://dx.doi.org/10.1021/acsaem.1c00015
ACS Appl. Energy Mater. XXXX, XXX, XXX−XXX

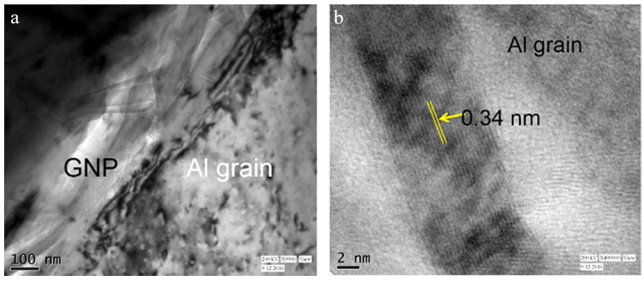

Figure 5. (a) TEM micrographs showing the Al−GNP interface and (b) high-resolution TEM image showing graphene layers in the GNP, along with its interface structure with an Al matrix.[55]

In this case, eq 10 can estimate the nanocomposite strength via the volume fraction and interfacial areas[58]

$$\sigma_{\text{nanocomposite}} = V_r\left(\frac{A}{CS}\right)\left(\frac{\tau}{2}\right) + \sigma_m V_m \tag{10}$$

where V_r shows the reinforcement's volume fraction, A and CS are interfacial surfaces and cross sections of reinforcements, respectively, τ stands for shear stress; σ_m is the matrix strength, and V_m is the matrix volume fraction. According to this equation, for the optimum dispersed GNPs in the matrix, the interfacial surface area (A) increases and the reinforcement's cross section (CS) decreases, which leads to an enhancement of the nanocomposite strength. In other words, the matrix reinforced by GNPs provides more effective interfaces and facilitates the load transfer from the matrices into GNPs via shear stress.[53] This mechanism causes load distribution and enables the strong reinforcing agent (GNPs) to take most of the applied load and prevent any local stress concentrations in the matrix and any subsequent premature nanocomposite failure.

1.2.3. Thermal Expansion Coefficient Mismatch. Dislocation can be generated due to the differences in the thermal expansion coefficients (TECs) contributed to matrices and GNPs.

Equation 11 describes the effective parameters in strength improvement, based on the TEC differences between the matrix and GNPs[59]

$$\sigma_{\text{TEC}} = \alpha G b\sqrt{\frac{12\Delta T\Delta C}{bd}} \tag{11}$$

where α is a constant, G shows the shear modulus, b represents the magnitude of the Burgers vector, ΔT is the temperature gradient between the process and the ambient, ΔC states the TEC difference, and d is the particle size.

As shown in this equation, the residual stress creation due to the TEC difference is directly related to ΔC. Moreover, the mismatch in the TECs is caused by residual stress.[60]

Equation 12 estimates the change in strength based on the density of the dislocations. In this equation, α is the geometric constant, μ_m shows the matrix shear modulus, b represents the Burgers vector magnitude, and ρ is the dislocation density.[60]

$$\Delta\sigma = \alpha\mu_m b\sqrt{\rho} \tag{12}$$

As represented in this equation, well-dispersed GNPs with a high level of interface areas with the matrix generate a higher density of dislocations and residual stress.

1.2.4. Orowan and Griffith Criteria. Orowan reinforcement is another mechanism that has been evaluated for reinforcing the matrix using GNPs. In this process, graphene may cause the pile-up of the dislocations and prevent them from moving freely throughout the matrix. Consequently, the dislocations need to pass around the graphene nanoplates due to their high mechanical stability. This extension in the dislocation paths (loops) results in higher ductility for the nanocomposites. Furthermore, these loops can create back stresses and prevent dislocation motions.[55] Equation 13[59] describes the strength regarding this mechanism, based on the effective parameters, such as

$$\sigma_o = \frac{Gb}{2\pi\sqrt{1 - \frac{\theta}{1.28}\left[\frac{1}{\sqrt{V_r}} - 1\right]d}}\ln\frac{d}{1.27b} \tag{13}$$

where G states the shear modulus, b is the Burgers vector magnitude, θ is Poisson's ratio, V_r is the reinforcement volume fraction, and d is the particle size.

Candidate thermoelectric materials for waste heat recovery applications such as heavily doped semiconductors and ceramic oxides are predominately brittle materials.[61] By considering this critical feature, the performance of the GNPs in strengthening the thermoelectric compounds against brittle fracture can be estimated via Griffith's fracture criterion (eq 14). In this equation, the critical stress intensity factor ($K_c = \sigma_c\sqrt{\pi a_0}$) depends on Young's modulus (E) and surface energy (γ) (i.e., the edge energy for 2D materials like graphene).

$$K_c = \sigma_c\sqrt{\pi a_0} = \sqrt{2\gamma E} \tag{14}$$

where a_0 stands for the half crack length and σ_c shows the critical stress at the fracture onset.[62]

Nevertheless, there is a crack length restriction (up to 10 nm) when using the Griffith criterion,[63] but as per an

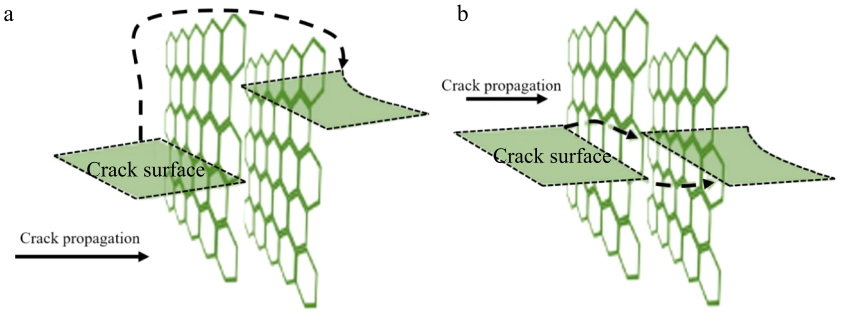

Figure 6. Schematic of crack growth inhibition by (a) crack deflection and (b) crack bifurcation/pinning, adapted from ref 65 with permission.

https://dx.doi.org/10.1021/acsaem.1c00015
ACS Appl. Energy Mater. XXXX, XXX, XXX−XXX

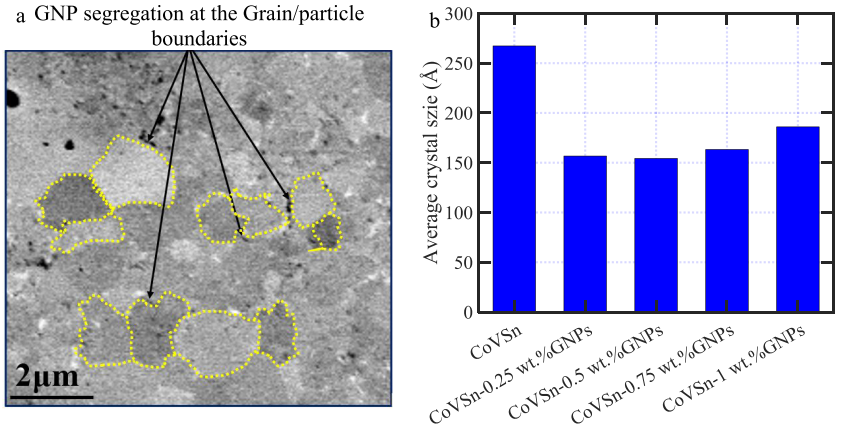

Figure 7. (a) GNP segregation at the grain/particle boundaries and (b) average crystal size of CoVSn heterostructure compositions.

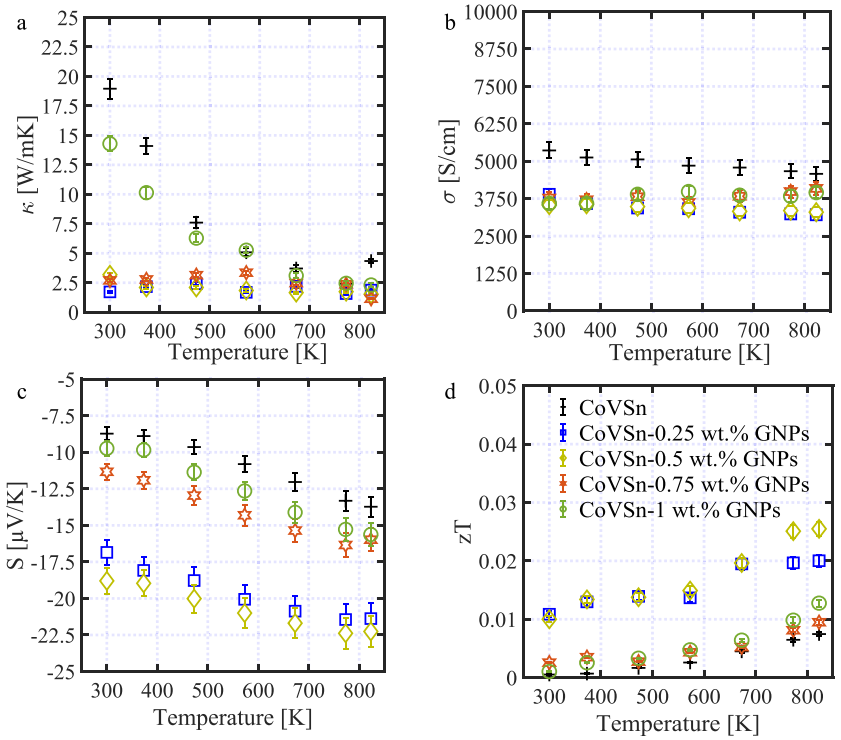

Figure 8. Temperature-dependent thermoelectric characteristics of CoVSn-GNP heterostructure compounds, (a) thermal conductivity, (b) electrical conductivity, (c) Seebeck coefficients, and (d) zT.

adequate dispersion of GNPs, these reinforcements with a high Young's modulus can improve the nanocomposite strength[64] and its resistance to crack propagation by improving the modulus (eq 14) as follows

$$\sigma_c = \sigma_{Gr} X_{Gr} + \sigma_m X_m \tag{15}$$

$$E_c = E_{Gr} X_{Gr} + E_m X_m \tag{16}$$

where E_c shows Young's modulus of the nanocomposites and E_{Gr}, E_m, X_{Gr}, and X_m are Young's moduli and volume fractions of the graphene nanoplates and the matrix, respectively.

Moreover, Figure 6 demonstrates schematically the crack growth blocking or halting by GNPs.

This process can also be interpreted based on eq 14, in which increasing the nanocomposite Young's modulus (E) and increasing K_c—fracture toughness—result in a lower crack propagation tendency.

In the following section, we report a case study on CoVSn and study the effect of graphene on the thermoelectric, microstructure, and mechanical properties of the nanocomposite structure. The CoVSn composition was studied in its pristine phase and presented in a prior publication.[66] Here, the heterogeneous composition is evaluated through reinforcement with graphene nanoplates.

2. MATERIALS AND METHODS

The synthesis of the CoVSn compound has been reported, and its multiphase composition and microstructure were discussed in an earlier work by the authors[66] (Figures S1 and S2). Here, the impacts of graphene nanoplate (GNP) reinforcement on the CoVSn microstructure and its properties are studied.

https://dx.doi.org/10.1021/acsaem.1c00015
ACS Appl. Energy Mater. XXXX, XXX, XXX−XXX

The CoVSn-xGNP (x: 0.25 wt % [0.047 atom %], 0.5 wt % [0.095 atom %], 0.75 wt % [0.142 atom %], and 1 wt % [0.19 atom %]) compounds were prepared using micromilling (reciprocating type, 1 h, a ball/powder volume ratio of 1:1, the stainless steel ball size of 1 mm) of the synthesized CoVSn powder with the GNPs (average particle: size 3 nm, surface area: 500 m^2 g^{-1}, Alfa Aesar) under an argon atmosphere. The bulk samples were fabricated with an average density (≈98 to 99% theoretical density measured by the Archimedes method, with isopropyl alcohol as a displacement medium) via spark plasma sintering (SPS) at a temperature of 850 °C and an applied pressure of 42 MPa, with a sintering time of 20 min under an argon atmosphere. The phase identification was implemented via X-ray diffraction (XRD) analysis (MiniFlex 300/600, 40 kV, 15 mA, Cu X-ray tube generation). Field emission scanning electron microscopy (FESEM) Quanta 450 SEM was employed for microstructural analysis. The Seebeck coefficient (S) and electrical conductivity (σ) were measured under a He environment at a temperature range of 300−820 K on a commercial Linseis LSR-3 system, using a differential voltage/temperature technique and a DC four-probe method, respectively. The thermal conductivity (κ) was calculated using $\kappa = D\rho C_P$ where ρ(g cm^{-3}) is the sample density. The thermal diffusivity D (m^2 s^{-1}) and specific heat capacity C_P (J Kg^{-1} K^{-1}) were measured with laser flash and differential scanning calorimetry methods, respectively, on Linseis LFA and DSC instruments, at a temperature range of 300−820 K. Moreover, the Vickers hardness values were measured using a microhardness device (LECO, LM-700AT-load: 1000 g, dwell time: 10 s) at room temperature.

3. RESULTS AND DISCUSSION

The segregation of GNPs at GBs in Figure 7 presents the range of the average crystal size of CoVSn-GNP heterostructure compounds estimated from the XRD analysis. The addition of GNPs has resulted in smaller crystallites, which are saturated at approximately 15−18 nm. The segregation of GNPs at the grain boundaries, creating new microstructural interfaces and providing extra boundaries, influenced the thermoelectric properties (Figure 8). The reduction in thermal conductivity is clearly illustrated in Figure 8a. Phonon scattering against the microstructural boundaries (grain/crystal boundaries and GNP distribution as a second phase) can be regarded as a reason for reducing the thermal conductivities. Based on the results, the primary reduction occurred at a lower temperature due to the main impact of phonon scattering with a longer wavelength (low frequencies) against the grain boundaries.[45]

Figure 8b shows the electrical conductivities of the samples after reinforcing with GNPs, which are in the range of conductive compounds. Moreover, Figure 8c illustrates the negative Seebeck coefficients for the samples to confirm the presence of electrons as the majority carriers. However, for the compounds with more than 0.5 wt % GNPs, there is a disruption in the improvement of the TE characteristics. This can be attributed to a lack of uniform GNP dispersion in the matrix and formation of the agglomerated GNP regions, as shown in Figure 9, which are also reported for other nanocomposites.[50,67]

Moreover, the microstructural analysis revealed multiphase microconstituents for the CoVSn-GNPs (e.g., CoVSn-1 wt % GNPs—Figure 10), similar to the pristine CoVSn sample, as discussed in ref 66 Figure 10 shows the elemental dispersion via X-ray mapping. It can be seen that the distributions of the main three elements, Co, V, and Sn, are not uniform, which confirms the presence of a multiphase microstructure. The comparison with the multiphase microstructure of the pristine CoVSn shows that the incorporation of GNPs does not influence the formation of the constituent phases in the microstructure (Figure S3).

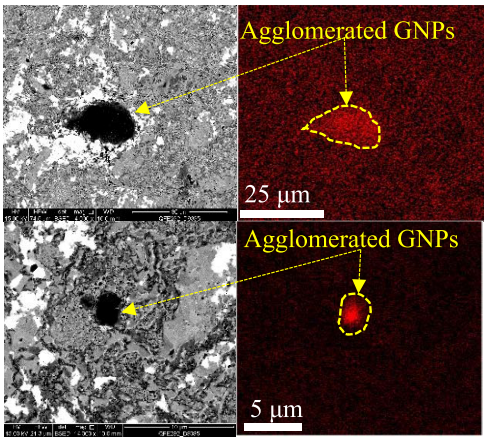

Figure 9. Backscattered electron micrographs with respective X-ray maps illustrating the GNP agglomerations in the matrix of the CoVSn-1 wt % GNPs nanocomposite.

Table 2 illustrates the hardness measurement results of the studied heterostructure compositions after reinforcement with the GNPs. The average hardness of the samples containing GNPs is higher than the pristine sample. This result can be explained by considering the presence of the GNPs as a second phase in the matrix and the smaller average crystal size—extra microstructural barriers (Hall−Petch effect[54]). In this regard, the dispersion of GNPs in the matrix is expected to hinder dislocation movements[68] and, consequently, strengthen the GNP-reinforced CoVSn heterostructure composition. It appears that the optimum concentration of GNPs to achieve the highest hardness is about 0.5%, and the further addition of GNPs reduces the hardness. Such an outcome may be attributed to the distribution of GNPs. A higher GNP concentration results in their agglomeration (Figure 9) and thus reduces the hardness.

Fracture toughness (K_{IC}, MPa$\sqrt{m}$) values were calculated based on the Shetty equation $K_{IC} = 0.0899\sqrt{\frac{HP}{4l}}$.[21] Here H, P, and l are the hardness, applied load of indentation, and indentation crack length, respectively. The average of the radial crack length was calculated from five indentations measured for each specimen (Figure 11). The calculations exhibit a higher fracture toughness for the sample containing 0.5 wt % GNPs (Table 2). This observation is attributable to halting the crack propagation against the extra microstructural interfaces/barriers, caused by the grain/crystal growth prevention (i.e., creating smaller grain/crystal sizes) in the graphene-reinforced CoVSn samples.

4. CONCLUSIONS

The scientific and engineering aspects of the graphene effects on mechanical, thermal, and electrical properties of thermoelectric materials were presented. The mechanisms under which GNPs affect the charge carrier concentration, carrier mobility, thermal conductivity, and thermopower were discussed. Special attention was paid to the incorporation of multilayer graphene as the reinforcing agent. As a case study, the impact of graphene nanoplates (GNPs) on the CoVSn heterostructure composition properties was analyzed.

https://dx.doi.org/10.1021/acsaem.1c00015
ACS Appl. Energy Mater. XXXX, XXX, XXX−XXX

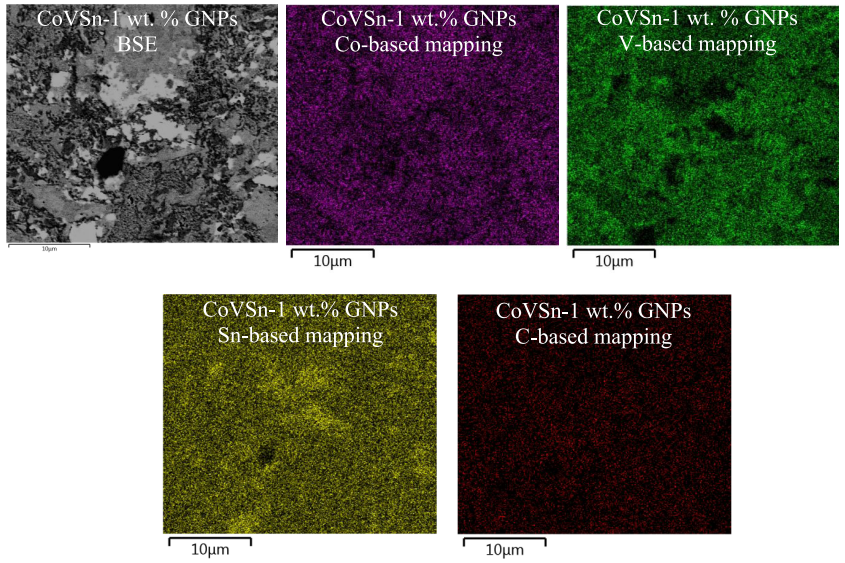

Figure 10. Backscattered electron micrograph along with X-ray maps showing the formation of multiphase microstructures in CoVSn-1 wt % GNPs.

Table 2. Mechanical Characteristics of the MnTe-GNP Samples

sample	CoVSn	CoVSn-0.25 wt % GNPs	CoVSn-0.5 wt % GNPs	CoVSn-0.75 wt % GNPs	CoVSn-1 wt % GNPs
hardness (HV)	592	636	737	695	682
SD: standard deviation	(SD: 15.3)	(SD: 17.2)	(SD: 12.4)	(SD: 16.7)	(SD: 12.6)
K_{IC}(MPa$\sqrt{m}$)	1.954	1.980	2.277	1.982	1.957

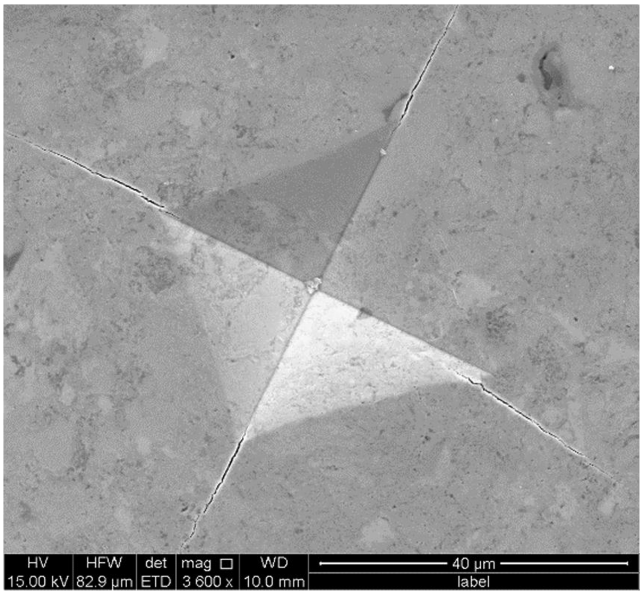

Figure 11. Crack length measurement to calculate the fracture toughness.

The mechanical assessment showed higher hardness (737 HV) in the sample reinforced with 0.5 wt % GNPs. This can be explained by the dispersion of the GNPs in the matrix and the excess microstructural barriers, due to small crystal sizes, hindering the dislocation movements and, consequently, strengthening the nanocomposite. The dispersion of GNPs did not significantly impact the CoVSn multiphase microstructure but enhanced the thermopower and reduced both the electrical and thermal conductivities. For some concentrations of the GNPs (0.25 and 0.5 wt %), zT was improved.

■ ASSOCIATED CONTENT

Supporting Information

The Supporting Information is available free of charge at https://pubs.acs.org/doi/10.1021/acsaem.1c00015.

Isopleth phase diagram of CoVSn composition; XRD pattern of CoVSn composition; X-ray line mapping of CoVSn-GNP scomposites (PDF)

■ AUTHOR INFORMATION

Corresponding Authors

Reza Ghomashchi − *School of Mechanical Engineering, University of Adelaide, Adelaide, SA 5005, Australia; ARC Research Hub for Graphene Enabled Industry Transformation and Institute for Photonics And Advanced Sensing, University of Adelaide, Adelaide, SA 5005, Australia*; Email: reza.ghomashchi@adelaide.edu.au

Daryoosh Vashaee − *Department of Electrical and Computer Engineering and Department of Materials Science and Engineering, North Carolina State University, Raleigh, North Carolina 27606, United States*; orcid.org/0000-0003-3667-3672; Email: dvashae@ncsu.edu

Author

Sadeq Hooshmand Zaferani − *School of Mechanical Engineering, University of Adelaide, Adelaide, SA 5005, Australia; Department of Electrical and Computer Engineering, North Carolina State University, Raleigh, North Carolina 27606, United States*; orcid.org/0000-0001-8923-6762

Complete contact information is available at: https://pubs.acs.org/10.1021/acsaem.1c00015

https://dx.doi.org/10.1021/acsaem.1c00015
ACS Appl. Energy Mater. XXXX, XXX, XXX−XXX

Notes

The authors declare no competing financial interest.

■ ACKNOWLEDGMENTS

This work was supported by the Australian Government Research Training Program Scholarship and the ARC Graphene Enabled Industry Transformation Hub at the University of Adelaide. This study is partially based upon work supported by the Air Force Office of Scientific Research (AFOSR) under contract number FA9550-19-1-0363 and the National Science Foundation (NSF) under grant numbers ECCS-1351533, ECCS-1515005, and ECCS-1711253.

■ REFERENCES

(1) Schwierz, F. Graphene transistors. *Nat. Nanotechnol.* **2010**, *5*, 487−496.
(2) Yazyev, O. V.; Louie, S. G. Electronic transport in polycrystalline graphene. *Nat. Mater.* **2010**, *9*, 806−809.
(3) Syama, S.; Mohanan, P. V. Comprehensive Application of Graphene: Emphasis on Biomedical Concerns. *Nano-Micro Lett.* **2019**, *11*, No. 6.
(4) Bullock, C. J.; Bussy, C. Biocompatibility Considerations in the Design of Graphene Biomedical Materials. *Adv. Mater. Interfaces* **2019**, No. 1900229.
(5) Nine, M. J.; Kabiri, S.; Diana, T. T. T.; Tran, N. H.; Losic, D. Electrostatic powder coatings of pristine graphene: A new approach for coating of granular and fibril substrates. *Appl. Surf. Sci.* **2018**, *441*, 187−193.
(6) Nine, M. J.; Cole, M. A.; Tran, D. N. H.; Losic, D. Graphene: a multipurpose material for protective coatings. *J. Mater. Chem. A* **2015**, *3*, 12580−12602.
(7) Wang, M.; Cui, M.; Zhao, M.; Cao, H. Sensitive determination of Amaranth in foods using graphene nanomeshes. *J. Electroanal. Chem.* **2018**, *809*, 117−124.
(8) Goh, K.; Yuan, Y.; Karahan, H. E.; Wei, L.; Zhai, S.; Htin, N. M.; Rong, W.; Fane, A. G.; Dekker; M.:Dehghani, F.; Chen, Y.; et al. Sandwich-Architectured Poly(lactic acid)−Graphene Composite Food Packaging Films. *ACS Appl. Mater. Interfaces* **2016**, *8*, 9994−10004.
(9) Shin, W. H.; Ahn, K.; Jeong, M.; Yoon, J. S.; Song, J. M.; Lee, S.; Seo, W. S.; Lim, Y. S. Enhanced thermoelectric performance of reduced graphene oxide incorporated bismuth-antimony-telluride by lattice thermal conductivity reduction. *J. Alloys Compd.* **2017**, *718*, 342−348.
(10) Zong, P.-a.; Liang, J.; Zhang, P.; Wan, C.; Wang, Y.; Koumoto, K. Graphene-Based Thermoelectrics. *ACS Appl. Energy Mater* **2020**, *3*, 2224−2239.
(11) Chakraborty, P.; Ma, T.; Zahiri, A.; Cao, L.; Wang, Y. Carbon-Based Materials for Thermoelectrics. *Adv. Condens. Matter Phys.* **2018**, No. 3898479.
(12) Kakaei, K.; Esrafili, M. D.; Ehsani, A. Atomic Properties and Electronic Structure. In *Interface Science and Technology*, 2019; pp *27*, 23−66.
(13) Nilsson, J.; Castro Neto, A. H.; Guinea, F.; Peres, N. M. R. Electronic Properties of Graphene Multilayers. *Phys. Rev. Lett.* **2006**, *97*, No. 266801.
(14) Amollo, T. A.; Mola, G. T.; Kirui, M. S. K.; Nyamori, V. O. Stacking order dependent electric field tuning of the band gap in graphene multilayers. *Phys. Rev. B* **2010**, *81*, No. 115432.
(15) El-Asfoury, M. S.; Nasr, M.; Nakamura, K.; Abdel-Moneim, A. Enhanced thermoelectric performance of Bi85Sb15-graphene composite by modulation carrier transport and density of state effective mass. *J. Alloys Compd.* **2018**, *745*, 331−340.
(16) Wu, C.; Li, J.; Fan, Y.; Xing, J.; Gu, H.; Zhou, Z.; Lu, X.; Zhang, Q.; Wang, L.; Jiang, W. The effect of reduced graphene oxide on microstructure and thermoelectric properties of Nb-doped A-site-deficient SrTiO3 ceramics. *J. Alloys Compd.* **2019**, *786*, 884−893.
(17) Chen, D.; Zhao, Y.; Chen, Y.; Wang, B.; Chen, H.; Zhou, J.; Liang, Z. One-Step Chemical Synthesis of ZnO/Graphene Oxide Molecular Hybrids for High-Temperature Thermoelectric Applications. *ACS Appl. Mater. Interfaces* **2015**, *7*, 3224−3230.
(18) Lin, Y.-H.; Lee, T.; Hsiao, Y.; Lin, W.; Whang, W.; Chen, C. Facile Synthesis of Diamino-Modified Graphene/Polyaniline Semi-Interpenetrating Networks with Practical High Thermoelectric Performance. *ACS Appl. Mater. Interfaces* **2018**, *10*, 4946−4952.
(19) Feng, B.; Xie, J.; Cao, G.; Zhua, T.; Zhao, X. Enhanced thermoelectric properties of p-type CoSb3/graphene nanocomposite. *J. Mater. Chem. A.* **2013**, *1*, 13111−13119.
(20) Kumar, A.; Kumari, K.; Ray, S. J.; Thakur, A. D. Graphene mediated resistive switching and thermoelectric behavior in lanthanum cobaltate. *J. Appl. Phys.* **2020**, *127*, No. 235103.
(21) Hooshmand Zaferani, S.; Ghomashchi, R.; Vashaee, D. Thermoelectric, Magnetic, and Mechanical Characteristics of Antiferromagnetic Manganese Telluride Reinforced with Graphene Nanoplates. *Adv. Eng. Mater.* **2021**, *23*, No. 2000816.
(22) Chen, H.; Yang, C.; Liu, H.; Zhang, G.; Wan, D.; Huang, F. Thermoelectric properties of CuInTe2/graphene composites. *CrystEngComm* **2013**, *15*, 6648−6651.
(23) Yang, S.; Si, J. X.; Su, Q.; Wu, H. Enhanced thermoelectric performance of SnSe doped with layered MoS2/graphene. *Mater. Lett.* **2017**, *193*, 146−149.
(24) Heremans, J. P.; Thrush, C. M.; Morelli, D. T. Thermopower enhancement in PbTe with Pb precipitates. *J. Appl. Phys.* **2005**, *98*, No. 063703.
(25) Li, Y.; Dou, Y.; Qin, X.; Zhang, J.; Xin, H.; Li, D.; Song, C.; Zou, T.; Liu, Y.; Li, C. Enhanced thermoelectric figure of merit in p-type b-Zn4Sb3/Bi0.4Sb1.6Te3 nanocomposites. *RSC Adv.* **2016**, *6*, 12243−12248.
(26) Kaydanov, V. I.; Coutts, T. J.; Young, D. L. In *Studies of Band Structure and Free-Carrier Scattering in Transparent Conducting Oxides Based on Combined Measurements of Electron Transport Phenomena*, Presented at the Material Research Society Workshop Denver, Colorado June 19-20, 2000.
(27) Puntambekar, K.; Dong, J.; Haugstad, G.; Frisbie, C. D. Structural and Electrostatic Complexity at a Pentacene/Insulator Interface. *Adv. Funct. Mater.* **2006**, *16*, 879−884.
(28) Yogev, S.; Matsubara, R.; Nakamura, M.; Rosenwaks, Y. Local charge accumulation and trapping in grain boundaries of pentacene thin film transistors. *Org. Electron.* **2010**, *11*, 1729−1735.
(29) Nan, G.; Li, Z. Modeling of charge transport in polycrystalline sexithiophene from quantum charge transfer rate theory beyond the first-order perturbation. *Org. Electron.* **2011**, *12*, 2198−2206.
(30) Vladimirov, I.; Kühn, M.; Geßner, T.; May, F.; Weitz, R. T. Energy barriers at grain boundaries dominate charge carrier transport in an electron-conductive organic semiconductor. *Sci. Rep.* **2018**, *8*, No. 14868.
(31) Steiner, F.; Poelking, C.; Niedzialek, D.; Andrienko, D.; Nelson, J. Influence of orientation mismatch on charge transport across grain boundaries in tri-isopropylsilylethynyl (TIPS) pentacene thin films. *Phys. Chem. Chem. Phys.* **2017**, *19*, 10854−10862.
(32) Qian, C.; Sun, J.; Zhang, L.; Huang, H.; Yang, J.; Gao, Y. Crystal-Domain Orientation and Boundary in Highly Ordered Organic Semiconductor Thin Film. *J. Phys. Chem. C* **2015**, *119*, 14965−14971.
(33) Kaake, L. G.; Barbara, P. F.; Zhu, X.-Y. Intrinsic Charge Trapping in Organic and Polymeric Semiconductors: A Physical Chemistry Perspective. *J. Phys. Chem. Lett.* **2010**, *1*, 628−635.
(34) Baier, R.; Leendertz, C.; Abou-Ras, D.; Ch.Lux-Steiner, M.; Sadewasser, S. Properties of electronic potential barriers at grain boundaries in Cu(In,Ga)Se2 thin films. *Sol. Energy Mater. Sol. Cells* **2014**, *130*, 124−131.
(35) Seto, J. Y. W. The electrical properties of polycrystalline silicon films. *J. Appl. Phys.* **1975**, *46*, 5247.

https://dx.doi.org/10.1021/acsaem.1c00015
ACS Appl. Energy Mater. XXXX, XXX, XXX−XXX

(36) Kamins, T. Hall Mobility in Chemically Deposited Polycrystalline Silicon. *J. Appl. Phys.* **1971**, 4357−4365.
(37) Grovenor, C. R. M. Grain boundaries in semiconductors. *J. Phys. C: Solid State Phys.* **1985**, *18*, 4079.
(38) Li, C.; Qin, X.; Yuanyue Li, Y.; Li, D.; Zhang, J.; Guo, H.; Xin, H.; Song, C. Simultaneous increase in conductivity and phonon scattering in a graphene nanosheets/(Bi2Te3)0.2(Sb2Te3)0.8 thermoelectric nanocomposite. *J. Alloys Compd.* **2016**, *661*, 389−395.
(39) Lu, M.-P.; Liao, C.-N. Mechanical and thermal processing effects on crystal defects and thermoelectric transport properties of Bi2(Se,Te)3 compounds. *J. Alloys Compd.* **2013**, *571*, 178−182.
(40) Paul, B.; Kumar, V. A.; Banerji, P. Embedded Ag-rich nanodots in PbTe: Enhancement of thermoelectric properties through energy filtering of the carriers. *J. Appl. Phys.* **2010**, *108*, No. 064322.
(41) Zamanipour, Z.; Shi, X.; Dehkordi, A. M.; Krasinski, J. S.; Vashaee, D. The effect of synthesis parameters on transport properties of nanostructured bulk thermoelectric p-type silicon germanium alloy. *phys. status solidi (a)* **2012**, *209*, 2049−2058.
(42) Horák, J.; Cermak, K.; Koudelka, L. Energy formation of antisite defects in doped Sb2Te3 and Bi2Te3 crystal. *J. Phys. Chem. Solids* **1986**, *47*, 805−809.
(43) Kumar, S.; Singh, S.; Dhawan, P. K.; Yadav, R. R.; Khare, N. Effect of graphene nanofillers on the enhanced thermoelectric properties of Bi2Te3 nanosheets: elucidating the role of interface in de-coupling the electrical and thermal characteristics. *Nanotechnology.* **2018**, *29*, No. 135703.
(44) Agarwal, K.; Kaushik, V.; Varandani, D.; Dhar, A.; Mehta, B. R. Nanoscale thermoelectric properties of Bi2Te3 − Graphene nanocomposites: Conducting atomic force, scanning thermal and kelvin probe microscopy studies. *J. Alloys Compd.* **2016**, *681*, 394−401.
(45) Hooshmand Zaferani, S.; Ghomashchi, R.; Vashaee, D. Strategies for engineering phonon transport in Heusler thermoelectric compounds. *Renewable Sustainable Energy Rev.* **2019**, *112*, 158−169.
(46) Ferry, D. K. *Semiconductor Transport*; Taylor & Francis: London, 2000.
(47) Mahan, G. D.; Bartkowiak, M. Wiedemann−Franz law at boundaries. *Appl. Phys. Lett.* **1999**, *74*, 953.
(48) McKinney, R. W.; Gorai, P.; Stevanovi′c, V.; Toberer, E. S. Search for new thermoelectric materials with low Lorenz number. *J. Mater. Chem. A.* **2017**, *5*, 17302−17311.
(49) Li, M.; L.Cortie, D. L.; Liu, J.; Yu, D.; Kazi NazrulIslam, S. M.; Zhao, L.; Mitchell, D. R. G.; A.Mole, R. A.; Cortie, M. B.; Dou, S.; Wang, X. Ultra-high thermoelectric performance in graphene incorporated Cu2Se: Role of mismatching phonon modes. *Nano Energy* **2018**, *53*, 993−1002.
(50) Zhao, D.; Wang, X.; Wu, D. Enhanced Thermoelectric Properties of Graphene/Cu2SnSe3 Composites. *Crystals* **2017**, *7*, 71.
(51) Yue, H.; Yao, L.; Gao, X.; Zhang, S.; Guo, E.; Zhang, H.; Lin, X.; Wang, B. Effect of ball-milling and graphene contents on the mechanical properties and fracture mechanisms of graphene nanosheets reinforced copper matrix composites. *J. Alloys Compd.* **2017**, *691*, 775−762.
(52) Hu, X.; Chan, Y. C.; Zhang, K.; Yung, K. C. Effect of graphene doping on microstructural and mechanical properties of Sn−8Zn−3Bi solder joints together with electromigration analysis. *J. Alloys Compd.* **2013**, *580*, 162−171.
(53) Yan, S. J.; Dai, S. L.; Zhang, X. Y.; Yang, C.; Hong, Q. H.; Chen, J. Z.; Lin, Z. M. Investigating aluminum alloy reinforced by graphene nanoflakes. *Mater. Sci. Eng. A* **2014**, *612*, 440−444.
(54) Taha, A. S.; Hammad, F. H. Application of the Hall-Petch Relation to Microhardness Measurements on Al, Cu, Al-MD 105, and Al-Cu Alloys. *phys. status solidi (a).* **1990**, *119*, 455.
(55) Bhadauria, A.; Singh, L. K.; Laha, T. Effect of physiochemically functionalized graphene nanoplatelet reinforcement on tensile properties of aluminum nanocomposite synthesized via spark plasma sintering. *J. Alloys Compd.* **2018**, *748*, 783−793.
(56) Shin, S. E.; Bae, D. H. Deformation behavior of aluminum alloy matrix composites reinforced with few-layer graphene. *Composites, Part A* **2015**, *78*, 42−47.
(57) Hooshmand Zaferani, S. Improvement if Thermoelectric Properties Through Manipulation of Microstructure: Effect of Graphene Reinforcement. PhD Project, School of Mechanical Engineering, The University of Adelaide: Australia.
(58) Rashad, M.; Pan, F.; Zhang, J.; Asif, M. Use of high energy ball milling to study the role of graphene nanoplatelets and carbon nanotubes reinforced magnesium alloy. *J. Alloys Compd.* **2015**, *646*, 223−232.
(59) Zhang, T.; J, S.; LÜ, L.-q.; Wang, C.-m.; Sang, J.-x.; Wu, D. Effects of graphene nanoplates on microstructures and mechanical properties of NSA-TIG welded AZ31 magnesium alloy joints. *Trans. Nonferrous Met. Soc. China* **2017**, *27*, 1285−1293.
(60) Rashad, M.; Pan, F.; Asif, M. Exploring mechanical behavior of Mg−6Zn alloy reinforced with graphene nanoplatelets. *Mater. Sci. Eng. A* **2016**, *649*, 263−269.
(61) Rowe, D. M. *Thermoelectrics and Its Energy Harvesting, Modules, Systems, AndApplications in Thermoelectrics*; CRC Press-Taylor & Francis Group: New york, 2012 © 2012 byTaylor & Francis Group, LLC, ISBN:978-1-4665-6030-7.
(62) Meng, Z.; Soler-Crespo, R. A.; Xia, W.; Gao, W.; Ruiz, L.; Espinosa, H. D.; Keten, S. A coarse-grained model for the mechanical behavior of graphene oxide. *Carbon* **2017**, *117*, 476−487.
(63) Yin, H.; Qi, H. J.; Fan, F.; Zhu, T.; Wang, B.; Wei, Y. Griffith Criterion for Brittle Fracture in Graphene. *Nano Lett.* **2015**, *15*, 1918−1924.
(64) Chung, J.-Y.; Sorkin, V.; Pei, Q.-X.; Chiu, C.-H.; Zhang, Y.-W. Mechanical properties and failure behaviour of graphene/silicene/graphene heterostructures. *J. Phys. D: Appl. Phys.* **2017**, *50*, No. 345302.
(65) Mefford, C. H.; Qiao, Y.; Salviato, M. Failure behavior and scaling of graphene nanocomposites. *Compos. Struct.* **2017**, *176*, 961−972.
(66) Hooshmand Zaferani, S.; Darebaghi, A.; Hong, S.; Vashaee, D.; Ghomashchi, R. Experimental Realization of Heavily p-doped Half-Heusler CoVSn Compound. *Energies* **2020**, *13*, No. 1459.
(67) Ghodrati, H.; Ghomashchi, R. Effect of Graphene Dispersion and Interfacial bonding on the Mechanical Properties of Metal Matrix Composites: An Overview. *FlatChem* **2019**, *16*, No. 100113.
(68) Cao, H.; Liang, Y. The microstructures and mechanical properties ofgraphene-reinforced titanium matrix composites. *J. Alloys Compd.* **2020**, *812*, No. 152057.

https://dx.doi.org/10.1021/acsaem.1c00015
ACS Appl. Energy Mater. XXXX, XXX, XXX−XXX

ADVANCED ENGINEERING MATERIALS
www.aem-journal.com

Thermoelectric, Magnetic, and Mechanical Characteristics of Antiferromagnetic Manganese Telluride Reinforced with Graphene Nanoplates

Sadeq Hooshmand Zaferani, Reza Ghomashchi,* and Daryoosh Vashaee**

Mechanical and thermal stability are the two challenging aspects of thermoelectric compounds and modules. Microcrack formation during material synthesis and mechanical failure under thermo-mechanical loading is commonly observed in thermoelectric materials made from brittle semiconductors. Herein, the results of graphene-nanoplates (GNPs) reinforcement on the mechanical and thermoelectric properties of MnTe compound are reported. The binary antiferromagnetic MnTe shown promising thermoelectric characteristics due to the paramagnon–hole drag above the Néel temperature. In this study, different bulk MnTe samples are synthesized with the addition of GNPs in a small quantity (0.25–1 wt%) by powder metallurgy and spark plasma sintering. The thermoelectric factors, magnetic behavior, microstructure, and mechanical properties of the samples are evaluated and analyzed. Nearly 33% improvement is observed in the fracture toughness of MnTe reinforced with 0.25 wt% GNPs compared to the pristine structure. The Néel temperature remains approximately unaffected with the GNP inclusion; however, the low-temperature ferromagnetic phase impurity is significantly suppressed. The thermal conductivity and power factor decrease almost equally by ≈34% at 600 K; hence, the thermoelectric figure-of-merit is not affected by GNP reinforcement in the optimized sample.

1. Introduction

To date, graphene in a 2D-carbon configuration allotrope with an atomic monolayer sheet has demonstrated itself as a promising material for novel products.[1–5] This material has shown various potentials in a broad range of applications such as bioscience,[6–9] electronics,[10,11] energy,[12–14] and polymeric/metallic nanocomposites.[15–18] As such, in the field of energy conversion, graphene products have been used in developing new thermoelectric (TE) compounds.[5,19–23] However, it may be unrealistic to expect to simultaneously achieve all the improving features by incorporating graphene compounds into TE materials. The TE material is often evaluated by the dimensionless figure of merit factor (zT), where $zT = \frac{S^2\sigma}{\kappa}T$, S is the Seebeck coefficient, σ is the electrical conductivity, κ is the thermal conductivity, and T is the absolute temperature. In this regard, Du et al.[24] synthesized orderly aligned poly3,4-ethylene-dioxythiophene (PEDOT) chains on the surface of graphene quantum dots (GQDs) by taking advantage of the strong interface interaction between PEDOT:polystyrene sulphonate (PSS) and GQDs. Such an ordered alignment of those chains resulted in improving the TE factors, including the electrical conductivity (30.99%) and Seebeck coefficient (113.2%), attributed to π–π interaction and low-energy carrier filtration, respectively. In another approach,[25] TE factors of Nb-doped $SrTiO_3$ were modified via reduced graphene oxide (rGO) and Sr deficiency cooperation. The outcome of this work was reported as a decrease in the grain size by a factor of ≈1.5 and a reduction of thermal conductivity due to increased phonon scattering at the boundaries. Also, Yadav et al.[26] identified a significant improvement (≈86% at RT) in the electrical conductivity of a

S. Hooshmand Zaferani, Dr. R. Ghomashchi
School of Mechanical Engineering
University of Adelaide
SA 5005, Australia
E-mail: sadeq.hooshmandzaferani@adelaide.edu.au;
reza.ghomashchi@adelaide.edu.au

S. Hooshmand Zaferani, Dr. D. Vashaee
Department of Electrical and Computer Engineering
North Carolina State University
NC 27606, USA
E-mail: dvashaee@ncsu.edu

The ORCID identification number(s) for the author(s) of this article can be found under https://doi.org/10.1002/adem.202000816.

DOI: 10.1002/adem.202000816

Dr. R. Ghomashchi
ARC Research Hub for Graphene Enabled Industry Transformation
University of Adelaide
Adelaide, SA 5005, Australia

Dr. R. Ghomashchi
Institute For Photonics and Advanced Sensing
University of Adelaide
SA 5005, Australia

Dr. D. Vashaee
Department of Materials Science and Engineering
North Carolina State University
NC 27606, USA

$CoSb_3$/G nanocomposite. They stated that the 2D graphene provides extra carrier conduction channels in addition to the low interface potential barrier for charge transport.

Along with discovering novel TE compounds and the continued interest in developing efficient chalcogenide TE materials,[27–32] lead-free MnTe, an antiferromagnetic (AFM) transition metal–semiconductor, has shown potential as an efficient TE material.[33,34] This material has been investigated since the late 1930s[35,36] as either undoped[37–40] or doped compounds such as MnTeLi,[38] $(GeTe)_{1-x}(MnTe)_x$,[41,42] $(Ge, Pb)_{1-x}Mn_xTe$,[43] $Cd_{1-x}Mn_xTe$,[44] $Sn_{1-x}Mn_xTe$,[45] and $Zn_{1-x}Mn_xTe$.[46] MnTe has a Néel temperature (T_N) of 307–310 K[47,48] and a bandgap of 1.27 eV,[47,49,50] with a high Seebeck coefficient ($\approx$450 μV K^{-1})[49,51] and spin-wave excitation (magnon) drag effect.[33,34] Also, in contrast to other manganese chalcogenides such as MnO, MnS, and MnSe, which form with a cubic NaCl–type crystal structure, MnTe has a hexagonal NiA-type crystal structure in its ground state.[49] However, MnTe suffers from two properties, mainly low electrical conductivity and chemical instability, which can compromise its potential application as an efficient TE material. The poor electrical conductivity originates from both a low hole concentration ($\approx 10^{18}$ cm^{-3} in comparison to the carrier concentration of 10^{19}–10^{21} cm^{-3} in typical TE tellurides)[49,52,53] and low carrier mobility due to the strong spin-disorder scattering.[54] The chemical and crystal structure instability is due to Te/Mn ion migration and Mn oxidation creating MnO and $MnTe_2$ impurity phases. Such reactions can alter the properties of MnTe-based devices during their service time,[55,56] and therefore warrant further investigation for improvement.

Aside from the TE material properties, a rational design of a reliable thermoelectric generator (TEG) demands thermomechanical stability to handle the stresses generated when the TE material is exposed to thermal gradients.[57–61]

To overcome the drawbacks mentioned previously for MnTe as a potential TE material, we tried to reinforce it with graphene nanoplates (GNPs). Also, we investigated if the high electrical conductivity of GNPs can enhance electrical conductivity of MnTe to attain a higher power factor. Another motivation for GNP addition was to prevent thermomechanical instability, through modification of the grain structure. As for the latter, mechanical sustainability due to graphene addition may result through grain refining or size reduction,[62,63] load transfer,[64,65] dislocation density increase,[66,67] and Orowan strengthening.[62,65] In this research, we characterized the magnetic, TE, and mechanical factors of GNP-reinforced MnTe compounds based on their microstructure manipulation and analysis.

2. Results and Discussion

Figure 1 shows the X-ray diffraction (XRD) pattern for the synthesized MnTe compound in which the majority of the diffraction peaks can be well indexed with NiAs-type crystal structure in good agreement with the literature.[40]

Magnetic characterization of the MnTe and MnTe–GNP compounds indicates that the Néel temperature ($T_N \cong 307$ K)[47,48] remains almost unaffected by GNP addition (**Figure 2** inset). The pristine MnTe shows a ferromagnetic (FM) phase over the temperature range of 0–50 K (Figure 2). The associated magnetic moment is smaller in the samples with more GNPs. Therefore, this reduction must be attributed to the dispersion of GNPs in the MnTe matrix. The magnetic susceptibility (Figure 2) shows a Curie temperature at the interval of 40–50 K. This observation indicates a probable existence of Mn_3O_4 because its Curie temperature is around 43 K.[68] Moreover, the XRD spectra, shown in **Figure 3**, reveal a minor peak ($2\theta = 49.2°$), which disappearing upon increasing the GNP mixing ratios (Figure 3 inset). All GNP-reinforced MnTe samples, except the MnTe–0.25 wt% GNP, also show XRD peaks at about $2\theta = 40.7°$ and $2\theta = 56.6°$, associated with the $Mn_{23}C_6$ phase.[69,70] The disappearance of the Mn_3O_4 XRD lines in the GNP-reinforced samples and the emergence of the $Mn_{23}C_6$ lines suggest a chemical reaction taking place between the bulk material and the GNPs (Figure 3 inset). Comparison of the formation energies for Mn_3O_4[71] and $Mn_{23}C_6$[72] confirms that $Mn_{23}C_6$ is chemically more stable than Mn_3O_4. As $Mn_{23}C_6$ is

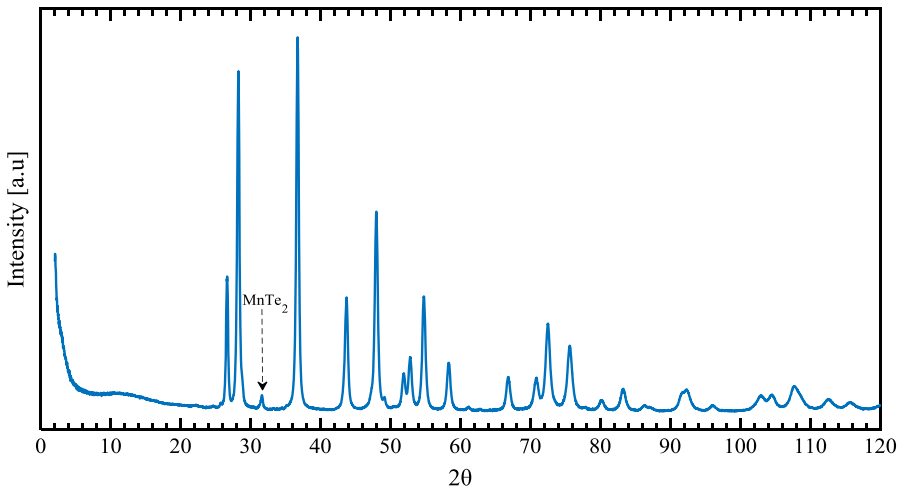

Figure 1. XRD spectra of the MnTe sintered powder. This plot confirms the primary phase is MnTe with a small peak corresponding to $MnTe_2$ binary compound.

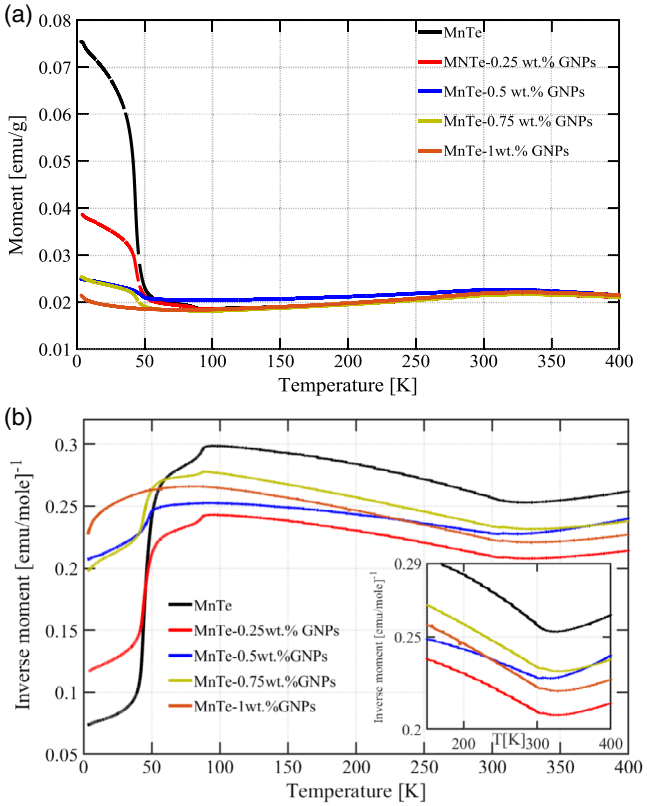

Figure 2. a) Regular magnetic susceptibility and b) inverse magnetic susceptibility of the MnTe–GNP compounds versus temperature under a magnetic field of 1000 Oe.

energetically more favourable, it is highly possible that in a thermally activated reaction, GNPs reduce Mn_3O_4 to make $Mn_{23}C_6$, as evidenced by the disappearance of Mn_3O_4 lines in the XRD data.

The Mn reaction with carbon consumes Mn, leading to Te-rich domains that favor the formation of $MnTe_2$, as confirmed by the XRD peak at $2\theta = 32$ (Figure 3). The formation of the $MnTe_2$ phase can be explained by thermodynamic considerations[73,74] based on three reaction steps for the formation of MnTe alloy in the current study: 1) $2Mn+2Te \rightarrow MnTe_2+Mn+ Q_1$ @ mechanical alloying and milling ($MnTe_2$ standard heat of formation = -26.4 kcal mol^{-1});[75] 2) $MnTe_2 \rightarrow MnTe+Te$ @ annealing process (T:750 °C) and spark plasma sintering (T: 950 °C); 3) $Mn+Te \rightarrow MnTe$ (MnTe standard heat of formation = -13.27 kcal mol^{-1}).[76]

It is worth noting that the second and third synthesis steps can happen simultaneously during the SPS process of the bulk samples. While these steps are likely to be completed in pristine MnTe samples, in the GNP-reinforced MnTe, the second reaction may not proceed further to the third one as the unreacted Mn can react with the carbon atoms (achieved by defected GNPs during the mechanical alloying) and create the stable manganese carbide of $Mn_{23}C_6$ (Figure 3).[70,77] In other words, $Mn_{23}C_6$ acts as a competitive phase with standard heat of formation of -58.5 kcal mol^{-1}[77] against the MnTe and $MnTe_2$ phases with the heat of formation equal to -13.27[76] and -26.4 kcal mol^{-1},[75] respectively.

Consistent with these claims, the equilibrium Mn–C phase diagram (**Figure 4**a) confirms that the $Mn_{23}C_6$ is stable up to the temperature of 1034 °C, which is higher than the melting point of $MnTe_2$ ($T = 735$ °C, Figure 4b). Consequently, Figure 3 shows higher peak intensities for $Mn_{23}C_6$ and $MnTe_2$ in the samples containing more GNPs (i.e., 0.75 and 1 wt% GNPs), which nearly compromises their magnetic properties (Figure 2) in comparison to the pristine MnTe.

The temperature-dependent TE characteristics of MnTe–GNP compounds are shown in **Figure 5** versus temperature from 300 to 820 K. The observed transport characteristics of the p-type MnTe near its Néel temperature (≈307 K) have already been noted in several reports.[78–80] GNP mixing did not make a significant difference in electrical conductivity at high temperatures. However, the room temperature electrical conductivity dropped with GNP inclusion. Electrical conductivity (σ) directly relates to the carrier concentration (n) and mobility (μ); i.e., $\sigma = en\mu$. To determine the impact of the graphene reinforcement on carrier concentration and mobility, the Hall effect data for two selected samples, namely, MnTe and MnTe–1 wt% GNP, were measured, as shown in **Figure 6**.

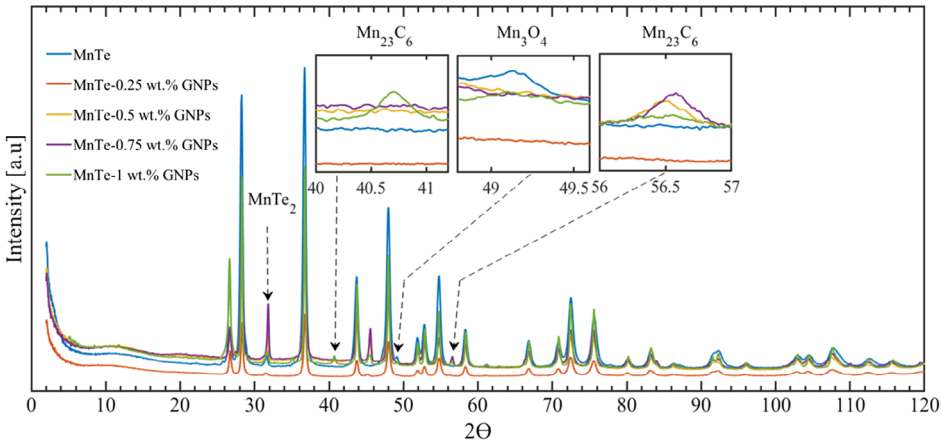

Figure 3. XRD spectrum showing the diffraction peaks for the MnTe–GNP samples. The formation of $Mn_{23}C_6$ peaks confirms the chemical reaction of Mn–C in addition to the formation of $MnTe_2$.

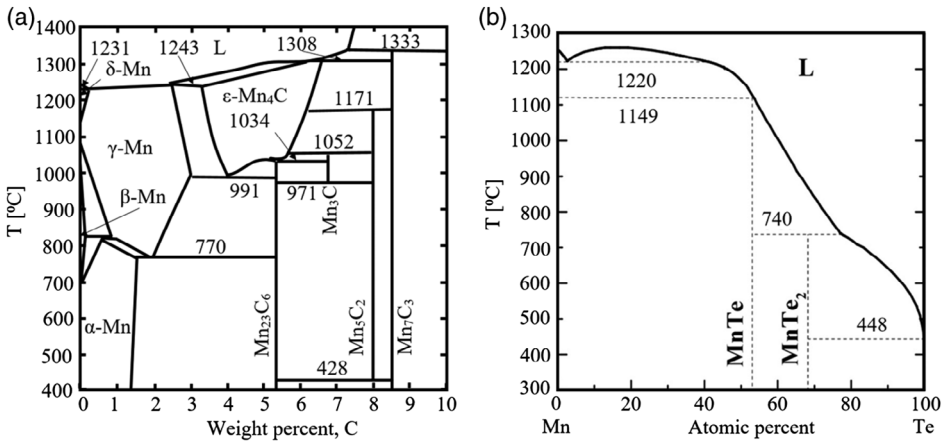

Figure 4. a) Mn–C binary phase diagram. Reproduced (Adapted) with permission.[96] Copyright 2018, Elsevier. b) Mn–Te phase diagrams. Reproduced (Adapted) with permission.[81] Copyright 2018, Elsevier.

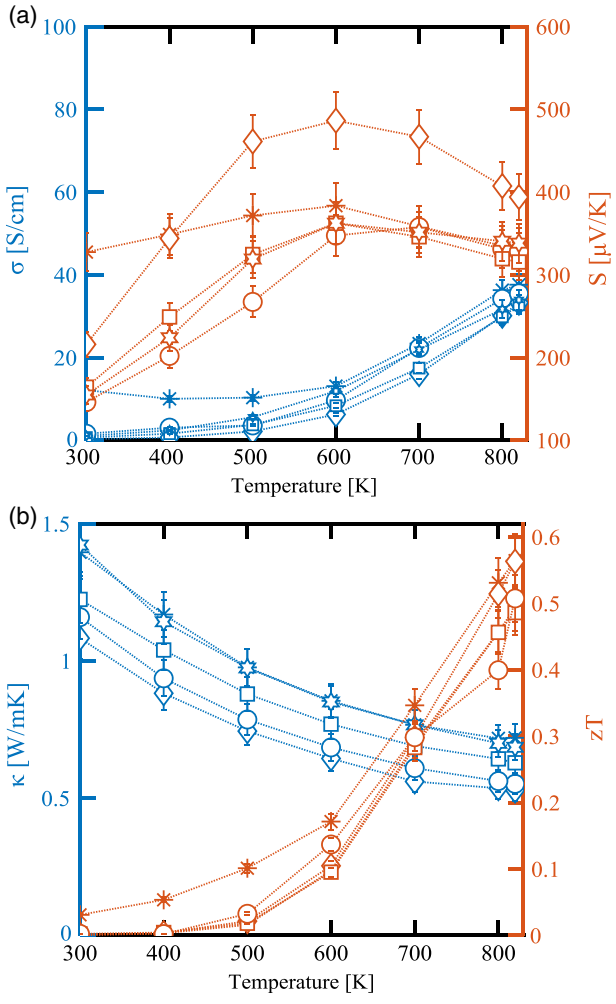

Figure 5. The temperature-dependent TE characteristics of the MnTe–*x*GNP compounds (0 wt% = asterisk (⋆); 0.25 wt% = diamond (◇); 0.5 wt% = circle (○); 0.75 wt% = square (□); and 1 wt% = hexagram (✱)).

The low-temperature side of the Hall data is limited to ≈312 K to stay away from the Néel temperature, where the critical fluctuations can distort the Hall voltage. As shown in the figure, the Hall data are in good agreement with the trends observed in the thermopower data. MnTe–1 wt% GNPs shows an ≈10× smaller hole concentration than MnTe. The electrical conductivity of this sample is also about the same order more diminutive than that of MnTe. The doping mechanism in pure MnTe is by stoichiometry and defects. For example, uncompensated ions such as Mn^{1+}—Mn vacancies as the major types of defect in MnTe—can donate a hole to the crystal.[81,82] GNP introduces carbon to the system that may compensate for some of such defects and reduce the hole concentration in MnTe, which can explain the smaller hole concentration in MnTe–1 wt% GNPs. The hole mobility for both samples is of the same order, which may seem counterintuitive, considering the larger density of interfaces in MnTe–1 wt% GNPs. To understand the insensitivity of the carrier mobility to the interface scattering in MnTe, one must take into consideration the magnetic properties. In AFM MnTe, the dominant scattering mechanism near and above the Néel temperature is due to spin-disorder scattering.[83] This scattering is about one to two orders of magnitude stronger than any other one in the material. For example, the relaxation times due to the acoustic phonons and impurity scatterings are typically in the range of picoseconds or fractions of picoseconds. However, the spin-disorder scattering in MnTe is in the range of a few tens of femtoseconds.[33] GNP addition will add more interface scattering to the material, although such defect scatterings are in the picosecond ranges and will not affect the carrier mobility significantly.

Therefore, the similar T_N and magnetic property, larger Seebeck coefficient, and smaller electrical conductivity of MnTe–GNP samples all indicate a lower carrier concentration in the GNP-added samples.

The segregation of the graphene phase (GNPs) at the microstructural boundaries is shown in **Figure 7**a,b. Moreover, Figure 7c shows the results of the X-ray line scan of the GNP (carbon) distribution in the microstructure. As shown in this figure, the path of this line was arranged to

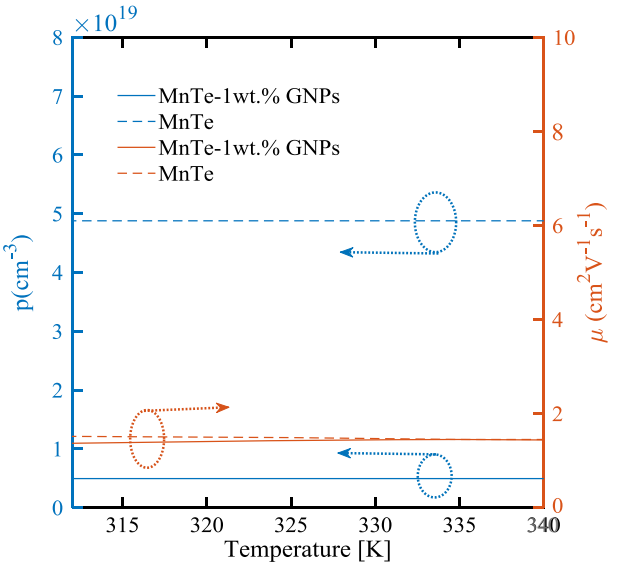

Figure 6. Carrier concentration (left axis) and carrier mobility (right axis) for two selected samples. MnTe (broken line) and MnTe–1 wt% GNPs (solid line).

cross the microstructural boundaries containing the GNP precipitation. Based on the results, by passing through the boundary regions, the carbon peaks increase, which confirms the precipitation of GNPs at the boundaries. It is noteworthy that the interfaces may scatter the low-energy carriers preferentially more than the high-energy ones and contribute to enhancing the Seebeck coefficient, a.k.a., the energy filtering mechanism.[84,85] However, considering the lower carrier concentration of MnTe–GNP samples, the energy filtering does not seem to be the dominant factor responsible for the observed improvement of the Seebeck coefficient in the paramagnetic region.

Concurrently, the thermal conductivities have also been reduced (Figure 5b), due to the interface scattering of the acoustic phonons in the MnTe–GNP matrix.[86,87] Overall, the samples with 0.5, 0.75, and 1 wt% GNPs did not show enhanced TE characteristics as much as the sample with 0.25 wt% GNPs despite the higher amount of GNP concentration.

This may be attributed to a few reasons such as the lack of uniform dispersion of GNPs in mixing ratios greater than 0.25 wt% GNPs (**Figure 8**), as similarly reported in another study.[88] Also, the phase impurities generated by the GNP reaction with MnTe can deteriorate the TE properties. GNP is also a pseudometallic phase with a small Seebeck coefficient; therefore, an excessive amount of GNPs can lead to the reduction of the thermopower. To this end, the zTmax was determined as ≈0.56 at 820 K for the MnTe–0.25 wt% GNP compound (Figure 5b).

The mechanical characteristics of the MnTe–GNP compounds were evaluated through the measurement of Vickers microhardness and calculation of fracture toughness, as given in **Table 1**. Fracture toughness (K_{IC}, MPa$\sqrt{m}$) values were calculated according to the Shetty equation $K_{IC} = 0.0899\sqrt{\frac{HP}{4l}}$,[89–91] where H, P, and l are the hardness, applied load of indentation, and indentation crack length, respectively. The average of the radial crack length was calculated from five indentations measured for each specimen. The calculations show a higher fracture toughness value for the samples containing 0.25 wt% GNPs (Table 1). Based on the shown crack growth path (**Figure 9**b), the presence of porosity in the bulk materials may influence the crack

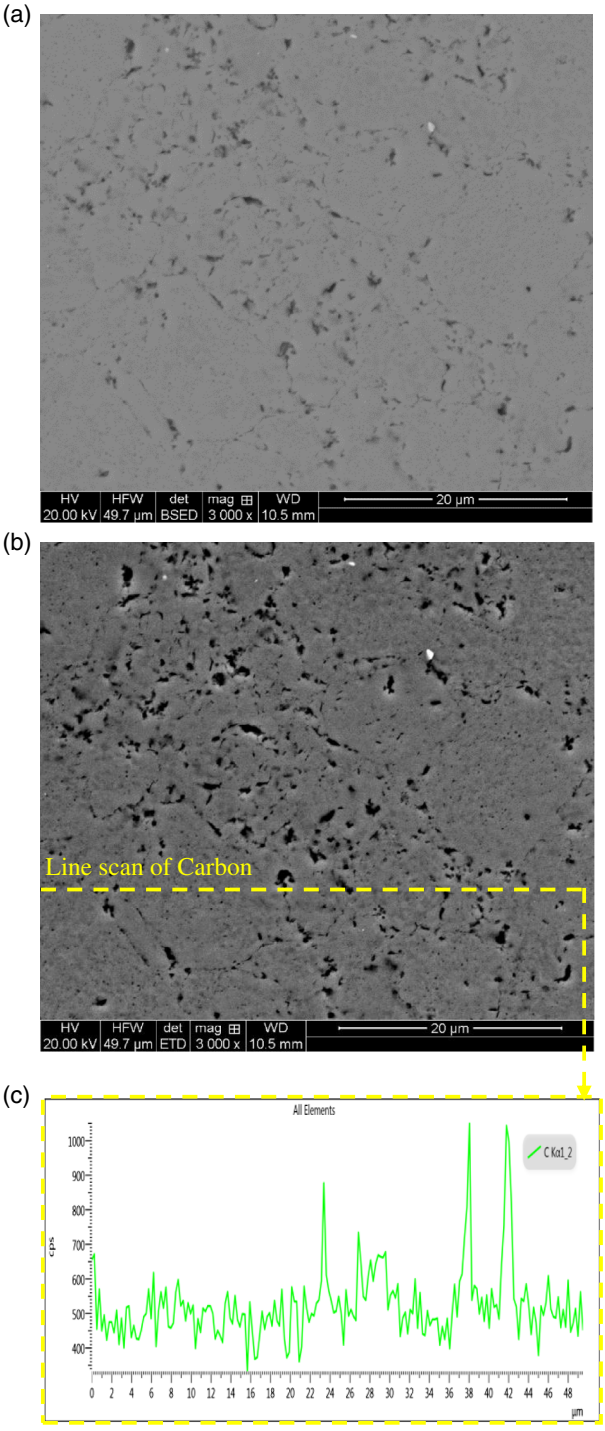

Figure 7. Graphene precipitation at the microstructural boundaries in the GNP-reinforced MnTe sample. a) Back-scattered electrons image, b) micrograph, and c) X-ray line scan of carbon distribution.

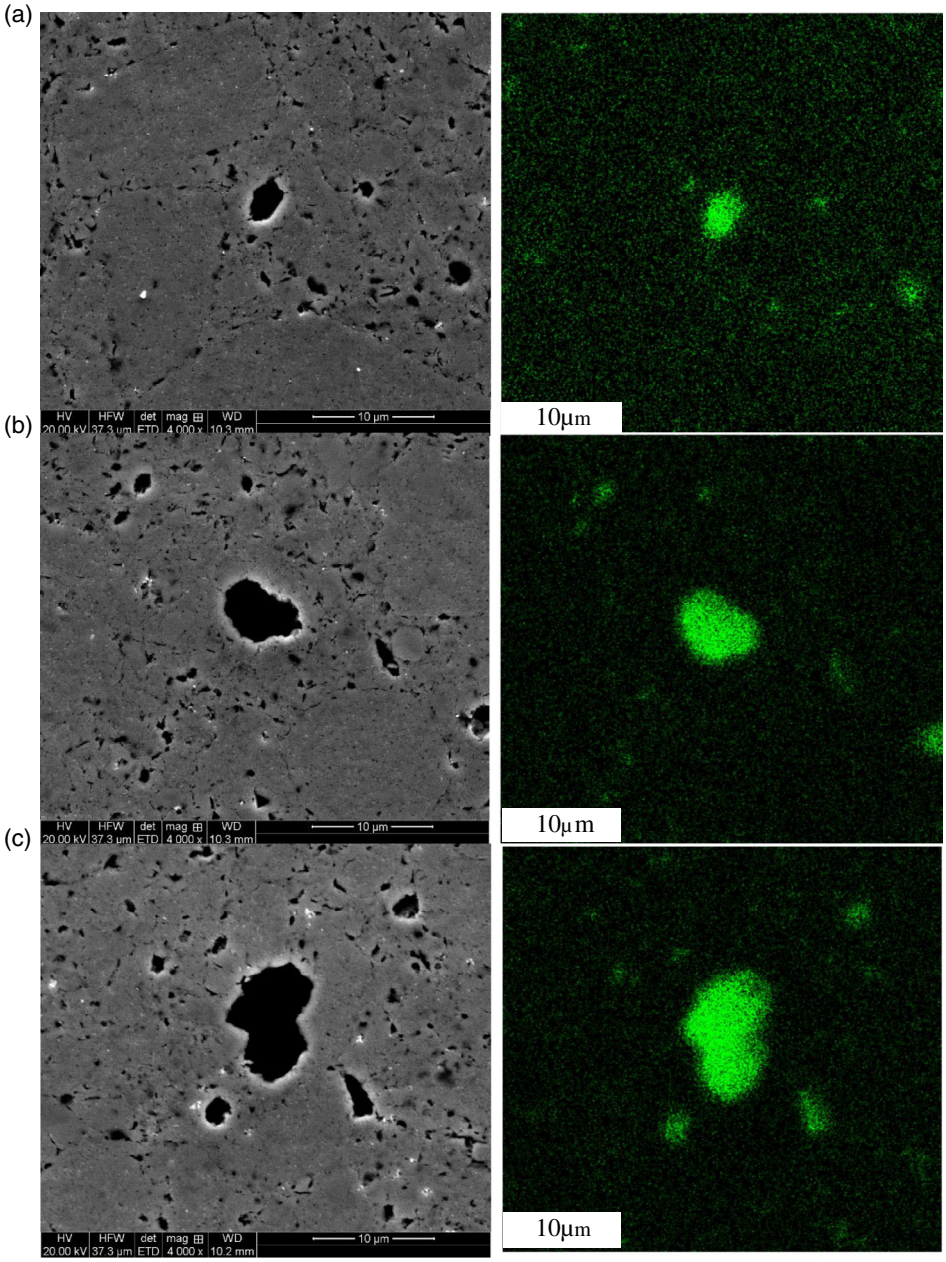

Figure 8. Graphene agglomeration in a) MnTe–0.5 wt% GNPs (left) and carbon distribution X-ray map (right), b) MnTe–0.75 wt% GNPs (left) and carbon distribution X-ray map (right), and c) MnTe–1 wt% GNPs (left) and carbon distribution X-ray map (right).

Table 1. Microstructure and mechanical characteristics of the MnTe–GNP samples.

Sample	MnTe	MnTe–0.25 wt% GNPs	MnTe–0.5 wt% GNPs	MnTe–0.75 wt% GNPs	MnTe–1 wt% GNPs
Porosity area percentage	0.6	1.12	0.5	0.5	0.65
Hardness [MPa]	1442	882	1497	1514	1379
K_{IC} (MPa$\sqrt{m}$)	0.69	0.919	0.792	0.785	0.786

deflection,[92] making the cracks reinitiate after passing through the pores. Moreover, the presence of porosity appears to have influenced the hardness values such that the samples with a higher concentration of porosity showed lower hardness (Table 1). The increase in porosity with GNP reinforcement may be attributed to the fact that in the SPS process of pristine MnTe, the local Joule heating produces melting at the particle contacts, and the applied force brings about the closure of inter-particle voids.[93] In contrast, in the GNP-reinforced samples, MnTe particles are separated by GNPs, preventing them from joining together due to the low wettability of graphene by the

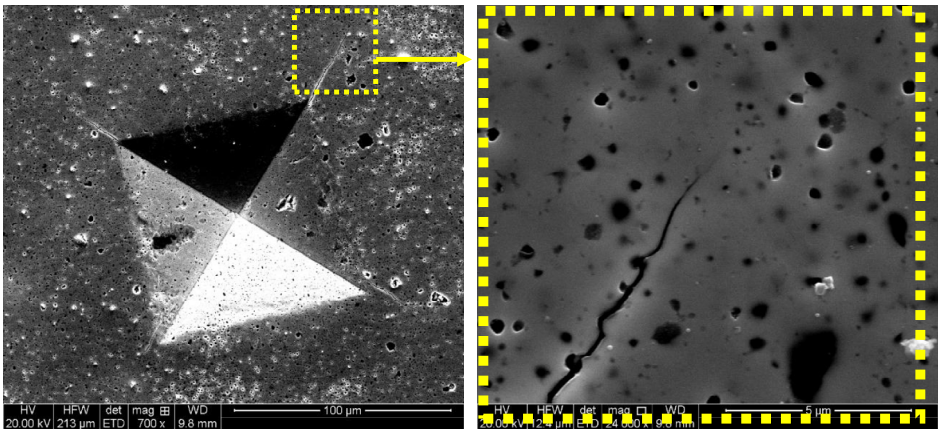

Figure 9. Microcrack formation due to the Vickers microhardness test (left side) and crack propagation path for 0.25 wt% GNP–MnTe (right side).

MnTe matrix.[94,95]. Furthermore, the formation of the impurity $Mn_{23}C_6$ phase (Figure 3) in the GNP-reinforced samples (GNPs $\geq$ 0.5 wt%), which is expected to increase with increasing GNP content, could increase the hardness values as carbides are hard and brittle.[94]

3. Conclusions

The effects of GNP inclusion on the magnetic, TE, and mechanical characteristics of an AFM MnTe compound were studied. The GNP precipitation in the MnTe matrix and the chemical reaction between GNPs and the bulk material during the synthesis process impact the magnetic, TE, and mechanical properties. Magnetic susceptibility at the AFM temperature range ($T < 307$ K) showed a monotonic reduction with the increase of the GNP mixing ratio at a temperature range of 0–50 K due to the Mn_3O_4 depletion. The XRD analysis indicated that the GNP reduces Mn_3O_4 impurities; however, it also introduces the $Mn_{23}C_6$ phase in the GNP-reinforced samples. No changes in the Néel temperature were identified; i.e., $T_N \cong 307$ K for all compounds. The GNP dispersion in the MnTe matrix decreased the thermal conductivities (34% @ T: 600 K, 0.25 wt% GNPs) due to the interface scattering of phonons. It also enhanced the Seebeck coefficients (27% @ T: 600 K, 0.25 wt% GNPs) by decreasing the carrier concentration. Approximately 33% improvement was observed in the mechanical properties of MnTe reinforced with 0.25 wt% GNPs in terms of K_{IC} as compared to the pristine MnTe.

4. Experimental Section

Synthesis: MnTe alloy was produced by chunk mixing of the pure elements (Mn and Te with 1:1 atomic ratio, Alfa Aesar 99.9%—https://www.alfa.com/en/) via a mechanical alloying/ ball milling process (Pulverisette 7, FRITSCH Planetary Ball Mill, 4 h at 600 rpm, ball/ powder mass ratio of 2:1, and stainless steel ball size of 10 mm). The powder mixture was annealed in a tube furnace under an argon atmosphere at a temperature of 750 °C for 24 h and then milled again at the same milling condition for a further 4 h. The MnTe–xGNP (x: 0.25, 0.5, 0.75, and 1 wt%) mixtures were then prepared by a micromilling (reciprocating type, 1 h, ball/powder volume ratio of 1:1, a steel ball size of 1 mm) of the synthesized MnTe powder with the GNPs (surface area 500 $m^2 g^{-1}$, Alfa Aesar) under an argon atmosphere. The bulk samples were fabricated with an average density (≈98–99% as-sintered density measured by the Archimedes method with isopropyl alcohol as a displacement medium) via spark plasma sintering (SPS) under the temperature of 950 °C and applied pressure of 42 MPa with a sintering time of 20 min under an argon atmosphere.

Microstructural Characterization: The phase identification was implemented via X-ray diffraction analysis (MiniFlex 300/600, 40 kV, 15 mA, Cu X-ray tube generation). Field emission scanning electron microscope Quanta 450 SEMs were used for the microstructural analysis.

TE, Mechanical, and Magnetic Measurements: The Seebeck coefficient (S) and electrical conductivity (σ) were measured under a He environment at a temperature range of 300 to 820 K on a commercial Linseis LSR-3 system using a differential voltage/temperature technique and a DC four-probe method, respectively. The thermal conductivity (κ) was calculated using $\kappa = D\rho C_p$, where ρ (g cm^{-3}) is the sample density. The specific heat capacity C_p (J $kg^{-1} K^{-1}$) and thermal diffusivity D ($m^2 s^{-1}$) were measured by a laser flash method on the Linseis LFA instrument at a temperature range of 300–820 K. Also, the Vickers hardness values were measured by a microhardness device (LECO, LM-700AT-load: 1000 g, dwell time:10 s) at room temperature. Moreover, the magnetic susceptibility measurement was implemented by a vibrating sample magnetometer (VSM), physical property measurement system (PPMS) (Dynacool) at a temperature range of 0–400 K.

Acknowledgements

This work has been supported by the Australian Government Research Training Program Scholarship, Faculty of Engineering and The ARC Graphene Enabled Industry Transformation Hub at the University of Adelaide. This study is partially based upon work supported by the Air Force Office of Scientific Research (AFOSR) under contract number FA9550-12-1-0225 and the National Science Foundation (NSF) under grant numbers ECCS-1351533, ECCS-1515005, and ECCS-1711253. Electron microscopy was carried out at the Adelaide Microscopy, University of Adelaide.

Conflict of Interest

The authors declare no conflict of interest.

Keywords

graphene nanoplates, MnTe, thermoelectric, waste heat recovery

Received: July 8, 2020
Revised: September 24, 2020
Published online:

[1] S. Shafraniuk, *Graphene: Fundamentals, Devices, and Applications*, CRC Press, Boca Raton, FL **2015**.
[2] S. C. Ray, *Applications of Graphene and Graphene-Oxide Based Nanomaterials*, Elsevier, Amsterdam **2015.**
[3] A. Tiwari, M. Syväjärvi, *Graphene Materials: Fundamentals and Emerging Applications*, John Wiley & Sons, Inc., Hoboken, NJ **2015**.
[4] L. Johnson, J. Meany, *Graphene: The Superstrong, Superthin, and Superversatile Material That Will Revolutionize the World*, Prometheus Books, Amherst, NY **2018.**
[5] D. Li, Y. Gong, Y. Chen, J. Lin, Q. Khan, Y. Zhang, Y. Li, H. Zhang, H. Xie, *Nano-Micro Lett.* **2020**, *12*, 36.
[6] V. Castagnola, W. Zhao, L. Boselli, M.C. Lo Giudice, F. Meder, E. Polo, K.R. Paton, C. Backes, J.N. Coleman, K.A. Dawson, *Nat. Commun.* **2018**, *9*, 1577.
[7] Md. Nurunnabi, J. R. McCarthy, *Nanomaterials*, Elsevier, Amsterdam **2019.**
[8] A. Pandikumar, P. Rameshkumar, *Graphene-Based Electrochemical Sensors For Biomolecules*, Elsevier, Amsterdam **2019.**
[9] K. M. Yocham, K. Fujimoto, R. Brown, E. Tanasse, J. T. Oxford, T. J. Lujan, D. Estrada, *Adv. Eng. Mater.* **2018**, *20*, 1800166.
[10] C-H. Liu, *Electrical and Optoelectronic Properties of the Nanodevices Composed of Two-Dimensional Materials*, Springer Nature, Singapore **2018.**
[11] P. M. Reddy, C-J. Chang, C-F. Lai, M Jusu, M-H. Tsai, *Composit. Sci. Technol.* **2018**, *165*, 95.
[12] J. Zhu, D. Yang, Z. Yin, Q. Yan, H. Zhang, *Small* **2014**, *10*, 3480.
[13] A. R. b. Mohd. Yusoff, *Graphene-Based Energy Devices*, Wiley-VCH Verlag, Weinheim, Germany, **2015**.
[14] J. Liu, *Nat. Nanotechnol*. **2014**, *9*, 739.
[15] S. Ramazani, Md. Karimi, *Mater. Sci. Eng. C*, **2015**, *56*, 325.
[16] L. Zhang, R. Wang, J. Wang, L. Wu, X. Zhang, *Nanoscale*, **2019**, *11*, 2343.
[17] Y. Wang, Y. Wang, *Adv. Energy Mater.* **2018**, *8*, 1800961.
[18] H. Ghodrati, R. Ghomashchi, *FlatChem* **2019**, *15*, 100113.
[19] V. Shautsova, T. Sidiropoulos, X. Xiao, N. A. Güsken, N. C. G. Black, *Nat. Commun.* **2018**, *9*, 1.
[20] A. Harzheim, J. Spiece, C. Evangeli, E. McCann, V. Falko, Y. Sheng, J. H. Warner, G. A. D. Briggs, J. A. Mol, P. Gehring, O. V. Kolosov, *Nano Lett.* **2018**, *18*, 7719.
[21] A. C. Kaleem, P-a. Z. Wan, *J. Mater. Sci.* **2019**, *30*, 11923.
[22] M. Li, D. L. Cortie, J. Liu, D. Yu, S. Md. K. NazrulIslam, L. Zhao, D. R. G. Mitchell, R. A. Mole, M. B. Cortie, S. Dou, X. Wang, *Nano Energy* **2018**, *53*, 993.
[23] C. Nath, C.-Y. Chueh, Y.-K. Kuo, J. P. Singh, *J. Appl. Phys.* **2019**, *125*, 185101.
[24] F-P. Du, N-N. Cao, Y-F. Zhang, P. Fu, Y-G. Wu, Z-D. Lin, R. Shi, A. Amini, C. Cheng, *Sci. Rep.* **2018**, *8*, 1.
[25] O. Okhay, S. Zlotnik, W. Xie, K. Orlinski, M. J. H. Gallo, G. Otero-Irurueta, A.J.S. Fernandes, D. A. Pawlak, A. Weidenkaff, A. Tkach, *Carbon* **2019**, *143*, 215.
[26] S. Yadav, S. Chaudhary, D. K. Pandya, *Ceramics Int.* **2018**, *44*, 10628.
[27] T. Caillat, M. Carle, P. Pierrat, H. Scherrer, S. Scherrer, *J. Phys. Chem. Solids* **1992**, *53* 1121.
[28] D. T. Morelli, V. Jovovic, J. P. Heremans, *Phys. Rev. Lett.* **2008**, *101*.
[29] H. Liu, X. Shi, F. Xu, L. Zhang, W. Zhang, L. Chen, Q. Li, C. Uher, T. Day, G. J. Snyder, *Nat. Mater.* **2012**, *11*, 422.
[30] M. D. Nielsen, V. Ozolins, J. P. Heremans, *Energy Environ. Sci.* **2013**, *6*, 570.
[31] R. Watanabe, R. Yoshimi, M. Shirai, T. Tanigaki, M. Kawamura, A. Tsukazaki, K. S. Takahashi, R. Arita, M. Kawasaki, Y. Tokura, *Appl. Phys. Lett.* **2018**, *113*, 181602.
[32] J. P. Heremans, V. Jovovic, E. S. Toberer, A. Saramat, K. Kurosaki, A. Charoenphakdee, S. Yamanaka, G. J. Snyder, *Science* **2008**, *321*, 554.
[33] Y. Zheng, T. Lu, M. M. H. Polash, M. Rasoulianboroujeni, N. Liu, M. E. Manley, Y. Deng, P. J. Sun, X. L. Chen, R. P. Hermann, D. Vashaee, J. P. Heremans, H. Zhao, *Sci. Adv.* **2019**, *5*, eaat9461.
[34] M. M. H. Polash, F. Mohaddes, M. Rasoulianboroujeni, D. Vashaee, *J. Mater. Chem. C*, **2020**, *8*, 4049.
[35] K. K. Kelley, *J. Am. Chem. Soc.* **1939**, *61*, 203.
[36] C. F. Squire, *Phys. Rev.* **1939**, *56*, 922.
[37] J. W. Allen, G. Lucovsky, J. C. Mikkelsen, *Solid State Commun.* **1977**, *24*, 367.
[38] A.J. Panson, W.D. Johnston, *J. Inorg. Nucl. Chem.* **1964**, *26*, 705.
[39] K. Ando, K. Takahashi, T. Okuda, *J. Magn. Magn. Mater.* **1992**, *104–107*, 993.
[40] W. Szuszkiewicz, E. Dynowska, B. Witkowska, B. Hennion, *Phys. Rev. B* **2006**, *73*, 104403.
[41] R. W. Cochrane, M. Plischke, J. O. Strom-Olsen, *Physical Review B* **1974**, *9*, 3013.
[42] W. D. Johnston, D. E. Sestrich, *J. Vnorg. Nucl. Chem.* **1961** *19*, 229.
[43] T. Hamasaki, *Solid State Commun.***1979**, *32*, 1069.
[44] R. Triboulet, G. Didier, *J. Cryst. Growth* **1981**, *52* 614.
[45] G. Tan, F. Shi, S. Hao, H. Chi, T. P. Bailey, L-D. Zhao, C. Uher, C. Wolverton, V. P. Dravid, M. G. Kanatzidis, *J. Am. Chem. Soc.* **2015**, *137*, 11507.
[46] T. M. Giebultowicz, P. KIosowski, N. Samarth, H. Luo, J. K. Furdyna, *Phys. Rev. B*, **1993**, *48*, 12817.
[47] C. Ferrer-Roca, A. Segura, C. Reig, V. Munoz, *Phys. Rev. B* **2000**, *61*, 13679.
[48] K. Walther, *Solid State Commun.* **1967**, *5*, 399.
[49] W. Xie, S. Populoh, K. Gałązka, X. Xiao, L. Sagarna, Y. Liu, M. Trottmann, J. He, A. Weidenkaff, *J. Appl. Phys.* **2014**, *115*, 103707.
[50] S. Mu, R. P. Hermann, S. Gorsse, H. Zhao, M. E. Manley, *Phys. Rev. Mater.* **2019**, *3*, 025403.
[51] Y. Ren, J. Yang, Q. Jiang, D. Zhang, Z. Zhou, X. Li, J. Xin, X. He, *J. Mater. Chem. C*, **2017**, *5*, 5076.
[52] Y. Magnin, T. Diep, *Phys. Rev. B* **2012**, *85*, 184413.
[53] A. Basit, J. Yang, Q. Jiang, J. Xin, X. Li, S. Li, S. Li, Q. Long, *J. Mater. Chem. A*, **2018**, *6*, 23473.
[54] K. Akabli, H. T. Diep, *Phys. Rev. B* **2008**, *77*, 165433.
[55] M. Jouannea, W. Szuszkiewiczb, J.F. Morhangea, M.A. Kanehisa, J. M. Hartmannc, H. Mariettec, E. Dynowskab, G. Karczewskib, T. Wojtowiczb, J. Kossutb, J. Barnasd, *J. Cryst. Growth* **1998**, *184/185*, 947.
[56] A. Gaj, W. Grieshaber, C. Bodin-Deshayes, J. Cibert, *Phys. Rev. B* **1994**, *50*, 5512.
[57] H. Chen, C. Yang, H. Liu, G. Zhang, D. Wan, F. Huang, *Cryst Eng Comm*,**2013**, *15* 6648.
[58] M. S. El-Asfoury, M. N.A. Nasr, K. Nakamura, A. Abdel-Moneim, *J. Alloys Compd.***2018**, *745,* 331.
[59] Y. Zhang, H. Ma, B. Sun, B. Liu, H. Liu, L. Kong, B. Liu, X. Jia, X. Chen, *J. Alloys Compd* **2017**, *715*, 344.
[60] K. Agarwal, V. Kaushik, D. Varandani, A. Dhar, B.R. Mehta, *J. Alloys Compd.* **2016**, *681*, 394.
[61] S. Kumar, S. Singh, P. K. Dhawan, R. R. Yadav, N. Khare, *Nanotechnology*,**2018**, *29*, 1.
[62] H. Yue, L. Yao, X. Gao, S. Zhang, E. Guo, H. Zhang, X. Lin, B. Wang, *J. Alloys Compd.* **2017**, *691*, 775.
[63] X. Hu, Y.C. Chan, K. Zhang, K.C. Yung, *J. Alloys Compd.* **2013**, *580* 162.
[64] A. Bhadauria, L. K. Singh, T. Laha, *J. Alloys Compd.* **2018**, *748,* 783.

[65] Q-H. Yuan, Z-Q Qiu, G-H Zhou, X-S. Zeng, L. Luo, X-X. Rao, Y. Ding, Y. Liu, *Mater. Character.* **2018**, *138*, 215.
[66] M. Rashad, F. Pan, M. Asif, A. Tang, *J. Industr. Eng. Chem.* **2014**, *20*, 4250.
[67] A. Sharma, H-R. Sohn, J. P. Jung, *Metall. Mater. Trans. A* **2016**, *47*, 494.
[68] C. W. Na, D. S. Han, D. S. Kim, J. Park, Y. T. Jeon, G. Lee, M-H. Jung, *Appl. Phys. Lett.* **2005**, *87*, 142504.
[69] W. M. Dawson, F. R. Sale, *Metal. Trans. A*, **1980**, *52*, 11A.
[70] M. Liu, J. M. Cowley, *Carbon*, **1995**, *33*, 749.
[71] K. T. Jacob, A. Kumar, G. Rajitha, Y. Waseda, *High Temp. Mater. Proc.* **2011**, *30* 459.
[72] U. V. Choudary, Y. A. Chang, *Calphad* **1978**, *2*,169.
[73] Z. Li, J-F. Dong, F-H. Sun, S. Hirono, J-F. Li, *Chem. Mater.* **2017**, *29*, 7378.
[74] X. She, X. Su, H. Xie, J. Fu, Y. Yan, W. Liu, P. F. Poudeu, X. Tang, *ACS Appl. Mater. Interfaces* **2018**, *10*, 25519.
[75] H. Wiedemeier, Growth of Single Crystals by Vapour Transport, Technical Report, NASA, **1987.**
[76] V. Vassiliev, M. Bykov, M. Gambino, J.P. Bros, *J. Chim. Phys.* **1993**, *90*, 463.
[77] W. M. Dawson, F. R. Sale, *Metall. Trans. A* **1980**, *11*, 1849.
[78] J. D. Wasscher, *Electrical Transport Phenomena in MnTe, an Antiferromagnetic Semiconductor*, Technische Hogeschool Eindhoven, Eindhoven **1969**.
[79] E. Uchida, H. Kondoh, N. Fukuoka, *J. Phys. Soc. Jpn.* **1956**, *11*, 27.
[80] H. Yadaka, T. Harada, E. Hirahara, *J. Phys. Soc. Jpn.* **1962**, *17*, 875.
[81] Y. Xu, W. Li, C. Wang, Z. Chen, Y. Wu, X. Zhang, J. Li, S. Lin, Y. Chen, Y. Pei, *J. Mater.* **2018**, *4* 215.
[82] W. D. Johnston, R. C. Miller, D. H. Damon, *J. Less-Common Metals* **1965**, *8*, 272.
[83] C. Hass, *Phys. Rev.* **1968**, *168*, 531.
[84] D. Vashaee, A. Shakouri, *Phys. Rev. Lett.*, **2004**, *92*, 106103,
[85] M. S. Dresselhaus, A. J. Minnich, Z. F. Ren, G. Chens, *Energy Environ. Sci.* **2009**, *2*, 466.
[86] W. Kims, *J. Mater. Chem. C*, **2015**, *3*, 10336.
[87] S. H. Zaferani, R. Ghomashchi, D. Vashaee, *Renew. Sustain. Energy Rev.* **2019**, *112* 158.
[88] D. Zhao, X. Wang, D. Wu, *Crystals* **2017**, *7*, 71.
[89] K. Markandan, J. K. Chin, M. T.T. Tan, *Appl. Mech. Mater.* **2014**, *625*, 81.
[90] D. K. Shetty, I. G. Wright, P. N. Mincer, A. H. Clauer, *J. Mater. Sci.* **1985**, *20*, 1873.
[91] L. Kvetková, A. Duszová, P. Hvizdoš, J. Duszá, P. Kunb, C. Balázsi, *Scr. Mater.* **2012**, *66*, 793.
[92] N. Joulaee, A. Makradi, S. Ahzi, M. A. Khaleel, *Mater. Sci. Forum* **2007**, *553*, 69.
[93] B. Du, F. Gucci, H. Porwal, S. Grasso, A. Mahajan, M. J. Reece, *J. Mater. Chem. C*, **2017**, *5*, 1514.
[94] M. Gurbuz, T. Mutuk, *J. Composite Mater.* **2018**, *52*, 543.
[95] H. R. Ezatpour, S. A. Sajjadi, M. H. Sabzevar, Y. Huang, *Mater. Des.* **2014**, *55* 921.
[96] F. Tang, D. Bogdanovski, I. Bajenova, A. Khvan, R. Dronskowski, B. Hallstedt, *Calphad*, **2018**, *60*, 231.

energies

MDPI

Article

Experimental Realization of Heavily p-doped Half-Heusler CoVSn Compound

Sadeq Hooshmand Zaferani [1,2,*], Alireza Darebaghi [1], Soon-Jik Hong [3], Daryoosh Vashaee [2,4,*] and Reza Ghomashchi [1,5,6,*]

1 School of Mechanical Engineering, University of Adelaide, Adelaide, SA 5005, Australia; alireza.darebaghi@adelaide.edu.au
2 Department of Electrical and Computer Engineering, North Carolina State University, Raleigh, NC 27606, USA
3 Division of Advanced Materials Engineering, Kongju National University, Chungnam 331-717, Korea; hongsj@kongju.ac.kr
4 Department of Materials Science and Engineering, North Carolina State University, Raleigh, NC 27606, USA
5 ARC Research Hub for Graphene Enabled Industry Transformation, University of Adelaide, Adelaide, SA 5005, Australia
6 Institute For Photonics And Advanced Sensing, University of Adelaide, Adelaide, SA 5005, Australia
* Correspondence: sadeq.hooshmandzaferani@adelaide.edu.au (S.H.Z.); dvashae@ncsu.edu (D.V.); reza.ghomashchi@adelaide.edu.au (R.G.)

Received: 24 February 2020; Accepted: 19 March 2020; Published: 20 March 2020

Abstract: Hypothetical half-Heusler (HH) ternary alloy of CoVSn has already been computationally investigated for possible spintronics and thermoelectric applications. We report the experimental realization of this compound and the characterizations of its thermoelectric properties. The material was synthesized by a solid-state reaction of the stoichiometric amounts of the elements via powder metallurgy (30 h mechanical milling and annealing at 900 °C for 20 h) and spark plasma sintering (SPS). The temperature-dependent ternary thermodynamic phase diagram of Co-V-Sn was further calculated. The phase diagram and detailed analysis of the synthesized material revealed the formation of the non-stoichiometry HH CoVSn, mixed with the binary intermetallic phases of SnV_3, Co_2Sn, and Co_3V. The combination of X-ray diffraction, energy-dispersive X-ray spectroscopy, and thermoelectric transport properties confirmed the formation of a multi-phase compound. The analysis revealed the predicted thermoelectric features (zT = 0.53) of the highly doped CoVSn to be compromised by the formation of intermetallic phases (zT ≈ 0.007) during synthesis. The additional phases changed the properties from p- to overall n-type thermoelectric characteristics.

Keywords: half-Heusler; CoVSn; thermoelectric; heterogeneous structure

1. Introduction

There have been substantial progress in thermoelectric (TE) materials over the last two decades. Thermoelectric technology, which was mainly based on alloys of bismuth telluride [1] for Peltier cooling modules, or silicon-germanium alloys [2] for radioisotope thermoelectric generators used in NASA spacecraft, has expanded to new compounds for power generation and cooling [3]. New materials and material structures have been discovered with considerably enhanced thermoelectric properties [4]. In particular, some materials like half-Heusler (HH) alloys have shown an inherently large thermoelectric power factor, although they have generally higher thermal conductivity than alloys such as Skutterudites [5] and Clathrates [6]. Since the thermal conductivity can be decreased by structural engineering, their potential to provide inherently significant power factors has attracted much attention lately. Recently, a new class of HH compounds was predicted with low thermal

conductivity [7]. In this regard, the sheer number of HH compounds to investigate is vast, and computational and predictive methods to shortlist the promising ones have become essential to making quick progress. First principle studies [8] and thermodynamic calculations [9] are some of the main methods to predict the new materials. Notably, HH alloys with the crystal structure of C1b (No. 216) and the atomic arrangement of XYZ [10] have attracted much attention due to their unusual TE characteristics, high-temperature stability, and doping capabilities (Figure 1, Table 1).

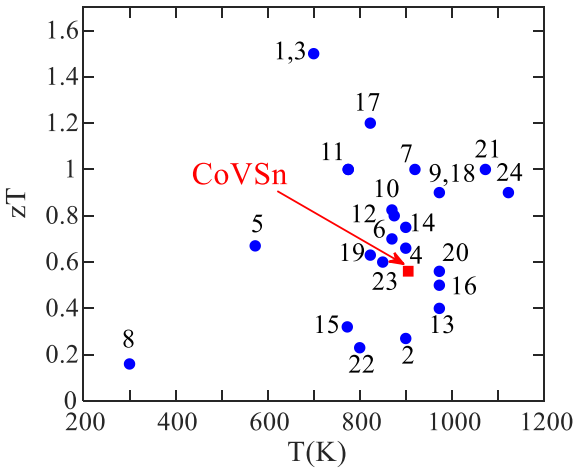

Figure 1. Selected alloys with their corresponding TE properties, which have been studied as half-Heusler (numbers are the items given in Table 1).

Table 1. Compounds cited in Figure 1.

Item	Compound	Ref.	Item	Compound	Ref.
1	$Ti_{0.5}(Zr_{0.5}Hf_{0.5})_{0.5}NiSn_{0.998}Sb_{0.002}$	[11]	13	NbCoSb	[12]
2	$TiCo_{0.95}Ni_{0.05}Sb$	[13]	14	Zr,Ni,Sn	[14]
3	$(Zr_{0.5}Hf_{0.5})_{0.5}Ti_{0.5}NiSn_{0.998}Sb_{0.002}$	[15]	15	Ti,Ni,Sn	[16]
4	$Ti_{0.5}(ZrHf)_{0.49}Nb_{0.01}Ni_{0.9}Pd_{0.1}Sn_{0.9}8Sb_{0.02}$	[17]	16	VCoSb	[18]
5	$ZrNiSn_{0.98}Sb_{0.02}$	[19]	17	$Ti_{0.5}Zr_{0.5}NiSn_{0.98}Sb_{0.02}$	[20]
6	$(Hf_{0.6}Zr_{0.4})_{0.99}Y_{0.01}NiSn_{0.98}Sb_{0.02}$	[21]	18	$(Hf_{0.25}Zr_{0.75})_{0.995}Nb_{0.005}NiSn$	[22]
7	$Hf_{0.75}Zr_{0.25}NiSn_{0.99}Sb_{0.01}$	[23]	19	$(TiNiSn)_{0.95}$ + $(MnNiSb)_{0.05}$	[24]
8	1.5% Y-Sb-doped Ti-Ni-Sn	[25]	20	$NbCoSb_{0.8}Sn_{0.2}$	[26]
9	$TiCoSb_{0.8}Sn_{0.2}$	[27]	21	$Zr_{0.5}Hf_{0.5}Co_{0.9}Ni_{0.1}Sb$	[28]
10	$(Zr_{0.3}Hf_{0.65}Ta_{0.05})NiSn$	[29]	22	$ZrCo_{0.97}Pd_{0.03}Bi$	[30]
11	$(Ti_{0.4}(Zr_{0.5}Hf_{0.5})_{0.6})_{0.99}Ta_{0.01}NiSn$	[31]	23	$TiNi_{1.06}Sn_{0.81}Sb_{0.17}$	[32]
12	$ZrNiSn_{0.99}Sb_{0.01}$	[33]	24	$Nb_{0.83}CoSb$	[34]
Predicted TE factors of CoVSn compound, κ = 4.1 W/mK, S = 175 μV K^{-1}, zT = 0.53 at 900 K.		[35]			

In 1995, Ögüt et al. [36] predicted CoVSn with a MgAgAs (C1b) crystal structure as an intermetallic semiconductor using density functional theory (DFT) band structure calculations. Another study [37] applied the full-potential linear muffin-tin orbital (FP-LMTO) method to evaluate the electronic properties of CoVSn alloy and showed an indirect energy bandgap of 0.75 eV. Shi et al. [38] calculated the electronic structure using the modified Becke-Johnson (MBJ) potential. Also, the transport coefficients were computed employing the Boltzmann theory within the constant scattering time approximation. Moreover, spin-orbit coupling (SOC) was considered in the electronic and transport calculations. Figure 2 shows the calculated electronic band structure and density of states (DOS) of CoVSn alloy [38]. Based on this electronic structure, the alloy was predicted as a p-type semiconductor with a bandgap (W-X) of 0.85 eV.

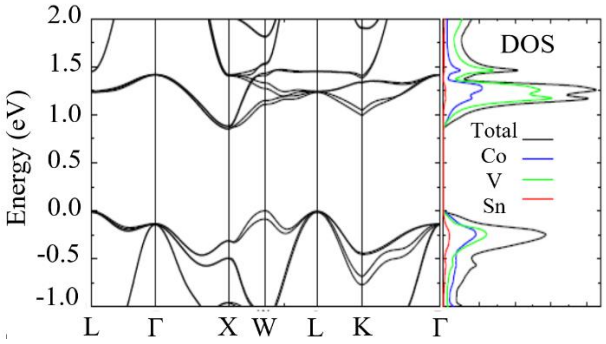

Figure 2. Calculated electronic band structure and density of states (DOS) of the CoVSn alloy. Reproduced from [38], Elsevier: 2017.

In the mentioned study, the maximum Seebeck coefficient with a carrier concentration of 1.0×10^{21} cm^{-3} was calculated at a temperature of 1150 K as 340 μV/K [38]. Zeeshan et al. [39] carried out combined ab initio and semiclassical calculations based on Boltzmann transport theory and determined the maximum doping concentration of the p-type CoVSn alloy. Assuming a relaxation time of 10^{-15} s for V- and Cr-group doping, they estimated a Seebeck coefficient of 175 μV/K and a maximum power factor in the range of 11–23 μW/K^{-2} at optimum 0.26 e/uc p-type doping. This value of the power factor is comparable to the power factor of many good HH thermoelectric alloys.

Despite the wide range of theoretical studies on CoVSn alloy with predicted promising thermoelectric characteristics, to the best of our knowledge, there is no report on the thermoelectric characterization of a synthesized sample of this alloy in the open literature. The current study presents an experimental synthesis and characterization of the CoVSn compound, and an empirical thermoelectric and microstructure analysis is performed.

2. Materials and Methods

The powder mixture of CoVSn compound was prepared by ball milling (SPEX-6, Metuchen, NJ, USA) (5:1 ball-powder weights) a stoichiometric ratio (1:1:1) of Co, V and Sn elements (Alfa Aesar Co., 99.9% commercial purity, Ward Hill, MA, USA) for 30 h following an annealing process at 900 °C for 20 h. The bulk samples were made by spark plasma sintering (SPS) at a temperature of 850 °C for 20 min at a pressure of 42 MPa. The phase identification was made via X-ray diffraction analysis (MiniFlex 300/600, 40 kV, 15 mA, Cu x-ray tube generation). The microstructure analysis was performed by field emission scanning electron microscopy (FESEM) (Quanta 450 FEG, FEI, Hillsboro, OR, USA). The thermal diffusivity (υ) was measured using a laser flash apparatus (LFA, Linseis, Selb, Germany) under an Ar environment from 30 to 550 °C. The Archimedes method was used to measure the density of materials with deionized water (DI) water as a displacement medium. Also, the specific heat was approximated by the Debye specific heat [40] for a temperature range of 30 to 600 °C. The electrical resistivity was measured using Linseis-LSR3 equipment (LSR3, Linseis, Selb, Germany) under He environment for the same temperature range. The Seebeck coefficient was measured simultaneously. The commercial Linsesis software calculates the thermopower from a single temperature gradient (ΔT) and voltage difference (ΔV), which is often erroneous. Therefore, the measurement was performed for five different temperature gradients, and each measurement was repeated four times, then averaged. The thermopower was calculated from the slope of the line fitted to five separate temperature and voltage differences. The accuracy of the measurement was verified by inspecting the linear fit to the (ΔT-ΔV) data set.

3. Results and Discussion

Figure 3 shows the X-ray diffraction data of the CoVSn powder after 15 and 30 h milling, and that of the SPS-consolidated bulk sample prepared from the milled powder mixture that was annealed at 900 °C for 20 h. The XRD patterns of the SPS-consolidated CoVSn bulk sample revealed the presence

of three binary intermetallics, namely, SnV_3, Co_2Sn, and Co_3V, in addition to the non-stoichiometry CoVSn half-Heusler alloy. Therefore, the synthesized compound was shown to be a multi-phase material. Further, the back-scattered electron (BSE) image and the energy dispersive spectroscopy (EDS) maps of the material, as shown in Figure 4, illustrated a heterogeneous microstructure, which agrees with the observation from the XRD analysis. The non-uniform dispersion of Co, V, and Sn provide evidence of the presence of a multiphase structure with various micro-clusters.

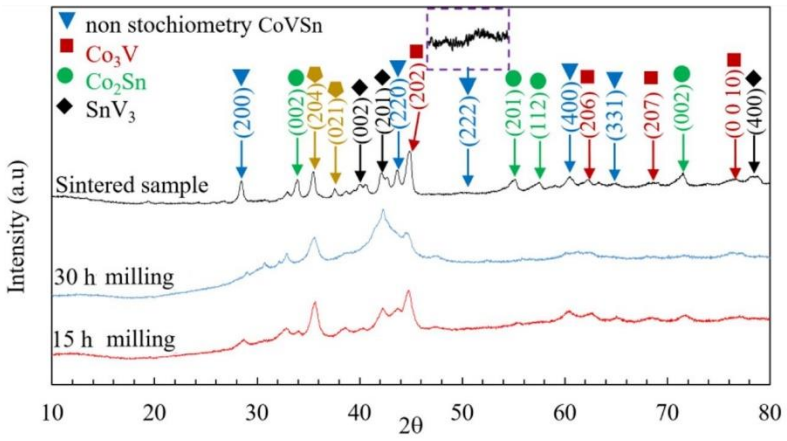

Figure 3. XRD patterns of the synthesized CoVSn compound.

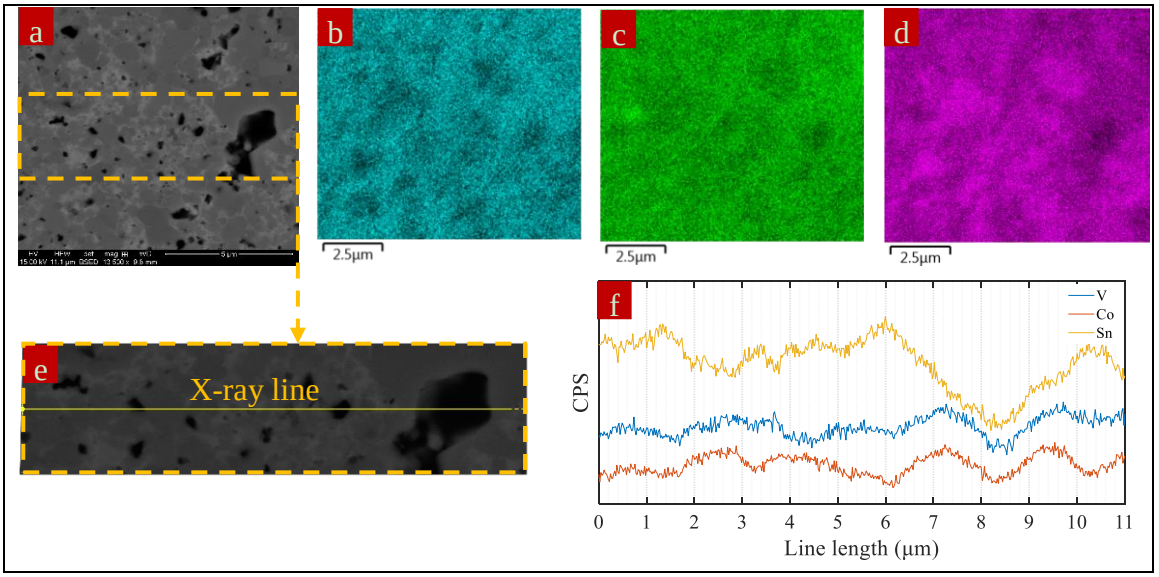

Figure 4. (**a**) BSE micrograph of the SPS-consolidated CoVSn composition and EDS-maps of (**b**) Co, (**c**) V, and (**d**) Sn. (**e**) X-ray line scan and (**f**) element distribution along with the X-ray line scan.

Figure 5 shows the thermoelectric parameters S, σ, κ (thermal conductivity), and zT of the synthesized compound over a temperature range of 25 to 550 °C. The Seebeck coefficient was negative, indicating an n-type semiconductor. This is in contrast with the theoretical prediction that the CoVSn compound should be a p-type semiconductor [38,39]. The physical properties of the Heusler-based compound are generally highly related to the crystallographic order [41]. The observed multiphase structure (Figure 5) combining metallic and semiconductor characteristics due to the presence of intermetallics (SnV_3, Co_2Sn, and Co_3V) and a semiconductor (CoVSn), respectively. Therefore, the carrier type of the composition cannot be assigned to the single-phase half-Heusler CoVSn compound.

As illustrated in Figure 4, the multi-phase structure containing various intermetallic compounds with both semiconductor and metallic characteristics provides semiconductor-metal interfaces [42]. The CoVSn compound containing the intermetallic phases has both ionic and covalent bonds. The presence of both ionic and covalent bonds in CoVSn (VSn: ionic-rock salt; CoSn: covalent-Zinc blend) can influence the stability of the semiconductor-metal interfaces (i.e., interface behavior) [43]. The metal–semiconductor contact lines up the chemical potentials and develops a Schottky barrier at the interface that can lead to distinct chemical and electrical properties different from the bulk compounds [44]. It is instructive to look at the thermodynamics of the ternary phase diagram of CoVSn. Such data are not currently available, being a new alloy. Therefore, we calculated the ternary phase diagram of the Co-V-Sn over the temperatures range of interest, 25 to 1200 °C. The Thermo-Calc 2016a package was used for this calculation. Figure 6 shows the ternary phase diagrams at the selected temperatures of 1100, 900, 600, and 25 °C.

Table 2. Phase compositions of the nominated areas in Figure 6.

Temperature (°C)	Label	Phase (s)
25	a_2	Co_3Sn_2_A + HCP_A3 + HCP_ORD
	b_2	Co_3Sn_2_A + CoSn + HCP_ORD
	c_2	CoSn + HCP_ORD + Sn_3V_2
	d_2	CoSn + $CoSn_2$ + Sn_3V_2
	e_2	BCT_A5 + $CoSn_2$ + Sn_3V_2
	f_2	HCP_ORD + $Sn3V_2$ + SnV_3
	g_2	CoV_3_A15 + HCP_ORD + SnV_3
	h_2	BCC_B2 + CoV_3_A15 + SnV_3
	i_2	BCC_B2 + CoV_3_A15
600	a_6	Co_3Sn_2_A + FCC_L12
	b_6	Co_3Sn_2_B + FCC_L12 + HCP_ORD
	c_6	Co_3Sn_2_B + HCP_ORD
	d_6	Co_3Sn_2_B + CoSn + HCP_ORD
	e_6	ALTA_SIGMA (V,Co) + CoSn + HCP_ORD
	f_6	ALTA_SIGMA (V, Co) + CoSn
	g_6	ALTA_SIGMA(V, Co) + CoSn+ SnV_3
	h_6	CoSn + Sn_3V_2 + SnV_3
	i_6	LIQUID + CoSn + Sn_3V_2
	j_6	LIQUID + Sn_3V_2
	k_6	ALTA_SIGMA(V, Co) + SnV_3
	l_6	ALTA_SIGMA(V, Co) + CoV_3_A15 + SnV_3
	h_2	BCC_B2 + CoV_3_A15 + SnV_3
	i_2	BCC_B2 + CoV_3_A15
	o_6	BCC_B2
	p_6	BCC_B2 + SnV_3

Table 2. *Cont.*

Temperature (°C)	Label	Phase (s)
900	a_9	FCC_L12
	b_9	Co_3Sn_2_B + FCC_L12
	c_9	Co_3Sn_2_B + FCC_L12 + HCP_ORD
	d_9	Co_3Sn_2_B + HCP_ORD
	e_9	ALTA_SIGMA(V, Co) + Co_3Sn_2_B + HCP_ORD
	f_9	ALTA_SIGMA(V, Co) + Co_3Sn_2_B
	g_9	Co_3Sn_2_B+BCC_B2+CoSn
	h_9	ALTA_SIGMA(V, Co) + Co_3Sn_2_B + BCC_B2
	i_9	BCC_B2 + Co_3Sn_2_B
	j_9	LIQUID + BCC_B2 + CoSn
	k_9	ALTA_SIGMA (V, Co) + CoV_3_A15 + BCC_B2
	l_9	BCC_B2 + CoSn
	i_2	BCC_B2 + CoV_3_A15
	o_6	BCC_B2
	o_9	LIQUID + SnV_3
	p_9	LIQUID + BCC_B2 + SnV_3
	p_6	BCC_B2 + SnV_3
	r_9	LIQUID + BCC_B2
	s_9	ALTA_SIGMA(V, Co) + BCC_B2
1100	a_9	FCC_L12
	b_9	Co_3Sn_2_B + FCC_L12
	c_{11}	LIQUID + Co_3Sn_2_B + FCC_L12
	d_{11}	LIQUID + FCC_L12
	e_{11}	LIQUID + ALTA_SIGMA
	f_{11}	LIQUID + ALTA_SIGMA (V, Co) + FCC_L12
	g_{11}	LIQUID
	h_{11}	LIQUID + ALTA_SIGMA(V, Co) + BCC_B2
	i_{11}	ALTA_SIGMA (V, Co) + BCC_B2
	o_6	BCC_B2
	p_6	BCC_B2 + SnV_3
	l_{11}	LIQUID + BCC_B2
	m_{11}	LIQUID + LIQUID #2 + SnV_3
	n_{11}	LIQUID + LIQUID #2 + BCC_B2
	l_{11}	LIQUID + BCC_B2
	o_9	LIQUID + SnV_3
	q_{11}	LIQUID + LIQUID #2

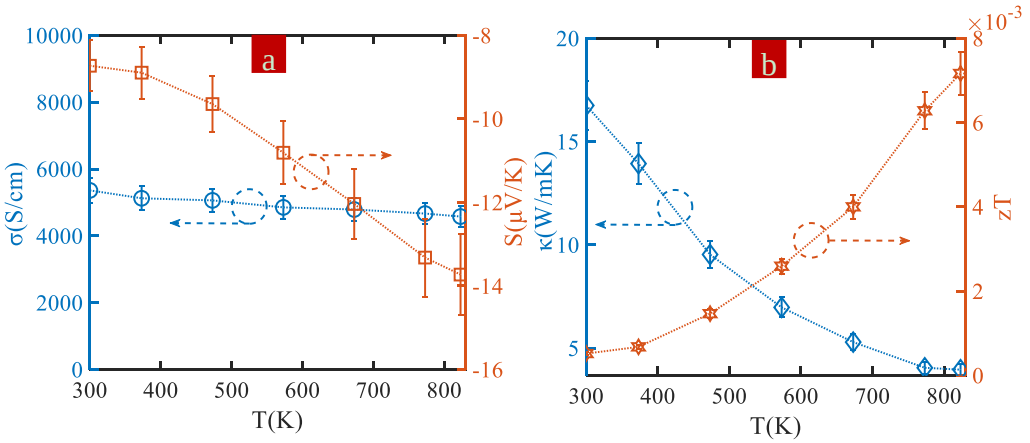

Figure 5. Temperature dependence thermoelectric parameters of CoVSn compounds. (**a**) electrical conductivity and Seebeck coefficient, (**b**) Thermal conductivity and zT.

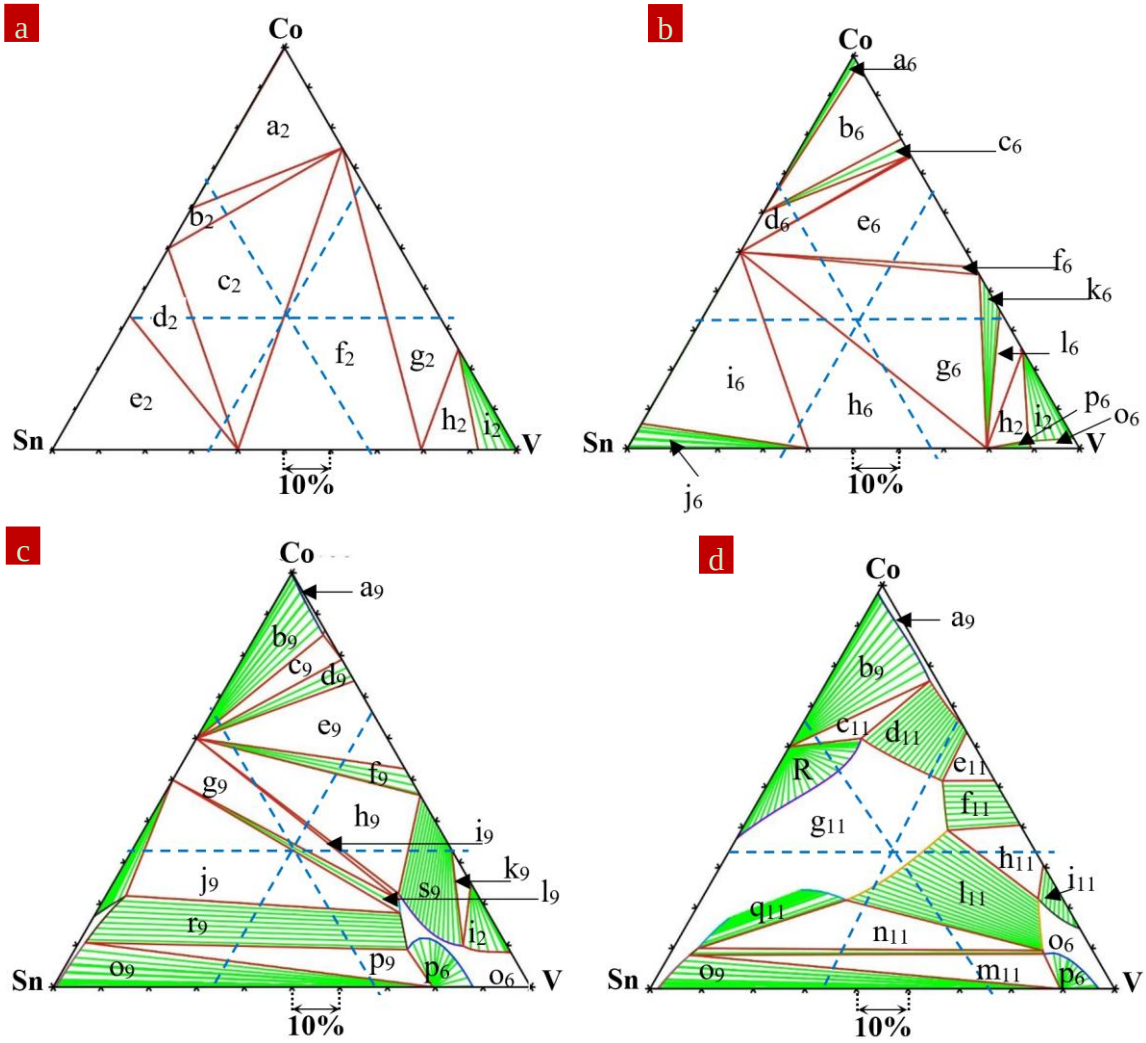

Figure 6. Calculated ternary phase diagrams (atomic ratio) of Co-V-Sn at (**a**) 25 °C, (**b**) 600 °C, (**c**) 900 °C and (**d**) 1100 °C. Crossing point showed a composition of 1:1:1 of atomic percent and a weight percent of Co: 26wt.%, V:22 wt.% and Sn: 52wt.%. Thermo-Calc 2016a package was employed to calculate the ternary phase diagrams under the atmospheric pressure. Table 2 give the phase compositions of the nominated areas in Figure 6.

Table 3 lists the different phases at the center of the phase diagram (i.e., the equal atomic concentration of the elements over 100-degree temperature steps from 25 to 1100 °C). These diagrams further confirm that at thermodynamic equilibrium, the material decomposes into multiple phases, as listed in Table 3, which agrees with the observation in the microstructural analysis (Figures 3 and 4).

Table 3. The phase composition of CoVSn compound (1:1:1) at the temperature of 25 to 1100 °C.

T (°C)	Phase/Crystal Structure/Elements
25	CoSn, HCP_ORD (Co, V) and Sn_3V_2
100	SnV_3, HCP_ORD (Co, V) and Sn_3V_2
200	SnV_3, HCP_ORD (Co, V) and Sn_3V_2
300	CoSn, HCP_ORD (Co, V) and Sn_3V_2
400	CoSn, HCP_ORD (Co, V) and Sn_3V_2
500	CoSn, HCP_ORD (Co, V) and Sn_3V_2
600	CoSn, SnV_3, ALTA_SIGMA (V, CO)
700	SnV_3, BCC_B2 (Co,V,Sn), ALTA_SIGMA (V, Co)
800	Equilibrium line between two areas of (CoSn, BCC_B2 (Co,V,Sn)) and (ALTA_SIGMA (V, Co), CoSn, BCC_B2 (Co,V,Sn))
900	Equilibrium line between two areas of (CoSn, BCC_B2 (Co,V,Sn)) and (LIQUID, CoSn, BCC_B2 (Co,V,Sn))
1000	LIQUID, BCC_B2 (Co,V,Sn)
1100	LIQUID

As shown in Table 3, there is no single phase of CoVSn, but mainly binary compounds of CoSn, SnV_3, Co_3V, and Sn_2V_3. Our observation of the multiphase structure, containing three binary intermetallics, contradicts previous studies [38,45]. In the theoretical analysis of this composition (1:1:1) [45], the calculated phase diagram showed a specific area for the stable CoVSn compound. However, the presence of this single-phase alloy was not experimentally confirmed.

4. Conclusions

The single-phase half-Heusler CoVSn was predicted theoretically as a stable thermodynamic material with prospective properties for spintronics and thermoelectric applications, although it was never experimentally confirmed. According to the theoretical and experimental data presented here, the CoVSn phase was found to be thermodynamically unstable, and its partial decomposition into metallic phases is unavoidable at the equilibrium state. In this study, the experimental realization of the CoVSn compound with a heterogeneous microstructure was represented. The material analysis showed the presence of the half-Heusler ternary alloy of non-stoichiometry CoVSn as the semiconductor phase, mixed with three binary intermetallics: SnV_3, Co_2Sn, and Co_3V. The combination of X-ray diffraction, energy-dispersive X-ray spectroscopy, and transport properties confirmed the formation of the composite structure. The composite material demonstrated a metallic electronic behavior with a degenerate carrier concentration.

Author Contributions: Conceptualization, S.H.Z., R.G., and D.V.; Methodology, S.H.Z., R.G., and D.V.; Validation, S.H.Z., R.G., and D.V.; Formal Analysis, S.H.Z.; Investigation, S.H.Z.; Resources, S.H.Z.; Data Curation, S.H.Z.; Writing-Original Draft Preparation, S.H.Z.; Writing-Review & Editing, S.H.Z., R.G., and D.V.; Visualization, S.H.Z., A.D., S.H.; Supervision, R.G., and D.V.; Project Administration, S.H.Z.; Funding Acquisition, R.G., D.V.and S.H. All authors have read and agreed to the published version of the manuscript.

Funding: This research was funded by the Australian Government Research Training Program Scholarship and The ARC Graphene Enabled Industry Transformation Hub at the University of Adelaide. Also, this study is partially based upon work supported by the AFOSR under contract number FA9550-12-1-0225 and the NSF under grant numbers ECCS-1351533, ECCS-1515005, and ECCS-1711253. Moreover, this research is partly supported by

the Basic Research Laboratory Program through the Ministry of Education of the Republic of Korea under grant number 2019R1A4A1026125.

Acknowledgments: Electron microscopy was carried out at the Adelaide Microscopy, University of Adelaide.

Conflicts of Interest: There is no conflict to declare.

References

1. Shafai, C. Optimization of Bi_2Te_3 thin films for microintegrated Peltier heat pumps. *J. Vac. Sci. Technol. A* **1997**, *15*, 2798–2801. [CrossRef]
2. Scoville, A.N.; Bajgar, C.; Vandersande, J.; Fleurial, J. High figure-of-merit n-type SiGe/GaP alloys, IECEC 91. In Proceedings of the 26th Intersociety Energy Conversion Engineering Conference, Boston, MA, USA, 4–9 August 1991; American Nuclear Society: La Grange Park, IL, USA, 1991; pp. 224–229.
3. Snyder, G.J.; Toberer, E.S. Complex thermoelectric materials. *Nat. Mater.* **2008**, *7*, 105–114. [CrossRef] [PubMed]
4. Beretta, D.; Neophytou, N.; Hodges, J.M.; Kanatzidis, M.G.; Narducci, D.; Martín-González, M.S.; Beekman, M.; Balke, B.; Cerretti, G.; Tremel, W.; et al. Thermoelectrics: From history, a window to the future. *Mater. Sci. Eng. R: Rep.* **2019**, *138*, 100501. [CrossRef]
5. Hermann, R.P.; Jin, R.; Schweika, W.; Grandjean, F.; Mandrus, D.G.; Sales, B.C.; Long, G.J. Einstein Oscillators in Thallium Filled Antimony Skutterudites. *Phys. Rev. Lett.* **2003**, *90*, 135505. [CrossRef]
6. Bentien, A.; Christensen, M.; Bryan, J.D.; Sanchez, A.; Paschen, S.; Steglich, F.; Stucky, G.D.; Iversen, B.B. Thermal conductivity of thermoelectric clathrates. *Phys. Rev. B* **2004**, *69*, 045107. [CrossRef]
7. Anand, S.; Wood, M.; Wolverton, C.; Snyder, G.J. *An Enormous Class of Double Half-Heusler Compounds with Low Thermal Conductivity*; Cornell University: Ithaca, NY, USA, 2019.
8. Jain, A.; Shin, Y.; Persson, K.A. Computational predictions of energy materials using density functional theory. *Nat. Rev. Mater.* **2016**, *1*, 15004. [CrossRef]
9. Fu, C.; Bai, S.; Liu, Y.; Tang, Y.; Chen, L.; Zhao, X.; Zhu, T. Realizing high figure of merit in heavy-band p-type half-Heusler thermoelectric materials. *Nat. Commun.* **2015**, *6*, 8144. [CrossRef]
10. Galanakis, I. *Theory of Heusler and Full-Heusler Compounds*; Springer: Cham, Switzerland, 2015; Volume 222, pp. 3–36.
11. Shutohs, S.S.N. Thermoelectric properties of the TiX (Zr0.5Hf0.5)1-XNiSn half-Heusler compounds. *J. Alloys Compd.* **2005**, *389*, 204–208. [CrossRef]
12. Huang, L.; He, R.; Chen, S.; Zhang, H.; Dahal, K.; Zhou, H.; Wang, H.; Zhang, Q.; Ren, Z. A new n-type half-Heusler thermoelectric material NbCoSb. *Mater. Res. Bull.* **2015**, *70*, 773–778. [CrossRef]
13. Zhou, M.; Feng, C.; Chen, L.; Huang, X. Effects of partial substitution of Co by Ni on the high-temperature thermoelectric properties of TiCoSb-based half-Heusler compounds. *J. Alloys Compd.* **2005**, *391*, 194–197. [CrossRef]
14. Chai, Y.W.; Oniki, T.; Kimura, Y. Microstructure and thermoelectric properties of a ZrNi1.1Sn half-Heusler alloy. *Acta Mater.* **2015**, *85*, 290–300. [CrossRef]
15. Sakurada, S.; Shutoh, N. Effect of Ti substitution on the thermoelectric properties of (Zr,Hf) NiSn half-Heusler compounds. *Appl. Phys. Lett.* **2005**, *86*, 82105. [CrossRef]
16. Misra, D.K.; Rajput, A.; Bhardwaj, A.; Chauhan, N.S.; Singh, S. Enhanced power factor and reduced thermal conductivity of a half-Heusler derivative Ti9Ni7Sn8: A bulk nanocomposite thermoelectric material. *Appl. Phys. Lett.* **2015**, *106*, 103901. [CrossRef]
17. Lee, P.-J.; Chao, L.-S. High-temperature thermoelectric properties of Ti0.5 (ZrHf) 0.5−xNbxNi0.9Pd0.1Sn0.98Sb0.02 half-Heusler alloys. *J. Alloys Compd.* **2010**, *504*, 192–196. [CrossRef]
18. Zhang, H.; Wang, Y.; Huang, L.; Chen, S.; Dahal, H.; Wang, D.; Ren, Z. Synthesis and thermoelectric properties of n-type half-Heusler compound VCoSb with valence electron count of 19. *J. Alloys Compd.* **2016**, *654*, 321–326. [CrossRef]
19. Katsuyama, S.; Kobayashi, T. Effect of mechanical milling on thermoelectric properties of half-Heusler ZrNiSn0.98Sb0.02 intermetallic compound. *Mater. Sci. Eng. B* **2010**, *166*, 99–103. [CrossRef]
20. Gürth, M.; Rogl, G.; Romaka, V.V.; Grytsiv, A.; Bauer, E.; Rogls, P. Thermoelectric high ZT half-Heusler alloys Ti 1−x−y Zr x Hf y NiSn ($0 \leq x \leq 1$; $0 \leq y \leq 1$). *Acta Mater.* **2016**, *104*, 210–222. [CrossRef]

21. Zhu, T.J.; Xiao, K.; Yu, C.; Shen, J.J.; Yang, S.H.; Zhou, A.J.; Zhao, X.B.; He, J. Effects of yttrium doping on the thermoelectric properties of Hf 0.6 Zr 0.4 NiSn 0.98 Sb 0.02 half-Heusler alloys. *J. Appl. Phys.* **2010**, *108*, 044903.
22. Zhang, H.; Wang, Y.; Dahal, K.; Mao, J.; Huang, L.; Zhang, Q.; Ren, Z. Thermoelectric properties of n-type half-Heusler compounds (Hf0.25Zr0.75)1–Nb NiSn. *Acta Mater.* **2016**, *113*, 41–47. [CrossRef]
23. Joshi, G.; Yan, X.; Wang, H.; Liu, W.; Chen, G.; Ren, Z. Enhancement in Thermoelectric Figure-Of-Merit of an N-Type Half-Heusler Compound by the Nanocomposite Approach. *Adv. Energy Mater.* **2011**, *1*, 643–647. [CrossRef]
24. Berry, T.; Fu, C.; Auffermann, G.; Fecher, G.H.; Schnelle, W.; Serrano-Sanchez, F.; Yue, Y.; Liang, H.; Felser, C. Enhancing Thermoelectric Performance of TiNiSn Half-Heusler Compounds via Modulation Doping. *Chem. Mater.* **2017**, *29*, 7042–7048. [CrossRef]
25. Hazama, H.; Matsubara, M.; Asahi, R. Thermoelectric Properties of Off-Stoichiometric Ti-Ni-Sn Half-Heusler Systems. *J. Electron. Mater.* **2012**, *41*, 1730–1734. [CrossRef]
26. Huang, L.; Zhang, Q.; Wang, Y.; He, R.; Shuai, J.; Zhang, J.; Wang, C.; Ren, Z. The effect of Sn doping on thermoelectric performance of n-type half-Heusler NbCoSb. *Phys. Chem. Chem. Phys.* **2017**, *19*, 25683–25690. [CrossRef] [PubMed]
27. Rausch, E.; Balke, B.; Ouardi, S.; Felser, C. Enhanced thermoelectric performance in the p-type half-Heusler (Ti/Zr/Hf)CoSb0.8Sn0.2 system via phase separation. *Phys. Chem. Chem. Phys.* **2014**, *16*, 25258–25262. [CrossRef] [PubMed]
28. He, R.; Zhu, H.; Sun, J.; Mao, J.; Reith, H.; Chen, S.; Schierning, G.; Nielsch, K.; Ren, Z. Improved thermoelectric performance of n-type half-Heusler MCo1-xNixSb (M = Hf, Zr). *Mater. Today Phys.* **2017**, *1*, 24–30. [CrossRef]
29. Gałązka, K.; Populoh, S.; Xie, W.; Yoon, S.; Saucke, G.; Hulliger, J.; Weidenkaff, A.; Büttner, G. Improved thermoelectric performance of (Zr0.3Hf0.7)NiSn half-Heusler compounds by Ta substitution. *J. Appl. Phys.* **2014**, *115*, 183704.
30. Zhao, D.; Zuo, M.; Bo, L.; Wang, Y. Synthesis and Thermoelectric Properties of Pd-Doped ZrCoBi Half-Heusler Compounds. *Materials* **2018**, *11*, 728. [CrossRef]
31. Geng, H.; Zhang, H. Effects of phase separation on the thermoelectric properties of (Ti, Zr, Hf) NiSn half-Heusler alloys. *J. Appl. Phys.* **2014**, *116*, 33708. [CrossRef]
32. Tang, Y.; Li, X.; Martin, L.H.J.; Ivas, T.; Leinenbach, C.; Anand, S.; Peters, M.; Snyder, G.J.; Battaglia, C.; Cuervo-Reyes, E. Impact of Ni content on the thermoelectric properties of half-Heusler TiNiSn. *Energy Environ. Sci.* **2018**, *11*, 311–320. [CrossRef]
33. Xie, H.; Wang, H.; Fu, C.; Liu, Y.; Snyder, G.J.; Zhao, X.; Zhu, T. The intrinsic disorder related alloy scattering in ZrNiSn half-Heusler thermoelectric materials. *Sci. Rep.* **2014**, *4*, 6888. [CrossRef]
34. Xia, K.; Liu, Y.; Anand, S.; Snyder, G.J.; Xin, J.; Yu, J.; Zhao, X.; Zhus, T. Enhanced Thermoelectric Performance in 18-Electron Nb0.8CoSb Half-Heusler Compound with Intrinsic Nb Vacancies. *Adv. Funct. Mater.* **2018**, *28*, 1705845. [CrossRef]
35. Zeeshan, M.; Brink, J.V.D.; Kandpal, H.C. Hole-doped cobalt-based Heusler phases as prospective high-performance high-temperature thermoelectrics. *Phys. Rev. Mater.* **2017**, *1*, 74401. [CrossRef]
36. Öğüt, S.; Rabe, K.M. Band gap and stability in the ternary intermetallic compounds NiSn M (M = Ti, Zr, Hf): A first-principles study. *Phys. Rev. B* **1995**, *51*, 10443–10453. [CrossRef] [PubMed]
37. Hichour, M.; Rached, D.; Khenata, R.; Rabah, M.; Merabet, M.; Reshak, A.; Bin-Omran, S.; Ahmed, R. Theoretical investigations of NiTiSn and CoVSn compounds. *J. Phys. Chem. Solids* **2012**, *73*, 975–981. [CrossRef]
38. Shi, H.; Ming, W.; Parker, D.S.; Du, M.H.; Singh, D.J. Prospective high thermoelectric performance of the heavily p-doped half-Heusler compound CoVSn. *Phys. Rev. B* **2017**, *95*, 195207. [CrossRef]
39. Zeeshan, M.; Singh, H.K.; Brink, J.V.D.; Kandpal, H.C. Ab initio design of new cobalt-based half-Heusler materials for thermoelectric applications. *Phys. Rev. Mater.* **2017**, *1*, 075407. [CrossRef]
40. Schroeder, D.V.; Gould, H. *An Introduction to Thermal Physics*; Addison-Wesley: Reading, MA, USA, 2000; pp. 149–220.
41. Tobola, J.; Kaprzyk, S.; Skolozdra, R.V.; A Kouacou, M.; Pierre, J. Crossover from semiconductor to magnetic metal in semi-Heusler phases as a function of valence electron concentration. *J. Phys.: Condens. Matter* **1998**, *10*, 1013–1032. [CrossRef]
42. Villars, P. *Inorganic Solid Phases, Springer Materials (Online Database)*; Springer: Heidelberg, Germany, 2016.

43. Brillson, L. Metal-semiconductor interfaces. *Surf. Sci.* **1994**, *299*, 909–927. [CrossRef]
44. Batra, I.; Tekman, E.; Ciraci, S. Theory of Schottky barrier and metallization. *Prog. Surf. Sci.* **1991**, *36*, 289–361. [CrossRef]
45. Lue, C.; Öner, Y.; Naugle, D.; Ross, J.J.H. Magnetism of new semi-Heusler compounds FeVSn and CoVSn. *IEEE Trans. Magn.* **2001**, *37*, 2138–2140. [CrossRef]

PAPER 5

Status: *Under review by Dr. Vashaee*

Planned journal for submission: *Journal of Environmental Science and Energy, RSC.*

Doping Engineering Approaches to Improve Power Factor of Thermoelectric Products

Thermoelectric energy conversion as an all-solid-state technology has achieved much interest due to its important applications in diverse science and engineering fields. They have potential capabilities for recycling industrial waste heat, space-based remote power generation, automobile exhaust heat recovery, solar power generation, and cooling system for electronics. In essence, thermoelectric generators/coolers work as heat engines, which are thermodynamically similar to conventional vapor power generators and heat pumps, with thermoelectric generators/coolers employing electrons as their working fluid instead of physical gaseous/liquid media. The possibility of controlling chemical and physical structuring at the nanometre scale, electronic band-structural, and microstructural engineering provides a variety of approaches for obtaining high thermoelectric performance in materials. To date, enhancing the efficiency of thermoelectric compounds has been practiced broadly by either improving the power factor ($S^2\sigma$) or reducing the lattice thermal conductivity (κ_l). Nonetheless, enhancing the thermoelectric power factor is still challenging because of the adverse interplay between Seebeck coefficient (S) and electrical conductivity (σ). Contemporary high-performance thermoelectric compounds require elaborate doping strategies and structural manipulation, particularly for electronic band-structure engineering. In this field, understanding the basis of electronic transport mechanisms and developing doping ideas to improve thermoelectric power factors are necessary to produce efficient thermoelectric compounds. This research focuses on doping engineering for electronic structural features, including band-structure distortions, transition-elements doping, spin fluctuation and entropy, modulation doping, the synergy of resonance levels, band convergence, and thermodynamic stability, which make up the thermoelectric quality factor. Experimental and theoretical studies of doping engineering based on frequent doping strategies are reviewed and analysed, directing on recent developments that have provided a more complete framework for understanding these subtle phenomena. We expect this study to serve as a practical guide to enhancing the power factor in thermoelectric compositions, based on electronic structural design and engineering.

Keywords*: Waste Heat Recovery; Doping Engineering; Thermoelectric; Optimization*

ANEM 2019 ADVANCED NANO AND ENERGY MATERIALS

December 4-6, 2019

The University of Western Australia, Perth, Australia

CERTIFICATE OF PARTICIPATION

This is to certify that

Sadeq Hooshmand Zaferani

has participated in ANEM2019 conference and has presented the work entitled

Thermoelectric Properties of P-type MnTe/Graphene Nanocomposites

in the session of Advanced Graphene Materials

Dr. Elby Titus (Conference Chair), 4th December 2019

Australian Government
Australian Research Council

ARC Research Hub for Graphene Enabled Industry Transformation

THE UNIVERSITY of ADELAIDE

Faculty of Engineering, Computer and Mathematical Sciences (ECMS)
School of Mechanical Engineering

Thermoelectric Properties of P-type MnTe/Graphene Nanocomposites

Sadeq Hooshmand Zaferani[1,3*], Reza Ghomashchi [1,2*] Daryoosh Vashaee [3,4*]

[1] School of Mechanical Engineering, University of Adelaide, SA, 5005, Australia
[2] ARC Research Hub for Graphene Enabled Industry Transformation, University of Adelaide, Adelaide, SA, 5005, Australia
[3] Department of Electrical and Computer Engineering, North Carolina State University, NC, 27606, United States
[4] Department of Materials Science and Engineering, North Carolina State University, NC, 27606, United States

ANEM 2019 ADVANCED NANO AND ENERGY MATERIALS
December 4-6, 2019
The University of Western Australia, Perth, Australia

OUTLINE

Step 1
- INTRODUCTION

Step 2
- EXPERIMENTAL

Step 3
- RESULTS AND DISCUSSION

Step 4
CONCLUSIONS

Australian Government
Australian Research Council

ARC Research Hub for Graphene Enabled Industry Transformation

THE UNIVERSITY of ADELAIDE

Faculty of Engineering, Computer and Mathematical Sciences (ECMS)
School of Mechanical Engineering

INTRODUCTION

Why Thermoelectric?

https://www.irishtimes.com/polopoly_fs/1.1663266.1390328306!/image/image.jpg_gen/derivatives/box_620_330/image.jpg

https://www.dogpollutionmask.com/wp-content/uploads/2017/11/Dog-Pollution-Mask-Air-Filter-1-e1511533953235.jpg

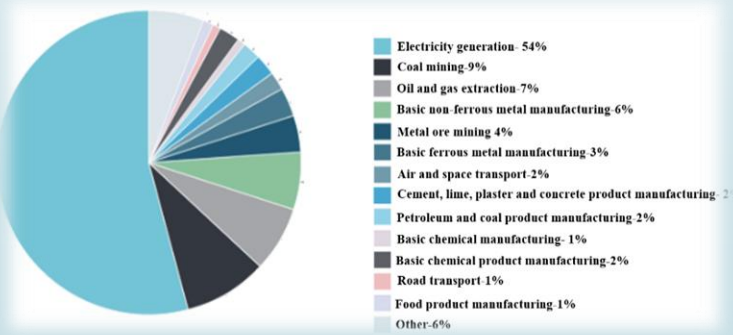

Reported list of Australia's top greenhouse gases emitters in 2015.

@ Makeover, E. Australia's Top 20 Greenhouse Gas Emitters. 2018.

Australian Government
Australian Research Council

ARC Research Hub for Graphene
Enabled Industry Transformation

THE UNIVERSITY of ADELAIDE

Faculty of Engineering, Computer and
Mathematical Sciences (ECMS)
School of Mechanical Engineering

Why Thermoelectric?

https://solyntaenergy.com/2018/01/05/top-six-renewable-energies-and-why-you-should-consider-using-them/

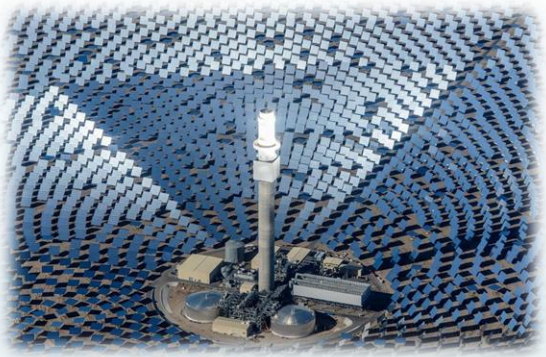

@https://www.usnews.com/dims4/USNEWS/8a29480/2147483647/thumbnail/970x647/quality/85/?url=http%3A%2F%2Fcom-usnews-beam-media.s3.amazonaws.com%2F3a%2Fa9%2Ffc1222614f81acdda3804df1e8f3%2F160219-crescentdunes-editorial.jpg

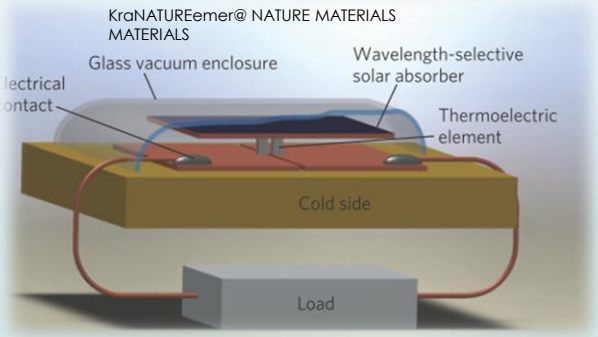

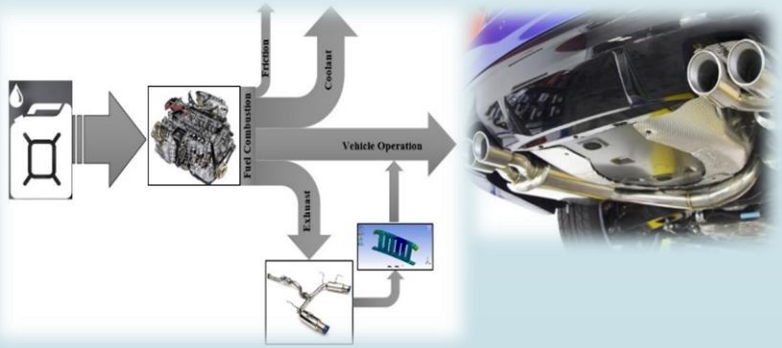

@Renewable and Sustainable Energy Reviews, 2018. 91: p. 376–393.

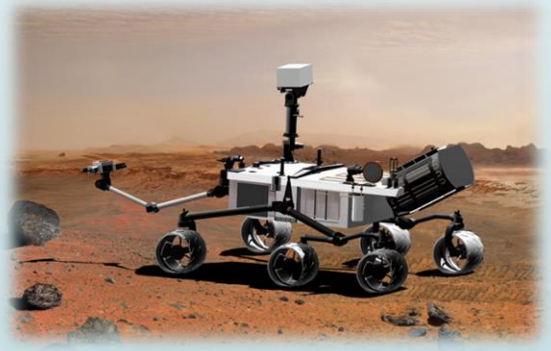

Mars Science Laboratory, aka Curiosity, is part of NASA's Mars Exploration Program, a long-term program of robotic exploration of the Red Planet. It's powered by the Multi-Mission Radioisotope Thermoelectric Generator (MMRTG).
@ Photo courtesy of NASA/JPL-Caltech.

Australian Government
Australian Research Council

ARC Research Hub for Graphene Enabled Industry Transformation

THE UNIVERSITY of ADELAIDE

Faculty of Engineering, Computer and Mathematical Sciences (ECMS)
School of Mechanical Engineering

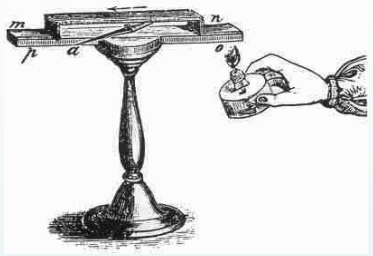

http://www.thermoelectrics.caltech.edu/thermoelectrics/history.html

The concept of thermoelectricity (TE) as the direct conversion of the temperature gradient (ΔT) to electricity was started by the ***German- Estonian physicist Thomas Johann Seebeck*** in the years between 1821 and 1831.

$$S = -\frac{\Delta V}{\Delta T}$$

@Materials Research Society, 2014. 17(5): p. 1260-1267.

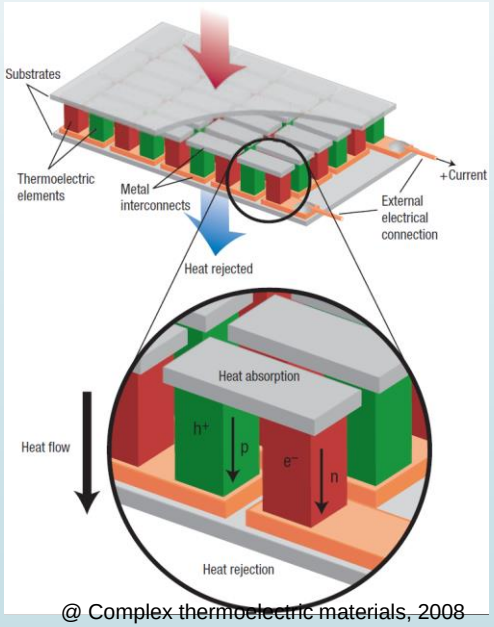

@ Complex thermoelectric materials, 2008 Nature Publishing Group

dimensionless figure-of-merit (zT)

$$zT = \frac{S^2\sigma}{k_e + k_l}T$$

S:Seebeck coefficient (VK^{-1}),
σ :electrical conductivity ($\Omega^{-1}m^{-1}$),
T :temperature (K),
k_e:electronic thermal conductivities ($Wm^{-1}K^{-1}$)
k_l :lattice thermal conductivities ($Wm^{-1}K^{-1}$)

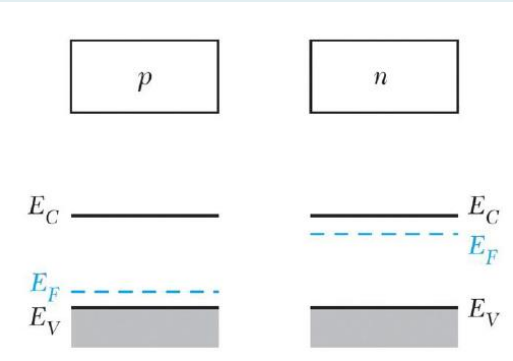

Hypothesis of Graphene performance

$$zT = \frac{S^2\sigma}{k_e + k_l}T$$

Increasing the Seebeck due to the electron filtering

Increasing the electrical conductivity

Decreasing thermal conductivity due to phonon scattering

Australian Government
Australian Research Council

ARC Research Hub for Graphene
Enabled Industry Transformation

THE UNIVERSITY of ADELAIDE

Faculty of Engineering, Computer and
Mathematical Sciences (ECMS)
School of Mechanical Engineering

EXPERIMENTAL

- Powder metallurgy
- Weighting & Mixing
- Loading into the cups and milling
- Annealing-750ºC
- Loading into the cups and milling
- Mixing with GNPs By a micro-milling

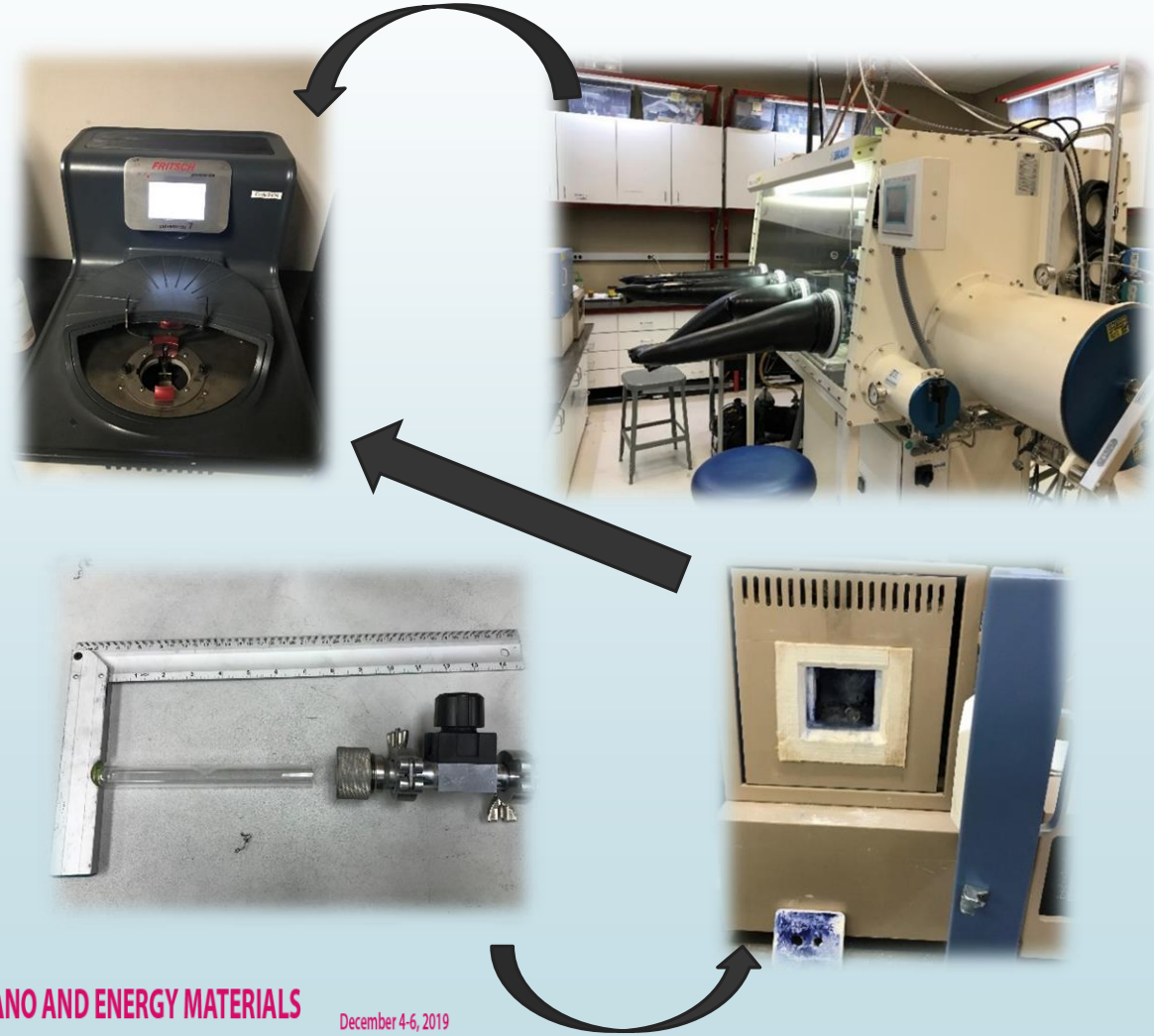

Australian Government
Australian Research Council

ARC Research Hub for Graphene Enabled Industry Transformation

THE UNIVERSITY of ADELAIDE

Faculty of Engineering, Computer and Mathematical Sciences (ECMS)
School of Mechanical Engineering

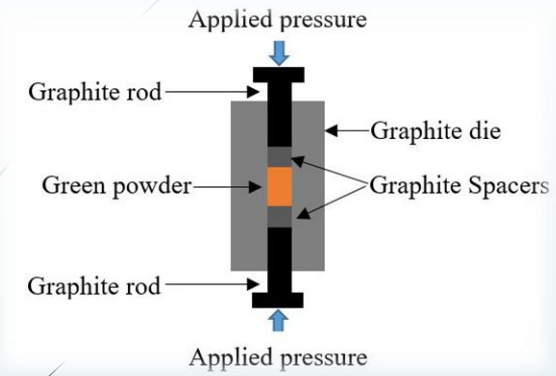

MnTe@T:950°C,
P:140psi and t:5 min
Density~ 98-99% theoretical values

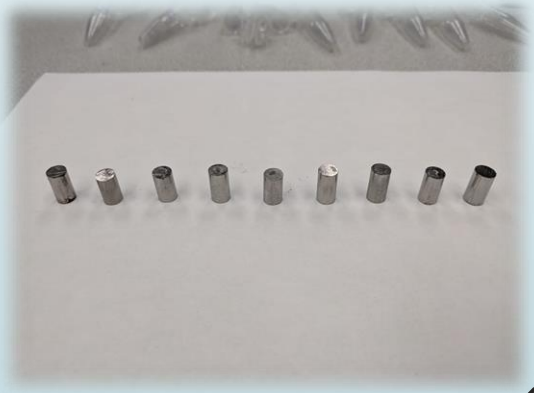

Measurement of XRD peaks @ RT

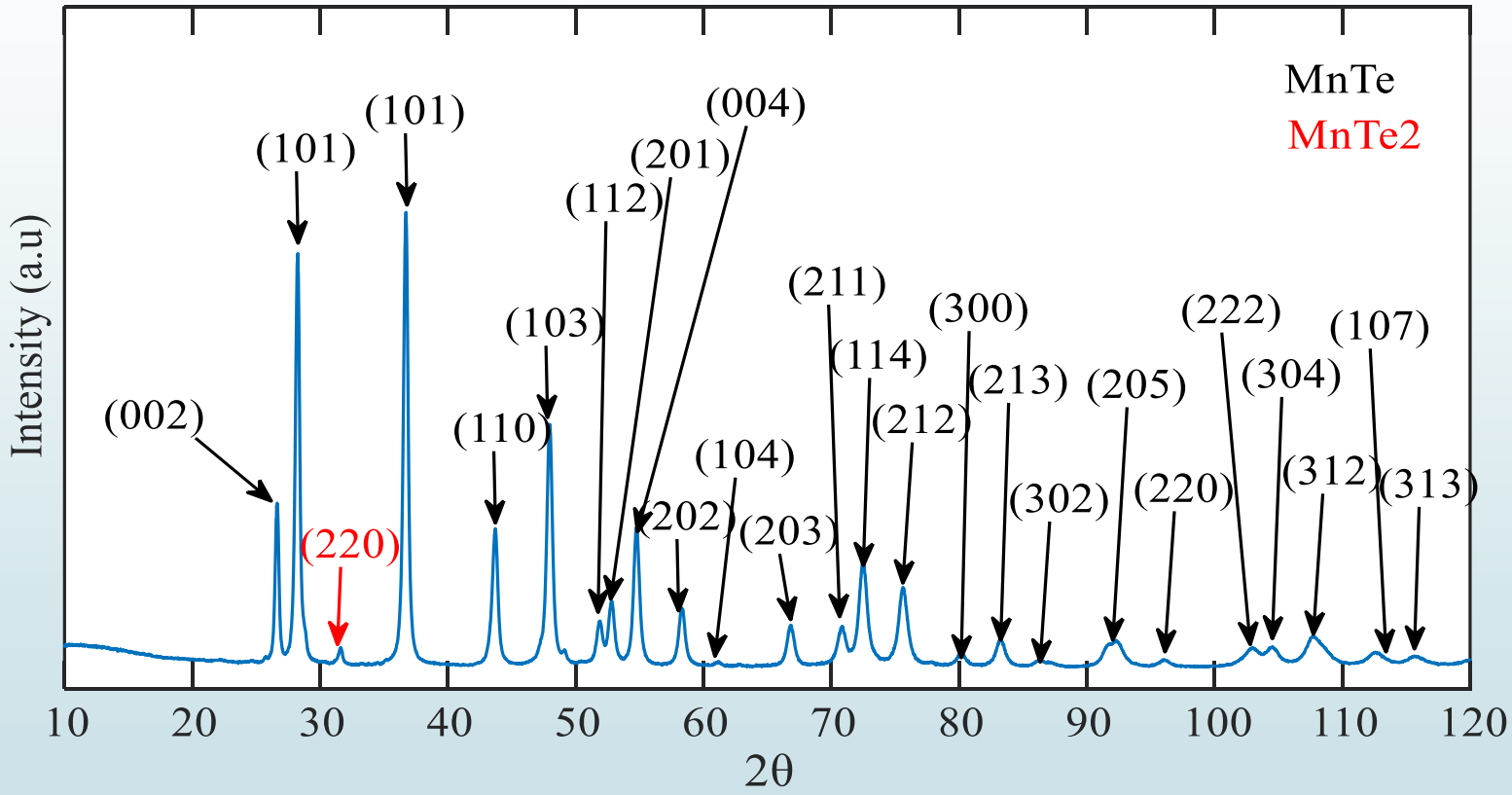

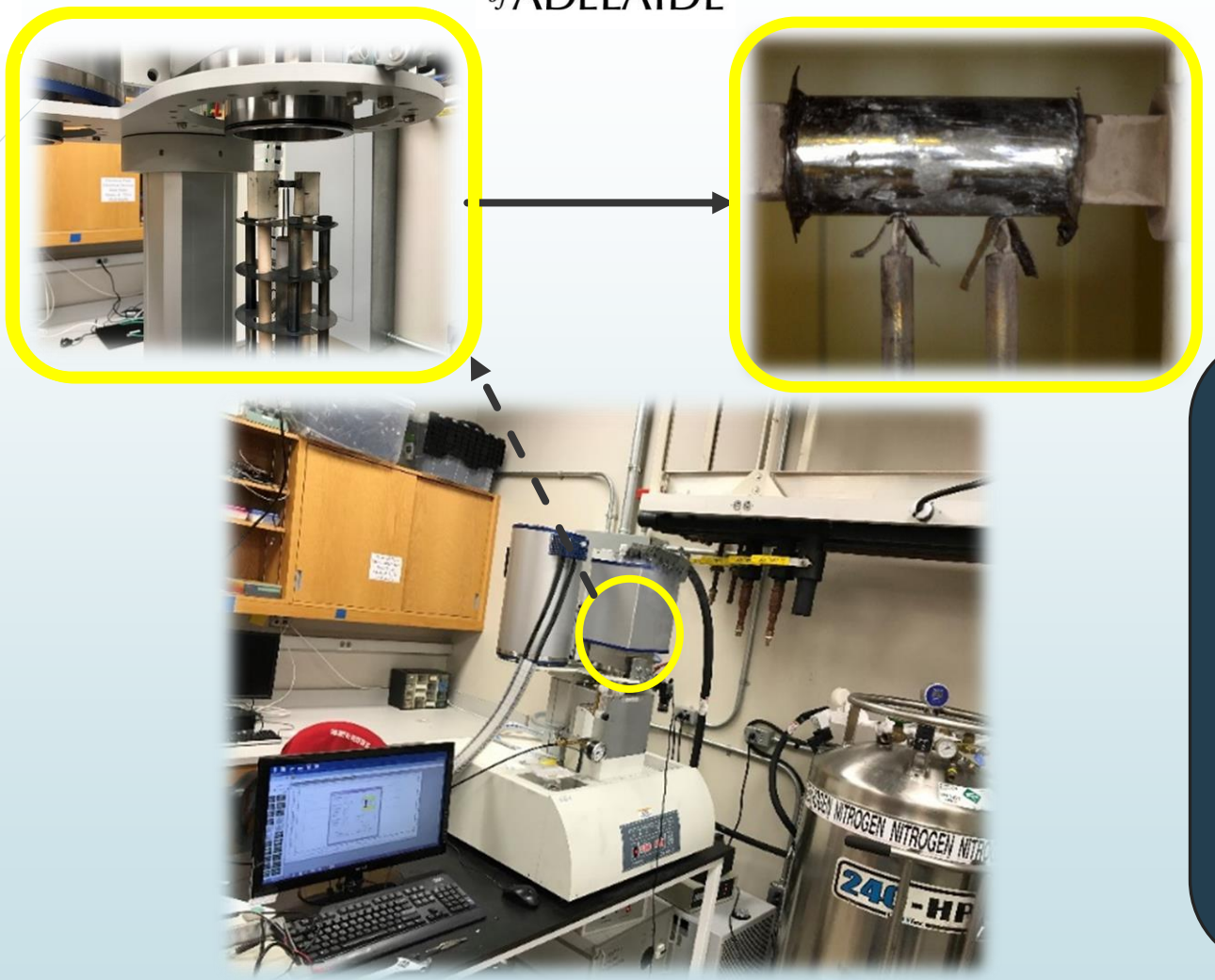

LSR-3, LINSEIS device
It measures:
Seebeck (S)
Electrical conductivity (σ)
Electronic thermal conductivity (κ_e)

Australian Government
Australian Research Council

ARC Research Hub for Graphene Enabled Industry Transformation

THE UNIVERSITY of ADELAIDE

Faculty of Engineering, Computer and Mathematical Sciences (ECMS)
School of Mechanical Engineering

Thermal diffusivity (m^2/s)

Australian Government
Australian Research Council
ARC Research Hub for Graphene Enabled Industry Transformation

THE UNIVERSITY of ADELAIDE

Faculty of Engineering, Computer and Mathematical Sciences (ECMS)
School of Mechanical Engineering

RESULTS AND DISCUSSION

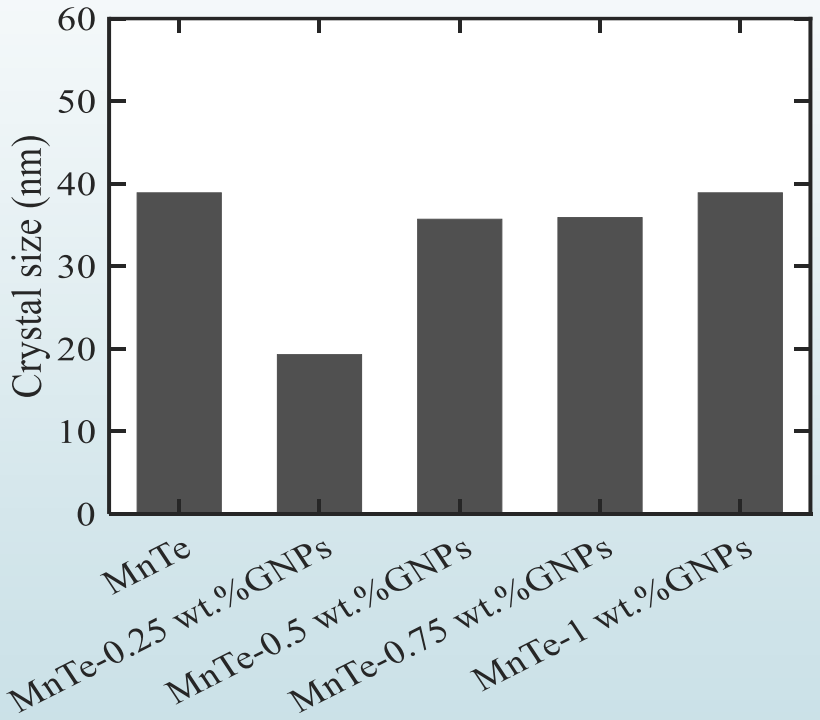

Crystal size

Thermoelectric results

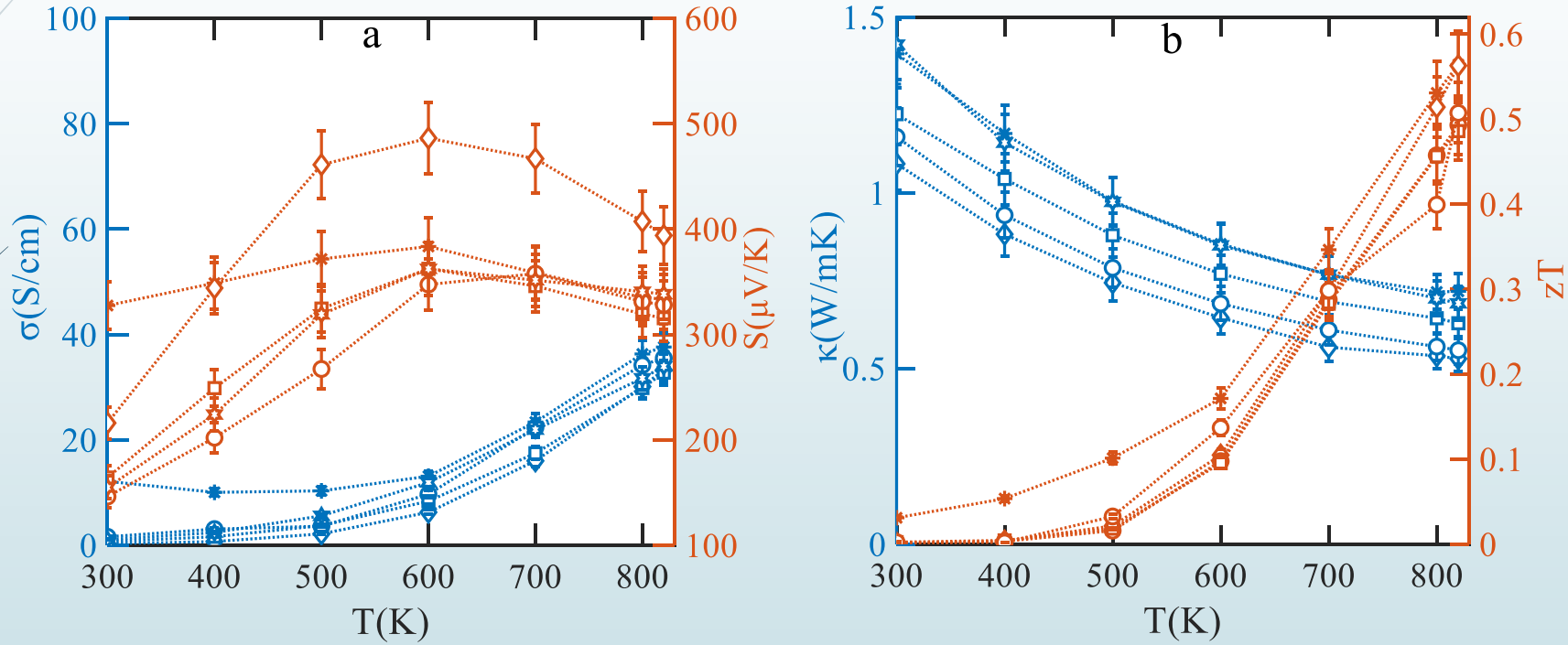

Figure 8: Thermoelectric characteristics of the MnTe-xGNP nanocomposites (0wt.%= Asterisk*, 0.250wt.%=Diamond, 0.5wt.%=Circle, 0.75wt.%=Square and 1wt.%=hexagram).

CONCLUSIONS

The GNP loading effects on magnetic, thermoelectric and mechanical characteristics of MnTe were represented.

The GNP settlement at the grain boundaries and grain growth reduction

Nanostructuring decreased thermal conductivity and enhanced Seebeck coefficients

$$zT = \frac{S^2\sigma}{k}T$$

ACKNOWLEDGMENTS

This work has been supported by the Australian Government Research Training Program Scholarship and The ARC Graphene Enabled Industry Transformation Hub at the University of Adelaide. In addition, this study is partially based upon work supported by the National Science Foundation (NSF) under grant numbers ECCS-1351533, ECCS-1711253, and CMMI-1363485. Electron microscopy was carried out at the Adelaide Microscopy, University of Adelaide.

REFERENCES

- Serhii Shafraniuk, Graphene : fundamentals, devices, and applications, Boca Raton, Florida : CRC Press, ISBN: 9780429068843, [2015]
- Liu, Jun, Charging graphene for energy, Nature Nanotechnology; London Vol. 9, Iss. 10, (Oct 2014): 739-41. DOI:10.1038/nnano.2014.233.
- Nano Lett.201818127719-7725, November 12, 2018
- E. S. T. G. Jeffrey Snyders,Complex thermoelectric materials,nature materials,7 (2008) 105-114.
- D. T. Morelli, V. Jovovic, J. P. Heremans, Intrinsically Minimal Thermal Conductivity in Cubic I-V-VI2 Semiconductors, PHYSICAL REVIEW LETTERS, 2008,035901-1-4. DOI: 10.1103/PhysRevLett.101.035901.
- Sai Mu, Raphaël P. Hermann, Stéphane Gorsse, Huaizhou Zhao, Michael E. Manley, Phonons, magnons, and lattice thermal transport in antiferromagnetic semiconductor MnTe, PHYSICAL REVIEW MATERIALS 3, 025403 (2019).
- C. Y. H.Chen, H.Liu, G.Zhang, D.Wan, F.Huangs, Thermoelectric properties of CuInTe2/graphene composites,Cryst Eng Comm,15 (2013,) 6648–6651
- Y. C. C. Xiao Hu, Kaili Zhang, K.C. Yungs,Effect of graphene doping on microstructural and mechanical properties of Sn–8Zn–3Bi solder joints together with electromigration analysis,Journal of Alloys and Compounds,580 (2013) 162-171.

Australian Government
Australian Research Council

ARC Research Hub for Graphene Enabled Industry Transformation

THE UNIVERSITY of ADELAIDE

Faculty of Engineering, Computer and Mathematical Sciences (ECMS)
School of Mechanical Engineering

Thanks for your attention

ANEM 2019 ADVANCED NANO AND ENERGY MATERIALS
December 4-6, 2019
The University of Western Australia, Perth, Australia

ANEM 2019 ADVANCED NANO AND ENERGY MATERIALS

December 4-6, 2019

The University of Western Australia, Perth, Australia

CERTIFICATE OF PARTICIPATION

This is to certify that

Sadeq Hooshmand Zaferani

has participated in ANEM2019 conference and has presented the work entitled

Design and Synthesis of Metal-Semiconductor Heterostructured CoV5.6Sn1.6

in the session of Advanced Energy Materials

Dr. Elby Titus (Conference Chair), 4th December 2019

Design and Synthesis of Metal-Semiconductor Heterostructured $CoV_{5.6}Sn_{1.6}$

Sadeq Hooshmand Zaferani[1,4]*, Reza Ghomashchi[1,2], Soon-Jik Hong[3], Daryoosh Vashaee[4, 5]*

[1]School of Mechanical Engineering, University of Adelaide, SA 5005, Australia
[2] ARC Research Hub for Graphene Enabled Industry Transformation, University of Adelaide, Adelaide, SA, 5005, Australia
[3]Division of Advanced Materials Engineering, Kongju National University, South Korea
[4]Department of Electrical and Computer Engineering, North Carolina State University, NC 27606, United States
[5]Department of Materials Science and Engineering, North Carolina State University, NC 27606, United States

Corresponding authors: sadeq.hooshmandzaferani@adelaide.edu.au (S. H. Zaferani), dvashae@ ncsu.edu (D. Vashaee)

THE UNIVERSITY of ADELAIDE

Faculty of Engineering, Computer and Mathematical Sciences (ECMS)
School of Mechanical Engineering

Australian Government
Australian Research Council

ARC Research Hub for Graphene

ANEM 2019 ADVANCED NANO AND ENERGY MATERIALS
December 4-6, 2019
The University of Western Australia, Perth, Australia

ABSTRACT

Following the discovering of metal-semiconductor characteristics for the multi-phase CoVSn compound, we investigated the $CoV_{5.6}Sn_{1.6}$ composition selected based on the thermodynamic calculation of ternary phase diagrams. The material was synthesized by solid-state reaction of the stoichiometric amounts of the elements in a vacuum induction melting furnace. The alloy analysis revealed the successful formation of the half-Heusler ternary alloy, as the semiconductor phase, and the mixture of binary intermetallics of SnV_3, Co_2Sn, and $CoSn_2$. The segregated microstructure was further confirmed by electron microscopy and Energy-dispersive X-ray spectroscopy. The material demonstrated metallic electronic behavior of a degenerate composite material.

Keywords: $CoV_{5.6}Sn_{1.6}$*; metal-semiconductor;* **Heterostructured**

INTRODUCTION

The investigating compounds which combine the characteristics of both semiconductors and metals cover a significant part of materials research [1]. Metal-semiconductor nanocomposites are particularly useful in various fields such as the design of energy and environment-related photocatalysts [2]. In this field, different techniques have been carried out to produce the metal-nanocomposite compounds, including laser nano-welding [1], photodeposition [3], hydrothermal [4] and electrochemical [5]. One crucial issue in designing the metal-semiconductor is the strength of interface bonding between the components of the nanocomposites [2]. Besides the mechanical properties, a stable and robust interface often helps the interfacial charge transfer process between the metallic and semiconductor phases [2]. Also, previous studies have shown that a good interface bonding between the metal and semiconductor improves the absorption of the optical frequencies [6].

In this regard, Li et.al [7] investigated an enhancement in optical transmission based on strong interference of metal/semiconductor for the Ag/Si double-layered and Si/Ag/Si triple-layered films. Also, Bates Jr. [8], evaluated the effects of microstructure on the metal-semiconductor composites and showed the heterogeneous structure as clustering causes a large absorption of infrared rather than the non-clustered compositions. In this research, to change the concentrations of the metallic phases, the nominated composition of $CoV_{5.6}Sn_{1.6}$ was synthesized and studied. This composition was chosen because it showed a single phase within the CoVSn ternary phase diagram (the temperature of 1070 K close to the melting point-Figure 1). The compound was synthesized by the vacuum induction melting and characterized for its electrical, thermal and mechanical properties.

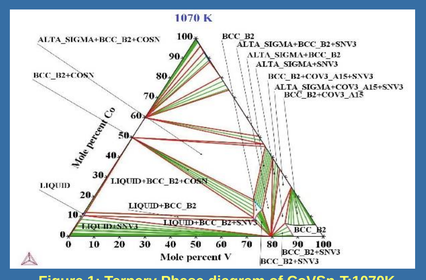

Figure 1: Ternary Phase diagram of CoVSn-T:1070K.

EXPERIMENTAL

Powders of Co, V, and Sn elements were weighed according to $CoV_{5.6}Sn_{1.6}$, mixed and melted by a vacuum induction furnace. The phase identification was carried out via X-ray diffraction analysis (MiniFlex 300/600, 40 kV, 15 mA). Differential scanning calorimetry (DSC) was carried out at a heating rate of 10 °C/min using SDT Q600 V20.9 Build 20 to evaluate the phase transitions. The microstructural analysis was performed by optical microscopy (Zeiss Axio Imager.M2m) and field emission scanning electron microscopy (FESEM Quanta 450 FEG). The electrical parameters, including the thermopower (S) and electrical conductivity (σ) were determined by LINSEIS-LSR - 3 at a temperature range of 30 to 550 °C.

RESULTS AND DISCUSSION

The XRD data of the synthesized $CoV_{5.6}Sn_{1.6}$ alloy was compared with the reported structures of the compounds containing the elements of Co, V, and Sn. Furthermore, XRD spectra were evaluated against the most renowned and stable half-Heusler alloys including, NiMnSb and MgAgAs alloys [9]. The phase identification of shows diffractions corresponding to ternary half-Heusler ($F\bar{4}3m, C1_b$) alloy and several other binary compositions, namely SnV_3, Co_2Sn, and $CoSn_2$.

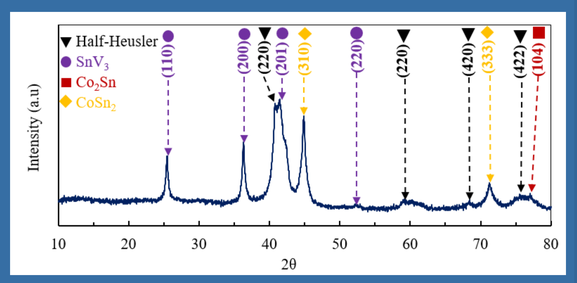

Figure 2: XRD pattern of the $CoV_{5.6}Sn_{1.6}$ alloy .

The optical micrograph shown in Figure 3a was taken from the as-cast $CoV_{5.6}Sn_{1.6}$ alloy. It displays the formation of multi-phase structures, which agrees with the multiphase XRD spectra. The dendritic characteristics of the segregated as-cast structure forming of several phases are evident by the SEM micrographs in Figures 3.b to 3.f.

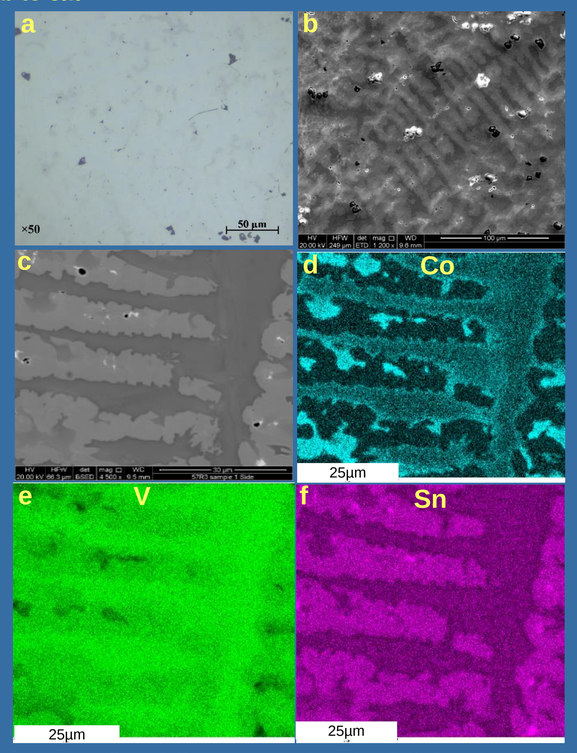

Figure 3: Microstructure analysis of the $CoV_{5.6}Sn_{1.6}$ alloy.

The results depicted the dispersion of three elements of Co, V, and Sn in the separated phases. Therefore, the properties of this alloy with a multi-phase crystal structure cannot be assigned to a half-Heusler composition containing three elements of Co, V, and Sn with a single phase, because, the presence of other three intermetallic phases with the metallic characteristics impact on the microstructure and electrical properties. This conclusion is in agreement with the multi-phase structure detected by the XRD analysis indicating the existence of the SnV_3, Co_2Sn, and $CoSn_2$ phases mixed with the deficient CoVSn phase. Therefore, this alloy contains four intermetallic compounds, which is combining both metallic, and semiconductor properties performing as a metal-semiconductor nanocomposite. The measured Seebeck coefficient (S), electrical conductivity (σ) are shown in Figure 4.

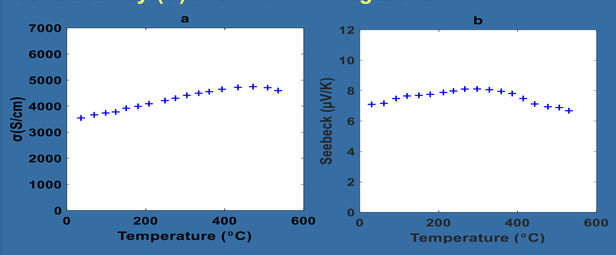

Figure 4: Microstructure analysis of the $CoV_{5.6}Sn_{1.6}$ alloy.

Due to the electrical measurement and microstructure analysis, it can be concluded the heterogeneous composition induced a metal-semiconductor. This heterostructured composition caused a conductivity mismatch between the metallic (SnV_3, Co_2Sn, and $CoSn_2$) and semiconductor (CoVSn) phases. Also, the contact of metal and semiconductor not only aligns the potential band (i.e.: making a common chemical potential), but also makes the interfaces with chemical and electrical properties different from the bulk compounds [10]

As illustrated in Figure 3 the presence of metallic microclusters in contact with half-Heusler CoVSn semiconductor provides various semiconductor-metal interfaces. In this regard, Freeouf [10] represented the Schottky model for these kinds of heterostrcutured compositions in which, the average of work function is considered for the microclusters (Φsb=Xsc- Φ_m^{eff} , Φsb: Schottky barrier, Φ_m^{eff} :effective work function, Xsc: electron affinity) rather than a uniform microstructure. Also, in these heterostrcutured microstructure containing semiconductor-metal interfaces, the structural stabilities is one of the crucial features influencing on the material performance [11].
Moreover, the $CoV_{5.6}Sn_{1.6}$ with a combination of ionic and covalent bonds can influence on the stability of semiconductor-metal interfaces (i.e.: interface behaviour). In this field, the sensitivity of the metal-semiconductor interfaces dependent on the covalent or ionic bonds of semiconductors [12]. Also, this matter influences on the formation energy and stability of the interfaces which provide specific electrical properties. Thus, this structure containing both ionic and covalent bonds can find an optimised stable occupation.

CONCLUSIONS

The $CoV_{5.6}Sn_{1.6}$ alloy was theoretical designed and experimentally synthesized elements in a high-frequency vacuum induction melting furnace. The material analysis showed a heterogeneous microstructure containing four phases including deficient CoVSn, SnV_3, Co_2Sn, and $CoSn_2$. This compound represented demonstrated the metallic electronic behaviour with degenerate carrier concentration.

ACKNOWLEDGEMENT

This work has been supported by the Australian Government Research Training Program Scholarship and The Graphene Enabled Industry Transformation Hub at the University of Adelaide. Also, this study is partially based upon work supported by the National Science Foundation (NSF) under grant numbers ECCS-1351533, ECCS-1711253, and CMMI-1363485. Also, the microscopic images were taken in the Adelaide Microscopy Center, Adelaide.

REFERENCES

1 Materials Letters 236 (2019) 271–275
2 Nanoscale,9, 2017, (7012–7015).
3 J Materiomics 4 (2018) 83-94.
4 ACS Catal 2012;2:949-56.
5 J Phys Chem C 2013;117:12949-57.
6 Nature Materials 12, 158–164 (2013).
7 Scientific Reports, 6:29195, 2016.
8 Materials Letters 18 (1993) 128-132.
9Journal of Alloys and Compounds, 509, (2011) 2611–2616.
10 J. L. Freeouf and J. M. Woodall, App. Phys. Lett. 39, 727 (1981).
11 Scientific Reports, Nature, 4, (2014) 1-6.
12 Acta Materialia, 104, (2016) 210-222.

Australian Government
Australian Research Council

The ARC Research Hub for Graphene Enabled Industry Transformation
Workshop 2020

Assessment of the Graphene-reinforced Thermoelectric Nanocomposites

Sadeq Hooshmand Zaferani[1,2], Daryoosh Vashaee [2,3], Soon-Jik Hong[4], Reza Ghomashchi[1,5]

1 School of Mechanical Engineering, University of Adelaide, SA, 5005, Australia
2 Department of Electrical and Computer Engineering, North Carolina State University, NC, 27606, United States
3 Department of Materials Science and Engineering, North Carolina State University, NC, 27606, United States
4 Division of Advanced Materials Engineering, Kongju National University 1223-24, Cheonan Daero, Seobuk-gu, Cheonan-si, Chungnam, 331-717, South Korea
5 ARC Research Hub for Graphene Enabled Industry Transformation, University of Adelaide, Adelaide, SA, 5005, Australia

THE UNIVERSITY of ADELAIDE

NC STATE UNIVERSITY

NSF

Australian Government
Australian Research Council

The ARC Research Hub for Graphene Enabled Industry Transformation
Workshop 2020

THE UNIVERSITY of ADELAIDE · MONASH University · THE UNIVERSITY OF MELBOURNE · University of South Australia · RMIT UNIVERSITY · first graphene · ARCHER · Graphene Technology Solutions · cleanfuture · NEMATIQ

Why Thermoelectric?

@https://www.irishtimes.com/polopoly_fs/1.1663266.1390328306!/image/image.jpg_gen/derivatives/box_620_330/image.jpg

@https://www.dogpollutionmask.com/wp-content/uploads/2017/11/Dog-Pollution-Mask-Air-Filter-1-e1511533953235.jpg

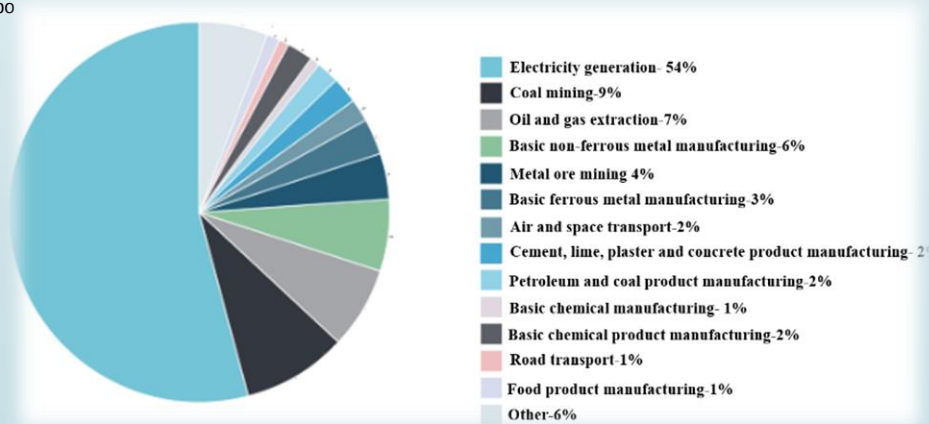

@Reported list of Australia's top greenhouse gases emitters in 2015.

@ Makeover, E. Australia's Top 20 Greenhouse Gas Emitters. 2018.

THE UNIVERSITY of ADELAIDE

NC STATE UNIVERSITY

NSF

Australian Government
Australian Research Council

The ARC Research Hub for Graphene Enabled Industry Transformation
Workshop 2020

THE UNIVERSITY of ADELAIDE · MONASH University · THE UNIVERSITY OF MELBOURNE · University of South Australia · RMIT UNIVERSITY · first graphene · ARCHER · Graphene Technology Solutions · cleanfuture · NEMATIQ

Why Thermoelectric?

https://solyntaenergy.com/2018/01/05/top-six-renewable-energies-and-why-you-should-consider-using-them/

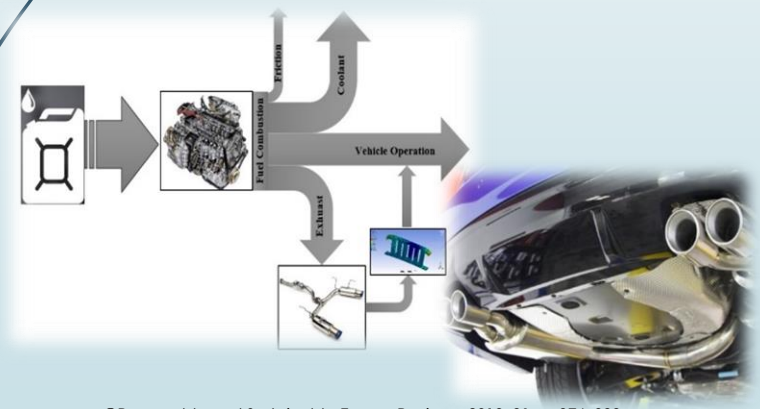

@Renewable and Sustainable Energy Reviews, 2018. 91: p. 376–393.

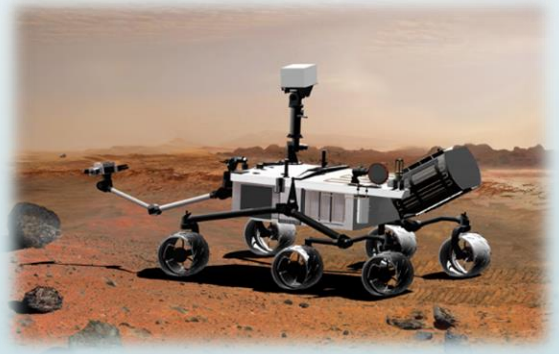

Mars Science Laboratory, aka Curiosity, is part of NASA's Mars Exploration Program, a long-term program of robotic exploration of the Red Planet. It's powered by the Multi-Mission Radioisotope Thermoelectric Generator (MMRTG). @ Photo courtesy of NASA/JPL-Caltech.

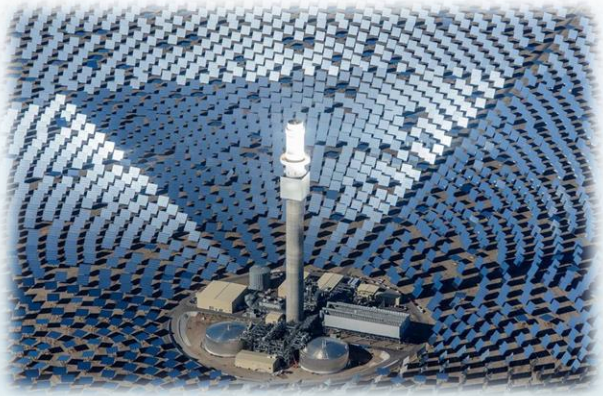

@https://www.usnews.com/dims4/USNEWS/8a29480/2147483647/thumbnail/970x647/quality/85/?url=http%3A%2F%2Fcom-usnews-beam-media.s3.amazonaws.com%2F3a%2Fa9%2Ffc1222614f81acdda3804df1e8f3%2F160219-crescentdunes-editorial.jpg

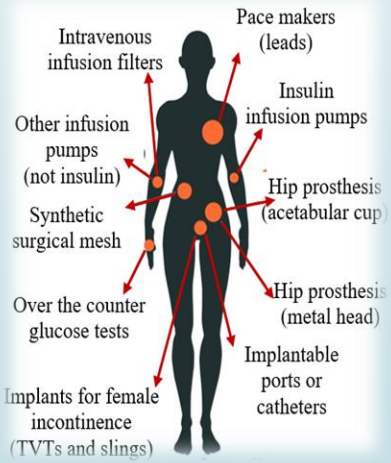

top 10 implantable medical devices (IMD) which have been carried out in the years between 2008 to 2018.
@https://www.cbc.ca/news/health/implanted-files-medical-devices-icij-1.4909196

THE UNIVERSITY of ADELAIDE

NC STATE UNIVERSITY

NSF

Australian Government
Australian Research Council

The ARC Research Hub for Graphene Enabled Industry Transformation
Workshop 2020

THE UNIVERSITY of ADELAIDE · MONASH University · THE UNIVERSITY OF MELBOURNE · University of South Australia · RMIT UNIVERSITY · first graphene · ARCHER · Graphene Technology Solutions · cleanfuture · NEMATIQ

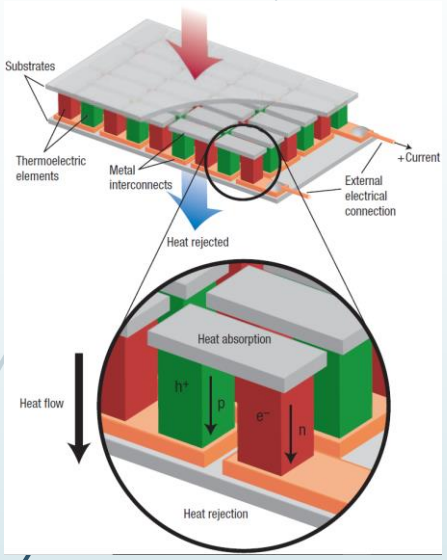

@ Complex thermoelectric materials, 2008 Nature Publishing Group

Potential modifications due to Graphene introduction

Increasing the Seebeck due to the carrier energy filtering

Modifying the carrier concentrations and mobility

Decreasing thermal conductivity due to phonon scattering

$$zT = \frac{S^2\sigma}{k_e + k_l}T$$

dimensionless figure-of-merit (zT)

S:Seebeck coefficient (VK^{-1}),
σ :electrical conductivity ($\Omega^{-1}m^{-1}$),
T :temperature (K),
k_e :electronic thermal conductivities ($Wm^{-1}K^{-1}$)
k_l :lattice thermal conductivities ($Wm^{-1}K^{-1}$)

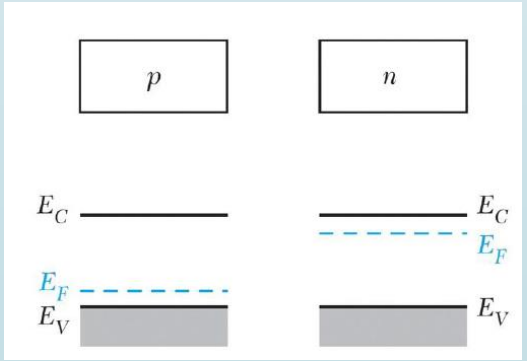

@John Willey & Sons, Inc. All rights reserved,

THE UNIVERSITY of ADELAIDE

NC STATE UNIVERSITY

NSF

Australian Government
Australian Research Council

The ARC Research Hub for Graphene Enabled Industry Transformation
Workshop 2020
Monash University, Clayton, VIC
12-13 March 2020

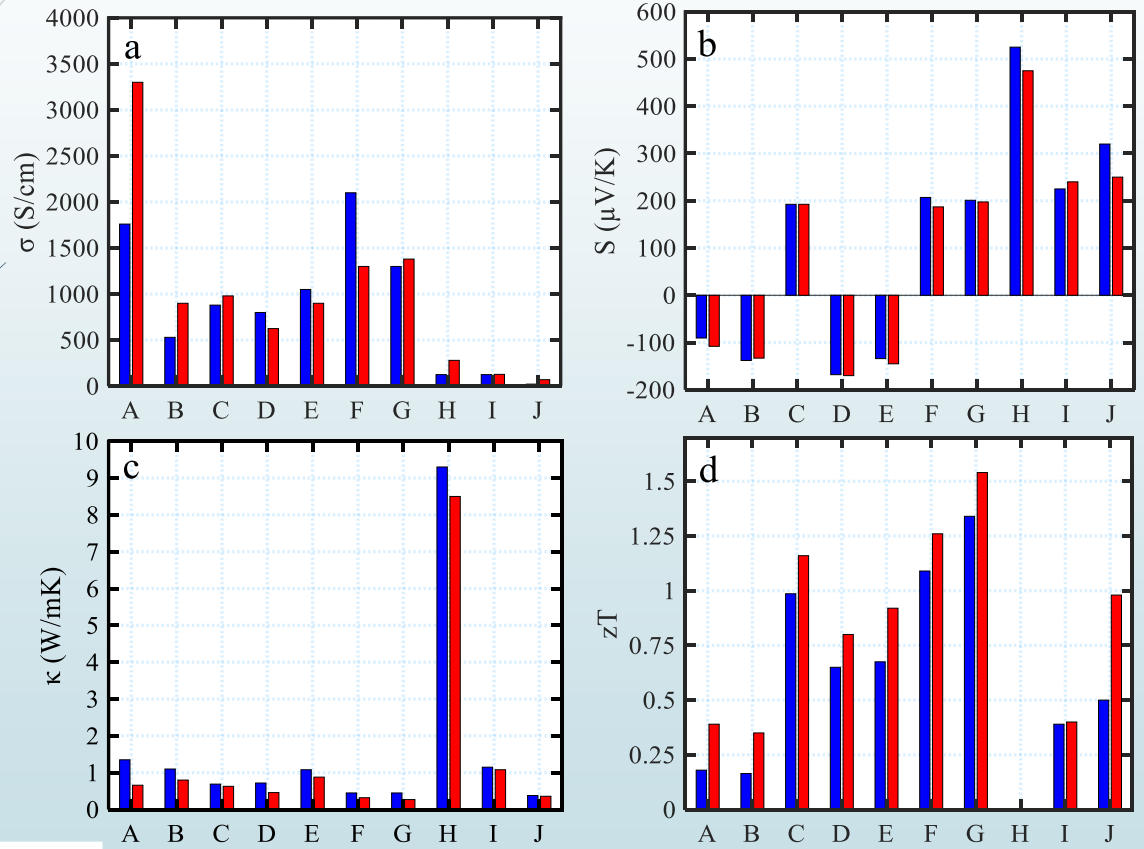

TE characteristics of the graphene-mixed compounds, a) Seebeck coefficients, b) electrical conductivities, c) lattice thermal conductivity and d) dimensionless figure of merit (zT)- the blue and red bars show the TE properties of pristine and nanocomposite samples, respectively. A) $Bi_{85}Sb_{15}$-0.5wt.%G , B) Bi_2Te_3–RGO, C) 0.4 vol%RGO-$Bi_{0.36}Sb_{1.64}Te_3$, D) 0.05 wt%-unoxidized graphene/$Bi_2Te_{2.7}Se_{0.3}$, E) 0.05 wt%.G/Bi_2Te_3, F) 0.05 wt%-$Bi_{0.4}Sb_{1.6}Te_3$, G) 0.4 vol.%G/$Bi_{0.4}Sb_{1.6}Te_3$, H) 1.7 wt% graphene oxide-$BaTiO_3$, I) 1:80 G/$CuInTe_2$, J) 3.2 wt% MoS_2/G&SnSe.

@ Sadeq H. Zaferani, Assessment of graphene-reinforced thermoelectric nanocomposites

THE UNIVERSITY of ADELAIDE

NC STATE UNIVERSITY

NSF

Australian Government
Australian Research Council

Seebeck coefficient- Energy filtering effect (EFE)

$$S = \frac{\pi^2 k_B^2 T}{3q}\left[\frac{\partial \ln(\partial(E))}{\partial E}\right]_{E=E_f}$$

$$= \frac{\pi^2 k_B^2 T}{3q}\left[\frac{1}{n}\frac{\partial n(E)}{\partial E} + \frac{1}{\mu}\frac{\partial \mu(E)}{\partial E}\right]_{E=E_f}$$

$$\mu(E) = q\tau/m_d^*$$

$$S \approx \frac{\pi^2 k_B^2 T}{3q}\left[\frac{N(E)}{n} + \frac{\lambda - \frac{1}{2}}{E}\right]_{E=E_f}$$

where, E is energy, n (E) stands for the energy dependent carrier density and m_d^* is the effective mass, and also n, μ, q, K_B, E_f and $\boldsymbol{\tau}$ are carrier concertation, carrier mobility, carrier charge, Boltzmann constant, Fermi energy, and relaxation time, respectively. By considering a solid with parabolic bands and dependency of the relaxation time (τ) to the energy and scattering factor (λ) via ($\boldsymbol{\tau = \tau_0 E^{\lambda - \frac{1}{2}}}$) (τ_0 is an energy-independent constant), equation 1 is expressed as,
in which N(E) is electronic density of states. Based on the equation 3, the Seebeck coefficients can be enhanced by increasing the scattering factor (λ).

Seebeck coefficient has an inverse relation with carrier concertation (n), thus increasing the charge density causes a decrease in the Seebeck coefficients.

THE UNIVERSITY of ADELAIDE

NC STATE UNIVERSITY

NSF

Australian Government
Australian Research Council

The ARC Research Hub for Graphene Enabled Industry Transformation
Workshop 2020
Monash University, Clayton, VIC
12-13 March 2020

Electrical conductivity

Mott equation (σ=enμ)

$$\frac{1}{\mu_T} = \frac{1}{\mu_m} + \frac{1}{\mu_{in}}$$

$$\mu_{in} = P_q \left(\frac{1}{2\pi m^* k_B T}\right)^{0.5} \exp\left(-\frac{E_B}{k_B T}\right)$$

e: standard electron charge
n: carrier concentration
μ:carrier mobility

μ_m :Carrier mobility in matrix
μ_{in} :Carrier mobility in interface

where P is the mean path between two adjacent potential barriers, E_B shows the height of the potentials at the interfaces, K_B is the Boltzmann constant, m* is the effective mass, and T is the absolute temperature.

@ Journal of Alloys and Compounds,661 (2016) 389-395.
@ Journal of Alloys and Compounds 681, (2016), 394-40.

THE UNIVERSITY of ADELAIDE
NC STATE UNIVERSITY
NSF

Australian Government
Australian Research Council

The ARC Research Hub for Graphene Enabled Industry Transformation
Workshop 2020
Monash University, Clayton, VIC
12-13 March 2020

Thermal conductivity

Phonon scattering against the grain/microstructure boundary/barriers

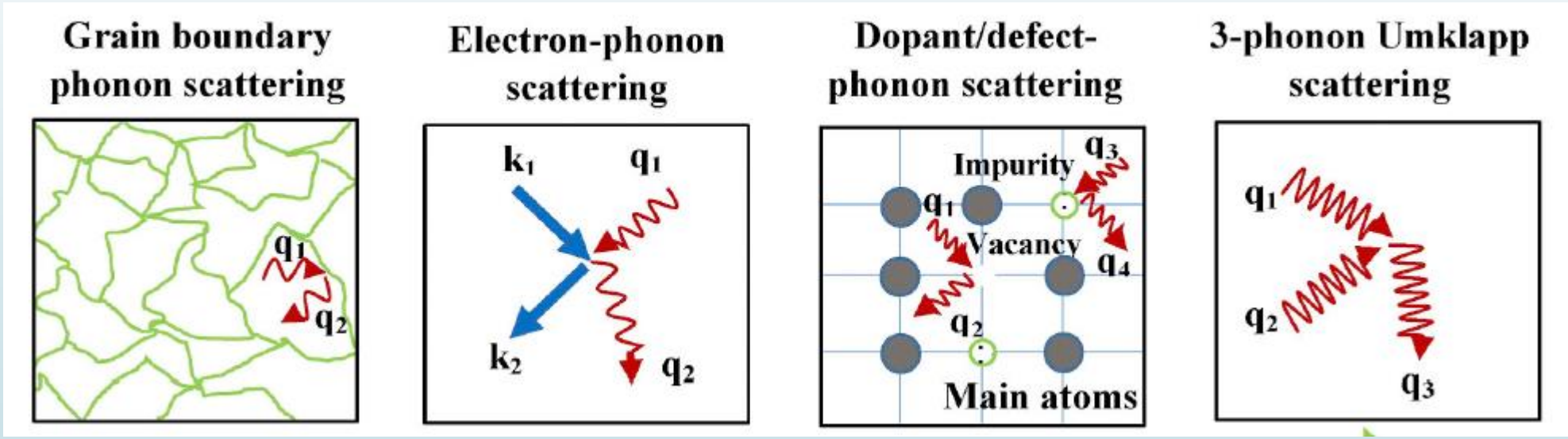

@ S.Hooshmand Zaferani, Renewable and Sustainable Energy Reviews 112 (2019) 158–169.

THE UNIVERSITY of ADELAIDE

NC STATE UNIVERSITY

NSF

Australian Government
Australian Research Council

The ARC Research Hub for Graphene Enabled Industry Transformation
Workshop 2020
Monash University, Clayton, VIC
12-13 March 2020

THE UNIVERSITY of ADELAIDE · MONASH University · THE UNIVERSITY OF MELBOURNE · University of South Australia · RMIT UNIVERSITY · first graphene · ARCHER · Graphene Technology Solutions · cleanfuture · NEMATIQ

Material synthesis of CoVSn-GNPs

- Powder metallurgy
- Weighting
- Mixing
- Loading into the cups
- Mechanical alloying






THE UNIVERSITY of ADELAIDE

NC STATE UNIVERSITY

NSF

Australian Government
Australian Research Council

The ARC Research Hub for Graphene Enabled Industry Transformation
Workshop 2020
Monash University, Clayton, VIC
12-13 March 2020

Sealing

Annealing

XRD-characterization

THE UNIVERSITY of ADELAIDE

NC STATE UNIVERSITY

NSF

Australian Government
Australian Research Council

The ARC Research Hub for Graphene Enabled Industry Transformation
Workshop 2020
Monash University, Clayton, VIC
12-13 March 2020

THE UNIVERSITY of ADELAIDE · MONASH University · THE UNIVERSITY OF MELBOURNE · University of South Australia · RMIT UNIVERSITY · first graphene · ARCHER · Graphene Technology Solutions · cleanfuture · NEMATIQ

SPS process

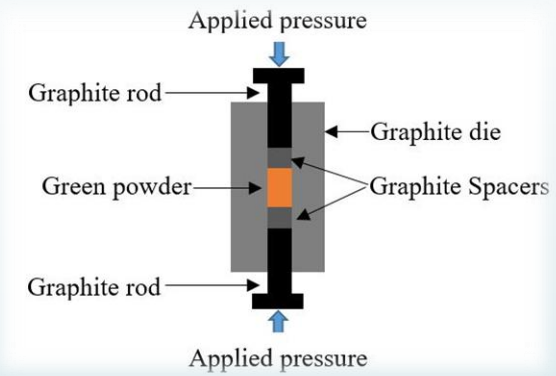

CoVSn@T:850° C, P:140 psi and t:20mins

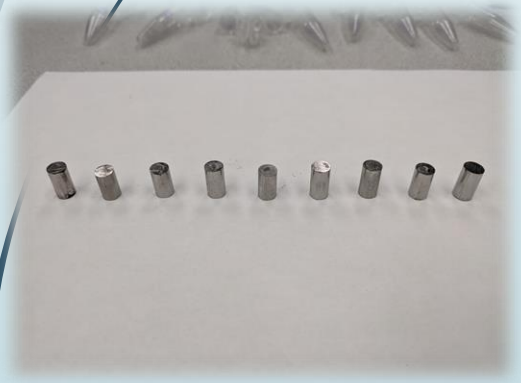

THE UNIVERSITY of ADELAIDE

NC STATE UNIVERSITY

NSF

Australian Government
Australian Research Council

The ARC Research Hub for Graphene Enabled Industry Transformation
Workshop 2020

THE UNIVERSITY of ADELAIDE · MONASH University · THE UNIVERSITY OF MELBOURNE · University of South Australia · RMIT UNIVERSITY · first graphene · ARCHER · Graphene Technology Solutions · cleanfuture · NEMATIQ

Thermoelectric characterization

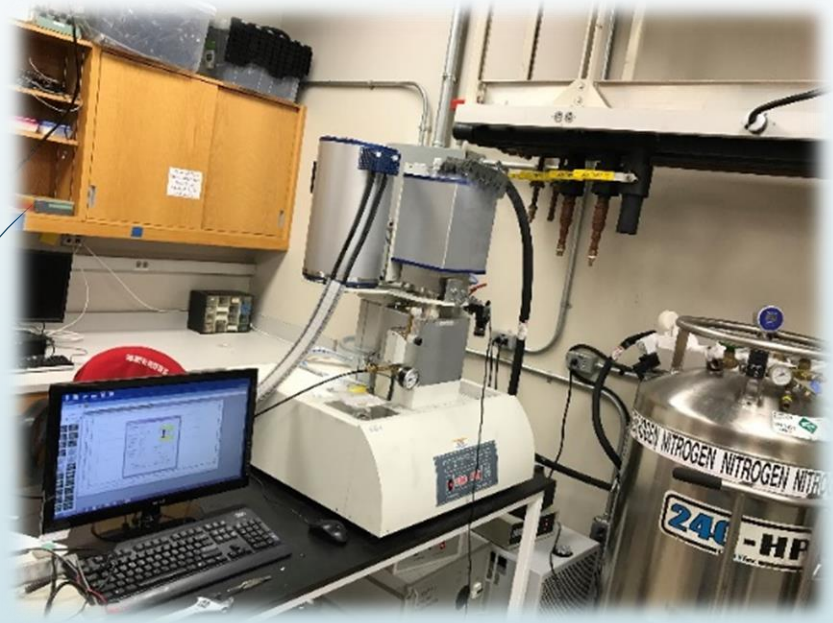

Seebeck and electrical conductivity

Thermal diffusivity

THE UNIVERSITY of ADELAIDE

NC STATE UNIVERSITY

NSF

Australian Government
Australian Research Council

The ARC Research Hub for Graphene Enabled Industry Transformation
Workshop 2020

THE UNIVERSITY of ADELAIDE · MONASH University · THE UNIVERSITY of MELBOURNE · University of South Australia · RMIT UNIVERSITY · first graphene · ARCHER · Graphene Technology Solutions · cleanfuture · NEMATIQ

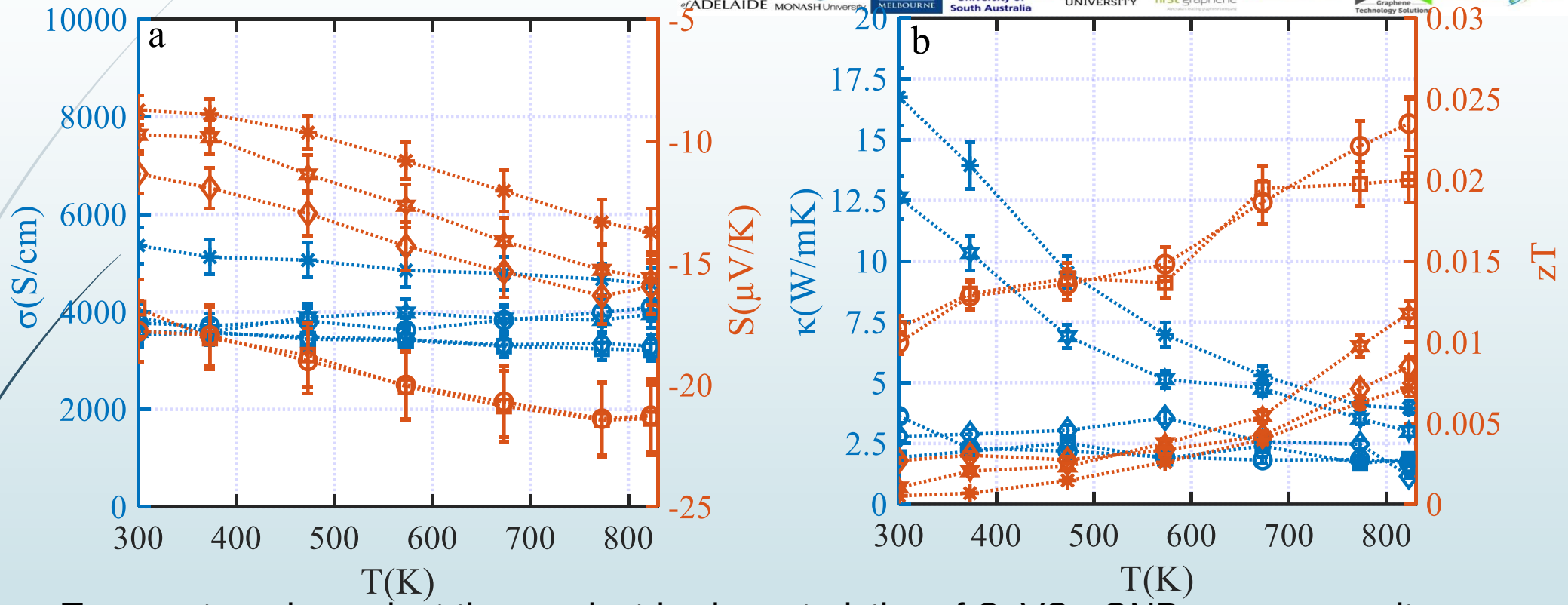

Temperature dependent thermoelectric characteristics of CoVSn-GNP nanocomposites: Asterisk* -0 wt. % GNPs, square-0.25 wt.%, GNPs circle-0.5 wt.% GNPs, diamond-0.75 wt.%, GNPs and hexagonal-1 wt.% GNPs.

THE UNIVERSITY of ADELAIDE

NC STATE UNIVERSITY

NSF

Australian Government
Australian Research Council

The ARC Research Hub for Graphene Enabled Industry Transformation
Workshop 2020
Monash University, Clayton, VIC
12-13 March 2020

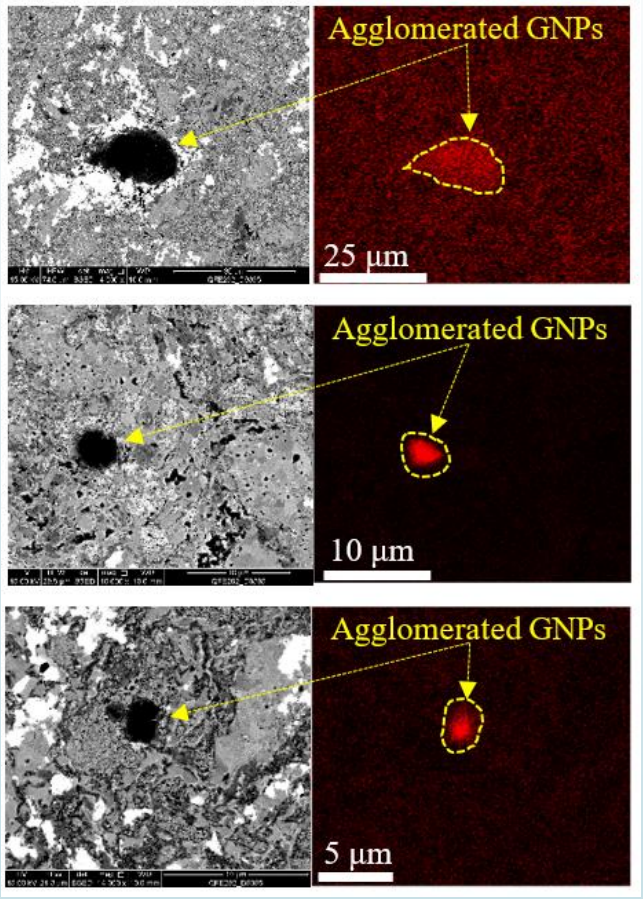

THE UNIVERSITY of ADELAIDE

NC STATE UNIVERSITY

NSF

Australian Government
Australian Research Council

Conclusions

GNPs may participate at the microstructural boundaries; however, graphene may not act with all the same physical factors as in the monolayer type due to any agglomeration,

Level of GNP dispersion impact on the thermoelectric properties.

GNP- dispersion provided ***energy filtering effect*** and ***phonon scattering*** which modified the thermoelectric properties of the GNP-reinforced CoVSn compositions.

THE UNIVERSITY of ADELAIDE

NC STATE UNIVERSITY

NSF

Acknowledgment

This work has been supported by the

- Australian Government Research Training Program Scholarship and
- The ARC Graphene Enabled Industry Transformation Hub at the University of Adelaide.

Also, this study is partially based upon work supported by

- National Science Foundation (NSF) under grant numbers ECCS-1351533, ECCS-1515005, and ECCS-1711253.

THE UNIVERSITY of ADELAIDE

NC STATE UNIVERSITY

NSF

Australian Government
Australian Research Council

Thanks for your attention

THE UNIVERSITY of ADELAIDE

NC STATE UNIVERSITY

NSF